SEPTEMBER 2018

AJNR

VOLUME 39 • PP 1583–1774

# AJNR

## AMERICAN JOURNAL OF NEURORADIOLOGY

SEPTEMBER 2018
VOLUME 39
NUMBER 9
WWW.AJNR.ORG

THE JOURNAL OF DIAGNOSTIC AND INTERVENTIONAL NEURORADIOLOGY

Convolutional neural network for hemorrhage on CT
Synthetic MR for spine imaging
Intracranial serpentine aneurysms

Official Journal ASNR • ASFNR • ASHNR • ASPNR • ASSR

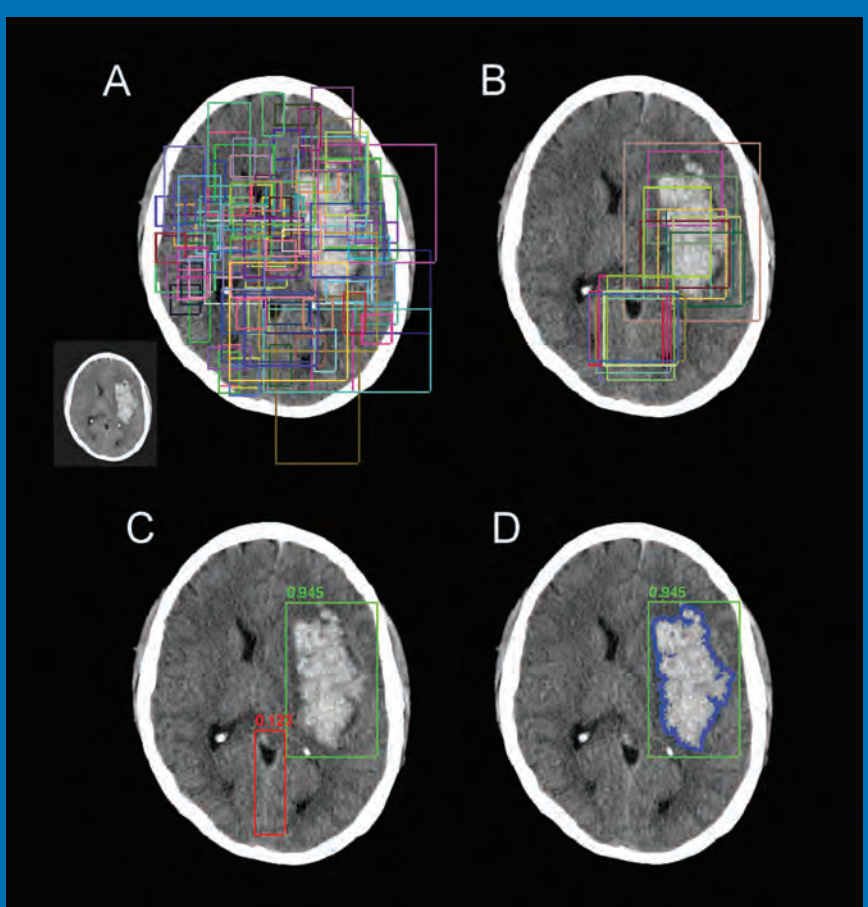

Aneurysm
Therapy
Solutions

# LVIS®

## Intraluminal Support Device

***The first and only stent with Premarket Approval (PMA) for use in stent-assisted coil embolization***

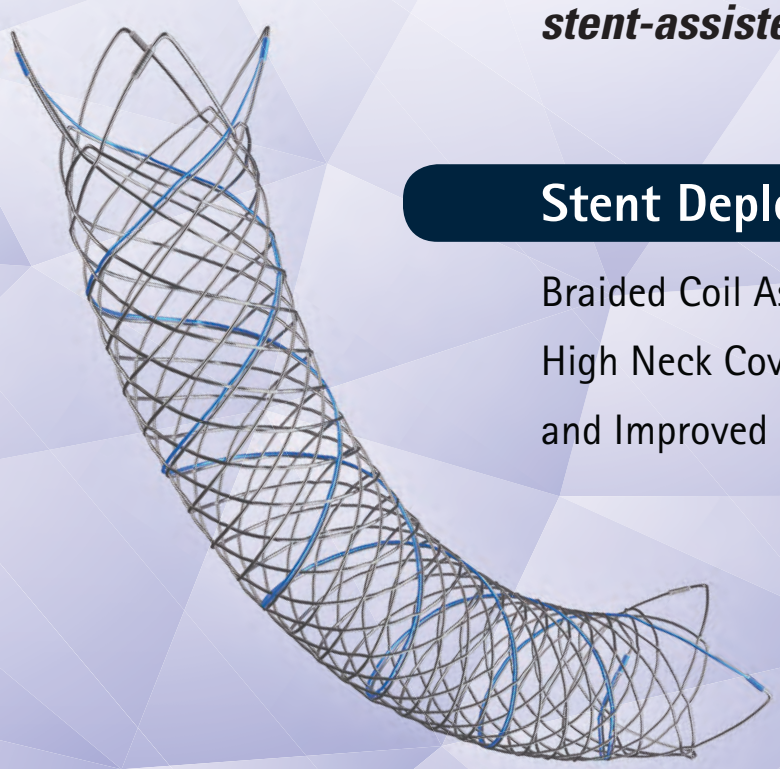

## Stent Deployment. Refined.

Braided Coil Assist Stents with
High Neck Coverage, Excellent Visibility
and Improved Conformability*

**L**ow-profile **V**isualized **I**ntraluminal **S**upport

INDICATIONS FOR USE:

**The LVIS® and LVIS® Jr. devices** are indicated for use with neurovascular embolization coils in patients ≥ 18 years of age for the treatment of wide-neck (neck width ≥ 4 mm or dome to neck ratio < 2) saccular intracranial aneurysms arising from a parent vessel with a diameter ≥ 2.0 mm and ≤ 4.5 mm.

Rx Only: Federal (USA) law restricts this device to sale by or on the order of a physician.

**The HydroCoil® Embolic System (HES) and MicroPlex® Coil System (MCS)** are intended for the endovascular embolization of intracranial aneurysms and other neurovascular abnormalities such as arteriovenous malformations and arteriovenous fistulae. The HES and MCS are also intended for vascular occlusion of blood vessels within the neurovascular system to permanently obstruct blood flow to an aneurysm or other vascular malformation and for arterial and venous embolizations in the peripheral vasculature.

The device should only be used by physicians who have undergone pre-clinical training in all aspects of HES/MCS procedures as prescribed by MicroVention.

CE 0297

# A Complete Coil Portfolio

## Hydrogel Embolic Coils & Platinum Coils

MicroVention's comprehensive portfolio features clinically proven Hydrogel coils, which can be used exclusively or in combination with our trusted Platinum coils to treat a wide range of aneurysms and neurovascular lesions.

## Breakthrough Hydrogel Technology

- Less Recurrence
- Less Retreatment
- More Progressive Occlusion

*Compared to platinum coils with comparable safety*[1]

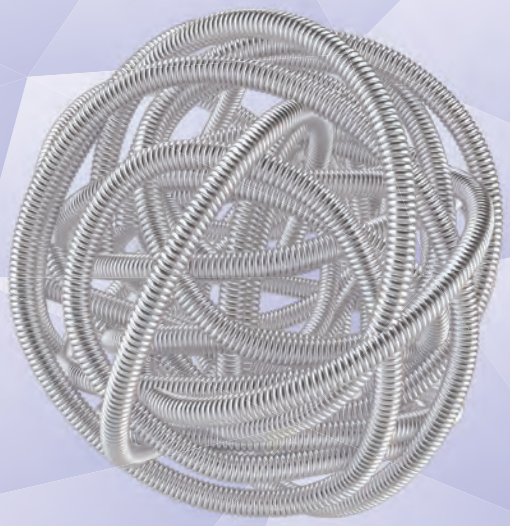

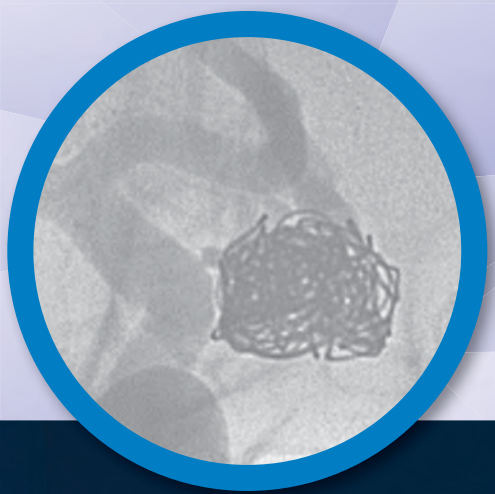


REFERENCES:

1. Taschner et al. Second-Generation Hydrogel Coils for the Endovascular Treatment of Intracranial Aneurysm; A Randomized Controlled Trial. 2018;49:00-00. DOI:10.1161/STROKEAHA.117.018707


**For more information or a product demonstration, contact your local MicroVention representative:**

MicroVention® TERUMO


**MicroVention Worldwide**

| | |
|---|---|
| **Innovation Center** | PH +1.714.247.8000 |
| 35 Enterprise | |
| Aliso Viejo, CA 92656 USA | |
| MicroVention UK Limited | PH +44 (0) 191 258 6777 |
| MicroVention Europe, S.A.R.L. | PH +33 (1) 39 21 77 46 |
| MicroVention Deutschland GmbH | PH +49 211 210 798-0 |

**microvention.com**



MICROVENTION, MicroPlex and HydroCoil are registered trademarks of MicroVention, Inc. • Refer to Instructions for Use, contraindications and warnings for additional information. Federal (USA) law restricts this device for sale by or on the order of a physician. ©2018 MicroVention, Inc. Jan. 2018

stryker | medela

# The one to choose when you choose aspiration.


- **Easily find clot**
  ClotFinder™ Specimen Cup retains the aspirated thrombus
- **High max vacuum**
  Adjustable up to -713mmHg
- **Aspirate on demand**
  Control aspiration from the sterile field

**0.218in ID**
AXS Universal Aspiration Tubing

## AXS Universal™
ASPIRATION SET

Copyright © 2018 Stryker
AP002176 v1.0

# Magic

BALT

## FLOW-DEPENDENT MICROCATHETER

## NOW AVAILABLE THROUGH BLOCKADE™ MEDICAL

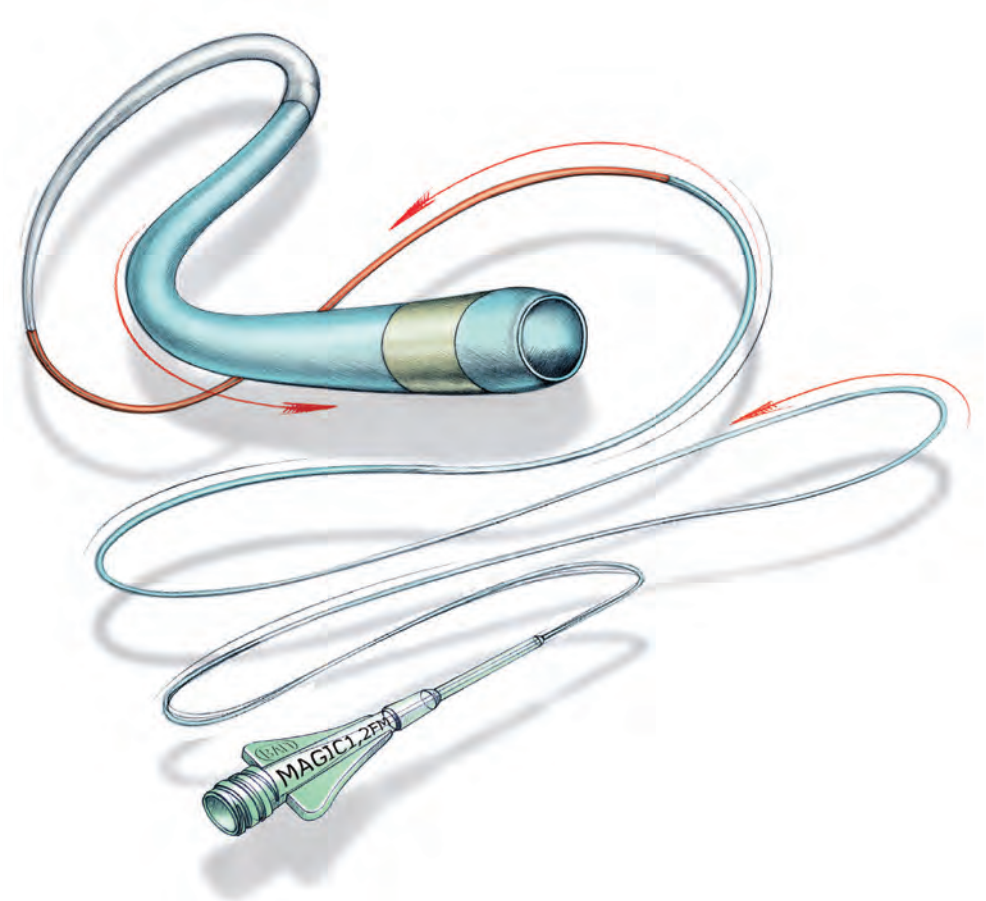


## ORDERMAGICS@BLOCKADEMEDICAL.COM

MAGIC catheters are designed for general intravascular use. They may be used for the controlled, selective regional infusion of therapeutic agents or embolic materials into vessels.[1]

1. Magic Catheters IFU – Ind 19

MKTG-068 Rev. A

18 Technology Drive #169, Irvine Ca 92618
**P** 949.788.1443 | **F** 949.788.1444

BLOCKADE MEDICAL
A BALT Company

CONNECTION SCIENCE & PRACTICE

ASNR

American Society of Neuroradiology

MAY 18-23, 2019 | BOSTON

ASNR 57th Annual Meeting & The Foundation of the ASNR Symposium 2019

# CALL FOR ABSTRACTS

You are invited! Join us next year in Boston to present the best scientific research in neuroradiology.

## Submit your abstract online at 2019.asnr.org
## Deadline: 5:00pm (PST), Wednesday, November 7, 2018

**Submit an abstract for the ASNR 57th Annual Meeting (May 18-23, 2019, Boston, MA) in one of the following presentation categories:**

- Scientific Paper ..... Oral
- Scientific Poster ..... Print
- Electronic Scientific Poster ..... Electronic
- Electronic Educational Exhibit ..... Electronic
- Educational Exhibit Poster ..... Print
- Excerpta ..... Oral

This activity has been approved for AMA PRA Category 1 Credits™.

**Abstract Submissions Information and Criteria**

1. Abstracts should describe the learning objectives of the presentation.
2. The *American Journal of Neuroradiology (AJNR)* encourages presenters to submit manuscripts based on their work to *AJNR* before considering other journals.
3. Presenters of accepted abstracts **must register** for the ASNR 57th Annual Meeting.
4. Published or previously presented works should NOT be submitted.
5. Format abstract text using headings required for submission category.
6. Submit each abstract in **one** category only.
7. Submission topic areas include: **Adult Brain, Spine, Head and Neck, Pediatrics, Functional Imaging, Interventional, Health Policy, and AI/ Informatics**.
8. Maximum length: **300 words** including graphics. Charts, graphs and tables may be included as an image, for all categories.
9. Submission site allows uploading of files into the system.
10. Changes can be made to the abstract until the deadline.

**Complete instructions for submissions are available online: 2019.asnr.org**

American Society of Pediatric Neuroradiology

**SAVE THE DATE**

*1st Annual Meeting of the*

AMERICAN SOCIETY OF

# Pediatric Neuroradiology

**January 18-20, 2019**

Royal Sonesta Hotel - New Orleans • New Orleans, Louisiana

Please contact Educational Symposia, at 813-806-1000 or ASPNR@edusymp.com or visit www.ASPNR.org for additional information.

# Simplify
## the MOC Process

# Manage
## your CME Credits Online

# CMEgateway.org

**Available to Members of Participating Societies**

- American Board of Radiology (ABR)
- American College of Radiology (ACR)
- American Roentgen Ray Society (ARRS)
- American Society of Neuroradiology (ASNR)
- Commnission on Accreditation of Medical Physics Educational Programs, Inc. (CAMPEP)
- Radiological Society of North America (RSNA)
- Society of Interventional Radiology (SIR)
- SNM
- The Society for Pediatric Radiology (SPR)

## It's Easy and Free!

Log on to CME Gateway to:

- View or print reports of your CME credits from multiple societies from a single access point.
- Print an aggregated report or certificate from each participating organization.
- Link to SAMs and other tools to help with maintenance of certification.

## American Board of Radiology (ABR) participation!

By activating ABR in your organizational profile, your MOC–fulfilling CME and SAM credits can be transferred to your own personalized database on the ABR Web site.

## Sign Up Today!

go to CMEgateway.org

# *We're Inside Every Great Neuroradiologist!*

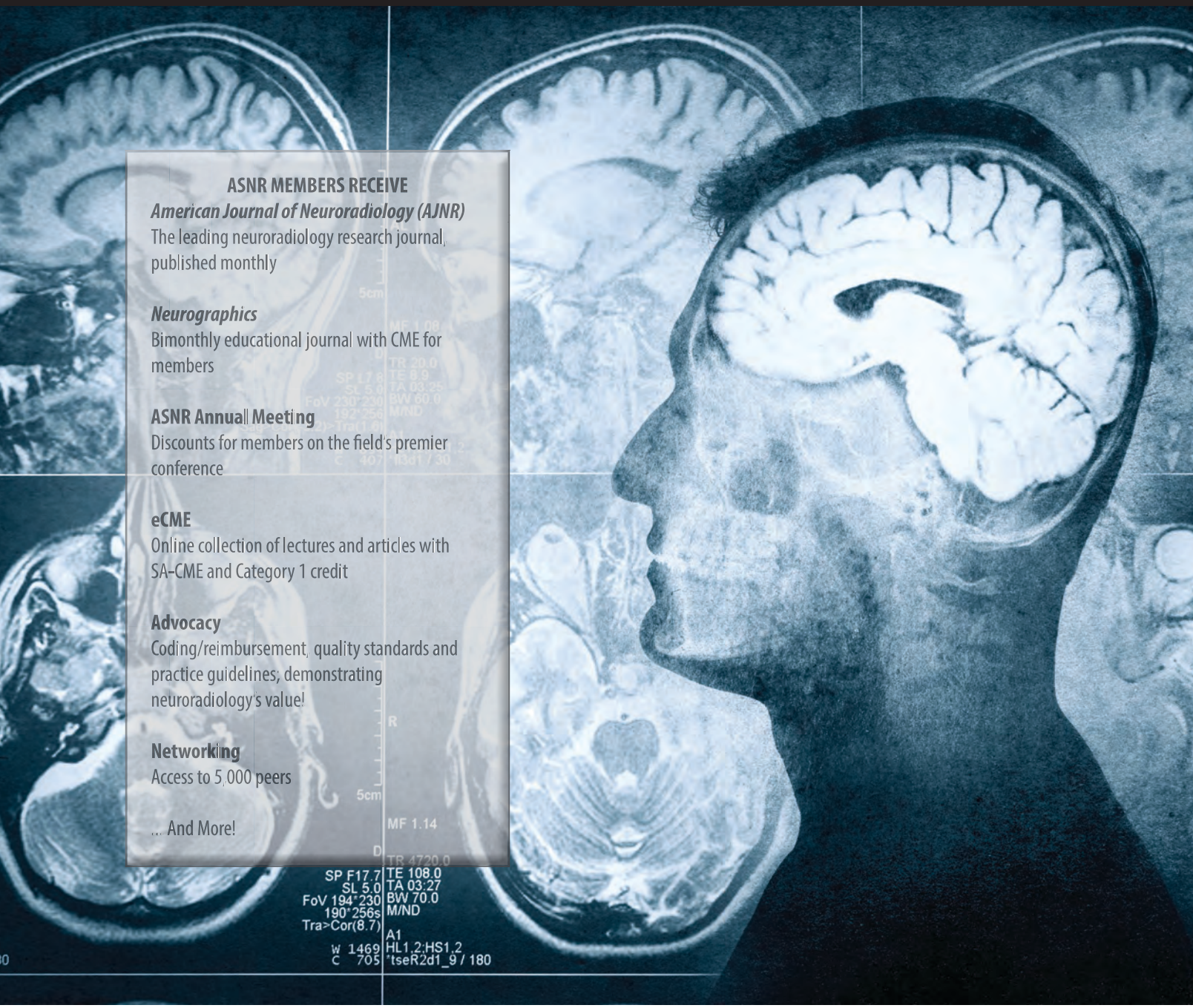


## Join the leaders in neuroradiology today!
## Learn more at www.asnr.org/join

ASNR
American Society of Neuroradiology

800 Enterprise Dr., Suite 205, Oak Brook, IL 60523 • (630)574-0220 • membership@asnr.org • www.asnr.org

## Dominant Flex Surgical Suction Pump

**See package insert for complete indications, complications, warnings, and instructions for use.**

### INDICATIONS FOR USE

The intended use of the Dominant Flex suction pump is the creation of a constant vacuum for use in hospitals and clinics. This vacuum can be used for general suction, to aspirate and remove: surgical fluids, tissue (including bone), gases, bodily fluids or infectious materials and during specific procedures which may include, vacuum extraction, aesthetic body contouring, aspiration during flexible endoscopy, use with cardiac tissue stabilizers during off-pump coronary artery bypass, and epicardial ablation probes.

### WARNINGS

- For use only by medically trained persons who have been adequately trained in suction procedures and in the use of aspirators.
- To avoid risk of electric shock, this equipment must only be connected to a fixed mains socket with protective earth.
- The device must not be used for suctioning explosive, easily flammable or corrosive liquids.
- The connecting tubing supplied with the device must never come into direct contact with the suction area. A sterile suction catheter must always be used (risk of infection).
- Before cleaning the device, pull the plug out of the fixed mains socket.
- No modification of this equipment is allowed.
- Consult the indications for use and consider risk factors and contraindications before using the Dominant Flex. Failure to read and follow all instructions in this manual prior to use may result in serious or fatal injury of the patient.
- Do not connect this device to a passive drainage tube.
- Not suitable for setting at a low vacuum, as needed for example for thoracic drainage without specialized accessories. Not approved for outdoor use or transport applications.

### PRECAUTIONS

- Incorrect use can cause pain and injury to the patient.
- Do not use sterile accessories when the sterile packaging is damaged.
- The use of mobile telephones, LAN / WLAN, walkie-talkies (two-way radios) and cordless telephones sets can affect the Dominant Flex pump. A safety distance of min. 3.3 ft (1 m) to the Dominant Flex pump is recommended.
- Portable and mobile RF communications equipment can affect medical devices.
- The rack version requires a minimum distance of 5 cm to the enclosure to prevent overheating of the device.
- The patient should be monitored regularly according to the physicians' instructions and facility guidelines. Objective indications or signs of a possible infection or complication must be met immediately (e.g. fever, pain, redness, increased warmth, swelling or purulent discharge).
- Non-observance can lead to considerable danger of the patient. Monitor the Dominant Flex frequently for operating status.
- To prevent the device from overheating, the exhaust at the bottom of the unit must be unobstructed when the unit is operational.

## AXS Universal™ Liner Set and Aspiration Tubing

**See package insert for complete indications, complications, warnings, and instructions for use.**

### INDICATIONS FOR USE

AXS Universal Liner Set and Aspiration Tubing is suitable for the safe collection and disposal of suctioned fluids. It is allowed for use only by medically trained staff who are aware of the in-house hygienic regulations. Medela can only guarantee the safe function if used in combination with Medela components.

**Stryker Neurovascular**
47900 Bayside Parkway
Fremont, CA 94538

**strykerneurovascular.com**

Date of Release: JUN/2018

EX_EN_US

Copyright © 2018 Stryker


## Trevo® XP ProVue Retrievers

**See package insert for complete indications, complications, warnings, and instructions for use.**

### INDICATIONS FOR USE

1. The Trevo Retriever is indicated for use to restore blood flow in the neurovasculature by removing thrombus for the treatment of acute ischemic stroke to reduce disability in patients with a persistent, proximal anterior circulation, large vessel occlusion, and smaller core infarcts who have first received intravenous tissue plasminogen activator (IV t-PA). Endovascular therapy with the device should start within 6 hours of symptom onset.
2. The Trevo Retriever is intended to restore blood flow in the neurovasculature by removing thrombus in patients experiencing ischemic stroke within 8 hours of symptom onset. Patients who are ineligible for intravenous tissue plasminogen activator (IV t-PA) or who fail IV t-PA therapy are candidates for treatment.
3. The Trevo Retriever is indicated for use to restore blood flow in the neurovasculature by removing thrombus for the treatment of acute ischemic stroke to reduce disability in patients with a persistent, proximal anterior circulation, large vessel occlusion of the internal carotid artery (ICA) or middle cerebral artery (MCA)-M1 segments with smaller core infarcts (0-50cc for age < 80 years, 0-20cc for age ≥ 80 years). Endovascular therapy with the device should start within 6-24 hours of time last seen well in patients who are ineligible for intravenous tissue plasminogen activator (IV t-PA) or who fail IV t-PA therapy.

### COMPLICATIONS

Procedures requiring percutaneous catheter introduction should not be attempted by physicians unfamiliar with possible complications which may occur during or after the procedure. Possible complications include, but are not limited to, the following: air embolism; hematoma or hemorrhage at puncture site; infection; distal embolization; pain/headache; vessel spasm, thrombosis, dissection, or perforation; emboli; acute occlusion; ischemia; intracranial hemorrhage; false aneurysm formation; neurological deficits including stroke; and death.

### COMPATIBILITY

3x20mm retrievers are compatible with Trevo® Pro 14 Microcatheters (REF 90231) and Trevo® Pro 18 Microcatheters (REF 90238). 4x20mm retrievers are compatible with Trevo® Pro 18 Microcatheters (REF 90238). 4x30mm retrievers are compatible with Excelsior® XT-27® Microcatheters (150cm x 6cm straight REF 275081) and Trevo® Pro 18 Microcatheters (REF 90238). 6x25mm Retrievers are compatible with Excelsior® XT-27® Microcatheters (150cm x 6cm straight REF 275081). Recommended minimum vessel ID for all Retriever sizes is 2.5mm. Compatibility of the Retriever with other microcatheters has not been established. Performance of the Retriever device may be impacted if a different microcatheter is used.

Balloon Guide Catheters (such as Merci® Balloon Guide Catheter and FlowGate® Balloon Guide Catheter) are recommended for use during thrombus removal procedures.

Retrievers are compatible with the Abbott Vascular DOC® Guide Wire Extension (REF 22260).

Retrievers are compatible with Boston Scientific Rotating Hemostatic Valve (Ref 421242).

### SPECIFIC WARNINGS FOR INDICATION 1

- The safety and effectiveness of the Trevo Retrievers in reducing disability has not been established in patients with large core infarcts (i.e. ASPECTS ≤ 7). There may be increased risks, such as intracerebral hemorrhage, in these patients.
- The safety and effectiveness of the Trevo Retrievers in reducing disability has not been established or evaluated in patients with occlusions in the posterior circulation (e.g., basilar or vertebral arteries) or for more distal occlusions in the anterior circulation.

### SPECIFIC WARNINGS FOR INDICATION 2

- To reduce risk of vessel damage, take care to appropriately size Retriever to vessel diameter at intended site of deployment.

### SPECIFIC WARNINGS FOR INDICATION 3

- The safety and effectiveness of the Trevo Retrievers in reducing disability has not been established in patients with large core infarcts (i.e., ASPECTS ≤ 7). There may be increased risks, such as intracerebral hemorrhage, in these patients.
- The safety and effectiveness of the Trevo Retrievers in reducing disabillity has not been established or evaluated in patients with occlusions in the posterior circulation (e.g., basilar or vertebral arteries) or for more distal occlusions in the anterior circulation.
- Users should validate their imaging software analysis techniques to ensure robust and consistent results for assessing core infarct size.

### WARNINGS APPLIED TO ALL INDICATIONS

- Administration of IV t-PA should be within the FDA-approved window (within 3 hours of stroke symptom onset).
- To reduce risk of vessel damage, adhere to the following recommendations:
  - Do not perform more than six (6) retrieval attempts in same vessel using Retriever devices.
  - Maintain Retriever position in vessel when removing or exchanging Microcatheter.
- To reduce risk of kinking/fracture, adhere to the following recommendations:
  - Immediately after unsheathing Retriever, position Microcatheter tip marker just proximal to shaped section. Maintain Microcatheter tip marker just proximal to shaped section of Retriever during manipulation and withdrawal.
  - Do not rotate or torque Retriever.
  - Use caution when passing Retriever through stented arteries.
- The Retriever is a delicate instrument and should be handled carefully. Before use and when possible during procedure, inspect device carefully for damage. Do not use a device that shows signs of damage. Damage may prevent device from functioning and may cause complications.
- Do not advance or withdraw Retriever against resistance or significant vasospasm. Moving or torquing device against resistance or significant vasospasm may result in damage to vessel or device. Assess cause of resistance using fluoroscopy and if needed resheath the device to withdraw.
- If Retriever is difficult to withdraw from the vessel, do not torque Retriever. Advance Microcatheter distally, gently pull Retriever back into Microcatheter, and remove Retriever and Microcatheter as a unit. If undue resistance is met when withdrawing the Retriever into the Microcatheter, consider extending the Retriever using the Abbott Vascular DOC guidewire extension (REF 22260) so that the Microcatheter can be exchanged for a larger diameter catheter such as a DAC® Catheter. Gently withdraw the Retriever into the larger diameter catheter.
- Administer anti-coagulation and anti-platelet medications per standard institutional guidelines.
- Users should take all necessary precautions to limit X-radiation doses to patients and themselves by using sufficient shielding, reducing fluoroscopy times, and modifying X-ray technical factors where possible.

### PRECAUTIONS

- Prescription only – device restricted to use by or on order of a physician.
- Store in cool, dry, dark place.
- Do not use open or damaged packages.
- Use by "Use By" date.
- Exposure to temperatures above 54°C (130°F) may damage device and accessories. Do not autoclave.
- Do not expose Retriever to solvents.
- Use Retriever in conjunction with fluoroscopic visualization and proper anti-coagulation agents.
- To prevent thrombus formation and contrast media crystal formation, maintain a constant infusion of appropriate flush solution between guide catheter and Microcatheter and between Microcatheter and Retriever or guidewire.
- Do not attach a torque device to the shaped proximal end of DOC® Compatible Retriever. Damage may occur, preventing ability to attach DOC® Guide Wire Extension.

DOC is a trademark of Abbott Laboratories.

**Stryker Neurovascular**
47900 Bayside Parkway
Fremont, CA 94538

**strykerneurovascular.com**

Date of Release: APR/2018

EX_EN_US

Copyright © 2018 Stryker

stryker

# Now you have **24 hours** to make a lifetime of difference in stroke patients like Nora

The Trevo Retriever is the only device cleared to **reduce disability in stroke patients up to 24 hours** from time last seen well.

For more information, visit strykerneurovascular.com/trevo24hours

**Trevo® XP**
PROVUE RETRIEVER

Copyright © 2018 Stryker
AP002078 v1.0

Not for sale within the territory of the United States

# FAST AND EASY

## ICAD* Treatment with NeuroSpeed® PTA Balloon Catheter and CREDO® Stent

- Over the wire system
- Flexible self-expanding highly visible stent
- Deliverable through 0.017" NeuroSpeed® PTA Balloon Catheter

* ICAD Intracranial Atherosclerotic Disease

**www.acandis.com**

acandis®

ENGINEERING STROKE SOLUTIONS

AJNR

AMERICAN JOURNAL OF NEURORADIOLOGY

SEPTEMBER 2018
VOLUME 39
NUMBER 9
WWW.AJNR.ORG

Publication Preview at www.ajnr.org features articles released in advance of print. Visit www.ajnrblog.org to comment on AJNR content and chat with colleagues and AJNR's News Digest at http://ajnrdigest.org to read the stories behind the latest research in neuroimaging.



**AJNR (Am J Neuroradiol** ISSN 0195–6108) is a journal published monthly, owned and published by the American Society of Neuroradiology (ASNR), 800 Enterprise Drive, Suite 205, Oak Brook, IL 60523. Annual dues for the ASNR include $170.00 for journal subscription. The journal is printed by Cadmus Journal Services, 5457 Twin Knolls Road, Suite 200, Columbia, MD 21045; Periodicals postage paid at Oak Brook, IL and additional mailing offices. Printed in the U.S.A. POSTMASTER: Please send address changes to American Journal of Neuroradiology, P.O. Box 3000, Denville, NJ 07834, U.S.A. Subscription rates: nonmember $400 ($470 foreign) print and online, $320 online only; institutions $460 ($530 foreign) print and basic online, $915 ($980 foreign) print and extended online, $380 online only (basic), extended online $825; single copies are $35 each ($40 foreign). Indexed by PubMed/Medline, BIOSIS Previews, Current Contents (Clinical Medicine and Life Sciences), EMBASE, Google Scholar, HighWire Press, Q-Sensei, RefSeek, Science Citation Index, SCI Expanded, and Meta/CZI. Copyright © American Society of Neuroradiology.

## ONLINE FEATURES

### LETTERS



### BOOK REVIEWS *R.M. Quencer, Section Editor*

Please visit www.ajnrblog.org to read and comment on Book Reviews.

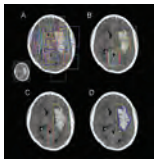

Mask R-CNN architectures provide a flexible and efficient framework for parallel evaluation of region proposal (attention), object detection (classification), and instance segmentation. *A*, Preconfigured bounding boxes are tested for the presence of a potential abnormality. *B*, Highest ranking bounding boxes are identified and used to generate region proposals that focus algorithm attention. *C*, Composite region proposals are pruned using nonmaximum suppression and are used as input to determine the presence or absence of hemorrhage. *D*, Segmentation masks are generated for cases positive for hemorrhage.


Indicates Editor's Choices selection

Indicates Fellows' Journal Club selection

Indicates open access to non-subscribers at www.ajnr.org

Indicates article with supplemental on-line table

Indicates article with supplemental on-line photo

Indicates article with supplemental on-line video

Evidence-Based Medicine Level 1

Evidence-Based Medicine Level 2

AJNR

# AMERICAN JOURNAL OF NEURORADIOLOGY

Publication Preview at www.ajnr.org features articles released in advance of print. Visit www.ajnrblog.org to comment on AJNR content and chat with colleagues and AJNR's News Digest at http://ajnrdigest.org to read the stories behind the latest research in neuroimaging.

SEPTEMBER 2018 • VOLUME 39 • NUMBER 9 • WWW.AJNR.ORG

**Official Journal:**
American Society of Neuroradiology
American Society of Functional Neuroradiology
American Society of Head and Neck Radiology
American Society of Pediatric Neuroradiology
American Society of Spine Radiology

**EDITOR-IN-CHIEF**

**Jeffrey S. Ross, MD**
*Professor of Radiology, Department of Radiology, Mayo Clinic College of Medicine, Phoenix, AZ*

**SENIOR EDITORS**

**Harry J. Cloft, MD, PhD**
Professor of Radiology and Neurosurgery, Department of Radiology, Mayo Clinic College of Medicine, Rochester, MN

**Thierry A.G.M. Huisman, MD**
Professor of Radiology, Pediatrics, Neurology, and Neurosurgery, Chairman, Department of Imaging and Imaging Science, Johns Hopkins Bayview, Director, Pediatric Radiology and Pediatric Neuroradiology, Johns Hopkins Hospital, Baltimore, MD

**Yvonne W. Lui, MD**
Associate Professor of Radiology, Chief of Neuroradiology, New York University School of Medicine, New York, NY

**C.D. Phillips, MD, FACR**
Professor of Radiology, Weill Cornell Medical College, Director of Head and Neck Imaging, New York-Presbyterian Hospital, New York, NY

**Pamela W. Schaefer, MD**
Clinical Director of MRI and Associate Director of Neuroradiology, Massachusetts General Hospital, Boston, Massachusetts, Associate Professor, Radiology, Harvard Medical School, Cambridge, MA

**Charles M. Strother, MD**
Professor of Radiology, Emeritus, University of Wisconsin, Madison, WI

**STATISTICAL SENIOR EDITOR**

**Bryan A. Comstock, MS**
Senior Biostatistician, Department of Biostatistics, University of Washington, Seattle, WA

*Founding Editor*
**Juan M. Taveras**
*Editors Emeriti*
**Mauricio Castillo, Robert I. Grossman, Michael S. Huckman, Robert M. Quencer**

**EDITORIAL BOARD**

Ashley H. Aiken, *Atlanta, GA*
Lea M. Alhilali, *Phoenix, AZ*
Kubilay Aydin, *Istanbul, Turkey*
John D. Barr, *Dallas, TX*
Ari Blitz, *Baltimore, MD*
Barton F. Branstetter IV, *Pittsburgh, PA*
Jonathan L. Brisman, *Lake Success, NY*
Keith Cauley, *Danville, PA*
James Y. Chen, *San Diego, CA*
Asim F. Choudhri, *Memphis, TN*
Daniel Chow, *Irvine, CA*
J. Matthew Debnam, *Houston, TX*
Seena Dehkharghani, *New York, NY*
Yonghong Ding, *Rochester, MN*
Clifford J. Eskey, *Hanover, NH*
Saeed Fakhran, *Phoenix, AZ*
Massimo Filippi, *Milan, Italy*
Reza Forghani, *Montreal, Quebec, Canada*
Nils D. Forkert, *Calgary, Alberta, Canada*
Wende N. Gibbs, *Los Angeles, CA*
Christine M. Glastonbury, *San Francisco, CA*
John L. Go, *Los Angeles, CA*
Philipp Gölitz, *Erlangen, Germany*
Allison Grayev, *Madison, WI*
Brent Griffith, *Detroit, MI*
Ajay Gupta, *New York, NY*
Rakesh Kumar Gupta, *Haryana, India*
Lotfi Hacein-Bey, *Sacramento, CA*
Christopher P. Hess, *San Francisco, CA*
Andrei Holodny, *New York, NY*
Benjamin Huang, *Chapel Hill, NC*
Mahesh V. Jayaraman, *Providence, RI*
Valerie Jewells, *Chapel Hill, NC*
Christof Karmonik, *Houston, TX*
Timothy J. Kaufmann, *Rochester, MN*
Hillary R. Kelly, *Boston, MA*
Toshibumi Kinoshita, *Akita, Japan*
Kennith F. Layton, *Dallas, TX*
Alexander Lerner, *Los Angeles, CA*
Michael Lev, *Boston, MA*
Karl-Olof Lovblad, *Geneva, Switzerland*
Franklin A. Marden, *Chicago, IL*
Joseph C. McGowan, *Merion Station, PA*
Stephan Meckel, *Freiburg, Germany*
Christopher J. Moran, *St. Louis, MO*
Takahisa Mori, *Kamakura City, Japan*
Suresh Mukherji, *Ann Arbor, MI*
Alexander J. Nemeth, *Chicago, IL*
Renato Hoffmann Nunes, *Sao Paulo, Brazil*
Sasan Partovi, *Cleveland, OH*
Laurent Pierot, *Reims, France*
Jay J. Pillai, *Baltimore, MD*
Whitney B. Pope, *Los Angeles, CA*
Joana Ramalho, *Lisbon, Portugal*
Otto Rapalino, *Boston, MA*
Álex Rovira-Cañellas, *Barcelona, Spain*
Paul M. Ruggieri, *Cleveland, OH*
Amit M. Saindane, *Atlanta, GA*
Erin Simon Schwartz, *Philadelphia, PA*
Lubdha M. Shah, *Salt Lake City, UT*
Maksim Shapiro, *New York, NY*
Timothy Shepherd, *New York, NY*
Mark S. Shiroishi, *Los Angeles, CA*
Bruno P. Soares, *Baltimore, MD*
Maria Vittoria Spampinato, *Charleston, SC*
Khin Khin Tha, *Sapporo, Hokkaido, Japan*
Krishnamoorthy Thamburaj, *Hershey, PA*
Cheng Hong Toh, *Taipei, Taiwan*
Aquilla S. Turk, *Charleston, SC*
Anja G. van der Kolk, *Madison, WI*
Willem Jan van Rooij, *Tilburg, Netherlands*
Arastoo Vossough, *Philadelphia, PA*
Elysa Widjaja, *Toronto, Ontario, Canada*
Max Wintermark, *Stanford, CA*
Ronald L. Wolf, *Philadelphia, PA*
Kei Yamada, *Kyoto, Japan*
Carlos Zamora, *Chapel Hill, NC*
Vahe M. Zohrabian, *New Haven, CT*

**EDITORIAL FELLOW**

Alireza Radmanesh, *New York, NY*

**SPECIAL CONSULTANTS TO THE EDITOR**

**AJNR Blog Editor**
Neil Lall, *Denver, CO*
**Case of the Month Editor**
Nicholas Stence, *Aurora, CO*
**Case of the Week Editors**
Juan Pablo Cruz, *Santiago, Chile*
Sapna Rawal, *Toronto, Ontario, Canada*
**Classic Case Editor**
Sandy Cheng-Yu Chen, *Taipei, Taiwan*
**Health Care and Socioeconomics Editor**
Pina C. Sanelli, *New York, NY*
**Physics Editor**
Greg Zaharchuk, *Stanford, CA*
**Podcast Editor**
Wende N. Gibbs, *Los Angeles, CA*
**Twitter Editor**
Jennifer McCarty, *Houston, TX*

*Managing Editor*
**Karen Halm**
*Assistant Managing Editor*
**Laura Wilhelm**
*Communications Coordinator*
**Rebecca Artz**
*Marketing and Social Media Manager*
**Kylie Mason**
*Executive Director, ASNR*
**Mary Beth Hepp**

Title: Surface Model of White Matter Tractography. What is unique about converting tractograms into surface models (.stl or .fbx file format) is that models like this can be used in virtual/augmented reality software such as Oculus Rift, HTC Vive, or Microsoft Hololens.

*Scott Collins, RT(R)(CT), Rhode Island Hospital 3D Lab, Providence, Rhode Island*

# Review of the Imaging Features of Benign Osteoporotic and Malignant Vertebral Compression Fractures

J.T. Mauch, C.M. Carr, H. Cloft, and F.E. Diehn


## ABSTRACT

**SUMMARY:** Vertebral compression fractures are very common, especially in the elderly. Benign osteoporotic and malignant vertebral compression fractures have extremely different management and prognostic implications. Although there is an overlap in appearances, characteristic imaging features can aid in the distinction between these 2 types of compression fractures. The aim of this review is to characterize the imaging features of benign and malignant vertebral compression fractures seen with CT, PET, SPECT, and MR imaging.


**ABBREVIATIONS:** SI = signal intensity; SUV = standard uptake value; VCF = vertebral compression fracture

Vertebral compression fractures (VCFs) can have a variety of etiologies, including trauma, osteoporosis, or neoplastic infiltration. Osteoporotic VCFs have a prevalence of approximately 25% among all postmenopausal women and occur less frequently in similarly aged men.[1] Trauma is the most common etiology in those younger than 50 years of age. However, many cancers, such as breast, prostate, thyroid, and lung, have a propensity to metastasize to bone, which can lead to malignant VCFs.[2] Indeed, the spine is a site of metastasis in 10%–15% of cancers.[3] In addition, primary tumors of bone and lymphoproliferative diseases such as lymphoma and multiple myeloma can be the cause of malignant VCFs. Differentiating benign and malignant VCFs can present a diagnostic dilemma, particularly in the elderly, with considerable management and prognostic implications. Advanced imaging is often used to attempt to distinguish benign from malignant VCFs.

The aim of this review is to describe and illustrate the imaging features of benign and malignant VCFs. The imaging modalities used in the clinical setting for this diagnostic purpose include CT, PET, SPECT, and MR imaging. MR imaging traditionally has been the technique of choice because characteristic morphologic features, enhancement patterns, and signal intensities are well-described in the literature. Relatively recently, chemical shift, dynamic contrast-enhanced imaging, and diffusion-weighted MR imaging have also been more thoroughly investigated. The multimodality imaging features and common pitfalls will be discussed.

From the Department of Radiology, Mayo Clinic, Rochester, Minnesota.

Please address correspondence to Justin Mauch, MD, Department of Radiology, Mayo Clinic, 200 First St SW, Rochester, MN 55905; e-mail: Mauch.Justin@Mayo.edu

Indicates open access to non-subscribers at www.ajnr.org

http://dx.doi.org/10.3174/ajnr.A5528

### *Pitfalls*

In the subsequent sections, technique and sign-related pitfalls will be discussed. In general, most pitfalls can be attributed to a few common issues: The first is that acute (<2 weeks) and subacute (2 weeks to 3 months) benign VCFs often have large areas of MR signal alteration or increased metabolism on nuclear medicine modalities that can mimic malignancy, owing to intertrabecular hemorrhage, edema, and the early reparative process.[4,5] Chronic (>3 months) benign VCFs have small areas of usually linear signal alteration and restoration of fatty marrow and normal metabolism, which make these easier to identify.[4] Unfortunately, precise timing of the fracture can often be difficult to elicit from the patient or medical records.

Multiple myeloma, a common cause of VCFs, is also an important pitfall. Myelomatous lesions can be present within vertebral bodies with normal bone marrow signal.[6] Multiple myeloma infiltrates bone marrow either diffusely or in a nodular pattern. When it is diffusely distributed in the bone marrow, it may give the appearance of osteoporosis, potentially from diffuse osteoclast activation.[6,7] VCFs from multiple myeloma can appear benign in 38% of cases.[7] Acute-subacute symptomatic myeloma-related VCFs may not demonstrate edema, either.[8] Inadvertent inclusion or exclusion of this patient population in studies may account for the sometimes discordant findings in the literature.

A summary of the key imaging features that can be helpful in differentiating benign and malignant fractures is found in the Table.

### *MR Imaging*

**Morphologic Features.** According to the literature, abnormal marrow signal involving the pedicles or other posterior elements

**Summary of imaging features of benign and malignant VCFs**

| Modality | Benign VCF Features | Malignant VCF Features |
|---|---|---|
| MRI: morphology | Normal posterior element signal,[20] retropulsed bone fragments,[9,12,14,17] additional benign VCFs[18,19] | Abnormal posterior element signal,[9-19] epidural or paravertebral soft-tissue mass,[9,10,12-15,17-19] expanded posterior vertebral contour,[9,11,12,14,18,24] metastasis in other vertebrae[9,14,18] |
| MRI: signal and enhancement patterns | Preserved normal marrow signal,[9-12,14,15,17] regular margins,[13,17,28] linear horizontal hypointense T1/T2 band,[4,9,11,14,18] fluid sign,[9,18,19,26] normal enhancement relative to adjacent vertebrae and at 3 mo[12,13,15,28] | Geographic replacement of normal marrow signal,[11,12,14-18,24,28] irregular margins,[13,17,28] increased enhancement relative to adjacent vertebrae and at 3 mo[12,13,15,28] |
| MRI: diffusion | No restricted diffusion[18,27,30,32-45] | Increased restricted diffusion[18,27,30,32-45] |
| MRI: chemical shift | Loss of SI on opposed-phase[18,51-53] | No change or slight loss of SI on opposed-phase,[18,51-53] ratio of opposed-phase to in-phase SI $>$ 0.8–1.0[18,51-53] |
| CT | Retropulsed bone,[54,55] puzzle sign,[10,54,55] sharp fracture lines,[10,54,55] intravertebral vacuum phenomenenon[55] | Bone destruction,[10,54,55] epidural or focal paravertebral soft tissue mass[54,55] |
| PET | SUV 2 SDs below liver SUV[57-60] | SUV of $>$3–4.7 or 2 SDs above liver SUV[57-60] |
| SPECT | Vertebral body and/or facet joint uptake[63] | Vertebral body with pedicle and/or spinous process uptake,[63] marginal uptake in cold lesion[63] |

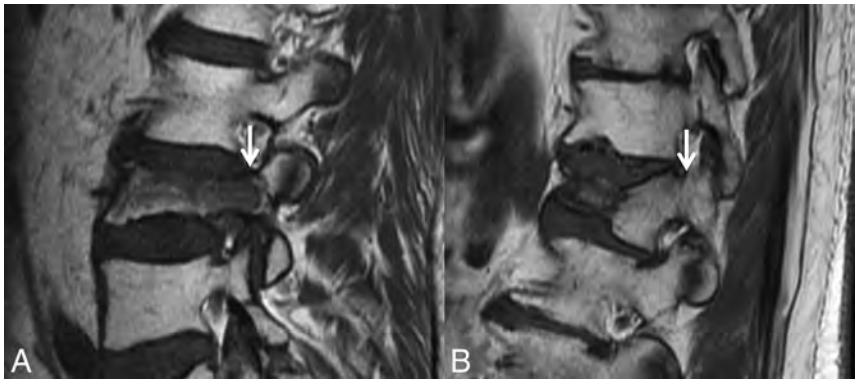


**FIG 1.** Abnormal pedicle marrow signal in a malignant VCF. *A*, Sagittal T1WI of the lumbar spine demonstrates a malignant VCF of L3 with loss of the high T1 normal marrow signal within the pedicle (*arrow*), indicating tumor infiltration. *B*, Sagittal T1WI of the lumbar spine demonstrates a typical benign VCF of L1 anteriorly, with preservation of the normal high T1 marrow signal within the pedicle (*arrow*).

is a strong indicator of malignancy in VCFs.[9-19] Tumor spread to the posterior elements typically occurs before tumor-associated structural instability leads to fracture within the vertebral body (Fig 1*A*). In contradistinction, according to the literature, osteoporotic fractures infrequently have signal change in the posterior elements (Fig 1*B*).[20] However, in our experience, as has been shown in the literature, osteoporotic fractures commonly cause such posterior element signal abnormalities.[21] Possible reasons include inflammation related to biomechanical stress and/or direct injury.[22]

Moreover, malignant VCFs may have preserved marrow signal within 1 or both pedicles (for example, preserved signal on the right in Fig 2) because the presence of abnormal signal is dependent on tumor infiltration.

The presence of abnormal epidural or paravertebral soft-tissue signal/enhancement is another finding suggesting a pathologic VCF.[9,10,12-15,17-19] When this is present, it represents direct extension of tumor from the vertebrae into the epidural or paravertebral space (Figs 3–5). This can occur without fracture or retropulsion. The morphology of this epidural or paravertebral infiltration tends to be masslike. A bilobed appearance in the ventral extradural space is more commonly seen in neoplastic disease, as opposed to non-neoplastic disease, in which there is preservation of the strong attachment of the central septum.[23] A potential pitfall in benign VCFs is when there is paravertebral or epidural hemorrhage with associated edema that mimics a soft-tissue mass. Except for acute posttraumatic fractures, the paravertebral hemorrhage and edema tend to be ill-defined, smooth, and/or rim-shaped about the vertebral body, as opposed to the appearance of a soft-tissue mass, which is seen with malignant VCFs. However, malignant VCFs may also demonstrate smooth and rim-shaped signal abnormality/enhancement about the vertebral body if peritumoral inflammation is present and/or there is no tumor infiltration of the cortex of the vertebral body.[13]

A convex vertebral contour, specifically expansion of the posterior aspect of the vertebral contour, is an imaging feature strongly suggestive of malignant fracture.[9,11,12,14,18,24] Because tumor infiltrates and destroys the cortex, an axial load causes bulging of the mass into the ventral epidural space. The bulge extends beyond the normal posterior margin of the vertebral body, resulting in a convexity, rather than the normal anatomic concavity of the vertebral body (Figs 3*A*, 4, and 5). Uncommonly, a similar finding can sometimes be seen in benign VCFs, primarily in the acute posttraumatic setting,[15,17] in which a ventral epidural hematoma can contribute to this appearance.[15,17]

Retropulsion of bone fragments from the posterior aspect of the vertebral body, rather than an expansile, convex contour, is characteristic of benign VCFs (Fig 6).[9,12,14,17] This is typical with axial loading from traumatic compression fractures, especially burst-type fractures.[20]

The location of a VCF within the spinal column has been reported to indicate the likelihood of benignity or malig-

nancy,[11,14,17-19,25] but this feature is of limited clinical utility. According to one study, thoracic and lumbar spine traumatic fractures were much more likely to be malignant than those occurring in the cervical spine.[25] In another study, lumbar fractures were more frequently malignant than thoracic fractures.[11]

Multiple VCFs throughout the spine typically favor a benign osteoporotic etiology. However, the possibility of underlying multiple myeloma should be considered in these patients[14]; multifocal metastases with multilevel pathologic fractures are less likely to cause this appearance. The presence of other healed benign VCFs or compression deformities without bone marrow edema suggests benignity of a new fracture.[18,19] Likewise, known spinal metastasis within other segments or indeterminate vertebral lesions suggest malignancy as the cause of new fractures.[9,14,18] A potential pitfall would be that it is possible to have both malignant and benign VCFs in the same patient.

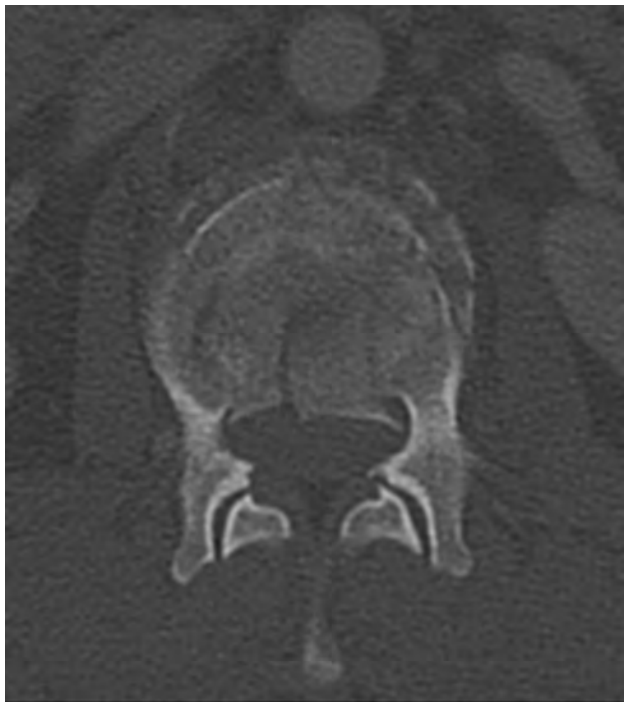

**FIG 2.** Fracture lines without cortical destruction in a benign VCF. Axial CT with bone windows shows the linear and well-delineated borders of the slightly displaced bone fragments within this benign VCF, an example of the puzzle sign.

**Signal Intensity and Enhancement Patterns.** An established strength of MR imaging lies in its ability to evaluate bone marrow. Both T1- and T2-weighted imaging have characteristic signal intensity patterns that can be used to discern a pathologic entity and differentiate benign and malignant VCFs.[10-18,24,26-28] The distinguishing signal intensities arise from 2 different mechanisms of fracture. In malignant VCFs, tumor infiltrates throughout the bone marrow and eventually the trabeculae and cortex, leading to a fracture.[17] Malignant or metastatic VCFs often have total replacement of the normally high T1 bone marrow signal intensity (SI), resulting in diffuse homogeneous low SI.[11,12,14-18,24,28] This was present in up to 88% of metastatic lesions in 1 series.[17] Meanwhile, in osteoporosis, the underlying mechanism leading to fracture is the loss of bone mineral density with preservation of the bone marrow.[17] Therefore, areas of preserved normal high T1 and intermediate T2 SI within the bone marrow of a collapsed vertebral body are more often found in benign VCFs.[9-12,14,15,17] Unfortunately, some VCFs with areas of spared normal bone marrow signal will also be malignant. Likewise, benign VCFs can also have abnormalities in bone marrow signal characteristics due to edema, which can demonstrate diffuse hypointensity on T1WI and patchy enhancement.[4,14,16]

Characterization of the margin between spared normal bone marrow signal and abnormal signal within the collapsed vertebrae can be a key to indicating the cause of the fracture. Ill-defined, irregular, or infiltrative margins are more likely to be found in malignant VCFs, while well-defined or regular margins are typical in benign VCFs.[13,17,28]

As an example of well-defined margins, a sign of benignity is a linear horizontal band of low T1 and T2 signal, often adjacent to the endplate (Fig 7).[4,9,11,14,18] The finding often correlates to a fracture line or area of cancellous bone compaction, which can sometimes be seen on CT.[12]

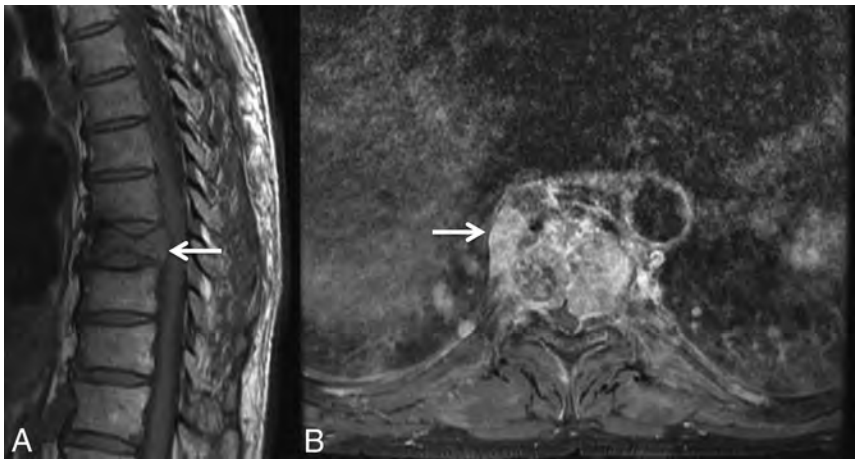


**FIG 3.** Masslike extension into the paravertebral and epidural space in a malignant VCF. *A*, Sagittal T1WI of the thoracic spine demonstrates a malignant VCF of T9 with loss of the high T1 normal marrow signal within the vertebral body and convex bowing of the posterior cortex (*arrow*), both signs indicating a malignant fracture. *B*, Axial postcontrast T1WI with fat saturation of the T9 fracture demonstrates an irregular enhancing mass (*arrow*) extending into the right paraspinal soft tissues and the epidural space in this malignant VCF.

A "fluid sign" refers to a focal, linear, or triangular area of T2 hyperintensity, best seen with fat-suppressed T2-weighted images, which can be present in acute, subacute, and chronic fractures.[29] This linear T2 hyperintensity occurs in a background of diffuse hyperintensity (edema) in the vertebral body (Fig 8).[26] It is thought to develop when fluid from bone marrow edema collects in an area of ischemic osteonecrosis after an acute fracture.[26] Sometimes a benign fracture/cleft may be filled with gas instead of or in addition to fluid; this can be recognized on MR imaging as strikingly hypointense signal on T1WI and T2WI, though this is generally more easily de-

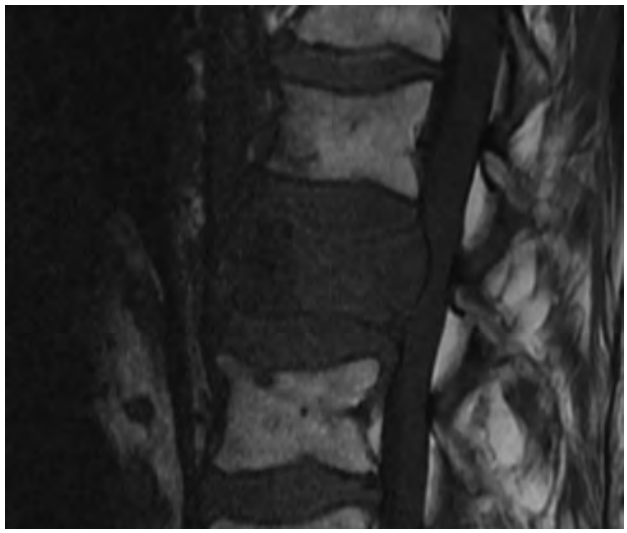

**FIG 4.** Diffuse abnormal marrow signal in a malignant VCF. Sagittal T1WI of the lumbar spine demonstrates a malignant VCF of L2 with marked complete replacement of the normal high T1 vertebral body marrow signal. The diffuse T1 hypointensity indicates tumor infiltration. Note the convex, expanded border of the posterior vertebral body versus the normal posterior concavity of the adjacent vertebral bodies.

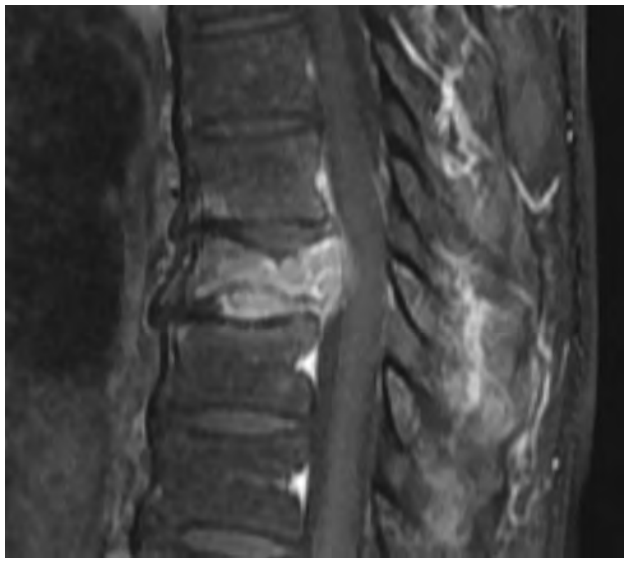

**FIG 5.** Increased enhancement in malignant VCF. Sagittal T1WI postgadolinium with fat saturation of the lumbar spine demonstrates an enhancing malignant VCF of L2. The enhancement is greater than that of the normal adjacent vertebral bodies. Also demonstrated is an expanded posterior convex border.

tected on CT (see subsequent "CT" section). The fluid sign has proved to be a strong indicator of benign VCFs in prediction models, though rarely it can develop in malignant VCFs.[9,18,19,26]

Use of postgadolinium T1WI, ideally with fat suppression, may also yield beneficial information.[11-13,15,16] As described above, findings in the epidural and paravertebral spaces on postcontrast MR imaging can help discriminate benign and malignant VCFs. In addition, the pattern and degree of intraosseous enhancement relative to normal adjacent vertebrae or noncontrast T1WI help to distinguish benign from malignant VCFs. Heterogeneous and relatively increased enhancement tends to be an indicator of malignancy (Fig 5).[12,13,15] Typically benign fractures will have enhancement that is equivalent to adjacent normal vertebrae, the so-called "return to normal signal intensity," with additional horizontal bands of high or low SI parallel to the fractured endplate.[12,13,15] In certain cases, an initial MR imaging, even with contrast, can be equivocal or can suggest malignancy even when clinical and other diagnostic tests do not indicate it. In equivocal cases, 1 option for problem solving is a follow-up gadolinium-enhanced MR imaging performed 2–3 months later. Benign VCFs will typically show a decrease or resolution of enhancement, while malignant VCFs will demonstrate persistent or progressive enhancement.[28]

Diffusion-Weighted Imaging. Application of DWI in relation to VCF evaluation is relatively new. As with its use intracranially, the technique is based on the ability to measure changes in the mobility of water molecules (Brownian motion) in various tissues.[30] Diffusion is presumed to be increased in osteoporotic fractures due to bone marrow edema, which allows relatively unimpeded extracellular water molecule movement (Fig 9). With malignant VCF, diffusion is predicted to be restricted due to the typically high cellularity of tumor tissue (Fig 9).[31] Restricted diffusion will appear as a hyperintensity, signifying tumor on DWI, with corresponding hypointensity on apparent coefficient images, whereas benign edema will be hypo- or isointense on DWI.[31,32]

DWI can also be quantitatively assessed. An ROI is selected within the vertebrae, and an ADC value is calculated. The ADC value is a measure of water molecule displacement per unit of time, with units of square millimeters/second.[30] Multiple MR imaging sequences have been explored to maximize the distinction between the signal intensity and ADC values of benign and malignant VCFs, including steady-state precession, spin-echo, fast spin-echo, echo-planar imaging, and single-shot fast spin-echo diffusion-weighted techniques, as well as optimization of b-values.[18,27,30,32-45] The results have been mixed because some of these studies can separate benign and malignant VCFs similar to conventional MR imaging, while others fail to find similar conclusions. Thus, it is unclear whether DWI provides an advantage over conventional MR imaging.[27] One possible reason for conflicting results is the presence of intravertebral hematoma. One study evaluated patients with low-impact trauma, high-impact trauma, and known metastatic VCFs. Those with high-impact trauma were found to have intermediate ADC values, similar to metastatic disease.[46] DWI may provide beneficial information in combination with conventional imaging; recently, Sung et al[42] have shown improved sensitivity, specificity, and accuracy when the 2 were used in conjunction.

Dynamic Contrast-Enhanced Imaging. Dynamic contrast-enhanced imaging is a technique in which contrast uptake is measured as changes in signal intensity across time. It allows qualitative and quantitative assessment of vascularity and hemodynamics, typically referred to as perfusion. Multiple perfusion parameters have been assessed, some of which included peak contrast percentage, enhancement slope, time-intensity curves, interstitial volume, plasma flow, plasma volume, permeability, wash-in slope, and area under the curve. The ability of perfusion parameters to differentiate benign and malignant VCFs is not convincingly different from that of conventional MR imaging. One early study was

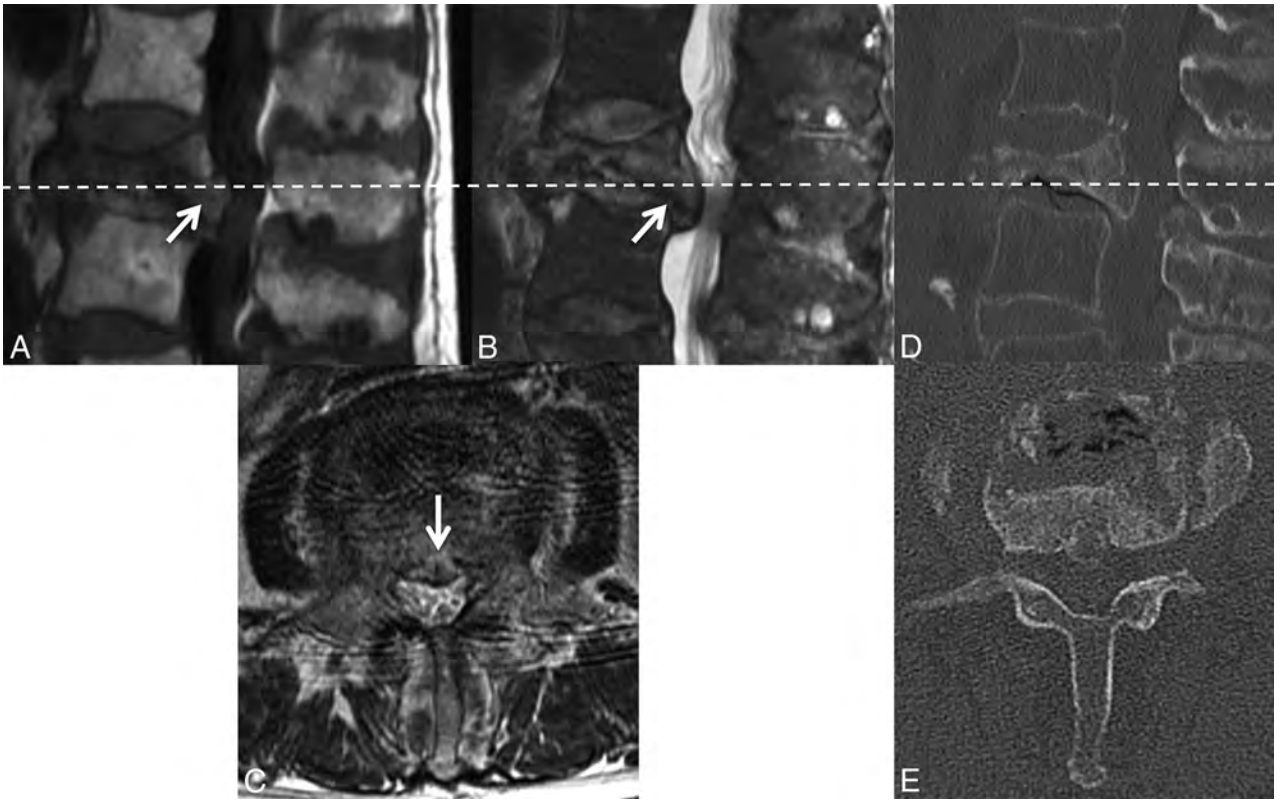


**FIG 6.** Retropulsion of a bone fragment in a benign VCF. Sagittal T1WI (*A*) and T2WI (*B*) with fat saturation of the lumbar spine demonstrate a retropulsed bone fragment (*arrow*) compressing the thecal sac and narrowing the spinal canal in this benign VCF (*C*), best seen on the axial T2WI. A similar appearance is demonstrated on the axial (*D*) and sagittal (*E*) reformatted thoracic spine CT scans.

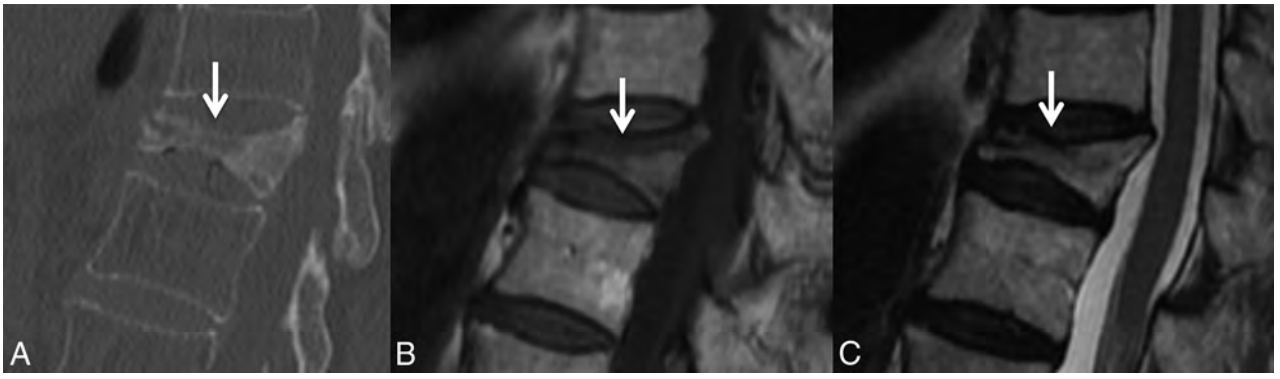


**FIG 7.** Linear horizontal fracture line in a benign VCF. As seen on the sagittal reformat from a thoracic spine CT in bone windows (*A*), there is a lucent fracture line (*arrow*) paralleling the superior endplate of T11. On MR imaging, this fracture is seen as a linear horizontal line (*arrow*) of T1 and T2 hypointensity through the T11 vertebral body, T1WI (*B*) and T2WI (*C*).

unable to find perfusion differences, specifically in cases of acute osteoporotic VCFs.[47] However, subsequent studies using more sophisticated analytic tools have been more successful in separating acute benign and malignant VCFs, though with slightly conflicting results based on the perfusion parameter assessed.[48-50]

Chemical Shift. In-phase and opposed-phase imaging is an additional MR imaging technique relatively recently being applied for the assessment of differentiating benign and malignant VCFs. With in-phase imaging, at 1.5T and a TE of 4.6 ms, both fat and water protons will contribute to the radiofrequency signal and increased SI.[51] On opposed-phase imaging, at 1.5T and a TE of 4.6 ms, the fat dipole is opposite that of water and cancels the radiofrequency signal of water, resulting in lower net signal intensity.[51] Normal red and yellow bone marrow has varying amounts of both fat and water components, which have loss of SI on opposed-phase imaging.[52] In contrast, malignant spinal lesions infiltrate bone marrow causing no or only slight loss on opposed-phase imaging.[52] The signal intensity ratio or the ratio of opposed-phase to in-phase SI is a measurement that, at values of $>0.8$, is a fairly sensitive and specific sign of malignancy.[18,52] Ratios of $\geq 1.0$ are even more specific.[53]

### *CT*

CT is a readily accessible technique that can be used to evaluate patients with back pain and suspected VCFs. Laredo et al[54] were

the earliest group to evaluate the diagnostic value of CT. They reported several CT features that were more frequently found in benign VCFs, with the following findings achieving statistical significance: fracture of the anterolateral or posterior cortex of the vertebral body, a retropulsed bone, fracture lines within cancellous bone, and a diffuse thin paraspinal soft-tissue thickening.

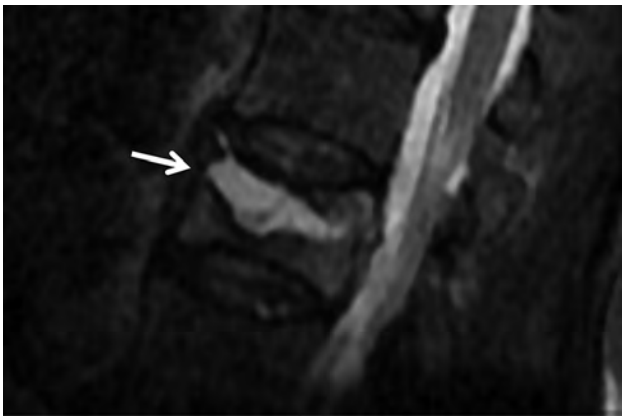

**FIG 8.** Fluid cleft in a benign VCF. Sagittal T2WI with fat saturation of the lumbar spine demonstrates a triangular fluid cleft (*arrow*) seen within this benign VCF.

The "puzzle sign" is a descriptive term of the presence of sharp fracture lines without cortical destruction so that the displaced bone fragments could be reconstructed into their original position to complete the "puzzle" (Fig 2). In addition, although uncommon and not reaching statistical significance, an intravertebral vacuum phenomenon (air-filled cleft) was never visualized in malignant fractures.

CT findings predictive of malignant VCFs revolve around destruction and the presence of masses. Any form of destruction whether of cortical bone, cancellous bone, or the pedicle was predictive of malignant VCF. As with MR imaging, an epidural or focal paravertebral soft-tissue mass also favors a malignant VCF.[54,55]

The use of various scoring systems and prediction models can be a helpful strategy for delineating benign from malignant VCFs.[10,19,56] Yuzawa et al[10] found that the combination of CT characteristics and MR imaging features enhanced the accuracy of differentiating benign from malignant fractures. The CT findings used in this scoring system included sharp fracture lines without osteolytic destruction in benign VCFs and osteolytic destruction in malignant VCFs. While MR imaging is typically superior in the depiction of most spine pathology, such studies exemplify the

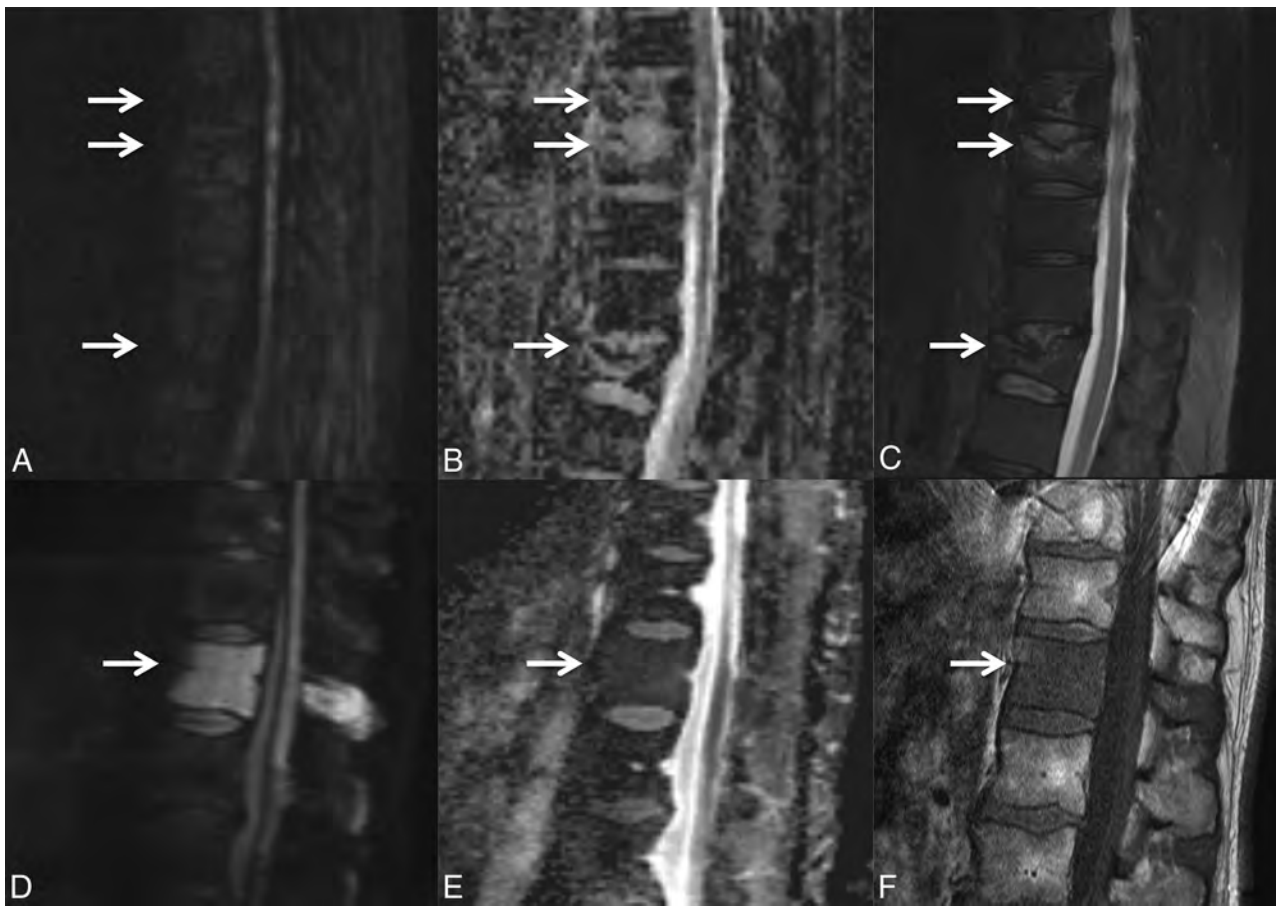


**FIG 9.** DWI of benign and malignant VCFs. Multiple benign osteoporotic VCFs (*A–C*, *arrows*) are seen in the lower thoracic spine. Sagittal DWI (*A*) and the corresponding ADC map (*B*) demonstrate the absence of diffusion restriction. Sagittal fat-saturated T2WI (*C*) demonstrates T2 hyperintensity about the fracture lines compatible with edema from an acute/subacute fracture. In contrast, malignant lymphomatous involvement of T12 (*D–F*, *arrow*) demonstrates diffuse diffusion restriction (*D*) with corresponding low ADC values (*E*). On the sagittal T1WI (*F*), there is slight loss of height of the superior and inferior endplates and diffuse T1 hypointensity compatible with marrow replacement.

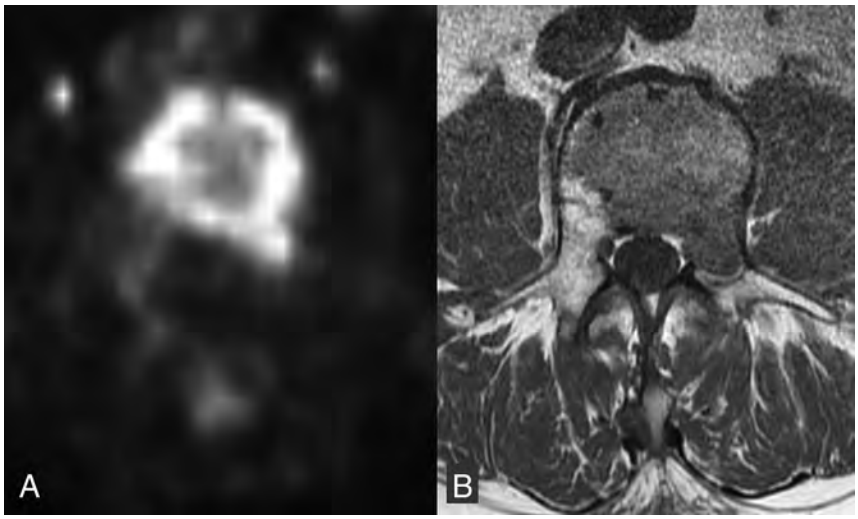


**FIG 10.** FDG avid malignant VCF. Axial non-attenuation-corrected PET (*A*) at the level of the malignant lumbar VCF with increased FDG activity throughout the vertebral body and into the left pedicle. Corresponding axial T1WI (*B*) shows the area of low T1 signal tumor infiltration throughout the vertebral body and left pedicle.

utility of CT in providing excellent characterization of cortical and cancellous bone and fracture margins.

### *FDG-PET/CT*

While MR imaging and CT are widely used in the assessment of VCFs, they provide primarily anatomic information and occasionally do not yield a definitive diagnosis. In addition, MR imaging may not be an option in patients unable to undergo it due to implanted devices or other limitations. FDG-PET/CT may have an adjunctive role in differentiating benign and malignant VCFs by providing metabolic information.[57-60] It has been shown that there is overlap in the appearance of benign and malignant bone lesions on this technique, but to date, published data are not extensive.[57,58]

Generally, fractures due to tumors are expected to accumulate FDG, while benign fractures are not expected to accumulate FDG to a similarly high degree. The maximum standard uptake value (SUV) on PET of malignant pathologic fractures of various bones (pelvis, long bones, spine, and rib) is significantly higher compared with benign fractures.[58] When evaluating vertebrae specifically, the SUV is significantly higher in malignant than in benign compression fractures (Fig 10).[57,59] Most of these studies used a threshold SUV to classify the lesions, while some incorporated comparison with liver SUV. The cutoff SUVs ranged from 3 to 4.7. Alternative criteria included 2 SDs above (malignant) or below (benign) the liver SUV or direct comparison with the SUV of the liver in indeterminate (SUV 2–3) lesions.

However, there are limitations to FDG-PET. Case reports have shown benign fractures with much higher-than-expected SUVs, even up to 9.3 in an acute pelvic fracture.[61] As such cases demonstrate, acute fractures can be a source of false-positive findings. FDG uptake was noted to be most intense in the acute phase of a benign fracture and returned to normal by approximately 3 months.[5,62] Failure of a fracture to return to a normal FDG uptake by 3 months may indicate malignancy or osteomyelitis.[5] An additional limitation is that patients receiving bone marrow–stimulating agents may have falsely elevated maximum SUVs related to increased bone marrow metabolism, so this factor should be considered in the interpretation of FDG uptake.[57] In summary, the precise role of FDG PET in imaging of benign and malignant VCFs has yet to be defined. It may provide the most benefit when CT or MR imaging findings are indeterminate and the exact age of the fracture is known.

### *SPECT*

Bone scintigraphy has long been used for the evaluation of intraosseous lesions in patients with known malignancy and back pain. In clinical practice, abnormal uptake within ≥1 vertebrae is seen relatively commonly, especially in the elderly who have a high rate of benign disease that can cause uptake. SPECT has the advantage over planar imaging of offering exact localization of vertebral lesions. Because MR imaging is sometimes not feasible due to implantable devices, claustrophobia, or length of the study, a single study evaluated whether SPECT could be used as a substitute for MR imaging to distinguish benign from malignant VCFs.[63] Imaging features signifying malignancy included the following: vertebral body + pedicle uptake, vertebral body + pedicle + spinous process uptake, and marginal uptake in a cold lesion. Lesions were classified as benign if they had uptake in the vertebral body + facet joint or just in the facet joint. SPECT was found to be comparable with MR imaging with similar sensitivity and specificity for differentiating benign and malignant VCFs, though there was significantly lower accuracy. In cases in which there was complete replacement of normal fatty marrow on MR imaging, no significant differences in sensitivity, specificity, or accuracy between SPECT and MR imaging were seen, suggesting that SPECT may be most useful in this subset of patients.[63]

## CONCLUSIONS

Advanced imaging plays a crucial role in distinguishing benign from malignant VCFs. The various modalities each have unique attributes. CT provides excellent information about the osseous integrity and fracture margins. PET-CT and SPECT have relatively sparse supporting literature, though with comparable diagnostic results to CT and MR imaging. MR imaging is the established technique of choice, with strong evidence for multiple distinguishing imaging features, which can allow relatively confident characterization of the nature of a VCF. Features strongly predictive of malignancy include expansion of the fractured vertebral body, an epidural and/or paraspinal soft tissue mass, and discrete lesions within the bone, especially if destructive. Features strongly predictive of benignity include lack of these malignant features and at least partial preservation of normal marrow signal, visible fluid- and/or air-filled fracture lines/clefts, and retropulsion of the cortex (Table).

## ACKNOWLEDGMENTS

The authors acknowledge the assistance of Sonia Watson, PhD, in editing and submission of the manuscript.

## REFERENCES

1. Melton LJ 3rd. **Epidemiology of spinal osteoporosis.** *Spine (Phila Pa 1976)* 1997;22:2S–11S CrossRef Medline
2. Coleman RE. **Skeletal complications of malignancy.** *Cancer* 1997;80: 1588–94 Medline
3. Porter BA, Shields AF, Olson DO. **Magnetic resonance imaging of bone marrow disorders.** *Radiol Clin North Am* 1986;24:269–89 Medline
4. Yamato M, Nishimura G, Kuramochi E, et al. **MR appearance at different ages of osteoporotic compression fractures of the vertebrae.** *Radiat Med* 1998;16:329–34 Medline
5. Zhuang H, Sam JW, Chacko TK, et al. **Rapid normalization of osseous FDG uptake following traumatic or surgical fractures.** *Eur J Nucl Med Mol Imaging* 2003;30:1096–103 CrossRef Medline
6. Lecouvet FE, Malghem J, Michaux L, et al. **Vertebral compression fractures in multiple myeloma, Part II: assessment of fracture risk with MR imaging of spinal bone marrow.** *Radiology* 1997;204: 201–05 CrossRef Medline
7. Lecouvet FE, Vande Berg BC, Maldague BE, et al. **Vertebral compression fractures in multiple myeloma, Part I: distribution and appearance at MR imaging.** *Radiology* 1997;204:195–99 CrossRef Medline
8. Layton KF, Thielen KR, Cloft HJ, et al. **Acute vertebral compression fractures in patients with multiple myeloma: evaluation of vertebral body edema patterns on MR imaging and the implications for vertebroplasty.** *AJNR Am J Neuroradiol* 2006;27:1732–34 Medline
9. Abdel-Wanis ME, Solyman MT, Hasan NM. **Sensitivity, specificity and accuracy of magnetic resonance imaging for differentiating vertebral compression fractures caused by malignancy, osteoporosis, and infections.** *J Orthop Surg (Hong Kong)* 2011;19: 145–50 CrossRef Medline
10. Yuzawa Y, Ebara S, Kamimura M, et al. **Magnetic resonance and computed tomography-based scoring system for the differential diagnosis of vertebral fractures caused by osteoporosis and malignant tumors.** *J Orthop Sci* 2005;10:345–52 CrossRef Medline
11. Moulopoulos LA, Yoshimitsu K, Johnston DA, et al. **MR prediction of benign and malignant vertebral compression fractures.** *J Magn Reson Imaging* 1996;6:667–74 CrossRef Medline
12. Cuénod CA, Laredo JD, Chevret S, et al. **Acute vertebral collapse due to osteoporosis or malignancy: appearance on unenhanced and gadolinium-enhanced MR images.** *Radiology* 1996; 199:541–49 CrossRef Medline
13. Shih TT, Huang KM, Li YW. **Solitary vertebral collapse: distinction between benign and malignant causes using MR patterns.** *J Magn Reson Imaging* 1999;9:635–42 Medline
14. Jung HS, Jee WH, McCauley TR, et al. **Discrimination of metastatic from acute osteoporotic compression spinal fractures with MR imaging.** *Radiographics* 2003;23:179–87 CrossRef Medline
15. Rupp RE, Ebraheim NA, Coombs RJ. **Magnetic resonance imaging differentiation of compression spine fractures or vertebral lesions caused by osteoporosis or tumor.** *Spine (Phila Pa 1976)* 1995;20: 2499–503; discussion 2504 CrossRef Medline
16. Tan DY, Tsou IY, Chee TS. **Differentiation of malignant vertebral collapse from osteoporotic and other benign causes using magnetic resonance imaging.** *Ann Acad Med Singapore* 2002;31:8–14 Medline
17. Yuh WT, Zachar CK, Barloon TJ, et al. **Vertebral compression fractures: distinction between benign and malignant causes with MR imaging.** *Radiology* 1989;172:215–18 CrossRef Medline
18. Thawait SK, Marcus MA, Morrison WB, et al. **Research synthesis: what is the diagnostic performance of magnetic resonance imaging to discriminate benign from malignant vertebral compression fractures? Systematic review and meta-analysis.** *Spine (Phila Pa 1976)* 2012;37:E736–44 CrossRef Medline
19. Thawait SK, Kim J, Klufas RA, et al. **Comparison of four prediction models to discriminate benign from malignant vertebral compression fractures according to MRI feature analysis.** *AJR Am J Roentgenol* 2013;200:493–502 CrossRef Medline
20. Kaplan PA, Orton DF, Asleson RJ. **Osteoporosis with vertebral compression fractures, retropulsed fragments, and neurologic compromise.** *Radiology* 1987;165:533–35 CrossRef Medline
21. Ishiyama M, Fuwa S, Numaguchi Y, et al. **Pedicle involvement on MR imaging is common in osteoporotic compression fractures.** *AJNR Am J Neuroradiol* 2010;31:668–73 CrossRef Medline
22. Lehman VT, Wood CP, Hunt CH, et al. **Facet joint signal change on MRI at levels of acute/subacute lumbar compression fractures.** *AJNR Am J Neuroradiol* 2013;34:1468–73 CrossRef Medline
23. Kim DH, Rosenblum JK, Panghaal VS, et al. **Differentiating neoplastic from nonneoplastic processes in the anterior extradural space.** *Radiology* 2011;260:825–30 CrossRef Medline
24. Baker LL, Goodman SB, Perkash I, et al. **Benign versus pathologic compression fractures of vertebral bodies: assessment with conventional spin-echo, chemical-shift, and STIR MR imaging.** *Radiology* 1990;174:495–502 CrossRef Medline
25. Dammers R, Bijvoet HW, Driesse MJ, et al. **Occurrence of malignant vertebral fractures in an emergency room setting.** *Emerg Med J* 2007; 24:707–09 CrossRef Medline
26. Baur A, Stäbler A, Arbogast S, et al. **Acute osteoporotic and neoplastic vertebral compression fractures: fluid sign at MR imaging.** *Radiology* 2002;225:730–35 CrossRef Medline
27. Castillo M, Arbelaez A, Smith JK, et al. **Diffusion-weighted MR imaging offers no advantage over routine noncontrast MR imaging in the detection of vertebral metastases.** *AJNR Am J Neuroradiol* 2000; 21:948–53 Medline
28. An HS, Andreshak TG, Nguyen C, et al. **Can we distinguish between benign versus malignant compression fractures of the spine by magnetic resonance imaging?** *Spine (Phila Pa 1976)* 1995;20:1776–82 CrossRef Medline
29. Ishiyama M, Numaguchi Y, Makidono A, et al. **Contrast-enhanced MRI for detecting intravertebral cleft formation: relation to the time since onset of vertebral fracture.** *AJR Am J Roentgenol* 2013;201: W117–23 CrossRef Medline
30. Raya JG, Dietrich O, Reiser MF, et al. **Methods and applications of diffusion imaging of vertebral bone marrow.** *J Magn Reson Imaging* 2006;24:1207–20 CrossRef Medline
31. Baur A, Stabler A, Huber A, et al. **Diffusion-weighted magnetic resonance imaging of spinal bone marrow.** *Semin Musculoskelet Radiol* 2001;5:35–42 CrossRef Medline
32. Baur A, Stäbler A, Brüning R, et al. **Diffusion-weighted MR imaging of bone marrow: differentiation of benign versus pathologic compression fractures.** *Radiology* 1998;207:349–56 CrossRef Medline
33. Zhou XJ, Leeds NE, McKinnon GC, et al. **Characterization of benign and metastatic vertebral compression fractures with quantitative diffusion MR imaging.** *AJNR Am J Neuroradiol* 2002;23:165–70 Medline
34. Tang G, Liu Y, Li W, et al. **Optimization of b value in diffusion-weighted MRI for the differential diagnosis of benign and malignant vertebral fractures.** *Skeletal Radiol* 2007;36:1035–41 CrossRef Medline
35. Baur A, Huber A, Ertl-Wagner B, et al. **Diagnostic value of increased diffusion weighting of a steady-state free precession sequence for differentiating acute benign osteoporotic fractures from pathologic vertebral compression fractures.** *AJNR Am J Neuroradiol* 2001; 22:366–72 Medline
36. Baur-Melnyk A. **Malignant versus benign vertebral collapse: are new imaging techniques useful?** *Cancer Imaging* 2009;9 Spec No A:S49–51 CrossRef Medline
37. Karchevsky M, Babb JS, Schweitzer ME. **Can diffusion-weighted imaging be used to differentiate benign from pathologic fractures? A meta-analysis.** *Skeletal Radiol* 2008;37:791–95 CrossRef Medline
38. Park SW, Lee JH, Ehara S, et al. **Single shot fast spin echo diffusion-weighted MR imaging of the spine; is it useful in differentiating**

**malignant metastatic tumor infiltration from benign fracture edema?** *Clin Imaging* 2004;28:102–08 CrossRef Medline
39. Biffar A, Baur-Melnyk A, Schmidt GP, et al. **Quantitative analysis of the diffusion-weighted steady-state free precession signal in vertebral bone marrow lesions.** *Invest Radiol* 2011;46:601–09 CrossRef Medline
40. Mubarak F, Akhtar W. **Acute vertebral compression fracture: differentiation of malignant and benign causes by diffusion weighted magnetic resonance imaging.** *J Pak Med Assoc* 2011;61:555–58 Medline
41. Wonglaksanapimon S, Chawalparit O, Khumpunnip S, et al. **Vertebral body compression fracture: discriminating benign from malignant causes by diffusion-weighted MR imaging and apparent diffusion coefficient value.** *J Med Assoc Thai* 2012;95:81–87 Medline
42. Sung JK, Jee WH, Jung JY, et al. **Differentiation of acute osteoporotic and malignant compression fractures of the spine: use of additive qualitative and quantitative axial diffusion-weighted MR imaging to conventional MR imaging at 3.0 T.** *Radiology* 2014;271:488–98 CrossRef Medline
43. Park HJ, Lee SY, Rho MH, et al. **Single-shot echo-planar diffusion-weighted MR imaging at 3T and 1.5T for differentiation of benign vertebral fracture edema and tumor infiltration.** *Korean J Radiol* 2016;17:590–97 CrossRef Medline
44. Luo Z, Litao L, Gu S, et al. **Standard-b-value vs low-b-value DWI for differentiation of benign and malignant vertebral fractures: a meta-analysis.** *Br J Radiol* 2016;89:20150384 CrossRef Medline
45. Dietrich O, Geith T, Reiser MF, et al. **Diffusion imaging of the vertebral bone marrow.** *NMR Biomed* 2017;30 CrossRef Medline
46. Rumpel H, Chong Y, Porter DA, et al. **Benign versus metastatic vertebral compression fractures: combined diffusion-weighted MRI and MR spectroscopy aids differentiation.** *Eur Radiol* 2013;23:541–50 CrossRef Medline
47. Chen WT, Shih TT, Chen RC, et al. **Blood perfusion of vertebral lesions evaluated with gadolinium-enhanced dynamic MRI: in comparison with compression fracture and metastasis.** *J Magn Reson Imaging* 2002;15:308–14 CrossRef Medline
48. Arevalo-Perez J, Peck KK, Lyo JK, et al. **Differentiating benign from malignant vertebral fractures using T1-weighted dynamic contrast-enhanced MRI.** *J Magn Reson Imaging* 2015;42:1039–47 CrossRef Medline
49. Geith T, Biffar A, Schmidt G, et al. **Quantitative analysis of acute benign and malignant vertebral body fractures using dynamic contrast-enhanced MRI.** *AJR Am J Roentgenol* 2013;200:W635–43 CrossRef Medline
50. Tokuda O, Hayashi N, Taguchi K, et al. **Dynamic contrast-enhanced perfusion MR imaging of diseased vertebrae: analysis of three parameters and the distribution of the time-intensity curve patterns.** *Skeletal Radiol* 2005;34:632–38 CrossRef Medline
51. Erly WK, Oh ES, Outwater EK. **The utility of in-phase/opposed-phase imaging in differentiating malignancy from acute benign compression fractures of the spine.** *AJNR Am J Neuroradiol* 2006;27:1183–88 Medline
52. Zajick DC Jr, Morrison WB, Schweitzer ME, et al. **Benign and malignant processes: normal values and differentiation with chemical shift MR imaging in vertebral marrow.** *Radiology* 2005;237:590–96 CrossRef Medline
53. Ogura A, Hayakawa K, Maeda F, et al. **Differential diagnosis of vertebral compression fracture using in-phase/opposed-phase and short TI inversion recovery imaging.** *Acta Radiol* 2012;53:450–55 CrossRef Medline
54. Laredo JD, Lakhdari K, Bellaïche L, et al. **Acute vertebral collapse: CT findings in benign and malignant nontraumatic cases.** *Radiology* 1995;194:41–48 CrossRef Medline
55. Kubota T, Yamada K, Ito H, et al. **High-resolution imaging of the spine using multidetector-row computed tomography: differentiation between benign and malignant vertebral compression fractures.** *J Comput Assist Tomogr* 2005;29:712–19 CrossRef Medline
56. Wang KC, Jeanmenne A, Weber GM, et al. **An online evidence-based decision support system for distinguishing benign from malignant vertebral compression fractures by magnetic resonance imaging feature analysis.** *J Digit Imaging* 2011;24:507–15 CrossRef Medline
57. Bredella MA, Essary B, Torriani M, et al. **Use of FDG-PET in differentiating benign from malignant compression fractures.** *Skeletal Radiol* 2008;37:405–13 CrossRef Medline
58. Shin DS, Shon OJ, Byun SJ, et al. **Differentiation between malignant and benign pathologic fractures with F-18-fluoro-2-deoxy-D-glucose positron emission tomography/computed tomography.** *Skeletal Radiol* 2008;37:415–21 CrossRef Medline
59. Cho WI, Chang UK. **Comparison of MR imaging and FDG-PET/CT in the differential diagnosis of benign and malignant vertebral compression fractures.** *J Neurosurg Spine* 2011;14:177–83 CrossRef Medline
60. Aggarwal A, Salunke P, Shekhar BR, et al. **The role of magnetic resonance imaging and positron emission tomography-computed tomography combined in differentiating benign from malignant lesions contributing to vertebral compression fractures.** *Surg Neurol Int* 2013;4:S323–26 CrossRef Medline
61. Ravenel JG, Gordon LL, Pope TL, et al. **FDG-PET uptake in occult acute pelvic fracture.** *Skeletal Radiol* 2004;33:99–101 CrossRef Medline
62. Shon IH, Fogelman I. **F-18 FDG positron emission tomography and benign fractures.** *Clin Nucl Med* 2003;28:171–75 CrossRef Medline
63. Tokuda O, Harada Y, Ueda T, et al. **Malignant versus benign vertebral compression fractures: can we use bone SPECT as a substitute for MR imaging?** *Nucl Med Commun* 2011;32:192–98 CrossRef Medline

# MR Thermography–Guided Head and Neck Lesion Laser Ablation

D.T. Ginat, S. Sammet, and G. Christoforidis

## ABSTRACT

**SUMMARY:** Interstitial laser ablation has been successfully used as a minimally invasive treatment option for tumors in many parts of the body, including the head and neck. In this article, we describe the use of MR imaging guidance and mapping sequences for accurate localization of the target lesion, percutaneous interstitial laser ablation methods, and the use of MR thermography for temperature monitoring during laser ablation, with a focus on applications in the head and neck region.

Laser ablation, also known as interstitial laser ablation/thermal therapy or stereotactically guided interstitial laser thermal ablation, is a minimally invasive treatment technique that can be performed as an outpatient percutaneous procedure. The technique uses the phenomenon that heat-induced protein denaturation and coagulative necrosis occur at temperatures above 43°C, such that the time to cell death varies exponentially with temperature.[1] This is accomplished with light at wavelengths of 800–1064 nm from diode or neodymium-doped yttrium aluminum garnet lasers, which is absorbed by chromophores in tissues, leading to the release of thermal energy.[2]

Commercial fiber-optic laser tips can be cooled using fluids, which allow higher initial power use without damaging the fiber-optic tip. The cooling process also removes heat from the probe-tissue interface, thereby preventing carbonization or vaporization and enabling the creation of larger ablation volumes. Furthermore, cooling prevents the probe tip from adhering to the ablated tissue.[1] Laser ablation of soft tissues results in 5 distinct concentric zones: 1) a core that corresponds to the probe tract; 2) a central zone of coagulation necrosis that contains damaged cell membranes and stains positive for markers of apoptosis; 3) a peripheral zone that contains thrombosed vessels and distended cell bodies, followed by liquefaction necrosis; 4) a peripheral rim of leaky vasculature; and 5) a marginal zone of reversible edema.[3,4] The volume of the necrosis induced by laser ablation depends on the probe size, duration of the procedure, and temperature setting. Larger lesions may require multiple probes or serial laser ablation with repositioning of the probe. Ultimately, laser ablation produces a sharp transition zone between dead and viable tissue.

Interstitial laser ablation has several advantages over other thermal therapy methods. Unlike high-intensity focused sonography, laser ablation is rapid and is less affected by target motion and heats more slowly. Unlike radiofrequency ablation, the laser fiber does not produce large MR imaging artifacts caused by electromagnetic interferences.[5,6] Thus, laser ablation can be used simultaneously with real-time MR temperature monitoring. Furthermore, patients who undergo percutaneous interstitial laser ablation tend to be discharged after a shorter stay compared with open surgical procedures.[2,7-12] Consequently, interstitial laser ablation has been found to be a cost-effective option for treating brain tumors. For example, this technique is less costly than craniotomy for patients with brain metastases.[13] Furthermore, interstitial laser ablation improves survival of patients with high-grade gliomas at a cost that appears to be of good value to society.[14] Although there is a paucity of data regarding the cost-effectiveness of interstitial laser ablation for head and neck lesions, we believe that in many cases, the procedure can provide good value as well.

### *Head and Neck Laser Ablation Indications and Complications*

Laser ablation has been successfully performed for treating various lesions in the head and neck, brain, breast, liver, prostate, and colon among other sites.[2,7-12,15-22] Regarding the head and neck in particular, percutaneous laser ablation has been implemented for treating benign solid thyroid nodules, lymphatic malforma-

Received January 1, 2018; accepted after revision April 19.

From the Department of Radiology, University of Chicago, Pritzker School of Medicine, Chicago, Illinois.

This work was supported by Toshiba America Medical Systems/RSNA Research Seed Grant.

Please address correspondence to Daniel Thomas Ginat, MD, MS, Department of Radiology, University of Chicago, Pritzker School of Medicine, 5841 S Maryland Ave, Chicago, IL 60637; e-mail: dtg1@uchicago.edu

http://dx.doi.org/10.3174/ajnr.A5726

tions, and various malignant neoplasms.[8,9,16-22] Laser ablation performed to shrink symptomatic benign solid thyroid nodules has been reported to yield a 47%–82% reduction in volume, a minor complication rate of 38%, and a major complication rate of 3%.[22] Major complications related to laser ablation of benign solid thyroid nodules include dysphonia, nodule rupture, hypothyroidism, and brachial plexus injury, while minor complications include hematoma, vomiting, skin burn, pain, edema, fever, and coughing,[22] though many of the procedures were not performed under MR thermography guidance.

In a small study of lymphangiomas in the tongue and neck, MR imaging–guided laser ablation performed via a percutaneous approach using a multiapplicator technique resulted in a considerable decrease in the size of all lesions by 3 months, with improvement in functions such as speech and swallowing in most patients.[20] In particular, the cystic components showed the most change as the treated lymphatic channels become surrounded by fibrous tissue. Recurrence of the lymphatic malformations is nevertheless a possibility, but laser ablation of these lesions can be performed to facilitate subsequent debulking surgery.

Recurrent head and neck cancers after major surgery and/or radiation therapy are difficult to manage via conventional treatment methods. Laser ablation is a relatively safe treatment option for recurrent head and neck cancers for which surgery is limited by the proximity of vital neurovascular structures and the aggressive nature of these tumors.[19] A 78% partial or complete response and a median survival of 19 months was achieved for recurrent head and neck cancers treated with laser ablation, which surpasses the results obtained via a standard regimen of cisplatin/fluorouracil (5-FU).[8] In particular, oral cavity squamous cell carcinomas showed the greatest response to the procedure.[8] Furthermore, laser ablation reduces clinical symptoms in most patients. Infusion of chemotherapy into the ablated tumor can potentially augment the effects of laser thermal therapy while mitigating systemic toxicity and is the subject of investigation.[8]

### MR Imaging Guidance for Head and Neck Laser Ablation

Various navigation techniques and devices have been developed for MR imaging–guided interventions.[23-25] The advantages and disadvantages mainly depend on the type of the MR imaging scanner and the interventional environment.[23] For example, open MR imaging scanners require minimal patient transfer during the procedure, which facilitates the interventional workflow. On the other hand, while most high-field-strength closed-bore MR imaging scanners provide better image quality, they do not enable instruments to be inserted within the bore of the magnet. Consequently, interventions in closed-bore scanners require the patient being moved out of the bore, though multimodal overlays, augmented reality displays, and robotic assistance devices can facilitate the process.[23]

Insertion of the laser probe can be accomplished under MR imaging using freehand or stereotactic approaches. In either case, the device can be advanced into the target lesion under MR imaging "fluoroscopic" guidance, in which the choice of tissue contrast weighting can be tailored to maximize lesion conspicuity on the basis of preprocedural imaging. Furthermore, MR imaging provides the ability to continuously visualize vessels throughout a procedure without using intravenous contrast.

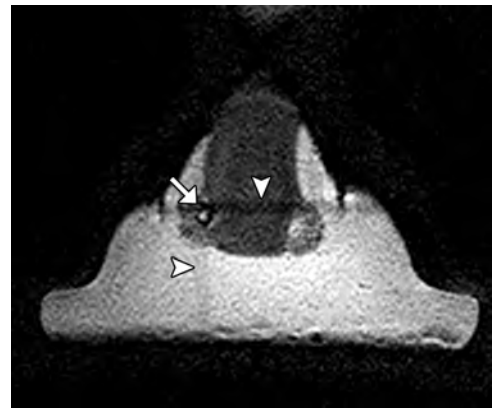

**FIG 1.** MR imaging guidance for laser applicator insertion. 3D T1-weighted fast-field echo image shows saturation bands *(arrowheads)* that are used to triangulate the target "lesion" (*arrow*) in the neck phantom.

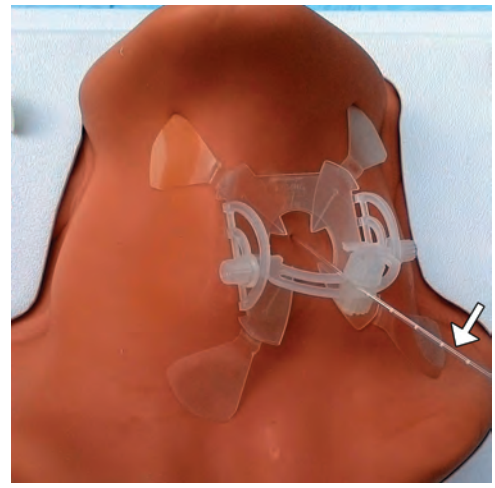

**FIG 2.** Photograph shows the laser applicator (Medtronic, Minneapolis, Minnesota) (*arrow*) inserted into the neck phantom (CIRS, Norfolk, Virginia) and supported by a skin-adhesive device (NeoRad).

Lesion targeting has traditionally been performed using "in-and-out" techniques in closed-bore MR imaging scanners with control imaging performed inside the bore, and needle adjustments, outside the bore. Alternatively, the process of targeting the lesion can be expedited using guidance and navigation systems, such as virtual 3D-MR imaging with real-time overlay of an optically tracked biopsy needle using reference markers or the interventional MR imaging suite (iSuite) image guidance and mapping system (Philips Research Labs, Hamburg, Germany), which facilitates triangulation of the laser probe insertion trajectory (Fig 1).[26] The biopsy needles and laser probe used for the procedure can be secured in position using commercially available skin-adhesive holder devices, such as the Simplify needle holder (NeoRad, Oslo, Norway) or Cradles Needle Localization Wire Protectors (Beekley Medical, Norcross, Georgia) (Fig 2).

### MR Thermography

In general, the success of laser interstitial thermal ablation depends on accurate insertion of the laser fiber into the target lesion,

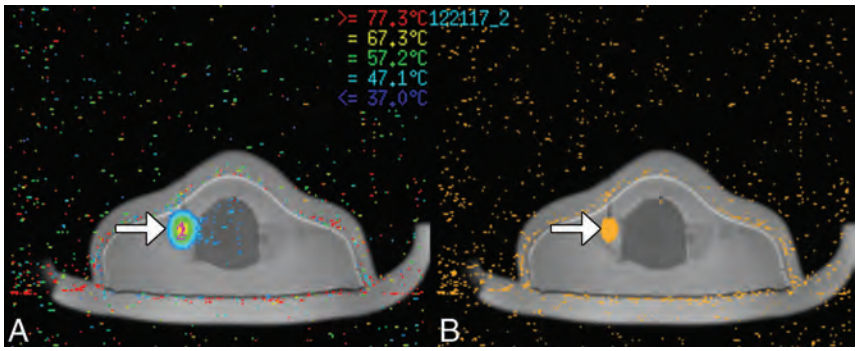


**FIG 3.** MR thermography during laser ablation. Temperature map acquired using the proton resonance frequency shift (*A*) and heat-damage model in a neck phantom (*B*) shows the ablation zone surrounding the tip of the probe (*arrows*).

real-time monitoring of the effects of the treatment, and subsequent evaluation of the extent of thermal tissue damage.[19] MR thermography is a validated noninvasive imaging technique that can provide accurate monitoring during laser ablation.[19,27] Several MR thermography methods have been developed, including sequences based on the proton resonance frequency, the diffusion coefficient, T1 and T2 relaxation times, magnetization transfer, proton density, and temperature-sensitive contrast agents.[4,24,27] In particular, proton resonance frequency techniques use temperature-induced effects of chemical shift, in which the temperature difference is directly proportional to the phase difference. This method provides accurate temperature measurements in the temperature range of interest for thermal ablation.[24]

A thermal dose can be calculated from a map of temperature as a function of time and is used for the prediction of tissue destruction (Fig 3).[7] Ultimately, continuous MR thermometry during thermal ablation procedures can help optimize safe thermal therapy delivery. Although the adequacy of ablation is estimated on the basis of the laser ablation system–generated damage model, it is important to obtain an immediate postablation MR imaging scan to ensure adequate ablation of the lesion.

Important technical considerations for performing MR imaging–guided laser ablation include coil selection and assessing the quality of MR imaging sequences in the head and neck region. For example, the use of whole-body coils contained within the closed bore of a high-field-strength MR imaging scanner is an ergonomic option with fewer obstacles between the interventionalist and the patient. Although these types of coils yield lower signal-to-noise compared with head and neck neurovascular coils, for example, the image quality may be generally adequate for clinical use.[28]

Furthermore, the quality of MR thermography can be limited by the presence of susceptibility artifacts from hemorrhage, calcifications, or underlying surgical hardware; the excessive presence of fat surrounding the lesion; and misregistration artifacts related to motion.[3] Ultimately, interstitial laser ablation should be performed only with MR thermography if a lesion can be adequately discerned on MR thermography images obtained as part of the pretreatment MR imaging.

## CONCLUSIONS

Interstitial laser ablation is a minimally invasive and potentially cost-effect technique that can be used to treat a variety of head and neck lesions, including benign thyroid nodules, vascular malformations, and cancers with low complication rates. In particular, the use of MR imaging guidance for inserting the laser applicator and the use of MR thermography for monitoring temperature changes during the procedure can help optimize safety and efficacy.

## ACKNOWLEDGMENTS

We thank Amy Schneider of Medtronic for assistance in performing the laser ablation procedure.

## REFERENCES

1. Mensel B, Weigel C, Hosten N. **Laser-induced thermotherapy.** *Recent Results Cancer Res* 2006;167:69–75 CrossRef Medline
2. Stafford RJ, Fuentes D, Elliott AA, et al. **Laser-induced thermal therapy for tumor ablation.** *Crit Rev Biomed Eng* 2010;38:79–100 CrossRef Medline
3. Medvid R, Ruiz A, Komotar RJ, et al. **Current applications of MRI-guided laser interstitial thermal therapy in the treatment of brain neoplasms and epilepsy: a radiologic and neurosurgical overview.** *AJNR Am J Neuroradiol* 2015;36:1998–2006 CrossRef Medline
4. Schober R, Bettag M, Sabel M, et al. **Fine structure of zonal changes in experimental Nd:YAG laser-induced interstitial hyperthermia.** *Lasers Surg Med* 1993;13:234–41 CrossRef Medline
5. Kickhefel A, Rosenberg C, Weiss CR, et al. **Clinical evaluation of MR temperature monitoring of laser-induced thermotherapy in human liver using the proton-resonance-frequency method and predictive models of cell death.** *J Magn Reson Imaging* 2011;33:704–12 CrossRef Medline
6. Boss A, Graf H, Müller-Bierl B, et al. **Magnetic susceptibility effects on the accuracy of MR temperature monitoring by the proton resonance frequency method.** *J Magn Reson Imaging* 2005;22:813–20 CrossRef Medline
7. Oto A, Sethi I, Karczmar G, et al. **MR imaging-guided focal laser ablation for prostate cancer: phase I trial.** *Radiology* 2013;267:932–40 CrossRef Medline
8. Sercarz JA, Bublik M, Joo J, et al. **Outcomes of laser thermal therapy for recurrent head and neck cancer.** *Otolaryngol Head Neck Surg* 2010;142:344–50 CrossRef Medline
9. Joo J, Sercarz JA, Paolini AA, et al. **Laser-induced thermal therapy and cisplatin for recurrent head and neck cancer: a case characterized by an unusually long disease-free survival.** *Ear Nose Throat J* 2009;88:E13–E16 Medline
10. Banerjee C, Snelling B, Berger MH, et al. **The role of magnetic resonance-guided laser ablation in neurooncology.** *Br J Neurosurg* 2015;29:192–96 CrossRef Medline
11. Carpentier A, McNichols RJ, Stafford RJ, et al. **Laser thermal therapy: real-time MRI-guided and computer-controlled procedures for metastatic brain tumors.** *Lasers Surg Med* 2011;43:943–50 CrossRef Medline
12. Carpentier A, McNichols RJ, Stafford RJ, et al. **Real-time magnetic resonance-guided laser thermal therapy for focal metastatic brain tumors.** *Neurosurgery* 2008;63:ONS21–28; discussion ONS28–29 Medline
13. Leuthardt EC, Voigt J, Kim AH, et al. **A single-center cost analysis of treating primary and metastatic brain cancers with either brain Laser Interstitial Thermal Therapy (LITT) or craniotomy.** *Pharmacoecon Open* 2017;1:53–63 CrossRef Medline
14. Voigt JD, Barnett G. **The value of using a brain laser interstitial thermal therapy (LITT) system in patients presenting with high**

**grade gliomas where maximal safe resection may not be feasible.** *Cost Eff Resour Alloc* 2016;14:6 CrossRef Medline
15. Eckardt A, Barth EL, Kokemueller H, et al. **Recurrent carcinoma of the head and neck: treatment strategies and survival analysis in a 20-year period.** *Oral Oncol* 2004;40:427–32 CrossRef Medline
16. Pacella CM, Bizzarri G, Spiezia S, et al. **Thyroid tissue: US-guided percutaneous laser thermal ablation.** *Radiology* 2004;232:272–80 CrossRef Medline
17. Shahrzad MK. **Laser thermal ablation of thyroid benign nodules.** *J Lasers Med Sci* 2015;6:151–56 CrossRef Medline
18. Achille G, Zizzi S, Di Stasio E, et al. **Ultrasound-guided percutaneous laser ablation in treating symptomatic solid benign thyroid nodules: our experience in 45 patients.** *Head Neck* 2016;38: 677–82 CrossRef Medline
19. Mack MG, Vogl TJ. **MR-guided ablation of head and neck tumors.** *Neuroimaging Clin N Am* 2004;14:853–59 CrossRef Medline
20. Eyrich GK, Bruder E, Hilfiker P, et al. **Temperature mapping of magnetic resonance-guided laser interstitial thermal therapy (LITT) in lymphangiomas of the head and neck.** *Lasers Surg Med* 2000;26: 467–76 CrossRef Medline
21. Feyh J, Gutmann R, Leunig A, et al. **MRI-guided laser interstitial thermal therapy (LITT) of head and neck tumors: progress with a new method.** *J Clin Laser Med Surg* 1996;14:361–66 Medline
22. Mainini AP, Monaco C, Pescatori LC, et al. **Image-guided thermal ablation of benign thyroid nodules.** *J Ultrasound* 2017;20:11–22 CrossRef Medline
23. Moche M, Trampel R, Kahn T, et al. **Navigation concepts for MR image-guided interventions.** *J Magn Reson Imaging* 2008;27:276–91 CrossRef Medline
24. Weiss CR, Nour SG, Lewin JS. **MR-guided biopsy: a review of current techniques and applications.** *J Magn Reson Imaging* 2008;27: 311–25 CrossRef Medline
25. Cleary K, Peters TM. **Image-guided interventions: technology review and clinical applications.** *Annu Rev Biomed Eng* 2010;12: 119–42 CrossRef Medline
26. Busse H, Riedel T, Garnov N, et al. **Targeting accuracy, procedure times and user experience of 240 experimental MRI biopsies guided by a clinical add-on navigation system.** *PLoS One* 2015;10:e0134370 CrossRef Medline
27. Quesson B, de Zwart JA, Moonen CT. **Magnetic resonance temperature imaging for guidance of thermotherapy.** *J Magn Reson Imaging* 2000;12:525–33 CrossRef Medline
28. Ginat DT, Anthony GJ, Christoforidis G, et al. **Comparison between whole-body and head and neck neurovascular coils for 3-T magnetic resonance proton resonance frequency shift thermography guidance in the head and neck region.** *Lasers Med Sci* 2018;33: 369–73 CrossRef Medline

# Gadolinium Deposition in Deep Brain Structures: Relationship with Dose and Ionization of Linear Gadolinium-Based Contrast Agents

H. Kang, M. Hii, M. Le, R. Tam, A. Riddehough, A. Traboulsee, S. Kolind, M.S. Freedman, and D.K.B. Li

## ABSTRACT

**BACKGROUND AND PURPOSE:** Dose-dependent association between hyperintensity in deep brain structures on unenhanced T1WIs and gadolinium-based contrast agent administrations has been demonstrated with subsequent histopathological confirmation of gadolinium deposition. Our aim was to determine whether greater exposure to linear gadolinium-based contrast agent administration is associated with higher signal intensity in deep brain structures on unenhanced T1-weighted MR imaging. Secondary objective was to compare signal intensity differences between ionic and nonionic linear gadolinium-based contrast agents.

**MATERIALS AND METHODS:** Subjects with secondary-progressive MS originally enrolled in a multicenter clinical trial were studied retrospectively. Eighty subjects (high-exposure cohort) received 9 linear gadolinium-based contrast agent administrations (30 nonionic/50 ionic) between week −4 and year 1 and a tenth administration by year 2. One hundred fifteen subjects (low-exposure cohort) received 2 administrations (40 nonionic/75 ionic) between week −4 and year 1 and a third administration by year 2. Signal intensities were measured on unenhanced T1WIs by placing sample-points on the dentate nucleus, globus pallidus, caudate, thalamus, pons, and white matter, and they were normalized using the following ratios: dentate/pons, globus pallidus/white matter, caudate/white matter, and thalamus/white matter.

**RESULTS:** Between week −4 and year 1, subjects in the high-exposure cohort showed increased signal intensity ratios in all regions ($P < .01$), while the low-exposure cohort showed only an increase in the dentate nucleus ($P = .003$). Between years 1 and 2, when both cohorts received only 1 additional gadolinium-based contrast agent, no significant changes were observed. In the high-exposure cohort, significantly higher changes in signal intensity ratios were observed in subjects receiving linear nonionic than in those receiving linear ionic gadolinium-based contrast agents.

**CONCLUSIONS:** Hyperintensity in deep brain structures from gadolinium deposition is related to the number of doses and the type of linear gadolinium-based contrast agent (nonionic greater than ionic) administration.

**ABBREVIATIONS:** CD = caudate; DN = dentate nucleus; GBCA = gadolinium-based contrast agent; GP = globus pallidus; SI = signal intensity; TH = thalamus

Gadolinium-based contrast agents (GBCAs) are frequently used in clinical MR imaging for their paramagnetic properties to shorten the T1 relaxation time of adjacent water protons and increase the visibility of abnormal tissues, hence improving diagnostic value.[1] However, free gadolinium is a toxic heavy metal *in vivo* and necessitates chelation to polyaminocarboxylic acid ligands to be excreted safely, primarily through the kidneys. Based on the chemical structures, there are 4 categories of chelating agents: macrocyclic ionic and nonionic, and linear ionic and nonionic. Stability and the ability to prevent free gadolinium from dissociating with the ligand differs for each type, with the macrocyclic being the most stable, followed by linear ionic, and linear nonionic being the least stable.[2,3]

In 2014, Kanda et al[4] first reported that increased signal intensity (SI) in the dentate nucleus (DN) and globus pallidus (GP) on unenhanced T1WI was associated with repeat GBCA exposure. Subsequent cadaveric histopathologic studies showed that the T1 hyperintensity represented deposition of gadolinium in neuronal tissues.[5,6] Since then, numerous studies have shown multiple ad-

Received April 14, 2018; accepted after revision June 20.

From the Department of Radiology (H.K., M.L., R.T., S.K., D.K.B.L.), University of British Columbia MS/MRI Research Group (M.H., R.T., A.R., A.T., S.K., D.K.B.L.), Department of Medicine and Division of Neurology (A.T., S.K., D.K.B.L.), Department of Physics and Astronomy (S.K.), University of British Columbia, Vancouver, British Columbia, Canada; and Department of Medicine and Division of Neurology (M.S.F.), University of Ottawa and the Ottawa Hospital Research Institute, Ottawa, Canada.

Paper previously presented at: Annual Meeting of the American Society of Neuroradiology and the Foundation of the ASNR Symposium, June 2–7, 2018; Vancouver, British Columbia, Canada.

Please address correspondence to Heejun Kang, MD, Department of Radiology, UBC Hospital, 2211 Wesbrook Mall, Vancouver, BC V6T 2B5; e-mail: tkang@alumni.ubc.ca; @tkang90


Indicates article with supplemental on-line photos.

http://dx.doi.org/10.3174/ajnr.A5751

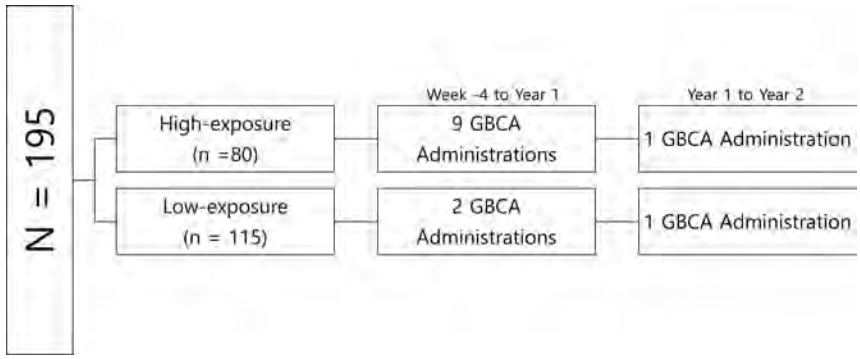


**FIG 1.** Gadolinium-based contrast agent administration schedule for high- and low-exposure cohorts.

ministrations of linear GBCAs to be associated with T1 hyperintensity in the deep brain structures.[4,6-13] However, many of these studies did not have a control group and had a relatively small and heterogeneous sample population.

Furthermore, there is a paucity of literature comparing linear ionic with linear nonionic GBCAs. Ramalho et al[14] was the only group at the time that directly compared the two and showed an increase in T1 hyperintensity with linear nonionic GBCA (gadodiamide) but not with linear ionic GBCA (gadobenate dimeglumine). Although other studies did demonstrate an increase in T1 hyperintensity with linear ionic GBCAs, direct comparison with linear nonionic GBCAs was not made.[4,7,10]

Our study used a cohort of 195 subjects with secondary-progressive MS who participated in a clinical trial and underwent 2 different contrast-enhanced MR imaging follow-up schedules (10 versus 3 GBCA administrations) over 2 years. Our goal was to determine whether multiple GBCA administrations were associated with increased T1 hyperintensity in deep brain structures on unenhanced T1WI and whether there was a dose relationship to these changes. Our secondary objective was to compare linear ionic with linear nonionic GBCAs to determine whether a difference could be observed in the degree of T1 SI change.

## MATERIALS AND METHODS

### Subjects

MR imaging data were obtained from subjects with secondary-progressive MS who were initially enrolled in a 2-year, randomized, double-blind, placebo-controlled trial assessing the efficacy of dirucotide (MBP8298) (clinicaltrials.gov NCT00869726 and ISRCTN98373474).[15] Six hundred twelve subjects were recruited from 47 centers in 10 countries.

Of the 612 subjects, 553 completed the trial and had usable MR imaging datasets. Ethics committees at each site approved the study, and all subjects signed written informed consents before protocol-required procedures. The details of the design, inclusion, and exclusion criteria and results of the 2-year study were previously reported.[15] There were no significant differences regarding clinical or MR imaging outcomes between the treatment and placebo cohorts, except the cumulative number of new and enlarging T2 lesions that favored the placebo cohort ($P = .03$).[15] Therefore, the subjects in both treatment and placebo arms were pooled together to be analyzed in the current study. MR imaging data were centrally analyzed by our research institution (UBC MS/MRI Research Group).

Exclusion criteria for the MR imaging data of this retrospective study were the absence of unenhanced T1WI, unsatisfactory image quality due to artifacts, and the presence of visible lesions in both the left and right DN, thalamus (TH), GP, caudate (CD), and/or frontal white matter in any of the time points. If the MR imaging data met the exclusion criteria, then all imaging studies for the same subject at other time points were removed from the study analysis. In addition, subjects who were administered macrocyclic GBCAs (the use of these agents was uncommon during the study period) and/or were scanned on a different MR imaging scanner for any of their follow-up studies were excluded.

### GBCA Administration and Type

The original study population followed 2 distinct contrast-enhanced MR imaging follow-up schedules: In the first 100 subjects (high-exposure cohort), 2 MRIs (week −4, week 0) were performed before the first dose of study medication, followed by further MRIs at weeks 4, 8, and 12. Another MR imaging was then performed immediately before the next dose (week 26), followed by 3 further MRIs at weeks 30, 34, and 38. Annual MRIs were then performed at years 1 and 2 (weeks 52 and 104). Overall, for the year 1 pre-GBCA assessment, 9 GBCA injections were given between week −4 and year 1, and for the year 2 pre-GBCA assessment, an additional GBCA was administered (from the year 1 MR imaging). The next 453 subjects (low-exposure cohort) had 2 MRIs performed before the first dose of medication (weeks −4 and 0) with annual MRIs at years 1 and 2 (weeks 52 and 104). Therefore, for the year 1 pre-GBCA assessment, 2 GBCA injections had been given, and similarly, for the year 2 pre-GBCA assessment, an additional GBCA injection was administered (from the year 1 MR imaging) (Fig 1). A random sample of the subjects in the low-exposure cohort was selected proportionately from each high-exposure cohort center. Subjects for this study received a standard single dose of either a linear nonionic agent (gadodiamide, Omniscan; GE Healthcare, Piscataway, New Jersey) or a linear ionic agent (gadopentetate dimeglumine, Magnevist; Bayer HealthCare Pharmaceuticals, Wayne, New Jersey), depending on the center preference. The same GBCA was used throughout the duration of the study.

### MR Imaging Protocol, Processing, and Analysis

Studies were performed with either 1T, 1.5T, or 3T MR imaging scanners (Table 1) using a standardized imaging protocol with whole-brain coverage, 3-mm contiguous axial proton density, T2WI, and pre- and postcontrast (0.1 mmol/kg gadolinium with a 5-minute delay) fast/turbo spin-echo T1WI (TE, 9–20 ms; TR, 600–800 ms; and slice gap, 0 mm). Changes to the MR imaging protocol were not permitted during the trial period.

Group-wise registration was performed using the T2WIs for

**Table 1: Demographics**

| Characteristic | High-Exposure Group (*n* = 80) | Low-Exposure Group (*n* = 115) | *P* Value |
|---|---|---|---|
| Age (yr)[a] | 51 ± 8 (34–64) | 52 ± 8 (27–82) | NS |
| Sex | | | |
| Female | 52 (65%) | 78 (68%) | |
| Male | 28 (35%) | 37 (32%) | |
| Weight (kg)[a] | 72 ± 16 (48–120) | 71 ± 15 (48–117) | |
| Gadolinium type | | | |
| Gadodiamide | 30 (37.5%) | 40 (34.8%) | |
| Gadopentetate dimeglumine | 50 (62.5%) | 75 (65.2%) | |
| Treatment assignment | | | |
| MBP8298 | 41 (51%) | 57 (50%) | |
| Placebo | 39 (49%) | 58 (50%) | |
| EDSS at week −4[a] | 5.57 ± 1.03 (3–6.5) | 5.34 ± 1.13 (3–6.5) | NS |
| EDSS at year 2[a] | 5.61 ± 1.00 (3.5–6.5) | 5.66 ± 1.19 (2–7.5) | NS |
| Disease duration (yr)[a] | 13.6 ± 5.5 (4–25) (*n* = 65) | 11.7 ± 5.1 (2–27) (*n* = 84) | NS |
| Magnet strength | | | |
| 1T | 0 (0%) | 4 (3%) | |
| 1.5T | 58 (73%) | 93 (81%) | |
| 3T | 22 (27%) | 18 (16%) | |

**Note:**—EDSS indicates Expanded Disability Status Scale; NS, not significant.
[a] Data are means ± SD (range).

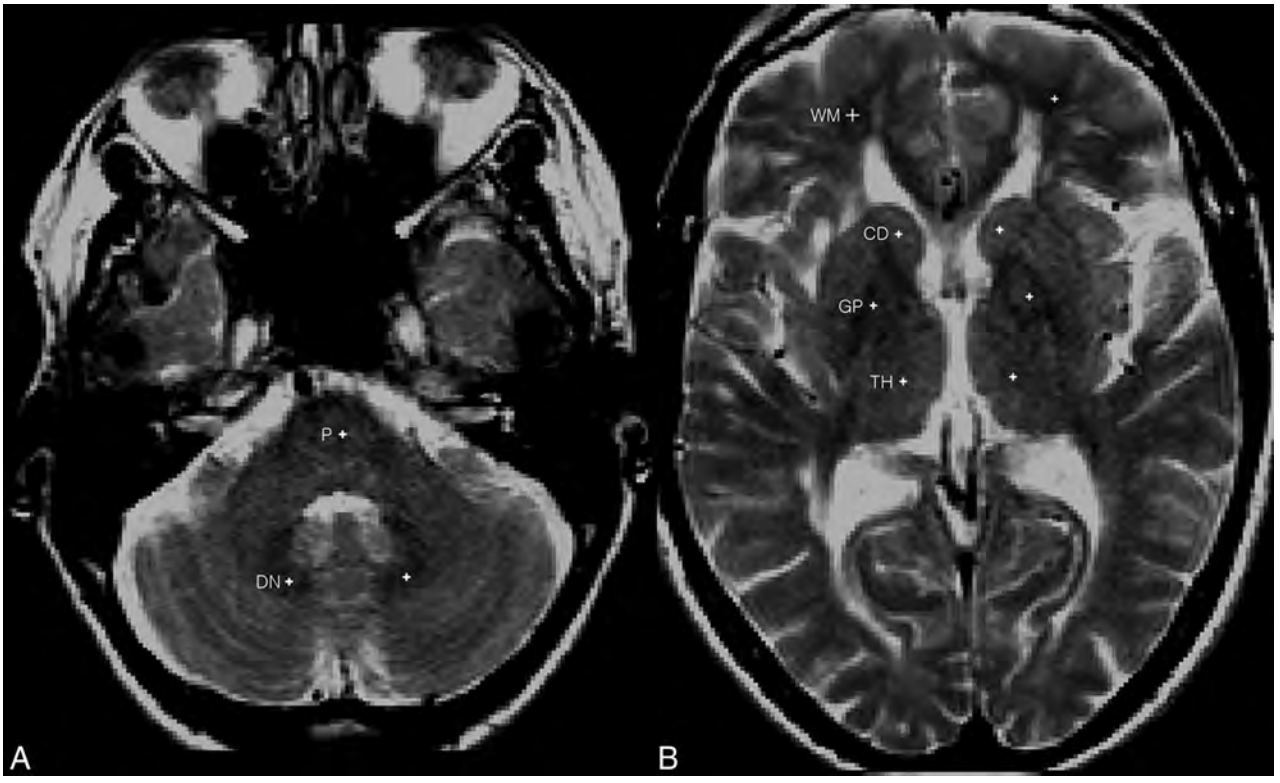


**FIG 2.** *A*, T2-weighted spin-echo images at the level of the posterior fossa with sample-points (*white cross*) placed at the center of the dentate and pons (P). *B*, T2-weighted spin-echo images at the level of the third ventricle with sample-points (*white cross*) placed at the center of the caudate, thalamus, globus pallidus, and white matter.

all subjects across 3 time points (week −4, year 1, and year 2) to ensure that the exact same location was measured across all time points. The sample-points (1 × 1 pixel; 1 pixel = 0.937 mm) were manually placed on the T2WIs by a single reader (M.L.) blinded to cohort assignment at our research institution. T2WIs were chosen instead of T1WIs to blind the reader from any visibly obvious T1 hyperintensity that may bias sample-point placement. In addition, T2WIs enabled the reader to identify the deep brain structures more easily. Sample-points were placed at the center of the left DN, left GP, left TH, left CD head, central pons, and left frontal WM (Fig 2). Normal-appearing WM that was free of any visible lesions was used. If the left side could not be assessed due to the presence of artifacts or visible lesions, then the right side was used. If the deep brain structures were unclear on T2WIs, the same section position of proton density images was used to guide placement. The final sample-point position was confirmed by a second reader (H.K.), and the sample-point measurement was conducted once. The sample-points were then mapped onto the

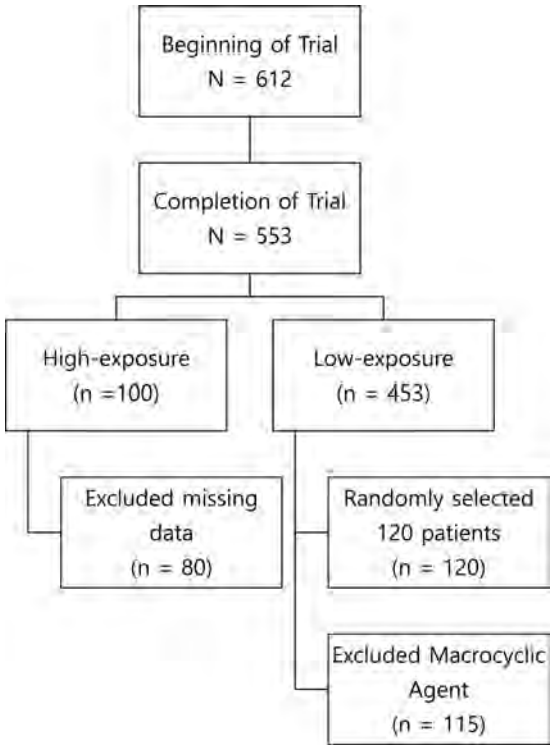


**FIG 3.** Patient disposition.

original precontrast (ie, unenhanced) T1WIs, and mean T1 SIs were obtained. Normalization of the mean T1 SI was performed by calculating the following ratios: DN/pons, GP/WM, CD/WM, and TH/WM.

### *Statistical Analysis*

Statistical analysis was performed with a commercially available medical statistical package (GraphPad Prism software; GraphPad Software, San Diego, California). The two-sample paired *t* test was used to evaluate the SI changes in the DN/pons, GP/WM, TH/WM, and CD/WM between week −4 and year 1, years 1 and 2, and week −4 and year 2 for the high-exposure and low-exposure cohorts. The two-sample unpaired *t* test was used to compare the SI changes in the DN/pons, GP/WM, TH/WM, and CD/WM between the subjects receiving linear nonionic versus the subjects receiving linear ionic GBCAs in the high-exposure cohort from week −4 to year 2. For all statistical tests, the level of significance was set at $P \leq .05$.

## RESULTS

Of the 100 subjects in the high-exposure cohort, 19 had missing MR imaging data at different time points and 1 subject had a major scanner change during follow-up, hence they were excluded. Overall, 80 subjects had complete MR imaging scan sets that also met the acceptance criteria for T1 SI analysis. Of the 453 subjects in the low-exposure cohort, 120 were randomly selected for analysis in which each high-exposure cohort center was proportionally represented (Fig 3). Five subjects from the low-exposure cohort were administered a macrocyclic agent and were excluded from the analysis. The high- and low-exposure cohorts had similar baseline characteristics (Table 1).

In the high-exposure cohort, 30 subjects received a linear nonionic agent (gadodiamide, Omniscan), while 50 subjects received a linear ionic agent (gadopentetate dimeglumine, Magnevist). For the low-exposure cohort, 40 subjects received a linear nonionic agent (gadodiamide, Omniscan) and 75 subjects received a linear ionic agent (gadopentetate dimeglumine, Magnevist). In the high-exposure cohort, the left DN or the left WM for 2 subjects was replaced with the right side for all 3 time points due to the presence of a visible lesion. In the low-exposure group, 1 subject's left WM showed a visible lesion and the right side was used instead for all 3 time points.

Between week −4 and year 1, there were significant absolute increases in all measured SI ratios (mean ± SD) in the high-exposure group (DN/pons: 0.04 ± 0.09 [relative increase of +4%]; GP/WM: 0.05 ± 0.09 [relative increase of +5%]; CD/WM: 0.03 ± 0.08 [relative increase of +3%]; and TH/WM: 0.03 ± 0.09 [relative increase of +3%]) (Table 2 and Fig 4), while only the DN/pons ratio showed a significant increase in the low-exposure group of 0.05 ± 0.17 (relative increase of +5%) (Table 3). Between years 1 and 2, when both cohorts received only 1 additional GBCA injection, no significant difference was observed in all SI ratios (Tables 2 and 3). Overall, from week −4 to year 2, significant SI increases were seen in all deep brain structures in the high-exposure cohort, but only the DN/pons ratio continued to show a significant increase in the low-exposure group (Tables 2 and 3). In the high-exposure group, 1 outlier was identified in the GP/WM and CD/WM SI measurements (On-Line Fig 1); and in the low-exposure group, 6 outliers in the DN/pons and 1 outlier in the GP/WM, CD/WM, and TH/WM SI measurements were demonstrated (On-Line Fig 2). The overall results and statistical significance remained consistent when the analysis was repeated with the outliers excluded.

Subgroup analysis of the subjects in the high-exposure cohort who received linear nonionic GBCA showed a significant increase in all SI ratios from week −4 to year 2 (Table 4). In comparison, for subjects who received a linear ionic GBCA, a significant increase was detected for only the DN/pons and CD/WM ratios (Table 4). There was more than a 2-fold difference in the DN/pons ratios, where the linear nonionic GBCA group demonstrated an average of 0.08 ± 0.09 (7.8%) increase, compared with 0.03 ± 0.09 (3.3%) in the linear ionic group ($P = .02$).

## DISCUSSION

There was a dose-dependent relationship between the number of linear GBCA administrations and the SI ratio increase in deep brain structures on unenhanced T1WI. After receiving 9 GBCA administrations, the high-exposure cohort demonstrated significant increases in all measured SI ratios (DN, GP, CD, and TH), while only the DN showed a significant increase in the low-exposure group after 2 GBCA administrations during the same period. This finding signifies that the larger number of GBCA administrations was a major factor in a greater number of deep brain structures demonstrating significant SI ratio increases in the high-exposure cohort compared to the low-exposure cohort, supporting a dose relationship. This result is in keeping with previous retrospective studies that have also demonstrated a greater increase in measured SI ratios to be related to multiple linear GBCA

**Table 2: Absolute and relative increase in signal intensity ratios for the high-exposure cohort[a]**

| | Δ Week −4 to Year 1 | *P* Value | Δ Year 1 to Year 2 | *P* Value | Δ Week −4 to Year 2 | *P* Value |
|---|---|---|---|---|---|---|
| L. DN | 0.04 ± 0.09 (4%) | <.001 | 0.01 ± 0.09 (1%) | NS | 0.05 ± 0.09 (5%) | <.001 |
| L. GP | 0.05 ± 0.09 (5%) | <.001 | −0.02 ± 0.11 (−1%) | NS | 0.03 ± 0.10 (3%) | .005 |
| L. CD | 0.03 ± 0.08 (3%) | <.001 | 0 ± 0.11 (0%) | NS | 0.03 ± 0.09 (3%) | .005 |
| L. TH | 0.03 ± 0.09 (3%) | .01 | 0 ± 0.11 (0%) | NS | 0.03 ± 0.09 (3%) | .01 |

**Note:**—L. indicates left; NS, not significant.
[a] Data are absolute (mean ± SD) and relative (%) increases.

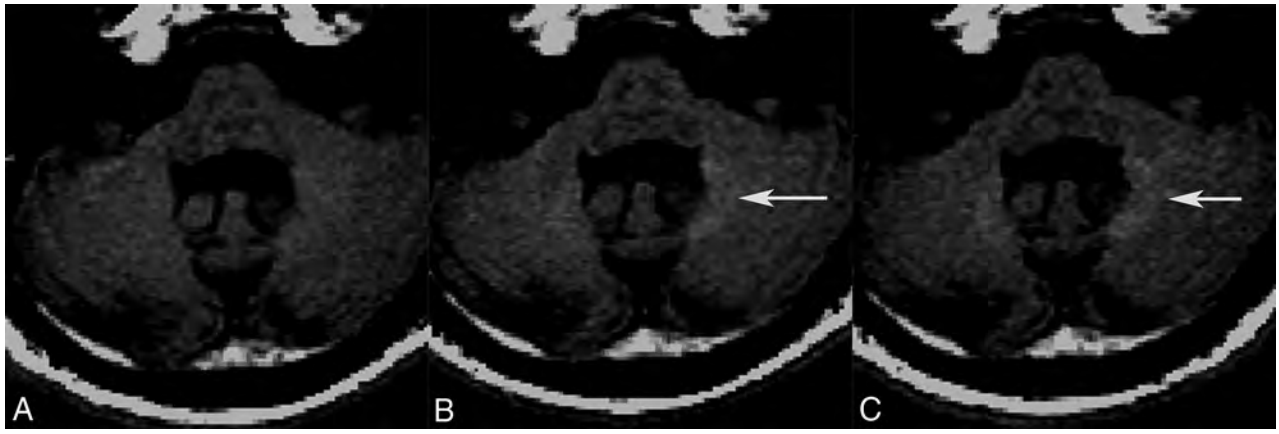


**FIG 4.** Unenhanced axial fast spin-echo T1-weighted MR images of a 48-year-old man in the high-exposure cohort who received linear nonionic GBCA. Images were obtained at week −4 (*A*), year 1 (*B*), and year 2 (*C*). A significant increase in T1 signal intensity is visualized in the dentate by year 1 (*arrow*), which persisted to year 2 (*arrow*).

**Table 3: Absolute and relative increase in signal intensity ratios for the low-exposure cohort[a]**

| | Δ Week −4 to Year 1 | *P* Value | Δ Year 1 to Year 2 | *P* Value | Δ Week −4 to Year 2 | *P* Value |
|---|---|---|---|---|---|---|
| L. DN | 0.05 ± 0.17 (5%) | .003 | 0 ± 0.20 (0%) | NS | 0.04 ± 0.15 (4%) | .003 |
| L. GP | 0.01 ± 0.09 (1%) | NS | 0 ± 0.17 (0%) | NS | 0 ± 0.18 (0%) | NS |
| L. CD | 0.01 ± 0.09 (1%) | NS | 0 ± 0.22 (0%) | NS | 0 ± 0.21 (0%) | NS |
| L. TH | 0 ± 0.09 (0%) | NS | 0.01 ± 0.18 (1%) | NS | 0.01 ± 0.19 (1%) | NS |

**Note:**—L. indicates left; NS, not significant.
[a] Data are absolute (mean ± SD) and relative (%) increases.

**Table 4: Absolute and relative increase in signal intensity ratios in subjects who received linear nonionic and linear ionic GBCA in the high-exposure cohort[a]**

| | Δ Week −4 to Year 2 | | | |
|---|---|---|---|---|
| | Linear Nonionic | *P* Value | Linear Ionic | *P* Value |
| L. DN | 0.08 ± 0.09 (8%) | <.001 | 0.03 ± 0.09 (3%) | .01 |
| L. GP | 0.06 ± 0.06 (6%) | <.001 | 0.02 ± 0.11 (2%) | NS |
| L. CD | 0.03 ± 0.06 (3%) | .03 | 0.03 ± 0.10 (3%) | .04 |
| L. TH | 0.04 ± 0.06 (4%) | .001 | 0.02 ± 0.10 (2%) | NS |

**Note:**—L. indicates left; NS, not significant.
[a] Data are absolute (mean ± SD) and relative (%) increases.

injections.[4,6,7,9-14,16-20] However, both the low- and the high-exposure cohorts had a significant-but-similar increase in the DN within the first year, and a clear dose effect was not seen for this structure. The DN is known to be more sensitive to gadolinium accumulation, and we could be seeing a dose-saturation effect in this structure, though the exact nature is not elucidated by our methodology. The importance of the number of GBCA administrations and its relationship with the T1 hyperintensities is further supported from the results between years 1 and 2, when no SI ratio changes were seen when the same high- and low-exposure cohorts received only 1 GBCA administration during the same period. We suspect that the increases in SI ratios were too minute and our measurement technique was not sensitive in detecting the changes.

The subgroup analysis in the high-exposure cohort comparing the linear ionic GBCA (gadopentetate dimeglumine) and the linear nonionic GBCA (gadodiamide) showed that the linear nonionic GBCA had the greatest increase in T1 hyperintensity in the deep brain structures. In particular, SI increases were demonstrated in all deep brain structures with the linear nonionic GBCA, whereas only the DN and CD demonstrated SI increase for the linear ionic GBCA. The DN demonstrated more than a 2-fold difference between the 2 classes of GBCAs, with an 8% increase in the linear nonionic GBCA compared with a 3% increase in the linear ionic GBCA ($P = .02$). These findings demonstrate *in vivo* the *in vitro* results by Frenzel et al,[2] who showed that the linear nonionic GBCAs was less stable than the linear ionic GBCAs. In their study, approximately 20% of the gadolinium of the linear nonionic GBCAs was released after 15 days of incubation in human serum, compared with 1%–2% of the gadolinium of the linear ionic GBCAs.[2] No gadolinium was released with the macrocyclic GBCAs.[2] Overall, these findings are in support of the hypothesis that the propensity of a GBCA to cause hyperintensity depends on the specific stability of the GBCA.[21]

Recent studies in rats propose that the penetration of GBCAs into the brain may occur through the blood-CSF barrier.[22,23] Once inside the brain tissue, the chemical stability and tendency of different GBCAs to dechelate may play an important role in the deposition of gadolinium in brain tissues. A new study by Frenzel et al[24] showed that after administration of linear ionic and linear nonionic GBCAs, a large portion of the gadolinium was detected in rat brain tissues as insoluble fractions or bound to soluble macromolecules, both presumed responsible for increased T1 SI due to their high relaxivity. These molecules were not found for macrocyclic GBCAs, which were exclusively detected in the soluble fraction, likely in their intact form, and demonstrated ongoing excretion.[24] However, more research is required to determine the clinical consequences of gadolinium deposition in either the chelated or dechelated form.

As demonstrated on a histopathologic study, the DN appears to be the most sensitive structure for detecting the T1 SI increase.[6] In our study, even after only 2 GBCA administrations, an increase in T1 hyperintensity was detected in the DN. One possible explanation is that the DN, along with other deep brain structures, is more susceptible to transmetalation, which allows dechelated gadolinium to form high-relaxivity macromolecules, as described above.[25]

Our study has several limitations. First, because the number of subjects receiving macrocyclic GBCA was small, this study could not examine the difference between the use of linear and macrocyclic GBCAs. Second, as with most studies on GBCA administration, the history of prior GBCA administrations and use of other agents could not be determined. Our study shows that there was at least a further increase in the SI during our observation window. Third, due to the multicenter nature of the study, several different MR imaging scanners were used, which may have introduced variations among scans, subjects, and scanners. Effort was made to minimize this issue by proportionately representing each center in both the high- and low-exposure cohorts. In addition, each follow-up MR imaging study was performed using the same MR imaging machine in the same center for each subject, and the SI was normalized with the reference standard extracted from the same image slice (pons and WM). The DN/pons ratio was chosen because McDonald et al[6] demonstrated in postmortem tissue 23-fold less gadolinium in the pons than in the DN. The WM tract was chosen for the CD, GP, and TH because it was hypothesized that the WM would accumulate less gadolinium than the gray matter structures, such as the TH. Fourth, the sample-point size used for the study measured 1 × 1 pixel, which likely introduced noise and fluctuations in the SI measurements. However, the small size was chosen to improve the accuracy of the sample-point placement on small structures such as the DN and CD, which was important when the sample-points were mapped from T2WI to T1WI. Furthermore, the degree of SI changes between the high- and low-exposure cohorts was large enough to overcome this limitation and demonstrated significant and relatively consistent results. Fifth, the study population had a pre-existing neurologic disease (MS), which may have confounded the results. However, the degree of interference is thought to be minimal because both cohorts had the same diagnosis with similar disease duration and Expanded Disability Status Scale scores without other potential confounding disease processes. Last, the physical, cognitive, and behavioral outcomes were not analyzed in this study; however, these are the subject of a current investigation.

## CONCLUSIONS

As little as 2 doses of GBCAs can result in an increased T1 SI in the DN that persists for at least 1 year after administration. T1 hyperintensity in the GP, CD, and TH is evident with greater cumulative doses. The degree of increase is related to the location (the DN being the most sensitive), the number of GBCA administrations, and the class of GBCA, with linear nonionic having the greater deposition.

Disclosures: Roger Tam—*RELATED*: *Other*: Jefferson Mooney, *Comments*: Mr Mooney donated $10,000 to support trainees in multiple sclerosis research at the University of British Columbia. This donation had no other restrictions on its use, and we used it to support Megan He, an undergraduate intern who worked on the technical aspects of the project*; *UNRELATED*: *Grants/Grants Pending*: Natural Sciences and Engineering Research Council of Canada, *Comments*: grant support from Natural Sciences and Engineering Research Council*; *Other*: Roche, Genzyme, *Comments*: Our group participates in sponsored clinical studies and clinical trials, which are unrelated to the submitted work.* Anthony Traboulsee—*UNRELATED*: *Other*: Consortium of Multiple Sclerosis Centers, *Comments*: honoraria to develop and disseminate MRI guidelines for diagnosing and monitoring patients with MS, including the role of gadolinium. Shannon Kolind—*UNRELATED*: *Consultancy*: Acorda Therapeutics; *Grants/Grants Pending*: Sanofi, Roche. Mark S. Freedman—*UNRELATED*: *Consultancy*: Actelion Pharmaceutical, Bayer Healthcare, Biogen, Chugai Pharmaceutical, Clene, EMD Serono Canada, Genzyme, Merck Serono, MedDay, Novartis, Roche, Sanofi, Teva Pharmaceutical Industries, *Comments*: consultant, ad board, steering committee; *Grants/Grants Pending*: Genzyme, *Comments*: Investigator Sponsored Studies (ISS)*; *Payment for Lectures Including Service on Speakers Bureaus*: Genzyme, Sanofi, Merck, Actelion, Biogen, EMD, Teva Pharmaceutical Industries; *Payment for Development of Educational Presentations*: Roche. David K.B. Li—*UNRELATED*: *Consultancy*: Vertex Pharmaceuticals, Opexa Therapeutics, Adelphi Group, *Comments*: I have been a consultant for Vertex Pharmaceuticals and served on the Data and Safety Advisory Board for Opexa Therapeutics and the Scientific Advisory Board for the Adelphi Group; *Grants/Grants Pending*: Genzyme, Hoffmann-la Roche, Merck Serono. Perceptive/Novartis, Sanofi-Aventis, *Comments*: I am the Emeritus Director of the University of British Columbia MS/MRI Research Group, which has received contracts to provide the central MRI analysis for MS clinical trials*; *Payment for Lectures Including Service on Speakers Bureaus*: Academy of Health Care Learning, Biogen Idec, Consortium of Multiple Sclerosis Centers, Novartis, Sanofi Genzyme, and Teva Pharmaceutical Industries; *Payment for Development of Educational Presentations*: Academy of Health Care Learning, *Comments*: Webinar. *Money paid to the institution in Canadian dollars.

## REFERENCES

1. Hao D, Ai T, Goerner F, et al. **MRI contrast agents: basic chemistry and safety.** *J Magn Reson Imaging* 2012;36:1060–71 CrossRef Medline
2. Frenzel T, Lengsfeld P, Schirmer H, et al. **Stability of gadolinium-based magnetic resonance imaging contrast agents in human serum at 37°C.** *Invest Radiol* 2008;43:817–28 CrossRef Medline
3. Tweedle MF, Wedeking P, Kumar K. **Biodistribution of radiolabeled, formulated gadopentetate, gadoteridol, gadoterate, and gadodiamide in mice and rats.** *Invest Radiol* 1995;30:372–80 CrossRef Medline
4. Kanda T, Ishii K, Kawaguchi H, et al. **High signal intensity in the dentate nucleus and globus pallidus on unenhanced T1-weighted MR images: relationship with increasing cumulative dose of a gadolinium-based contrast material.** *Radiology* 2014; 270:834–41 CrossRef Medline
5. Murata N, Gonzalez-Cuyar LF, Murata K, et al. **Macrocyclic and other non–group 1 gadolinium contrast agents deposit low levels of gadolinium in brain and bone tissue: preliminary results from 9 patients with normal renal function.** *Invest Radiol* 2016;51:447–53 CrossRef Medline
6. McDonald RJ, McDonald JS, Kallmes DF, et al. **Intracranial gadolin-**

**ium deposition after contrast-enhanced MR imaging.** *Radiology* 2015;275:772–82 CrossRef Medline
7. Kanda T, Osawa M, Oba H, et al. **High signal intensity in dentate nucleus on unenhanced T1-weighted MR images: association with linear versus macrocyclic gadolinium chelate administration.** *Radiology* 2015;275:803–09 CrossRef Medline
8. Quattrocchi CC, Mallio CA, Errante Y, et al. **Gadodiamide and dentate nucleus T1 hyperintensity in patients with meningioma evaluated by multiple follow-up contrast-enhanced magnetic resonance examinations with no systemic interval therapy.** *Invest Radiol* 2015; 50:470–72 CrossRef Medline
9. Errante Y, Cirimele V, Mallio CA, et al. **Progressive increase of T1 signal intensity of the dentate nucleus on unenhanced magnetic resonance images is associated with cumulative doses of intravenously administered gadodiamide in patients with normal renal function, suggesting dechelation.** *Invest Radiol* 2014;49: 685–90 CrossRef Medline
10. Radbruch A, Weberling LD, Kieslich PJ, et al. **Gadolinium retention in the dentate nucleus and globus pallidus is dependent on the class of contrast agent.** *Radiology* 2015;275:783–91 CrossRef Medline
11. Cao Y, Huang DQ, Shih G, et al. **Signal change in the dentate nucleus on T1-weighted MR images after multiple administrations of gadopentetate dimeglumine versus gadobutrol.** *AJR Am J Roentgenol* 2016;206:414–19 CrossRef Medline
12. Weberling LD, Kieslich PJ, Kickingereder P, et al. **Increased signal intensity in the dentate nucleus on unenhanced T1-weighted images after gadobenate dimeglumine administration.** *Invest Radiol* 2015;50:743–48 CrossRef Medline
13. Radbruch A, Weberling LD, Kieslich PJ, et al. **Intraindividual analysis of signal intensity changes in the dentate nucleus after consecutive serial applications of linear and macrocyclic gadolinium-based contrast agents.** *Invest Radiol* 2016;51:683–90 CrossRef Medline
14. Ramalho J, Castillo M, AlObaidy M, et al. **High signal intensity in globus pallidus and dentate nucleus on unenhanced T1-weighted MR images: evaluation of two linear gadolinium-based contrast agents.** *Radiology* 2015;276:836–44 CrossRef Medline
15. Freedman MS, Bar-Or A, Oger J, et al; MAESTRO-01 Investigators. **A phase III study evaluating the efficacy and safety of MBP8298 in secondary progressive MS.** *Neurology* 2011;77:1551–60 CrossRef Medline
16. Adin ME, Kleinberg L, Vaidya D, et al. **Hyperintense dentate nuclei on T1-weighted MRI: relation to repeat gadolinium administration.** *AJNR Am J Neuroradiol* 2015;36:1859–65 CrossRef Medline
17. Flood TF, Stence NV, Maloney JA, et al. **Pediatric brain: repeated exposure to linear gadolinium-based contrast material is associated with increased signal intensity at unenhanced T1-weighted MR imaging.** *Radiology* 2017;282:222–28 CrossRef Medline
18. Hu HH, Pokorney A, Towbin RB, et al. **Increased signal intensities in the dentate nucleus and globus pallidus on unenhanced T1-weighted images: evidence in children undergoing multiple gadolinium MRI exams.** *Pediatr Radiol* 2016;46:1590–98 CrossRef Medline
19. Ramalho J, Semelka RC, Ramalho M, et al. **Gadolinium-based contrast agent accumulation and toxicity: an update.** *AJNR Am J Neuroradiol* 2016;37:1192–98 CrossRef Medline
20. Zhang Y, Cao Y, Shih GL, et al. **Extent of signal hyperintensity on unenhanced T1-weighted brain MR images after more than 35 administrations of linear gadolinium-based contrast agents.** *Radiology* 2017;282:516–25 CrossRef Medline
21. Radbruch A. **Are some agents less likely to deposit gadolinium in the brain?** *Magn Reson Imaging* 2016;34:1351–54 CrossRef Medline
22. Jost G, Frenzel T, Lohrke J, et al. **Penetration and distribution of gadolinium-based contrast agents into the cerebrospinal fluid in healthy rats: a potential pathway of entry into the brain tissue.** *Eur Radiol* 2017;27:2877–85 CrossRef Medline
23. Öner AY, Barutcu B, Aykol Ş, et al. **Intrathecal contrast-enhanced magnetic resonance imaging-related brain signal changes: residual gadolinium deposition?** *Invest Radiol* 2017;52:195–97 CrossRef Medline
24. Frenzel T, Apte C, Jost G, et al. **Quantification and assessment of the chemical form of residual gadolinium in the brain after repeated administration of gadolinium-based contrast agents: comparative study in rats.** *Invest Radiol* 2017;52:396–404 CrossRef Medline
25. Gulani V, Calamante F, Shellock FG, et al; International Society for Magnetic Resonance in Medicine. **Chelated or dechelated gadolinium deposition: authors' reply.** *Lancet Neurol* 2017;16:955–56 CrossRef Medline

# Gadolinium Deposition within the Pediatric Brain: No Increased Intrinsic T1-Weighted Signal Intensity within the Dentate Nucleus following the Administration of a Minimum of 4 Doses of the Macrocyclic Agent Gadoteridol

J.R. Young, W.B. Pope, and M. Bobinski

## ABSTRACT

**BACKGROUND AND PURPOSE:** Our aim was to evaluate whether serial administration of the macrocyclic gadolinium-based contrast agent gadoteridol in children is associated with T1-weighted hyperintensity within the dentate nucleus, an imaging surrogate for gadolinium deposition.

**MATERIALS AND METHODS:** We identified a retrospective cohort of 10 patients younger than 18 years of age who underwent between 4 and 8 gadoteridol-enhanced MR imaging examinations of the brain from 2016 to 2017. For comparison, we identified a retrospective cohort of 9 pediatric patients who each underwent 6 gadodiamide-enhanced MR imaging examinations. For each examination, both dentate nuclei were contoured on unenhanced images and the mean dentate-to-pons signal intensity ratio was calculated. Dentate-to-pons signal intensity ratios from the first and last scans were compared using paired *t* tests.

**RESULTS:** In the gadoteridol group, there was no significant change in the mean dentate-to-pons signal intensity ratio from the first to the last scan (0.99 versus 0.99, $P = .59$). In the gadodiamide group, there was a significant increase in the mean dentate-to-pons signal intensity ratio from the first to the last scan (0.99 versus 1.10, $P = .001$).

**CONCLUSIONS:** Repeat administration of the macrocyclic gadolinium-based contrast agent gadoteridol in children was not associated with T1-weighted dentate hyperintensity, while the repeat administration of the linear gadolinium-based contrast agent gadodiamide was associated with T1-weighted dentate hyperintensity, presumably due to gadolinium deposition.

**ABBREVIATIONS:** DN-P SI = dentate-to-pons signal intensity; GBCA = gadolinium-based contrast agent

A number of recent studies have shown retention or deposition of gadolinium within multiple organs in the body, including the brain, following the serial administration of gadolinium-based contrast agents (GBCAs) for clinical MR imaging.[1-9] Intracranial gadolinium deposition has been associated with intrinsic T1-weighted hyperintensity, which is most detectable within the dentate nucleus and globus pallidus. To date, most studies investigating intracranial gadolinium deposition have focused on adults, with few studies evaluating gadolinium deposition in the pediatric brain.[1-16]

The clinical significance of intracranial gadolinium deposition has been controversial and remains uncertain. However, the pediatric brain may be more vulnerable to the potentially deleterious effects of gadolinium deposition because the pediatric brain is generally more susceptible to a variety of toxins.[17,18] Furthermore, the cumulative lifetime dose and duration of exposure to GBCAs may be greater in children than in adults. Thus, it remains important to identify the safest GBCAs for use in children. Recent studies evaluating pediatric intracranial gadolinium deposition have generally focused on the linear GBCA gadopentetate dimeglumine.[10-13] Few studies have evaluated the effect of the repeat administration of macrocyclic GBCAs in children. Radbruch et al[14] found that the repeat administration of the macrocyclic GBCA gadoterate meglumine in pediatric patients was not associated with T1-weighted dentate hyperintensity. Additionally, Tibussek et al[15] found that the serial administration of 2 macrocyclic agents gadoterate meglumine and gadoteridol was not associated with an increase in T1-weighted signal intensity in the dentate nucleus.

The lack of association between macrocyclic GBCAs and T1-weighted dentate hyperintensity was recently questioned by Rossi Espagnet et al,[16] who found that the repeat administration of gadoterate meglumine was associated with increased T1-weighted

Received February 9, 2018; accepted after revision June 5.

From the Department of Radiology (J.R.Y., M.B.), University of California Davis School of Medicine, Sacramento, California; and Department of Radiology (W.B.P.), David Geffen School of Medicine at University of California at Los Angeles, Los Angeles, California.

Please address correspondence to Jonathan R. Young, MD, University of California Davis School of Medicine, Department of Radiology, 4860 Y St, Suite 3100, Sacramento, CA 95817; e-mail: jroyoung@ucdavis.edu

http://dx.doi.org/10.3174/ajnr.A5748

**Patient characteristics**[a]

| Parameter | All Patients (*n* = 19 Patients) | Gadoteridol Group (*n* = 10 Patients) | Gadodiamide Group (*n* = 9 Patients) |
|---|---|---|---|
| Sex (No.) | | | |
| Male | 11 (58%) | 7 (70%) | 5 (56%) |
| Female | 8 (42%) | 3 (30%) | 4 (44%) |
| Age at first scan (yr)[a] | 7.5 (0.5–16.5) | 5.6 (0.5–13.4) | 9.6 (1.7–16.5) |
| No. of scans[a] | 6.1 (4–8) | 6.1 (4–8) | 6 (6) |
| Interval between first and last scans (yr)[a] | 0.92 (0.05–1.58) | 1.01 (0.31–1.58) | 0.81 (0.06–1.35) |
| History of chemotherapy (No.) | 9 (47%) | 4 (40%) | 5 (56%) |
| History of radiation (No.) | 6 (32%) | 1 (10%) | 5 (56%) |
| Diagnosis (No.) | | | |
| Tumor | 16 (84%) | 8 (80%) | 8 (89%) |
| Other[b] | 3 (16%) | 2 (20%) | 1 (11%) |

[a] Data are means. Ranges are in parentheses.

[b] Other diagnoses include a subgaleal abscess, an intracranial abscess, and a cavernous malformation.

hyperintensity within the dentate nucleus by quantitative ROI analysis. However, in the study by Rossi Espagnet et al,[16] there was no visible increase in T1-weighted dentate signal intensity.[19] To date, no published studies have examined the association between the repeat exclusive administration of the macrocyclic GBCA gadoteridol and T1-weighted signal intensity within the pediatric brain. The goal of this study was to determine whether the repeat exclusive administration of the macrocyclic GBCA gadoteridol in pediatric patients is associated with the development of T1-weighted hyperintensity within the dentate nucleus, an imaging surrogate for gadolinium deposition.

## MATERIALS AND METHODS

### *Patients*

With UC Davis School of Medicine institutional review board approval for this Health Insurance Portability and Accountability Act–compliant retrospective study and a waiver of informed consent, we queried the PACS of our institution and the electronic medical record to identify all pediatric patients younger than 18 years of age without posterior fossa disease who underwent between 4 and 8 gadoteridol-enhanced MR imaging examinations of the brain performed at our institution from 2016 to 2017 and who had not had prior exposure to any other GBCA. Patients with <4 MR imaging examinations were excluded because prior published studies have shown that at least 4 doses of gadolinium are required before progressively increasing T1-weighted hyperintensity within the brain is identified.[5] This query resulted in a historical cohort of 10 patients. For comparison, we identified a separate retrospective cohort of 9 patients younger than 18 years of age without posterior fossa disease who each underwent 6 gadodiamide-enhanced MR imaging examinations of the brain performed at our institution from 2008 to 2015 and who had not had prior exposure to any other GBCA. The standard pediatric dose of 0.1 mmol/kg was administered for both gadoteridol and gadodiamide.

Patient characteristics, including age, sex, diagnosis, history of chemotherapy, history of radiation, number of MR imaging examinations, and the time interval between the first and last scans are presented in the Table. Patient diagnoses were classified as tumoral (ganglioglioma, astrocytoma, choroid plexus carcinoma, lymphoma, dysembryoplastic neuroepithelial tumor, craniopharyngioma, germ cell tumor [including germinoma], neuroblastoma, pineoblastoma, Ewing sarcoma, and Langerhans cell histiocytosis) and nontumoral (subgaleal abscess, intracranial abscess, and cavernous malformation). None of the patients had a history of renal disease.

### *MR Imaging Examination*

All MR imaging examinations were performed on 1.5T (Signa HDxt or Optima MR450w; GE Healthcare, Milwaukee, Wisconsin) or 3T scanners (Signa HDxt; GE Healthcare). Three MR imaging protocols were used to obtain precontrast T1-weighted images of the brain: a routine axial T1-weighted spin-echo sequence (slice thickness = 5 mm, TR = 667 ms, TE = 14 ms, flip angle = 90°), an axial echo-spoiled gradient-echo volumetric sequence (slice thickness = 1 mm, TR = 10 ms, TE = 4 ms, flip angle = 20°), and an axial T1-weighted fluid-attenuated inversion recovery sequence (slice thickness = 5 mm, TR = 3180 ms, TE = 29 ms, TI = 1238 ms, flip angle = 90°). For each patient, the same MR imaging protocol was used for the first and last MR imaging examinations. Fifty-eight percent of patients (11/19) had a routine axial T1-weighted spin-echo sequence on the first and last MR imaging examinations; 21% of patients (4/19) had an axial echo-spoiled gradient-echo sequence on the first and last MR imaging examinations, while 21% of the patients (4/19) had an axial T1-weighted FLAIR sequence on the first and last MR imaging examinations. Furthermore, for 84% of the patients (16/19), imaging was performed on scanners of the same magnetic field strength for the first and last MR imaging examinations. Of these 16 patients, 8 (50%) had the first and last MR imaging examinations performed on a 1.5T scanner and 8 (50%) had the first and last MR imaging examinations performed on a 3T scanner.

### *Image Analysis*

For each axial precontrast T1-weighted examination, the right and left dentate nuclei were manually contoured on a single axial slice using polygonal ROIs on the PACS of our institution. The dentate nucleus was selected because it is the most frequently studied site of progressively increasing T1-weighted hyperintensity in the brain following repeat exposure to GBCAs. Additionally, McDonald et al[5,6] found that the dentate nucleus contained that highest median concentration of deposited gadolinium in their postmortem cohorts. For each patient, the dentate nuclei were identified on later MR imaging examinations in which the dentate nuclei appeared relatively hyperintense in comparison with surrounding cerebellar tissue. This information was then used to guide the contouring of the dentate nuclei on earlier MR imaging examinations in which the margins of the dentate nucleus were not well-delineated. In addition, T2-weighted images were used to help identify the dentate nuclei in some cases. Subsequently, a circular ROI with a diameter of 8 mm was manually placed in the central pons. The ratio of the mean signal intensity of

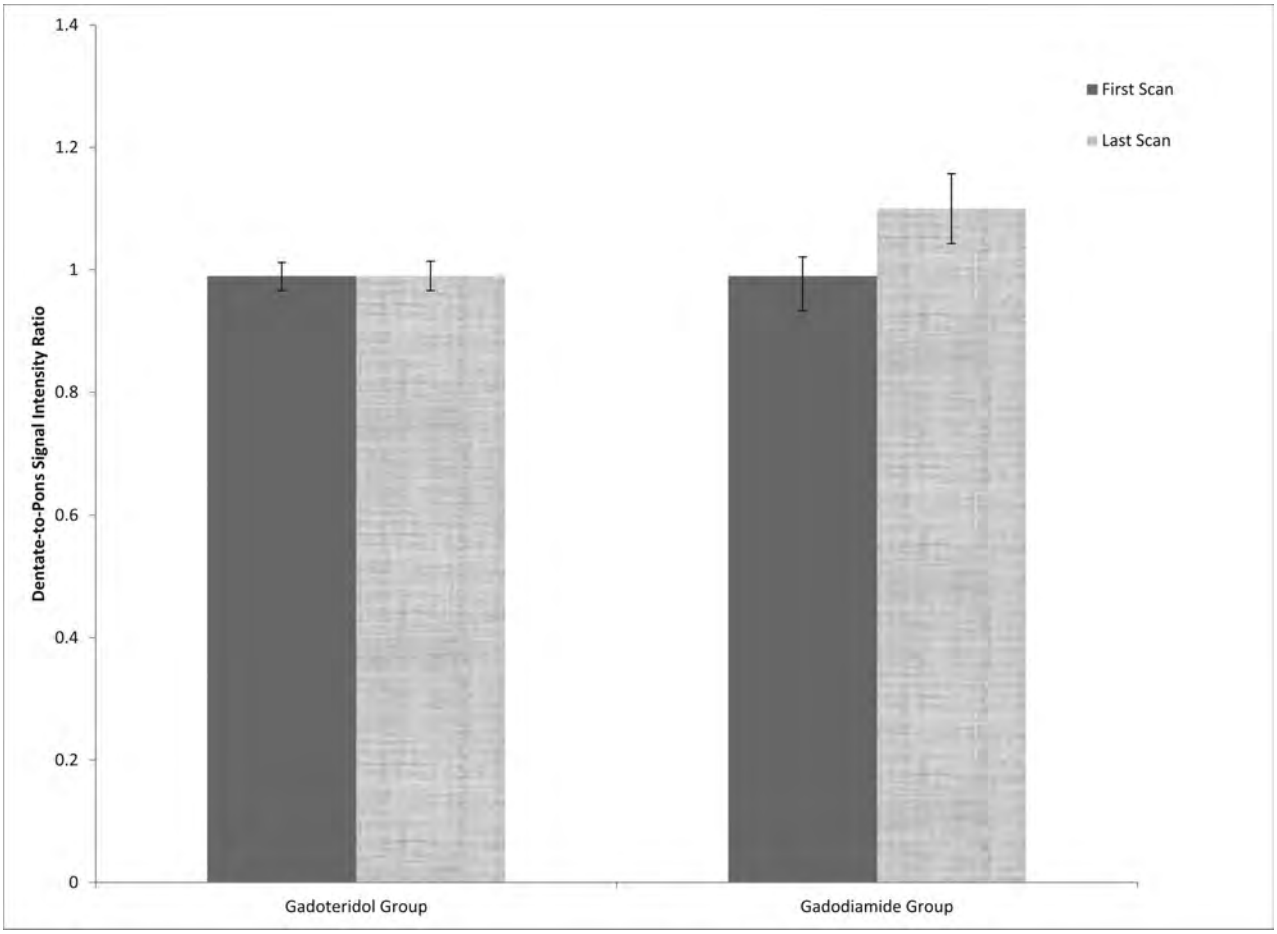


**FIG 1.** Dentate-to-pons signal intensity ratios on the first and last scans for patients in the gadoteridol and gadodiamide groups. Data are means. *Errors bars* represent 95% confidence intervals.

the dentate nuclei to the mean signal intensity of the pons was calculated for each MR imaging examination for each patient.

### *Statistical Analysis*

Dentate-to-pons signal intensity (DN-P SI) ratios for the first and last MR imaging examinations were compared using paired *t* tests. The number of doses of gadolinium received and patient age in the gadoteridol and gadodiamide groups were compared using *t* tests. Patient diagnosis (tumoral versus nontumoral), history of chemotherapy, and history of radiation in the gadoteridol and gadodiamide groups were compared using Fisher exact tests. *P* values $< .05$ were considered statistically significant. Analyses were performed using SPSS 23 for Windows (IBM, Armonk, New York).

## RESULTS

### *Patients*

Our study cohort comprised 11 male (58%) and 8 female (42%) pediatric patients (Table). On average, each patient underwent 6.1 MR imaging examinations (range, 4–8 examinations). There was no significant difference in the number of MR imaging examinations between the gadoteridol group and the gadodiamide group ($P = .85$). In the gadoteridol group, each patient underwent an average of 6.1 MR imaging examinations (range, 4–8 examinations). Within the gadodiamide group, each patient underwent 6 MR imaging examinations. Eighty-four percent of the patients (16/19) had brain tumors. Forty-seven percent of the patients (9/19) had a history of chemotherapy, and 32% (6/19) had a history of radiation therapy. There was no significant difference in the proportion of patients with tumoral diagnoses, history of chemotherapy, and history of radiation between the gadoteridol and gadodiamide groups ($P = 1.00, .66, .06$, respectively). The time elapsed between the first and last MR imaging examinations ranged from 1 month to 1.6 years, which is similar to prior published studies in children with a range of 1.2–12.9 years.[12] There was no significant difference in age between the gadoteridol and gadodiamide groups ($P = .13$).

### *Dentate Signal Intensity following Repeat Gadoteridol and Gadodiamide Administration*

In the gadoteridol cohort, there was no significant change in the mean DN-P SI ratio from the first to the last scan (0.99 versus 0.99, $P = .59$), as shown in Figs 1 and 2. However, in the gadodiamide cohort, there was a significant increase in the mean DN-P SI ratio from the first to the last scan (0.99 versus 1.10, $P = .001$, Figs 1 and 2).

All patients had the same MR imaging protocol on the first and last scans. However, 3 patients in the gadoteridol cohort had differing magnetic field strengths on the first and last scans. All patients in the gadodiamide cohort had the same magnetic field strength on the first and last scans. Thus, we considered the possibility that changes in magnetic field strength could impact T1-

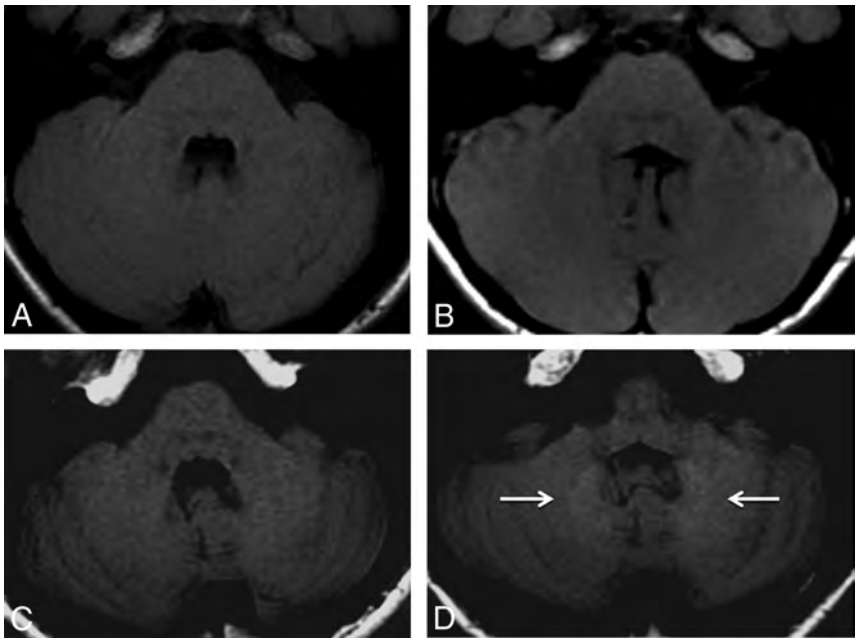


**FIG 2.** Dentate signal intensity in a patient in the gadoteridol group and in a patient in the gadodiamide group. *A* and *B*, An 11-year-old boy with a subgaleal abscess who underwent 6 gadoteridol-enhanced MR imaging examinations. *A*, Axial T1-weighted image on the first MR imaging examination. *B*, Axial T1-weighted image on the sixth MR imaging examination. *C* and *D*, A 15-year-old boy with a germinoma who underwent 6 gadodiamide-enhanced MR imaging examinations. *C*, Axial T1-weighted image on the first MR imaging examination. *D*, Axial T1-weighted image on the sixth MR imaging examination. There is intrinsic T1-weighted hyperintensity within the dentate nuclei (*arrows*).

weighted hyperintensity. After we excluded these 3 patients from the analyses, the results were similar. In the gadoteridol cohort, there was no significant change in the mean DN-P SI ratio from the first to the last scan (0.99 versus 0.99, $P = .24$).

## DISCUSSION

In this study, we sought to evaluate whether the serial administration of the macrocyclic GBCA gadoteridol in pediatric patients (who received between 4 and 8 doses) was associated with the development of T1-weighted hyperintensity in the dentate nucleus, an imaging surrogate for gadolinium retention. We found that in children who received serial administrations of gadoteridol, there was no significant change in the mean DN-P SI ratio from the first to the last MR imaging examination. However, in children who received serial administrations of the linear GBCA gadodiamide, there was a significant increase in the mean DN-P SI ratio from the first to the last scan, consistent with prior published studies in adults.[2,3,5,7,9] These findings are also consistent with recently published studies in pediatric patients that found an association between serial administration of the linear GBCA gadopentetate dimeglumine and T1-weighted hyperintensity in the dentate nucleus.[10-12] Our findings suggest that the macrocyclic GBCA gadoteridol may be less likely to deposit within the dentate nucleus in comparison with the linear GBCA gadodiamide. However, an alternative possibility is that gadoteridol may be retained within the dentate nucleus but may result in less T1 shortening than gadodiamide.

Our findings are consistent with those in a prior published study in adults by Kanda et al,[4] which demonstrated that the macrocyclic GBCA gadoteridol is less likely to deposit within the brain in comparison with the linear GBCA gadopentetate dimeglumine. Our results are also consistent with the results from 2 studies in adults by Radbruch et al,[8,20] who found that the macrocyclic GBCAs gadoterate meglumine and gadobutrol may be less likely to deposit in the brain in comparison with the linear GBCA gadopentetate dimeglumine.

Furthermore, our findings are consistent with those in a recently published study by Tibussek et al,[15] who evaluated a cohort of 24 pediatric patients who received serial administrations of the macrocyclic GBCAs gadoterate meglumine and gadoteriodol and did not find an association with T1-weighted hyperintensity in the dentate nuclei. An important difference between our study and the study by Tibussek et al is that our macrocyclic subcohort received exclusively gadoteridol. The patients in the study of Tibussek et al received both gadoteridol and gadoterate meglumine. Additionally, we compared our gadoteridol subcohort with a subcohort of patients who exclusively received the linear GBCA gadodiamide. The study by Tibussek et al did not include a linear GBCA subcohort for comparison. Our findings are also consistent with a recent study by Radbruch et al,[14] who found that the serial administration of the macrocyclic GBCA gadoterate meglumine in pediatric patients was not associated with T1-weighted hyperintensity in the dentate nuclei. The conclusions of the Radbruch et al study[14] have recently been called into question because Rossi Espagnet et al[16] found that the repeat administration of gadoterate meglumine was associated with increasing T1-weighted hyperintensity in the dentate nucleus by quantitative ROI analysis. However, in the study by Rossi Espagnet et al, there was no visible increase in the T1-weighted signal intensity in the dentate nucleus.[16,19] In our study, we found a visible increase in dentate T1-weighted signal intensity in the gadodiamide subcohort, but we did not find a visible increase in dentate T1-weighted signal intensity in the gadoteridol subcohort (Fig 2).

Our study has several potential limitations. First, because of the retrospective nature of this study, all patients were not imaged on the same scanner with the same precontrast T1-weighted protocol. However, in accordance with the recommendations of Ramalho et al,[21] for each patient, the same MR imaging protocol was used for the first and last MR imaging examinations and thus should allow satisfactory comparison. For 84% of the patients in our cohort (16/19), imaging was performed on scanners of the same magnetic field strength for the first and last MR imaging examinations. The 3 patients who had the first and last MR imaging examinations on scanners of differing magnetic field strengths were from the gadoteridol subcohort. We analyzed the data after

excluding these 3 patients, and the results were similar. In the gadoteridol subcohort, there was no significant change in the mean DN-P SI ratio when comparing the first scan with the last scan. Furthermore, we normalized the dentate signal intensity to the signal intensity of the pons, which should limit the effects of scanner variability (specifically variability in magnetic field strength) and protocol variability.

Second, we used T1-weighted hyperintensity in the dentate nucleus as an imaging surrogate for gadolinium deposition. While the direct measurement of gadolinium in cerebellar tissue is preferable, this is much more challenging to acquire. Additionally, the generation of T1-weighted hyperintensity within the dentate nucleus may potentially depend on factors that may vary between different gadolinium-based contrast agents. As a result, T1-weighted hyperintensity may be an imperfect measure of gadolinium concentration in the brain. A quantitative method based on susceptibility mapping has recently been studied and used by other groups.[22]

Third, our study did not include an age-matched control cohort of patients who did not receive any GBCA. However, each patient in our study cohort was followed serially across time, thus serving as his or her own internal control. Fourth, patients in our gadoteridol subcohort received, on average, 6 doses of gadoteridol. We cannot exclude the possibility that T1-weighted hyperintensity within the dentate nucleus may appear after >6 doses of gadoteridol in pediatric patients. Despite these limitations, our results suggest that in children, the macrocyclic GBCA gadoteridol may be less likely than linear GBCAs such as gadodiamide to deposit in the dentate nuclei.

## CONCLUSIONS

To our knowledge, our study is the first to demonstrate that the repeat exclusive administration of the macrocyclic GBCA gadoteridol in children is not associated with T1-weighted hyperintensity in the dentate nucleus. Thus, the macrocyclic GBCA gadoteridol may be less likely than linear GBCAs, such as gadodiamide, to deposit within the pediatric brain, consistent with prior published studies in adults.[4,8,20]

Disclosures: Whitney B. Pope—*UNRELATED*: *Consultancy*: Bracco; *Grants/Grants Pending*: Guerbet.* *Money paid to the institution.

## REFERENCES


1. Adin ME, Kleinberg L, Vaidya D, et al. **Hyperintense dentate nuclei on T1-weighted MRI: relation to repeat gadolinium administration.** *AJNR Am J Neuroradiol* 2015;36:1859–65 CrossRef Medline
2. Errante Y, Cirimele V, Mallio CA, et al. **Progressive increase of T1 signal intensity of the dentate nucleus on unenhanced magnetic resonance images is associated with cumulative doses of intravenously administered gadodiamide in patients with normal renal function, suggesting dechelation.** *Invest Radiol* 2014;49:685–90 CrossRef Medline
3. Kanda T, Ishii K, Kawaguchi H, et al. **High signal intensity in the dentate nucleus and globus pallidus on unenhanced T1-weighted MR images: relationship with increasing cumulative dose of a gadolinium-based contrast material.** *Radiology* 2014;270:834–41 CrossRef Medline
4. Kanda T, Osawa M, Oba H, et al. **High signal intensity in dentate nucleus on unenhanced T1-weighted MR images: association with linear versus macrocyclic gadolinium chelate administration.** *Radiology* 2015;275:803–09 CrossRef Medline
5. McDonald RJ, McDonald JS, Kallmes DF, et al. **Intracranial gadolinium deposition after contrast-enhanced MR imaging.** *Radiology* 2015;275:772–82 CrossRef Medline
6. McDonald RJ, McDonald JS, Kallmes DF, et al. **Gadolinium deposition in human brain tissues after contrast-enhanced MR imaging in adult patients without intracranial abnormalities.** *Radiology* 2017;285:546–54 CrossRef Medline
7. Quattrocchi CC, Mallio CA, Errante Y, et al. **Gadodiamide and dentate nucleus T1 hyperintensity in patients with meningioma evaluated by multiple follow-up contrast-enhanced magnetic resonance examinations with no systemic interval therapy.** *Invest Radiol* 2015;50:470–72 CrossRef Medline
8. Radbruch A, Weberling LD, Kieslich PJ, et al. **Gadolinium retention in the dentate nucleus and globus pallidus is dependent on the class of contrast agent.** *Radiology* 2015;275:783–91 CrossRef Medline
9. Ramalho J, Castillo M, AlObaidy M, et al. **High signal intensity in globus pallidus and dentate nucleus on unenhanced T1-weighted MR images: evaluation of two linear gadolinium-based contrast agents.** *Radiology* 2015;276:836–44 CrossRef Medline
10. Flood TF, Stence NV, Maloney JA, et al. **Pediatric brain: repeated exposure to linear gadolinium-based contrast material is associated with increased signal intensity at unenhanced T1-weighted MR imaging.** *Radiology* 2017;282:222–28 CrossRef Medline
11. Roberts DR, Chatterjee AR, Yazdani M, et al. **Pediatric patients demonstrate progressive T1-weighted hyperintensity in the dentate nucleus following multiple doses of gadolinium-based contrast agent.** *AJNR Am J Neuroradiol* 2016;37:2340–47 CrossRef Medline
12. Hu HH, Pokorney A, Towbin RB, et al. **Increased signal intensities in the dentate nucleus and globus pallidus on unenhanced T1-weighted images: evidence in children undergoing multiple gadolinium MRI exams.** *Pediatr Radiol* 2016;46:1590–98 CrossRef Medline
13. Young JR, Orosz I, Franke MA, et al. **Gadolinium deposition in the paediatric brain: T1-weighted hyperintensity within the dentate nucleus following repeated gadolinium-based contrast agent administration.** *Clin Radiol* 2018;73:290–95 CrossRef Medline
14. Radbruch A, Haase R, Kickingereder P, et al. **Pediatric brain: no increased signal intensity in the dentate nucleus on unenhanced T1-weighted MR images after consecutive exposure to a macrocyclic gadolinium-based contrast agent.** *Radiology* 2017;283:828–36 CrossRef Medline
15. Tibussek D, Rademacher C, Caspers J, et al. **Gadolinium brain deposition after macrocyclic gadolinium administration: a pediatric case-control study.** *Radiology* 2017;285:223–30 CrossRef Medline
16. Rossi Espagnet MC, Bernardi B, Pasquini L, et al. **Signal intensity at unenhanced T1-weighted magnetic resonance in the globus pallidus and dentate nucleus after serial administrations of a macrocyclic gadolinium-based contrast agent in children.** *Pediatr Radiol* 2017;47:1345–52 CrossRef Medline
17. Blakemore SJ. **Imaging brain development: the adolescent brain.** *Neuroimage* 2012;61:397–406 CrossRef Medline
18. Stein J, Schettler T, Wallinga D, et al. **In harm's way: toxic threats to child development.** *J Dev Behav Pediatr* 2002;23:S13–22 CrossRef Medline
19. Radbruch A, Quattrocchi CC. **Interpreting signal-intensity ratios without visible T1 hyperintensities in clinical gadolinium retention studies.** *Pediatr Radiol* 2017;47:1688–89 CrossRef Medline
20. Radbruch A, Haase R, Kieslich PJ, et al. **No signal intensity increase in the dentate nucleus on unenhanced T1-weighted MR images after more than 20 serial injections of macrocyclic gadolinium-based contrast agents.** *Radiology* 2017;282:699–707 CrossRef Medline
21. Ramalho J, Ramalho M, AlObaidy M, et al. **Technical aspects of MRI signal change quantification after gadolinium-based contrast agents' administration.** *Magn Reason Imaging* 2016;34:1355–58 CrossRef Medline
22. Hinoda T, Fushimi Y, Okada T, et al. **Quantitative assessment of gadolinium deposition in dentate nucleus using quantitative susceptibility mapping.** *J Magn Reason Imaging* 2017;45:1352–58 CrossRef Medline

# Hybrid 3D/2D Convolutional Neural Network for Hemorrhage Evaluation on Head CT

P.D. Chang, E. Kuoy, J. Grinband, B.D. Weinberg, M. Thompson, R. Homo, J. Chen, H. Abcede, M. Shafie, L. Sugrue, C.G. Filippi, M.-Y. Su, W. Yu, C. Hess, and D. Chow

## ABSTRACT

**BACKGROUND AND PURPOSE:** Convolutional neural networks are a powerful technology for image recognition. This study evaluates a convolutional neural network optimized for the detection and quantification of intraparenchymal, epidural/subdural, and subarachnoid hemorrhages on noncontrast CT.

**MATERIALS AND METHODS:** This study was performed in 2 phases. First, a training cohort of all NCCTs acquired at a single institution between January 1, 2017, and July 31, 2017, was used to develop and cross-validate a custom hybrid 3D/2D mask ROI-based convolutional neural network architecture for hemorrhage evaluation. Second, the trained network was applied prospectively to all NCCTs ordered from the emergency department between February 1, 2018, and February 28, 2018, in an automated inference pipeline. Hemorrhage-detection accuracy, area under the curve, sensitivity, specificity, positive predictive value, and negative predictive value were assessed for full and balanced datasets and were further stratified by hemorrhage type and size. Quantification was assessed by the Dice score coefficient and the Pearson correlation.

**RESULTS:** A 10,159-examination training cohort (512,598 images; 901/8.1% hemorrhages) and an 862-examination test cohort (23,668 images; 82/12% hemorrhages) were used in this study. Accuracy, area under the curve, sensitivity, specificity, positive predictive value, and negative-predictive value for hemorrhage detection were 0.975, 0.983, 0.971, 0.975, 0.793, and 0.997 on training cohort cross-validation and 0.970, 0.981, 0.951, 0.973, 0.829, and 0.993 for the prospective test set. Dice scores for intraparenchymal hemorrhage, epidural/subdural hemorrhage, and SAH were 0.931, 0.863, and 0.772, respectively.

**CONCLUSIONS:** A customized deep learning tool is accurate in the detection and quantification of hemorrhage on NCCT. Demonstrated high performance on prospective NCCTs ordered from the emergency department suggests the clinical viability of the proposed deep learning tool.

**ABBREVIATIONS:** CNN = convolutional neural networks; EDH/SDH = epidural/subdural hemorrhage; GPU = graphics processing unit; ICH = intracranial hemorrhage; IPH = intraparenchymal hemorrhage; mask R-CNN = mask ROI-based CNN

Intracranial hemorrhages (ICHs) represent a critical medical event that results in 40% patient mortality despite aggressive care.[1] Early and accurate diagnosis is necessary for the management of acute ICHs.[2,3] However, increasing imaging use and distractions from noninterpretive tasks are known to cause delays in diagnosis[4] with turn-around time for noncontrast CT head examinations reported up to 1.5–4 hours in the emergency department.[4] These delays impact patient care because acute deterioration from hemorrhage expansion often results early, within the initial 3–4.5 hours of symptom onset.[5-7] Therefore, a tool for expeditious and accurate diagnosis of ICHs may facilitate a prompt therapeutic response and ultimately improved outcomes.

In addition to ICH detection, a tool for automated quantification of hemorrhage volume may provide a useful metric for patient monitoring and prognostication.[8,9] For intraparenchymal hemorrhage (IPH) specifically, the current clinical standard for quantification relies on a simplified formula (ABC/2) calculation

Received April 10, 2018; accepted after revision June 6.

From the Departments of Radiology (P.D.C., E.K., M.T., R.H., M.-Y.S., D.C.), Neurosurgery (J.C.), and Neurology (H.A., M.S., W.Y.), University of California Irvine; Departments of Radiology (P.D.C., L.S., C.H.), University of California, San Francisco, California; Department of Radiology (J.G.), Columbia University, New York, New York; Department of Radiology (B.D.W.), Emory University School of Medicine, Atlanta, Georgia; and Department of Radiology (C.G.F.), North Shore University Hospital, Long Island, New York.

The work of P.C. was, in part, supported by grant T32EB001631 from the National Institutes of Health (National Institute of Biomedical Imaging and Bioengineering). The work of D.C. was, in part, supported by Canon Medical Systems.

Please address correspondence to Daniel Chow, MD, University of California, Irvine Medical Center, 101 The City Drive South, Douglas Hospital, Route 140, Room 0115, Orange, CA 92868-3201; e-mail: chowd3@uci.edu; @TheCAIDM

Indicates open access to non-subscribers at www.ajnr.org

http://dx.doi.org/10.3174/ajnr.A5742

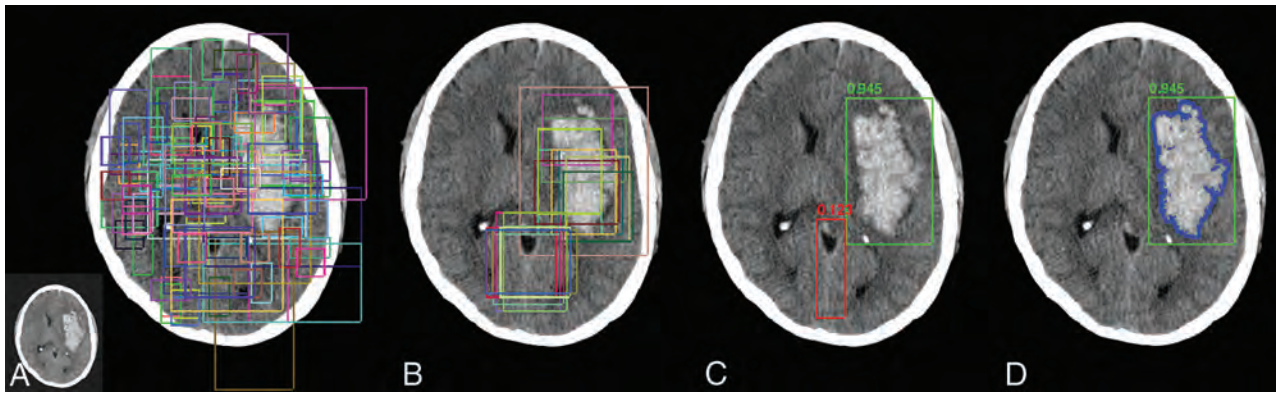


**FIG 1.** Overview of the mask R-CNN approach. Mask R-CNN architectures provide a flexible and efficient framework for parallel evaluation of region proposal (attention), object detection (classification), and instance segmentation. *A*, Preconfigured bounding boxes at various shapes and resolutions are tested for the presence of a potential abnormality. *B*, The highest ranking bounding boxes are identified and used to generate region proposals that focus algorithm attention. *C*, Composite region proposals are pruned using nonmaximum suppression and are used as input into a classifier to determine the presence or absence of hemorrhage. *D*, Segmentation masks are generated for cases positive for hemorrhage.

that commonly overestimates true IPH volumes by up to 30%.[10] Alternatively, while manual delineation of hemorrhage may provide accurate volume estimates, time constraints make this impractical in the emergency setting. Accordingly, a fully automated and objective tool for rapid quantification of ICH volume may be a compelling alternative to current approaches, offering more accurate, detailed information to guide clinical decision-making.

In this study, we propose a tool based on deep learning convolutional neural networks (CNN), an emerging technology now capable of image interpretation tasks that were once thought to require human intelligence.[11] The effectiveness of CNNs is based on the capacity of the algorithm for self-organization and pattern recognition without explicit human programming. Using a deep learning approach, Prevedello et al[12] previously described a generic algorithm for broad screening of various acute NCCT findings (hemorrhage, mass effect, hydrocephalus) with an overall sensitivity and specificity of 90% and 85%, respectively. We extend this preliminary work by customizing a new mask ROI-based CNN (mask R-CNN) architecture optimized specifically for ICH evaluation and training the network on an expanded cohort of NCCT head examinations. In addition to validation on a retrospective cohort, the trained algorithm will be tested for real-time interpretation of new, prospectively acquired NCCT examinations as part of an automated inference pipeline. By testing performance in a realistic environment of consecutive NCCT examinations, we hope to assess the feasibility of future implementation in clinical practice.

In summary, the 3 key objectives of this study include deep learning algorithm development and assessment of final trained CNN performance in the following: 1) detection of ICH including intraparenchymal, epidural/subdural (EDH/SDH), and subarachnoid hemorrhages; 2) quantification of ICH volume; and 3) prospective, real-time inference on an independent test set as part of an automated pipeline.

## MATERIALS AND METHODS

### *Patient Selection*

After approval of the institutional review board of the University of California, Irvine Medical Center, 2 separate cohorts were identified for this study: one cohort for training (combined with cross-validation) and a second cohort as an independent test set. The initial retrospectively defined training cohort consisted of every NCCT examination acquired at the study institution between January 1, 2017, and July 31, 2017. The subsequent prospectively acquired independent test set cohort consisted of every NCCT examination ordered from the emergency department between February 1, 2018, and February 28, 2018. For both cohorts, cases positive for hemorrhage (IPH, EDH/SDH, and SAH) were identified from clinical reports and confirmed with visual inspection by a board-certified radiologist. 3D ground truth masks were generated for all cases positive for hemorrhage using a custom semiautomated Web-based annotation platform developed at our institution, implementing a variety of tools for level-set segmentation and morphologic operations. All masks were visually inspected for accuracy by a board-certified radiologist.

### *Convolutional Neural Network*

A custom architecture derived from the mask R-CNN algorithm was developed for detection and segmentation of hemorrhage.[13] In brief, the mask R-CNN architecture provides a flexible and efficient framework for parallel evaluation of region proposal (attention), object detection (classification), and instance segmentation (Fig 1). In the first step, a preconfigured distribution of bounding boxes at various shapes and resolutions is tested for the presence of a potential abnormality. Next, the highest ranking bounding boxes are identified and used to generate region proposals, thus focusing algorithm attention on specific regions of the image. These composite region proposals are pruned using nonmaximum suppression and are used as input into a classifier to determine the presence or absence of hemorrhage. In the case of detection positive for hemorrhage, a final segmentation branch of the network is used to generate binary masks.

The efficiency of a mask R-CNN architecture arises from a common backbone network that generates a shared set of image features for the various parallel detection, classification, and segmentation tasks (Fig 2). The backbone network used in this article is a custom hybrid 3D/2D variant of the feature pyramid network.[14] This custom backbone network was constructed using standard residual bottleneck blocks[15] without iterative tuning,

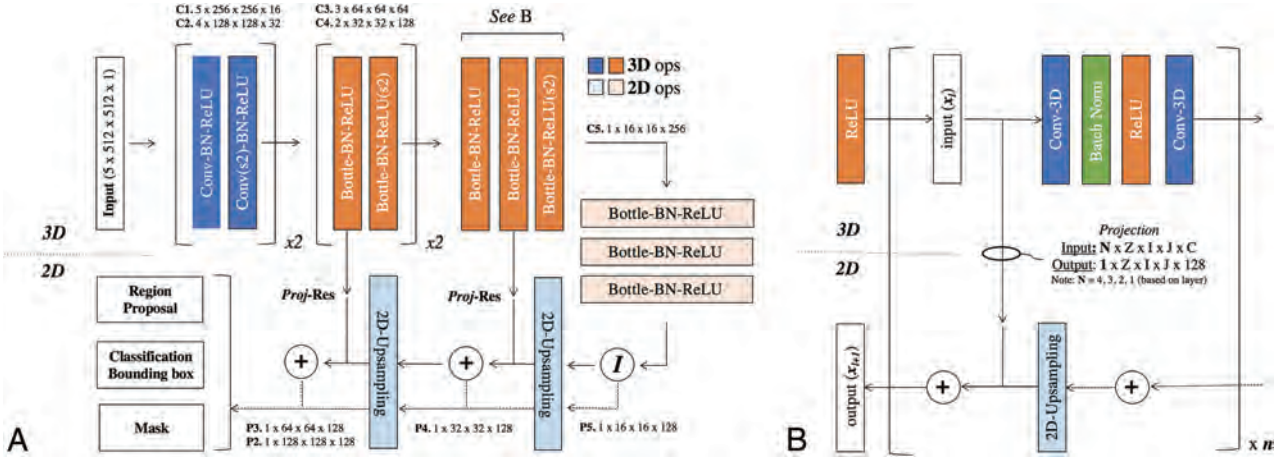


**FIG 2.** Convolutional neural network architecture. *A*, Hybrid 3D-contracting (bottom-up) and 2D-expanding (top-down) fully convolutional feature-pyramid network architecture used for the mask R-CNN backbone. The architecture incorporates both traditional 3 × 3 filters (blue) as well as bottleneck 1 × 1–3 × 3–1 × 1 modules (orange). The contracting arm is composed of 3D operations and convolutional kernels. Subsampling in the x- and y-directions is implemented via 1 × 2 × 2 strided convolutions (marked by s2). Subsampling in the *z*-direction is mediated by a 2 × 1 x 1 convolutional kernel with valid padding. The expanding arm is composed entirely of 2D operations. *B*, Connections between the contracting and expanding arms are facilitated by residual addition operations between corresponding layers. 3D layers in the contracting arm are mapped to 2D layers in the expanding arm by projection operations, which are designed both to match in the input (N) and output (1) *z*-dimension shape in addition to input (C) and output (128) feature map sizes. Ops indicates operations; Conv, convolutions; BN-ReLU, Batch Normalization Rectified Linear Unit; Proj-Res, Projection-Residual; Z, Z-axis; I, In plane axis; J, In plane axis.

given the observation that mask R-CNN architectures, particularly those based on pyramid networks, are robust to many design choices. In this implementation, a 3D input matrix of 5 × 512 × 512 is mapped to 2D output feature maps at various resolutions, with 3D input from the pyramid network bottom-up pathway added to the 2D feature maps of the top-down pathway using a projection operation to match the matrix dimensions. Thus, the network can use contextual information from the 5 slices immediately surrounding the ROI to predict the presence and location of hemorrhage.

### Implementation

The approximate joint training method as described in the original faster mask R-CNN implementation[16] was used for parallel optimization of the region-proposal network classifier and segmentation heads. The mask R-CNN architecture was trained using 128 sampled ROIs per image, with a ratio of positive-to-negative samples fixed at 1:3. During inference, the top 256 proposals by the region-proposal network are pruned using nonmaximum suppression and are used to generate detection boxes for classification. The region-proposal network anchors span 4 scales (128 × 128, 64 × 64, 32 × 32, 16 × 16) and 3 aspect ratios (1:1, 1:2, 2:1).

Network weights were initialized using the heuristic described by He et al.[17] The final loss function included a term for L2 regularization of the network parameters. Optimization was implemented using the Adam method, an algorithm for first-order gradient-based optimization of stochastic objective functions based on adaptive estimates of lower order moments.[18] An initial learning rate of $2 \times 10^{-4}$ was used and annealed whenever a plateau in training loss was observed.

The software code for this study was written in Python 3.5 using the open-source TensorFlow r1.4 library (Apache 2.0 license; https://github.com/tensorflow/tensorflow/blob/master/LICENSE).[19] Experiments were performed on a graphics processing unit (GPU)-optimized workstation with 4 GeForce GTX Titan X cards (12GB, Maxwell architecture; NVIDIA, Santa Clara, California). Inference benchmarks for speed were determined using a single-GPU configuration.

### Image Preprocessing

For each volume, the axial soft-tissue reconstruction series was automatically identified by a custom CNN-based algorithm. If necessary, this volume was resized to an in-plane resolution matrix of 512 × 512. Furthermore, all matrix values less than −240 HU or greater than +240 HU were clipped, and the entire volume was rescaled to a range of [−3, 3].

### Statistical Analysis

The primary end point of this study was the detection of hemorrhage on a per-study basis. A given NCCT volume was considered positive for hemorrhage if any single region-proposal prediction on any given slice was determined to contain hemorrhage. Thus, algorithm performance including accuracy, sensitivity, specificity, positive predictive value, and negative predictive value was calculated. Furthermore, by varying the softmax score threshold for hemorrhage classification, we calculated an area under the curve.

In addition to complete dataset evaluation, performance statistics on a balanced dataset (an equal number of positive and negative cases) were also calculated. By means of a balanced distribution, accuracy could also be further stratified by hemorrhage type (IPH, EDH/SDH, and SAH) and size (punctate, small, medium, and large, defined as <0.01, 0.01–5.0, 5.0–25, and >25 mL).

The secondary end point of this study was the ability of the algorithm to accurately estimate hemorrhage volume. This was assessed in 2 ways. First, predicted binary masks of hemorrhage

**Table 1: Distribution of hemorrhages by type and size[a]**

| | IPH | | EDH/SDH | | SAH | |
|---|---|---|---|---|---|---|
| Size | Valid | Test | Valid | Test | Valid | Test |
| Large | 192 | 13 | 188 | 19 | 85 | 9 |
| Medium | 88 | 8 | 79 | 15 | 53 | 3 |
| Small | 63 | 1 | 49 | 4 | 52 | 6 |
| Punctate | 15 | 1 | 3 | 0 | 34 | 3 |
| Total | 358 | 23 | 319 | 38 | 224 | 21 |

[a] Large, medium, small, and punctate hemorrhages were defined as >25, 5–25, 0.01–5.0, and <0.01 mL, respectively.

were compared with criterion standard manual segmentations using a Dice score coefficient. Second, predicted volumes of hemorrhage were compared with criterion standard annotated volumes using a Pearson correlation coefficient ($r$). As a comparison, estimates of IPH volume were also calculated using the simplified ABC/2 formula.

### *Training Cohort Evaluation*

A 5-fold cross-validation scheme was used for evaluation of the initial training cohort. In this experimental paradigm, 80% of the data are randomly assigned into the training cohort, while the remaining 20% are used for validation. This process is then repeated 5 times until each study in the entire dataset is used for validation once. Validation results below are reported for the cumulative statistics across the entire dataset.

### *Independent Test Cohort Evaluation*

After fine-tuning the algorithm design and parameters, we applied the final trained network to a new, prospective cohort of all consecutive NCCT examinations ordered from the emergency department for 1 month. The entire pipeline for inference was fully automated, including real-time transfer of newly acquired examinations to a custom GPU server from the PACS, identification of the correct input series, and trained network inference. In addition to initial validation statistics, results from this independent test dataset are also reported.

## RESULTS

### *Patient Selection*

The initial training set cohort comprised 10,159 NCCT examinations, 901 (8.9%) of which contained hemorrhage including IPH ($n$ = 358/10,159, 3.5%), EDH/SDH ($n$ = 319, 3.1%), and SAH ($n$ = 224, 2.2%), yielding a total of 512,598 images. The median hemorrhage size was 28.2 mL (interquartile range, 9.4–44.7 mL).

The independent test set cohort compromised 682 prospective NCCT examinations, 82 (12.0%) of which contained hemorrhage including IPH ($n$ = 23, 3.4%), EDH/SDH ($n$ = 38, 5.6%), and SAH ($n$ = 21, 3.1%), yielding 23,668 images. The median hemorrhage size was 24.9 mL (interquartile range, 8.3–35.6 mL). Further baseline stratification of both training and test set cohorts by hemorrhage type and size can be found in Table 1.

### *ICH Detection*

Overall algorithm performance on the full dataset as measured by accuracy, area under the curve, sensitivity, specificity, positive predictive value, and negative predictive value was 0.975, 0.983, 0.971, 0.975, 0.793, and 0.997 for the cross-validation cohort and 0.970, 0.981, 0.951, 0.973, 0.829, and 0.993 for the prospective test set. When stratified by ICH type, the sensitivity for IPH, EDH/SDH, and SAH detection was 98.6% (353/358), 97.4% (311/319), and 94.2% (211/224) for the cross-validation cohort and 100% (23/23), 94.7% (36/38), and 90.5% (19/21) for the prospective test set. In total, 26/901 (2.9%) hemorrhages were missed in the cross-validation cohort compared with 4/81 (4.9%) hemorrhages in the prospective test set (Figs 3 and 4).

Balanced dataset results stratified by hemorrhage size show that in general, algorithm accuracy for hemorrhages of >5 mL (range, 0.977–0.999 mL) is higher than for hemorrhages of <5 mL (range, 0.872–0.965 mL) with only 4 cases of missed hemorrhage of >5 mL across both cohorts (all representing EDH/SDH). Detection accuracy of punctate hemorrhages of <0.01 mL (range, 0.872–0.883 mL) is noticeably more challenging than that of small hemorrhages between 0.01 and 5 mL (range, 0.906–0.965 mL). When we further stratify results by hemorrhage type, the most challenging combinations to detect are punctate SAH or EDH/SDH with accuracy ranges of 0.830–0.881 across both cohorts. Complete stratification of balanced dataset results by hemorrhage and size can be found in Table 2.

### *ICH Quantification*

Estimates of IPH, EDH/SDH, and SAH segmentation masks by the CNN demonstrated Dice score coefficients of 0.931, 0.863, and 0.772, respectively, compared with manual segmentations. Estimates of IPH, EDH/SDH, and SAH volume by the CNN demonstrated Pearson correlation coefficients of 0.999, 0.987, and 0.953 compared with volumes derived from manual segmentations. By comparison, estimates of IPH volume derived from the simplified ABC/2 formula demonstrated a Pearson correlation of 0.954. On average, the ABC/2-derived hemorrhage volumes overestimated ground truth by an average of 20.2%, while the CNN-derived hemorrhage volumes underestimated ground truth by an average of just 2.1%.

### *Network Statistics*

Each network for a corresponding validation fold trained for approximately 100,000 iterations before convergence. Depending on the number of GPU cards for training distribution, this process required, on average, 6–12 hours per fold. Once trained, the mask R-CNN network was able to determine the presence of hemorrhage in a new test case within an average of 0.121 seconds, including all preprocessing steps on a single GPU workstation.

## DISCUSSION

In this study, we demonstrate that a deep learning solution is highly accurate in the detection of ICHs, including IPHs, EDHs/SDHs, and SAHs. In addition, this study demonstrates that a CNN can quantify ICH volume with high accuracy as reflected by Dice score coefficients (0.772–0.931) and Pearson correlations (0.953–0.999). Finally, while embedded for 1 month in an automated inference pipeline, the deep learning tool was able to accurately detect and quantify ICHs from prospective NCCT examinations ordered from the emergency department.

There are several previously described approaches to ICH detection with traditional machine-learning techniques such as fuzzy clustering,[20,21] Bayesian classification,[22] level-set thresh-

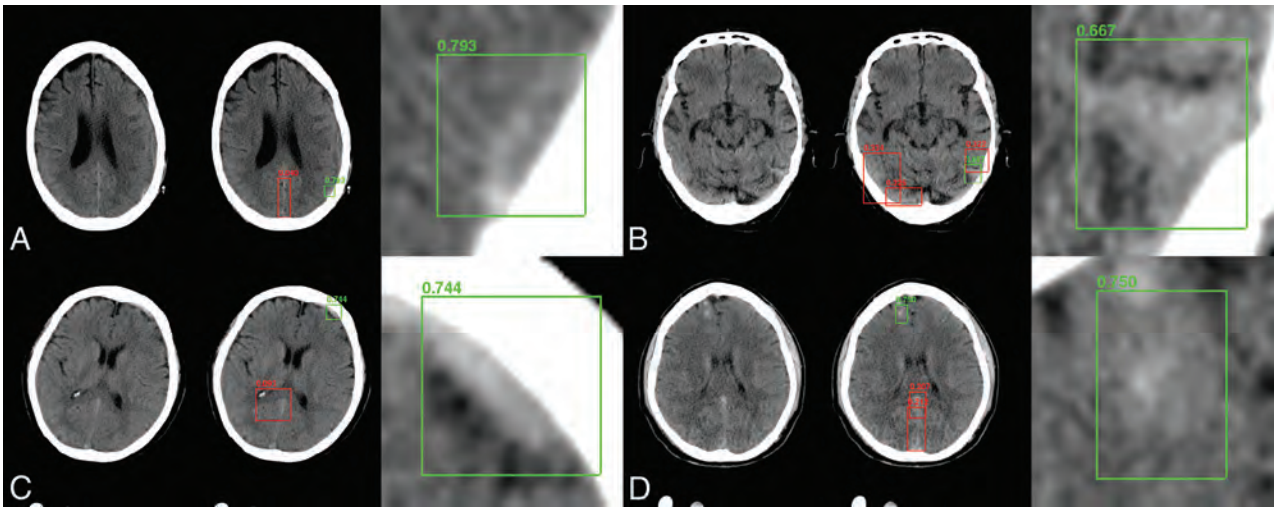


**FIG 3.** Sample network predictions: true-positives. Network predictions by the algorithm include bounding-box region proposals for potential areas of abnormality (to focus algorithm attention) and final network predictions, including confidence of results. Correctly identified areas of hemorrhage (green) include subtle abnormalities representing subarachnoid (*A*), subdural (*B* and *C*), and intraparenchymal (*D*) hemorrhage. Correctly identified areas of excluded hemorrhage often include common mimics for blood on NCCT, including thickening/high density along the falx (*A*, *C*, and *D*) and beam-hardening along the periphery (*B*).

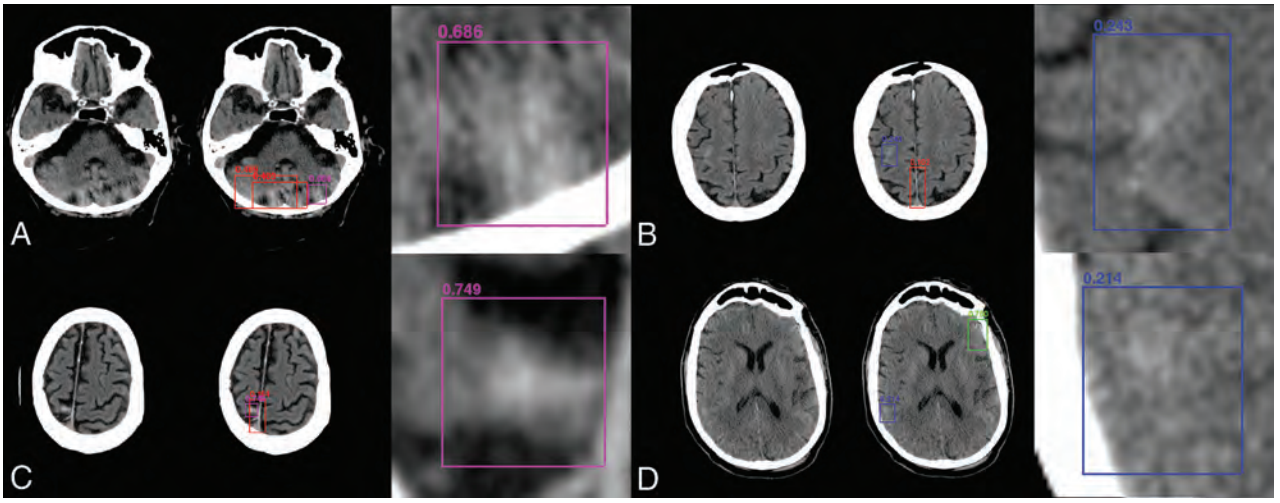


**FIG 4.** Sample network predictions: false-positives and false-negatives. Network predictions by the algorithm include bounding-box region proposals for potential areas of abnormality (to focus algorithm attention) and final network predictions including confidence of results. False-positive predictions for hemorrhage (purple) often include areas of motion artifacts and/or posterior fossa beam-hardening (*A*) or high-density mimics such as cortical calcification (*C*). False-negative predictions for excluded hemorrhage often include small volume abnormalities with relatively lower density, resulting in decreased conspicuity. Examples include subtle subarachnoid hemorrhage along the posterior right frontal lobe (*B*) and right inferior parietal lobe (*D*).

olds,[23] and decision tree analysis.[24] However, the image diversity present on any given NCCT head examination ultimately limits the accuracy of algorithms that are derived from a priori rules and hard-coded assumptions. For example, Gong et al[24] reported a sensitivity of 0.60 and a positive predictive value of 0.447 for IPH detection using decision tree analysis. Furthermore, hard-coded logic tends to produce narrow algorithms optimized for just a single task. For example, Prakash et al[23] reported a level-set technique for hemorrhage quantification yielding a Dice score range between 0.858 and 0.917; however, the algorithm is limited for hemorrhage detection because it is not designed to exclude hemorrhage on an examination with negative findings.

Given the increasing awareness of deep learning potential in medical imaging, there has been a gradual paradigm shift increasingly favoring convolutional neural networks over other approaches. For example, Shen et al[25] developed a multiscale CNN for lung nodule detection with CT images, while Wang et al[26] devised a 12-layer CNN for predicting cardiovascular disease from mammograms as well as for detecting spine metastasis.[27] More recently, Phong et al[28] described a deep learning approach for hemorrhage detection using several pretrained networks on a small test set of 20 cases.

However, while this preliminary effort is important, there are several key limitations to be addressed before clinical deployment of deep learning tools. First, in addition to high algorithm performance, a clinically viable tool must address the traditional "black box" critique of being unable to rationalize a given interpretation. While there are some techniques to ameliorate this through gen-

**Table 2: Balanced dataset performance statistics stratified by hemorrhage type and size[a]**

| | Accuracy | | AUC | | Sensitivity | | Specificity | | PPV | | NPV | |
|---|---|---|---|---|---|---|---|---|---|---|---|---|
| Size | Valid | Test | Valid | Test | Valid | Test | Valid | Test | Valid | Test | Valid | Test |
| All ICHs | 0.984 | 0.972 | 0.991 | 0.989 | 0.971 | 0.951 | 0.975 | 0.973 | 0.975 | 0.972 | 0.971 | 0.952 |
| Large | 0.999 | 0.997 | 0.999 | 0.999 | 1.000 | 1.000 | 0.975 | 0.973 | 0.975 | 0.973 | 1.000 | 1.000 |
| Medium | 0.992 | 0.977 | 0.995 | 0.982 | 0.986 | 0.962 | 0.975 | 0.973 | 0.975 | 0.972 | 0.986 | 0.962 |
| Small | 0.965 | 0.906 | 0.972 | 0.987 | 0.933 | 0.818 | 0.975 | 0.973 | 0.974 | 0.968 | 0.936 | 0.843 |
| Punctate | 0.883 | 0.872 | 0.895 | 0.903 | 0.769 | 0.750 | 0.975 | 0.973 | 0.968 | 0.965 | 0.809 | 0.796 |
| IPH | 0.992 | 0.997 | 0.996 | 0.999 | 0.986 | 1.000 | 0.975 | 0.973 | 0.975 | 0.973 | 0.986 | 1.000 |
| Large | 0.999 | 0.997 | 0.999 | 0.999 | 1.000 | 1.000 | 0.975 | 0.973 | 0.975 | 0.973 | 1.000 | 1.000 |
| Medium | 0.999 | 0.997 | 0.999 | 0.999 | 1.000 | 1.000 | 0.975 | 0.973 | 0.975 | 0.973 | 1.000 | 1.000 |
| Small | 0.983 | 0.997 | 0.999 | 0.999 | 0.968 | 1.000 | 0.975 | 0.973 | 0.974 | 0.973 | 0.968 | 1.000 |
| Punctate | 0.899 | 0.997 | 0.921 | 0.999 | 0.800 | 1.000 | 0.975 | 0.973 | 0.969 | 0.973 | 0.830 | 1.000 |
| EDH/SDH | 0.986 | 0.970 | 0.989 | 0.974 | 0.975 | 0.947 | 0.975 | 0.973 | 0.975 | 0.972 | 0.975 | 0.949 |
| Large | 0.999 | 0.997 | 0.999 | 0.999 | 1.000 | 1.000 | 0.975 | 0.973 | 0.975 | 0.973 | 1.000 | 1.000 |
| Medium | 0.980 | 0.963 | 0.983 | 0.971 | 0.962 | 0.933 | 0.975 | 0.973 | 0.974 | 0.971 | 0.963 | 0.936 |
| Small | 0.958 | 0.872 | 0.968 | 0.882 | 0.918 | 0.750 | 0.975 | 0.973 | 0.973 | 0.965 | 0.923 | 0.796 |
| Punctate | 0.832 | NA | 0.857 | NA | 0.667 | NA | 0.975 | 0.973 | 0.963 | NA | 0.745 | NA |
| SAH | 0.970 | 0.949 | 0.972 | 0.953 | 0.942 | 0.905 | 0.975 | 0.973 | 0.974 | 0.971 | 0.944 | 0.911 |
| Large | 0.999 | 0.997 | 0.999 | 0.999 | 1.000 | 1.000 | 0.975 | 0.973 | 0.975 | 0.973 | 1.000 | 1.000 |
| Medium | 0.999 | 0.997 | 0.999 | 0.999 | 1.000 | 1.000 | 0.975 | 0.973 | 0.975 | 0.973 | 1.000 | 1.000 |
| Small | 0.950 | 0.913 | 0.960 | 0.928 | 0.904 | 0.833 | 0.975 | 0.973 | 0.973 | 0.968 | 0.910 | 0.854 |
| Punctate | 0.881 | 0.830 | 0.891 | 0.833 | 0.765 | 0.667 | 0.975 | 0.973 | 0.968 | 0.961 | 0.806 | 0.745 |

**Note:**—AUC indicates area under the curve; NA, not applicable; PPV, positive predictive value; NPV, negative predictive value.

[a] Large, medium, small, and punctate hemorrhages were defined as >25, 5–25, 0.01–5.0, and <0.01 mL, respectively.

eration of saliency maps[29] or class-activation maps,[30] this is a known limitation of conventional global CNN-based classification of an image (or volume). By contrast, the proposed custom mask R-CNN architecture, through combining an attention-based object-detection network with more traditional classification and segmentation components, allows the algorithm to explicitly localize suspicious CT findings and provide visual feedback regarding which findings are likely to represent ICH or a mimic.

Second, a clinically viable tool needs to be tested on unfiltered data in a setting that reflects the expected context for deployment. In this study, we attempted to simulate this by deploying the trained network in a fully automated inference pipeline that can perform all the requisite steps to support algorithm prediction, ranging from PACS image transfer to series identification to GPU-enabled inference, all without human supervision. Furthermore, the prospectively acquired, independent test set used in this context is a reflective sample of the target population used, namely every NCCT head examination performed in the emergency radiology department. That algorithm performance in this setting remains favorable suggests that the deep learning tool has promising potential for clinical utility in the near future.

An additional point should also be made of the requisite data base size for proper algorithm validation. While large datasets are rare in medical imaging, a representative sample of pathology is critical for validating algorithm accuracy. As evidenced in this study, it is often the uncommon findings for which a neural network has the most difficultly learning and generalizing to (eg, punctate hemorrhages of <0.01 mL represent approximately 56/10,841 = 0.5% of all examinations yet are also the most difficult to detect); thus, a large representative dataset is required to assess performance on these critical rare entities. A large data base also facilitates algorithm learning, whereby the increased diversity of training examples helps the network choose more generalizable and predictive features. Finally, cases without ICH are just as important as those with ICH because the algorithm must also be able to correctly identify the absence of hemorrhage in most cases despite any possible underlying pathology that may be present. To address these issues, this study takes advantage of a large training dataset comprising over 512,598 images from >10,000 patients, at least an order of magnitude higher than that in any previous study.

The most salient use case of an accurate tool for hemorrhage detection is a triage system that alerts physicians of examinations potentially positive for hemorrhage for expedited interpretation, thus facilitating reduced turn-around time. The recent 2013 Imaging Performance Partnership survey of >80 institutions rated the importance of reduced turn-around time as one of their highest priorities, scoring 5.7 of a 6.0 rating,[31] allowing an expedited triage of patients for therapeutic management. As an example, rapid identification of patients with IPH would facilitate immediate control of blood pressure during the vulnerable first few 3–4.5 hours of symptom onset when acute deterioration is most likely.[5-7] The importance of rapid diagnosis is supported further by the recent Intensive Blood Pressure Reduction in Acute Cerebral Hemorrhage Trial-2, which concluded that intensive treatment afforded by early diagnosis was associated with improved functional outcome.[32]

In addition to hemorrhage detection, ICH volume metrics can be used to precisely and efficiently quantify the initial burden of disease as well as serial changes, which, in turn, may have important clinical implications.[33,34] For IPHs, this is most relevant within the first 2–3 hours of onset when the hemorrhagic volume can shift dramatically.[5-7] Furthermore, the volume of hemorrhage is a known predictor of 30-day mortality and morbidity.[8,9] Presently, the clinical standard for estimation of IPH volume is by the ABC/2 formula of Kwak et al,[10,35] in which A and B represent maximum single-dimensional perpendicular measurements on the largest axial region of hemorrhage and C represents a graded estimate of the craniocaudal extent. While easy to use, this limited

approach assumes an ellipsoid shape for all IPHs. In this study, we show that this assumption results in overestimation of hemorrhage by 20.2%, a statistic that has been previously reported with discrepancies up to 30% compared with manual segmentation.[10] While the criterion standard remains manual delineation, this approach can be both time-consuming and technically challenging in the emergency department setting. By comparison, the ability of the trained CNN to rapidly and accurately quantify IPH volume with >0.999 correlations to human experts offers a clinically feasible, improved alternative to the current standards of practice.

Several limitations should be addressed when considering our results. First, examinations in this study were performed at a single academic institution. Therefore, while we have demonstrated that our results generalize well to independent datasets obtained at our hospital center, further work is necessary to evaluate performance on a variety of vendors and scanning protocols at other institutions. While we acknowledge this drawback, CT examinations are inherently normalized by Hounsfield Units and show less image variability than plain radiographs or MR imaging. Second, deep learning algorithms are known to be susceptible to the phenomenon of adversarial noise,[36] where small but highly patterned perturbations in images may result in unexpected predictions. However, this is rare and was not encountered in the current dataset and, to some extent, can be mitigated using network ensembles and denoising autoencoders.[37] Finally, while the current dataset is quite large, there are, nonetheless, rare findings and contexts that occur at a prevalence of less than our 1/10,000 cases, and it is foreseeable that such studies may be incorrectly interpreted. To this end, we plan to incorporate continued iterative algorithm updates as new, increasingly larger datasets become available.

## CONCLUSIONS

This study demonstrates the high performance of a fully automated, deep learning algorithm for detection and quantification of IPH, EDH/SDH, and SAH on NCCT examinations of the head. Furthermore, confirmation of high algorithm performance on a prospectively acquired, independent test set while embedded in an automated inference environment suggests the clinical viability of this deep learning tool in the near future. Such a tool may be implemented either as a triage system to assist radiologists in identifying high-priority examinations for interpretation and/or as a method for rapid quantification of ICH volume, overall expediting the triage of patient care and offering more accurate, detailed information to guide clinical decision-making.

Disclosures: Peter Chang—*RELATED*: *Grant*: National Institutes of Health (National Institute of Biomedical Imaging and Bioengineering) T32 Training Grant T32EB001631.* Christopher G. Filippi—*UNRELATED*: *Consultancy*: Syntactx, *Comments*: I read MR imaging brain scans for their clinical trials; *Grants/Grants Pending*: The Foundation of the American Society of Neuroradiology (FASNR), *Comments*: Alzheimer research study grant*; *Payment for Lectures Including Service on Speakers Bureaus*: Grand Rounds Lectures: Montefiore, Albert Einstein College of Medicine, and Iowa University. Daniel Chow—*RELATED*: *Grant*: Canon Medical. *Money paid to the institution.

## REFERENCES

1. van Asch CJ, Luitse MJ, Rinkel GJ, et al. **Incidence, case fatality, and functional outcome of intracerebral haemorrhage over time, according to age, sex, and ethnic origin: a systematic review and meta-analysis.** *Lancet Neurol* 2010;9:167–76 CrossRef Medline
2. Goldstein JN, Gilson AJ. **Critical care management of acute intracerebral hemorrhage.** *Curr Treat Options Neurol* 2011;13: 204–16 CrossRef Medline
3. Heit JJ, Iv M, Wintermark M. **Imaging of intracranial hemorrhage.** *J Stroke* 2017;19:11–27 CrossRef Medline
4. Glover M 4th, Almeida RR, Schaefer PW, et al. **Quantifying the impact of noninterpretive tasks on radiology report turn-around times.** *J Am Coll Radiol* 2017;14:1498–1503 CrossRef Medline
5. Davis SM, Broderick J, Hennerici M, et al. Recombinant Activated Factor VII Intracerebral Hemorrhage Trial Investigators. **Hematoma growth is a determinant of mortality and poor outcome after intracerebral hemorrhage.** *Neurology* 2006;66:1175–81 CrossRef Medline
6. Kazui S, Naritomi H, Yamamoto H, et al. **Enlargement of spontaneous intracerebral hemorrhage: incidence and time course.** *Stroke* 1996;27:1783–87 CrossRef Medline
7. Qureshi A, Palesch Y, ATACH II Investigators. **Expansion of recruitment time window in antihypertensive treatment of acute cerebral hemorrhage (ATACH) II trial.** *J Vasc Interv Neurol* 2012; 5:6–9 Medline
8. Broderick JP, Brott TG, Duldner JE, et al. **Volume of intracerebral hemorrhage: a powerful and easy-to-use predictor of 30-day mortality.** *Stroke* 1993;24:987–93 CrossRef Medline
9. Butcher K, Laidlaw J. **Current intracerebral haemorrhage management.** *J Clin Neurosci* 2003;10:158–67 CrossRef Medline
10. Scherer M, Cordes J, Younsi A, et al. **Development and validation of an automatic segmentation algorithm for quantification of intracerebral hemorrhage.** *Stroke* 2016;47:2776–82 CrossRef Medline
11. Goodfellow I, Bengio Y, Courville A. *Deep Learning.* Cambridge: MIT Press; November 2016. ISBN: 9780262035613
12. Prevedello LM, Erdal BS, Ryu JL, et al. **Automated critical test findings identification and online notification system using artificial intelligence in imaging.** *Radiology* 2017;285:923–31 CrossRef Medline
13. He K, Gkioxari G, Dollár P, et al. **Mask R-CNN.** arXiv:1703.06870. 2017. In: *Proceedings of the IEEE International Conference on Computer Vision,* Venice, Italy. October 22–29, 2017
14. Lin TY, Dollár P, Girshick R, et al. **Feature pyramid networks for object detection.** arXiv:1612.03144. 2017. In: *Proceedings of the IEEE* Conference on *Computer Vision and Pattern Recognition,* Honolulu, Hawaii. July 21–27, 2017
15. He K, Zhang X, Ren S, et al. **Deep residual learning for image recognition.** arXiv:1512.03385. 2016. In: *Proceedings of the IEEE Conference on Computer Vision and Pattern Recognition*, Las Vagas, Nevada. June 27–30, 2016
16. Ren S, He K, Girshick R, et al. **Faster R-CNN: towards real-time object detection with region proposal networks.** *IEEE Trans Pattern Anal Mach Intell* 2017;39:1137–49 CrossRef Medline
17. He K, Zhang X, Ren S, et al. **Delving deep into rectifiers: surpassing human-level performance on imagenet classification.** arXiv:1502. 01852. 2015. In: *Proceedings of the IEEE International Conference on Computer Vision,* Santiago, Chile. December 7–13, 2015:1026–34
18. Kingma DP, Ba J Adam. **A method for stochastic optimization.** arXiv:1412.6980. 2015. In: *Proceedings of the International Conference for Learning Representations*, San Diego, California. May 7–9, 2015
19. Abadi M, Agarwal A, Barham P, et al. Tensorflow: large-scale machine learning on heterogeneous distributed systems. http://download.tensorflow.org/paper/whitepaper2015.pdf. Accessed March 25, 2018
20. Yuh EL, Gean AD, Manley GT, et al. **Computer-aided assessment of head computed tomography (CT) studies in patients with suspected traumatic brain injury.** *J Neurotrauma* 2008;25:1163–72 CrossRef Medline
21. Cósić D, Lončarić S. **Rule-based labeling of CT head image.** In: Keravnou E, Garbay C, Baud R, et al, eds. *Artificial Intelligence in Medicine: 6th Conference on Artificial Intelligence in Medicine Europe, AIME'97 Grenoble, France, March 23–26, 1997 Proceedings.* Berlin: Springer-Verlag;1997:453–56

22. Li YH, Zhang L, Hu QM, et al. **Automatic subarachnoid space segmentation and hemorrhage detection in clinical head CT scans.** *Int J Comput Assist Radiol Surg* 2012;7:507–16 CrossRef Medline
23. Prakash KN, Zhou S, Morgan TC, et al. **Segmentation and quantification of intra-ventricular/cerebral hemorrhage in CT scans by modified distance regularized level set evolution technique.** *Int J Comput Assist Radiol Surg* 2012;7:785–98 CrossRef Medline
24. Gong T, Liu R, Tan CL, et al. **Classification of CT brain images of head trauma.** In: Rajapakse JC, Schmidt B, Volkert G, eds. *Pattern Recognition in Bioinformatics: Second IAPR International Workshop, PRIB 2007, Singapore, October 1–2, 2007 Proceedings.* Berlin: Springer-Verlag; 2007:401–08
25. Shen W, Zhou M, Yang F, et al. **Multi-scale convolutional neural networks for lung nodule classification.** *Inf Process Med Imaging* 2015;24:588–99 Medline
26. Wang J, Ding H, Bidgoli FA, et al. **Detecting cardiovascular disease from mammograms with deep learning.** *IEEE Trans Med Imaging* 2017;36:1172–81 CrossRef Medline
27. Wang J, Fang Z, Lang N, et al. **A multi-resolution approach for spinal metastasis detection using deep Siamese neural networks.** *Comput Biol Med* 2017;84:137–46 CrossRef Medline
28. Phong TD, Duong HN, Nguyen HT, et al. **Brain hemorrhage diagnosis by using deep learning.** In: *Proceedings of the International Conference on Machine Learning and Soft Computing,* Ho Chi Minh City, Vietnam. January 13–16, 2017:34–39
29. Simonyan K, Vedaldi A, Zisserman A. Deep inside convolutional networks: visualising image classification models and saliency maps. https://arxiv.org/abs/1312.6034. Accessed March 25, 2018
30. Selvaraju RR, Das A, Vedantam R, et al. Grad-CAM: why did you say that? visual explanations from deep networks via gradient-based localization. https://www.researchgate.net/publication/308964930_GradCAM_Why_did_you_say_that_Visual_Explanations_from_Deep_Networks_via_Gradient-based_Localization. Accessed March 25, 2018
31. Nataraj S. 2013 Imaging Turnaround Times Survey Results. 2014. https://www.advisory.com/research/imaging-performance-partnership/expert-insights/2014/2013-turnaround-times-survey-results. Accessed March 25, 2018
32. Anderson CS, Heeley E, Huang Y, et al; INTERACT2 Investigators. **Rapid blood-pressure lowering in patients with acute intracerebral hemorrhage.** *N Engl J Med* 2013;368:2355–65 CrossRef Medline
33. Jung SW, Lee CY, Yim MB. **The relationship between subarachnoid hemorrhage volume and development of cerebral vasospasm.** *J Cerebrovasc Endovasc Neurosurg* 2012;14:186–91 CrossRef Medline
34. Bullock MR, Chesnut R, Ghajar J, et al; Surgical Management of Traumatic Brain Injury Author Group. **Surgical management of acute epidural hematomas.** *Neurosurgery* 2006;58:S7–S15; discussion Si-iv Medline
35. Kwak R, Kadoya S, Suzuki T. **Factors affecting the prognosis in thalamic hemorrhage.** *Stroke* 1983;14:493–500 CrossRef Medline
36. Goodfellow IJ, Shlens J, Szegedy C. **Explaining and harnessing adversarial examples.** In: *Proceedings of the International Conference for Learning Representations,* San Diego, California. May 7–9, 2015
37. Gu S, Rigazio L. **Towards deep neural network architectures robust to adversarial examples.** https://arxiv.org/abs/1412.5068. Accessed March 25, 2018

# Vessel Wall Enhancement in Unruptured Intracranial Aneurysms: An Indicator for Higher Risk of Rupture? High-Resolution MR Imaging and Correlated Histologic Findings

N. Larsen, C. von der Brelie, D. Trick, C.H. Riedel, T. Lindner, J. Madjidyar, O. Jansen, M. Synowitz, and C. Flüh

## ABSTRACT

**BACKGROUND AND PURPOSE:** Recent studies have suggested that wall enhancement of unruptured intracranial aneurysms in high-resolution MR imaging might serve as an imaging biomarker for higher risk of rupture. Histologic studies have revealed a possible association among inflammatory processes, degeneration, and destabilization of the aneurysm wall preceding rupture. Understanding the histologic condition underlying aneurysm wall enhancement could be an important step toward assessing the value of this method for risk stratification. We present our observations of aneurysm wall enhancement in MR vessel wall imaging and underlying histologic changes.

**MATERIALS AND METHODS:** We reviewed records of patients with an unruptured middle cerebral artery aneurysm who underwent MR vessel wall imaging before aneurysm clipping. Contrast enhancement of the aneurysm wall was dichotomized into either none/faint or strong. Histologic analysis included myeloperoxidase stain for detection of inflammatory cell invasion and CD34 stain for assessment of neovascularization and vasa vasorum.

**RESULTS:** Thirteen aneurysms were included. Five aneurysms showed strong wall enhancement. Among these, myeloperoxidase staining revealed inflammatory cell infiltration in 4. Three showed neovascularization. In 2 aneurysms, vasa vasorum were present. Seven aneurysms did not show wall enhancement; 1 had only mild enhancement. None of these bore evidence of inflammatory cell invasion or neovascularization, and they all lacked vasa vasorum.

**CONCLUSIONS:** Wall enhancement in MR vessel wall imaging is associated with inflammatory cell invasion, neovascularization, and the presence of vasa vasorum. Enhancement does not occur when histologic signs of inflammation are absent. Our results support the hypothesis that MR vessel wall imaging could provide valuable information for risk stratification.

**ABBREVIATIONS:** MPO = myeloperoxidase; PHASES = Population, Hypertension, Age, Size, Earlier subarachnoid hemorrhage, and Site; VWI = vessel wall imaging

Unruptured intracranial saccular aneurysms have a prevalence of 3%–4% and generally have a low risk of rupture. Risk of rupture has been shown to depend on size and location, with the lowest risk for small aneurysms (<7 mm) in the anterior circulation. About 11% of patients show symptoms attributable to the unruptured aneurysm (eg, cranial nerve palsies).[1,2] In daily practice, subarachnoid hemorrhage from aneurysms of <7 mm is often encountered, while on the other hand, giant aneurysms in older patients sometimes are followed up for years without rupture. Treatment options are endovascular management with platinum coils, intrasaccular flow disruptors, or flow diverters and the neurosurgical approach: microsurgical clipping. Aneurysm rupture resulting in subarachnoid hemorrhage is associated with considerable morbidity and mortality.[3] Therefore, risk stratification is crucial, but optimal management remains controversial. Patient counseling in cases of incidental aneurysms can be challenging and should be based on well-established data.

Recent studies have proposed intracranial aneurysm wall enhancement detected by high-resolution MR imaging as a possible imaging biomarker for a high risk of rupture. Wall enhancement was more frequently observed in unstable (ruptured, symptomatic, or morphologically progressing) than in stable aneurysms and may identify the site of rupture in patients with multiple aneurysms.[4-7]

Received September 6, 2017; accepted after revision June 1, 2018.

From the Department of Radiology and Neuroradiology (N.L., C.H.R., T.L., J.M., O.J.), Department of Neurosurgery (C.v.d.B., M.S., C.F.), and Institute of Pathology (D.T.), University Hospital Schleswig-Holstein Campus Kiel, Kiel, Germany; and Department of Neurosurgery (C.v.d.B.), University Hospital Göttingen, Göttingen, Germany.

Paper previously presented orally at: Annual Meeting of the American Society of Neuroradiology and the Foundation of the ASNR Symposium, April 22–27, 2017; Long Beach, California.

Please address correspondence to Naomi Larsen, MD, Department of Radiology and Neuroradiology, University Hospital Schleswig-Holstein Campus Kiel, Arnold-Heller-Str 3, 24105 Kiel, Germany; e-mail: naomi.larsen@uksh.de

http://dx.doi.org/10.3174/ajnr.A5731

**Patient characteristics**

| Patient | Age (yr) | Sex | ASA | Nicotine | Estimated 5-Year Rupture Risk (PHASES) | Size of Aneurysm (mm) | Location of Aneurysm | Multiple Aneurysms | Enhancement in VWI | MPO | CD34 | Vasa Vasorum |
|---|---|---|---|---|---|---|---|---|---|---|---|---|
| 1 | 48 | Male | Yes | No | 3.2% | 17 | Right MCA | No | Strong | + | + | No |
| 2 | 64 | Male | Yes | Yes | 0.4% | 6 | Right MCA | No | Strong | + | + | No |
| 3 | 73 | Female | Yes | Yes | 5.3% | 10 | Right MCA | No | Strong | + | + | No |
| 4 | 48 | Female | No | Yes | 3.2% | 10 | Left MCA | No | Faint | − | − | No |
| 5 | 52 | Female | Yes | Yes | 0.7% | 5 | Right MCA | Yes | None | − | − | No |
| 6 | 53 | Male | Yes | Yes | 4.3% | 14 | Right MCA | No | Strong | − | − | Yes |
| 7 | 53 | Female | Yes | Yes | 0.7% | 7 | Left MCA | No | None | − | − | No |
| 8 | 46 | Male | No | Yes | 0.4% | 6 | Left MCA | Yes | Strong (partial) | + | − | Yes |
| 9 | 48 | Male | No | Yes | 0.4% | 8 | Left MCA | No | None | − | − | No |
| 10 | 57 | Female | No | No | 1.7% | 9 | Right MCA | No | None | − | − | No |
| 11 | 67 | Female | No | Yes | 0.7% | 4 | Right MCA | No | None | − | − | No |
| 12 | 36 | Female | No | No | 0.4% | 4 | Right MCA | No | None | − | − | No |
| 13 | 49 | Female | No | Yes | 1.3% | 9 | Right MCA | No | None | − | − | No |

**Note:**—ASA indicates acetylsalicylic acid; +, positive; −, negative.

Multiple histologic studies have contributed detailed descriptions of remodelling and inflammatory processes that occur during the evolution of intracranial saccular aneurysms. These processes include invasion of macrophages and other inflammatory cells in the aneurysm wall. Infiltration of mast cells is associated with neovascularization and degeneration of the aneurysm wall.[8,9]

Gounis et al[10] have shown that myeloperoxidase (MPO), an enzyme mainly secreted by neutrophilic granulocytes, is abundant in the walls of aneurysms with a higher estimated 5-year-rupture risk. The results suggest that MPO could possibly function as a biomarker for instability.

Vasa vasorum have been associated with neutrophilic MPO infiltration of the aneurysm wall by facilitating an outside-in pathway.[11] Nondiseased intracranial arteries in children and young adults usually do not have vasa vasorum. They develop with age, mainly in the proximal intracranial segments of the internal carotid, vertebral, and basilar arteries, reflecting degenerative processes. Moreover, vasa vasorum can be found in intracranial vessel segments affected by atherosclerosis, vasculitis, or aneurysm formation. It has been shown that intracranial vasa vasorum not only develop because of atherosclerotic wall remodelling, inflammation, or wall injury but also play a crucial role in further promotion of atherosclerotic remodelling changes by enabling the inflammatory outside-in pathway.[12,13]

Both neovascularization and the presence of vasa vasorum have been shown to correlate with contrast enhancement of the vessel wall in fusiform basilar aneurysms.[14]

Whether wall enhancement in saccular intracranial aneurysms correlates with remodelling changes, inflammatory activity, the presence of vasa vasorum, or rather a combination of factors has not explicitly been investigated.

Understanding the histopathologic condition underlying aneurysm wall enhancement could be an important step toward assessing the significance of wall enhancement and the value of MR vessel wall imaging (VWI) for risk stratification.

We present our first observations of aneurysm wall enhancement in MR VWI and underlying histopathologic changes in unruptured intracranial aneurysms.

## MATERIALS AND METHODS

This study was approved by the Ethics Committee at the Faculty of Medicine of Christian-Albrechts-University Kiel. We retrospectively reviewed records of all patients with an unruptured saccular middle cerebral artery aneurysm who underwent preoperative high-resolution MR VWI and microsurgical aneurysm clipping in our institution between May 2015 and June 2017. VWI was performed on a 3T MR imaging scanner (Achieva; Philips Healthcare, Best, the Netherlands) and comprised time-of-flight angiography and a T1-weighted black-blood 3D volume isotropic turbo spin-echo acquisition (TE/TR, 27/700 ms; matrix, 268 × 332; FOV, 200 × 250 × 160 mm; voxel size, 0.75 × 0.75 × 0.75 mm; acquisition time, 4 minutes 45 seconds) before and after administration of 0.1 mmol/kg of gadoterate meglumine (Dotarem; Guerbet, Aulnay-sous-Bois, France). Contrast enhancement of the aneurysm wall was visually rated as none/faint and strong. All patients underwent microsurgical clipping of the aneurysm via a pterional, transsylvian approach. Pre-, post-, and intraoperative management of the patients was performed according to institutional standards. This included pre- and postoperative digital subtraction angiography of the intracranial vessels and, in most cases, intraoperative angiography with indocyanine green. After clipping the aneurysm, the aneurysm sac was removed.

Histologic analysis was performed as described elsewhere.[15] In brief, formalin-fixed and paraffin-embedded resection specimens were cut into 2.5-$\mu$m-thin tissue sections. Slides were either stained with hematoxylin-eosin or using rabbit anti-MPO polyclonal antibody (1:1000; DAKO, Glostrup, Denmark) after antigen retrieval with ER2 (EDTA-buffer Bond pH 8.9) or a monoclonal antibody against CD34 (Clone QBEnd10, 1:700; Beckman Coulter, Sykesville, Maryland) without antigen retrieval using the autostainer Bond Max System (Leica Microsystems, Wetzlar, Germany).

## RESULTS

Fifteen patients who met the inclusion criteria were identified. Two were not further analyzed because there was not a sufficient amount of resected tissue for a comprehensive histologic analysis.

We analyzed MR VWI and histologic findings in 13 patients, 5

men, 8 women; age range, 36–73 years. All had middle cerebral artery aneurysms with maximum diameters ranging from 4 to 17 mm. Patient characteristics are shown in the Table. None of the patients had major complications during or after the operation. There was no case of intraoperative rupture.

Five aneurysms showed strong wall enhancement (Fig 1), with circumferential enhancement in 4 and partial enhancement in 1. Among these, 4 were MPO-positive. Three showed neovascularization as detected by CD34 staining. In 2 of these aneurysms, vasa vasorum were present (Fig 2).

Seven aneurysms did not show wall enhancement; 1 showed only faint enhancement. They were MPO- and CD 34-negative, and they all lacked vasa vasorum.

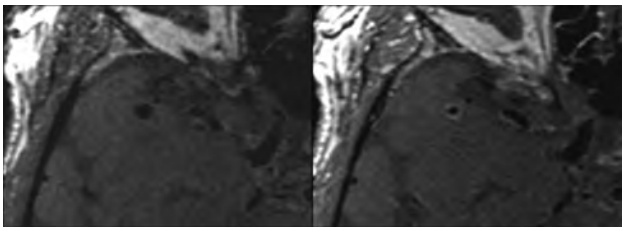

**FIG 1.** Nonenhanced (*left*) and contrast-enhanced (*right*) MR vessel wall imaging shows circumferential strong contrast enhancement of a right middle cerebral artery aneurysm.

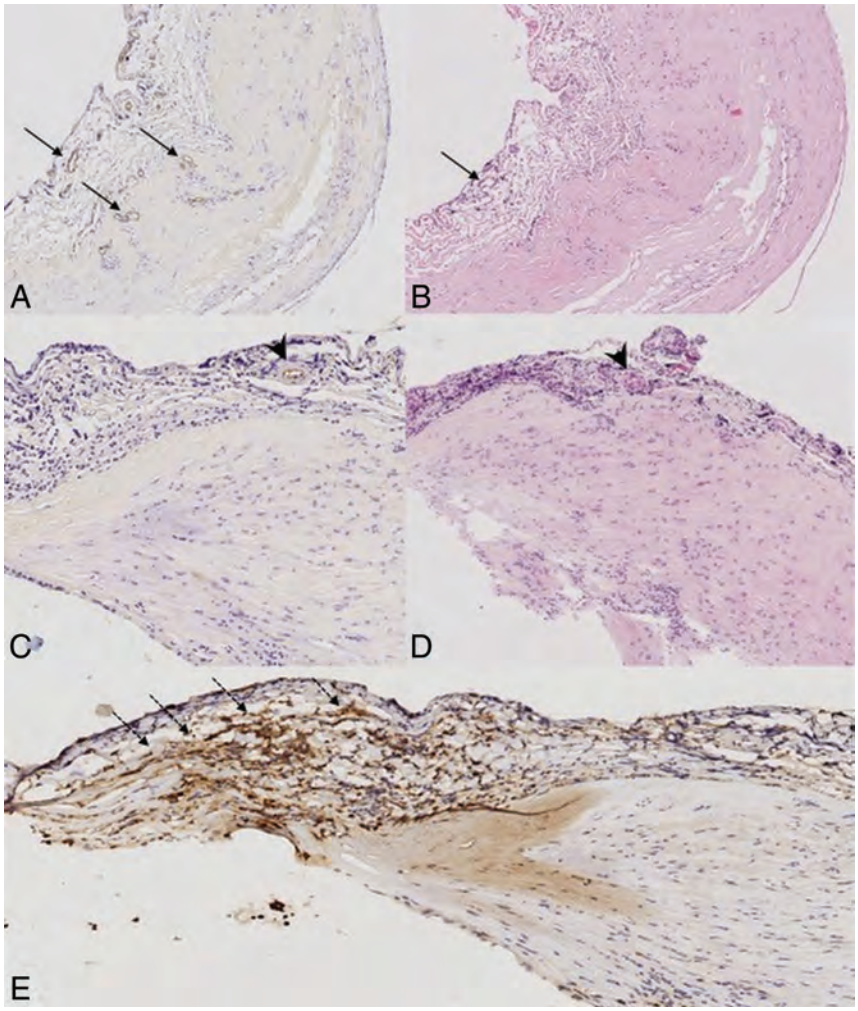


**FIG 2.** CD34 (*A* and *C*), hematoxylin-eosin (*B* and *D*), and MPO stain (*E*) at 10x magnification. *A* and *B*, Patient 3: aneurysm wall with evidence of neovascularization (*arrows*). *C* and *D*, Patient 8, vasa vasorum are present (*arrowheads*). There is no sign of neovascularization. *E*, The same patient as in *C* and *D*. MPO-positive aneurysm wall with accumulation of MPO-positive inflammatory cells in the tunica media (*dotted arrows*).

## DISCUSSION

Various histologic markers of aneurysm wall inflammation and degeneration have been identified. Furthermore, there is growing evidence from MR imaging studies suggesting a connection of wall enhancement and an unstable state of the aneurysm. How imaging findings reflect histologic changes associated with aneurysm formation, growth, and rupture has not yet been explored. In our study, we attempted to correlate histologic markers with a promising and easily assessable imaging marker. We found that MPO could only be detected in aneurysms with mural enhancement, but not in all (4/5). In the MPO-negative aneurysm with mural enhancement, vasa vasorum were present. Furthermore, not all MPO-positive aneurysms showed evidence of neovascularization and vasa vasorum. Abundance of inflammatory cells such as mast cells has been associated with a higher density of neovessels,[8] which does not necessarily imply a coexistence in every aneurysm. Vasa vasorum can be detected in intracranial aneurysms of >4 mm and are thought to form not only in association with chronic mural inflammation but also because of vascular remodeling.[12]

Vessel wall enhancement possibly occurs not only in the context of inflammatory cell invasion but with various types of histologic changes, likely representing different stages and phenotypes of vasculopathy, leading to aneurysm formation and growth. Still, this hypothesis should be validated in studies with larger sample sizes.

Clinical scoring systems are frequently used in counseling patients with unruptured intracranial aneurysms. The PHASES (Population, Hypertension, Age, Size, Earlier subarachnoid hemorrhage, and Site) model is often used to estimate the absolute risk of rupture for the initial 5 years. It takes 6 baseline patient characteristics into account, including population (P), hypertension (H), age (A), aneurysm size (S), earlier subarachnoid hemorrhage from another aneurysm (E), and the site of the aneurysm (S).[16] However, the PHASES model may not be applicable to certain patient subgroups.

The Unruptured Intracranial Aneurysm Treatment Score includes more factors that possibly influence rupture risk

than the PHASES score. Nonetheless, it is not a predictive model because it is partially derived from consensus among cerebrovascular specialists.[17]

Both scores aimed to assess the patient-specific risk of rupture by accumulating established risk factors. They do not serve to estimate the individual aneurysm-related risk of rupture.

Additionally, imaging-based approaches have identified numerous morphologic and flow characteristics associated with a higher risk of rupture.[18-29] Easily assessable characteristics such as aneurysm size or the presence of a daughter sac are usually already being considered in clinical practice for risk stratification. More complex geometric measurements or the assessment of intrasaccular hemodynamics, which require specialized image postprocessing or analysis software, cannot be easily performed in all centers and are therefore not readily available for patient management. Furthermore, these methods focus on the morphologic changes resulting from aneurysm wall degeneration without being able to directly visualize a correlate of the causative processes.

Our results support the assumption that contrast-enhanced MR vessel wall imaging might be able to directly detect inflammatory and degenerative changes associated with aneurysm progression and thereby enable the clinician to estimate the individual risk of rupture.

The influence of additional factors that possibly affect inflammatory activity in the aneurysm wall, such as acetylsalicylic acid or statin intake, should be investigated in further studies.

Drawbacks of this study include the retrospective study design with an inherent selection bias toward patients with morphologically dangerous-appearing lesions or higher PHASES scores who were scheduled for therapy. Another drawback is the low sample size, which does not allow a comprehensive correlation of the diverse histologic changes that occur during the different stages of aneurysm progression and mural enhancement.

Further prospective studies analyzing data from larger patient cohorts are warranted to consolidate the value of this method.

## CONCLUSIONS

Our results suggest that wall enhancement correlates with destabilizing inflammatory changes of the aneurysm wall and does not occur when histologic signs of inflammation are absent. The results support the hypothesis that MR VWI may be a valuable tool for risk stratification of patients with unruptured intracranial aneurysms and could aid in the decision-making process and patient management.

Disclosures: David Trick—*UNRELATED*: *Payment for Lectures Including Service on Speakers Bureaus*: Boehringer Ingelheim, *Comments*: lecture on interstitial lung disease. Olav Jansen—*UNRELATED*: *Payment for Lectures Including Service on Speakers Bureaus*: Stryker, Medtronic, Bayer Pharma AG. Charlotte Flüh—*UNRELATED*: *Employment*: Resident at University Medical Center Schleswig-Holstein, Campus Kiel, Germany.

## REFERENCES

1. Wiebers DO, Whisnant JP, Huston J 3rd, et al; International Study of Unruptured Intracranial Aneurysms Investigators. **Unruptured intracranial aneurysms: natural history, clinical outcome, and risks of surgical and endovascular treatment.** *Lancet* 2003;362:103–10 Medline
2. Vlak MH, Algra A, Brandenburg R, et al. **Prevalence of unruptured intracranial aneurysms, with emphasis on sex, age, comorbidity, country, and time period: a systematic review and meta-analysis.** *Lancet Neurol* 2011;10:626–36 CrossRef Medline
3. Nieuwkamp DJ, Setz LE, Algra A, et al. **Changes in case fatality of aneurysmal subarachnoid haemorrhage over time, according to age, sex, and region: a meta-analysis.** *Lancet Neurol* 2009;8:635–42 CrossRef Medline
4. Edjlali M, Gentric JC, Régent-Rodriguez C, et al. **Does aneurysmal wall enhancement on vessel wall MRI help to distinguish stable from unstable intracranial aneurysms?** *Stroke* 2014;45:3704–06 CrossRef Medline
5. Hu P, Yang Q, Wang DD, et al. **Wall enhancement on high-resolution magnetic resonance imaging may predict an unsteady state of an intracranial saccular aneurysm.** *Neuroradiology* 2016;58:979–85 CrossRef Medline
6. Nagahata S, Nagahata M, Obara M, et al. **Wall enhancement of the intracranial aneurysms revealed by magnetic resonance vessel wall imaging using three-dimensional turbo spin-echo sequence with motion-sensitized driven-equilibrium: a sign of ruptured aneurysm?** *Clin Neuroradiol* 2016;26:277–83 CrossRef Medline
7. Matouk CC, Mandell DM, Günel M, et al. **Vessel wall magnetic resonance imaging identifies the site of rupture in patients with multiple intracranial aneurysms: proof of principle.** *Neurosurgery* 2013; 72:492–96; discussion 496 CrossRef Medline
8. Ollikainen E, Tulamo R, Frösen J, et al. **Mast cells, neovascularization, and microhemorrhages are associated with saccular intracranial artery aneurysm wall remodeling.** *J Neuropathol Exp Neurol* 2014;73:855–64 CrossRef Medline
9. Hoh BL, Hosaka K, Downes DP, et al. **Stromal cell-derived factor-1 promoted angiogenesis and inflammatory cell infiltration in aneurysm walls.** *J Neurosurg* 2014;120:73–86 CrossRef Medline
10. Gounis MJ, Vedantham S, Weaver JP, et al. **Myeloperoxidase in human intracranial aneurysms: preliminary evidence.** *Stroke* 2014;45: 1474–77 CrossRef Medline
11. Gounis MJ, van der Marel K, Marosfoi M, et al. **Imaging inflammation in cerebrovascular disease.** *Stroke* 2015;46:2991–97 CrossRef Medline
12. Portanova A, Hakakian N, Mikulis DJ, et al. **Intracranial vasa vasorum: insights and implications for imaging.** *Radiology* 2013; 267:667–79 CrossRef Medline
13. Maiellaro K, Taylor WR. **The role of the adventitia in vascular inflammation.** *Cardiovasc Res* 2007;75:640–48 CrossRef Medline
14. Nakatomi H, Segawa H, Kurata A, et al. **Clinicopathological study of intracranial fusiform and dolichoectatic aneurysms: insight on the mechanism of growth.** *Stroke* 2000;31:896–900 CrossRef Medline
15. Warneke VS, Behrens HM, Haag J, et al. **Prognostic and putative predictive biomarkers of gastric cancer for personalized medicine.** *Diagn Mol Pathol* 2013;22:127–37 CrossRef Medline
16. Greving JP, Wermer MJ, Brown RD Jr, et al. **Development of the PHASES score for prediction of risk of rupture of intracranial aneurysms: a pooled analysis of six prospective cohort studies.** *Lancet Neurol* 2014;13:59–66 CrossRef Medline
17. Etminan N, Brown RD Jr, Beseoglu K, et al. **The unruptured intracranial aneurysm treatment score: a multidisciplinary consensus.** *Neurology* 2015;85:881–89 CrossRef Medline
18. Dhar S, Tremmel M, Mocco J, et al. **Morphology parameters for intracranial aneurysm rupture risk assessment.** *Neurosurgery* 2008; 63:185–96; discussion 196–97 CrossRef Medline
19. Rahman M, Smietana J, Hauck E, et al. **Size ratio correlates with intracranial aneurysm rupture status: a prospective study.** *Stroke* 2010;41:916–20 CrossRef Medline
20. Xiang J, Natarajan SK, Tremmel M, et al. **Hemodynamic-morphologic discriminants for intracranial aneurysm rupture.** *Stroke* 2011; 42:144–52 CrossRef Medline
21. Cebral JR, Mut F, Weir J, et al. **Quantitative characterization of the hemodynamic environment in ruptured and unruptured brain aneurysms.** *AJNR Am J Neuroradiol* 2011;32:145–51 CrossRef Medline
22. Chien A, Sayre J, Viñuela F. **Comparative morphological analysis of**

**the geometry of ruptured and unruptured aneurysms.** *Neurosurgery* 2011;69:349–56 CrossRef Medline
23. Baharoglu MI, Lauric A, Gao BL, et al. **Identification of a dichotomy in morphological predictors of rupture status between sidewall- and bifurcation-type intracranial aneurysms**. *J Neurosurg* 2012;116: 871–81 CrossRef Medline
24. Lin N, Ho A, Gross BA, et al. **Differences in simple morphological variables in ruptured and unruptured middle cerebral artery aneurysms.** *J Neurosurg* 2012;117:913–19 CrossRef Medline
25. Cai W, Shi D, Gong J, et al. **Are morphologic parameters actually correlated with the rupture status of anterior communicating artery aneurysms?** *World Neurosurg* 2015;84:1278–83 CrossRef Medline
26. Kang H, Ji W, Qian Z, et al. **Aneurysm characteristics associated with the rupture risk of intracranial aneurysms: a self-controlled study.** *PLoS One* 2015;10:e0142330 CrossRef Medline
27. Ho AL, Lin N, Frerichs KU, et al. **Intrinsic, transitional, and extrinsic morphological factors associated with rupture of intracranial aneurysms.** *Neurosurgery* 2015;77:433–41; discussion 441–42 CrossRef Medline
28. Zheng Y, Xu F, Ren J, et al. **Assessment of intracranial aneurysm rupture based on morphology parameters and anatomical locations.** *J Neurointerv Surg* 2016 Jan 11. [Epub ahead of print]. CrossRef Medline
29. Cebral J, Ollikainen E, Chung BJ, et al. **Flow conditions in the intracranial aneurysm lumen are associated with inflammation and degenerative changes of the aneurysm wall.** *AJNR Am J Neuroradiol* 2017;38:119–26 CrossRef Medline

# Quantitative MRI of Perivascular Spaces at 3T for Early Diagnosis of Mild Cognitive Impairment

M. Niazi, M. Karaman, S. Das, X.J. Zhou, P. Yushkevich, and K. Cai

## ABSTRACT

**BACKGROUND AND PURPOSE:** The limitations inherent in the current methods of diagnosing mild cognitive impairment have constrained the use of early therapeutic interventions to delay the progression of mild cognitive impairment to dementia. This study evaluated whether quantifying enlarged perivascular spaces observed on MR imaging can help differentiate those with mild cognitive impairment from cognitively healthy controls and, thus, have an application in the diagnosis of mild cognitive impairment.

**MATERIALS AND METHODS:** We automated the identification of enlarged perivascular spaces in brain MR Images using a custom quantitative program designed with Matlab. We then quantified the densities of enlarged perivascular spaces for patients with mild cognitive impairment ($n = 14$) and age-matched cognitively healthy controls ($n = 15$) and compared them to determine whether the density of enlarged perivascular spaces can serve as an imaging surrogate for mild cognitive impairment diagnosis.

**RESULTS:** Quantified as a percentage of volume fraction (v/v%), densities of enlarged perivascular spaces were calculated to be 2.82 ± 0.40 v/v% for controls and 4.17 ± 0.57 v/v% for the mild cognitive impairment group in the subcortical brain ($P < .001$), and 2.74 ± 0.57 v/v% for the controls and 3.90 ± 0.62 v/v% for the mild cognitive impairment cohort in the basal ganglia ($P < .001$). Maximum intensity projections exhibited a visually conspicuous difference in the distributions of enlarged perivascular spaces for a patient with mild cognitive impairment and a control patient. By means of receiver operating characteristic curve analysis, we determined the sensitivity and specificity of using enlarged perivascular spaces as a differentiating biomarker between mild cognitive impairment and controls to be 92.86% and 93.33%, respectively.

**CONCLUSIONS:** The density of enlarged perivascular spaces was found to be significantly higher in those with mild cognitive impairment compared with age-matched healthy control subjects. The density of enlarged perivascular spaces, therefore, may be a useful imaging biomarker for the diagnosis of mild cognitive impairment.

**ABBREVIATIONS:** AD = Alzheimer disease; aMCI = amnestic mild cognitive impairment; EPVS = enlarged perivascular spaces; MCI = mild cognitive impairment; PVS = perivascular spaces; v/v % = percentage of volume fraction

Perivascular spaces (PVS) are cavities filled with cerebrospinal and interstitial fluids that lie between the perforating blood vessels of the brain and the pia mater.[1,2] They act as conduits for the drainage of interstitial fluid and solutes from the brain.[3] These spaces can become dilated and are termed enlarged perivascular spaces (EPVS) when large enough to be visible on imaging.[4] The presence of EPVS has been shown to be increased in a variety of physiologic and pathologic neurologic conditions, such as aging, hypertension, arteriosclerosis, dementia, mild cognitive impairment (MCI), Alzheimer disease (AD), and Parkinson disease.[5-8]

Current research suggests that MCI can be a harbinger of AD development, with annual rates of progression variably reported to be 10%–15%.[9-12] Individuals with MCI exhibit cognitive impairment beyond that expected for their age, a feature shared with AD, with no overt impact on their activities of daily living.[13] The MCI population is of particular clinical interest because it is hypothesized that early therapeutic interventions can be used to delay or even thwart their deterioration to AD.[14] The challenge lies in detecting MCI early enough for such interventions to be successful. Several assessment tools, such as the Mini-Mental

Received February 8, 2018; accepted after revision June 2.

From the Department of Radiology (M.N., X.J.Z., K.C.) and Center for MR Research (M.K., X.J.Z., K.C.), College of Medicine, University of Illinois at Chicago, Chicago, Illinois; Chicago College of Osteopathic Medicine (M.N.), Midwestern University, Downers Grove, Illinois; and Department of Radiology (S.D., P.Y.), School of Medicine, University of Pennsylvania, Philadelphia, Pennsylvania.

This study was supported by the National Institute of Biomedical Imaging and Bioengineering of the National Institutes of Health under award number R21 EB023516.

Please address correspondence to Kejia Cai, PhD, Department of Radiology, Center for MR Research, College of Medicine, University of Illinois at Chicago, 2242 W Harrison St, Suite 103, Chicago, IL 60612; e-mail: kcai@uic.edu

Indicates open access to non-subscribers at www.ajnr.org

http://dx.doi.org/10.3174/ajnr.A5734

State Examination,[15] are used by physicians to clinically assess MCI. However, a failure to detect the condition, especially in its early stages, is an important limitation of these tools[11,16,17] and underscores an emergent need for more quantitative diagnostic approaches.

Aided by a discovery of several sensitive and specific imaging biomarkers, including the EPVS, MR imaging continues to find increasing utility in the diagnosis of AD.[18] Logically, these biomarkers hold the most promise for becoming indicators of MCI as well.[19,20] Owing to the difficulties involved in their quantification, EPVS are a relatively understudied biomarker.[21] Current evaluation of their properties, such as their shape, size, and number, remains a subjective process.[22] Development of objective methods for quantifying these properties is, thus, highly desirable, with a great potential for clinical utility.

A quantitative method for mapping brain PVS in the MR images of healthy patients and those with AD acquired on a 7T whole-body MR imaging scanner has previously been reported by Cai et al.[23] Using a train of algorithms, including a pixel-wise spatial gradient, we segmented the hyperintense PVS and calculated their density as a percentage of volume fraction (v/v%). The initial results demonstrated that the PVS density is significantly higher in patients with AD compared with healthy controls.[23]

In this retrospective study based on brain imaging datasets collected previously for other research purposes,[24] we aimed to evaluate whether the quantitative EPVS MR imaging at the clinically prevalent 3T can help differentiate subjects with MCI from age-matched healthy controls. We tested our method on patients diagnosed with amnestic MCI (aMCI), 1 of the 2 main subtypes of MCI; the other is nonamnestic MCI. Individuals with aMCI have memory impairment as their predominant symptom and have a higher risk of conversion to AD than individuals with nonamnestic MCI, who present with a decline in cognitive domains other than memory and convert more frequently to other dementia forms, such as Lewy body dementia.[25,26]

## MATERIALS AND METHODS

### Subjects

The subjects, 15 controls and 14 patients who met the Petersen criteria for aMCI, were recruited from the Penn Memory Center/Alzheimer Disease Center at the University of Pennsylvania between 2011 and 2014.[27]

To be included, all subjects required the following: age of 55–89 years, at least 2 years postmenopausal or surgically sterile if female, fluent in English, 6 grades of education or sufficient work experience to exclude mental retardation, in good health without any diseases that could interfere with the study, visual and auditory acuity to allow neuropsychological testing, a geriatric depression scale of <6, and willing and able to complete all the required study procedures. Additional inclusion criteria for patients were a diagnosis of probable aMCI and a Mini-Mental State Examination score between 24 and 30. Exclusion criteria were neurologic diseases other than aMCI or AD; the presence of devices contraindicated for MR imaging; a history of major depression, bipolar disorder, schizophrenia, substance abuse or dependency within the past 2 years; illnesses or medical conditions that could lead to difficulty complying with the study protocol; anxiety disorders; and pregnancy.

The mean age for controls and the patients with aMCI was 66.3 ± 9.5 and 71.9 ± 6.2 years, respectively ($P = .07$). The male/female ratios were 7:8 and 6:8 for the control and the aMCI groups respectively ($P = 1.00$). Education, measured in years of schooling, was 15.6 ± 2.6 years for controls and 16.9 ± 2.8 years for the aMCI cohort ($P = .19$). The subjects' performance on the Mini-Mental State Examination was 29.5 ± 1.0 for the controls and 26.9 ± 1.7 for the aMCI group ($P < .001$); on the Consortium to Establish a Registry for Alzheimer Disease Word List Memory Task, it was 24.7 ± 2.9 for the controls and 16.2 ± 3.2 for the aMCI group ($P < .001$); and on the Delayed-Recall Test, it was 8.7 ± 1.8 for the controls and 3.4 ± 2.1 for the aMCI group ($P < .001$).[24]

All subjects provided informed consent, and the research was performed in compliance with the standards set by the National Institutes of Health, the institutional review board, and the International Code of Medical Ethics of the World Medical Association. All subjects underwent high-resolution T2-weighted MR imaging of the brain.[24]

### MR Imaging

T2-weighted MR images were acquired on a 3T MAGNETOM Trio scanner (Siemens, Erlangen, Germany) with an 8-channel array head coil at the Hospital of the University of Pennsylvania. In total, 30 coronal slices of the middle brain were acquired with a slice thickness of 2 mm and a 0.6-mm gap, covering a total of 78 mm. The other parameters for the T2-weighted scans included the following: TR/TE = 5310/68 ms, echo-train length = 15, echo spacing = 18.3 ms, phase oversampling = 0%, FOV = 180 × 180 $mm^2$, image matrix = 448 × 448, rendering an in-plane resolution of 0.4 × 0.4 $mm^2$. The total acquisition time for the T2-weighted dataset is about 7 minutes.[24]

### Image Processing

A custom script was written using Matlab (R2012b; MathWorks, Natick, Massachusetts) to automate the segmentation of EPVS in the brain scans. We focused on the EPVS in the white matter and the basal ganglia, areas that previous research identified as ROIs for studying the EPVS.[4]

For each image, first, pixels of background noise were excluded using a preset threshold to create a brain mask. To segment out the white matter and the subcortical nuclei from the brain, we performed 2 successive rounds of 3- and 6-level k-means clustering to filter out the CSF and cortical gray matter, respectively. Hole-filling, edge-detection, and contrast-enhancement algorithms were used throughout this process to prevent the EPVS from being filtered out and to keep the edges with their high spatial gradient from being erroneously labeled as EPVS in the subsequent steps. The pixel-wise spatial gradient was then calculated using the Matlab function "imgradient." EPVS were then automatically identified as pixels with a spatial gradient and top 92% of gradient values. The threshold was determined heuristically, given that pixels for brain tissues have 8% of the lowest gradient values. Eventually, the function "bwconncomp" in Matlab was applied to preserve the fusiform structures corresponding

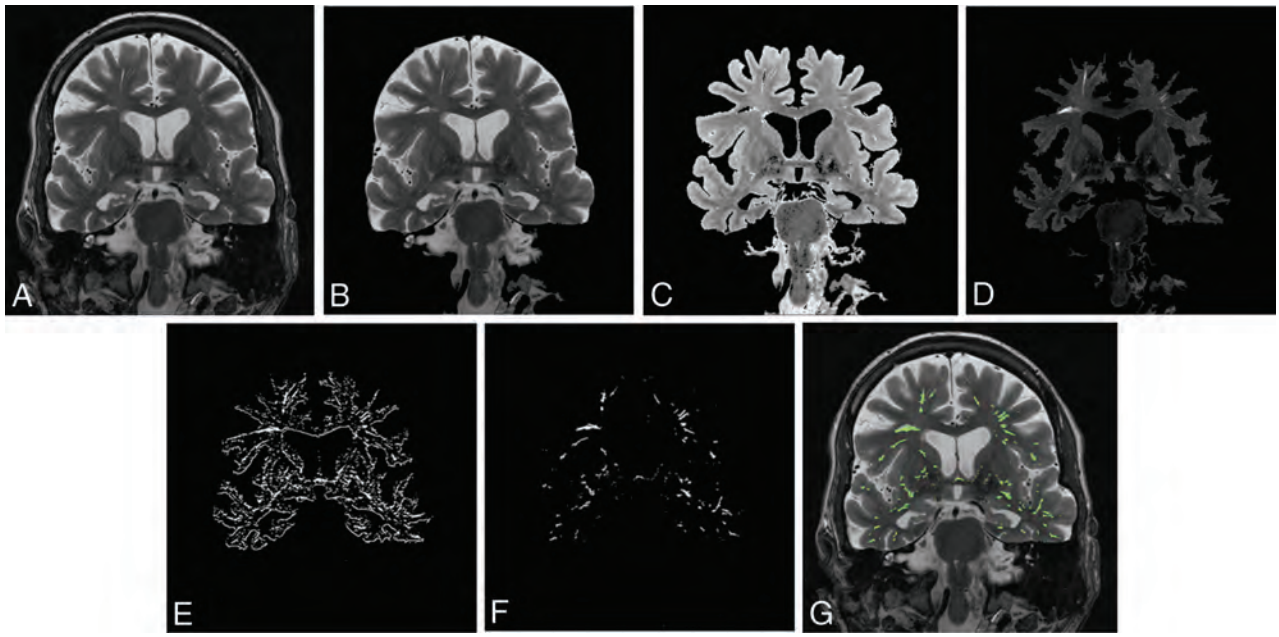


**FIG 1.** Illustration of the EPVS segmentation process. *A*, A coronal MR brain image of a patient with aMCI. The original image fitted with a brain mask (*B*) and the original image fitted with a mask generated with first-order k-means clustering to remove the CSF (*C*). *D*, Contrast-enhanced image of the brain fitted with the mask generated with second-order k-means clustering to exclude the cortical gray matter. *E*, A mask for pixels with high and positive spatial gradient values obtained from a pixel-wise spatial gradient map. The brain stem was manually removed. *F*, EPVS selected on the basis of object size after removing the edges of the brain structures. *G*, Color-coded EPVS overlaid on the original brain image.

to the EPVS with a prescribed object size (20–200 pixels) and to generate EPVS maps of the brain. False-positive and false-negative rates for the automatic EPVS-segmentation method were estimated on the basis of visual counting from 10 randomly selected brain slices from 10 distinct subjects, of which 5 were patients with aMCI and 5 were controls.

The density of EPVS as a volume fraction was calculated as the total volume of segmented EPVS divided by the total volume of the white matter and the subcortical nuclei.

EPVS images from brain slices were interpolated to create a 3D volume of isotropic voxels (0.4 × 0.4 × 0.4 mm) as was performed in Cai et al.[28] Using ImageJ (National Institutes of Health, Bethesda, Maryland), we created maximum intensity projections. These projections were color-coded using the cyan hot color map available in ImageJ.

MIPs and the calculation of EPVS density were limited to the brain volume bounded anteriorly by the anterior-most part of the hippocampus and posteriorly by the anterior-most part of the cerebellum for 2 reasons: First, this limitation is consistent with previous studies that have identified this region, which contains structures such as the subcortical nuclei, as the most relevant area for studying the EPVS distribution.[4] Second, the cerebellum was excluded, given that it contains fine linear structures with high and positive spatial gradients that can be erroneously labeled as EPVS by our algorithms.

To specifically study the EPVS distribution within the basal ganglia, the region of interest for most previous studies on EPVS,[4] we manually drew masks corresponding to these subcortical nuclei in reference to the original T2-weighted brain images. MIPs and the calculation of EPVS density in the basal ganglia were then separately performed.

### *Statistical Analysis*

Experimental results are presented as mean ± SD. To determine whether a statistically significant difference existed between the EPVS densities in the healthy controls and the MCI cohorts, we performed 2-tailed unpaired Student *t* tests with the statistical significance defined as $P < .05$. A receiver operating characteristic curve was generated to evaluate the performance of our method for differentiating individuals with aMCI from controls using EPVS density as an imaging biomarker. EPVS densities were used as the test variables when the state variable was considered the "true" group category obtained from thorough clinical evaluation. The best cutoff sensitivity and specificity values of the receiver operating characteristic curves were determined using the Youden index, which maximizes the sum of sensitivity and specificity. The performance of our method for the differentiation of patients with aMCI from healthy controls was subsequently assessed by these sensitivity and specificity cutoff values as well as the diagnostic accuracy and the area under the curve. The receiver operating characteristic curve analysis was performed in Matlab (R2012b).

## RESULTS

Figure 1 outlines the major steps involved in the automatic identification of EPVS on an MR image of a subject with aMCI. The algorithm sequentially masks the brain (Fig 1*B*), removes CSF with first-order k-means clustering (Fig 1*C*), removes cortical gray matter with second-order k-means clustering (Fig 1*D*), creates a pixel-wise spatial gradient map after manually removing the brain stem, generates the mask for pixels with high and positive spatial gradient values (Fig 1*E*), and selects EPVS on the basis of object size after removing the edges of the brain structures

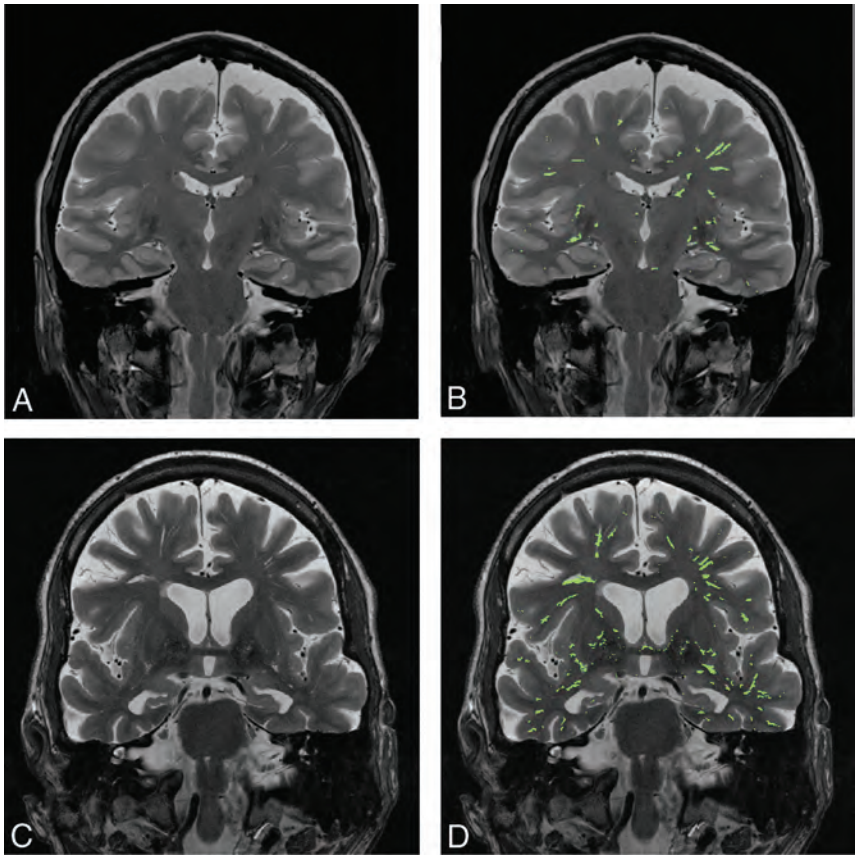


**FIG 2.** A side-by-side comparison of EPVS in a cognitively healthy control versus a patient with aMCI *A*, A coronal MR brain image of a cognitively healthy control. *B*, Segmented EPVS color-overlaid on the MR brain image of a cognitively healthy control. *C*, A coronal MR brain image of a patient with aMCI. *D*, Color-coded EPVS overlaid on the MR brain image of a patient with aMCI.

(Fig 1*F*). Finally, the EPVS are color-coded and subsequently overlaid on the original brain image (Fig 1*G*).

Figure 2 shows side-by-side comparison of the automatically segmented EPVS on MR images of a cognitively healthy individual (Fig 2*A*, -*B*) and a subject with aMCI (Fig 2*C*, -*D*). Compared with visual counting of the number of EPVS pixels, the automatic EPVS segmentation from 10 randomly selected brain slices produced 0.77% ± 0.29% of false-positive pixels and 19.39% ± 6.92% of false-negative pixels. The difference between the false-positive and false-negative pixels among the control and the aMCI subjects was not statistically significant ($P = .44$).

Figure 3 depicts the MIPs generated from ordered middle-brain slices of EPVS images in a control and a subject with aMCI. These MIP images are generated for the white matter and subcortical nuclei as a whole (Fig 3*A*, -*B*) and separately for the basal ganglia (Fig 3*C*, -*D*). There is a visually appreciable increase in the density of EPVS in the subject with aMCI compared with the cognitively healthy subject in both the white matter and subcortical nuclei as well as the basal ganglia.

Quantified as a percentage of volume fraction, EPVS density in the white matter and the subcortical structures was calculated to be 2.82 ± 0.40 v/v% for the controls and 4.17 ± 0.57 v/v% for the aMCI group with $P < .001$. EPVS density in the basal ganglia was 2.74 ± 0.57 v/v% for the controls and 3.90 ± 0.62 v/v% for the aMCI cohort with $P < .001$. Figure 4 depicts these findings in a boxplot form.

Figure 5 depicts the receiver operating characteristic curve for using EPVS as a differentiating biomarker between subjects with aMCI and controls. The area under the curve is 0.96, with the 95% confidence interval between 0.89 and 1.00 and the standard error being 0.04. The threshold value that achieves the best compromise between sensitivity (92.86%) and specificity (93.33%) is 3.35 v/v%.

## DISCUSSION

In this study, we quantified the EPVS density with an automatic segmentation algorithm in patients with MCI and investigated whether EPVS density may be a useful imaging biomarker for the diagnosis of MCI at the clinically available magnetic field strength of 3T.

Improving on the previous study at 7T,[23] we implemented the EPVS quantification method for the MR imaging dataset collected on a clinical 3T scanner. Compared with 7T EPVS MR imaging, the lower magnetic field strength of these scanners entails a lower detection sensitivity and a reduced signal-to-noise ratio.[29] However, it has the benefit of a more homogeneous radiofrequency $B_1$ field, a feature that is appreciated for segmenting EPVS on the basis of a pixel-wise spatial gradient. Most important, EPVS quantification from clinically accessible 3T MR imaging has a higher potential for clinical applications.

The algorithm used in this study performed better at correctly identifying true EPVS at the cost of capturing all the true EPVS pixels in any given brain slice, as evidenced by its lower false-positive rate and the comparatively higher false-negative rate. This lower false-positive rate and the comparatively higher false-negative rate can be explained by the threshold values used in the segmentation process. These values were selected via trial and error, with the aim of maximizing identification of true EPVS, minimizing segmentation of unrelated structures, and using consistent threshold parameters across all subjects. If one assumed that healthy brains are associated with smaller PVS, this conservative PVS recognition strategy may overestimate the difference between MCI and healthy subjects to some extent. Our results show that the EPVS density in a patient with aMCI is significantly higher than that in controls, both in the subcortical brain as a whole and in the basal ganglia separately. This finding suggests that quantitative EPVS density may be a sensitive imaging biomarker with utility in aiding the diagnosis of aMCI.

The detection of MCI remains one of the biggest clinical challenges in the management of neurologic pathologies.[11,16,17] MCI is a relatively common condition in the elderly, with its prevalence reported to be 15%–20% in individuals 65 years of age or older.[30]

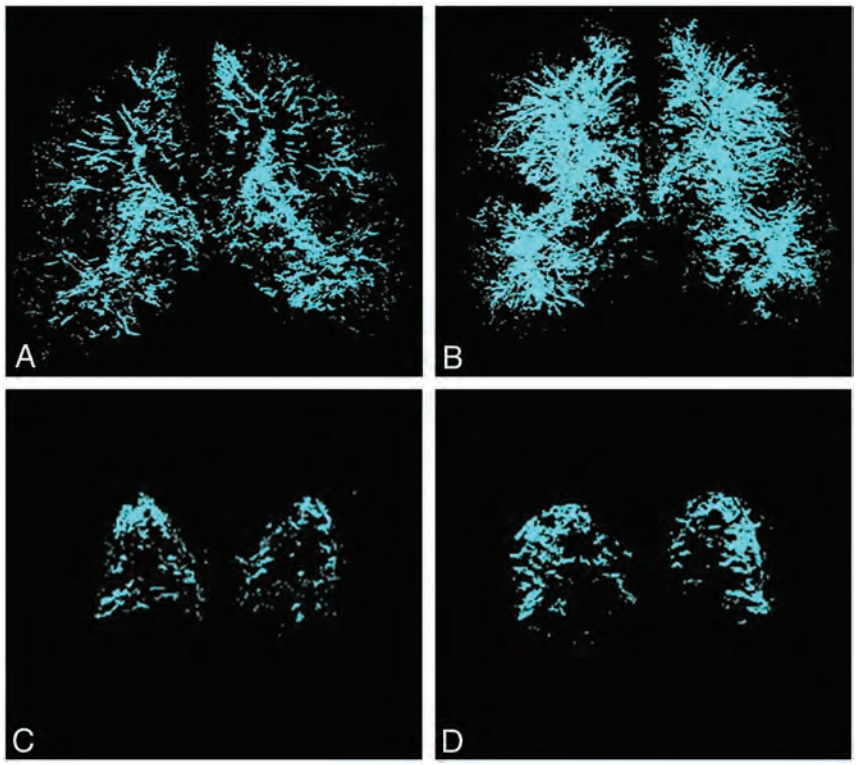


**FIG 3.** Representative multislice MIP projections of EPVS in the subcortical brain structures and the basal ganglia of a control and a subject with aMCI. *A*, MIP image of subcortical structures within the middle of the brain of a control subject. *B*, The MIP image of subcortical structures within the middle of the brain of a subject with aMCI. *C*, MIP image of the basal ganglia of a control subject. *D*, MIP image of the basal ganglia of a subject with aMCI.

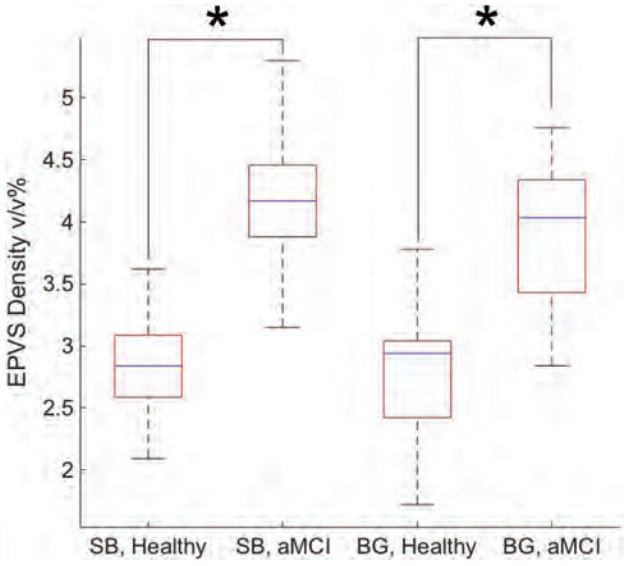


**FIG 4.** Summarized EPVS densities within the middle part of the subcortical brain (SB) and the basal ganglia (BG) of healthy controls and subjects with aMCI. The *asterisk* indicates $P < .001$.

Current research suggests that the MCI population progresses to dementia at a greater rate than those without this condition.[31,32] Anywhere from 32%–38% of individuals with MCI progress to AD in 5 years or longer.[32,33] Annual rates of progression have been estimated to be 10%–15%.[9-12] These findings have naturally generated an interest in using disease-modifying agents to not only preserve cognitive function in individuals with MCI but also slow their conversion to dementia.[14] Given the significant difference between the EPVS densities in patients with MCI and cognitively intact individuals as evidenced by our results, incorporating EPVS quantification into the diagnostic work-up of MCI could help eliminate some of the prevailing uncertainty surrounding its diagnosis, allowing earlier intervention and better clinical outcomes.

Past literature has demonstrated that the entire CSF space and the cerebral ventricular volume increase due to brain tissue atrophy in patients with MCI and AD.[34] Measurement of total CSF space or cerebral ventricular volume with MR imaging may provide a simpler quantitative method to examine neuropathologic changes associated with MCI and AD.[35] However, given that PVS function as a conduit for the drainage of interstitial fluid and solutes from the brain, the measurement of EPVS reflects brain functionality that may be independent of brain tissue atrophy. Hence, EPVS may be an earlier functional signature than structural brain atrophy during the aging process. Testing such a hypothesis will be our future research interest.

Although receiver operating characteristic curve analysis demonstrated >90% sensitivity and specificity for the differentiation of patients with MCI and healthy controls on the basis of quantified EPVS density, some caution is warranted because fundamentally increased EPVS density may not be a specific feature of MCI. It has been observed in a variety of other physiologic and pathologic neurologic conditions, such as normal aging, hypertension, and Parkinson disease.[5-8] EPVS density may therefore be best used to substantiate a suspected diagnosis of MCI in the presence of its other clinical features as opposed to being used as a screening test. Nevertheless, the higher sensitivity of our method underscores its potential as a confirmatory test for the early diagnosis of MCI.[36]

One limitation of this study is that we confined our analyses to the middle region of the brain because the cerebellum posed a unique challenge to our segmentation process. A large volume of the cerebellum is occupied by its finely structured cortex,[37] which appears hyperintense with respect to its surrounding tissues on T2-weighted MR images, a feature it shares with EPVS. This leads our algorithm to misidentify the cerebellar cortex as part of the EPVS. Thereafter, we excluded this brain region from our analysis. Additionally, given that the quantification of the pixel-wise spatial gradient can be affected by the signal-to-noise ratio, spatial resolution, and so forth, our technique for EPVS segmentation requires the MR images to be collected under the same imaging

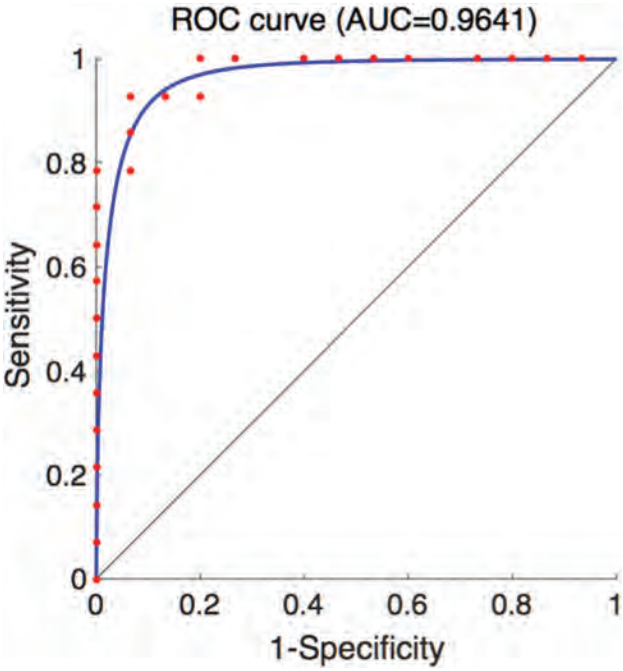


**FIG 5.** The receiver operating characteristic curve for using EPVS as a differentiating biomarker between aMCI and cognitively healthy individuals. The area under the curve is 0.96, the 95% confidence interval is 0.89–1.00, and the standard error is 0.04. The cutoff point that gives the best sensitivity (92.86%) and the specificity (93.33%) is 3.35 v/v%.

setup as well as with the same acquisition sequence and parameters. This may pose a challenge for large-scale multicenter studies or studies involving the use of MR imaging scanners from different vendors. A way to make the EPVS quantification consistent across multiple sites and vendors remains to be studied.

A second limitation is the lack of data on the prevalence of vascular disease, such as diabetes and hypertension, within the study population. Such conditions can precipitate microvascular changes within the brain and are well-known risk factors for lacunar infarcts. The presence of subcortical infarcts was additionally not assessed in these subjects. Because both lacunar and subcortical strokes leave MR imaging footprints within the regions that contain the PVS, they can confound our algorithm, causing it to mistake those footprints for EPVS. Whether our algorithm performs just as well in patients with known vascular disease and brain infarcts would be an intriguing question to probe in our future studies. Additional features of the brain with MCI, such as the severity of hippocampal atrophy, could also be incorporated in future investigations to provide a more detailed picture of the imaging features of MCI.

Another limitation is the lack of 3T MR imaging data for patients with AD. Although Cai et al[23] have already established that the EPVS density is similarly increased in patients with AD in MR images acquired at 7T, it would be interesting to compare the EPVS level between patients with MCI and those with AD at 3T to understand the time course of PVS enlargement during the development of AD from cognitively intact, to MCI, and, finally, to clinically manifest dementia or AD. With a large sample size, it will also be interesting to see whether EPVS density can discriminate patients with MCI whose clinical symptoms are less evident and who have low neuropsychiatric testing scores. These characteristics could further enhance the utility of EPVS quantification as a tool for monitoring dementia progression and regression in response to treatment.

## CONCLUSIONS

The quantitative EPVS segmentation method allows automatic mapping of EPVS from MR images acquired on a clinical 3T MR imaging scanner. EPVS density was found to be significantly higher in patients with aMCI compared with age-matched cognitively healthy control subjects. Therefore, EPVS density may be a useful imaging biomarker for the diagnosis of MCI.

## ACKNOWLEDGMENTS

We thank Dr David Wolk, Associate Professor of Neurology at the University of Pennsylvania and Co-Director of the Penn Memory Center, and his clinical research coordinator, Ms Grace Stockbower, for recruiting and acquiring the MR images of the subjects used in this study.

Disclosures: Xiaohong J. Zhou—*UNRELATED*: *Consultancy*: Horizon Medical Physics Services, *Comments*: consultant and ownership interest; *Employment*: University of Illinois at Chicago, *Comments*: faculty employee; *Grants/Grants Pending*: AbbVie, *Comments*: contracts with AbbVie on research projects; *Royalties*: Elsevier, *Comments*: royalty payment for a book. Paul Yushkevich—*RELATED*: *Grant*: National Institutes of Health, *Comments*: AG037376.* *Money paid to the institution.

## REFERENCES

1. Virchow R. **Ueber die Erweiterung kleinerer Gefäfse**. *Archiv für Pathologische Anatomie und Physiologie und für Klinische Medicin* 1851;3:427–62
2. Heier LA, Bauer CJ, Schwartz L, et al. **Large Virchow-Robin spaces: MR-clinical correlation.** *AJNR Am J Neuroradiol* 1989;10:929–36 Medline
3. Rolyan H, Feike AC, Upadhaya AR, et al. **Amyloid-β protein modulates the perivascular clearance of neuronal apolipoprotein E in mouse models of Alzheimer's disease.** *J Neural Transm* 2011;118:699–712 CrossRef Medline
4. Salzman KL, Osborn AG, House P, et al. **Giant tumefactive perivascular spaces.** *AJNR Am J Neuroradiol* 2005;26:298–305 Medline
5. Davis PC, Mirra SS, Alazraki N. **The brain in older persons with and without dementia: findings on MR, PET, and SPECT images.** *AJR Am J Roentgenol* 1994;162:1267–78 CrossRef Medline
6. Miyakawa T, Hattori E, Shikai I, et al. **Histopathological changes of chronic alcoholism.** *Folia Psychiatr Neurol Jpn* 1977;31:253–61 Medline
7. Poirier J, Derouesné C. **Distinguishing lacunar infarcts from dilatations of the perivascular space.** *J Neurol* 1998;245:813–14 CrossRef Medline
8. Achiron A, Faibel M. **Sandlike appearance of Virchow-Robin spaces in early multiple sclerosis: a novel neuroradiologic marker.** *AJNR Am J Neuroradiol* 2002;23:376–80 Medline
9. Flicker C, Ferris SH, Reisberg B. **Mild cognitive impairment in the elderly: predictors of dementia.** *Neurology* 1991;41:1006–09 CrossRef Medline
10. Tierney MC, Szalai JP, Snow WG, et al. **Prediction of probable Alzheimer's disease in memory-impaired patients: a prospective longitudinal study.** *Neurology* 1996;46:661–65 CrossRef Medline
11. Devanand DP, Folz M, Gorlyn M, et al. **Questionable dementia: clinical course and predictors of outcome.** *J Am Geriatr Soc* 1997;45:321–28 CrossRef Medline
12. Bowen J, Teri L, Kukull W, et al. **Progression to dementia in patients with isolated memory loss.** *Lancet* 1997;349:763–65 CrossRef Medline

13. Petersen RC. **Apolipoprotein E status as a predictor of the development of Alzheimer's disease in memory-impaired individuals.** *JAMA* 1995;273:1274–78 Medline
14. Sherwin BB. **Mild cognitive impairment: potential pharmacological treatment options.** *J Am Geriatr Soc* 2000;48:431–41 CrossRef Medline
15. O'Bryant SE, Humphreys JD, Smith GE, et al. **Detecting dementia with the Mini-Mental State Examination in highly educated individuals.** *Arch Neurol* 2008;65:963–67 Medline
16. Herlitz A. **Detection of mild dementia in community surveys: is it possible to increase the accuracy of our diagnostic instruments?** *Arch Neurol* 1997;54:319–24 CrossRef Medline
17. Stewart R. **Mild cognitive impairment: the continuing challenge of its "real-world" detection and diagnosis.** *Arch Med Res* 2012;43:609–14 CrossRef Medline
18. Mueller SG, Weiner MW, Thal LJ, et al. **The Alzheimer's Disease Neuroimaging Initiative.** *Neuroimaging Clin N Am* 2005;15:869–77 CrossRef Medline
19. Chen W, Song X, Zhang Y. **Assessment of the Virchow-Robin Spaces in Alzheimer disease, mild cognitive impairment, and normal aging, using high-field MR imaging.** *AJNR Am J Neuroradiol* 2011;32:1490–95 CrossRef Medline
20. Ramirez J, Berezuk C, McNeely AA, et al. **Visible Virchow-Robin spaces on magnetic resonance imaging of Alzheimer's disease patients and normal elderly from the Sunnybrook Dementia Study.** *J Alzheimers Dis* 2015;43:415–24 CrossRef Medline
21. Hernández Mdel C, Piper RJ, Wang X, et al. **Towards the automatic computational assessment of enlarged perivascular spaces on brain magnetic resonance images: a systematic review.** *J Magn Reson Imaging* 2013;38:774–85 CrossRef
22. Doubal FN, MacLullich AM, Ferguson KJ, et al. **Enlarged perivascular spaces on MRI are a feature of cerebral small vessel disease.** *Stroke* 2010;41:450–54 CrossRef Medline
23. Cai K, Tain R, Das S, et al. **The feasibility of quantitative MRI of perivascular spaces at 7T.** *J Neurosci Methods* 2015;256:151–56 CrossRef Medline
24. Yushkevich PA, Pluta JB, Wang H, et al. **Automated volumetry and regional thickness analysis of hippocampal subfields and medial temporal cortical structures in mild cognitive impairment.** *Hum Brain Mapp* 2015;36:258–87 CrossRef Medline
25. Grundman M, Petersen RC, Ferris SH, et al; Alzheimer's Disease Cooperative Study. **Mild cognitive impairment can be distinguished from Alzheimer disease and normal aging for clinical trials.** *Arch Neurol* 2004;61:59–66 CrossRef Medline
26. Csukly G, Sirály E, Fodor Z, et al. **The differentiation of amnestic type MCI from the non-amnestic types by structural MRI.** *Front Aging Neurosci* 2016;8:52 CrossRef Medline
27. Petersen RC. **Mild cognitive impairment as a diagnostic entity.** *J Intern Med* 2004;256:183–94
28. Cai K, Shore A, Singh A, et al. **Blood oxygen level dependent angiography (BOLDangio) and its potential applications in cancer research.** *NMR Biomed* 2012;25:1125–32 CrossRef Medline
29. Trattnig S, Springer E, Bogner W, et al. **Key clinical benefits of neuroimaging at 7T.** *Neuroimage* 2018;168:477–89 CrossRef Medline
30. Roberts R, Knopman DS. **Classification and epidemiology of MCI.** *Clin Geriatr Med* 2013;29:753–72 CrossRef Medline
31. Kantarci K, Weigand SD, Przybelski SA, et al. **Risk of dementia in MCI: combined effect of cerebrovascular disease, volumetric MRI, and 1H MRS.** *Neurology* 2009;72:1519–25 CrossRef Medline
32. Mitchell AJ, Shiri-Feshki M. **Rate of progression of mild cognitive impairment to dementia–meta-analysis of 41 robust inception cohort studies.** *Acta Psychiatr Scand* 2009;119:252–65 CrossRef Medline
33. Ward A, Tardiff S, Dye C, et al. **Rate of conversion from prodromal Alzheimer's disease to Alzheimer's dementia: a systematic review of the literature.** *Dement Geriatr Cogn Dis Extra* 2013;3:320–32 CrossRef Medline
34. Apostolova LG, Green AE, Babakchanian S, et al. **Hippocampal atrophy and ventricular enlargement in normal aging, mild cognitive impairment (MCI), and Alzheimer disease.** *Alzheimer Dis Assoc Disord* 2012;26:17–27 CrossRef Medline
35. Jack CR Jr, Shiung MM, Gunter JL, et al. **Comparison of different MRI brain atrophy rate measures with clinical disease progression in AD.** *Neurology* 2004;62:591–600 CrossRef Medline
36. Parikh R, Mathai A, Parikh S, et al. **Understanding and using sensitivity, specificity and predictive values.** *Indian J Ophthalmol* 2008;56:45–50 CrossRef Medline
37. Press GA, Murakami JW, Courchesne E, et al. **The cerebellum, 3: anatomic-MR correlation in the coronal plane.** *AJNR Am J Neuroradiol* 1990;11:41–50 Medline

# Prognostic Value of the Metabolic and Volumetric Parameters of $^{11}$C-Methionine Positron-Emission Tomography for Gliomas: A Systematic Review and Meta-Analysis

Y.-i. Kim, Y. Kim, J.Y. Lee, and S.J. Jang

## ABSTRACT

**BACKGROUND:** Several studies have demonstrated that $^{11}$C-methionine positron-emission tomography provides information on prognosis.

**PURPOSE:** We performed a systematic review and meta-analysis of the prognostic value of the metabolic and volumetric parameters of $^{11}$C-methionine-PET for gliomas.

**DATA SOURCES:** A systematic search was performed using the following combination of keywords: "methionine," "PET," "glioma," and "prognosis."

**STUDY SELECTION:** The inclusion criteria were the use of $^{11}$C-methionine-PET as an imaging tool, studies limited to gliomas, studies including metabolic parameters (tumor-to-normal ratio) and/or volumetric parameters (metabolic tumor volume), and studies reporting survival data. The electronic search first identified 181 records, and 14 studies were selected.

**DATA ANALYSIS:** Event-free survival and overall survival were the outcome measures of interest. The effect of the tumor-to-normal ratio and metabolic tumor volume on survival was determined by the effect size of the hazard ratio. Hazard ratios were extracted directly from each study when provided or determined by analyzing the Kaplan-Meier curves.

**DATA SYNTHESIS:** The combined hazard ratios of the tumor-to-normal ratio for event-free survival was 1.74 with no significance and that of the tumor-to-normal ratio for overall survival was 2.02 with significance. The combined hazard ratio of the metabolic tumor volume for event-free survival was 2.72 with significance and that of the metabolic tumor volume for overall survival was 3.50 with significance.

**LIMITATIONS:** The studies selected were all retrospective, and there were only 4 studies involving the metabolic tumor volume.

**CONCLUSIONS:** The present meta-analysis of $^{11}$C-methionine-PET suggests that the tumor-to-normal ratio for overall survival and the metabolic tumor volume for event-free survival and overall survival are significant prognostic factors for patients with gliomas.

**ABBREVIATIONS:** EFS = event-free survival; HR = hazard ratio; MTV = metabolic tumor volume; OS = overall survival; SUVmax = maximum standardized uptake value; SUVmean = mean standardized uptake value; TNR = tumor-to-normal ratio

Primary brain tumors are a heterogeneous tumor group with its own biology, prognosis, and treatment approach. Gliomas constitute the most frequent pathology and account for approximately 50% of primary brain tumors.[1] Glioblastomas are the most common of all malignant central nervous system tumors (46.6%), and their relative survival estimates are rather low: Only 5.5% of patients have been reported to survive 5 years postdiagnosis.[2]

Among various imaging modalities, MR imaging has been found to be the most effective tool for characterizing gliomas.[3] However, the limitations of MR imaging have encouraged the development of other imaging modalities for the clinical management of gliomas. Not only the MR imaging enhancement patterns of local treatment-related changes but also the T2- or fluid-attenuated inversion recovery MR imaging after antiangiogenic treatment has limited value in differentiating disease progression from post-therapy changes.[4] To overcome these drawbacks, advanced imaging techniques such as perfusion MR imaging, MR spectroscopy, and positron-emission tomography have been developed

Received November 28, 2017; accepted after revision March 29, 2018.

From the Department of Nuclear Medicine (Y.-i.K.), Asan Medical Center, University of Ulsan College of Medicine, Seoul, Republic of Korea; Department of Nuclear Medicine (Y.-i.K., J.Y.L., S.J.J.), CHA Bundang Medical Center, CHA University, Seongnam, Republic of Korea; and Veterans Health Service Medical Center (Y.K.), Seoul, Republic of Korea.

This work was supported by a grant of the Research Driven Hospital R&D project, funded by the CHA Bundang Medical Center (grant No. BDCHA R&D 2017-018).

Please address correspondence to Su Jin Jang, MD, PhD, Department of Nuclear Medicine, CHA Bundang Medical Center, CHA University, 59, Yatap-ro, Bundang-gu, Seongnam-si, Gyeongi-do, 13496, Republic of Korea; e-mail: jsjnm07@cha.ac.kr

Indicates article with supplemental on-line tables.

http://dx.doi.org/10.3174/ajnr.A5707

and used for the accurate characterization of tumors. Among them, amino acid PET has additive value compared with MR imaging when assessing the response to antiangiogenic treatments because amino acid uptake occurs independent of regional tumor perfusion and blood-brain barrier permeability.[5,6] Several amino acid radiotracers for PET, such as $^{11}$C-methionine, [$^{18}$F]fluoroethyl tyrosine, and 6-[$^{18}$F]-fluoro-L-dopa, have been used for the metabolic imaging of brain tumors.[7] Various studies have demonstrated the advantages of $^{11}$C-methionine-PET in diagnosis, grading, and the differential diagnosis between tumor recurrence and radiation necrosis.[8,9] In addition, $^{11}$C-methionine-PET also provides information on patient prognosis because a high uptake in the glioma indicates a high chance of tumor progression and a poor survival rate.[10]

Most previous studies with $^{11}$C-methionine-PET have used a semiquantitative tumor-to-normal ratio (TNR, metabolic parameter) to identify the uptake and evaluate the prognosis of brain tumors. The TNR is usually defined as the maximum standard uptake value (SUVmax) of the brain tumor divided by the mean SUV (SUVmean) of the contralateral normal cerebral cortex.[11,12] However, because the TNR reflects only the single voxel with the highest SUV in the tumor, this parameter does not reflect the total tumor uptake.[13] In recent years, volumetric parameters, including the metabolic tumor volume (MTV), have been reported to have prognostic significance for several types of tumors.[14-16] The MTV is defined as the tumor volume within the boundary determined by a certain threshold and theoretically reflects the total tumor amount or tumor burden.[17,18] Currently, there is a lack of comprehensive and detailed reviews on the prognostic value of the MTV and/or TNR of $^{11}$C-methionine-PET for gliomas, which could guide physicians in the management of the tumor.

Therefore, we conducted a comprehensive systematic review of the literature on metabolic and volumetric parameters and designed a meta-analysis to assess the prognostic value of the TNR and MTV of $^{11}$C-methionine-PET for patients with gliomas.

## MATERIALS AND METHODS

### Data Search and Selection

We performed a systematic search of MEDLINE and EMBASE and a manual search on July 31, 2017, to identify publications using the following combination of keywords: "methionine," "PET," "glioma," and "prognosis." All searches were limited to human studies. The inclusion criteria were the use of $^{11}$C-methionine-PET as an imaging tool, studies limited to gliomas, studies that reported survival data, and studies that included metabolic parameters (TNR) and/or volumetric parameters (MTV). Reviews, abstracts, case reports, and editorials were excluded. Two authors independently conducted the search and screening, and they selected eligible studies for inclusion. Any discrepancies were resolved by consensus.

### Data Extraction and Quality Assessment

Two reviewers independently extracted data from the selected publications and recorded the following information: study design, first author, year of publication, country of origin, number of patients, treatment, end point, and evaluated PET parameters. The 2 reviewers scored each publication according to a quality scale used in previous studies.[19] This quality scale was divided into 4 categories: scientific design, generalizability, result analysis, and PET report (On-line Table 1). A value between 0 and 2 was assigned to each item, and each category had a maximum score of 10 points. Scores were expressed as a percentage of the maximum, which was 40 points. All data were extracted, and scores were graded by 2 reviewers who performed comparisons at each step. Any discrepancies were resolved by consensus.

### Statistical Analysis

The primary outcome was event-free survival (EFS). Disease-free survival and progression-free survival were defined as EFS, which was measured from the date of the initiation of therapy to the date of recurrence or metastasis.[20] The secondary end point was overall survival (OS), defined as the time from the initiation of therapy until death. The effect of the TNR or MTV on survival was measured by the effect size of the hazard ratio (HR). Survival data were extracted using a methodology proposed by Parmar et al.[21] We extracted the univariate HR estimate and 95% confidence interval directly from each study when provided by the authors. Otherwise, the *P* values of the log-rank test, 95% CI, number of events, and at-risk numbers were extracted to estimate the HR indirectly. We determined the survival rates from the Kaplan-Meier curves using the Engauge Digitizer (http://markummitchell.github.io/engauge-digitizer/) to reconstruct the HR estimate and its variance, assuming that patients were censored at a constant rate during follow-up. An HR of $>1$ implied worse survival for patients with a high TNR or MTV, whereas an HR $<1$ implied better survival for patients with a high TNR or MTV. Heterogeneity between the studies was assessed by a $\chi^2$ test and $I^2$ statistics as described by Higgins et al.[22] A fixed-effects model was used with Higgins $I^2 \leq 50\%$ and Cochran Q at $P \geq .1$, and a random-effects model was used with Higgins $I^2 > 50\%$ or Cochran Q at $P < .1$. Subgroup analyses were performed according to the tumor grade, tumor stage, calculation methods of the TNR, and references for the MTV. Funnel plots were used to assess publication bias graphically.[23] $P < .05$ was considered statistically significant, and $.05 \leq P \leq .1$ indicated a significant trend. Data from each study were analyzed using Review Manager (RevMan, Version 5.3; The Nordic Cochrane Centre, Copenhagen, Denmark).

## RESULTS

### Characteristics of the Study

The results of the data search and selection are summarized in Fig 1. A total of 14 studies involving 735 patients were included in our meta-analysis. All 14 studies were of a retrospective design.[24-37] The grade of glioma was low in 3 studies,[25,29,31] high in 4 studies,[30,32,35,37] and mixed in 7 studies.[24,26-28,33,34,36] The prognostic value of the TNR was determined in all 14 studies,[24-37] and the prognostic value of the MTV was determined in 4 studies.[32,34,35,37] The tumor parameters used were SUVmax in 13 studies[24-32,34-37] and SUVmean in 1 study.[33] The reference parameters were contralateral cortex SUVmean in 10 studies,[24-27,30-35] SUVmax in 2 studies,[36,37] and undefined in 2 studies.[28,29] The cutoff values of the TNR ranged from 1.51 to 3.42, and those of the MTV ranged from 35 to 60 cm$^3$ (On-line Table 2). The mean quality score of the selected studies was 58.0%, with a range of 41.9%–71.3% (On-line Table 3).

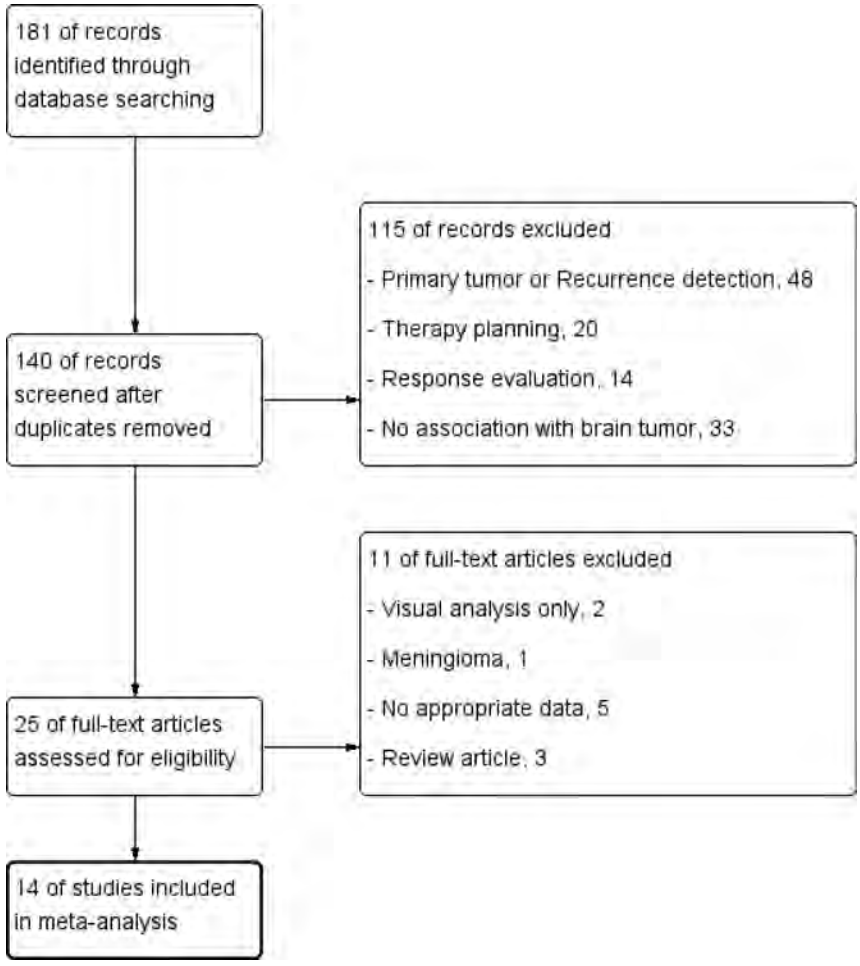


**FIG 1.** A flow diagram of the study.

### *Prognostic Value of the TNR and MTV*

The effect of the TNR on EFS was analyzed using 5 studies. The combined HR of 1.74 for adverse events was not statistically significant (95% CI, 0.86–3.49; $P = .12$). Heterogeneity was high with statistical significance ($\chi^2 = 16.19$, $P = .003$; $I^2 = 75\%$). The effect of the TNR on OS was analyzed using 11 studies. The combined HR of 2.02 for death was statistically significant (95% CI, 1.55–2.64; $P < .001$). Heterogeneity was moderate with statistical significance ($\chi^2 = 18.86$, $P = .04$; $I^2 = 47\%$) (Fig 2).

The effect of the MTV on EFS was analyzed using 2 studies. The combined HR of 2.72 for adverse events was statistically significant (95% CI, 1.51–4.90; $P < .001$). Heterogeneity was not statistically significant ($\chi 2 = 0.73$, $P = .39$; $I^2 = 0\%$). The effect of the MTV on OS was analyzed using 3 studies. The combined HR of 3.50 for death was statistically significant (95% CI, 1.52–8.06; $P < .003$). Heterogeneity was moderate with statistical significance ($\chi^2 = 6.50$, $P = .04$; $I^2 = 69\%$) (Fig 3).

The results of the meta-analysis are summarized in Table 1, and a visual inspection of the funnel plot suggests no evidence of publication bias, as shown in Fig 4.

### *Subgroup Analysis*

Subgroup analysis was performed in relation to the tumor grade, tumor stage, methods of TNR calculation, and references for the MTV (Table 2). According to the variables, eligible studies were divided into 2 subgroups. Among studies of OS in terms of the TNR, high-grade glioma had a significant HR of 1.76 (95% CI, 1.36–2.28; $P < .001$), and low-grade glioma had an HR of 2.19 with a significant trend (95% CI, 0.98–4.86; $P = .05$). Studies of primary tumors had a significant HR of 1.95 (95% CI, 1.45–2.63; $P < .001$), and those of recurrent tumors had a significant HR of 2.58 (95% CI, 1.31–5.08; $P = .006$). Studies of TNR calculation methods (tumor SUVmax divided by normal contralateral cortex SUVmean) had a significant HR of 1.97 (95% CI, 1.42–2.74; $P < .001$), and those of other calculation methods had a significant HR of 2.15 (95% CI, 1.29–3.60; $P = .003$). Among studies that included the OS in terms of the MTV, high-grade glioma (HR = 5.54; 95% CI, 3.11–9.86; $P < .001$), primary tumor (HR = 3.51; 95% CI, 1.04–11.88; $P = .04$), and references for the MTV (1.3 × SUVmean of the normal contralateral cortex; HR = 3.51; 95% CI, 1.04–11.88; $P = .04$) showed significant results.

## DISCUSSION

In the current study, the prognostic value of the TNR and MTV of $^{11}$C-methionine-PET for patients with gliomas was evaluated through a meta-analysis of published studies. The TNR for OS and the MTV for EFS and OS were useful in predicting the prognosis of patients. In addition, subgroup analysis demonstrated that tumor grade may affect the prognosis. To our knowledge, this is the first meta-analysis that has investigated the prognostic value of metabolic and volumetric parameters for patients with gliomas.

Most of the previous studies have used the TNR to quantify the intensity of $^{11}$C-methionine uptake to determine the prognosis.[24-31,33,36] Our meta-analysis indicated that the TNR for OS (but not the TNR for EFS) of $^{11}$C-methionine-PET could be a significant prognostic parameter. A previous study compared $^{11}$C-methionine uptake with the pathologic features of tumors and showed that the malignant portions of lesions were coincident with the areas with higher $^{11}$C-methionine uptake.[28] In subgroup analysis, the TNR showed significant prognostic value for OS in high-grade tumors; however, only a significant trend was found in low-grade tumors. Regarding the tumor stage for OS, the TNR demonstrated significant prognostic value for both primary and recurrent tumors. Regarding the calculation methods of the TNR for OS, the SUVmax of the tumor divided by the SUVmean of the normal contralateral cortex and other TNR calculation methods revealed significant prognostic values.

The TNR represents the high metabolic activity of the tumor, and the MTV reflects the size of the metabolically active tumor. In theory, volumetric parameters should be more useful than meta-

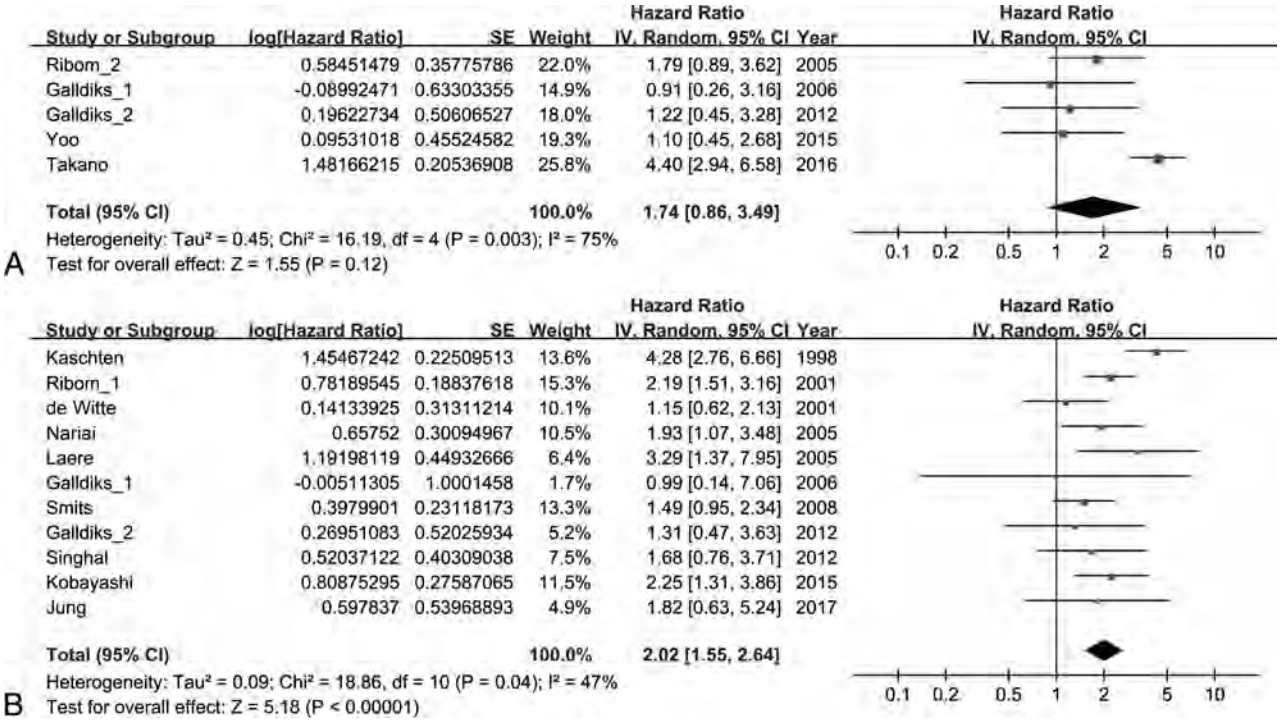


**FIG 2.** Forest plot results of the EFS (*A*) and OS (*B*) based on the TNR.

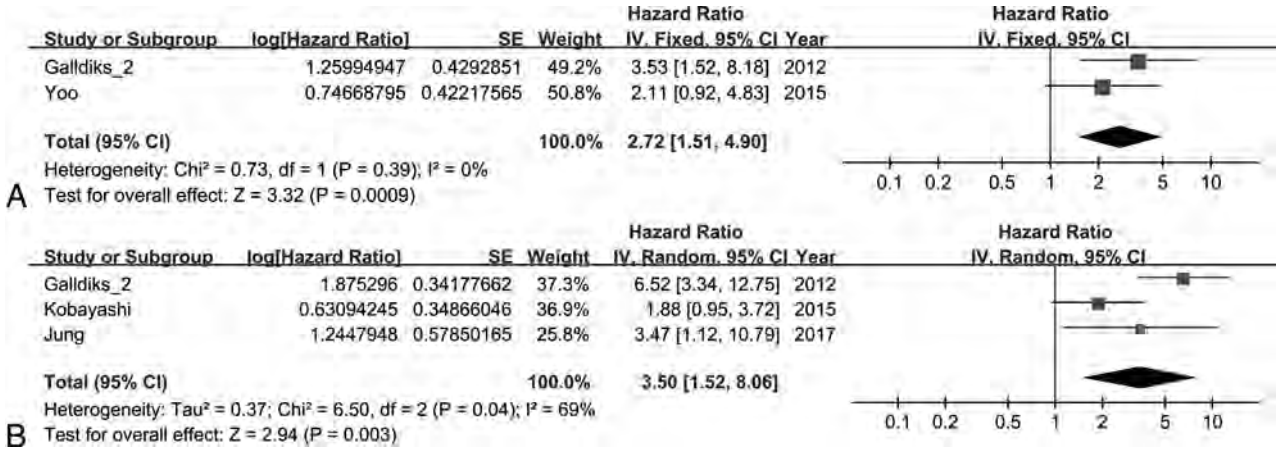


**FIG 3.** Forest plot results of the EFS (*A*) and OS (*B*) based on the MTV.

**Table 1: Summary of the meta-analysis results**

| Parameters | End Point | No. of Studies | HR | 95% CI of HR | *P* Value | $I^2$ (%) | Model |
|---|---|---|---|---|---|---|---|
| TNR | EFS | 5 | 1.74 | 0.86–3.49 | .12 | 75 | Random |
| TNR | OS | 11 | 2.02 | 1.55–2.64 | <.001[a] | 47 | Random |
| MTV | EFS | 2 | 2.72 | 1.51–4.90 | <.001[a] | 0 | Fixed |
| MTV | OS | 3 | 3.50 | 1.52–8.06 | .003[a] | 69 | Random |

[a] Statistically significant ($P < .05$).

bolic parameters in the prediction of tumor behavior because both metabolic activity and tumor burden are taken into consideration.[17,18] Our meta-analysis indicated that the MTV of $^{11}$C-methionine-PET could reflect patient prognosis. The results revealed its significance for both EFS and OS. In comparison with the HR of the TNR, the HR of the MTV for EFS was significant, whereas the HR of the TNR for EFS was not significant. The HR of the MTV for OS was higher than the HR of the TNR for OS; however, it was not statistically significant ($P = .19$; data not shown). Furthermore, previous direct comparison studies reported that the MTV has a better prognostic value than the TNR.[32,34,35,37] The direct comparison results are summarized in On-line Table 4. In subgroup analysis, the MTV had significant prognostic value for OS in high-grade tumors, and its statistical significance was compared with that of the TNR for OS in high-grade tumors ($P < .001$; data not shown). With respect to the tumor stage for OS, the MTV demonstrated significant prognostic value for primary gliomas with higher HRs than those of

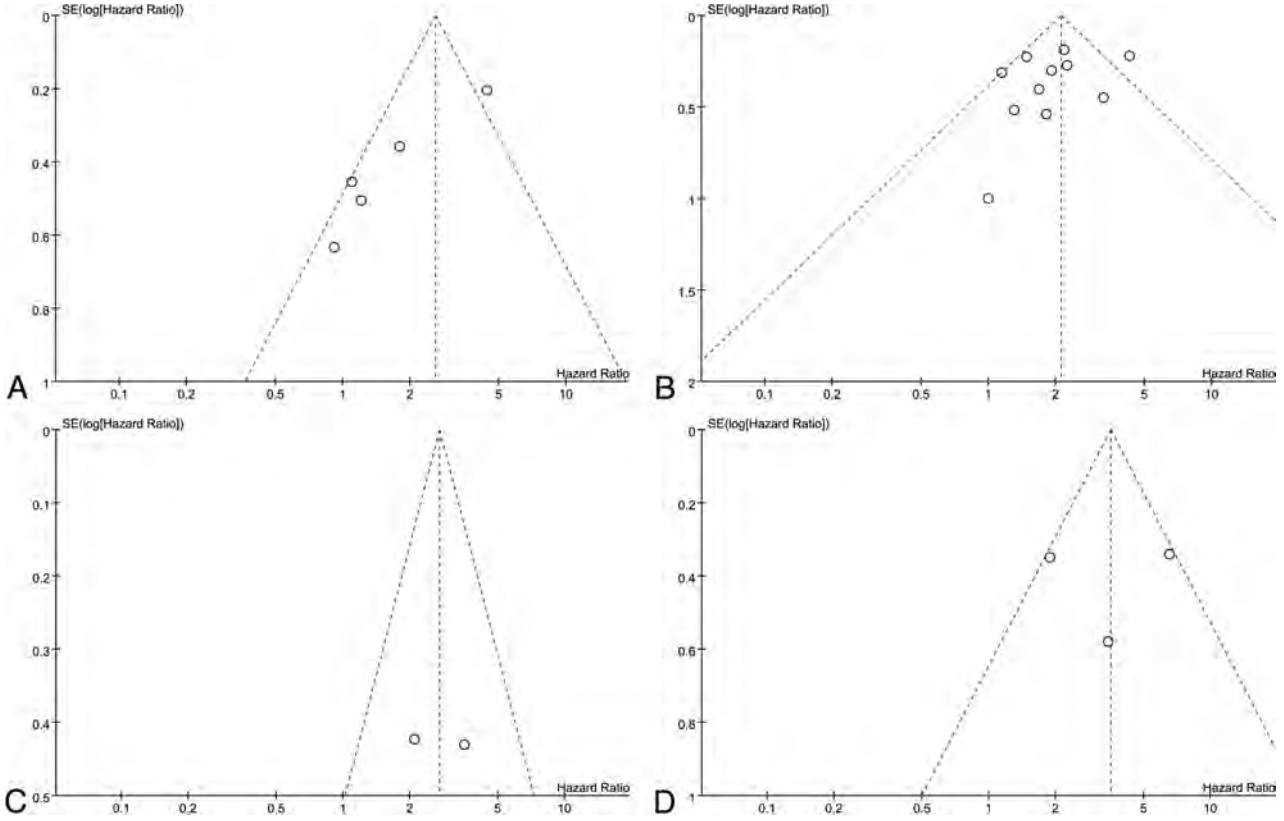


**FIG 4.** Funnel plot results of the EFS based on the TNR (*A*), OS based on the TNR (*B*), EFS based on the MTV (*C*), and OS based on the MTV (*D*).

**Table 2: Results of subgroup analysis**

| Parameters | End Point | Factor | No. of Studies | HR | 95% CI of HR | *P* Value | $I^2$ (%) | Model |
|---|---|---|---|---|---|---|---|---|
| TNR | OS | Tumor grade (high) | 7 | 1.76 | 1.36–2.28 | <.001[a] | 22 | Fixed |
| | | Tumor grade (low) | 6 | 2.19 | 0.98–4.86 | .05[b] | 97 | Random |
| TNR | OS | Tumor stage (primary) | 9 | 1.95 | 1.45–2.63 | <.001[a] | 55 | Random |
| | | Tumor stage (recurrence) | 2 | 2.58 | 1.31–5.08 | .006[a] | 0 | Fixed |
| TNR | OS | Calculation method of TNR (tumor SUVmax/ normal contralateral SUVmean) | 8 | 1.97 | 1.42–2.74 | <.001[a] | 60 | Random |
| | | Calculation method of TNR (others) | 3 | 2.15 | 1.29–3.60 | .003[a] | 0 | Fixed |
| MTV | OS | Tumor grade (high) | 2 | 5.54 | 3.11–9.86 | <.001[a] | 0 | Fixed |
| MTV | OS | Tumor stage (primary) | 2 | 3.51 | 1.04–11.88 | .04[a] | 85 | Random |
| MTV | OS | Reference for MTV (1.3 × SUVmean of normal contralateral cortex) | 2 | 3.51 | 1.04–11.88 | .04[a] | 85 | Random |

[a] Statistically significant ($P < .05$).
[b] Significant trend ($.05 \leq P \leq .10$).

the TNR. MTV defined by normal contralateral cortex SUVmean × 1.3, was prognostic and showed higher HRs than those of TNR calculation methods.

According to our systematic review and meta-analysis, the TNR could be used for the prognosis of OS, especially in cases of high-grade gliomas. In addition, the MTV could be used for the prognosis of both EFS and OS. Furthermore, the MTV could be superior to the TNR for the prognosis of high-grade gliomas.

There are some limitations to this study. First, the studies selected were all retrospective. There were only 4 studies involving the MTV, and the number of patients in each study was relatively small. In addition, a possible publication bias was not excluded; nevertheless, the funnel plot did not clearly show this. Furthermore, we were unable to determine an optimal cutoff value to categorize the TNR and MTV as high or low due to the lack of individual data. Last, a comparison between the MTV and total lesion glycolysis (TLG = SUVmean multiplied by the MTV, a frequently used parameter in FDG-PET studies) should be performed in the future.[34]

## CONCLUSIONS

The TNR and MTV of $^{11}$C-methionine-PET are significant prognostic parameters for patients with gliomas. Patients with a high TNR have a higher risk of death, and patients with a high MTV have a higher risk of adverse events or death. The MTV could be used as an incremental predictor of prognosis instead of the TNR.

Disclosures: Yong-il Kim—*RELATED: Grant*: Research Driven Hospital R&D project, funded by the CHA Bundang Medical Center, *Comments*: grant No. BDCHA R&D 2017-018.

## REFERENCES


1. Rigau V, Zouaoui S, Mathieu-Daudé H, et al; Société Française de Neuropathologie (SFNP), Société Française de Neurochirurgie (SFNC), Club de Neuro-Oncologie of the Société Française de Neurochirurgie (CNO-SFNC), Association des Neuro-Oncologues d'Expression Française (ANOCEF). **French brain tumor database: 5-year histological results on 25 756 cases.** *Brain Pathol* 2011;21:633–44 CrossRef Medline
2. Ostrom QT, Gittleman H, Liao P, et al. **CBTRUS statistical report: primary brain and central nervous system tumors diagnosed in the United States in 2007–2011.** *Neuro Oncol* 2014;16(Suppl 4):iv1–63 CrossRef Medline
3. Behin A, Hoang-Xuan K, Carpentier AF, et al. **Primary brain tumours in adults.** *Lancet* 2003;361:323–31 CrossRef Medline
4. van den Bent MJ, Vogelbaum MA, Wen PY, et al. **End point assessment in gliomas: novel treatments limit usefulness of classical Macdonald's criteria.** *J Clin Oncol* 2009;27:2905–08 CrossRef Medline
5. Hutterer M, Hattingen E, Palm C, et al. **Current standards and new concepts in MRI and PET response assessment of antiangiogenic therapies in high-grade glioma patients.** *Neuro Oncol* 2015;17:784–800 CrossRef Medline
6. Galldiks N, Rapp M, Stoffels G, et al. **Response assessment of bevacizumab in patients with recurrent malignant glioma using [$^{18}$F]fluoroethyl-L-tyrosine PET in comparison to MRI.** *Eur J Nucl Med Mol Imaging* 2013;40:22–33 CrossRef Medline
7. Galldiks N, Langen K. **Applications of PET imaging of neurological tumors with radiolabeled amino acids.** *Q J Nucl Med Mol Imaging* 2015;59:70–82 Medline
8. Glaudemans AW, Enting RH, Heesters MA, et al. **Value of $^{11}$C-methionine PET in imaging brain tumours and metastases.** *Eur J Nucl Med Mol Imaging* 2013;40:615–35 CrossRef Medline
9. Terakawa Y, Tsuyuguchi N, Iwai Y, et al. **Diagnostic accuracy of $^{11}$C-methionine PET for differentiation of recurrent brain tumors from radiation necrosis after radiotherapy.** *J Nucl Med* 2008;49:694–99 CrossRef Medline
10. Kim S, Chung JK, Im SH, et al. **$^{11}$C-methionine PET as a prognostic marker in patients with glioma: comparison with $^{18}$F-FDG PET.** *Eur J Nucl Med Mol Imaging* 2005;32:52–59 CrossRef Medline
11. Cicuendez M, Lorenzo-Bosquet C, Cuberas-Borrós G, et al. **Role of [$^{11}$C] methionine positron emission tomography in the diagnosis and prediction of survival in brain tumours.** *Clin Neurol Neurosurg* 2015;139:328–33 CrossRef Medline
12. Watanabe A, Muragaki Y, Maruyama T, et al. **Usefulness of $^{11}$C-methionine positron emission tomography for treatment-decision making in cases of non-enhancing glioma-like brain lesions.** *J Neurooncol* 2016;126:577–83 CrossRef Medline
13. Boellaard R, Krak NC, Hoekstra OS, et al. **Effects of noise, image resolution, and ROI definition on the accuracy of standard uptake values: a simulation study.** *J Nucl Med* 2004;45:1519–27 Medline
14. Kang CM, Lee SH, Hwang HK, et al. **Preoperative volume-based PET parameter, MTV2. 5, as a potential surrogate marker for tumor biology and recurrence in resected pancreatic cancer.** *Medicine* 2016;95:e2595 CrossRef Medline
15. Hyun SH, Choi JY, Shim YM, et al. **Prognostic value of metabolic tumor volume measured by $^{18}$F-fluorodeoxyglucose positron emission tomography in patients with esophageal carcinoma.** *Ann Surg Oncol* 2010;17:115–22 CrossRef Medline
16. La TH, Filion EJ, Turnbull BB, et al. **Metabolic tumor volume predicts for recurrence and death in head-and-neck cancer.** *Int J Radiat Oncol Biol Phys* 2009;74:1335–41 CrossRef Medline
17. Kim Y-i, Paeng JC, Cheon GJ, et al. **Prediction of posttransplantation recurrence of hepatocellular carcinoma using metabolic and volumetric indices of $^{18}$F-FDG PET/CT.** *J Nucl Med* 2016;57:1045–51 CrossRef Medline
18. Fonti R, Larobina M, Del Vecchio S, et al. **Metabolic tumor volume assessed by $^{18}$F-FDG PET/CT for the prediction of outcome in patients with multiple myeloma.** *J Nucl Med* 2012;53:1829–35 CrossRef Medline
19. Berghmans T, Dusart M, Paesmans M, et al; European Lung Cancer Working Party for the IASLC Lung Cancer Staging Project. **Primary tumor standardized uptake value (SUVmax) measured on fluorodeoxyglucose positron emission tomography (FDG-PET) is of prognostic value for survival in non-small cell lung cancer (NSCLC): a systematic review and meta-analysis (MA) by the European Lung Cancer Working Party for the IASLC Lung Cancer Staging Project.** *J Thorac Oncol* 2008;3:6–12 CrossRef Medline
20. Zhao Q, Feng Y, Mao X, et al. **Prognostic value of fluorine-18-fluorodeoxyglucose positron emission tomography or PET-computed tomography in cervical cancer: a meta-analysis.** *Int J Gynecol Cancer* 2013;23:1184–90 CrossRef Medline
21. Parmar MK, Torri V, Stewart L. **Extracting summary statistics to perform meta-analyses of the published literature for survival endpoints.** *Stat Med* 1998;17:2815–34 Medline
22. Higgins J, Thompson SG, Deeks JJ, et al. **Measuring inconsistency in meta-analyses.** *BMJ* 2003;327:557–60 CrossRef Medline
23. Egger M, Davey Smith GD, Schneider M, et al. **Bias in meta-analysis detected by a simple, graphical test.** *BMJ* 1997;315:629–34 CrossRef Medline
24. Kaschten B, Stevenaert A, Sadzot B, et al. **Preoperative evaluation of 54 gliomas by PET with fluorine-18-fluorodeoxyglucose and/or carbon-11-methionine.** *J Nucl Med* 1998;39:778–85 Medline
25. Ribom D, Eriksson A, Hartman M, et al. **Positron emission tomography (11)C-methionine and survival in patients with low-grade gliomas.** *Cancer* 2001;92:1541–49 Medline
26. De Witte O, Goldberg I, Wikler D, et al. **Positron emission tomography with injection of methionine as a prognostic factor in glioma.** *J Neurosurg* 2001;95:746–50 CrossRef Medline
27. Van Laere K, Ceyssens S, Van Calenbergh F, et al. **Direct comparison of $^{18}$F-FDG and $^{11}$C-methionine PET in suspected recurrence of glioma: sensitivity, inter-observer variability and prognostic value.** *Eur J Nucl Med Mol Imaging* 2005;32:39–51 CrossRef Medline
28. Nariai T, Tanaka Y, Wakimoto H, et al. **Usefulness of L-[methyl-11C] methionine-positron emission tomography as a biological monitoring tool in the treatment of glioma.** *J Neurosurg* 2005;103:498–507 CrossRef Medline
29. Ribom D, Smits A. **Baseline $^{11}$C-methionine PET reflects the natural course of grade 2 oligodendrogliomas.** *Neurol Res* 2005;27:516–21 CrossRef Medline
30. Galldiks N, Kracht LW, Burghaus L, et al. **Use of $^{11}$C-methionine PET to monitor the effects of temozolomide chemotherapy in malignant gliomas.** *Eur J Nucl Med Mol Imaging* 2006;33:516–24 CrossRef Medline
31. Smits A, Westerberg E, Ribom D. **Adding $^{11}$C-methionine PET to the EORTC prognostic factors in grade 2 gliomas.** *Eur J Nucl Med Mol Imaging* 2008;35:65–71 CrossRef Medline
32. Galldiks N, Dunkl V, Kracht LW, et al. **Volumetry of [$^{11}$C]-methionine positron emission tomographic uptake as a prognostic marker before treatment of patients with malignant glioma.** *Mol Imaging* 2012;11:516–27 Medline Medline
33. Singhal T, Narayanan TK, Jacobs MP, et al. **$^{11}$C-methionine PET for grading and prognostication in gliomas: a comparison study with $^{18}$F-FDG PET and contrast enhancement on MRI.** *J Nucl Med* 2012;53:1709–15 CrossRef Medline
34. Kobayashi K, Hirata K, Yamaguchi S, et al. **Prognostic value of volume-based measurements on (11)C-methionine PET in glioma patients.** *Eur J Nucl Med Mol Imaging* 2015;42:1071–80 CrossRef Medline
35. Yoo MY, Paeng JC, Cheon GJ, et al. **Prognostic value of metabolic tumor volume on (11)C-methionine PET in predicting progression-free survival in high-grade glioma.** *Nucl Med Mol Imaging* 2015;49:291–97 CrossRef Medline
36. Takano K, Kinoshita M, Arita H, et al. **Diagnostic and prognostic value of 11C-methionine PET for nonenhancing gliomas.** *AJNR Am J Neuroradiol* 2016;37:44–50 CrossRef Medline
37. Jung TY, Min JJ, Bom HS, et al. **Prognostic value of post-treatment metabolic tumor volume from $^{11}$C-methionine PET/CT in recurrent malignant glioma.** *Neurosurg Rev* 2017;40:223–29 CrossRef Medline

# Evaluation of Thick-Slab Overlapping MIP Images of Contrast-Enhanced 3D T1-Weighted CUBE for Detection of Intracranial Metastases: A Pilot Study for Comparison of Lesion Detection, Interpretation Time, and Sensitivity with Nonoverlapping CUBE MIP, CUBE, and Inversion-Recovery-Prepared Fast-Spoiled Gradient Recalled Brain Volume

B.C. Yoon, A.F. Saad, P. Rezaii, M. Wintermark, G. Zaharchuk, and M. Iv

## ABSTRACT

**BACKGROUND AND PURPOSE:** Early and accurate identification of cerebral metastases is important for prognostication and treatment planning although this process is often time consuming and labor intensive, especially with the hundreds of images associated with 3D volumetric imaging. This study aimed to evaluate the benefits of thick-slab overlapping MIPs constructed from contrast-enhanced T1-weighted CUBE (overlapping CUBE MIP) for the detection of brain metastases in comparison with traditional CUBE and inversion-recovery prepared fast-spoiled gradient recalled brain volume (IR-FSPGR-BRAVO) and nonoverlapping CUBE MIP.

**MATERIALS AND METHODS:** A retrospective review of 48 patients with cerebral metastases was performed at our institution from June 2016 to October 2017. Brain MRIs, which were acquired on multiple 3T scanners, included gadolinium-enhanced T1-weighted IR-FSPGR-BRAVO and CUBE, with subsequent generation of nonoverlapping CUBE MIP and overlapping CUBE MIP. Two blinded radiologists identified the total number and location of metastases on each image type. The Cohen $\kappa$ was used to determine interrater agreement. Sensitivity, interpretation time, and lesion contrast-to-noise ratio were assessed.

**RESULTS:** Interrater agreement for identification of metastases was fair-to-moderate for all image types ($\kappa$ = 0.222–0.598). The total number of metastases identified was not significantly different across the image types. Interpretation time for CUBE MIPs was significantly shorter than for CUBE and IR-FSPGR-BRAVO, saving at least 50 seconds per case on average ($P < .001$). The mean lesion contrast-to-noise ratio for both CUBE MIPs was higher than for IR-FSPGR-BRAVO. The mean contrast-to-noise ratio for small lesions (<4 mm) was lower for nonoverlapping CUBE MIP (1.55) than for overlapping CUBE MIP (2.35). For both readers, the sensitivity for lesion detection was high for all image types but highest for overlapping CUBE MIP and CUBE (0.93–0.97).

**CONCLUSIONS:** This study suggests that the use of overlapping CUBE MIP or nonoverlapping CUBE MIP for the detection of brain metastases can reduce interpretation time without sacrificing sensitivity, though the contrast-to-noise ratio of lesions is highest for overlapping CUBE MIP.

**ABBREVIATIONS:** CNR = contrast-to-noise ratio; IR-FSPGR-BRAVO = inversion-recovery-prepared fast-spoiled gradient recalled brain volume; nC-MIP = non-overlapping CUBE MIP; oC-MIP = overlapping CUBE MIP; SRS = stereotactic radiosurgery; XR = cross-reference

The early and accurate identification of brain metastases in patients with systemic cancers has important implications for patient prognosis and treatment strategy because a greater number of lesions at presentation correlates with decreased survival.[1] In patients with a small number of metastases, surgical resection or stereotactic radiosurgery (SRS) may be pursued, while whole-brain radiation therapy is generally recommended for those with an extensive lesion burden.[2,3] Previous studies have shown that SRS alone is an effective treatment and provides good local tumor control in patients with up to 10 brain metastases.[4,5] Additionally, the rate of local control with SRS is greater for small lesions, which further stresses the importance of early detection. The choice of SRS or whole-brain radiation therapy for the treatment of brain metastases in individuals with a specific number of lesions is important because the risk of radiation-induced dementia and neurocognitive decline associated with whole-brain radiation therapy can be potentially avoided with SRS.

Counting multiple small metastases is often laborious and time-consuming, especially with the hundreds of images associated with 3D volumetric imaging. Multiple investigators have demonstrated improved lesion detection using 3D T1-weighted volumetric fast spin-echo sequences (CUBE, GE Healthcare, Mil-

Received September 23, 2017; accepted after revision June 16, 2018.

From the Department of Radiology, Division of Neuroimaging and Neurointervention, Stanford University, Stanford, California.

Paper previously presented as an electronic exhibit at: Annual Meeting of the American Society of Neuroradiology and the Foundation of the ASNR Symposium, April 22–27, 2017; Long Beach, California (#eP-50).

Please address correspondence to Michael Iv, MD, Department of Radiology, Division of Neuroimaging and Neurointervention, Stanford University, 300 Pasteur Dr, Grant Building, Room S031E, Stanford, CA 94305; e-mail: miv@stanford.edu, @Michael_Iv_MD

http://dx.doi.org/10.3174/ajnr.A5747

waukee, Wisconsin; sampling perfection with application optimized contrasts by using different flip angle evolution [SPACE], Siemens, Erlangen, Germany; volume isotropic turbo spin-echo [VISTA], Philips Healthcare, Best, the Netherlands).[6-13] CUBE (and similar sequences) uses a variable flip angle technique and higher echo-train length to acquire gap-free volumetric images with reduced acquisition time and specific absorption rate.[7] Furthermore, the black-blood properties offered by CUBE allow good background vascular suppression and provide a higher contrast-to-noise ratio (CNR) than 3D T1-weighted gradient-echo sequences (inversion-recovery-prepared fast spoiled gradient recalled brain volume [IR-FSPGR-BRAVO], GE Healthcare; MPRAGE, Siemens; 3D TFE, Phillips Healthcare).[7]

The use of maximum-intensity-projection images has become standard in chest imaging when evaluating pulmonary nodules because MIPs have been shown to enhance lesion detection and reduce the total amount of time the radiologist spends searching for small nodules.[14-17] In neuroimaging, 3D volumetric fast spin-echo imaging is ideally suited to MIP reconstruction because of its black-blood and increased CNR properties. However, the use of MIP images in the detection of brain metastases has been limited.[18,19] Recently, Bae et al[18] have shown that nonoverlapping 5-mm-thick MIPs of 3D T1-weighted turbo spin-echo significantly reduced interpretation time without sacrificing diagnostic accuracy but with an increased false-positive rate, compared with the source 1-mm images. Thick-section MIPs reconstructed with slice overlapping can potentially reduce artifacts from partial volume averaging and improve visualization of lesions. Therefore, in this study, we examined whether the use of thick-slab overlapping MIPs constructed from gadolinium-enhanced 3D T1-weighted CUBE (overlapping CUBE MIP [oC-MIP]) would allow improved visualization and quicker and more sensitive detection of brain metastases compared with nonoverlapping CUBE MIP (nC-MIP) as well as source 3D T1-weighted CUBE and IR-FSPGR-BRAVO.

## MATERIALS AND METHODS

We performed an institutional review board–approved retrospective study of patients with brain metastases who had MRIs from June 2016 to October 2017 at a single academic institution. Patients with a diagnosis of metastatic disease from any primary cancer who had brain MR imaging during the study period were identified through our PACS imaging data base by keyword search criteria. The specific keywords used were "metastasis" and "metastases." On the basis of finalized reports associated with the MRIs, patients with at least 2 intra-axial brain metastases were included in the study.

### MR Imaging Protocol

All brain MRIs were performed on multiple 3T scanners (Discovery 750; GE Healthcare) using our institutional brain metastasis protocol, which consisted of precontrast and postcontrast images, the latter acquired following the intravenous administration of 0.1 mmol/kg of gadobenate dimeglumine (MultiHance; Bracco Diagnostics, Princeton, New Jersey). Gadobenate dimeglumine is the specific contrast agent used at our institution because of its high relaxivity, which allows improved lesion conspicuity. Postgadolinium sequences were obtained in the following order: sagittal 3D T1-weighted CUBE (TR = 600 ms, TE = 13 ms, slice thickness = 1 mm, echo-train length = 28, flip angle = 90°, matrix = 256 × 256 mm, FOV = 250 mm, in-plane resolution = 0.977 mm, bandwidth = 244 Hz, number of averages = 1, imaging time = 2 minutes 15 seconds) with 1-mm axial and coronal reformats and axial 3D T1-weighted IR-FSPGR-BRAVO (TR = 9.2 ms, TE = 3.7 ms, TI = 400 ms, slice thickness = 1 mm, echo-train length = 1, flip angle = 13°, matrix = 256 × 256 mm, FOV = 240 mm, in-plane resolution = 0.938 mm, bandwidth = 195 Hz, number of averages = 1, imaging time = 3 minutes 30 seconds) with 1-mm sagittal and coronal reformats. IR-FSPGR-BRAVO was the last sequence performed in our protocol because increased scan time delay after contrast administration allows improved lesion detection.

Axial MIP images (oC-MIP: 10-mm sections reconstructed at 4-mm intervals; nC-MIP: 5-mm sections at 5-mm intervals) were then constructed from the contrast-enhanced T1-weighted CUBE images. Image parameters for the nC-MIPs were chosen on the basis of results from a recent prior study showing their benefits for the detection of brain metastases.[18] Image parameters for the oC-MIPs were chosen on the basis of our clinical experience of using thick-slabbed MIPs for detection of enhancing brain lesions because no prior studies, to our knowledge, have reported optimal values for overlapping MIPs. Axial MIPs of IR-FSPGR-BRAVO (10-mm sections reconstructed at 4-mm intervals) were also generated solely for comparison of CNR with CUBE MIPs. These specific MIPS were not used for detection of metastases in this study because we and others have found them to be of little clinical utility, in large part due to the difficulty in distinguishing true enhancing metastases from excessive background vascular enhancement.[18]

### Determination of Ground Truth for Brain Metastases

A neuroradiologist with >10 years of experience who did not participate in counting of the metastases as part of the study carefully reviewed all sequences from the initial MR imaging, including precontrast (diffusion-weighted imaging, gradient recalled, T2-weighted fast spin-echo, 3D T1 CUBE) and postcontrast (3D T1 CUBE, IR-FSPGR-BRAVO, 3D CUBE FLAIR) images as well as any follow-up MRIs that were acquired before any intervening treatment. A brain metastasis was positively identified and recorded (image slice number of the lesion and its anatomic location) if the following criteria were present: a nonvascular enhancing lesion with or without associated FLAIR or diffusion signal intensity, surrounding edema, or hemorrhage that was unchanged or increased in size on follow-up MR imaging. For this study, any postsurgical enhancement (defined as enhancement contiguous with a remote surgical resection cavity) and leptomeningeal enhancement were excluded.

### Image Analysis

A neuroradiologist with 10 years of experience (reader 1) and a radiology resident with 2 years of experience (reader 2) counted the number of brain metastases for each patient during 4 sessions separated by 1 week between each session. Each reader independently evaluated CUBE in 1 session, nC-MIP alone in the second

session, oC-MIP alone in the third session, and IR-FSPGR-BRAVO in the last session. In additional sessions separated by 1 week, each reader also independently evaluated nC-MIP and oC-MIP with the option to cross-reference a lesion with source images to confirm the authenticity of a questionable lesion (nC-MIP+ cross-reference [XR] and oC-MIP+XR, respectively); this was performed to determine whether the simultaneous use of cross-referencing affected interpretation time and detection sensitivity. The order of patients during each session was randomized. The number of metastases identified and the time for each reader to identify and count all lesions (time for interpretation) were recorded. During the counting process, readers also recorded the image slice number and anatomic location of each lesion on each sequence using speech recognition software (Nuance PowerScribe 360 Reporting; Nuance Communications, Burlington, Massachusetts).

The contrast-to-noise ratio was calculated using the smallest (<4 mm) and largest metastatic lesions identified on CUBE, both CUBE MIPs, IR-FSPGR-BRAVO, and IR-FSPGR-BRAVO MIPs with the following formula: Mean Signal Intensity of Lesion − Mean Signal Intensity of Normal White Matter / SD of Lesion Signal Intensity.[8]

### *Statistical Analysis*

Due to the lack of histopathologic data, our study did not have an absolute standard of truth. Our ground truth was based on the evaluation of all sequences on the initial MR imaging and comparison of lesions with any follow-up MR imaging in which there was no intervening treatment. Therefore, we aimed to compare the sensitivities and discrepancy rates of all image types rather than to determine diagnostic accuracy; this method has been similarly used in previous analyses of pulmonary nodules.[20]

Interrater agreement for identification of metastases was calculated using the Cohen $\kappa$ coefficient with the following interpretation model of $\kappa$: 0-.20, slight; 0.21–0.40, fair; 0.41–0.60, moderate; 0.61–0.80, substantial; and 0.81–1, almost perfect.[21] Specifically, of the total pool of ground truth metastases, agreement for the presence of each individual lesion was assessed as follows: 1) both readers agreed that a lesion was present, 2) reader 1 identified a lesion but reader 2 did not, 3) reader 2 identified a lesion but reader 1 did not, and 4) both readers agreed that a lesion was not present. The total number of lesions detected on each image type and time for interpretation were compared between readers using 1-way analysis of variance with a Bonferroni adjustment. A $P < .013$ (calculated by .05/4) was considered statistically significant in comparing the 4 image types (CUBE, nC-MIP, oC-MIP, IR-FSPGR-BRAVO), as determined by the Bonferroni adjustment.[22] The CNR of the smallest and largest lesions on each series was reported as mean ± SD. In a subgroup analysis, the time for interpretation was compared between all CUBE MIPs (nC-MIP, oC-MIP, nC-MIP+XR, oC-MIP+XR) and source CUBE, using 1-way analysis of variance with a Bonferroni adjustment. A $P < .01$ (calculated by .05/5) was considered statistically significant in comparing these 5 image types, as determined by the Bonferroni adjustment.[22] Lesion-detection sensitivity, mean false-negative, mean false-positive, and mean discrepancy (total number of false-positives and false-negatives) per case were assessed for all image analysis types.

**Table 1: Interrater agreement using the Cohen $\kappa$ coefficient for T1-weighted CUBE, nC-MIP, oC-MIP, and IR-FSPGR-BRAVO**

| Image Type | $\kappa$ | 95% Confidence Interval | Agreement |
|---|---|---|---|
| CUBE | 0.235 | 0.024–0.447 | Fair |
| nC-MIP | 0.222 | 0.069–0.374 | Fair |
| oC-MIP | 0.598 | 0.371–0.825 | Moderate |
| IR-FSPGR-BRAVO | 0.445 | 0.290–0.599 | Moderate |

## RESULTS

A total of 308 metastases were identified in 48 patients, consisting of 37 women and 11 men (mean age: 62.4 ± 13 years; age range, 29–81 years). Twenty-six patients had primary non-small cell lung cancer, 1 had small cell lung cancer, 13 had breast cancer, 2 had melanoma, 2 had renal cell carcinoma, 1 had esophageal cancer, and 2 had ovarian cancer. One patient had a history of Li-Fraumeni syndrome and had multiple primary cancers, including colon, lung, breast, uterine, and hepatocellular carcinoma. Of the 48 patients, 27 had undergone prior treatment for brain metastases, including surgical resection, whole-brain radiation therapy, and/or SRS.

Interrater agreement for the presence of individual metastatic lesions was fair-to-moderate across all image types ($\kappa = 0.222$–$0.598$) but highest for oC-MIP ($\kappa = 0.598$) (Table 1). No significant difference was found among the total number of metastases on any of the 4 main image types ($P = .062$): CUBE (319 for reader one, 336 for reader 2), nC-MIP (325 for reader one, 313 for reader 2), oC-MIP (327 for reader one, 333 for reader 2), IR-FSPGR-BRAVO (289 for reader one, 303 for reader 2) (Fig 1).

A significant difference in the time for interpretation among the image types was found for both readers ($P < .001$) (Fig 2*A*). The time for interpretation using oC-MIP (mean: 55.2 ± 25.1 seconds for reader one, 94.7 ± 36.5 seconds for reader 2) and nC-MIP (58.2 ± 32.9 seconds for reader one, 97.0 ± 23.4 seconds for reader 2) was significantly reduced compared with CUBE (109.8 ± 47.5 seconds for reader one, $P < .001$; 173.5 ± 67.7 seconds for reader 2, $P < .001$) and IR-FSPGR-BRAVO (124.6 ± 48 seconds for reader one, $P < .001$; 195 ± 64.8 seconds for reader 2, $P < .001$), with a savings of at least 50 seconds per case (on average). In a subgroup analysis of all CUBE image types, time for interpretation using oC-MIP+XR (61.9 ± 27.7 seconds for reader one, 91.7 ± 35.0 seconds for reader 2) and nC-MIP+XR (71.7 ± 32.0 seconds for reader one, 94.3 ± 33.0 seconds for reader 2) was significantly reduced compared with CUBE ($P < .001$) (Fig 2*B*). However, time for interpretation was not significantly different among oC-MIP, nC-MIP, oC-MIP+XR, and nC-MIP+XR.

The conspicuity of the lesions as indicated by CNR on the 4 image types also differed for both small (<4 mm) and large lesions (Table 2 and Fig 3). For both lesion groups, the mean CNR was the highest for oC-MIP and higher with CUBE and both CUBE MIPs than with IR-FSPGR-BRAVO and IR-FSPGR-BRAVO MIP. The mean CNR for small lesions was lower with nC-MIP (1.55 ± 0.3) than with CUBE (2.35 ± 2.0) or oC-MIP (2.35 ± 1.64).

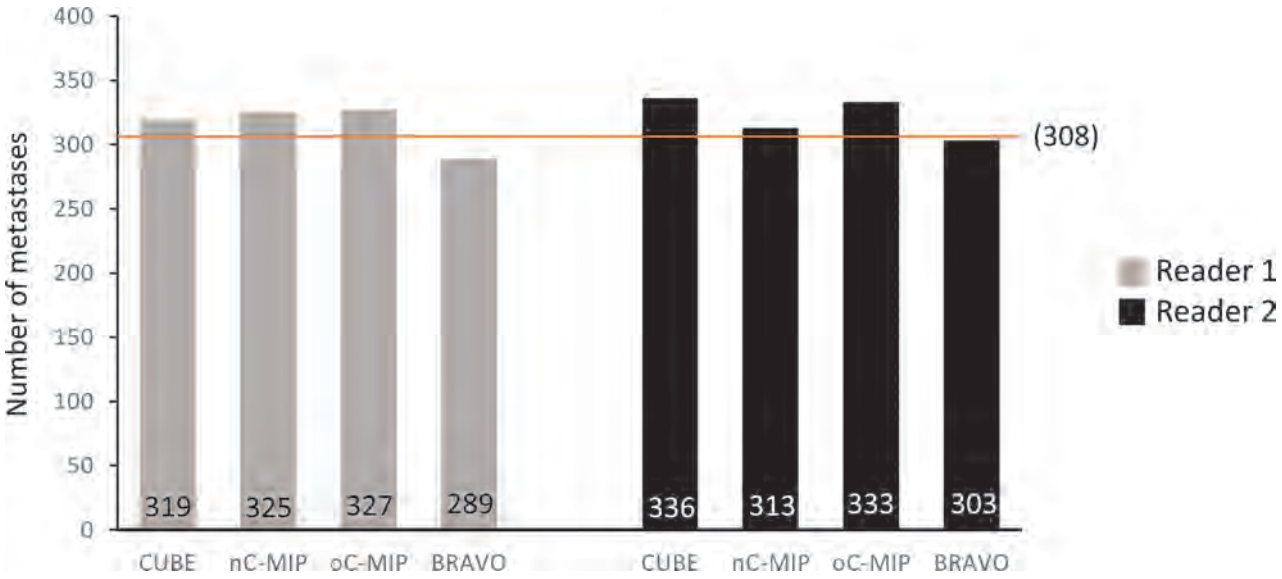


**FIG 1.** Total number of brain metastases detected. No significant difference was found among the total number of metastases detected using CUBE, nC-MIP, oC-MIP, and IR-FSPGR-BRAVO ($P = .062$) using 1-way ANOVA with a Bonferroni adjustment. The *orange line* denotes the total number of ground truth lesions ($n = 308$).

For both readers, the sensitivity for lesion detection was high for all image types. Of CUBE, nC-MIP, oC-MIP, and IR-FSPGR-BRAVO, sensitivity was highest for oC-MIP (0.96 for both readers) and CUBE (0.97 for reader one, 0.93 for reader 2) (Table 3). Sensitivity was slightly lower for nC-MIP (0.95 for reader one, 0.90 for reader 2) and even lower for IR-FSPGR-BRAVO (0.92 for reader one, 0.89 for reader 2). On average, there was <1 false-negative and 1 false-positive case per patient across all image types (Table 3). The mean discrepancy rate (total number of false-negative and false-positive lesions per case) was also <1 lesion per patient on all image types except with nC-MIP and IR-FSPGR-BRAVO for reader 2. Mean false-positives per case were reduced with oC-MIP+XR (0.21 for reader one, 0.23 for reader 2) compared with oC-MIP (0.54 for reader one, 0.33 for reader 2) and with nC-MIP+XR (0.25 for reader one, 0.29 for reader 2) compared with nC-MIP (0.58 for reader one, 0.71 for reader 2).

## DISCUSSION

In this study, we found that the use of oC-MIP or nC-MIP reduced interpretation time without sacrificing lesion detection sensitivity compared with traditional CUBE and IR-FSPGR-BRAVO. The coupling of CUBE MIPs with the option to cross-reference a questionable lesion to source images further reduced false-positives without significantly changing the time for interpretation compared with MIPs alone. The CNR of brain metastases was higher with CUBE and both CUBE MIPs than with IR-FSPGR-BRAVO and IR-FSPGR-BRAVO MIP, though the CNR of small and large metastases was highest with thick-slab oC-MIP. Interrater agreement for the detection of brain metastases was fair-to-moderate across all image types but highest with oC-MIP. The findings in our study are consistent with those of other investigators regarding enhanced lesion detection and increased CNR using 3D fast spin-echo imaging compared with gradient-echo imaging.[7,8] CUBE images are ideally suited for MIP reconstruction because there is an inherent reduction in the amount of background vascular enhancement, which further reduces background image noise and increases lesion conspicuity.

An issue of clinical importance for practicing radiologists that has received less research attention is interpretation time, a particularly relevant issue with the increasing use of 3D volumetric sequences. Tasks such as counting individual millimetric metastases is of high importance in patient management, but this remains time-consuming and laborious. A recent study demonstrated that the use of nonoverlapping 5-mm-thick MIP reformations of contrast-enhanced 3D T1-weighted turbo spin-echo imaging yielded a shorter time for interpretation with sensitivity comparable with that of the 1-mm source images.[18] Similarly, we found that the use of CUBE MIPs resulted in significantly reduced interpretation times compared with both source CUBE and IR-FSPGR-BRAVO, without a reduction in detection sensitivity. When we compared the 5-mm-thick nC-MIP (used in the study of Bae et al[18]) and 10-mm-thick oC-MIP, the sensitivity for detection of cerebral metastases was slightly higher with the latter. Moreover, while the mean discrepancy (number of missed lesions) was <1 lesion per case between the 2 MIPs for reader 1, the mean discrepancy and the SD were slightly higher for reader 2, the radiology resident. This is not surprising because the CNR is dependent on the SNR, which increases with MIP technique and slice thickness. There is also less effect of partial volume averaging with overlapping than nonoverlapping MIPs, which contributes to increased lesion conspicuity and detection. As an example, Fig 4 demonstrates a small lesion that is visible over a greater number of slices on oC-MIP than on nC-MIP. There is also easier tracking of vessels on oC-MIP because vessels are seen continuously over multiple slices. Thus, the use of thick-slab oC-MIP can be a useful tool for less experienced radiologists, such as trainees, to detect cerebral metastases.

The absolute number of brain metastases identified on MR imaging is important in determining treatment planning (eg, selection of SRS or whole-brain radiation therapy). Our results

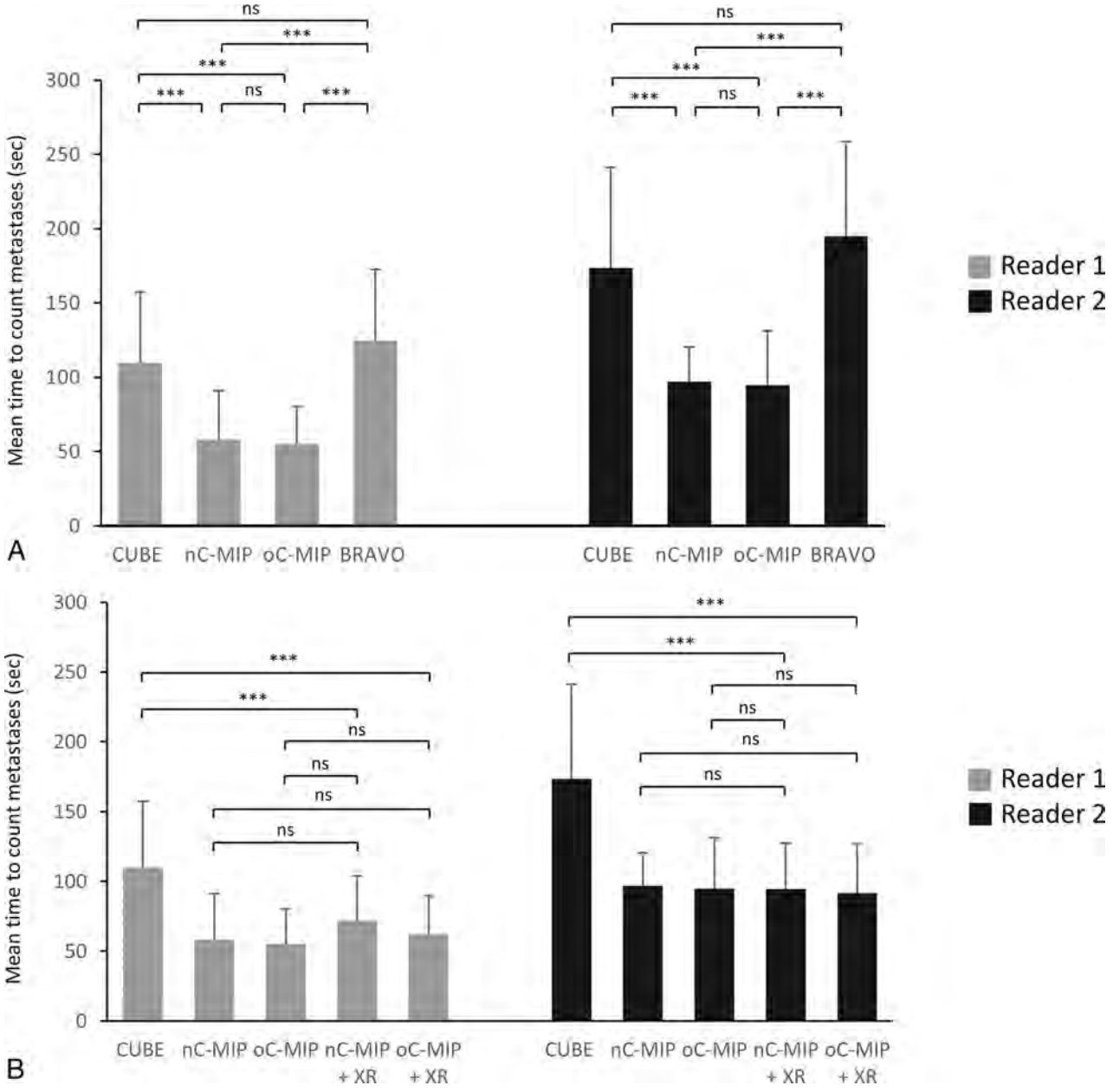


**FIG 2.** Mean time for interpretation. *A*, Both readers had significantly reduced interpretation time using nC-MIP and oC-MIP compared with CUBE and IR-FSPGR-BRAVO, saving at least 50 seconds per case (on average). *B*, The use of nC-MIP and oC-MIP with the option to cross-reference an equivocal lesion to the source images (nC-MIP+XR and oC-MIP+XR, respectively) did not result in a significant change in interpretation time compared with the use of nC-MIP or oC-MIP alone. However, time for interpretation for all CUBE MIPs was significantly reduced compared with CUBE. *Error bars* represent the SD. One-way ANOVA with a Bonferroni adjustment. *Triple asterisks* indicate $P < .001$; ns, no significance.

**Table 2: CNR of the smallest and largest metastases on CUBE, nC-MIP, oC-MIP, IR-FSPGR-BRAVO, and overlapping IR-FSPGR-BRAVO MIP[a]**

| Image Type | CNR of the Smallest Lesion (<4 mm) | CNR of the Largest Lesion |
|---|---|---|
| CUBE | 2.35 ± 2.0 | 2.49 ± 1.84 |
| nC-MIP | 1.55 ± 0.53 | 2.69 ± 0.93 |
| oC-MIP | 2.35 ± 1.64 | 3.23 ± 1.92 |
| IR-FSPGR-BRAVO | 0.62 ± 0.39 | 1.45 ± 1.14 |
| IR-FSPGR-BRAVO MIP | 0.90 ± 0.78 | 1.69 ± 1.14 |

[a] Numbers are means.

indicate a small number of discrepant lesions per case using oC-MIP and CUBE, with both image types averaging <1 missed lesion per case in both readers. While not statistically significant, the total number of metastases detected with IR-FSPGR-BRAVO was also slightly less than with CUBE and both CUBE MIPs. This feature may have been related to IR-FSPGR-BRAVO failing to conspicuously demonstrate some lesions, which is likely due to the lower CNR associated with gradient-echo imaging (despite this sequence being the last acquired in our imaging protocol). Regarding lesion detection using MIPs, the discrepancy rate can be decreased by concurrently cross-referencing any lesions in question to the source images to confirm that they are true lesions.

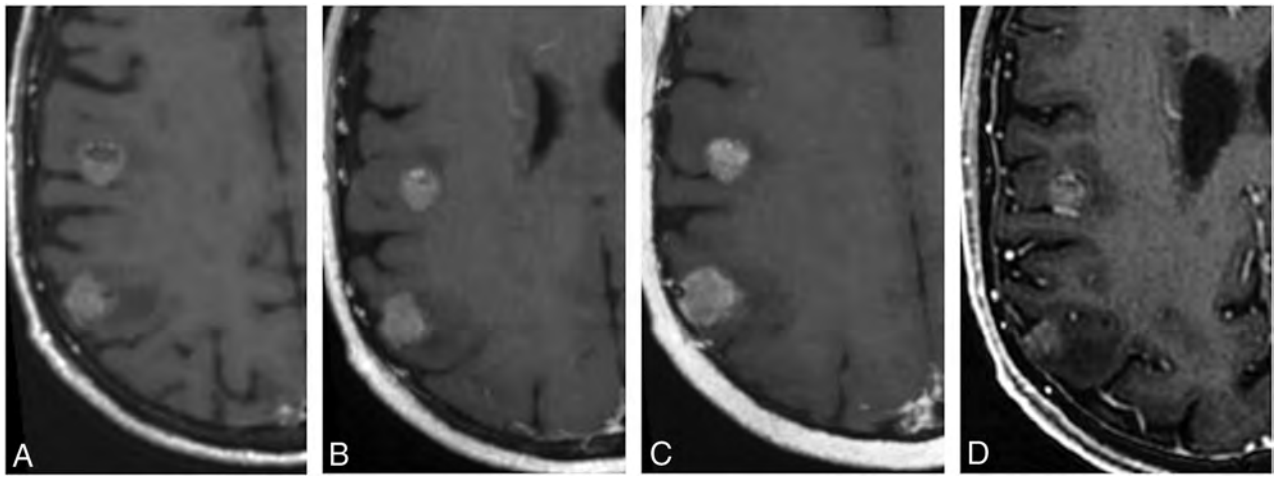


**FIG 3.** Enhancing cerebral metastases in a 74-year-old male with metastatic tongue squamous cell carcinoma. Postcontrast T1-weighted CUBE (*A*), nonoverlapping CUBE MIP (nC-MIP) (*B*), overlapping CUBE MIP (oC-MIP) (*C*), and IR-FSPGR-BRAVO (*D*) images demonstrate enhancing metastatic lesions. The lesions appear most conspicuous with CUBE MIPs (*B* and *C*). The contrast-to-noise ratio of lesions was highest for oC-MIP (*C*).

**Table 3: Sensitivity, number of false-negatives, number of false-positives, and number of discrepant lesions (FN + FP) per case for CUBE, nC-MIP, oC-MIP, IR-FSPGR-BRAVO, and non-overlapping and overlapping CUBE MIPs[a]**

| | Reader 1 | | | | Reader 2 | | | |
|---|---|---|---|---|---|---|---|---|
| | % Sensitivity | Mean FN | Mean FP | Mean Discrepancy | % Sensitivity | Mean FN | Mean FP | Mean Discrepancy |
| CUBE | 97.1 ± 14.8 | 0.08 ± 0.28 | 0.31 ± 0.63 | 0.40 ± 0.65 | 93.0 ± 16.8 | 0.38 ± 0.70 | 0.38 ± 0.82 | 0.75 ± 0.93 |
| nC-MIP | 94.7 ± 20.4 | 0.08 ± 0.28 | 0.58 ± 0.98 | 0.65 ± 0.96 | 90.2 ± 16.8 | 0.60 ± 0.96 | 0.71 ± 1.98 | 1.31 ± 2.00 |
| oC-MIP | 95.8 ± 15.4 | 0.19 ± 0.49 | 0.54 ± 0.92 | 0.73 ± 0.94 | 95.8 ± 15.4 | 0.19 ± 0.50 | 0.33 ± 0.69 | 0.75 ± 0.93 |
| BRAVO | 91.5 ± 17.0 | 0.58 ± 0.99 | 0.21 ± 0.50 | 0.79 ± 0.99 | 89.0 ± 19.5 | 0.85 ± 1.49 | 0.31 ± 0.59 | 1.17 ± 1.42 |
| nC-MIP + XR | 95.5 ± 9.8 | 0.33 ± 0.66 | 0.25 ± 0.70 | 0.58 ± 0.87 | 91.2 ± 12.3 | 0.67 ± 0.93 | 0.29 ± 0.74 | 0.95 ± 1.01 |
| oC-MIP + XR | 96.6 ± 7.3 | 0.29 ± 0.62 | 0.21 ± 0.46 | 0.68 ± 0.96 | 94.8 ± 12.3 | 0.38 ± 0.79 | 0.23 ± 0.47 | 0.60 ± 0.82 |

**Note:**—FN indicates false-negative; FP, false-positive.

[a] With the option to cross-reference a lesion to the source images (nC-MIP+XR and oC-MIP+XR, respectively) for both readers. Numbers are means.

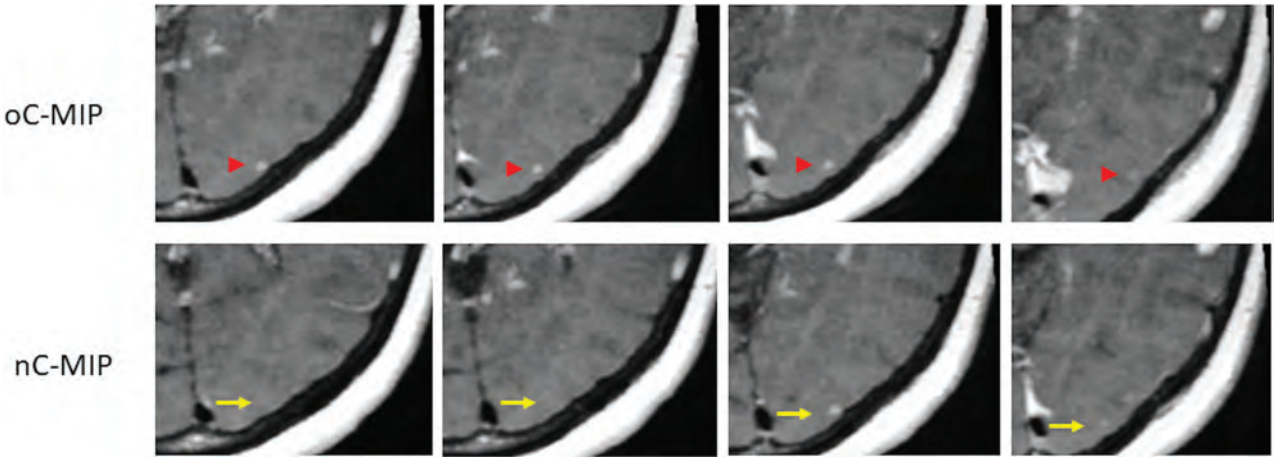


**FIG 4.** Comparison between nonoverlapping and overlapping CUBE MIP. A small 3-mm metastasis in a 57-year-old woman with non-small cell lung cancer is seen across 4 different slices with oC-MIP but is only identified on 2 slices with nC-MIP.

While missing a few metastatic lesions may not mean much in an individual with innumerable lesions, it may potentially change management in patients with fewer lesions who are being considered for SRS because certain institutions may only offer SRS to patients with up to a specific number of lesions.

In chest imaging, MIPs have been shown to enhance the detection of small lesions with increased sensitivity and decreased interpretation time; however, increased false-positive rates have been found.[14-17] Many authors have found that MIPs are of greatest benefit when used for the detection of smaller lesions (<4 mm) because larger lesions were detected at an equivalent rate when using thin-section source images. Axial source images yield a lower false-positive rate, consistent with the results in our study, and thus a higher positive predictive value. Thus, given the importance of lesion-detection accuracy, we believe that the use of CUBE MIPs for the evaluation of brain metastases should play a

role similar to the use of MIPs in chest imaging; MIPs can help provide a global overview of the presence of lesions, which can subsequently help focus the reader on a particular area in the brain for a more targeted assessment. Specifically, an equivocal lesion that is identified on MIPs can be cross-referenced to source images to confirm its authenticity as a true metastasis. Our study suggests that this can be achieved without significantly increasing the interpretation time.

A limitation of our study, which was also encountered by Kato et al,[8] is the identification of false-positive lesions on CUBE images. Despite the predominant black-blood contrast of CUBE, scattered regions of short-segment vascular enhancement persist. Thus, small vessels may be difficult to differentiate from punctate enhancing metastases, and often in clinical practice, concurrent review of IR-FSPGR-BRAVO is necessary to confirm the nature of these enhancing foci by showing their continuity with vascular structures. This issue persists on MIP and may even be more problematic given the reduced ability to trace the origin of a given focus of enhancement due to thicker slabs and fewer images. Future investigation using improved blood flow suppression techniques with CUBE may help to address this dilemma. The use of MIPs in patients with innumerable (>20) lesions also poses a challenge because superimposition of lesions may occur with thick-slab MIPs, thereby hampering differentiation of separate-but-adjacent metastases. Finally, the generalizability of our study results is somewhat limited because this study was performed at a single institution on 3T MR imaging scanners of a single vendor type using a specific gadolinium-based contrast agent (gadobenate dimeglumine). Additional studies that include a larger sample size, more scanner types and of different magnet strength, more raters with varying levels of experience, and different contrast agents including macrocyclic agents (especially given the issue of intracranial gadolinium deposition) are needed to further validate our results. Future studies can also explore the potential use of MIPs for characterization of metastases beyond the total number of lesions, including defining tumor extent, intratumoral features, and effects of radiation treatment.

## CONCLUSIONS

MIPs have been established in chest imaging for pulmonary nodule assessment and can be successfully extrapolated to brain metastatic disease. The use of oC-MIP or nC-MIP for the detection of multiple brain metastases yields reduced reading time without sacrificing diagnostic sensitivity compared with source CUBE and IR-FSPGR-BRAVO. However, the use of thick-slab oC-MIP provides higher lesion conspicuity, which can aid in overall lesion detection, especially of smaller lesions. While MIPs may not entirely replace the use of thin source images, given the limitations described in this study, they may serve as a complementary tool to enhance visualization of lesions.

Disclosures: Max Wintermark—*UNRELATED*: *Board Membership*: GE NFL Advisory Board. Greg Zaharchuk—*UNRELATED*: *Board Membership*: GE Healthcare, *Comments*: Research funding*. *Money paid to the institution.

## REFERENCES

1. Lam TC, Sahgal A, Chang EL, et al. **Stereotactic radiosurgery for multiple brain metastases.** *Expert Rev Anticancer Ther* 2014;14:1153–72 CrossRef Medline
2. Tsao MN, Lloyd NS, Wong RKS, et al; Supportive Care Guidelines Group of Cancer Care Ontario's Program in Evidence-Based Care. **Radiotherapeutic management of brain metastases: a systematic review and meta-analysis.** *Cancer Treat Rev* 2005;31:256–73 CrossRef Medline
3. Sills AK. **Current treatment approaches to surgery for brain metastases.** *Neurosurgery* 2005;57(5 Suppl):S24–32; discusssion S1–S4 Medline
4. Yamamoto M, Serizawa T, Shuto T, et al. **Stereotactic radiosurgery for patients with multiple brain metastases (JLGK0901): a multi-institutional prospective observational study.** *Lancet Oncol* 2014;15:387–95 CrossRef Medline
5. Serizawa T, Hirai T, Nagano O, et al. **Gamma knife surgery for 1–10 brain metastases without prophylactic whole-brain radiation therapy: analysis of cases meeting the Japanese prospective multi-institute study (JLGK0901) inclusion criteria.** *J Neurooncol* 2010;98:163–67 CrossRef Medline
6. Park J, Kim J, Yoo E, et al. **Detection of small metastatic brain tumors: comparison of 3D contrast-enhanced whole-brain black-blood imaging and MP-RAGE imaging.** *Invest Radiol* 2012;47:136–41 CrossRef Medline
7. Majigsuren M, Abe T, Kageji T, et al. **Comparison of brain tumor contrast-enhancement on T1-CUBE and 3D-SPGR Images.** *Magn Reson Med Sci* 2016;15:34–40 CrossRef Medline
8. Kato Y, Higano S, Tamura H, et al. **Usefulness of contrast-enhanced T1-weighted sampling perfection with application-optimized contrasts by using different flip angle evolutions in detection of small brain metastasis at 3T MR imaging: comparison with magnetization-prepared rapid acquisition of gradient echo imaging.** *AJNR Am J Neuroradiol* 2009;30:923–29 CrossRef Medline
9. Fukuoka H, Hirai T, Okuda T, et al. **Comparison of the added value of contrast-enhanced 3D fluid-attenuated inversion recovery and magnetization-prepared rapid acquisition of gradient echo sequences in relation to conventional postcontrast T1-weighted images for the evaluation of leptomeningeal diseases at 3T.** *AJNR Am J Neuroradiol* 2010;31:868–73 CrossRef Medline
10. Komada T, Naganawa S, Ogawa H, et al. **Contrast-enhanced MR imaging of metastatic brain tumor at 3 Tesla: utility of T(1)-weighted SPACE compared with 2D spin echo and 3D gradient echo sequence.** *Magn Reson Med Sci* 2008;7:13–21 CrossRef Medline
11. Takeda T, Takeda A, Nagaoka T, et al. **Gadolinium-enhanced three-dimensional magnetization-prepared rapid gradient-echo (3D MP-RAGE) imaging is superior to spin-echo imaging in delineating brain metastases.** *Acta Radiol* 2008;49:1167–73 CrossRef Medline
12. Yoshida A, Tha KK, Fujima N, et al. **Detection of brain metastases by 3-dimensional magnetic resonance imaging at 3 T: comparison between T1-weighted volume isotropic turbo spin echo acquisition and 3-dimensional T1-weighted fluid-attenuated inversion recovery imaging.** *J Comput Assist Tomogr* 2013;37:84–90 CrossRef Medline
13. Kwak HS, Hwang S, Chung GH, et al. **Detection of small brain metastases at 3 T: comparing the diagnostic performances of contrast-enhanced T1-weighted SPACE, MPRAGE, and 2D FLASH imaging.** *Clin Imaging* 2015;39:571–75 CrossRef Medline
14. Valencia R, Denecke T, Lehmkuhl L, et al. **Value of axial and coronal maximum intensity projection (MIP) images in the detection of pulmonary nodules by multislice spiral CT: comparison with axial 1-mm and 5-mm slices.** *Eur Radiol* 2006;16:325–32 CrossRef Medline
15. Kilburn-Toppin F, Arthurs OJ, Tasker AD, et al. **Detection of pulmonary nodules at paediatric CT: maximum intensity projections and axial source images are complementary.** *Pediatr Radiol* 2013;43:820–26 CrossRef Medline
16. Jankowski A, Martinelli T, Timsit JF, et al. **Pulmonary nodule detection on MDCT images: evaluation of diagnostic performance using**

**thin axial images, maximum intensity projections, and computer-assisted detection.** *Eur Radiol* 2007;17:3148–56 CrossRef Medline

17. Diederich S, Lentschig MG, Overbeck TR, et al. **Detection of pulmonary nodules at spiral CT: comparison of maximum intensity projection sliding slabs and single-image reporting.** *Eur Radiol* 2001;11:1345–50 CrossRef Medline
18. Bae YJ, Choi BS, Lee KM, et al. **Efficacy of maximum intensity projection of contrast-enhanced 3D turbo-spin echo imaging with improved motion-sensitized driven-equilibrium preparation in the detection of brain metastases.** *Korean J Radiol* 2017;18:699–709 CrossRef Medline
19. Sepulveda F, Yáñez P, Carnevale MD, et al. **MIP improves detection of brain metastases.** *J Comput Assist Tomogr* 2016;40:997–1000 CrossRef Medline
20. Peloschek P, Sailer J, Weber M, et al. **Pulmonary nodules: sensitivity of maximum intensity projection versus that of volume rendering of 3D multidetector CT data.** *Radiology* 2007;243:561–69 CrossRef Medline
21. Landis JR, Koch GG. **The measurement of observer agreement for categorical data.** *Biometrics* 1977;33:159–74 CrossRef Medline
22. Bland JM, Altman DG. **Multiple significance tests: the Bonferroni method.** *BMJ* 1995;310:170 CrossRef Medline

# MRI Findings in Tumefactive Demyelinating Lesions: A Systematic Review and Meta-Analysis

C.H. Suh, H.S. Kim, S.C. Jung, C.G. Choi, and S.J. Kim

## ABSTRACT

**BACKGROUND:** Accurate diagnosis of tumefactive demyelinating lesions is clinically important to avoid unnecessary invasive biopsy or inappropriate treatment.

**PURPOSE:** We aimed to evaluate conventional and advanced MR imaging findings of tumefactive demyelinating lesions and determine the diagnostic performance of MR imaging for differentiating tumefactive demyelinating lesions from primary brain tumor.

**DATA SOURCES:** A systematic search of Ovid MEDLINE and EMBASE up to December 6, 2017, was conducted.

**STUDY SELECTION:** Original articles describing MR imaging findings in patients with tumefactive demyelinating lesions were selected.

**DATA ANALYSIS:** The pooled incidences of conventional MR imaging findings of tumefactive demyelinating lesions were obtained with the DerSimonian and Liard random-effects model. The pooled sensitivity and specificity of MR imaging for differentiating tumefactive demyelinating lesions from primary brain tumor were obtained using the bivariate random-effects model.

**DATA SYNTHESIS:** Nineteen eligible studies with 476 patients with tumefactive demyelinating lesions were included. The pooled incidence of open ring or incomplete rim enhancement was 35% (95% CI, 24%–47%), which was significantly higher than the incidence of closed ring or complete rim enhancement (18% [95% CI, 11%–29%]; $P = .0281$). The pooled incidences of T2 hypointense rim, absent or mild mass effect, and absent or mild perilesional edema were 48%, 67%, and 57%, respectively. On advanced MR imaging, tumefactive demyelinating lesions showed a high apparent diffusion coefficient, peripheral restricted diffusion, and low cerebral blood volume. The pooled sensitivity and specificity of MR imaging for differentiating tumefactive demyelinating lesions from primary brain tumor were 89% (95% CI, 82%–93%) and 94% (95% CI, 89%–97%), respectively.

**LIMITATIONS:** Seventeen of 19 studies were retrospective studies.

**CONCLUSIONS:** Conventional MR imaging findings may help differentiate tumefactive demyelinating lesions from primary brain tumor, though further study is needed to determine the added value of advanced MR imaging.

**ABBREVIATIONS:** DSC = dynamic susceptibility-weighted contrast-enhanced imaging; PCNSL = primary central nervous system lymphoma; TDL = tumefactive demyelinating lesion

Tumefactive demyelinating lesions (TDLs) are large (usually >2 cm) demyelinating brain lesions that mimic primary brain tumors, including primary central nervous system lymphoma (PCNSL) and high-grade glioma.[1-3] Accurate diagnosis of TDL is clinically important to avoid unnecessary invasive biopsy or inappropriate treatment.

Several characteristic conventional MR imaging findings and advanced MR imaging techniques have been introduced for the diagnosis of TDLs.[4-22] Conventional MR imaging findings,[23] including open ring or incomplete rim enhancement, a T2 hypointense rim, absent or mild mass effect, and absent or mild perilesional edema, demonstrate variable frequencies. In addition, 1 review article classified TDLs into 4 different subtypes based on

Received March 10, 2018; accepted after revision May 9.

From the Department of Radiology and Research Institute of Radiology, University of Ulsan College of Medicine, Asan Medical Center, Seoul, Republic of Korea.

This study was supported by a grant from the National R&D Program for Cancer Control, Ministry of Health and Welfare, Republic of Korea (1720030).

Please address correspondence to Ho Sung Kim, MD, PhD, Department of Radiology and Research Institute of Radiology, University of Ulsan College of Medicine, Asan Medical Center, 86 Asanbyeongwon-Gil, Songpa-Gu, Seoul 138-736, Republic of Korea; e-mail: radhskim@gmail.com

Indicates open access to non-subscribers at www.ajnr.org
Indicates article with supplemental on-line photo.

http://dx.doi.org/10.3174/ajnr.A5775

the most prominent conventional MR imaging characteristics as follows: megacystic, Balò-like, infiltrative, and ringlike.[24] Several studies have reported the use of advanced MR imaging techniques, including diffusion-weighted imaging, dynamic susceptibility-weighted contrast-enhanced imaging (DSC), MR spectroscopy, and diffusion tensor imaging.[5,8,10,12,14,15,18,19]

To our knowledge, the MR imaging findings of TDLs and their diagnostic performance for differentiating TDLs from primary brain tumors have not yet been systematically reviewed. Therefore, we aimed to evaluate conventional and advanced MR imaging findings of TDLs and to determine the diagnostic performance of MR imaging for differentiating TDL from primary brain tumor.

## MATERIALS AND METHODS

### Search Methods and Study Selection

A systematic search of the literature in MEDLINE and EMBASE was performed to identify published original articles describing MR imaging findings in patients with TDL. The search term combined synonyms of "TDL" and "MR imaging" as follows: ((tumefactive demyelinating lesion*) OR (TDL) OR (atypical demyelination lesion) OR (Balò sclerosis)) AND ((MR imaging) OR (MR imaging) OR (MR imaging)). The data base was searched for literature published on or before April 21, 2018. The literature search was limited to English-language publications. The bibliographies of articles were explored to identify additional relevant articles.

### Data Extraction

Conventional MR imaging findings and advanced MR imaging findings in patients with TDL and the diagnostic performance of MR imaging for differentiating TDL from primary brain tumor were extracted from the eligible articles. A TDL was defined as a large (usually >2 cm) demyelinating brain lesion mimicking a primary brain tumor.[25,26] The conventional MR imaging findings of TDLs were recorded as the following: 1) an open ring or incomplete rim enhancement, 2) a closed ring or complete rim enhancement, 3) a T2 hypointense rim, 4) an absent or mild mass effect, and 5) absent or mild perilesional edema. Advanced MR imaging findings from the techniques of DWI, DSC, and MR spectroscopy were also recorded. Two-by-2 tables (true-positive, false-positive, false-negative, true-negative) for the determination of the diagnostic performance of MR imaging for differentiating TDLs from primary brain tumors were also constructed.

The following information was recorded from the selected studies: 1) the institution, the patient recruitment period, a retrospective or prospective design, consecutive or nonconsecutive patient enrollment, the reference standard, and the follow-up period; 2) the number of patients with TDLs, mean age, age range, and male-to-female ratio; 3) the magnetic field strength of the scanner, scanner manufacturer, scanner model, number of head coil channels, slice thickness, and advanced MR imaging techniques used, including DWI, DSC, and MR spectroscopy; and 4) the number of MR imaging readers, reader experience, and blindness to the reference standard.

Quality assessment was performed using the Quality Assessment of Diagnostic Accuracy Studies-2 (QUADAS-2) criteria.[27] The study selection, data extraction, and quality assessment were performed by 2 reviewers (C.H.S., H.S.K.) and were independently reviewed by a third reviewer (S.J.K.), in accordance with the Preferred Reporting Items for Systematic Reviews and Meta-Analyses guidelines.[28]

### Statistical Methods

The pooled incidences for conventional MR imaging findings of TDL were obtained with the inverse variance method for calculating weights and the DerSimonian and Liard random-effects model.[29-31] The difference between the incidences of open ring or incomplete rim enhancement versus closed ring or complete rim enhancement was evaluated using mixed-effects model meta-regression. Heterogeneity was evaluated using the inconsistency index ($I^2$) test of Higgins et al,[32] with values of >50% indicating substantial heterogeneity. Publication bias was visually assessed using a funnel plot, and the statistical significance was assessed using the Egger test.[33] Meta-regression was performed to explain the effects of heterogeneity across the studies. We considered the following covariates: 1) the number of patients with TDL (<15 [median value of the included studies] versus ≥15); 2) age (younger than 34.5 years [median value of the included studies] versus 34.5 years and older); 3) male-to-female ratio (<0.76 [median value of the included studies] versus ≥0.76); 4) reference standard (histopathology only versus others); 5) magnetic field of the scanner (1.5T versus 3T); and 6) slice thickness (<5 mm versus ≥5 mm).

The pooled sensitivity and specificity and their 95% confidence interval were obtained using the bivariate random-effects model.[29-31] A hierarchic summary receiver operating characteristic curve with 95% confidence and prediction regions was obtained. Publication bias was assessed by the Deeks funnel plot, and the statistical significance was assessed by the Deeks asymmetry test.[34]

All statistical analyses were performed by 1 reviewer (C.H.S., with 5 years of experience in performing systematic reviews and meta-analysis) using the "metafor" and "mada" packages in R, Version 3.4.1 (http://www.r-project.org/) and the "metandi" and "MIDAS" modules in STATA 15.0 (StataCorp, College Station, Texas).

## RESULTS

### Eligible Studies and Characteristics

The search identified 195 articles. After removing 21 duplicated articles, we performed screening of the 174 remaining titles and abstracts. From these, a further 147 articles were excluded (Fig 1). Full-text reviews of the remaining 27 potentially eligible articles were performed, and a further 8 studies were excluded for the following reasons: no mention of the MR imaging findings of TDL ($n = 4$), partially overlapping patient cohorts ($n = 3$), and case series ($n = 1$). Finally, 19 eligible studies covering 476 patients with TDLs were included in the analyses.[4-22]

The Table lists the characteristics of the eligible studies published between 2001 and 2017. The mean age ranged from 10.4 to 42 years. One study was prospective in design,[22] 17 studies were retrospective,[4-10,12-21] and 1 study did not mention the design.[11] The clinical follow-up ranged from 9.6 months to 5 years.

### *Quality Assessment*

The quality of the 19 included studies was moderate, with >4 of the 7 domains being satisfied (On-line Fig 1). With regard to patient selection, 17 studies were considered to have an unclear risk of bias due to nonconsecutive enrollment.[4,5,8-22] With regard to the reference standard, 5 studies were considered to have a high risk of bias because they only used clinical diagnosis for the reference standard.[4,7,10,15,16] In the flow and timing domain, 5 studies had an unclear risk of bias because the follow-up interval was not reported,[6,7,12,14,21] and 13 studies had a high risk because different reference standards were used in the study.[4-6,8,11,12,14,16,18-22]

### *Incidence of Conventional MR Imaging Findings in Patients with TDL: Meta-Analysis*

First, we evaluated the pooled incidences of conventional MR imaging findings in patients with TDL (Fig 2). The pooled incidence of open ring or incomplete rim enhancement was 35% (95% CI, 24%–47%), and the pooled incidence of closed ring or complete rim enhancement was 18% (95% CI, 11%–29%), with the incidence of open ring or incomplete rim enhancement being significantly higher than that of closed ring or complete rim enhancement ($P = .028$). The pooled incidence of a T2 hypointense rim was 48% (95% CI, 36%–60%), the pooled incidence of an absent or mild mass effect was 67% (95% CI, 48%–83%), and the pooled incidence of absent or mild perilesional edema was 57% (95% CI, 36%–76%).

There was no publication bias with respect to open ring or incomplete rim enhancement ($P = .81$), though publication bias was noted with respect to closed ring or complete rim enhancement ($P < .001$). Heterogeneity was observed for all conventional MR imaging findings ($I^2 = 63\%–80\%$). To explore the effects of heterogeneity, we conducted a meta-regression for open ring or incomplete rim enhancement. None of the variables, including the number of patients with TDL ($P = .43$), age ($P = .26$), male-to-female ratio ($P = .24$), reference standard ($P = .51$), magnetic field strength of the scanner ($P = .45$), and slice thickness ($P = .07$), showed a statistically significant relationship.

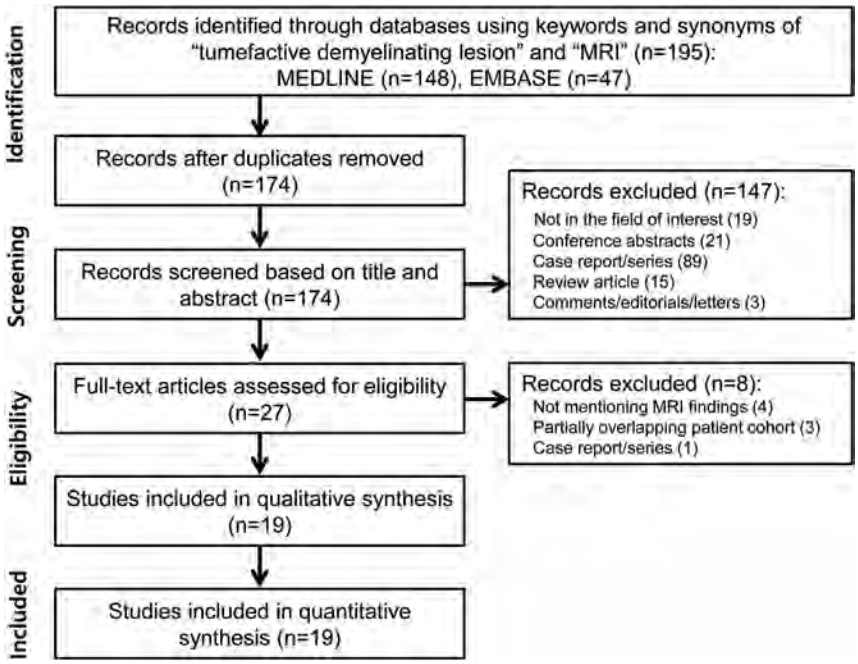


**FIG 1.** Flow diagram for the literature-selection process.

**Characteristics of the eligible studies**

| Author (yr) | Patients with TDL (No.) | Male (No.) | Female (No.) | Mean Age (yr) | Age Range (yr) | Duration of Patient Recruitment | Institution |
|---|---|---|---|---|---|---|---|
| Altintas et al (2012)[4] | 54 | 17 | 37 | 31.8 | 18–63 | NA | 5 Medical centers, Turkey |
| Cha et al (2001)[5] | 10 | 3 | 7 | 34.5 | 13–57 | NA | New York University Medical Center |
| Hiremath et al (2017)[6] | 14 | 10 | 4 | 37.5 | NA | 2011.1–2015.12 | Sree Chitra Tirunal Institute for Medical Sciences and Technology, India |
| Jain et al (2017)[7] | 11 | 7 | 4 | 19.6 | 10–41 | 2014.8–2017.3 | Sawai Man Singh Medical College, India |
| Kilic et al (2013)[8] | 25 | 8 | 17 | 29 | 15–56 | 1993.2–2011.6 | Hacettepe University, Faculty of Medicine, Turkey |
| Kim et al (2009)[9] | 15 | 8 | 7 | 42 | 27–57 | 1998.12–2005.12 | Seoul National University Hospital and Samsung Medical Center, Republic of Korea |
| Kiriyama et al (2011)[10] | 12 | 6 | 6 | 27 (Median) | 17–64 | 1993.1–2009.6 | Nara Medical University, Japan |
| Kuan et al (2013)[11] | 12 | 1 | 11 | 41.5 | 16–62 | 1985.1–2010.12 | Taipei Veterans General Hospital, Taiwan |
| Lu et al (2015)[12] | 18 | 10 | 8 | NA | 22–66 | 2007.4–2012.5 | Asan Medical Center, Republic of Korea |
| Lucchinetti et al (2008)[13] | 151 | NA | NA | NA | NA | 1987.9–2005.8 | Mayo Clinic and Georg–August University, Germany |
| Mabray et al (2015)[14] | 24 | 10 | 14 | 35.1 | 16–53 | 2002–2011 | University of California at San Francisco |
| Malhotra et al (2009)[15] | 18 | 8 | 10 | 26 | 4–50 | NA | Chhatrapati Sahuji Maharaj Medical University and Sanjay Gandhi Post Graduate Institute of Medical Sciences, India |
| Miron et al (2013)[16] | 10 | 2 | 8 | 26.8 | NA | 2007.1–2007.12 | Sheba Medical Center, Israel |
| Qi et al (2015)[17] | 14 | 9 | 5 | 24 (Median) | 4–51 | 2004.1–2009.1 | Beijing Tiantan Hospital, China |
| Saini et al (2011)[18] | 18 | 10 | 8 | 31.8 | 10–61 | 2001.1–2009.12 | Sree Chitra Tirunal Institute for Medical Sciences and Technology, India |
| Sánchez et al (2017)[19] | 15 | 3 | 12 | 36 | NA | 2010.1–2017.2 | Hospital Universitario de La Princesa, Spain |
| Siri et al (2015)[20] | 16 | 5 | 11 | 35.7 | 20–65 | NA | 10 Medical centers, France |
| Toh et al (2012)[21] | 8 | 2 | 6 | 37.3 | 23–51 | NA | National Yang–Ming University, Taiwan |
| Yiu et al (2014)[22] | 31 | 14 | 17 | 10.4 | NA | 2004.9–2009.12 | 23 Medical centers, Canada |

**Note:**—NA indicates not available.

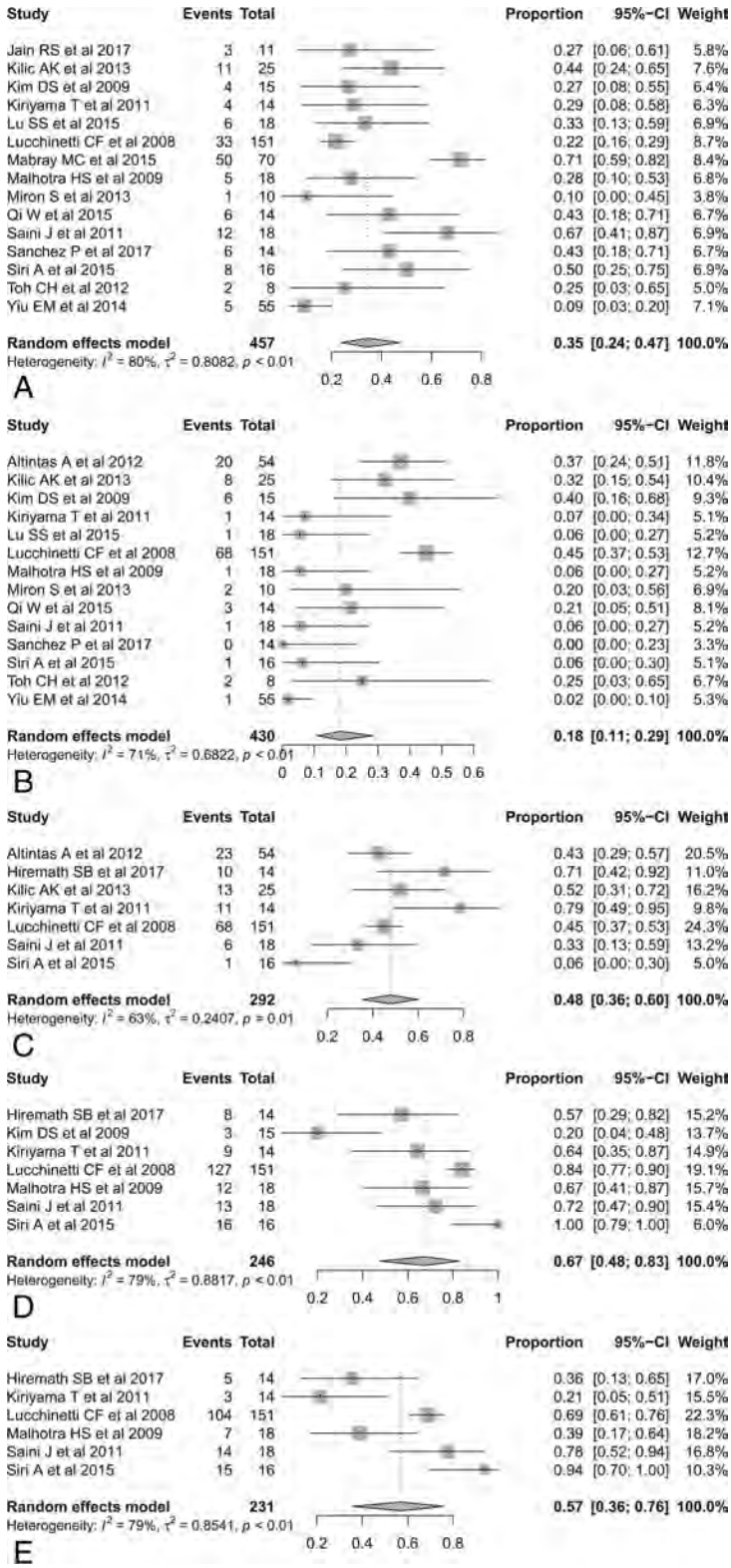


**FIG 2.** Forest plots to show the pooled incidences of conventional MR imaging findings in patients with TDL: open ring or incomplete rim enhancement (*A*), closed ring or complete rim enhancement (*B*), T2 hypointense rim (*C*), absent or mild mass effect (*D*), and absent or mild perilesional edema (*E*). Numbers are estimates with 95% confidence intervals in parentheses.

### *Advanced MR Imaging Findings in Patients with TDL*

On DWI, 2 studies demonstrated a significantly higher apparent diffusion coefficient for TDL than for PCNSL[12,14] and high-grade glioma.[14] Three studies also reported peripheral, restricted diffusion in TDLs.[8,15,19,21] One study reported that TDLs showed higher intralesional hyperintensities on fractional anisotropy maps but lower perilesional fractional anisotropy values in the rim than high-grade gliomas.[21] On perfusion imaging, 1 study demonstrated that TDLs showed a significantly lower relative cerebral blood volume than intracranial neoplasms,[5] and 2 studies showed decreased CBV in TDLs on MR[8,19] or CT perfusion.[8] In addition, 1 study reported the presence of an intact vein traversing the TDL on DSC.[5] For MR spectroscopy, several studies reported increased choline[8,10,15,19] and decreased *N*-acetylaspartate,[8,10,18,19] the presence of a lactate peak,[8,15,18] and the presence of a glutamate/glutamine peak.[15,18] The representative case studied by conventional and advanced MR imaging is shown in Fig 3.

### *Individual Diagnostic Performance of MR Imaging for the Diagnosis of TDLs*

The diagnostic performance of conventional MR imaging for the diagnosis of TDLs was reported in 3 studies.[6,9,14] By means of open ring or incomplete rim enhancement for the diagnosis of TDLs, the individual sensitivity showed substantial variation (27%–71%), though the specificity was consistently high (98%–100%).[9,14] In addition, 1 study using conventional MR imaging and CT criteria (less attenuation than cortical and basal ganglia gray matter) showed a sensitivity of 87% and specificity of 100% for distinguishing TDLs from gliomas or PCNSLs.[9] Another study showed that conventional MR imaging had a sensitivity of 81% and specificity of 57% for the differentiation of TDLs from high-grade gliomas.[6]

The diagnostic performance of an advanced MR imaging technique for the diagnosis of TDL was noted in 4 studies.[9,12,14,21] In a comparison of TDLs with PCNSLs, 1 study demonstrated that the high $ADC_{minimum}$ value with a threshold of $556 \times 10^{-6}$ $mm^2/s$ was the best indicator for differentiating TDLs from atypical PCNSLs (a sensitivity of 81% and specificity of 89%).[12] In comparisons of TDLs with high-grade gliomas, 1 study using combined DTI and DSC perfusion showed a sen-

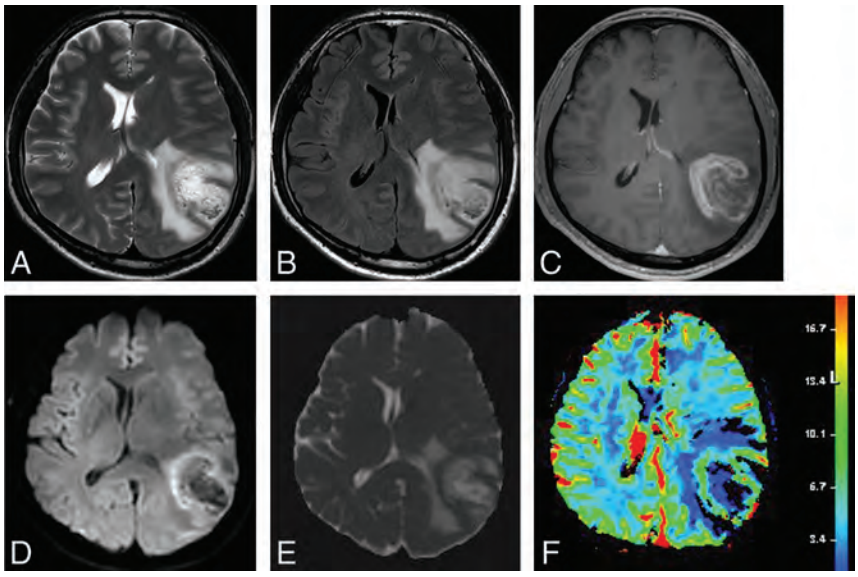


**FIG 3.** Images obtained in a 44-year-old man with biopsy-proved TDL. T2-weighted (*A*) and FLAIR (*B*) images show a well-defined high-signal-intensity lesion in the left cerebral hemisphere with mild perilesional edema. *C*, Contrast-enhanced T1-weighted image shows open ring enhancement. DWI (*D*) and the corresponding ADC map (*E*) reveal high ADC within the lesion and peripheral restricted diffusion. *F*, DSC demonstrates low cerebral blood volume.

sitivity of 71% and specificity of 93%,[6] while another study using DTI showed a sensitivity of 92% and specificity of 88%.[21] Two studies revealed that the combination of conventional MR imaging and advanced MR imaging improved the diagnostic performance.[6,14]

### *Diagnostic Performance of MR Imaging for the Diagnosis of TDLs: Meta-Analysis*

Five original articles evaluated the overall diagnostic performance of MR imaging for differentiating a TDL from primary brain tumor.[6,9,12,14,21] The individual sensitivities and specificities were 67%–91% and 79%–100%. The pooled sensitivity was 89% (95% CI, 82%–93%), and the pooled specificity was 94% (95% CI, 89%–97%; Fig 4). The area under the hierarchic summary receiver operating characteristic curve was 0.93 (95% CI, 0.90–0.95; On-line Fig 2). There was no heterogeneity in the sensitivity ($I^2 = 0.0\%$) or specificity ($I^2 = 45.72\%$). The Deeks funnel plot demonstrated that the likelihood of publication bias was low ($P = .48$, On-line Fig 3).

## DISCUSSION

The current study reports the conventional MR imaging findings for TDLs, covering 19 studies with 476 patients. The pooled incidence of open ring or incomplete rim enhancement was 35% (95% CI, 24%–47%). In addition, the pooled incidences of a T2 hypointense rim, absent or mild mass effect, and absent or mild perilesional edema were 48% (95% CI, 25%–68%), 67% (95% CI, 42%–87%), and 57% (95% CI, 27%–82%), respectively. The overall diagnostic performance of MR imaging for differentiating TDL from primary brain tumor demonstrated a pooled sensitivity of 89% (95% CI, 82%–93%) and a pooled specificity of 94% (95% CI, 89%–97%). Open ring or incomplete rim enhancement showed a high specificity (98%–100%). Therefore, conventional MR imaging findings can be of help in the accurate diagnosis of TDL. In addition, our work could prove useful to the literature and may prompt the conduct of prospective case collections or consortial work.

In routine clinical practice, the differentiation of TDL from primary brain tumor is difficult. Open ring or incomplete rim enhancement as a conventional MR imaging finding was described as highly specific (94%) for atypical brain demyelination in 32 illustrated cases identified on a MEDLINE search.[35] The present study demonstrated a pooled incidence of open ring or incomplete rim enhancement of 35% (95% CI, 24%–47%); however, a high specificity (98%–100%) was noted. In addition, the pooled incidence of open ring or incomplete rim enhancement was significantly higher than the incidence of closed ring or complete rim enhancement (18% [95% CI, 11%–29%]). The enhancing area of the ring is regarded as representing the leading edge of demyelination and therefore favors the white matter side of the lesion.[36] Open ring or incomplete rim enhancement may be useful for differentiating a TDL from primary brain tumor.

The differentiation of a TDL from a PCNSL can sometimes be challenging, clinically, radiologically, and even pathologically. A few studies have tried to differentiate TDLs from PCNSLs using advanced MR imaging techniques. Two studies demonstrated a significantly higher $ADC_{minimum}$ in TDL than in PCNSL,[12,14] with 1 study demonstrating that $ADC_{minimum}$ with a threshold of $556 \times 10^{-6}$ mm$^2$/s was the best indicator for differentiating TDL from atypical PCNSL (a sensitivity of 81% and specificity of 89%).[12] Histologically, TDLs may demonstrate peripheral active breakdown of myelin and a dense inflammatory infiltrate consisting of activated macrophages.[37] Another study showed a lower choline/NAA ratio in TDLs than in PCNSLs, with a threshold for differentiation of 1.73 (a sensitivity of 89% and specificity of 76%).[38] In addition, noncontrast CT hypoattenuation of MR imaging–enhanced regions was observed in 93% of TDL cases, but only 4% of primary brain tumors.[9] One study revealed that the combination of conventional MR imaging and advanced MR imaging improved the diagnostic performance for differentiating TDL from PCNSLs or high-grade gliomas.[14] ADC values, MR spectroscopy, and noncontrast CT may help in diagnosing TDLs; however, further study is required to determine the added value of advanced MR imaging techniques in the differentiation of TDLs from PCNSLs.

A previous article reported that most patients with TDLs showed an excellent response to corticosteroid treatment, with a substantial decrease in lesion size or disappearance on follow-up imaging.[25] One of the studies included in the present meta-analysis reported that all patients with TDLs received corticosteroid treatment after surgical biopsy and showed no evidence of recurrence or radiologic aggravation during the 4.2 years of the follow-

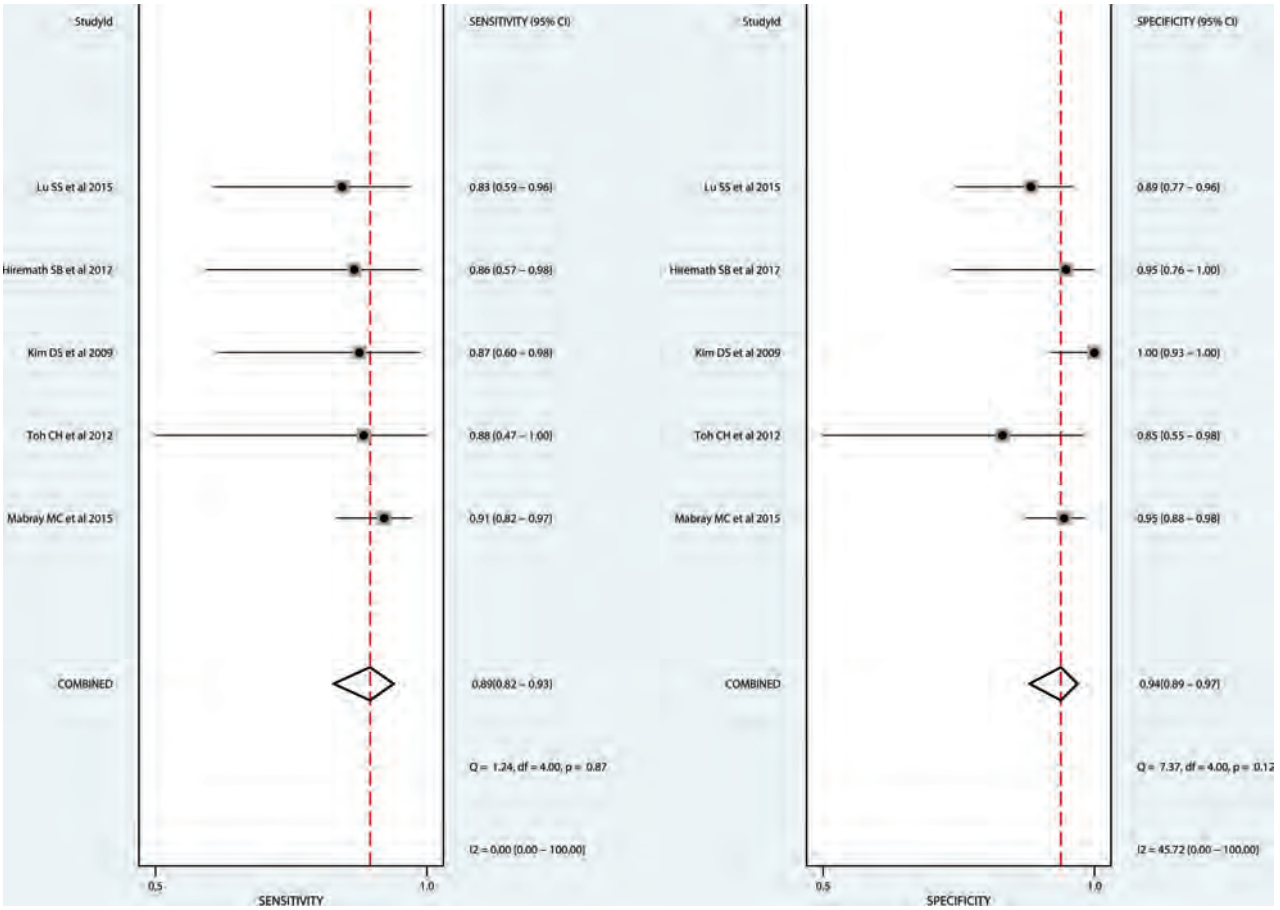


**FIG 4.** Coupled forest plots of the sensitivity and specificity of MR Imaging for the diagnosis of a TDL. Numbers are estimates with 95% confidence intervals in parentheses.

up.[9] Other studies revealed that 35%–62% of patients with TDLs had a monophasic course and were diagnosed with a clinically isolated syndrome.[4,8] A correlation between MR imaging findings and treatment response in patients with TDL has not yet been established, and further study on this may be needed.

This study has several limitations. First, 17 of the 19 studies were retrospective observational studies with a small sample size, and there were only 5 studies differentiating a TDL from primary brain tumor. However, the included studies represented the full extent of the currently available evidence. Our study may prompt prospective studies or consortial work. Second, heterogeneity was noted for conventional MR imaging findings. We therefore performed meta-regression to explore the effects of heterogeneity but found no covariates. Conventional MR imaging findings are inherently subjective, and the small samples due to the rarity of TDLs may affect the heterogeneity. Third, it is unclear how many of the included patients were positive for aquaporin 4 antibodies or myelin oligodendrocyte glycoprotein antibodies and whether this influences MR imaging findings in TDLs. To overcome these limitations, we performed our systematic review and meta-analysis using recent robust methodology, including hierarchic logistic regression modeling,[29-31] and reported our findings according to the following guidelines: Preferred Reporting Items for Systematic Reviews and Meta-Analyses,[28] the Handbook for Diagnostic Test Accuracy Reviews published by the Cochrane Collaboration,[39] and the Agency for Health Care Research and Quality.[40]

## CONCLUSIONS

Conventional MR imaging findings may help in the accurate diagnosis of TDLs. However, further study is required to determine the added value of advanced MR imaging techniques in the differentiation of a TDL from primary brain tumor.

## REFERENCES


1. Hardy TA, Chataway J. **Tumefactive demyelination: an approach to diagnosis and management.** *J Neurol Neurosurg Psychiatry* 2013;84:1047–53 CrossRef Medline
2. Ayrignac X, Menjot de Champfleur N, Menjot de Champfleur S, et al. **Brain magnetic resonance imaging helps to differentiate atypical multiple sclerosis with cavitary lesions and vanishing white matter disease.** *Eur J Neurol* 2016;23:995–1000 CrossRef Medline
3. Wallner-Blazek M, Rovira A, Fillipp M, et al. **Atypical idiopathic inflammatory demyelinating lesions: prognostic implications and relation to multiple sclerosis.** *J Neurol* 2013;260:2016–22 CrossRef Medline
4. Altintas A, Petek B, Isik N, et al. **Clinical and radiological characteristics of tumefactive demyelinating lesions: follow-up study.** *Mult Scler* 2012;18:1448–53 CrossRef Medline
5. Cha S, Pierce S, Knopp EA, et al. **Dynamic contrast-enhanced T2*-weighted MR imaging of tumefactive demyelinating lesions.** *AJNR Am J Neuroradiol* 2001;22:1109–16 Medline
6. Hiremath SB, Muraleedharan A, Kumar S, et al. **Combining diffusion tensor metrics and DSC perfusion imaging: can it improve the diagnostic accuracy in differentiating tumefactive demyelination from high-grade glioma?** *AJNR Am J Neuroradiol* 2017;38:685–90 CrossRef Medline

7. Jain RS, Khan I, Kandelwal K, et al. **Tumefactive demyelinating lesions (TDLs): a case series of clinicoradiological features.** *Clin Neurol Neurosurg* 2017;162:91–94 CrossRef Medline
8. Kilic AK, Kurne AT, Oguz KK, et al. **Mass lesions in the brain: tumor or multiple sclerosis? Clinical and imaging characteristics and course from a single reference center.** *Turk Neurosurg* 2013;23: 728–35 CrossRef Medline Medline
9. Kim DS, Na DG, Kim KH, et al. **Distinguishing tumefactive demyelinating lesions from glioma or central nervous system lymphoma: added value of unenhanced CT compared with conventional contrast-enhanced MR imaging.** *Radiology* 2009;251:467–75 CrossRef Medline
10. Kiriyama T, Kataoka H, Taoka T, et al. **Characteristic neuroimaging in patients with tumefactive demyelinating lesions exceeding 30 mm.** *J Neuroimaging* 2011;21:e69–77 CrossRef Medline
11. Kuan YC, Wang KC, Yuan WH, et al. **Tumefactive multiple sclerosis in Taiwan**. *PLoS One* 2013;8:e69919 CrossRef Medline
12. Lu SS, Kim SJ, Kim N, et al. **Histogram analysis of apparent diffusion coefficient maps for differentiating primary CNS lymphomas from tumefactive demyelinating lesions.** *AJR Am J Roentgenol* 2015; 204:827–34 CrossRef Medline
13. Lucchinetti CF, Gavrilova RH, Metz I, et al. **Clinical and radiographic spectrum of pathologically confirmed tumefactive multiple sclerosis.** *Brain* 2008;131:1759–75 CrossRef Medline
14. Mabray MC, Cohen BA, Villanueva-Meyer JE, et al. **Performance of apparent diffusion coefficient values and conventional MRI features in differentiating tumefactive demyelinating lesions from primary brain neoplasms.** *AJR Am J Roentgenol* 2015;205:1075–85 CrossRef Medline
15. Malhotra HS, Jain KK, Agarwal A, et al. **Characterization of tumefactive demyelinating lesions using MR imaging and in-vivo proton MR spectroscopy.** *Mult Scler* 2009;15:193–203 CrossRef Medline
16. Miron S, Tal S, Achiron A. **Diffusion tensor imaging analysis of tumefactive giant brain lesions in multiple sclerosis.** *J Neuroimaging* 2013;23:453–59 CrossRef Medline
17. Qi W, Jia GE, Wang X, et al. **Cerebral tumefactive demyelinating lesions.** *Oncol Lett* 2015;10:1763–68 CrossRef Medline
18. Saini J, Chatterjee S, Thomas B, et al. **Conventional and advanced magnetic resonance imaging in tumefactive demyelination.** *Acta Radiol* 2011;52:1159–68 CrossRef Medline
19. Sánchez P, Meca-Lallana V, Barbosa A, et al. **Tumefactive demyelinating lesions of 15 patients: clinico-radiological features, management and review of the literature.** *J Neurol Sci* 2017;381:32–38 CrossRef Medline
20. Siri A, Carra-Dalliere C, Ayrignac X, et al. **Isolated tumefactive demyelinating lesions: diagnosis and long-term evolution of 16 patients in a multicentric study.** *J Neurol* 2015;262:1637–45 CrossRef Medline
21. Toh CH, Wei KC, Ng SH, et al. **Differentiation of tumefactive demyelinating lesions from high-grade gliomas with the use of diffusion tensor imaging.** *AJNR Am J Neuroradiol* 2012;33:846–51 CrossRef Medline
22. Yiu EM, Laughlin S, Verhey LH, et al; Canadian Pediatric Demyelinating Disease Network. **Clinical and magnetic resonance imaging (MRI) distinctions between tumefactive demyelination and brain tumors in children.** *J Child Neurol* 2014;29:654–65 CrossRef Medline
23. Given CA 2nd, Stevens BS, Lee C. **The MRI appearance of tumefactive demyelinating lesions.** *AJR Am J Roentgenol* 2004;182:195–99 CrossRef Medline
24. Seewann A, Enzinger C, Filippi M, et al. **MRI characteristics of atypical idiopathic inflammatory demyelinating lesions of the brain: a review of reported findings.** *J Neurol* 2008;255:1–10 CrossRef Medline
25. Kepes JJ. **Large focal tumor-like demyelinating lesions of the brain: intermediate entity between multiple sclerosis and acute disseminated encephalomyelitis? A study of 31 patients.** *Ann Neurol* 1993; 33:18–27 CrossRef Medline
26. Dagher AP, Smirniotopoulos J. **Tumefactive demyelinating lesions.** *Neuroradiology* 1996;38:560–65 CrossRef Medline
27. Whiting PF, Rutjes AW, Westwood ME, et al; QUADAS-2 Group. **QUADAS-2: a revised tool for the quality assessment of diagnostic accuracy studies.** *Ann Intern Med* 2011;155:529–36 CrossRef Medline
28. Liberati A, Altman DG, Tetzlaff J, et al. **The PRISMA statement for reporting systematic reviews and meta-analyses of studies that evaluate health care interventions: explanation and elaboration.** *Ann Intern Med* 2009;151:W65–94 Medline
29. Suh CH, Park SH. **Successful publication of systematic review and meta-analysis of studies evaluating diagnostic test accuracy.** *Korean J Radiol* 2016;17:5–6 CrossRef Medline
30. Kim KW, Lee J, Choi SH, et al. **Systematic review and meta-analysis of studies evaluating diagnostic test accuracy: a practical review for clinical researchers, Part I: general guidance and tips.** *Korean J Radiol* 2015;16:1175–87 CrossRef Medline
31. Lee J, Kim KW, Choi SH, et al. **Systematic review and meta-analysis of studies evaluating diagnostic test accuracy: a practical review for clinical researchers, Part II: statistical methods of meta-analysis.** *Korean J Radiol* 2015;16:1188–96 CrossRef Medline
32. Higgins JP, Thompson SG, Deeks JJ, et al. **Measuring inconsistency in meta-analyses.** *BMJ* 2003;327:557–60 CrossRef Medline
33. Egger M, Davey Smith G, Schneider M, et al. **Bias in meta-analysis detected by a simple, graphical test.** *BMJ* 1997;315:629–34 CrossRef Medline
34. Deeks JJ, Macaskill P, Irwig L. **The performance of tests of publication bias and other sample size effects in systematic reviews of diagnostic test accuracy was assessed.** *J Clin Epidemiol* 2005;58:882–93 CrossRef Medline
35. Masdeu JC, Quinto C, Olivera C, et al. **Open-ring imaging sign: highly specific for atypical brain demyelination.** *Neurology* 2000;54: 1427–33 CrossRef Medline
36. He J, Grossman RI, Ge Y, et al. **Enhancing patterns in multiple sclerosis: evolution and persistence.** *AJNR Am J Neuroradiol* 2001; 22:664–69 Medline
37. Lassmann H. **The pathologic substrate of magnetic resonance alterations in multiple sclerosis.** *Neuroimaging Clin N Am* 2008;18:563–76, ix CrossRef Medline
38. Lu SS, Kim SJ, Kim HS, et al. **Utility of proton MR spectroscopy for differentiating typical and atypical primary central nervous system lymphomas from tumefactive demyelinating lesions.** *AJNR Am J Neuroradiol* 2014;35:270–77 CrossRef Medline
39. Deeks JJ, Bossuyt PM, Gatsonis C, eds. 2013 Cochrane Handbook for DTA Reviews, Version 1.0.0. The Cochrane Collaboration. http://srdta.cochrane.org/handbook-dta-reviews. Accessed October 9, 2017
40. Trikalinos TA, Balion CM, Coleman CI, et al. **Chapter 8: meta-analysis of test performance when there is a "gold standard."** *J Gen Intern Med* 2012;27(Suppl 1):S56–66 CrossRef Medline

# Longitudinal Microstructural Changes in Traumatic Brain Injury in Rats: A Diffusional Kurtosis Imaging, Histology, and Behavior Study

M.-L. Wang, M.-M. Yu, D.-X. Yang, Y.-L. Liu, X.-E. Wei, and W.-B. Li

## ABSTRACT

**BACKGROUND AND PURPOSE:** Traumatic brain injury is a major public health problem worldwide. Accurately evaluating the brain microstructural changes in traumatic brain injury is crucial for the treatment and prognosis assessment. This study aimed to assess the longitudinal brain microstructural changes in traumatic brain injury in the rat using diffusional kurtosis imaging.

**MATERIALS AND METHODS:** Diffusional kurtosis imaging was performed in a group of 5 rats at preinjury and 3, 14, and 28 days after traumatic brain injury. The diffusional kurtosis imaging parameters were measured in the bilateral cortex, hippocampus, and corpus callosum. Another 4 groups of 5 rats were used in brain immunohistochemistry analysis of neuron (neuron-specific nuclear protein [NeuN]), astroglia (glial fibrillary acidic protein [GFAP]), microglia (ionized calcium binding adaptor molecule 1 [Iba-1]), and myelin (myelin basic protein [MBP]) in the same area as the diffusional kurtosis imaging parameter measurements. Furthermore, 2 groups of 6 rats underwent a Morris water maze test at 28 days after traumatic brain injury. The diffusional kurtosis imaging parameters, immunohistochemistry results, and Morris water maze test results were compared longitudinally or between traumatic brain injury and control groups.

**RESULTS:** Compared with baseline, traumatic brain injury in the rat showed higher mean kurtosis and mean diffusivity values in the ipsilateral perilesional cortex and hippocampus and lower fractional anisotropy values in the corpus callosum ($P < .05$). The traumatic brain injury group showed higher staining of GFAP and Iba-1 and lower immunohistochemistry staining of NeuN and MBP in all ipsilateral ROIs ($P < .05$). There was no significant difference in the contralateral ROIs in diffusional kurtosis imaging parameters or immunohistochemistry results. The Morris water maze test revealed lower platform crossing times in the probe test ($P < .05$).

**CONCLUSIONS:** Our study indicated that there were longitudinal changes in diffusional kurtosis imaging parameters, accompanied by multiple pathologic changes at different time points following traumatic brain injury, and that mean kurtosis is more sensitive to detect microstructural changes, especially in gray matter, than mean diffusivity and fractional anisotropy.

**ABBREVIATIONS:** Da = axial diffusion; DKI = diffusional kurtosis imaging; Dr = radial diffusion; FA = fractional anisotropy; GFAP = glial fibrillary acidic protein; Iba-1 = ionized calcium binding adaptor molecule 1; IHC= immunohistochemistry; Ka = axial kurtosis; Kr = radial kurtosis; MBP = myelin basic protein; MD = mean diffusivity; MK = mean kurtosis; NeuN = neuron-specific nuclear protein; TBI = traumatic brain injury

Traumatic brain injury (TBI) is one of the most serious public health problems worldwide. After injury, a significant number of patients with TBI will experience neurologic and non-neurologic disorders, among which cognitive impairment is most common.[1] Although most patients recover to baseline cognitive function within 1–3 months, some patients have persistent cognitive impairment.[2,3] At present, how TBI could lead to the occurrence and persistence of cognitive impairment is poorly understood. Finding a reliable noninvasive biomarker to accurately evaluate brain pathologic changes after TBI is crucial for TBI management and prognosis assessment.

MR imaging, as a noninvasive tool, is increasingly used to assess the pathologic changes in TBI. Diffusion tensor imaging has shown great promise in evaluating the brain microstructural

Received March 28, 2018; accepted after revision June 2.

From the Departments of Radiology (M.-L.W., M.-M.Y., X.-E.W., W.-B.L.) and Neurosurgery (D.-X.Y., Y.-L.L.), Shanghai Jiao Tong University Affiliated Sixth People's Hospital, Shanghai Jiao Tong University School of Medicine, Shanghai, China; and Imaging Center (W.-B.L.), Kashgar Prefecture Second People's Hospital, Kashgar, China.

Ming-Liang Wang and Meng-Meng Yu contributed equally to this work.

This work was supported by the National Natural Science Foundation of China (No. 81271540, 81301213), Natural Science Foundation of Xinjiang Province (No. 2016D01C083), Medical-Engineering Cross Project of Shanghai Jiao Tong University (No. YG2015MS19), the Shanghai Health and Family Planning Commission research projects (No. 20164Y0065), and the Shanghai Key Discipline of Medical Imaging (No. 2017ZZ02005).

Please address correspondence to Wen-Bin Li, MD, No. 600, Yi Shan Rd, Shanghai 200233, China; e-mail: liwenbin@sjtu.edu.cn

Indicates open access to non-subscribers at www.ajnr.org

Indicates article with supplemental on-line photos.

http://dx.doi.org/10.3174/ajnr.A5737

changes. DTI assumes a Gaussian distribution for the water molecule in measured tissue and could quantify water molecule directional diffusion characteristics.[4] The DTI parameters, including fractional anisotropy (FA) and mean diffusivity (MD) changes, have been widely used to assess white matter injury in both human[5-8] and animal studies.[9-12] However, the actual distribution of water in brain tissue is usually non-Gaussian, especially for the largely isotropic gray matter. The DTI technique might not detect the real microstructural pathologic changes.

Diffusional kurtosis imaging (DKI), using the non-Gaussian model of water diffusion, could overcome this limitation.[13,14] Apart from DTI parameters, it provides additional kurtosis metrics, including mean kurtosis (MK), to depict the heterogeneity of brain microstructure. Previous studies have shown that the MK value in the thalamus might be useful in the early prediction of brain damage and cognitive outcome.[15,16] As for the underlying pathologic changes, only reactive astrogliosis has proved to be directly linked to increased MK values in an acute and subacute TBI animal study.[17]

However, apart from reactive astrogliosis, TBI has other pathologic processes, including but not limited to neuron loss, axonal damage, demyelination, and microgliosis, which may also have an effect on diffusional kurtosis.[18-20] The MR imaging parameters should be a summary marker of all the possible TBI microstructural pathologic changes.[21] Figuring out the radiologic-pathologic relationship and the evolving laws in the process of TBI will improve the interpretation of DKI parameter changes and finally promote the application of the DKI sequence in the clinical diagnosis and assessment of patients with TBI.

In this study, we hypothesized the following: 1) There would be changes in DKI parameters at different time points following TBI, and 2) DKI parameters could reflect multiple pathologic changes in the process of TBI. Our study aimed to investigate the longitudinal changes of DKI parameters and pathologic changes in the TBI rat brain. These findings will deepen our knowledge of longitudinal microstructural pathologic changes of TBI and promote the use of the DKI sequence in clinical practice.

## MATERIALS AND METHODS

### Traumatic Brain Injury Rat Model

All work was performed in accordance with the Institutional Animal Care and Experiment Committee of Shanghai Jiao Tong University Affiliated Sixth People's Hospital. Five adult male Sprague-Dawley rats (250–300 g) underwent longitudinal MR imaging examinations preinjury and 3, 14, and 28 days after TBI. Another 20 adult male rats were assigned to 4 groups (preinjury and 3, 14, and 28 days after TBI) for histopathologic analysis. Furthermore, 2 groups of adult male rats (TBI group, $n = 6$ and control group, $n = 6$) had a Morris water maze test at 28 days after TBI.

The induction of TBI was done by a controlled cortical impact device (PinPoint Precision Cortical Impactor PCI3000; Hatteras Instruments, Cary, North Carolina). First, Sprague-Dawley rats were anesthetized with ketamine and mounted in a stereotaxic frame. Second, a Ø4-mm craniotomy was created at 3.5 mm posterior and 4 mm lateral to the bregma, exposing the dura mater. Third, a 3-mm impactor tip connected to the controlling system was used to deliver the controlled cortical impact at a deformation depth of 1.5 mm, a velocity of 2 m/s, and a dwell time of 100 ms. Rats were excluded if the dura mater integrity was breached. Last, the cranial opening was sealed with bone wax. Control animals underwent the same operation without the impact intervention.

### MR Imaging Protocol and DKI Data Analysis

MR imaging was performed on a BioSpec 7T 20-cm horizontal bore scanner (Bruker BioSpin, Rheinstetten, Germany). The rats were fixed in an MR imaging–compatible rat head stereotaxic holder with ear and tooth bars. During the imaging time, the rat was anesthetized with 1%–2% isoflurane anesthesia and 1 L/min of oxygen administration. An MR imaging–compatible small-animal monitoring system was used to monitor the animal's respiration rate and body temperature. The rats underwent T2-weighted and DKI examinations at preinjury and 3, 14, and 28 days after TBI.

T2-weighted images were obtained to observe the general brain lesion using the following parameters: TR, 4500 ms; TE, 20, 60, 100, 140 ms; FOV, 30 × 30 mm; matrix, 128 × 128; slice thickness, 1 mm; rare factor, 2. DKI was acquired using a spin-echo echo-planar imaging diffusion sequence with 2 repetitions, using 20 different diffusion-encoding directions. Four b-values ($b$=0, 650, 1300, 2000 s/mm$^2$) were acquired for each direction. Other imaging parameters were as follows: TR/TE, 3500/50 ms; $\delta/\Delta$, 5ms/18ms; 19 axial slices; FOV, 30 × 30 mm; matrix, 128 × 128; slice thickness, 1 mm.

Diffusional Kurtosis Estimator software was used to calculate the DKI parameters (https://www.nitrc.org/projects/dke/).[22] The calculated DKI parameters included MK, axial kurtosis (Ka), and radial kurtosis (Kr); FA, MD, axial diffusion (Da); and radial diffusion (Dr). Using ITK-SNAP software (www.itksnap.org),[23] we manually drew multiple ROIs, including ipsilateral and contralateral to the injury in the cortex, hippocampus, and corpus callosum (Fig 1) on the $b$=0 image at around 3–4 mm posterior to bregma. These ROIs were selected because they were all possibly related to cognitive impairment in the TBI animal model.[24,25] The individual drawing the ROI was trained before analysis of the study data. The ROIs should be sufficiently large but not defined to the edge of the tissues on the section. A single voxel width was used for the delineation of corpus callosum. Then, the ROIs were transferred to identical sites on the FA, MD, Da, Dr, MK, Ka, and Kr maps in the same rat. The average regional value for each DKI parameter was recorded from the voxels within each ROI.

### Immunohistochemistry Staining and Semiquantitative Analysis

The rats were deeply anesthetized with ketamine and transcardially perfused with saline followed by 4% paraformaldehyde. Then the brains were extracted, and a 5-mm-thick section surrounding the lesion site of the rat brain was dissected, postfixed further, dehydrated with alcohols embedded in paraffin, and then cut as coronal sections at around 3–4 mm posterior to bregma, similar to the sections of DKI analysis. Immunohistochemistry (IHC) staining was performed on these coronal sections, stained with established markers for neurons (neuron-specific nuclear protein [NeuN]; 1:100; Wuhan Servicebio Technology, Hubei, China), astroglia (glial fibrillary acidic protein [GFAP]; 1:400; Wuhan

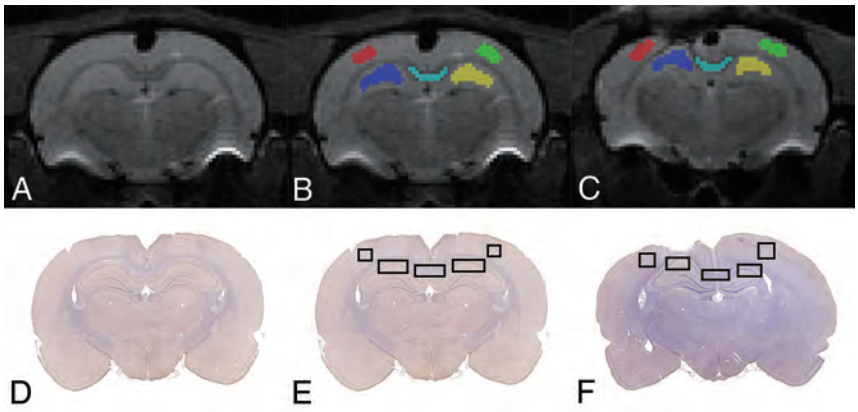


**FIG 1.** Illustration of ROIs on $B_0$ (*A–C*) and histology (*D–F*) maps for a representative control and TBI rat. Regions shown are the bilateral cortex, bilateral hippocampus, and corpus callosum.

Servicebio Technology), microglia (ionized calcium binding adaptor molecule 1 [Iba-1]; 1:1000; Wuhan Servicebio Technology), and myelin (myelin basic protein [MBP]; 1:100; Wuhan Servicebio Technology).

Brain IHC images were captured using a microscope for cell counting of $NeuN^+$, $GFAP^+$, and Iba-$1^+$ cells and the IHC staining area of MBP. Three random FOVs of each section at a magnification of ×20 were obtained to quantify the IHC result to match the MR imaging measured area (Fig 1). The mean values were used to indicate the positive cell numbers or area percentage in each region. Quantification of positive stained cells or area was performed manually using a computer-based image analysis system (Image J 1.51; National Institutes of Health, Bethesda, Maryland).

### Cognitive Assessment

Morris water maze tests were performed to assess spatial learning and memory at 28 days after TBI.[26] The testing paradigm included 5 daily training trials and a probe trial.

Another two groups of rats (TBI group, $n = 6$ and control group, $n = 6$) underwent the Morris water maze tests. First, all the rats underwent a block of 4 trials per day on 5 consecutive days to locate the hidden platform. The interval between trials was 15 minutes, and the start position was different for each trial. Each rat was allowed 90 seconds to find the hidden platform and stay on it for 15 seconds. The latency to locate the platform was recorded as the escape latency time. If the rat could not find the platform within 90 seconds, it was guided to the platform and stayed on the platform for 15 seconds, and the latency time was recorded as 90 seconds.

One day after the last training trial, the platform was removed, and the rats were placed in the opposite quadrant and allowed to explore the removed platform in water for 60 seconds. During the probe trial, 3 parameters, including the number of platform-site crossovers, the time spent in the target quadrant, and the swimming speed during 60 seconds, were recorded for each rat.

### Statistical Analysis

Statistical analysis was performed with the Statistical Package for Social Sciences (IBM, Armonk, New York) software for Windows, Version 20.0, and graphs were plotted using GraphPad Prism 6.0 software (GraphPad Software, San Diego, California). The Morris water maze and IHC data were expressed as the mean ± standard error of the mean. DKI parameter data were expressed as mean ± SD. The DKI parameters and the Morris water maze data were compared by repeated-measures ANOVA, followed by paired *t* tests. Differences in IHC qualitative data were analyzed using 1-way ANOVA, followed by post hoc LSD (least significant difference) tests. Statistical significance was set at $P < .05$.

## RESULTS

### DKI Parameter Changes in TBI

Representative DKI parameter maps at all time points from baseline to 28 days after TBI are shown in On-line Fig 1. Figure 2 shows the longitudinal DKI parameter changes.

In the ipsilateral perilesional cortex, significant differences were found in MK ($F = 9.703$, $P = .002$) and MD ($F = 16.528$, $P = .014$). Compared with baseline, TBI rats had higher MK at 3 days ($P = .034$), 14 days ($P = .015$), and 28 days ($P = .02$), reaching the peak at 14 days and recovering at 28 days after TBI. TBI rats also had higher MD at 3 days ($P = .013$). Compared with 3 days after TBI, higher MD was also found at 14 days ($P = .005$) and 28 days ($P = .019$) after TBI. There was no significant difference in FA values ($P > .05$). Furthermore, no significant changes were found in the contralateral perilesional cortex ($P > .05$).

There were also significant differences in the ipsilateral hippocampus in MK ($F = 13.291$, $P < .001$), MD ($F = 3.671$, $P = .044$), and FA ($F = 6.358$, $P = .008$). Compared with baseline, similar higher MK at 3 days ($P = .02$), 14 days ($P = .013$), and 28 days ($P = .042$) and higher MD at 3 days after TBI ($P = .023$) were found. Compared with 28 days after TBI, lower MK was found at 3 days ($P = .023$) and 14 days ($P = .003$) after TBI. Furthermore, higher FA was also found at 3 days ($P = .002$) and 28 days ($P = .008$). No significant changes were found in the contralateral hippocampus either ($P > .05$).

As for the corpus callosum, significant differences were also found in MK ($F = 6.713$, $P = .007$), MD ($F = 4.162$, $P = .031$), FA ($F = 9.255$, $P = .002$), Dr ($F = 3.478$, $P = .05$), and Kr ($F = 11.828$, $P = .001$). Compared with baseline, TBI rats had higher MK at 3 days ($P = .008$), 14 days ($P = .009$), and 28 days ($P = .014$); higher MD at 3 days ($P = .005$) and 14 days ($P = .043$); lower FA at 3 days ($P = .005$), 14 days ($P = .036$), and 28 days ($P = .013$); higher Dr at 3 days ($P = .005$) as well as higher Kr at 3 days ($P < .001$) and 14 days ($P = .014$) after TBI. The Kr at 14 days was also higher ($P = .008$) than that at 28 days after TBI.

### IHC Quantitative Changes in TBI

On-line Fig 2 shows the representative IHC staining of NeuN, GFAP, Iba-1, and MBP in the ipsilateral perilesional cortex, hippocampus, and corpus callosum at preinjury and 3, 14, and 28 days after TBI. Fig 3 shows the IHC staining changes at each time point.

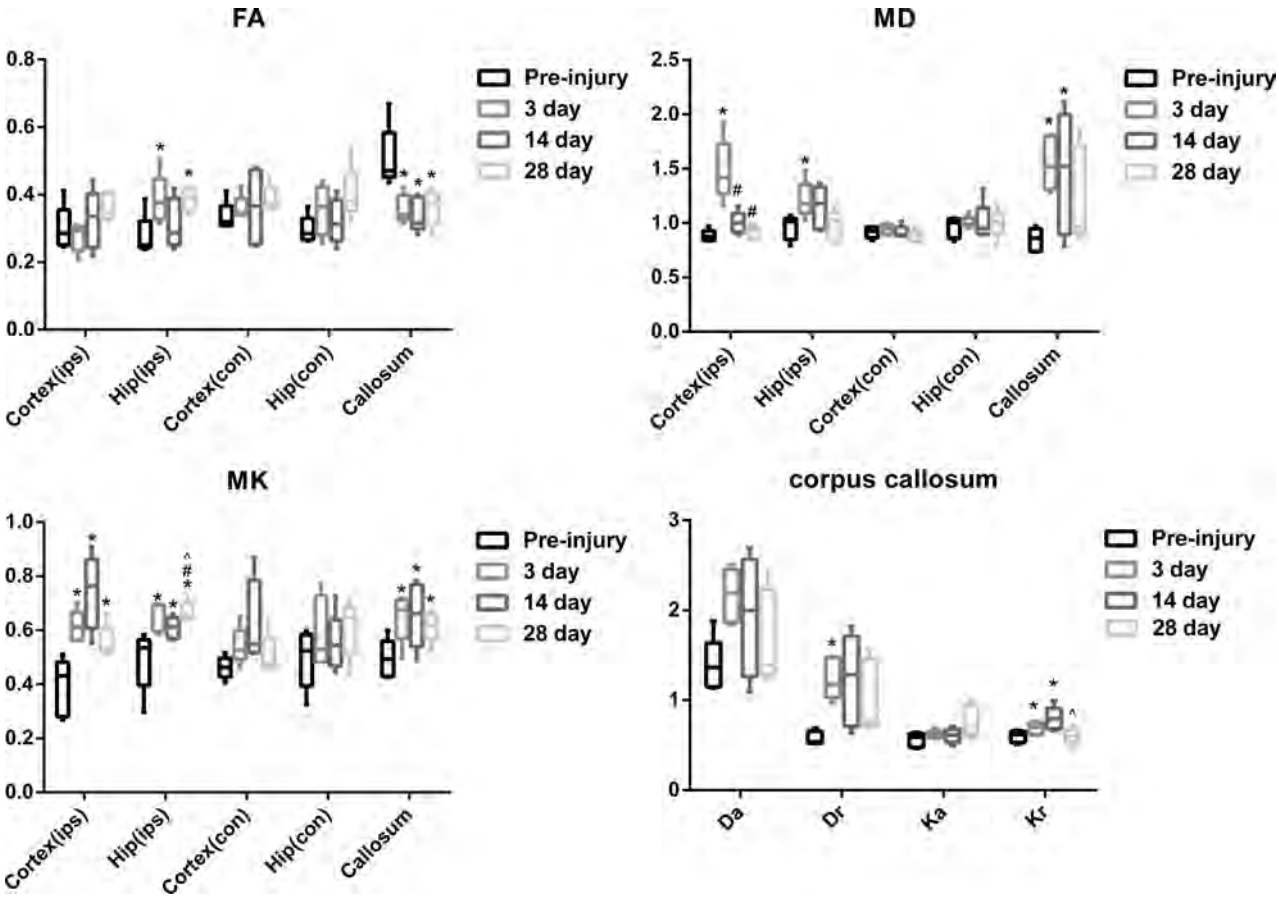


**FIG 2.** Changes in FA, MD, and MK values for the bilateral cortex (ips, con), bilateral hippocampus (ips, con), and corpus callosum and changes in Da, Dr, Ka, and Kr values for the corpus callosum. The *asterisk* indicates $P < .05$, compared with preinjury; *hash tag*, $P < .05$, compared with 3 days after TBI; *caret*, $P < .05$, compared with 14 days after TBI; ips, ipsilateral; con, contralateral.

In the ipsilateral perilesional cortex, $GFAP^+$ and Iba-$1^+$ cells increased significantly at 3 days ($P < .001$; $P < .001$), 14 days ($P < .001$; $P < .001$), and 28 days ($P < .001$; $P = .012$) compared with preinjury, reaching the peak at 3 days after TBI. On the other hand, $NeuN^+$ cells and the IHC staining area of MBP decreased significantly at 3 days ($P = .001$; $P < .001$), 14 days ($P = .045$; $P = .049$), and 28 days ($P = .003$; $P < .001$), reaching the lowest point at 3 days and beginning to recover at 14 days after TBI. There was no significant difference in the contralateral perilesional cortex ($P > .05$).

In the ipsilateral hippocampus, $GFAP^+$ cells also increased significantly at 3 days ($P = .012$), 14 days ($P = .014$), and 28 days ($P = .027$). Iba-$1^+$ cells increased significantly at 3 days ($P = .005$) and 14 days ($P < .001$), reaching the peak at 14 days after TBI. $NeuN^+$ cells and the IHC staining area of MBP decreased significantly at 3 days ($P < .001$; $P < .001$), 14 days ($P = .001$; $P = .001$), and 28 days ($P < .001$; $P = .001$). There was also no significant difference in the contralateral hippocampus ($P > .05$).

Like the ipsilateral perilesional cortex, $GFAP^+$ and Iba-$1^+$ cells increased significantly at 3 days ($P = .001$; $P = .007$), 14 days ($P = .034$; $P = .018$), and 28 days ($P = .046$; $P = .048$) in the corpus callosum, reaching a peak at 3 days after TBI. MBP decreased significantly at 3 days ($P < .001$), 14 days ($P < .001$), and 28 days ($P < .001$), reaching the lowest point at 3 days and beginning to recover at 14 days after TBI.

### *Cognitive Changes in TBI*

Compared with the control group, the TBI group demonstrated no significant difference in escape latency time in training trials ($P > .05$). In the probe test, the TBI group had lower platform crossing times ($P = .017$). Furthermore, there was no statistical significance in the time in the target quadrant and swimming speed between the 2 groups ($P > .05$) (Fig 4).

## DISCUSSION

DKI is a useful tool for detecting brain abnormalities. Figuring out the radiologic-pathologic relationship and the evolving laws in the process of TBI is important. Our study revealed that there were longitudinal changes in DKI parameters, which were suggestive of multiple pathologic changes at different time points following TBI. Moreover, MK is more sensitive for detecting microstructural changes, especially in gray matter, than MD and FA. Overall, our findings indicate that DKI could be used to detect and reflect brain microstructural changes induced by TBI.

In a previous study, Zhuo et al[17] investigated the TBI rat brain microstructural changes using the DKI technique in a mild controlled cortical impact TBI rat model at both acute (2 hours) and subacute (7 days) stages following injury. Our study further extended their study stages using 3 time points: 3, 14, and 28 days after TBI. Compared with baseline, the study of Zhuo et al revealed increased MK values in the ipsilateral perilesional cortex at

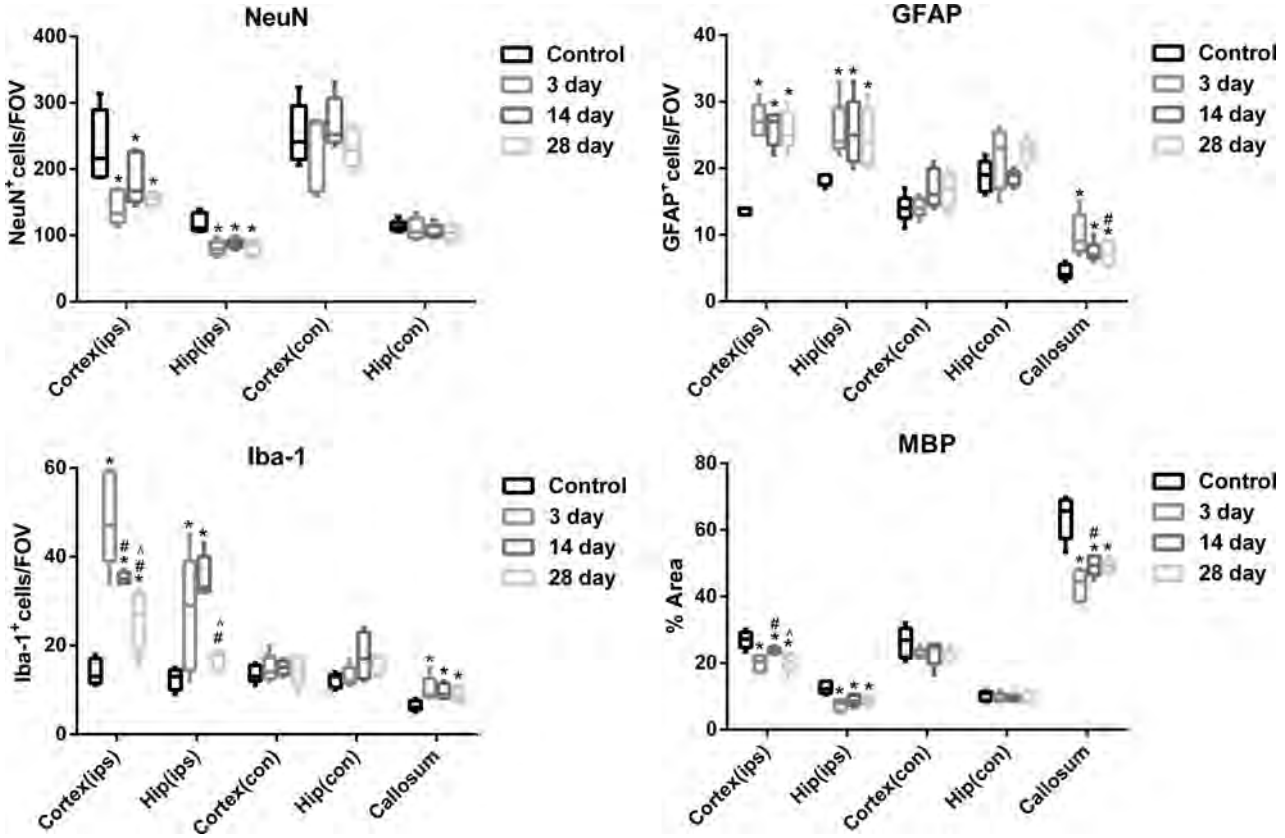


**FIG 3.** Changes in NeuN$^+$, GFAP$^+$, and Iba-1$^+$ cells and MBP area for the bilateral cortex (ips, con), bilateral hippocampus (ips, con), and corpus callosum. *Asterisk* indicates $P < .05$, compared with preinjury; *hash tag*, $P < .05$, compared with 3 days after TBI; *caret*, $P < .05$, compared with 14 days after TBI; ips, ipsilateral; con, contralateral.

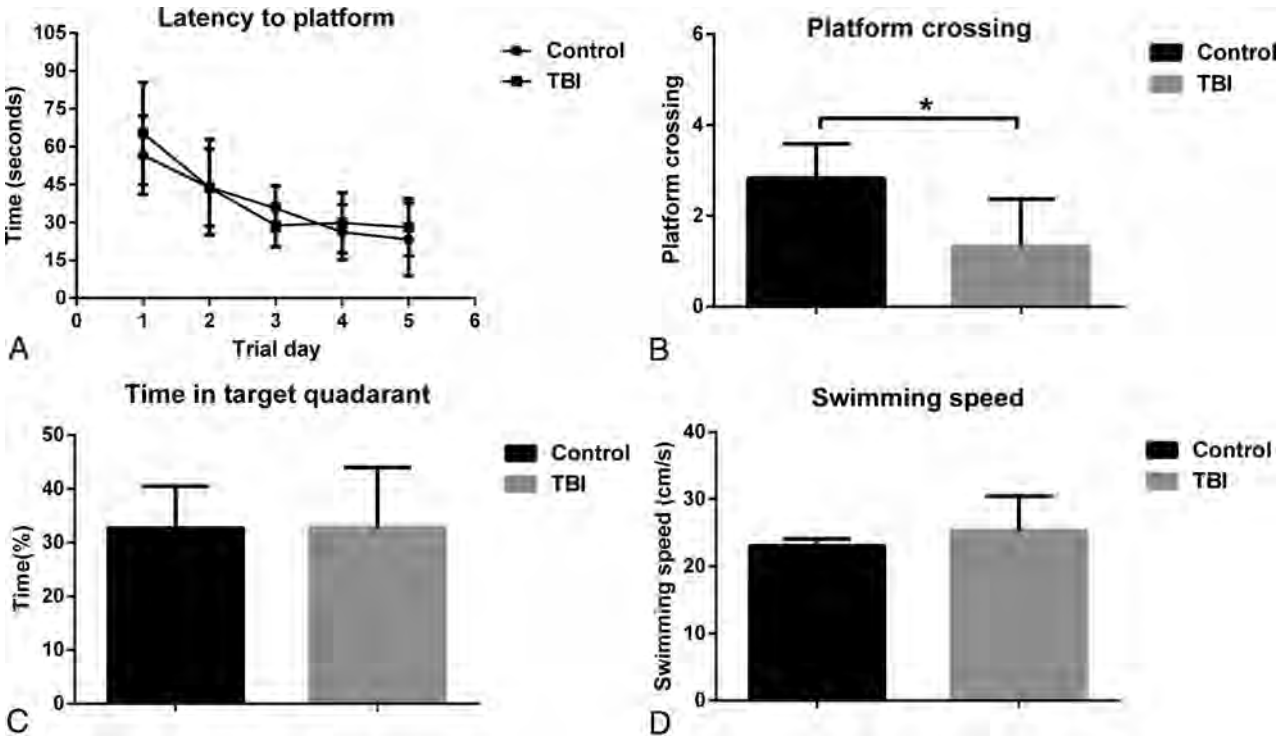


**FIG 4.** The Morris water maze tests results. *A*, Latency to find the platform. *B*, Platform-crossing times. *C*, Time spent in target quadrant. *D*, The swimming speed. *Error bars* indicate standard error. *Asterisk* indicates $P < .05$.

2 time points. Because our study also demonstrated higher MK values in the ipsilateral perilesional cortex at all 3 time points, our results are relatively consistent with those in their study. Furthermore, significantly higher MD values were only observed at 3 days after TBI, and no significant difference was found in FA values. Our study indicates that MK is more sensitive for detecting microstructural changes in the cortex.

As for the underlying pathologic changes, our study showed increased $GFAP^+$ and Iba-$1^+$ cells in the ipsilateral perilesional cortex, reaching a peak at 3 days after TBI. This finding was consistent with those in previous studies.[27,28] With the proliferation of $GFAP^+$ and Iba-$1^+$ cells, the perilesional cortex tissue would become more complex and thus have higher MK values. At present, reactive astrogliosis has been proved to be associated with higher MK values.[17] However, the MK values peaked at 14 days after TBI seemed inconsistent with the peak of $GFAP^+$ and Iba-$1^+$ cells. This inconsistency was possible because there would be other pathologic changes after TBI contributing to the MK peak. Our study also revealed decreased $NeuN^+$ and MBP staining in the ipsilateral perilesional cortex, reaching the lowest point at 3 days and beginning to recover at 14 days after TBI. This was relatively consistent with previous studies. Wiley et al[29] found neuron loss at 1 day and increased NeuN staining at 7 days after TBI. The study of Liu et al[30] found the lowest MBP expression at 3 days, and it increased in the ipsilateral perilesional cortex at 14 days after TBI. Because neuron loss and myelin disruption will cause loose cellular structure, these pathologic changes might lower the MK values, which have been found in patients with Alzheimer disease[31] and demyelinating disease.[32] Thus, the MK value could peak at 14 days, not 3 days, after TBI.

Because the obtained voxel diffusion signal is a summation of all brain microstructural effects, which have different or even similar effect on the diffusion signal, the relationship between brain microstructural changes and diffusion behavior was rather complex.[33] Thus, the MK value change in the perilesional cortex could result from all or only a subset of the investigated pathologic changes.

In the ipsilateral hippocampus, our study revealed higher MK values at all 3 time points. This was relatively consistent with findings in previous studies. Zhuo et al[17] found higher MK values in the ipsilateral hippocampus at 7 days after TBI. Another study using a blast TBI model also revealed higher MK values at 7, 14, and 28 days after TBI.[34] Our study also found higher MD values only at 3 days after TBI, and higher FA values at 3 and 28 days after TBI. Our study indicated that MK is more sensitive to detect microstructural changes in the hippocampus.

Like the perilesional cortex, the perilesional hippocampus had increased $GFAP^+$ and Iba-$1^+$ cells and decreased $NeuN^+$ and MBP staining. These findings were consistent with those in previous studies.[27,30] At present, the reactive astrogliosis has also been proved to be associated with higher MK values in the hippocampus.[17] The FA value was also increased significantly in the perilesional hippocampus. A previous study indicated that gliosis contributes to the higher FA values in gray matter.[9] Our study suggests that the DKI parameters in the perilesional hippocampus could also result from all or only a subset of the investigated pathologic changes.

In the corpus callosum, higher MK values were found at all 3 time points. The study of Zhuo et al[17] also indicated higher MK values in the corpus callosum at 7 days after TBI. Lower FA values and higher MD values were found in the corpus callosum, which was consistent with previous studies.[12,35] Furthermore, our study found higher Dr at 3 days and higher Kr at 3 and 14 days after TBI. As for the pathologic changes, the corpus callosum showed increased $GFAP^+$ and Iba-$1^+$ cells and decreased MBP staining, findings consistent with those in previous studies.[10,12,35] After TBI, primary axonal damage and further Wallerian degeneration will cause myelin loss. This could cause a decrease in FA and an increase in MD. MK might mainly result from the proliferation of astrocyte and microglia cells, which was further confirmed by higher Kr values. Our study suggests that DKI could provide supplementary information.

In our study, rats in the TBI group had lower platform crossing times in the probe test at 1 month after TBI, which was suggestive of cognitive impairment. In fact, previous studies have reported poorer performance on the Morris water maze tests as early as 2 weeks after TBI.[36-38] We speculated that persistent cortex, hippocampus, and corpus callosum abnormalities revealed by the DKI parameter changes would cause disruption of the brain cognitive network, thus leading to cognitive impairment.

Our study has limitations. First, because the MR imaging, histologic analysis, and neurocognitive tests were performed on different groups of rats, we could not perform a correlational study between DKI parameters and histologic and neurocognitive data directly. Second, although we did multiple pathologic analyses of IHC in our study, other pathologic changes might also exist and contribute to the DKI parameter changes. Furthermore, we only investigated the brain histologic cell number. However, the cell distribution patterns could also influence the DKI parameters. Third, although the controlled cortical impact model has been widely used in TBI animal studies, the animal model still has differences compared with clinical patients with TBI. Clinical TBI encompasses diverse injury mechanisms, injury locations, and injury severity.[39] One should be careful in the interpretation of DKI parameters in clinical patients with TBI. Fourth, the sample size used in this study was relatively small. A future large-sample study is needed to replicate our results.

## CONCLUSIONS

Our study indicated that there were longitudinal changes in DKI parameters, accompanied by multiple pathologic changes at different time points following TBI. MK is more sensitive for detecting microstructural changes, especially in gray matter, than MD and FA. Overall, DKI could be a potentially useful tool for detecting and reflecting brain microstructural changes induced by TBI.

Disclosures: Wen-Bin Li—*RELATED*: *Grant*: National Natural Science Foundation of China (No. 81271540), Natural Science Foundation of Xinjiang Province (No. 2016D01C083), and the Shanghai Key Discipline of Medical Imaging (No. 2017ZZ02005). Xiao-Er Wei—*RELATED*: National Natural Science Foundation of China (No.81301213), Medical-Engineering Cross Project of Shanghai Jiao Tong University (No. YG2015MS19), and the Shanghai Health and Family Planning Commission research projects (No. 20164Y0065).

## REFERENCES


1. Masel BE, DeWitt DS. **Traumatic brain injury: a disease process, not an event.** *J Neurotrauma* 2010;27:1529–40 CrossRef Medline
2. Langlois JA, Rutland-Brown W, Wald MM. **The epidemiology and impact of traumatic brain injury: a brief overview.** *J Head Trauma Rehabil* 2006;21:375–78 CrossRef Medline
3. Schretlen DJ, Shapiro AM. **A quantitative review of the effects of traumatic brain injury on cognitive functioning.** *Int Rev Psychiatry* 2003;15:341–49 CrossRef Medline
4. Basser PJ, Mattiello J, LeBihan D. **MR diffusion tensor spectroscopy and imaging.** *Biophys J* 1994;66:259–67 CrossRef Medline
5. Salmond CH, Menon DK, Chatfield DA, et al. **Diffusion tensor imaging in chronic head injury survivors: correlations with learning and memory indices.** *Neuroimage* 2006;29:117–24 CrossRef Medline
6. Kraus MF, Susmaras T, Caughlin BP, et al. **White matter integrity and cognition in chronic traumatic brain injury: a diffusion tensor imaging study.** *Brain* 2007;130:2508–19 CrossRef Medline
7. Kinnunen KM, Greenwood R, Powell JH, et al. **White matter damage and cognitive impairment after traumatic brain injury.** *Brain* 2011; 134:449–63 CrossRef Medline
8. Fakhran S, Yaeger K, Alhilali L. **Symptomatic white matter changes in mild traumatic brain injury resemble pathologic features of early Alzheimer dementia.** *Radiology* 2013;269:249–57 CrossRef Medline
9. Budde MD, Janes L, Gold E, et al. **The contribution of gliosis to diffusion tensor anisotropy and tractography following traumatic brain injury: validation in the rat using Fourier analysis of stained tissue sections.** *Brain* 2011;134:2248–60 CrossRef Medline
10. Tu TW, Williams RA, Lescher JD, et al. **Radiological-pathological correlation of diffusion tensor and magnetization transfer imaging in a closed head traumatic brain injury model.** *Ann Neurol* 2016;79: 907–20 CrossRef Medline
11. Singh K, Trivedi R, Devi MM, et al. **Longitudinal changes in the DTI measures, anti-GFAP expression and levels of serum inflammatory cytokines following mild traumatic brain injury.** *Exp Neurol* 2016; 275(Pt 3):427–35 CrossRef Medline
12. Pischiutta F, Micotti E, Hay JR, et al. **Single severe traumatic brain injury produces progressive pathology with ongoing contralateral white matter damage one year after injury.** *Exp Neurol* 2018;300: 167–178 CrossRef Medline
13. Jensen JH, Helpern JA, Ramani A, et al. **Diffusional kurtosis imaging: the quantification of non-Gaussian water diffusion by means of magnetic resonance imaging.** *Magn Reason Med* 2005; 53:1432–40 CrossRef Medline
14. Jensen JH, Helpern JA. **MRI quantification of non-Gaussian water diffusion by kurtosis analysis.** *NMR Biomed* 2010;23:698–710 CrossRef Medline
15. Grossman EJ, Ge Y, Jensen JH, et al. **Thalamus and cognitive impairment in mild traumatic brain injury: a diffusional kurtosis imaging study.** *J Neurotrauma* 2012;29:2318–27 CrossRef Medline
16. Grossman EJ, Jensen JH, Babb JS, et al. **Cognitive impairment in mild traumatic brain injury: a longitudinal diffusional kurtosis and perfusion imaging study.** *AJNR Am J Neuroradiol* 2013;34:951–57, s1–3 CrossRef Medline
17. Zhuo J, Xu S, Proctor JL, et al. **Diffusion kurtosis as an in vivo imaging marker for reactive astrogliosis in traumatic brain injury.** *Neuroimage* 2012;59:467–77 CrossRef Medline
18. Johnson VE, Stewart W, Smith DH. **Axonal pathology in traumatic brain injury.** *Exp Neurol* 2013;246:35–43 CrossRef Medline
19. Kou Z, VandeVord PJ. **Traumatic white matter injury and glial activation: from basic science to clinics.** *Glia* 2014;62:1831–55 CrossRef Medline
20. Faden AI, Loane DJ. **Chronic neurodegeneration after traumatic brain injury: Alzheimer disease, chronic traumatic encephalopathy, or persistent neuroinflammation?** *Neurotherapeutics* 2015;12: 143–50 CrossRef Medline
21. Wang ML, Li WB. **Cognitive impairment after traumatic brain injury: the role of MRI and possible pathological basis.** *J Neurol Sci* 2016;370:244–50 CrossRef Medline
22. Tabesh A, Jensen JH, Ardekani BA, et al. **Estimation of tensors and tensor-derived measures in diffusional kurtosis imaging.** *Magn Reason Med* 2011;65:823–36 CrossRef Medline
23. Yushkevich PA, Piven J, Hazlett HC, et al. **User-guided 3D active contour segmentation of anatomical structures: significantly improved efficiency and reliability.** *Neuroimage* 2006;31: 1116–28 CrossRef Medline
24. Vertes RP. **Interactions among the medial prefrontal cortex, hippocampus and midline thalamus in emotional and cognitive processing in the rat.** *Neuroscience* 2006;142:1–20 CrossRef Medline
25. Chida Y, Kokubo Y, Sato S, et al. **The alterations of oligodendrocyte, myelin in corpus callosum, and cognitive dysfunction following chronic cerebral ischemia in rats.** *Brain Res* 2011;1414:22–31 CrossRef Medline
26. Vorhees CV, Williams MT. **Morris water maze: procedures for assessing spatial and related forms of learning and memory.** *Nat Protoc* 2006;1:848–58 CrossRef Medline
27. Chen S, Pickard JD, Harris NG. **Time course of cellular pathology after controlled cortical impact injury.** *Exp Neurol* 2003;182:87–102 CrossRef Medline
28. Susarla BT, Villapol S, Yi JH, et al. **Temporal patterns of cortical proliferation of glial cell populations after traumatic brain injury in mice.** *ASN Neuro* 2014;6:159–70 CrossRef Medline
29. Wiley CA, Bissel SJ, Lesniak A, et al. **Ultrastructure of diaschisis lesions after traumatic brain injury.** *J Neurotrauma* 2016;33:1866–82 CrossRef Medline
30. Liu MC, Akle V, Zheng W, et al. **Extensive degradation of myelin basic protein isoforms by calpain following traumatic brain injury.** *J Neurochem* 2006;98:700–12 CrossRef Medline
31. Gong NJ, Chan CC, Leung LM, et al. **Differential microstructural and morphological abnormalities in mild cognitive impairment and Alzheimer's disease: evidence from cortical and deep gray matter.** *Hum Brain Mapp* 2017;38:2495–508 CrossRef Medline
32. Guglielmetti C, Veraart J, Roelant E, et al. **Diffusion kurtosis imaging probes cortical alterations and white matter pathology following cuprizone induced demyelination and spontaneous remyelination.** *Neuroimage* 2016;125:363–77 CrossRef Medline
33. Umesh Rudrapatna S, Wieloch T, Beirup K, et al. **Can diffusion kurtosis imaging improve the sensitivity and specificity of detecting microstructural alterations in brain tissue chronically after experimental stroke? Comparisons with diffusion tensor imaging and histology.** *Neuroimage* 2014;97:363–73 CrossRef Medline
34. Zhuo J, Keledjian K, Xu S, et al. **Changes in diffusion kurtosis imaging and magnetic resonance spectroscopy in a direct cranial blast traumatic brain injury (dc-bTBI) model.** *PLoS One* 2015;10: e0136151 CrossRef Medline
35. Harris NG, Verley DR, Gutman BA, et al. **Bi-directional changes in fractional anisotropy after experiment TBI: disorganization and reorganization?** *Neuroimage* 2016;133:129–43 CrossRef Medline
36. Scheff SW, Baldwin SA, Brown RW, et al. **Morris water maze deficits in rats following traumatic brain injury: lateral controlled cortical impact.** *J Neurotrauma* 1997;14:615–27 CrossRef Medline
37. Radabaugh HL, Carlson LJ, O'Neil DA, et al. **Abbreviated environmental enrichment confers neurobehavioral, cognitive, and histological benefits in brain-injured female rats.** *Exp Neurol* 2016;286: 61–68 CrossRef Medline
38. Brabazon F, Wilson CM, Jaiswal S, et al. **Intranasal insulin treatment of an experimental model of moderate traumatic brain injury.** *J Cereb Blood Flow Metab* 2017;37:3203–18 CrossRef Medline
39. Maas AI, Stocchetti N, Bullock R. **Moderate and severe traumatic brain injury in adults.** *Lancet Neurol* 2008;7:728–41 CrossRef Medline

# Adult-Onset Leukoencephalopathy with Axonal Spheroids and Pigmented Glia: An MRI Study of 16 French Cases

P. Codjia, X. Ayrignac, F. Mochel, K. Mouzat, C. Carra-Dalliere, G. Castelnovo, E. Ellie, F. Etcharry-Bouyx, C. Verny, S. Belliard, D. Hannequin, C. Marelli, Y. Nadjar, I. Le Ber, I. Dorboz, S. Samaan, O. Boespflug-Tanguy, S. Lumbroso, and P. Labauge

## ABSTRACT

**SUMMARY:** Adult-onset leukoencephalopathy with axonal spheroids and pigmented glia is an autosomal dominant leukoencephalopathy related to *CSF1R* gene mutations. A growing number of clinicoradiologic phenotypes have been described. In this study, we analyzed brain imaging findings in 16 patients with adult-onset leukoencephalopathy with axonal spheroids and pigmented glia to refine radiologic diagnostic clues. T2/FLAIR white matter hyperintensities were present in all patients with frontal or frontoparietal predilection, with asymmetric distribution in more than one-third. Brain atrophy and callosal involvement were almost constant, and corticospinal tract involvement was frequent. Moreover, deep white matter hyperintense dots on DWI and deep punctate calcifications on CT were often found. Conversely, deep gray matter nuclei, external capsules, and brain stem were rarely involved. Our series emphasized the great variability of MR imaging findings seen in adult-onset leukoencephalopathy with axonal spheroids and pigmented glia. A complete imaging screening including DWI, T2*, and CT is mandatory to accurately assess patients with suspected inherited adult-onset leukoencephalopathy.

**ABBREVIATIONS:** ALSP = adult-onset leukoencephalopathy with axonal spheroids and pigmented glia; FTLD = frontotemporal lobar degeneration; WMH = white matter hyperintensities

Adult-onset leukoencephalopathy with axonal spheroids and pigmented glia (ALSP) is an autosomal dominant leukoencephalopathy related to heterozygous mutations in the *colony stimulating factor 1 receptor* (*CSF1R*) gene.[1] To date, >50 *CSF1R* mutations and multiple clinicoradiologic phenotypes have been described.[2] ALSP is increasingly recognized as one of the most common causes of adult-onset inherited leukoencephalopathy.[3]

Received January 28, 2018; accepted after revision May 1.

From the Department of Neurology (P.C., X.A., C.C.-D., C.M., P.L.), Montpellier University Hospital, Montpellier, France; Departments of Biochemistry and Molecular Biology (K.M., S.L.) and Neurology (G.C.), Nîmes University Hospital, Nîmes, France; Department of Neurology (E.E.), Côte Basque Hospital, Bayonne, France; Department of Neurology (F.E.-B., C.V.), Angers University Hospital, Angers, France; Department of Neurology (S.B.), Rennes University Hospital, Rennes, France; Department of Neurology (D.H.), Rouen University Hospital, Rouen, France; Departments of Neurology (Y.N., I.L.B.) and Genetics (F.M.), Assistance Publique–Hôpitaux de Paris, Pitié-Salpêtrière University Hospital, Paris, France; and Department of Neuropediatrics and Metabolic Disorders (I.D., S.S., O.B.-T.), Assistance Publique–Hôpitaux de Paris, Robert Debré University Hospital, Paris, France.

Serge Lumbroso and Pierre Labauge contributed equally as last authors.

The research leading to these results has received funding from the program "Investissements d'avenir" ANR-10-IAIHU-06. This work was funded by the PHRC (Programme Hospitalier de Recherche Clinique) FTLD exome (promotion Assistance Publique–Hôpitaux de Paris to I.L.B.).

Please address correspondence to Xavier Ayrignac, MD, Department of Neurology, Montpellier University Hospital, 80 Rue Augustin Fliche, 34295 Montpellier, Cedex 05, France; e-mail: xavier.ayrignac@yahoo.fr

Indicates open access to non-subscribers at www.ajnr.org

http://dx.doi.org/10.3174/ajnr.A5744

ALSP diagnosis is still challenging because of the multiple presentations that can mimic frontotemporal lobar degeneration (FTLD), atypical parkinsonism, CADASIL, or primary-progressive MS.[1,3-5] Indeed, initial descriptions of ALSP included late-onset psychiatric and cognitive impairment with MR imaging frontal white matter changes and atrophy. Following the genetic characterization of the disease, more distinctive imaging findings have been identified, including deep punctate calcifications, persistent DWI small diffusion-restricted lesions, and corpus callosum thinning.[6-8] In this study, we analyzed imaging findings in 16 patients with genetically confirmed ALSP to refine imaging characteristics and improve its diagnostic rate.

### Case Series

Sixteen patients with ALSP (9 women, 7 men) from 10 unrelated families were identified in 7 neurologic centers. Five patients had a longitudinal MR imaging evaluation. T1WI, T2WI, and FLAIR were available for all patients. T1WI with gadolinium contrast medium ($n = 6$), DWI ($n = 8$), and T2* ($n = 8$) were available for some patients. Six patients had a brain CT. Seven patients have been previously described.[3,4,9,10]

### Clinical and Genetic Findings

Thirteen patients had a positive family history of ALSP (Table 1). The mean age of onset was 45.8 years (range, 28–60 years). Initial

**Table 1: Clinical and genetic findings**

| Case | Sex | Age at Onset (yr) | Family History | Initial Symptoms | First Suspected Diagnosis | *CSF1R Mutation* | MRI Delay (yr) |
|---|---|---|---|---|---|---|---|
| 1 | M | 57 | Yes | Cognitive/psychiatric | FTLD (genetic form) | c.2330G>A(p.Arg777Gln) | 1 |
| 2 | M | 44 | Yes | Cognitive | FTLD (genetic form) | c.2330G>A(p.Arg777Gln) | 4 |
| 3 | F | 42 | Yes | Parkinsonism | Corticobasal degeneration | c.2566T>C(p.Tyr856His) | 3 |
| 4 | M | 28 | Yes | Gait | CNS lesions related to celiac disease | c.2381T>C(p.Ile794Thr) | 4 |
| 5 | M | 57 | Yes | Speech | Undetermined leukoencephalopathy | c.2381T>C(p.Ile794Thr) | 5 |
| 6 | F | 28 | No | Gait/apraxia | Undetermined leukoencephalopathy | c.2381T>C(p.Ile794Thr) | 0.5 |
| 7 | F | 31 | No | Motor | PPMS | c.2342C>T(p.Ala781Val) | 1.5 |
| 8 | M | 60 | Yes | Cognitive/apraxia | Corticobasal degeneration | c.2525G>T(p.Gly842Val)[a] | 1 |
| 9 | F | 47 | Yes | Parkinsonism | Vascular leukoencephalopathy (inherited) | c.2522A>G(p.Tyr841Cys)[a] | 1 |
| 10 | F | 60 | Yes | Cognitive/parkinsonism | Vascular leukoencephalopathy (inherited) | c.2522A>G(p.Tyr841Cys)[a] | 1 |
| 11 | M | 36 | Yes | Cognitive | LCC | c.2534T>C(p.Leu845Pro)[a] | 2 |
| 12 | F | 55 | Yes | Psychiatric/speech | LCC | c.2534T>C(p.Leu845Pro)[a] | 2 |
| 13 | F | – | Yes | Asymptomatic | NA | c.2498C>A(p.Thr833Lys)[a] | 49[b] |
| 14 | F | 57 | Yes | Cognitive | FTLD (genetic form) | c.2498C>A(p.Thr833Lys)[a] | 1 |
| 15 | F | 33 | Yes | Gait | NA | c.2498C>A(p.Thr833Lys)[a] | 0.5 |
| 16 | M | 52 | No | Cognitive/psychiatric | Vascular leukoencephalopathy (inherited) | c.2308G>C(p.Ala770Pro) | 2 |

**Note:**—NA indicates not applicable (diagnosis already known in family member); PPMS, primary-progressive MS; LCC, leukoencephalopathy with calcifications and cysts.
[a] Mutation not previously described.
[b] Patient asymptomatic at the time of MRI. Each family is separated by dashed lines.

symptoms included cognitive impairment (44%), psychiatric symptoms (19%), parkinsonism (19%), gait ataxia (19%), apraxia (13%), speech problems (13%), and motor dysfunction (6%). Nine different pathogenic *CSF1R* mutations were identified, including 5 previously reported mutations. All mutations involved the *CSF1R* tyrosine kinase domain with no overt correlation between mutations and the patient's phenotypes or MR imaging findings.

### *Imaging Findings*

**White Matter Hyperintensities.** The mean delay between symptom onset and MR imaging was 2.0 years (range, 0.5–5 years). Bilateral, predominantly frontal and parietal T2/FLAIR white matter hyperintensities (WMH) associated with T1 hypointensities were present in all patients, even if they were subtle in some patients (Fig 1*A* and Table 2). Temporal and occipital abnormalities were observed in, respectively, 69% and 50% of the cases. WMH were confluent in 63% (Fig 1*B*) and patchy in 37% (Fig 1*C*), and a clear asymmetry was seen 37% of the patients (Fig 1*D*).

Pyramidal tract hyperintensities were noted in 63% of the patients (Fig 1*A*, -*E*), with an involvement of the internal capsules in 10 and of the brain stem in 3. Three patients had spinal cord MR imaging; findings were always normal. Corpus callosum abnormalities were almost always present with hyperintensities in 81% (Fig 1*F*) and atrophy in 88% of cases (Fig 1*G*). Deep gray matter nuclei and external capsules were involved in, respectively, 13% and 44% of patients. Posterior fossa hyperintensities were seen in 37% of the patients: Half of these patients had pontine vascular-like lesions (Fig 1*H*). The cerebellum was always spared. Enlarged perivascular spaces were seen in 25% of patients (Fig 1*I*).

**Atrophy.** Brain atrophy was almost constant (94%), and 4 patients had marked atrophy (Fig 1*J*). It was usually more pronounced in patients with diffuse WMH and predominated in the frontal (40%) or frontoparietal (53%) areas.

**DWI and Calcifications.** Multiple small deep white matter DWI diffusion-restricted lesions were observed in 6 of 8 patients, including 4 with a restriction of the apparent diffusion coefficient (Fig 2). On CT, calcifications were found in 4 of 6 patients (Fig 3), but they were not identified with T2* imaging.

**Other Features.** None of the 6 patients with contrast MR imaging showed gadolinium enhancement. Ventricular abnormalities, including cavum septum pellucidum and/or cavum vergae (Fig 1*A*, -*B*), were seen in 50% of the patients. Five patients (cases 7, 8, 11, 14, and 15) had an MR imaging follow-up after a mean of 15.3 months (range, 5–32 months): Supratentorial WMH worsened in all patients (Fig 1*K*, -*L*), usually associated with marked brain volume loss.

## DISCUSSION

Our series emphasizes the great variability of MR imaging findings seen in ALSP. Likewise, only 44% of our patients corresponded to the initial description (before the era of genetic screening) of patients with ALSP with cognitive impairment and psychiatric symptoms associated with marked frontoparietal hyperintensities and atrophy.[11] FTLD is one of the main differential diagnoses of ALSP, though WMH are rarely seen in FTLD, with the exception of patients with *GRN* mutations.[12] Recent data suggest that patients can also be misdiagnosed as having inflammatory disorders or vascular leukoencephalopathies.[5,13,14] In our series, inflammatory diseases (primary-progressive MS and celiac disease–related CNS lesions) were initially suspected in 2 patients, and a vascular leukoencephalopathy, in 3. In patients who had MR imaging with patchy and sometimes periventricular lesions like those potentially seen in MS, in the absence of CSF oligoclonal bands and in patients with a rapid worsening of disability, ALSP should be suspected. In these cases, absence of typical periventricular Dawson finger lesions, marked corpus callosum atrophy, and persistent DWI hyperintensities and CT microcalcifications should be sought and, if present, should warrant *CSF1R* gene sequencing.

WMH, as previously described, always involved frontal and parietal white matter, but temporal and occipital involvement (though usually mild) was also common, respectively, in 69% and 50% of the cases compared with <20% in previous studies.[7,8] Moreover, the "patchy" pattern frequently observed in ALSP is

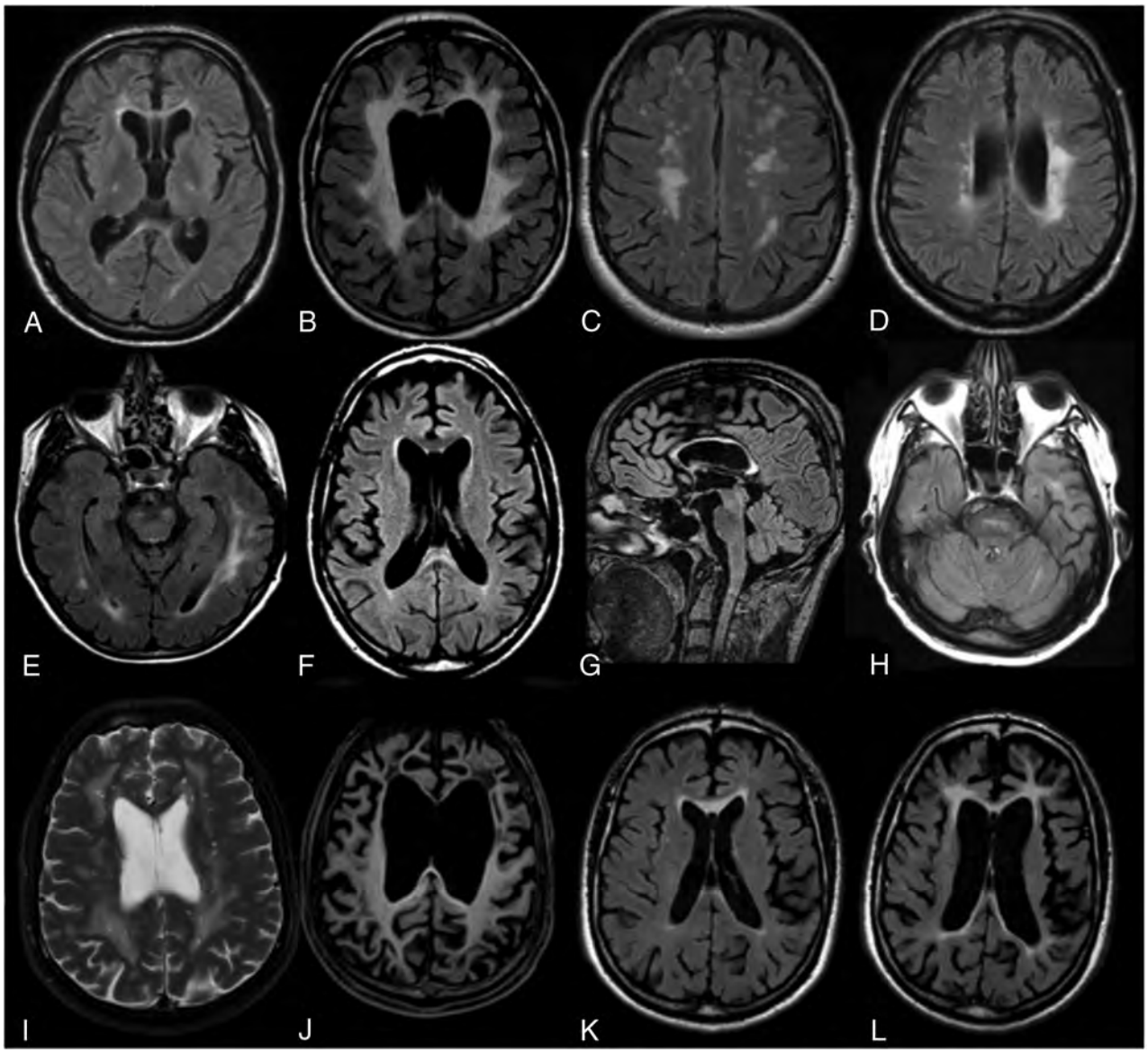


**FIG 1.** Characteristic MR imaging abnormalities in patients with ALSP on FLAIR (*A–H*, *K*, *L*), T2WI (*I*), and T1WI (*J*) images. MR imaging usually discloses subtle (*A*) or marked (*B*) white mater hyperintensities with frontal predilection (*B*). WMH can be confluent (*B*) or patchy (*C*) and are usually asymmetric (*D*). Corticospinal tract involvement (*A* and *E*) and corpus callosum involvement (*F* and *G*) are frequent. At the posterior fossa level, WMH can be of a vascular-like type (*H*). Some patients can present with enlarged perivascular spaces on T2WI (*I*). T1WI frequently reveals atrophy, usually marked, with frontal predominance (*J*). During a 32-month follow-up (case 8), a clear increase of WMH and atrophy is seen (*K* and *L*). A cavum septum pellucidum is frequently observed (*A* and *B*).

rarely seen in other adult-onset leukoencephalopathies and usually suggests an inflammatory or vascular (acquired or inherited) etiology.[5] Finally, asymmetric hyperintensities are rarely reported in inherited white matter disorders. Besides ALSP, they have been mainly described in *AARS2*-related leukoencephalopathy, retinal vasculopathy with cerebral leukoencephalopathy, Alexander disease, and leukoencephalopathy with calcifications and cysts.[7,15,16] Our data confirmed that asymmetric lesions are present in ALSP (37%), and a recent series reported an even higher occurrence of asymmetric WMH (90%).[7]

Deep small white matter DWI diffusion-restricted lesions, often associated with a restriction on an ADC map, were found in 6/8 patients. They are characteristic of the disease because they have only been reported in ALSP (two-thirds of the patients) and in *AARS2*-related leukoencephalopathy (100%).[2,7,14,17] As previously described, our single patient with serial MR imaging and DWI sequences had persistent $b=1000$ hyperintensities.[7,17] Other series have suggested that small calcifications with a stepping stone distribution were characteristic of the disease, but their frequency has not been reported to date.[6,18] Here, we found calcifications in 4/6 patients who had undergone CT, stressing that they are likely frequent in ALSP. Of note, none of our patients with calcifications on CT had identifiable T2* hypointensities.

Atrophy (88%) and/or hyperintensities (81%) were frequently seen in the corpus callosum. In some patients, the corpus callosum was markedly involved, despite very subtle white matter abnormalities.[19] Conversely, deep gray matter nuclei (13%) and the external capsule (44%) were rarely involved. Accordingly, such

**Table 2: Neuroimaging findings**

| Imaging Findings | No. | % | Imaging Findings | No. | % |
|---|---|---|---|---|---|
| White matter abnormalities | 16/16 | 100 | Atrophy | 15/16 | 94 |
| Symmetry | | | Atrophy predominance | | |
| Symmetric | 10/16 | 63 | Frontal | 6/15 | 40 |
| Asymmetric | 6/16 | 37 | Frontoparietal | 8/15 | 53 |
| Confluence of lesions | | | Parietal | 1/15 | 7 |
| Confluent | 10/16 | 63 | Corpus callosum involvement | | |
| Patchy | 6/16 | 37 | Hyperintensities | 13/16 | 81 |
| White matter abnormalities predominance | | | Atrophy | 14/16 | 88 |
| Frontal | 13/16 | 81 | Corticospinal tract | 10/16 | 63 |
| Frontoparietal | 3/16 | 19 | Deep gray matter nuclei | 2/16 | 13 |
| Lobar distribution | | | External capsule | 7/16 | 44 |
| Frontal | 16/16 | 100 | Posterior fossa | 6/16 | 37 |
| Parietal | 16/16 | 100 | Enlarged perivascular spaces | 4/16 | 25 |
| Temporal | 11/16 | 69 | Diffusion-weighted imaging | | |
| Occipital | 8/16 | 50 | Hyperintensities | 6/8 | 75 |
| U-fiber involvement | 8/16 | 50 | Restricted ADC | 4/6 | 67 |
| White matter rarefaction | 0/16 | 0 | Calcifications | | |
| | | | T2* | 0/8 | 0 |
| | | | CT | 4/6 | 67 |
| | | | Gadolinium enhancement | 0/6 | 0 |
| | | | Cavum septum pellucidum | 8/16 | 50 |

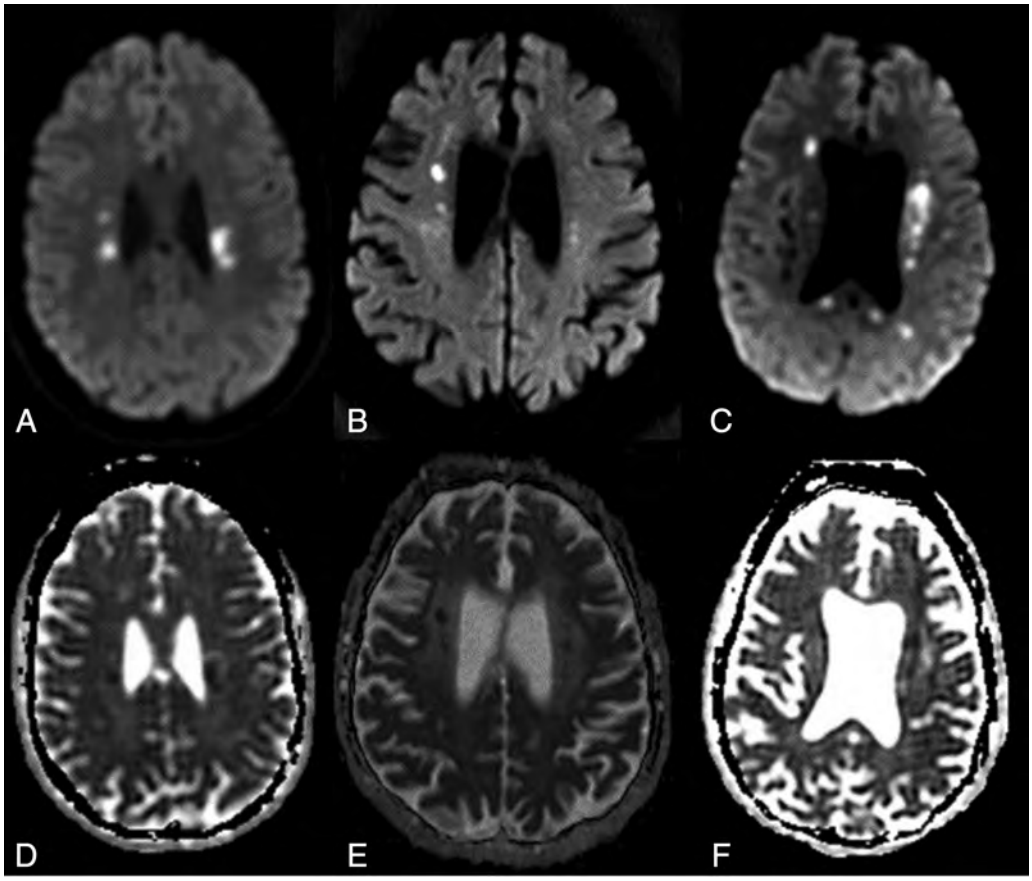


**FIG 2.** Typical DWI in ALSP. Persistent deep white matter diffusion-restricted lesions (*A–C*) with corresponding low ADC values (*D–F*) are found.

features in patients with patchy WMH, along with the absence of T2* microbleeds, help distinguish acquired or inherited vascular leukoencephalopathy from ALSP.[7,8,20] Similarly, of the 6 patients with pontine hyperintensities, only 3 had lesions suggestive of a vascular origin, whereas the other patients had corticospinal tract hyperintensities.

Altogether, this series emphasized the striking variability of MR imaging patterns in ALSP, suggesting that to date, this condition is probably markedly underestimated. Moreover, in patients suspected of having inherited leukoencephalopathy, we confirmed that an asymmetric distribution of WMH, persistent DWI hyperintense white matter diffusion-restricted lesions, and

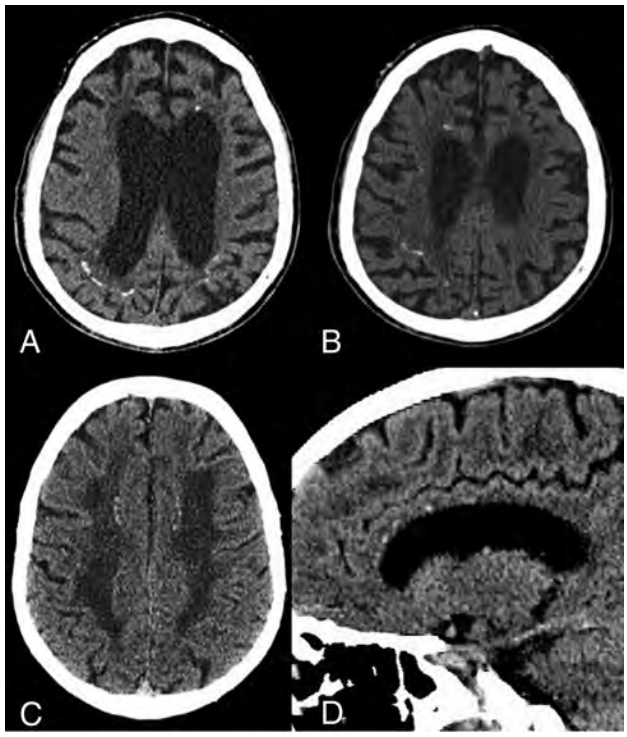


**FIG 3.** Small calcifications in ALSP. CT images reveal punctate calcifications located in the subcortical parietal WM and the periventricular frontal WM (*A*–*C*). Sagittal reconstruction shows the typical stepping stone distribution (*D*).

punctate calcifications are highly suggestive of ALSP. Likewise, a complete imaging screening, including DWI, T2*, and CT, is key to accurately assess patients suspected of having inherited adult-onset leukoencephalopathy. The early detection of *CSF1R*-related leukoencephalopathy is even more critical because hematopoietic stem cell transplantation may be a promising therapy for patients and their at-risk relatives.[21]

Disclosures: Fanny Mochel—*UNRELATED*: *Consultancy*: Ultragenyx Pharmaceuticals, *Comments*: expert at investigator meetings for Phase 3 study; *Expert Testimony*: Haute Autorité de Santé, *Comments*: expert opinion on an Orphan drug for a rare neurometabolic disease; *Grants/Grants Pending*: Programme Hospitalier de Recherche Clinique, Direction Générale de l'Offre de Soins, Ultragenyx, *Comments*: clinical trial: NCT02336633, clinical trial: NCT02639871, clinical trial: NCT02453061*; *Patents (Planned, Pending or Issued)*: EP1929995 A1. Serge Belliard—*UNRELATED*: *Board Membership*: Lilly, *Comments*: board for development of antiamyloid treatments. Cecilia Marelli—*UNRELATED*: *Payment for Development of Educational Presentations*: Actelion Pharmaceuticals; *Travel/Accommodations/Meeting Expenses Unrelated to Activities Listed*: Nutricia Metabolics. Yann Nadjar—*UNRELATED*: *Grants/Grants Pending*: Leadiant and Retrophin, *Comments*: financial support for clinical studies about cerebrotendinous xanthomatosis from 2 pharmaceutical companies*; *Payment for Lectures Including Service on Speakers Bureaus*: lectures about Fabry disease (from Amicus Therapeutics) and dementias from inherited metabolic disease (from Orphan Europe); *Payment for Manuscript Preparation*: from Orphan Europe, concerning a manuscript about MTHFR deficiency*; *Patents (Planned, Pending or Issued)*: from Orphan Europe, to develop a Web site concerning neurometabolic diseases. *Money paid to the institution.

## REFERENCES

1. Rademakers R, Baker M, Nicholson AM, et al. **Mutations in the colony stimulating factor 1 receptor (CSF1R) gene cause hereditary diffuse leukoencephalopathy with spheroids.** *Nat Genet* 2011;44:200–05 CrossRef Medline
2. Konno T, Yoshida K, Mizuno T, et al. **Clinical and genetic characterization of adult-onset leukoencephalopathy with axonal spheroids and pigmented glia associated with CSF1R mutation.** *Eur J Neurol* 2017;24:37–45 CrossRef Medline
3. Guerreiro R, Kara E, Le Ber I, et al. **Genetic analysis of inherited leukodystrophies: genotype-phenotype correlations in the CSF1R gene.** *JAMA Neurol* 2013;70:875–82 CrossRef Medline
4. Prieto-Morin C, Ayrignac X, Ellie E, et al. **CSF1R-related leukoencephalopathy mimicking primary progressive multiple sclerosis.** *J Neurol* 2016;263:1864–65 CrossRef Medline
5. Lynch DS, Jaunmuktane Z, Sheerin UM, et al. **Hereditary leukoencephalopathy with axonal spheroids: a spectrum of phenotypes from CNS vasculitis to parkinsonism in an adult onset leukodystrophy series.** *J Neurol Neurosurg Psychiatry* 2016;87:512–19 CrossRef Medline
6. Konno T, Broderick DF, Mezaki N, et al. **Diagnostic value of brain calcifications in adult-onset leukoencephalopathy with axonal spheroids and pigmented glia.** *AJNR Am J Neuroradiol* 2017;38:77–83 CrossRef Medline
7. Lakshmanan R, Adams ME, Lynch DS, et al. **Redefining the phenotype of ALSP and AARS2 mutation-related leukodystrophy.** *Neurol Genet* 2017;3:e135 CrossRef Medline
8. Sundal C, Van Gerpen JA, Nicholson AM, et al. **MRI characteristics and scoring in HDLS due to CSF1R gene mutations.** *Neurology* 2012;79:566–74 CrossRef Medline
9. Letournel F, Etcharry-Bouyx F, Verny C, et al. **Two clinicopathological cases of a dominantly inherited, adult onset orthochromatic leucodystrophy.** *J Neurol Neurosurg Psychiatry* 2003;74:671–73 CrossRef Medline
10. Labauge P, Berger E, Magnin E, et al. **A new form of leukoencephalopathy with calcifications and cysts with nonrecessive inheritance and absence of gadolinium enhancement.** *Eur Neurol* 2012;67:151–53 CrossRef Medline
11. van der Knaap MS, Naidu S, Kleinschmidt-Demasters BK, et al. **Autosomal dominant diffuse leukoencephalopathy with neuroaxonal spheroids.** *Neurology* 2000;54:463–68 CrossRef Medline
12. Caroppo P, Le Ber I, Camuzat A, et al. **Extensive white matter involvement in patients with frontotemporal lobar degeneration: think progranulin.** *JAMA Neurol* 2014;71:1562–66 CrossRef Medline
13. Sundal C, Baker M, Karrenbauer V, et al. **Hereditary diffuse leukoencephalopathy with spheroids with phenotype of primary progressive multiple sclerosis.** *Eur J Neurol* 2015;22:328–33 CrossRef Medline
14. Battisti C, Di Donato I, Bianchi S, et al. **Hereditary diffuse leukoencephalopathy with axonal spheroids: three patients with stroke-like presentation carrying new mutations in the CSF1R gene.** *J Neurol* 2014;261:768–72 CrossRef Medline
15. Stam AH, Kothari PH, Shaikh A, et al. **Retinal vasculopathy with cerebral leukoencephalopathy and systemic manifestations.** *Brain* 2016;139:2909–22 CrossRef Medline
16. Wang M, Zhang M, Wu L, et al. **Leukoencephalopathy with cerebral calcification and cysts: cases report and literature review.** *J Neurol Sci* 2016;370:173–79 CrossRef Medline
17. Terasawa Y, Osaki Y, Kawarai T, et al. **Increasing and persistent DWI changes in a patient with hereditary diffuse leukoencephalopathy with spheroids.** *J Neurol Sci* 2013;335:213–15 CrossRef Medline
18. Ayrignac X, Nicolas G, Carra-Dallière C, et al. **Brain calcifications in adult-onset genetic leukoencephalopathies: a review.** *JAMA Neurol* 2017;74:1000–08 CrossRef Medline
19. Kondo Y, Kinoshita M, Fukushima K, et al. **Early involvement of the corpus callosum in a patient with hereditary diffuse leukoencephalopathy with spheroids carrying the de novo K793T mutation of CSF1R.** *Intern Med* 2013;52:503–06 CrossRef Medline
20. Ayrignac X, Carra-Dalliere C, Menjot de Champfleur N, et al. **Adult-onset genetic leukoencephalopathies: a MRI pattern-based approach in a comprehensive study of 154 patients.** *Brain* 2015;138(Pt 2):284–92 CrossRef Medline
21. Eichler FS, Li J, Guo Y, et al. **CSF1R mosaicism in a family with hereditary diffuse leukoencephalopathy with spheroids.** *Brain* 2016;139:1666–72 CrossRef Medline

# Intracranial Serpentine Aneurysms: Spontaneous Changes of Angiographic Filling Pattern

S.G. Kandemirli, S. Cekirge, I. Oran, I. Saatci, O. Kizilkilic, C. Cinar, C. Islak, and N. Kocer

## ABSTRACT

**BACKGROUND AND PURPOSE:** Serpentine aneurysms are partially thrombosed aneurysms with an eccentrically located tortuous intra-aneurysmal vascular channel. The large size, distinctive neck anatomy, and supply of the brain parenchyma by the outflow tract pose technical challenges in treatment. The aim of this study was to discuss the endovascular treatment results and illustrate the dynamic nature of serpentine aneurysms. Spontaneous transformation of saccular and fusiform aneurysms into serpentine morphology, along with a case of serpentine-into-fusiform aneurysm transformation during follow-up, is presented.

**MATERIALS AND METHODS:** A retrospective analysis from 3 institutions revealed 15 patients with serpentine aneurysms who underwent diagnostic evaluation and endovascular treatment. Nine of the 15 patients underwent endovascular occlusion of the parent vessel with detachable balloon or coils. Six of the 15 patients underwent aneurysm and parent artery occlusion with coiling.

**RESULTS:** In 11 patients, improvement or resolution of symptoms was achieved by an endovascular approach without any treatment-related morbidity. Morbidity related to treatment in the immediate postoperative period was seen in 3 patients, with resolution of the deficits at long-term follow-up in 2 patients and persistence of a mild deficit in 1 patient. Endovascular treatment failed to achieve resolution of symptoms in a case with a basilar tip aneurysm treated by aneurysm coiling.

**CONCLUSIONS:** Serpentine aneurysms are dynamic structures with spontaneous transformation possible from a saccular or fusiform shape into a serpentine configuration. An endovascular approach by parent vessel occlusion or intra-aneurysmal occlusion is a successful treatment technique for serpentine aneurysms.

**ABBREVIATIONS:** ACA = anterior cerebral artery; BTO = balloon test occlusion; ECA = external carotid artery; PAO = parent artery occlusion; PCA = posterior cerebral artery

Serpentine aneurysms constitute a rare form of intracranial aneurysms with unique radiologic and pathologic features.[1,2] Serpentine aneurysms are partially thrombosed aneurysms and contain an eccentrically located tortuous intra-aneurysmal vascular channel.[3,4] The main distinctive features are the presence of separate inflow and outflow tracts and supply of the brain parenchyma by the outflow tract.[4,5] The pathogenesis of serpentine aneurysms is not clear, and several hypotheses have been proposed to explain the evolutionary features.[6-8] The most widely accepted mechanism is continued expansion of a saccular aneurysm into a serpentine configuration termed the "Coanda effect."[6] The common entity in the pathophysiology of serpentine aneurysms is the dynamic nature of thrombosis and aneurysm formation.[4]

The large size, distinctive neck anatomy, and supply of the brain parenchyma by the outflow tract pose technical challenges in treatment.[4] In the initial reports, surgical obliteration alone was the mainstay treatment; however, surgical external carotid artery (ECA)-ICA anastomosis and an endovascular approach have expanded the treatment options.[4,8]

This study focused on the clinical and imaging findings of 15 patients with serpentine aneurysms treated by endovascular routes. We present cases of saccular and fusiform aneurysms evolving into serpentine aneurysms during follow-up to illustrate the possible formation mechanisms of serpentine aneurysms. Additionally, a case of spontaneous transformation of a serpentine aneurysm into a fusiform aneurysm is presented that has not been

Received April 9, 2018; accepted after revision June 12.

From the Division of Neuroradiology (S.G.K., O.K., C.I., N.K.), Department of Radiology, Cerrahpasa Medical Faculty, Istanbul University, Istanbul, Turkey; Interventional Neuroradiology Department (S.C.), Koru and Bayındır Hospital, Ankara, Turkey; Division of Neuroradiology (I.O., C.C.), Department of Radiology, Ege University Medical Faculty, İzmir, Turkey; and Interventional Neuroradiology Department (S.C., I.S.), Yuksek Ihtisas University, Koru Hospital, Ankara, Turkey.

Please address correspondence to Naci Kocer, MD, Department of Radiology, Division of Neuroradiology, Cerrahpasa Medical Faculty, Istanbul University, Kocamustafapasa/Istanbul 34098, Turkey; e-mail: nkocer@istanbul.edu.tr

Indicates article with supplemental on-line tables.

http://dx.doi.org/10.3174/ajnr.A5746

reported in the literature previously. These cases illustrate the dynamic nature of the mechanisms involved in serpentine aneurysm pathogenesis.

## MATERIALS AND METHODS

A retrospective analysis of the medical records from 3 institutions revealed 21 patients with serpentine aneurysms who had endovascular or surgical treatment. Fifteen patients who underwent endovascular treatment constituted the study group. Patients with surgical intervention alone were not included in this study.

All patients underwent selective cerebral angiography in addition to a CT scan and/or MR imaging. At the time of diagnosis, 5 of the 15 patients had not received treatment initially. However, 4 of them were subsequently treated with an endovascular route due to worsening of symptoms at follow-up.

The age range was 17–70 years (mean, 40.2 years) with a male-to-female ratio of 1.14. The main presenting features were headache, neurologic deficits secondary to mass effect, or distal emboli (On-line Table 1). The neurologic deficits included hemiparesis, sensory symptoms, cranial nerve involvement, and brain stem compression symptoms. One patient initially presenting with headache refused treatment and later presented with rupture of the aneurysm.

Ten aneurysms involved the anterior circulation (7 at the MCA, 2 at the ICA, and 1 at the anterior cerebral artery [ACA]), whereas 5 aneurysms involved the posterior circulation (1 basilar artery, 4 posterior cerebral arteries [PCAs]) (On-line Table 1). Mean aneurysm size was 4.9 cm, with a minimum size of 2.5 cm and maximum size of 8 cm.

Nine of the 15 patients underwent endovascular occlusion of the parent vessel with detachable balloons (2 patients) and detachable coils (7 patients). Six of the 15 patients underwent aneurysm and parent artery occlusion with coiling (in 2 of them, Onyx [Covidien, Irvine, California] was used as an adjunctive embolic material). In a single case, bypass surgery was performed before endovascular aneurysm occlusion.

Systemic anticoagulation during endovascular treatment was achieved by bolus infusion of 5000 IU of heparin after insertion of a femoral sheath. The bolus infusion of heparin was followed by a continuous drip (1000–1500 IU/h) to double the baseline activated clotting time.

Balloon test occlusion (BTO) before endovascular treatment was performed for 5 of 15 patients (a single cavernous ICA aneurysm and 4 proximal MCA aneurysms). During BTO, collateral filling of the occluded side through the circle of Willis or via other collaterals (such as pial-pial) and the transit time to the venous phase (which should demonstrate a $<$2-second difference compared with nonoccluded regions) were evaluated. While BTO showed adequate collateral flow in 4 patients (cases 2, 3, 8, and 9), there was inadequate flow in 1 patient (case 11) in whom intracranial bypass surgery was performed before the endovascular parent artery occlusion. Test occlusion before endovascular treatment was not performed for distally located aneurysms (4 PCA, 3 MCA M2–M3, 1 ACA, and 1 basilar tip aneurysm). Additionally, BTO could not be performed due to technical difficulty in a case with a supraclinoid ICA aneurysm.

## RESULTS

In 11 patients, improvement or resolution of symptoms was achieved by an endovascular approach without any treatment-related morbidity.

New MR imaging positive for ischemic complications was seen in 3 patients (cases 3, 11, and 14). Deficits totally resolved in 2 cases, whereas 1 case had a mild deficit at follow-up. No clinically silent new ischemic region in the postoperative period was observed in the remaining 12 patients. Additionally, no hemorrhagic findings complicated the postoperative course.

Case 11 had a left MCA inferior trunk aneurysm and presented with multiple transient ischemic attacks before treatment. In this patient, BTO showed inadequate collateral supply, and intracranial bypass was performed before aneurysm occlusion. This patient still had a slight right hemiparesis and facial paresis in the immediate postoperative period with resolution of deficits at the 3-month follow-up. Case 14 had a left PCA aneurysm treated by parent artery occlusion (PAO). BTO was not performed in this case. Right hemihypesthesia and right thalamic hand syndrome developed in the immediate postembolization period with total resolution at the 1-year follow-up.

Case 3 with a left MCA (M1–M2 segments) aneurysm had adequate collateral supply during BTO occlusion. Following intra-aneurysmal coiling and PAO, the patient had new-onset dysphasia and right hemiparesis. During follow-up, deficits partially ameliorated, the patient presented with intense headache at the 2-month follow-up. MR imaging revealed abscess formation along with extensive edema around the aneurysm sac. The patient underwent total resection of the abscess cavity and aneurysm. On the postoperative course, the patient had persistence of mild dysphasia with total resolution of right hemiparesis.

Endovascular treatment failed to achieve resolution of symptoms in a case (case 5) with a basilar tip aneurysm treated by aneurysm coiling. There was a substantial increase in brain stem compression with worsening of symptoms at the 6-month follow-up.

At follow-up (mean duration of 27 months), no recanalization of the aneurysm sac was observed. In a single case (case 5), there was an increase in brain stem compression at the 6-month follow-up. Perianeurysmal edema regressed in all other cases; additionally, aneurysm mass size decreased in 8 cases.

Among the 15 aneurysms, 12 patients presented with serpentine morphology; 3 of 15 aneurysms (cases 1, 3, and 8) did not have a serpentine morphology initially and changed into a serpentine configuration spontaneously during follow-up. Aneurysms in case 8 had a saccular shape, and cases 1, 3 had a fusiform shape initially. In a single case, spontaneous transformation of a serpentine aneurysm into a fusiform aneurysm was seen at the 2-year follow-up (case 2).

Herein, we describe these cases in detail to illustrate the different formation mechanisms of serpentine aneurysms.

### *Spontaneous Transformation of a Saccular Aneurysm into a Serpentine Aneurysm (Case 8)*

A 37-year-old woman presented with severe headache (Fig 1). Diagnostic imaging revealed a saccular aneurysm at the left MCA bifurcation. Per the patient's preference, she did not undergo treatment at the initial presentation. Five years later, the patient

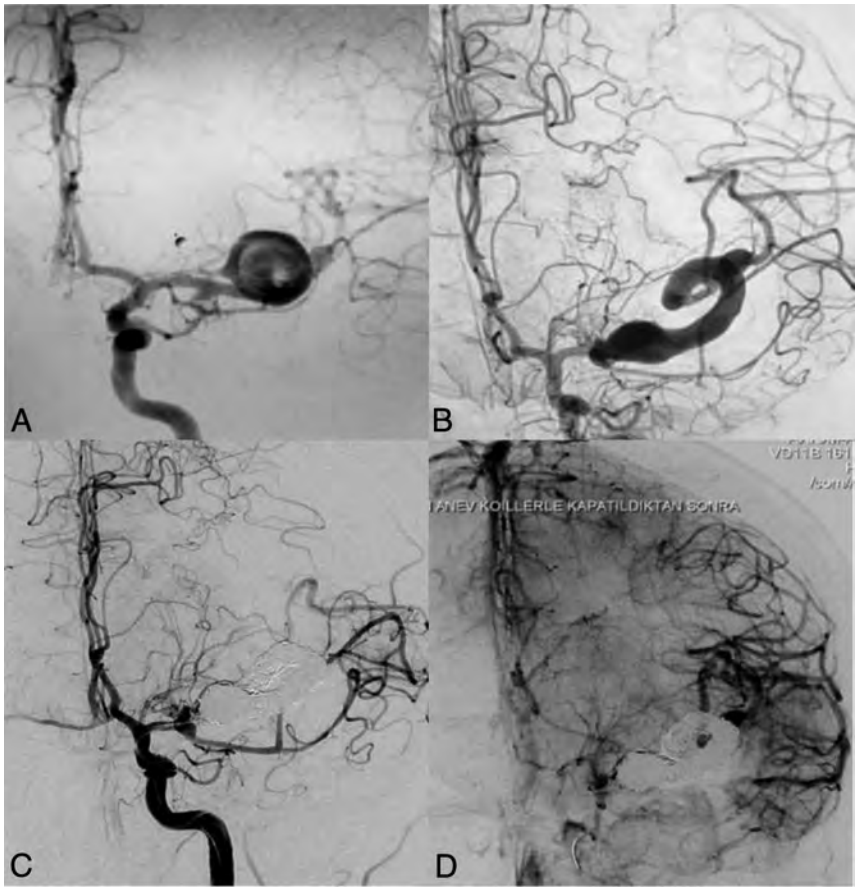


**FIG 1.** A 37-year-old woman who presented with severe headache. *A*, Left ICA angiography shows a saccular aneurysm (1.44 × 1.65 cm) at the left MCA bifurcation. *B*, Repeat angiography 5 years later reveals marked enlargement of the aneurysm (5 × 4 × 4 cm) with incorporation of the upper MCA trunk into the serpentine aneurysm lumen. *C* and *D*, Endovascular occlusion of the serpentine aneurysm and the parent artery by coiling and Onyx injection was performed.

presented with worsening of symptoms. On DSA, marked enlargement of the aneurysm with a change into a serpentine configuration was noted. The patient tolerated a balloon test occlusion, and the lumen of the serpentine aneurysm was occluded by coiling and Onyx injection. At 1-year follow-up, the patient was neurologically intact with resolution of the perianeurysmal edema and absence of flow in the aneurysm.

### *Spontaneous Transformation of a Fusiform Aneurysm into a Serpentine Aneurysm (Cases 1 and 3)*

At the initial presentation, 2 cases with fusiform aneurysms were managed conservatively (Figs 2 and 3). These cases presented with worsening of symptoms at the long-term follow-up (1 and 6 years), at which time the diagnostic examinations revealed enlargement of the aneurysms and evolution of fusiform aneurysms into serpentine aneurysms.

In case 1, a 32-year-old man presented with headache and diaphoresis. Cerebral angiography at the time of initial evaluation showed fusiform enlargement of the right PCA. No treatment was performed initially. Six years later, the patient presented with worsening of symptoms, and diagnostic imaging revealed marked enlargement of the aneurysm along with edema. The initially fusiform aneurysm had transformed into a serpentine configuration. The patient was treated by parent vessel occlusion of the PCA with detachable coils. The distal PCA branches were opacified by pial-pial collaterals through the MCA. At 1-year follow-up, the patient was neurologically intact with resolution of symptoms. DSA at 1 year showed exclusion of the aneurysm lumen from circulation and stable perfusion of the distal PCA territory with a thrombosed mass.

Case 3 was a fusiform aneurysm of the left MCA (M1–M2 segments) in a 39-year-old female patient who presented with headache. The patient presented with worsening of symptoms 1 year later, when DSA revealed marked enlargement of the fusiform aneurysm. Endovascular treatment was contemplated. Six days later, during endovascular treatment, the aneurysm acquired a doughnut shape with partial intra-aneurysmal thrombosis. Intra-aneurysmal coiling was performed. In the immediate postoperative period, the patient had dysphasia and right hemiparesis. The postoperative course was further complicated by abscess formation adjacent to the coiled aneurysm, which required surgical drainage and resection of the abscess cavity. At the 6-month follow-up, the patient had mild dysphasia with resolution of right hemiparesis.

### *Spontaneous Transformation of a Serpentine Aneurysm into a Fusiform Aneurysm (Case 2)*

A 39-year-old woman presented with headache and diplopia; cerebral DSA revealed a giant serpentine aneurysm in the cavernous segment of the right ICA (Fig 4). No treatment was contemplated at the time of initial evaluation. At 2-year follow-up, DSA revealed transformation of the serpentine aneurysm into a fusiform aneurysm with no change in patient symptoms. The patient opted for treatment and was treated by PAO using a detachable balloon. Postoperatively, the patient had no neurologic deficit.

## DISCUSSION

In our review of the literature, there were 101 giant serpentine aneurysms (On-line Table 2). Serpentine aneurysms were seen more commonly in young males, with a male-to-female ratio of 1.86 at an average age of 35.6 years (range, 4–71 years) (On-line Table 2). Seventy aneurysms (69.3%) involved the anterior circulation, where 48 aneurysms (47.5%) were in the MCA territory, 18 aneurysms (12.9%) were within the ICA, and 9 aneurysms (8.9%) were within the ACA. Thirty-one aneurysms (30.7%) involved the posterior circulation, where 17 aneurysms (16.8%) were in the PCA and 14 aneurysms (13.9%) involved the vertebral artery,

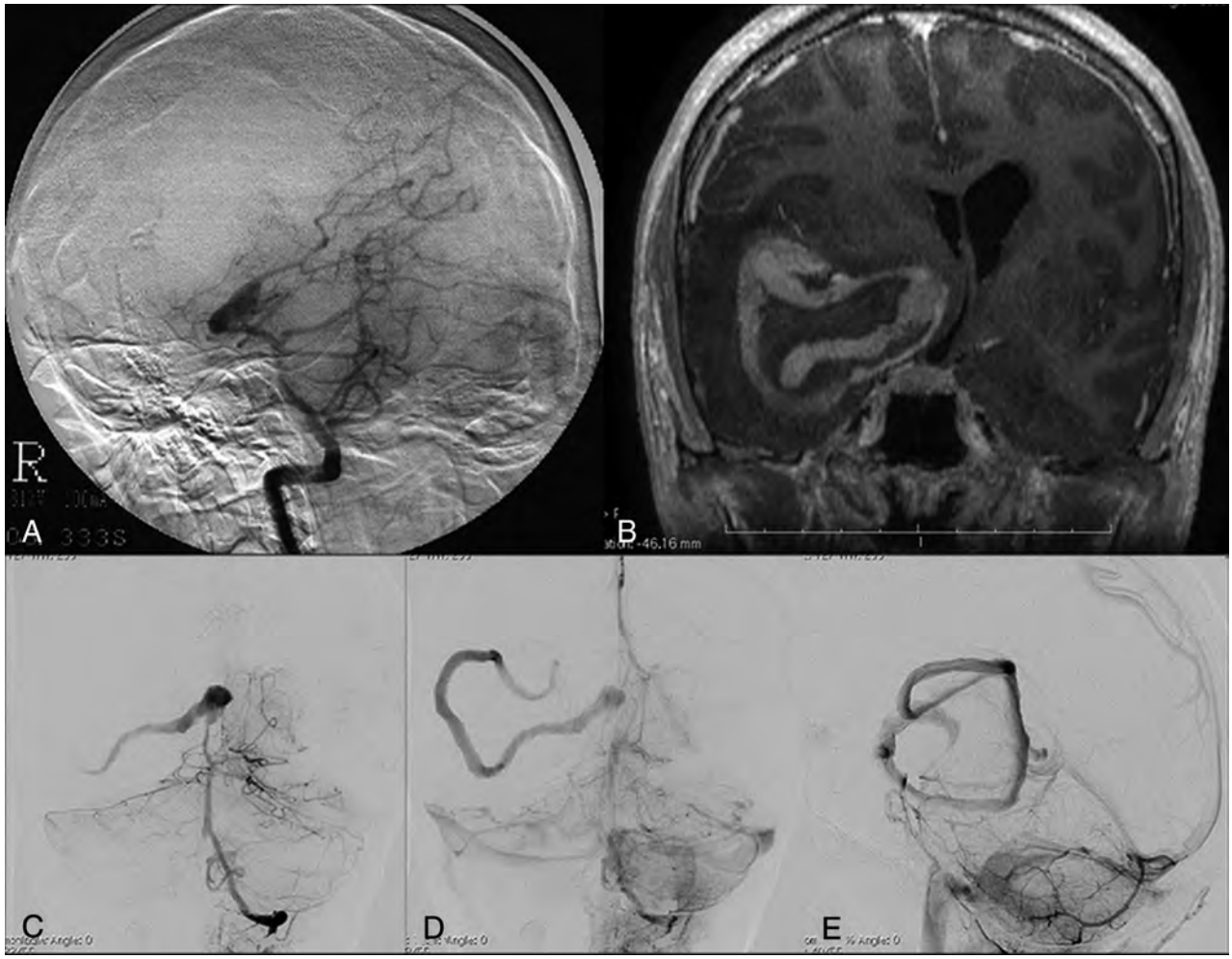


**FIG 2.** A 32-year-old man who presented with headache and diaphoresis. *A*, Cerebral angiography shows fusiform enlargement of the right PCA (P2 and P3 segments). *B*, Six years later, postcontrast MR imaging reveals an enhancing vascular channel on the postgadolinium T1-weighted image surrounded by nonenhancing thrombus. Note the associated mass effect and midline shift. *C–E*, Cerebral angiography demonstrates marked enlargement of the aneurysm with a tortuous vascular channel.

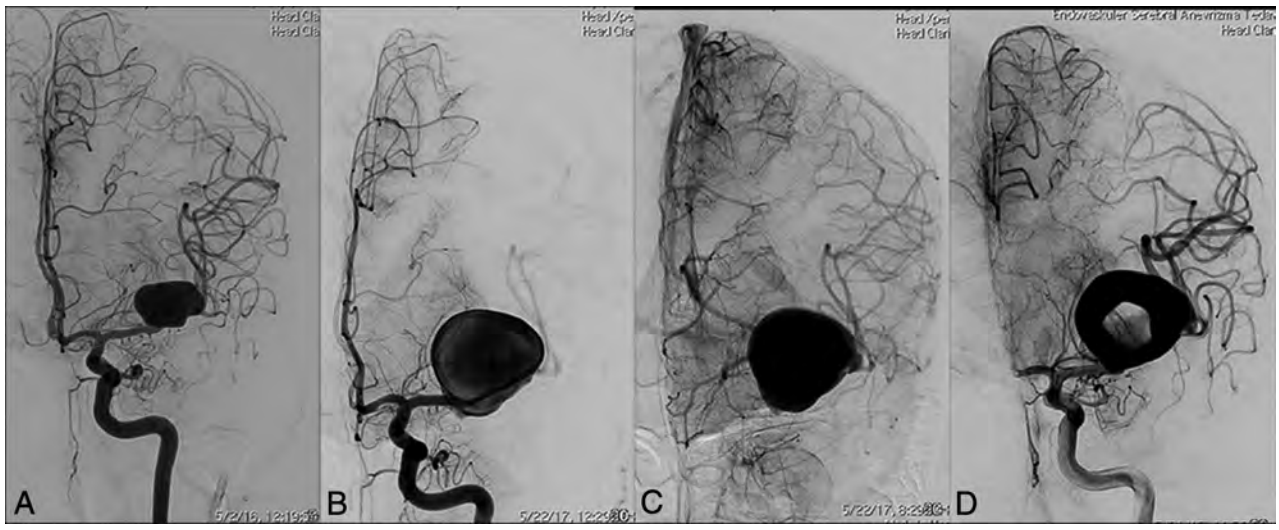


**FIG 3.** A 39-year-old woman who presented with headache. *A*, Cerebral angiography shows a fusiform aneurysm involving the left MCA M1 and M2 segments. *B* and *C*, DSA 1 year later demonstrates marked enlargement of the fusiform aneurysm with sluggish intra-aneurysmal blood flow. *D*, Six days later, angiography before endovascular treatment reveals partial intra-aneurysmal thrombosis with the classic doughnut shape evident.

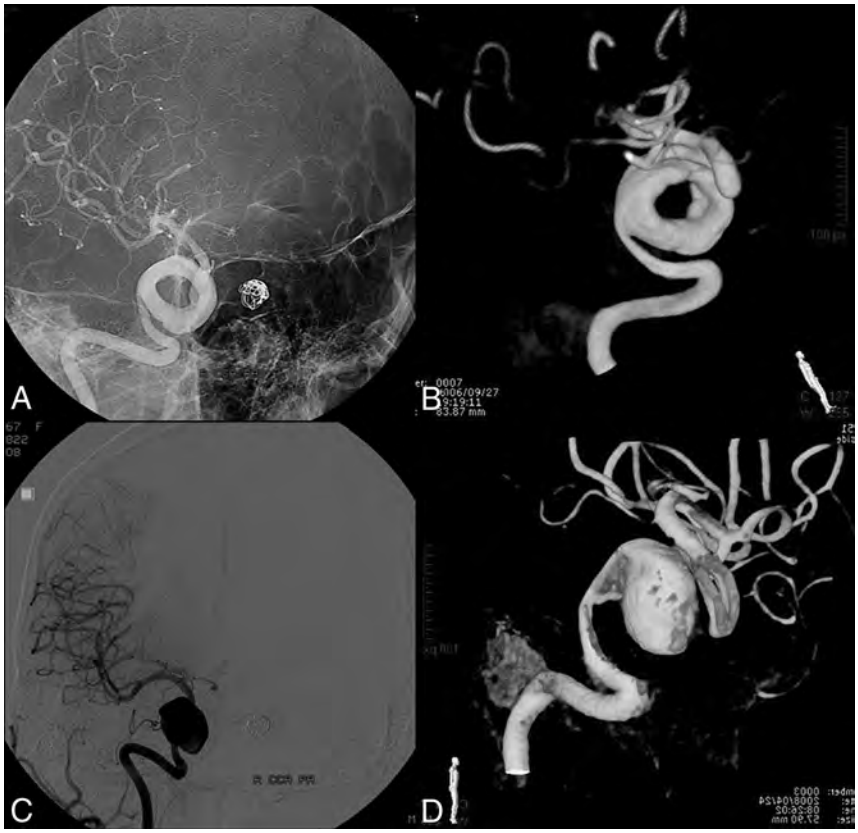


**FIG 4.** A 39-year-old woman who presented with headache and diplopia. *A* and *B*, Initial cerebral angiography shows a giant serpentine aneurysm in the cavernous segment of the right ICA. *C* and *D*, Repeat angiogram at the 2-year follow-up demonstrates that the aneurysm has lost its serpentine formation and acquired a fusiform morphology.

vertebrobasilar junction, basilar artery, posterior communicating artery, PICA, or superior cerebellar artery (On-line Table 2). The main presenting feature was symptoms related to mass effect, in which distinct symptomatology was based on the location of the aneurysm.[4,5,8-10] Although it is generally accepted that serpentine aneurysms are protected against rupture by the thick fibrous wall, Suzuki et al[11] reported a 28% rate of subarachnoid hemorrhage in 39 serpentine aneurysms. Another cause of morbidity and mortality is related to ischemic stroke in the territory supplied by the serpentine aneurysm.[12] In our series, up to treatment time, 2 patients had distal emboli, whereas a case of rupture was seen in a single patient who initially presented with headache and refused treatment and later presented with SAH.

The pathologic examinations of serpentine aneurysms have shown tortuous vascular channels within old organized thrombus containing revascularization.[3,6,13-16] The walls of the aneurysms are composed primarily of acellular, fibrous tissue and lack an internal elastic lamina or endothelial layer.[3,4] Additionally, arterial vessels similar to the vasa vasorum that course through the adventitial layer of the aneurysm have been described.[4,6]

In conservative management of serpentine aneurysms, there is a high rate of neurologic deterioration and death.[11] The aim of treatment is to decrease the mass effect while maintaining adequate distal circulation. A variety of surgical techniques has been used in the treatment of serpentine aneurysms. Visualization of perforating vessels and separation from the parent vessel, brain retraction required for proximal control, and the rich peripheral vascular supply of the aneurysm could cause challenges and marked blood loss during an operation.[4,5] Additionally, the outflow channel of the aneurysm supplies the normal brain parenchyma. If there is inadequate collateral supply of the brain parenchyma, revascularization procedures (like ECA-ICA bypass) may be needed before aneurysm occlusion.[17-19] We assessed collateral flow by BTO in certain aneurysms; no Wada testing was performed in this study group. We have not performed BTO in certain regions like the PCA or distal MCA territory because there is a risk of endothelial damage with possible retrograde thrombosis.[1] Especially for the PCA supply region, which has a rich collateral supply from the ACA and MCA, a low incidence of visual field deficits complicating parent artery occlusion has been reported.[10]

An endovascular approach by parent vessel occlusion using coils or detachable balloons has been successfully used in cases with an established adequate distal collateral supply.[5,9,20] Aneurysm occlusion by trapping or proximal occlusion using coils or glue has been reported.[2,21] In our series, 11 patients (73.3%) achieved improvement or resolution of symptoms following therapy without treatment-related morbidity, whereas 3 cases (20%) had distal infarction, with total resolution of symptoms in 2 of these patients.

The pathogenesis of serpentine aneurysms is not clear. Unlike saccular aneurysms, serpentine aneurysms do not have a predilection for arterial branch points, indicating a different pathophysiology compared with saccular aneurysms.[3] The most accepted hypothesis is the Coanda effect proposed by Fodstad et al.[6] In their initial report, Fodstad et al treated a giant intracavernous aneurysm by carotid artery ligation. Following ligation, partial thrombi formed in the aneurysm with incomplete occlusion of the aneurysm. Six months later, the incompletely occluded aneurysm evolved into a giant serpentine aneurysm. This transformation of a saccular aneurysm into a serpentine aneurysm can be explained by continuing blood flow into a large incompletely occluded aneurysm. This mechanism is termed as the Coanda effect, in which the jet flow of blood is directed and reinforced toward one wall instead of the central portion of the aneurysm.[15] Subsequently, blood flow in the central portion of the aneurysm and adjacent arterial wall is markedly decreased, with predisposition to stagnant blood flow and thrombus formation. Because of thrombus formation, the aneurysm enlarges and evolves into a serpentine configuration. The Coanda effect also explains the

higher predilection of serpentine aneurysms in the MCA territory compared with the ICA. The higher jet force of the blood flow prevents stagnation of blood in the ICA, whereas the jet force of blood flow is lower in the MCA with predisposition to stagnation and thrombus formation. Another reason for higher MCA predilection is the absence of dural or osseous structures to limit expansion of the aneurysm in the MCA territory.[6,22]

In the literature, there are also cases reporting spontaneous evolution of fusiform aneurysms into giant serpentine aneurysms.[1,7,23,24] Initially, Tomasello et al[23] described a case of a small MCA fusiform aneurysm that progressed to a serpentine aneurysm during 5 years. In a similar case, Senbokuya et al[7] reported a case of a distal ACA aneurysm that evolved into a serpentine aneurysm after 5 months. In our series, there were 2 cases of spontaneous transformation of fusiform aneurysms into serpentine aneurysms during 6 days to 6 years. In case 3, a fusiform aneurysm was transformed into a serpentine aneurysm 6 days later, following diagnostic angiography. Six days later, thrombosis within the aneurysm and a doughnut-like configuration were noted. This phenomenon of angiography inducing thrombosis in a giant aneurysm has also been reported in the literature.[25] In this case, the authors proposed that thrombosis might be related to the internal thrombosis initiated by the contrast agent used in angiography.[25] Arterial dissection may also be the initial event in the development of serpentine aneurysms; Verny et al[26] reported a case of an MCA dissecting aneurysm that evolved into a serpentine aneurysm during 11 years.

Spontaneous complete occlusion of a giant saccular aneurysm is a well-recognized phenomenon that can occur in 13%–20% of cases; however, spontaneous thrombosis in serpentine aneurysms is rarely reported, with 3 cases available in the literature.[5,25,27] The first case was reported by Aletich et al,[5] in which an MCA serpentine aneurysm was spontaneously thrombosed with persistent thrombosis documented at the 1-year follow-up. Similarly, Sari et al[25] have reported a case of spontaneous and complete thrombosis of a serpentine aneurysm with persistent thrombosis documented at the 3-year follow-up. Spontaneous occlusion of a serpentine aneurysm can be related to slow blood flow and thrombus formation.[28] Endothelial damage related to turbulent blood flow may also be an important factor in thrombus formation. However, even complete thrombosis of a serpentine aneurysm should not be considered stable because Lee et al[29] reported recanalization of a completely thrombosed serpentine aneurysm. The exact mechanism of recanalization is not clear; however, thrombus liquefaction and subsequent intrathrombotic dissection by blood flow might be involved. In addition to spontaneous thrombosis, as demonstrated in our series, spontaneous transformation of serpentine aneurysms into fusiform aneurysms may occur. This reflects the dynamic nature of intra-aneurysmal thrombosis that can spontaneously recanalize.

## CONCLUSIONS

Serpentine aneurysms are partially thrombosed aneurysms with a patent, tortuous vascular lumen coursing through the aneurysm. We presented cases of spontaneous evolution of saccular and fusiform aneurysms into serpentine aneurysms during follow-up. Additionally, a case of spontaneous transformation of a serpentine aneurysm into a fusiform aneurysm is presented, indicating the dynamic nature of thrombosis involved in serpentine aneurysm pathogenesis.

Disclosures: Saruhan Cekirge—*UNRELATED*: *Consulting Fee or Honorarium*: Medtronic, MicroVention; *Stock/Stock Options*: eLUM Technologies, NDI Inc. Isil Saatci—*UNRELATED*: *Consultancy*: Medtronic, MicroVention. Civan Islak—*UNRELATED*: *Patents (Planned, Pending or Issued)*: floating diameter embolic coil US 2015/0327868; *Stock/Stock Options*: Neuro Device Innovations Inc, *Comments*: 10% shareholder. Naci Kocer—*UNRELATED*: *Consultancy:* MicroVention; *Payment for Lectures Including Service on Speakers Bureaus*: MicroVention; *Travel/Accommodations/Meeting Expenses Unrelated to Activities Listed*: MicroVention.

## REFERENCES

1. Coley SC, Hodgson TJ, Jakubowski J. **Coil embolization of giant serpentine aneurysms: report of two cases arising from the posterior cerebral artery.** *Br J Neurosurg* 2002;16:43–47 CrossRef Medline
2. van Rooij WJ, Sluzewski M, Beute GN. **Endovascular treatment of giant serpentine aneurysms.** *AJNR Am J Neuroradiol* 2008;29:1418–19 CrossRef Medline
3. Segal HD, McLaurin RL. **Giant serpentine aneurysm: report of two cases.** *J Neurosurg* 1977;46:115–20 CrossRef Medline
4. Christiano LD, Gupta G, Prestigiacomo CJ, et al. **Giant serpentine aneurysms.** *Neurosurg Focus* 2009;26:E5 CrossRef Medline
5. Aletich VA, Debrun GM, Monsein LH, et al. **Giant serpentine aneurysms: a review and presentation of five cases.** *AJNR Am J Neuroradiol* 1995;16:1061–72 Medline
6. Fodstad H, Liliequist B, Wirell S, et al. **Giant serpentine intracranial aneurysm after carotid ligation: case report.** *J Neurosurg* 1978;49:903–09 CrossRef Medline
7. Senbokuya N, Kanemaru K, Kinouchi H, et al. **Giant serpentine aneurysm of the distal anterior cerebral artery.** *J Stroke Cerebrovasc Dis* 2012;21:910.e917–11 CrossRef Medline
8. Xu K, Yu T, Guo Y, et al. **Study and therapeutic progress on intracranial serpentine aneurysms.** *In J Med Sci* 2016;13:432–39 CrossRef Medline
9. Mawad ME, Klucznik RP. **Giant serpentine aneurysms: radiographic features and endovascular treatment.** *AJNR Am J Neuroradiol* 1995;16:1053–60 Medline
10. Xianli L, Youxiang L, Liu A, et al. **Endovascular treatment of intracranial giant serpentine aneurysms.** *Neuroradiol J* 2007;20:237–41 CrossRef Medline
11. Suzuki S, Takahashi T, Ohkuma H, et al. **Management of giant serpentine aneurysms of the middle cerebral artery: review of literature and report of a case successfully treated by STA-MCA anastomosis only.** *Acta Neurochir (Wien)* 1992;117:23–29 CrossRef Medline
12. Mahadevan A, Tagore R, Siddappa NB, et al. **Giant serpentine aneurysm of vertebrobasilar artery mimicking dolichoectasia: an unusual complication of pediatric AIDS—report of a case with review of the literature.** *Clin Neuropathol* 2008;27:37–52 CrossRef Medline
13. Sadik AR, Budzilovich GN, Shulman K. **Giant aneurysm of middle cerebral artery: a case report.** *J Neurosurg* 1965;22:177–81 CrossRef Medline
14. Terao H, Muraoka I. **Giant aneurysm of the middle cerebral artery containing an important blood channel: case report.** *J Neurosurg* 1972;37:352–56 CrossRef Medline
15. Cantu RC, LeMay M. **A large middle cerebral aneurysm presenting as a bizarre vascular malformation.** *Br J Radiol* 1966;39:317–19 CrossRef
16. Belec L, Cesaro P, Brugieres P, et al. **Tumor-simulating giant serpentine aneurysm of the posterior cerebral artery.** *Surg Neurol* 1988;29:210–15 CrossRef Medline
17. Amin-Hanjani S, Chen PR, Chang SW, et al. **Long-term follow-up of giant serpentine MCA aneurysm treated with EC-IC bypass and proximal occlusion.** *Acta Neurochir (Wien)* 2006;148:227–28 CrossRef Medline
18. Isla A, Alvarez F, Roda JM, et al. **Serpentine aneurysm: regrowth after a superficial temporal artery-middle cerebral artery bypass**

**and internal carotid artery ligation: case report.** *Neurosurgery* 1994; 34:1072–74 Medline
19. Greene KA, Anson JA, Spetzler RF. **Giant serpentine middle cerebral artery aneurysm treated by extracranial-intracranial bypass: case report.** *J Neurosurg* 1993;78:974–78 CrossRef Medline
20. Fanning NF, Kelleher MO, Ryder DQ. **The pretzel sign: angiographic pattern of tortuous intra-aneurysmal blood flow in a giant serpentine aneurysm.** *Br J Neurosurg* 2003;17:67–71 Medline
21. Otsuka G, Miyachi S, Handa T, et al. **Endovascular trapping of giant serpentine aneurysms by using Guglielmi detachable coils: successful reduction of mass effect: report of two cases.** *J Neurosurg* 2001; 94:836–40 CrossRef Medline
22. Kumabe T, Kaneko U, Ishibashi T, et al. **Two cases of giant serpentine aneurysm.** *Neurosurgery* 1990;26:1027–32; discussion 1032–33 CrossRef Medline
23. Tomasello F, Albanese V, Cioffi FA. **Giant serpentine aneurysms: a separate entity.** *Surg Neurol* 1979;12:429–32 Medline
24. Anson JA, Lawton MT, Spetzler RF. **Characteristics and surgical treatment of dolichoectatic and fusiform aneurysms.** *J Neurosurg* 1996;84:185–93 CrossRef Medline
25. Sari A, Kandemir S, Kuzeyli K, et al. **Giant serpentine aneurysm with acute spontaneous complete thrombosis.** *AJNR Am J Neuroradiol* 2006;27:766–68 Medline
26. Verny C, Marc G, Pasco A, et al. **Middle cerebral artery dissection gives rise to giant serpentine aneurysm.** *Cerebrovasc Dis* 2008;25: 283–85 CrossRef Medline
27. McLaughlin N, Denis D, Bojanowski MW. **Neoangiogenesis of a serpentine middle cerebral artery aneurysm.** *Acta Neurochir (Wien)* 2012;154:63–64 CrossRef Medline
28. Pany A, Sobri M, Valarmathi S, et al. **Giant serpentine middle cerebral artery aneurysm.** *Med J Malaysia* 2004;59:422–24 Medline
29. Lee KC, Joo JY, Lee KS, et al. **Recanalization of completely thrombosed giant aneurysm: case report.** *Surg Neurol* 1999;51:94–98 CrossRef Medline

# Acutely Ruptured Intracranial Aneurysms Treated with Flow-Diverter Stents: A Systematic Review and Meta-Analysis

F. Cagnazzo, D.T. di Carlo, M. Cappucci, P.-H. Lefevre, V. Costalat, and P. Perrini

## ABSTRACT

**BACKGROUND:** The implantation of flow-diverter stents for the treatment of ruptured intracranial aneurysms required further investigation.

**PURPOSE:** Our aim was to analyze the outcomes after flow diversion of ruptured intracranial aneurysms.

**DATA SOURCES:** A systematic search of 3 databases was performed for studies published from 2006 to 2018.

**STUDY SELECTION:** According to the Preferred Reporting Items for Systematic Reviews and Meta-Analyses guidelines, we included studies (from 2010 to 2018) reporting acutely ruptured intracranial aneurysms treated with flow diversion.

**DATA ANALYSIS:** Random-effects meta-analysis was used to pool the following: aneurysm occlusion rate, complications, rebleeding, and factors influencing the studied outcomes.

**DATA SYNTHESIS:** We included 20 studies evaluating 223 patients with acutely ruptured intracranial aneurysms treated with flow-diverter stents. Immediate angiographic occlusion was obtained in 32% (29/86; 95% CI, 15.4%–48%; $I^2 = 79.6\%$) of aneurysms, whereas long-term complete/near-complete aneurysm occlusion was 88.9% (162/189; 95% CI, 84%–93.5%; $I^2 = 20.9\%$) (mean radiologic follow-up of 9.6 months). The treatment-related complication rate was 17.8% (42/223; 95% CI, 11%–24%; $I^2 = 52.6\%$). Complications were higher in the posterior circulation (16/72 = 27%; 95% CI, 14%–40%; $I^2 = 66\%$ versus 18/149 = 11.7%; 95% CI, 7%–16%; $I^2 = 0\%$) ($P = .004$) and after treatment with multiple stents (14/52 = 26%; 95% CI, 14%–45%; $I^2 = 59\%$) compared with a single stent (20/141 = 10%; 95% CI, 5%–15%; $I^2 = 0\%$) ($P = .004$). Aneurysm rebleeding after treatment was 4% (5/223; 95% CI, 1.8%–7%; $I^2 = 0\%$) and was higher in the first 72 hours.

**LIMITATIONS:** Small and retrospective series.

**CONCLUSIONS:** Flow-diversion treatment of ruptured intracranial aneurysms yields a high rate of long-term angiographic occlusion with a relatively low rate of aneurysm rebleeding. However, treatment is associated with a complication rate of 18%. When coiling or microsurgical clipping are not feasible strategies, anterior circulation ruptured aneurysms can be effectively treated with a flow-diversion technique, minimizing the number of stents deployed. Given the 27% rate of complications, flow diversion for ruptured posterior circulation aneurysms should be considered only in selected cases not amenable to other treatments.

**ABBREVIATIONS:** ASA = acetylsalicylic acid; CP = clopidogrel; IQR = interquartile range; PRISMA = Preferred Reporting Items for Systematic Reviews and Meta-Analyses

Flow diversion is increasingly used for a variety of intracranial aneurysms, especially complex lesions difficult to treat with conventional surgical or endovascular techniques. The thin, fragile walls and poorly defined neck make blister aneurysms particularly challenging lesions to treat with simple coiling or clipping, with not negligible rates of intraoperative aneurysm rupture.[1,2] Similarly, the lack of a true neck in the dissecting/fusiform aneurysms usually renders coiling and clipping impossible.[3] In addition, embolization of wide-neck and wide-neck bifurcation aneurysms without the use of adjunctive devices is difficult because of the instability of the coil mass. The flow-diversion devices work by diverting the flow away from the aneurysm, promoting progres-

Received April 13, 2018; accepted after revision May 25.

From the Department of Neurosurgery (F.C., D.T.d.C., P.P.), University of Pisa, Pisa, Italy; Radiology Department (M.C.), University of Rome Sapienza, Sant'Andrea Hospital, Rome, Italy; and Neuroradiology Department (P.-H.L., V.C.), University Hospital Güi-de-Chauliac, Centre Hospitalo-Universitaire de Montpellier, Montpellier, France.

Please address correspondence to Federico Cagnazzo, MD, Department of Neurosurgery, University of Pisa, Via Paradisa 2, 56100, Pisa, Italy; e-mail: f.cagnazzo86@gmail.com

Indicates article with supplemental on-line tables.

Indicates article with supplemental on-line photos.

http://dx.doi.org/10.3174/ajnr.A5730

sive intra-aneurysmal thrombosis, leading the treatment of complex lesions.[4] While a growing body of evidence corroborates the efficacy and safety of flow-diversion treatment of unruptured lesions,[5,6] the off-label indications of these devices are constantly extended, including acutely ruptured intracranial aneurysms.[7-26]

There are 2 main concerns when flow-diverter stents are used in acute SAH: 1) the management of the antiplatelet therapy (loading and maintaining dose), which is potentially associated with hemorrhagic complications, especially when additional surgical maneuvers are required (ventriculostomy or decompressive craniectomy); and 2) the prevention of aneurysm rebleeding.[17] The aim of our meta-analysis was to evaluate the safety and efficacy of the implantation of flow-diverter stents in the acute phase (0–30 days) of SAH for the treatment of ruptured intracranial aneurysms. In addition, we investigated the influence of aneurysm-related factors (type of aneurysm, location, and size), technical factors (number of devices or adjunctive coiling), patient-related factors, and the antiplatelet therapy administration on the studied outcomes.

## MATERIALS AND METHODS

### Literature Search

A comprehensive literature search of PubMed, Ovid MEDLINE, and Ovid EMBASE was conducted for studies published from January 2006 to March 2018. The Preferred Reporting Items for Systematic Reviews and Meta-Analyses (PRISMA[27]) guidelines were followed. Key words and the detailed search strategy are reported in On-line Table 1, and the studies included in our review (from 2010 to 2018) are reported in On-line Table 2. The inclusion criteria were the following: studies reporting series with >3 patients with ruptured intracranial aneurysms treated with flow-diverter stents in the acute phase. Treatment in the acute phase was considered within 30 days of SAH. Exclusion criteria were the following: 1) case reports, 2) review articles, 3) studies published in languages other than English, 4) in vitro/animal studies, and 5) flow diversion after 30 days of hemorrhage. In cases of overlapping patient populations, only the series with the largest number of patients or the most detailed data were included. Two independent readers screened articles in their entirety to determine eligibility for inclusion. A third author solved discrepancies.

### Data Collection

Data were extracted by 2 independent readers. A prespecified data-collection template was used for the data collection. A third author solved discrepancies about data extraction. We extracted the following: 1) occlusion rate, 2) treatment-related complications, 3) aneurysm rebleeding rate, and 4) clinical outcome. Occlusion and complication rates were analyzed on the basis of the influence of the following: 1) anterior-versus-posterior circulation aneurysms; 2) distal-versus-proximal location; 3) patient age (younger than 60 years versus older than 60 years); 4) low-grade SAH (Fisher 1–2 or Hunt and Hess 1–2 or World Federation of Neurosurgical Societies I–II) versus high-grade SAH (Fisher 3–4 or Hunt and Hess 3–5 or World Federation of Neurosurgical Societies III–V); 5) aneurysm size (saccular aneurysms small-medium-sized versus large-giant); 6) flow diverter alone versus flow diverter plus coiling; and 7) single-versus-multiple devices. Distal location was considered for lesions arising distal to the circle of Willis or located in small vessels: A2–3 segments, middle cerebral artery, posterior cerebral artery, posterior/anterior inferior cerebellar artery, and superior cerebellar artery. Complete/near-complete aneurysm occlusion was defined on the basis of the following: 1) the Raymond-Roy classification[28] (class 1–2); 2) the O'Kelly-Marotta grading scale[29] (grades C–D); or 3) when "complete occlusion" and "neck remnant" were used in the study. Treatment-related complications were divided into the following: 1) periprocedural/early events (within 30 days) and delayed events (after 30 days); 2) transient (asymptomatic events or complete neurologic recovery) and permanent complications (symptomatic events with permanent deficits). Finally, good outcome was defined as a modified Rankin Scale score of 0–2 or a Glasgow Outcome Score of 4–5; or good outcome was assumed if the study used terms such as "no morbidity," "good recovery," or "no symptoms."

### Outcomes

The primary objectives of this meta-analysis were to define the safety (treatment-related complications, mortality rate, and neurologic outcomes) and the efficacy (aneurysm occlusion and rebleeding rates) of the flow diversion of acutely ruptured intracranial aneurysms. The secondary objectives were to define the influence of aneurysm and patient characteristics as well as the effect of the antiplatelet therapy (loading dose and maintaining dose) on the analyzed outcomes.

### Quality Scoring

The Newcastle-Ottawa Scale[30] was used for the quality assessment of the included studies. The detailed scale evaluation is reported in On-lines Tables 3 and 4. In general, "high-quality" studies were defined on the basis of the following: 1) the presence of a predefined study protocol, 2) defined inclusion and exclusion criteria, 3) the presence of detailed information about treatment-related outcomes, and 4) adequate clinical and radiologic follow-up (it was considered when the follow-up time was longer than the median follow-up time of the reported studies). Accordingly, a star rating of 0–9 was allocated to each study. The quality assessment was performed by 2 authors independently, and a third author solved discrepancies. Studies receiving ≥6 stars were considered "high-quality."

### Statistical Analysis

We estimated, from each cohort, the cumulative prevalence (percentage) and 95% confidence interval for each outcome. To assess the heterogeneity of the data, we used the Higgins index ($I^2$); and subsequently, the DerSimonian and Laird random-effects model was applied. The graphic representation of the meta-analysis was performed with a forest plot. To evaluate the heterogeneity and bias, we analyzed the meta-regression and funnel plot followed by the Egger linear regression test, respectively. To compare the percentages and to calculate the $P$ values, a $Z$-test for 2 proportions was used. Differences were considered significant at $P < .05$. Statistical analyses were performed with SPSS, Version 2.3 (IBM, Armonk, New York), Prometa, Version 2 (Internovi, Cesena, Italy), and OpenMeta [Analyst] (http://www.cebm. brown.edu/openmeta/).

## RESULTS

### Literature Review

Studies included in our meta-analysis are summarized in On-line Table 2. The search flow diagram is shown in On-line Fig 1.

Twenty studies and 223 patients with acutely ruptured intracranial aneurysms treated with flow-diverter stents were included in our review.

### Quality of Studies

Overall, 15 studies (75%)[7, 8,10,12-14,16-18,21-26] were retrospective single-center series, 2 studies were retrospective multicentric series,[11,15] and 3 articles had a prospective design.[9,19,20] Two prospective articles were rated "high quality" (On-line-Table 4).

### Patient Population

Overall, 223 patients/aneurysms were treated with flow-diverter stents in the setting of SAH (On-line Table 5). The mean age of patients was 53.3 years (range, 5–80 years), and the proportion of male patients was 66% (95% CI, 59%–72%). Overall, 18.8% (42/223; 95% CI, 14%–24%) of aneurysms were saccular, 34.5% (77/223; 95% CI, 28%–40%) were dissecting/fusiform, and 46.6% (104/223; 95% CI, 40%–53%) were blister. Most of the aneurysms (150/223 = 67%; 95% CI, 60%–73%) were in the anterior circulation. The mean aneurysm size was 5.6 mm (median, 4 mm; interquartile range [IQR], 2–7 mm; range, 2–16 mm).

### Treatment Characteristics

The mean time between SAH and flow-diversion treatment was 6.7 days (median, 4 days; IQR, 3–9.6 days). Pipeline Embolization Devices (PED; Covidien, Irvine, California) were the most common stents used (86%; 95% CI, 81%–89%), followed by the Silk flow diverter (Balt Extrusion, Montmorency, France) (10.6%; 95% CI, 7.5%–14%), the Flow-Redirection Endoluminal Device (FRED; MicroVention, Tustin, California) (3%; 95% CI, 1.4%–5%), and the Surpass stent (Stryker Neurovascular, Kalamazoo, Michigan) (0.4%; 95% CI, 0.1%–2.2%). Most patients were treated with a single stent (75%; 95% CI, 68%–80%) and without adjunctive coils (81%; 95% CI, 75%–85%). The mean radiologic follow-up was 9.6 months (median, 7.5 months; IQR, 6–12 months), and the mean clinical follow-up was 7.5 months (median, 8.7 months; IQR, 6–12 months).

### Angiographic Outcomes

During a mean angiographic follow-up of 9.6 months, the overall rate of complete/near-complete occlusion was 88.9% (162/189; 95% CI, 84%–93.5%; $I^2$ = 20.9%). Meta-regression showed a nonsignificant variation of the effect size during the analyzed period ($P$ = .348), and the funnel plot followed by the Egger linear regression test excluded publication bias ($P$ = .058) (On-line Fig 2). Complete/near-complete occlusion was achieved in 79% (20/25; 95% CI, 64%–93%; $I^2$ = 0%) of saccular aneurysms, 89% (51/58; 95% CI, 82%–96%; $I^2$ = 0%) of dissecting/fusiform lesions, and 88% (76/89; 95% CI, 81%–95%; $I^2$ = 26%) of blister aneurysms. Immediate angiographic occlusion after stent deployment was obtained in 32% (29/86; 95% CI, 15.4%–48%; $I^2$ = 79.6%) of aneurysms: Twenty-eight percent (2/7; 95% CI, 3%–50%; $I^2$ = 0%) of saccular aneurysms, 45% (10/25; 95% CI, 18%–91%; $I^2$ = 90%) of dissecting/fusiform lesions, and 35% (17/54; 95% CI, 14%–56%; $I^2$ = 77%) of blister aneurysms were occluded immediately after flow-diversion treatment.

### Treatment-Related Complications

The overall complication rate was 17.8% (42/223; 95% CI, 11%–24%; $I^2$ = 52.6%) (On-line Table 6). Meta-regression showed a nonsignificant variation of the effect size during the analyzed period ($P$ = .111), and the funnel plot followed by the Egger linear regression test excluded publication bias ($P$ = .666) (On-line Fig 3). Complications were higher among saccular aneurysms (7/31 = 23%; 95% CI, 11%–49%; $I^2$ = 43%) compared with dissecting/fusiform (11/69 = 13%; 95% CI, 5%–20%; $I^2$ = 9%) and blister aneurysms (16/97 = 18%; 95% CI, 8%–27%; $I^2$ = 50%). Periprocedural/early and delayed complication rates were 16% (37/223; 95% CI, 10%–22%; $I^2$ = 47%) and 3% (5/223; 95% CI, 0.9%–6%; $I^2$ = 37.7%), respectively. The overall rates of transient and permanent complications were 9% (28/223; 95% CI, 4%–11%; $I^2$ = 0%) and 7% (16/223; 95% CI, 4%–11%; $I^2$ = 0%), respectively.

Overall, ischemic/thromboembolic and hemorrhagic events were 8% (26/223; 95% CI, 4.4%–11%; $I^2$ = 22%) and 7% (16/223; 95% CI, 3.5%–10%; $I^2$ = 0%), respectively. The rate of ischemic complications was 9.9% (4/31; 95% CI, 0.5%–19%; $I^2$ = 0%) among saccular aneurysms, 8.3% (6/69; 95% CI, 2%–14%; $I^2$ = 0%) among dissecting/fusiform lesions, and 10.2% (12/97; 95% CI, 4.5%–16%; $I^2$ = 0%) among blister aneurysms. The rate of hemorrhagic complications was 12% (3/31; 95% CI, 2%–22%; $I^2$ = 0%) among saccular aneurysms, 7.5% (5/69; 95% CI, 2%–13%; $I^2$ = 0%) among dissecting/fusiform lesions, and 6% (3/84; 95% CI, 1.2%–10%; $I^2$ = 0%) among blister aneurysms. The rate of acute in-stent thrombosis was 4% (6/223; 95% CI, 1.6%–6%; $I^2$ = 0%). The incidence of aneurysm rebleeding after treatment was 4% (5/223; 95% CI, 1.8%–7%; $I^2$ = 0%): Aneurysm rerupture occurred within the first 72 hours among one 21-mm fusiform aneurysm, 2 saccular giant lesions, and two 3- and 8-mm saccular aneurysms. The rate of rebleeding after treatment among the anterior and posterior circulation aneurysms was 4.6% (4/150; 95% CI, 1.3%–7.4%; $I^2$ = 0%) and 3% (1/73; 95% CI, 1.7%–12%; $I^2$ = 0%), respectively ($P$ = .56).

Treatment-related mortality was 4.5% (6/223; 95% CI, 2%–7%; $I^2$ = 0%), and the rate of good neurologic outcome was 83% (169/210; 95% CI, 76%–89%; $I^2$ = 0%).

### Factors Related to Aneurysm Occlusion

Overall, the occlusion rate was comparable among anterior-versus-posterior circulation aneurysms ($P$ = .27), proximal-versus-distally located aneurysms ($P$ = .28), low-versus-high-grade SAH ($P$ = .2), small-medium-sized versus large-giant aneurysms ($P$ = .6), flow diverter alone versus flow diverter plus coiling ($P$ = .12), and single-versus-multiple stents ($P$ = .61) (On-line Table 7). Patients younger than 60 years of age had a statistically significant higher rate of occlusion (105/120 = 90%; 95% CI, 85%–95%; $I^2$ = 0%) compared with older patients (older than 60 years) (43/52 = 76%; 95% CI, 64%–88%; $I^2$ = 49%) ($P$ = .01).

### Factors Related to Complications after Treatment

The complication rate was higher for ruptured aneurysms located in the posterior circulation (16/72 = 27%; 95% CI, 14%–40%; $I^2$ = 66%) compared with the anterior circulation (18/149 = 11.7%; 95% CI, 7%–16%; $I^2$ = 0%) ($P$ = .004) (On-line Table 7). In addition, complications were higher after treatment with multiple flow diverters (14/52 = 26%; 95% CI, 14%–45%; $I^2$ = 59%) compared with a single stent (20/141 = 10%; 95% CI, 5%–15%; $I^2$ = 0%) ($P$ = .004). There was no statistically significant difference in complication rates in relation to aneurysm location, patient age, aneurysm size, and flow diverter alone versus flow diverter plus coiling.

### Relationship between the Timing of Flow Diversion and Treatment-Related Outcomes

Flow diversion within and after 72 hours of SAH allowed comparable rates of aneurysm occlusion (50/61 = 85%; 95% CI, 7%–93%; $I^2$ = 0% versus 64/70 = 89%; 95% CI, 8%–9.5%; $I^2$ = 0%) ($P$ = .49) and treatment-related complications (16/81 = 18.6%; 95% CI, 10%–26%; $I^2$ = 0% versus 15/79 = 16%; 95% CI, 8%–23%; $I^2$ = 0%) ($P$ = .66) (On-line Table 8). Although not statistically significant, ischemic complications were higher after treatment between 72 hours and 30 days (12/79 = 14%; 95% CI, 7%–21%; $I^2$ = 0%) compared with flow diversion before 72 hours (8/81 = 10%; 95% CI, 4%–16%; $I^2$ = 0%) ($P$ = .43). On the contrary, there was a slightly higher rate of hemorrhagic complications when flow diversion was performed in the early phase (8/81 = 10%; 95% CI, 5%–18%; $I^2$ = 0%) compared with flow diversion after 72 hours (3/79 = 4%; 95% CI, 2%–13%; $I^2$ = 0%) ($P$ = .13). Similarly, the rebleeding rate was slightly higher after treatment within 72 hours (3/81 = 4%; 95% CI, 2%–10%; $I^2$ = 0% versus 1/79 = 1.2%; 95% CI, 0.8%–5%; $I^2$ = 0%) ($P$ = .26).

### Relationship between Antiplatelet Therapy and Treatment-Related Outcomes

There were 4 main groups of antiplatelet therapy: dual antiplatelet therapy with clopidogrel (CP) and acetylsalicylic acid (ASA), tirofiban, prasugrel, and abciximab (On-line Table 9). Overall, 67.7% (95% CI, 60%–73%) of patients were treated with CP + ASA. The occlusion rates and the treatment-related complications were quite comparable among the different types of antiplatelet therapy. Aneurysm rebleeding was 3% (95% CI, 9.6%–8%) and 2.8% (95% CI, 0.1%–15%) in the group of patients treated with CP + ASA and tirofiban, respectively.

### Study Heterogeneity

Substantial heterogeneity was reported in the following outcomes: overall rate of treatment-related complications, occlusion rate of anterior circulation aneurysms, and complication rate of aneurysms treated with a flow-diverter alone.

## DISCUSSION

The aim of the endovascular treatment of ruptured intracranial aneurysms is to give effective protection against aneurysm rerupture while minimizing the complications related to the treatment. While large multicentric studies and meta-analyses have demonstrated the safety and efficacy of flow-diversion treatment of unruptured aneurysms,[6,31] few, small reports described treatment-related results of flow-diverter stents in acute SAH.[7-26] In general, the use of flow diverters in ruptured lesions is controversial and theoretically contraindicated due to the necessity of dual antiplatelet therapy administration.[9] Pooling the results of 20 studies, our analysis provides more representative data on the angiographic and clinical outcomes after flow-diversion treatment of ruptured intracranial aneurysms.

### Angiographic Outcomes

Due to the high pore density, flow-diverter stents disrupt the flow from the parent artery into the aneurysm, promoting a progressive thrombosis and shrinkage of the lesion.[4] While only 32% of the ruptured aneurysms were occluded immediately after treatment, nearly 90% of the lesions had complete/near-complete occlusion during the 9.6 months of radiologic follow-up. Flow diversion was particularly effective in the treatment of blister and dissecting/fusiform aneurysms, allowing a slightly higher occlusion rate (89%) compared with saccular lesions (79%). Aydin et al[7] reported complete occlusion of 9 of 10 blood-blister-like aneurysms during 6 months of angiographic follow-up, though only 1 aneurysm presented with near-complete occlusion immediately after the stent deployment. However, a recent series and meta-analysis demonstrated that deconstructive techniques are also an effective treatment option for ruptured dissecting and blister aneurysms. In a meta-analysis of 265 ruptured blisterlike aneurysms, Rouchaud et al[2] showed that endovascular deconstructive techniques achieved higher rates of initial and long-term complete occlusion (77% and 81%) compared with reconstructive treatments (33% and 73%), albeit with higher rates of periprocedural ischemic complications.

Given that aneurysm occlusion is a progressive process requiring weeks or months, along with the need for the antiplatelet therapy administration, there is a theoretic risk of rebleeding after flow diversion of ruptured aneurysms. The results of the 1-year follow-up of the International Subarachnoid Aneurysm Trial study[32] showed 2.7% rebleeding among 1073 patients treated with endovascular coiling. In our review, rebleeding was higher during the first 72 hours of flow diversion, occurring in 4% of treated patients (1 large fusiform, 1 small, and 3 giant saccular aneurysms) without statistically significant differences between the anterior and posterior circulation. Although rebleeding occurred predominantly among large-giant lesions, treatment of large and giant aneurysms has higher rates of complications regardless of the treatment.[33] In a previous review of flow-diversion treatment of ruptured intracranial aneurysms, rerupture occurred in approximately 5% of patients, with 67% of rebleedings among lesions measuring >2 cm.[34] Series of ruptured aneurysms treated with coiling or stent-assisted coiling showed a rebleeding rate ranging from 2% to 17%[35,36]: Rerupture was higher during the first 3 days, and it was influenced by the degree of aneurysm occlusion and the SAH grade, with a trend toward higher rebleeding after stent-assisted coiling and for larger aneurysms.

Assessing factors related to aneurysm occlusion, we found that patients younger than 60 years of age had a higher occlusion rate compared with the older group (90% versus 76%, $P$ = .01). Adeeb et al,[37] after treatment of 465 intracranial aneurysms with PEDs,

showed that older age was a significant predictor of incomplete occlusion at last follow-up. Although the exact reasons are currently unknown, the lower occlusion rates in the elderly may be related to a deficiency in the endothelial repair pathway, with incomplete endothelization of the stent.[37]

### Treatment-Related Complications

Based on the literature, the overall rate of complications after coiling of ruptured aneurysms is approximately 12%,[38] whereas the rate of thromboembolic and hemorrhagic events after stent-assisted coiling in the acute phase is 11% and 5.5%,[39] respectively. In our meta-analysis, flow diversion was associated with 17.8% complications, which mostly occurred in the periprocedural/early period after treatment, with a 7% treatment-related morbidity. Most interesting, flow-diversion treatment of acutely ruptured saccular aneurysms was associated with a higher rate (23%) of complications compared with dissecting/fusiform and blister aneurysms (13% and 18%, respectively). Treatment-related complications after coiling and stent-assisted coiling of ruptured saccular lesions are reported close to 12%[38] and 16%, respectively.[40,41] Accordingly, given the possibility of other treatment strategies, flow diversion for acutely ruptured saccular aneurysms should be considered salvage therapy when traditional treatment methods are unfeasible.

Overall, the rates of thromboembolism and hemorrhagic events (intracerebral hemorrhage and vessel perforation) were quite comparable (8% and 7%, respectively). However, hemorrhagic complications were higher when flow diversion was performed during the first 72 hours, whereas ischemic events were more frequent when the treatment was in the subacute phase. The higher rate of hemorrhages in the early period can be related to the loading dose of antiplatelet therapy needed to achieve a platelet inhibition rate high enough to prevent ischemic complications, in combination with additional surgical intracranial procedures, such as ventriculostomy or decompressive craniectomy, usually performed in the early phase of SAH.[15] Accordingly, 18% of the reported hemorrhagic complications were ventriculostomy-related bleeding,[15,17,22] while 30% were related to aneurysm rerupture, which is generally higher in the first 72 hours.[42] On the contrary, the higher ischemic rate during the following weeks after SAH can be related to the higher incidence of vasospasm in this period (within 5 and 21 days).[43] In this setting, passage of a microcatheter/microwire through vasospastic vessels might be associated with a higher risk of vessel dissection or thromboembolic complications caused by the temporary flow reduction in the narrowed arteries.[43] Despite decades of advances in microsurgical techniques, dissecting and blister aneurysms also remain very challenging lesions for the surgical approach, and many techniques (clipping and clip reconstruction of the arterial wall, wrapping, revascularization plus trapping, and primary suture repair) have been developed.[44] In a recent surgical series of 17 blister aneurysms, intraoperative rupture was not negligible and occurred in 7 patients (41%): Direct clipping was possible in 71% of patients, whereas the other lesions were treated with bypass and trapping or with clip-reinforced wrapping.[45]

Flow diversion in the posterior circulation is associated with a not negligible rate of ischemic complications related to perforators infarcts. We found 27% complications when the stents were deployed in the posterior circulation, compared with 11.7% for anterior circulation aneurysms ($P = .004$). Similarly, in the International Retrospective Study of the Pipeline Embolization Device, the rates of morbidity and mortality after flow-diversion treatment were higher among the posterior circulation (16.5%) compared with the anterior circulation lesions (7%).[6] In addition, considering only the ruptured lesions, morbidity and mortality were significantly higher after the treatment of posterior circulation aneurysms (50% versus 14%).[6]

Finally, multiple stents were associated with an increased rate (26%) of complications, compared with treatment with a single device (10%). This finding is in accordance with reports in the literature,[46] and it might be related to the increased metal density of the overlapped multiple stents that promotes platelet aggregation, increasing the ischemic complications.

### Antiplatelet Therapy and Treatment-Related Outcomes

In a meta-analysis of stent-assisted coiling in SAH, Ryu et al[39] showed that the event rate of ischemic complications varied among the different methods of antiplatelet therapy administration. The standard management of flow diversion of unruptured aneurysms is pretreatment with ASA and CP 5–10 days before the procedure.[9] However, for the off-label use of flow-diverter stents among ruptured aneurysms, there is no consensus regarding the antiplatelet pretreatment. We found 4 main groups of antiplatelet therapy administration (On-line Table 9). There were no statistically significant differences among the analyzed subgroups of antiplatelet therapy, with an overall complication rate ranging from 17% to 23%. The most common drugs were CP plus ASA, administered intraoperatively and maintained after treatment (19.5% complications and 3% rebleeding). In 4 studies,[9,18,21,25] a protocol with tirofiban infusion, a glycoprotein IIb/IIIa inhibitor, was proposed starting immediately after the stent deployment and continuing for 12 hours after the procedure. The authors reported 17% complications and 2.8% aneurysm rebleeding. Lozupone et al[17] reported a series of 17 patients with ruptured aneurysms treated with flow diversion: Immediately after stent deployment, a bolus dose of 0.25 mg/kg of abciximab (an irreversible glycoprotein IIb/IIIa inhibitor) was administered, followed by a 12-hour infusion of 0.125 ng/kg/min. Although there were no rebleeding events, the authors reported 11% hemorrhagic and 11% ischemic complications. Finally, only 1 study[21] described 50 mg of intraoperative prasugrel administration for 9 acutely treated blood-blister aneurysms, reporting similar rates of complications.

### Strengths and Limitations

Our study has limitations. Most of the series are retrospective studies and small single-institution experiences. Details of platelet inhibition after the antiplatelet therapy administration were infrequently specified. Because of the small number of cases in some subgroups of analysis, the comparison among them may not provide sufficient power to show a statistically significant difference among the studied outcomes. However, publication bias was reasonably excluded from the analysis, and this review is currently the largest available, to our knowledge. It does provide a comprehensive summary and statistical analysis of the published data to

help guide the initial treatment of a selected subgroup of ruptured aneurysms with flow-diverter stents.

## CONCLUSIONS

In our study, flow-diversion treatment of ruptured intracranial aneurysms yielded high rates of long-term angiographic occlusion, with a relatively low rate of aneurysm rebleeding. However, independent of the type of antiplatelet therapy, flow diversion is associated with approximately 18% treatment-related complications. When simple coiling or microsurgical clipping is not feasible, anterior circulation ruptured aneurysms can be effectively treated with a flow-diversion technique, minimizing the number of stents deployed. Given the 27% rate of complications, flow diversion for ruptured posterior circulation aneurysms should be considered only in selected cases not amenable to other treatments.


## ACKNOWLEDGMENTS

We thank Professor Beth De Felici for the English revision.

Disclosures: Federico Cagnazzo—*UNRELATED*: *Employment*: University of Florence. Pierre-Henri Lefevre—*UNRELATED*: *Payment for Development of Educational Presentations*: Medtronic, Stryker, MicroVention, Balt. Vincent Costalat—*UNRELATED*: *Consultancy*: Medtronic, Balt, Stryker; *Grants/Grants Pending*: Medtronic, Stryker, MicroVention*; *Payment for Development of Educational Presentations*: Medtronic, Stryker. Paolo Perrini—*UNRELATED*: *Employment*: University of Pisa, Azienda Ospedaliero Universitaria Pisana, *Comments*: Consultant Neurosurgeon. *Money paid to the institution.


## REFERENCES


1. Garrett M, Spetzler RF. **Surgical treatment of blister-like aneurysms.** *World Neurosurg* 2012;77:76–77 CrossRef Medline
2. Rouchaud A, Brinjikji W, Cloft HJ, et al. **Endovascular treatment of ruptured blister-like aneurysms: a systematic review and meta-analysis with focus on deconstructive versus reconstructive and flow-diverter treatments.** *AJNR Am J Neuroradiol* 2015;36:2331–39 CrossRef Medline
3. Awad AJ, Mascitelli JR, Haroun RR, et al. **Endovascular management of fusiform aneurysms in the posterior circulation: the era of flow diversion.** *Neurosurg Focus* 2017;42:E14 CrossRef Medline
4. Kallmes DF, Ding YH, Dai D, et al. **A new endoluminal, flow-disrupting device for treatment of saccular aneurysms.** *Stroke* 2007;38:2346–52 CrossRef Medline
5. Kallmes DF, Brinjikji W, Boccardi E, et al. **Aneurysm Study of Pipeline in an Observational Registry (ASPIRe).** *Interv Neurol* 2016;5:89–99 CrossRef Medline
6. Kallmes DF, Hanel R, Lopes D, et al. **International retrospective study of the Pipeline embolization device: a multicenter aneurysm treatment study.** *AJNR Am J Neuroradiol* 2015;36:108–15 CrossRef Medline
7. Aydin K, Arat A, Sencer S, et al. **Treatment of ruptured blood blister-like aneurysms with flow diverter SILK stents.** *J Neurointerv Surg* 2015;7:202–09 CrossRef Medline
8. Cerejo R, Bain M, John S, et al. **Flow diverter treatment of cerebral blister aneurysms.** *Neuroradiology* 2017;59:1285–90 CrossRef Medline
9. Chalouhi N, Zanaty M, Whiting A, et al. **Treatment of ruptured intracranial aneurysms with the Pipeline embolization device.** *Neurosurgery* 2015;76:165–72; discussion 172 CrossRef Medline
10. Chan RS, Mak CH, Wong AK, et al. **Use of the Pipeline embolization device to treat recently ruptured dissecting cerebral aneurysms.** *Interv Neuroradiol* 2014;20:436–41 CrossRef Medline
11. Cruz JP, O'Kelly C, Kelly M, et al. **Pipeline embolization device in aneurysmal subarachnoid hemorrhage.** *AJNR Am J Neuroradiol* 2013;34:271–76 CrossRef Medline
12. de Barros Faria M, Castro RN, Lundquist J, et al. **The role of the Pipeline embolization device for the treatment of dissecting intracranial aneurysms.** *AJNR Am J Neuroradiol* 2011;32:2192–95 CrossRef Medline
13. Duman E, Coven I, Yildirim E, et al. **Endovascular treatment of wide necked ruptured saccular aneurysms with flow-diverter stent.** *Turk Neurosurg* 2017;27:362–67 CrossRef Medline
14. Kulcsár Z, Wetzel SG, Augsburger L, et al. **Effect of flow diversion treatment on very small ruptured aneurysms.** *Neurosurgery* 2010;67:789–93 CrossRef Medline
15. Lin N, Brouillard AM, Keigher KM, et al. **Utilization of Pipeline Embolization Device for treatment of ruptured intracranial aneurysms: US multicenter experience.** *J Neurointerv Surg* 2015;7:808–15 CrossRef Medline
16. Linfante I, Mayich M, Sonig A, et al. **Flow diversion with Pipeline Embolic Device as treatment of subarachnoid hemorrhage secondary to blister aneurysms: dual-center experience and review of the literature.** *J Neurointerv Surg* 2017;9:29–33 CrossRef Medline
17. Lozupone E, Piano M, Valvassori L, et al. **Flow diverter devices in ruptured intracranial aneurysms: a single-center experience.** *J Neurosurg* 2018;128:1037–43 CrossRef Medline
18. Maus V, Mpotsaris A, Dorn F, et al. **The use of flow diverter in ruptured, dissecting intracranial aneurysms of the posterior circulation.** *World Neurosurg* 2018;111:e424–33 CrossRef Medline
19. McAuliffe W, Wenderoth JD. **Immediate and midterm results following treatment of recently ruptured intracranial aneurysms with the Pipeline embolization device.** *AJNR Am J Neuroradiol* 2012;33:487–93 CrossRef Medline
20. Möhlenbruch MA, Herweh C, Jestaedt L, et al. **The FRED flow-diverter stent for intracranial aneurysms: clinical study to assess safety and efficacy.** *AJNR Am J Neuroradiol* 2015;36:1155–61 CrossRef Medline
21. Parthasarathy R, Gupta V, Gupta A. **Safety of Prasugrel loading in ruptured blister like aneurysm treated with a Pipeline device.** *Br J Radiol* 2018;91:20170476 CrossRef Medline
22. Peschillo S, Caporlingua A, Cannizzaro D, et al. **Flow diverter stent treatment for ruptured basilar trunk perforator aneurysms.** *J Neurointerv Surg* 2016;8:190–96 CrossRef Medline
23. Peschillo S, Caporlingua A, Resta MC, et al. **Endovascular treatment of large and giant carotid aneurysms with flow-diverter stents alone or in combination with coils: a multicenter experience and long-term follow-up.** *Oper Neurosurg (Hagerstown)* 2017;13:492–502 CrossRef Medline
24. Ryan RW, Khan AS, Barco R, et al. **Pipeline flow diversion of ruptured blister aneurysms of the supraclinoid carotid artery using a single-device strategy.** *Neurosurg Focus* 2017;42:E11 CrossRef Medline
25. Volker M, Anastasios M, Jan B, et al. **Treatment of intracranial aneurysms with the Pipeline Embolization Device only: a single center experience.** *Neurointervention* 2018;13:32–40 CrossRef Medline
26. Yang C, Vadasz A, Szikora I. **Treatment of ruptured blood blister aneurysms using primary flow-diverter stenting with considerations for adjunctive coiling: a single-centre experience and literature review.** *Interv Neuroradiol* 2017;23:465–76 CrossRef Medline
27. Moher D, Liberati A, Tetzlaff J, et al. **Preferred reporting items for systematic reviews and meta-analyses: the PRISMA statement.** *Int J Surg* 2010;8:336–41 CrossRef Medline
28. Roy D, Milot G, Raymond J. **Endovascular treatment of unruptured aneurysms.** *Stroke* 2001;32:1998–2004 CrossRef Medline
29. O'Kelly CJ, Krings T, Fiorella D, et al. **A novel grading scale for the angiographic assessment of intracranial aneurysms treated using flow diverting stents.** *Interv Neuroradiol* 2010;16:133–37 CrossRef Medline
30. Wells G, Shea B, O'Connell D, et al. **The Newcastle-Ottawa Scale (NOS) for assessing the quality of nonradomized studies in meta-analyses.** Ottawa: Ottawa Hospital Research Institute. 2011. http://www.evidencebasedpublichealth.de/download/Newcastle_Ottawa_Scale_Pope_Bruce.pdf. Accessed March 28, 2018
31. Brinjikji W, Murad MH, Lanzino G, et al. **Endovascular treatment of**

**intracranial aneurysms with flow diverters: a meta-analysis.** *Stroke* 2013;44:442–47 CrossRef Medline

32. Molyneux AJ, Kerr RS, Yu LM, et al; International Subarachnoid Aneurysm Trial (ISAT) Collaborative Group. **International Subarachnoid Aneurysm Trial (ISAT) of neurosurgical clipping versus endovascular coiling in 2143 patients with ruptured intracranial aneurysms: a randomised comparison of effects on survival, dependency, seizures, rebleeding, subgroups, and aneurysm occlusion.** *Lancet* 2005;366:809–17 CrossRef Medline
33. Cagnazzo F, Mantilla D, Rouchaud A, et al. **Endovascular treatment of very large and giant intracranial aneurysms: comparison between reconstructive and deconstructive techniques—a meta-analysis.** *AJNR Am J Neuroradiol* 2018;39:852–58 CrossRef Medline
34. Madaelil TP, Moran CJ, Cross DT 3rd, et al. **Flow diversion in ruptured intracranial aneurysms: a meta-analysis.** *AJNR Am J Neuroradiol* 2017;38:590–95 CrossRef Medline
35. White AC, Roark CD, Case DE, et al. **Factors associated with rerupture of intracranial aneurysms after endovascular treatment: a retrospective review of 11 years experience at a single institution and review of the literature.** *J Clin Neurosci* 2017;44:53–62 CrossRef Medline
36. Zhao B, Tan X, Yang H, et al. **Stent-assisted coiling versus coiling alone of poor-grade ruptured intracranial aneurysms: a multicenter study.** *J Neurointerv Surg* 2017;9:165–68 CrossRef Medline
37. Adeeb N, Moore JM, Wirtz M, et al. **Predictors of incomplete occlusion following Pipeline embolization of intracranial aneurysms: is it less effective in older patients?** *AJNR Am J Neuroradiol* 2017;38:2295–2300 CrossRef Medline
38. Renowden SA, Benes V, Bradley M, et al. **Detachable coil embolisation of ruptured intracranial aneurysms: a single center study, a decade experience.** *Clin Neurol Neurosurg* 2009;111:179–88 CrossRef Medline
39. Ryu CW, Park S, Shin HS, et al. **Complications in stent-assisted endovascular therapy of ruptured intracranial aneurysms and relevance to antiplatelet administration: a systematic review.** *AJNR Am J Neuroradiol* 2015;36:1682–88 CrossRef Medline
40. Lodi YM, Latorre JG, El-Zammar Z, et al. **Stent assisted coiling of the ruptured wide necked intracranial aneurysm.** *J Neurointerv Surg* 2012;4:281–86 CrossRef Medline
41. Amenta PS, Dalyai RT, Kung D, et al. **Stent-assisted coiling of wide-necked aneurysms in the setting of acute subarachnoid hemorrhage: experience in 65 patients.** *Neurosurgery* 2012;70:1415–29; discussion 1429 CrossRef Medline
42. Guo LM, Zhou HY, Xu JW, et al. **Risk factors related to aneurysmal rebleeding.** *World Neurosurg* 2011;76:292–98; discussion 253–54 CrossRef Medline
43. Alaraj A, Wallace A, Mander N, et al. **Outcome following symptomatic cerebral vasospasm on presentation in aneurysmal subarachnoid hemorrhage: coiling vs. clipping.** *World Neurosurg* 2010;74:138–42 CrossRef Medline
44. Kazumata K, Nakayama N, Nakamura T, et al. **Changing treatment strategy from clipping to radial artery graft bypass and parent artery sacrifice in patients with ruptured blister-like internal carotid artery aneurysms.** *Neurosurgery* 2014;10(Suppl 1):66–72; discussion 73 CrossRef Medline
45. Owen CM, Montemurro N, Lawton MT. **Blister aneurysms of the internal carotid artery: microsurgical results and management strategy.** *Neurosurgery* 2017;80:235–47 CrossRef Medline
46. Brinjikji W, Lanzino G, Cloft HJ, et al. **Risk factors for ischemic complications following Pipeline Embolization Device treatment of intracranial aneurysms: results from the IntrePED study.** *AJNR Am J Neuroradiol* 2016;37:1673–78 CrossRef Medline

# Feasibility, Safety, and Periprocedural Complications Associated with Endovascular Treatment of Ruptured Intracranial Aneurysms according to the Depth of Anesthesia

J. Song, C.-Y. Lee, and H.-W. Kim

## ABSTRACT

**BACKGROUND AND PURPOSE:** The aim of the present study was to report the feasibility, safety, and periprocedural complications associated with EVT of ruptured intracranial aneurysms according to the depth of anesthesia. In most centers, endovascular treatment of intracranial aneurysm is performed under general anesthesia.

**MATERIALS AND METHODS:** Between March 2011 and December 2016, a total of 183 consecutive patients with 183 aneurysms were treated endovascularly at the authors' center. The data about the depth of anesthesia (local anesthesia, conscious sedation, deep sedation, and general anesthesia), procedural details, and clinical and radiologic outcomes were reviewed.

**RESULTS:** A total of 183 consecutive patients with 183 aneurysms (mean age, 60.2 ± 14.8 years; 54 men and 129 women) were successfully treated. Of these, 70 (38.3%) patients underwent endovascular treatment under local anesthesia, 33 (18.0%) patients underwent endovascular treatment under conscious sedation, 78 (42.6%) patients underwent endovascular treatment under deep sedation, and only 2 (1.1%) patients underwent endovascular treatment under general anesthesia. For patients who presented with Hunt and Hess grades 1, 2, 3, 4, and 5, 75%, 59.6%, 59.1%, 53.3%, and 35.3% were treated under local anesthesia or conscious sedation, respectively. The procedure-related complication rates amounted to 8.7% (16/183, with 11 thromboembolic complications and 5 intraprocedural ruptures) overall, and 7.7% (14/183) of complications were symptomatic events. In the patients with good clinical grade (Hunt and Hess 1 or 2), the procedure-related complication rate was 4.1% (4/97), and all complications were symptomatic events under local anesthesia or conscious sedation.

**CONCLUSIONS:** In the authors' experience, local anesthesia or conscious sedation seemed safe and feasible for the patients with good clinical grade SAH.

**ABBREVIATIONS:** EVT = endovascular treatment; HH = Hunt and Hess scale

In the past decade, endovascular treatment (EVT) has evolved to the mainstream treatment for the patients with ruptured intracranial aneurysms. In most centers, EVT of aneurysms is performed with the patient under general anesthesia to ensure control of hemodynamic and respiratory profiles, improved image quality in an immobile patient, and patient comfort.[1-3] However, general anesthesia has potential risk of respiratory and hemodynamic instability during induction, interrupting the neurologic examination during the procedure and causing respiratory complications due to mechanical ventilation.[3,4]

Sedation is a drug-induced depression of consciousness, a continuum culminating in general anesthesia. The American Society of Anesthesiology defines 3 levels of sedation and general anesthesia (Table 1). Minimal sedation is a depressed level of consciousness in which the patient retains the ability to respond normally to verbal commands. Conscious sedation is the level at which the patient can respond purposefully to verbal commands or tactile stimulation. Deep sedation allows the patient to respond to painful stimulation. Patients may require assistance in maintaining the airway and ventilation. General anesthesia is a loss of consciousness in which patients are not arousable and require assistance in maintaining the airway and positive pressure ventilation. Cardiovascular function may be impaired.

At the authors' center, we considered EVT with the patient under local anesthesia or conscious sedation first, according to the patient's

Received April 13, 2018; accepted after revision June 6.

From the Department of Neurosurgery, College of Medicine, Konyang University Hospital, Konyang University Myunggok Medical Research Institute, Daejeon, Republic of Korea.

Please address correspondence to Cheol-Young Lee, MD, Department of Neurosurgery, College of Medicine, Konyang University Hospital, Konyang University Myunggok Medical Research Institute, 58, Gwanjeodong-ro, Seo-gu, Daejeon, Republic of Korea; e-mail: milelon@kyuh.ac.kr

Indicates article with supplemental on-line table.

http://dx.doi.org/10.3174/ajnr.A5753

**Table 1: Continuum of depth of sedation—definition of general anesthesia and levels of sedation/analgesia**

| | Minimal Sedation/ Anxiolysis | Moderate Sedation/Analgesia (Conscious Sedation) | Deep Sedation Analgesia | General Anesthesia |
|---|---|---|---|---|
| Responsiveness | Normal response to verbal stimulation | Purposeful[a] response to verbal or tactile stimulation | Purposeful[a] response after repeat or painful stimulation | Unarousable even with painful stimulus |
| Airway | Unaffected | No intervention required | Intervention may be required | Intervention often required |
| Spontaneous ventilation | Unaffected | Adequate | May be inadequate | Frequently inadequate |
| Cardiovascular function | Unaffected | Usually maintained | Usually maintained | May be impaired |

[a] Reflex withdrawal from a painful stimulus is not considered a purposeful response.

clinical SAH grade. The purpose of this study was to examine the feasibility and safety of the use of local anesthesia or conscious sedation for EVT of ruptured intracranial aneurysms.

## MATERIALS AND METHODS

### *Patient Population*

The present study was approved by our institutional review board. A total of 388 consecutive cases were treated with EVT in our institution from March 2011 to December 2016. Of these, 203 procedures were unruptured and 185 procedures were ruptured intracranial aneurysms. The patients with ruptured aneurysms who underwent EVT during the study period were included. Two patients who had no imaging follow-up were excluded. The remaining 183 patients were included in this study.

### *Baseline Characteristics*

We retrospectively reviewed the patients' medical records, focusing on the following characteristics: sex, age, multiplicity of aneurysms, location, size of aneurysms, procedure details (eg, devices, coils, and medications used for anesthesia), procedure-related complications, procedure outcome with regard to technical success and underlying reasons for unsuccessful procedures, image findings after postoperative CT or MR imaging, procedure-related mortality and morbidity, and mRS score (at discharge and at 1 and 6 months).

### *Anesthetic Technique and Patient Selection*

For the patients who did not require airway control because they were sufficiently alert and stable to undergo the procedure in the awake condition, local anesthesia or conscious sedation was administered. The patients who were in poor neurologic status (Glasgow Coma Scale Score $\leq$8 at the time of the procedure) or unable to undergo the procedure in the awake state underwent deep sedation or general anesthesia. The information about the process of EVT was repeated and reinforced at the time of treatment by the nursing staff, technicians, and treating physicians. In our experience, this approach enhances the patient's cooperation throughout the various stages of the intervention.

Before each intervention, a Foley catheter and 2 intravenous lines were inserted in each patient in the intensive care unit. For a further reduction of head motion during the intervention, a custom-made, rigid, radiolucent headholder attached to the angiography table was used (Fig. 1). Electrocardiography, blood pressure cuffs, and pulse oximetry were applied throughout the procedure to monitor the patients. For real-time clinical assessment, frequent neurologic examinations (motor, sensory, and speech) were performed. In all procedures performed with the patient under local anesthesia, conscious sedation, or deep sedation, to ensure the possibility to convert to general anesthesia if needed (eg, due to the patient's intolerance, deterioration, or intraprocedural complications), an anesthesiologist was always available. After the intervention, all patients were returned to the intensive care unit for monitoring of periprocedural complications and vasospasm. Noncontrast CT was performed immediately after the procedure, and diffusion MR imaging was performed on the day after procedure to evaluate ischemic or hemorrhagic complications.

**FIG 1.** Rigid and radiolucent head holder.

### *Definitions and Outcome Variables*

Levels of sedation and anesthesia were defined according to the American Society of Anesthesiologists (Table 1). Local anesthesia is infiltration of local anesthetics into the groin without conscious sedation. Conscious sedation is a drug-induced depression of consciousness during which patients respond purposefully to verbal commands, either alone or accompanied by light tactile stimulation. Drugs were administered by a neurosurgeon. They consisted of an intravenous injection of 1 mg of midazolam and/or 50 mg of fentanyl. To ensure that the patients could still respond to commands while resting comfortably, we administered an additional dose of midazolam when necessary (Ramsay sedation scale score of 2 or 36). Deep sedation is a drug-induced depression of consciousness during which patients cannot be easily aroused but are able to respond to repeat or painful stimulation. It was induced by intravenous injection of propofol (40 mg). General anesthesia is a drug-induced loss of consciousness during which patients are not arousable, even by painful stimulation. Intravenous general anesthetic drugs were administered (fentanyl or midazolam) and, to achieve a concomitant neuromuscular blockade, pancuronium was used under the direction of the operating

neurosurgeon. Infrequently, an anesthesiologist administered inhalational anesthetic agents.

Any undesirable events and/or abnormal angiographic findings related to the procedures were recorded, regardless of the symptom development, as procedure-related complications. In such cases, the neurosurgeon thoroughly reviewed procedural records and charts. We defined hemorrhagic complications as intraoperative rupture and thromboembolic complications as any thrombus formation during the procedure or abnormal findings on diffusion MR imaging regardless of the symptom development.

### Statistical Analysis

The data were analyzed using the R statistical and computing software (http://www.r-project.org/). Continuous data were expressed as the mean ± SD. The $\chi^2$ test or Fisher exact test was used to compare categoric values. Logistic regression models were used to evaluate independent associations between significant variables and treatment type. The odds ratio and 95% confidence interval were calculated. A $P$ value $< .05$ was considered significant.

## RESULTS

### Characteristics of Patients and Aneurysms

During the study period, 183 consecutive patients with 183 aneurysms (mean age, 60.2 ± 14.8 years; range, 30–92 years; 54 men and 129 women) were successfully treated. Of these, 31 (16.9%) patients had multiple aneurysms. Eighty (43.7%) aneurysms were in the anterior cerebral artery, and 68 (39.9%) aneurysms were <5 mm in maximal diameter. Ninety-seven (53%) patients were Hunt and Hess grade 1 or 2, 52 (28.4%) patients were 3 or 4, and 34 (18.6%) patients were grade 5. One hundred three (56.3%) patients underwent EVT under local anesthesia or conscious sedation, and only 2 (1.1%) patients underwent EVT under general anesthesia (Table 2). Figure 2 demonstrates the distribution of patients according to clinical grade and depth of anesthesia.

**Table 2: Baseline demographic data**

| Variable | No. |
|---|---|
| No. of aneurysms | 183 |
| No. of patients | 183 |
| Age (mean) (SD) (yr) | 60.2 (14.8) |
| Younger than 40 | 13 (7.1%) |
| 40–50 | 44 (24.0%) |
| 50–60 | 43 (23.5%) |
| 60–70 | 26 (14.2%) |
| 70–80 | 40 (21.9%) |
| Older than 80 | 17 (9.3%) |
| Sex | |
| Female | 129 (70.5%) |
| Male | 54 (29.5%) |
| Multiplicity | 31 (16.9%) |
| Location | |
| ACA | 80 (43.7%) |
| ICA | 56 (30.6%) |
| MCA | 31 (16.9%) |
| VB | 15 (8.2%) |
| Aneurysm size (mm) | |
| ≤5 | 68 (39.9%) |
| 5–10 | 92 (47.5%) |
| 10–15 | 21 (11.5%) |
| >15 | 2 (1.1%) |
| Modalities of EVT | |
| Simple catheter | 114 (62.3%) |
| Double catheter | 47 (25.7%) |
| Stent-assisted | 22 (12.0%) |
| Anesthesia grade | |
| Local anesthesia | 70 (38.3%) |
| Conscious sedation | 33 (18.0%) |
| Deep sedation | 78 (42.6%) |
| General anesthesia | 2 (1.1%) |
| Hunt and Hess scale grade | |
| 1 | 40 (21.9%) |
| 2 | 57 (31.1%) |
| 3 | 22 (12.0%) |
| 4 | 30 (16.4%) |
| 5 | 34 (18.6%) |

**Note:**—ACA indicates anterior cerebral artery; VB, vertebrobasilar artery.

### Aborted Procedures, Periprocedural Complications, and Outcomes

All 183 procedures were successfully completed. Procedure-related complications occurred in 16 (8.7%) of 183 procedures, including 11 thromboembolic (6%) and 5 hemorrhagic (2.7%) complications. Fourteen (7.7%) complications were symptomatic events. Among 11 thromboembolic complications, 3 procedures were performed with the patient under local anesthesia, 2 were performed with the patient under conscious sedation, and 6 were performed with the patient under deep sedation. Two thromboembolic complications resolved with intra-arterial abciximab (ReoPro) injection without clinical symptoms and imaging abnormalities. Intraoperative perforation occurred in 5 procedures: 3 with the patient under conscious sedation, and 2, under deep sedation. One of the patients developed an increased SAH requiring craniectomy and surgical evacuation, 2 patients died, and 2 patients had clinical deterioration (only 1 patient was asymptomatic). At the last follow-up (average, 12.4 months), 21 of the 183 patients had died; of these 21, two had an intraprocedural rupture and 1 had a thromboembolic event (mortality rate of 11.5%). The mortality rate in the local anesthesia or conscious sedation group amounted to 1% (1 of 103 patients) (On-line Table).

### Clinical Grade and the Depth of Anesthesia

For the patients who presented with Hunt and Hess grades 1, 2, 3, 4, and 5, 75%, 77.2%, 59.1%, 53.3%, and 35.3% were treated under local anesthesia or conscious sedation, respectively (Fig 1). In patients with good clinical grade (Hunt and Hess grade 1 or 2), 76.3% (74/97) were treated under local anesthesia or conscious sedation. In patients with Hunt and Hess (HH) grades 3, 4, or 5, 33.7% (29/86) were treated under local anesthesia or conscious sedation. Among the 183 procedures, 16 procedures had procedure-related complications. Six patients (6.2%) were HH 1 or 2, and 4 complications occurred with the patient under local anesthesia or conscious sedation. Ten patients (10/86, 11.6%) were HH 3, 4, or 5, and 4 complications occurred under local anesthesia or conscious sedation (Fig 3). There was no statistically significant difference between the rates of overall adverse events and clinical or angiographic factors (Table 3).

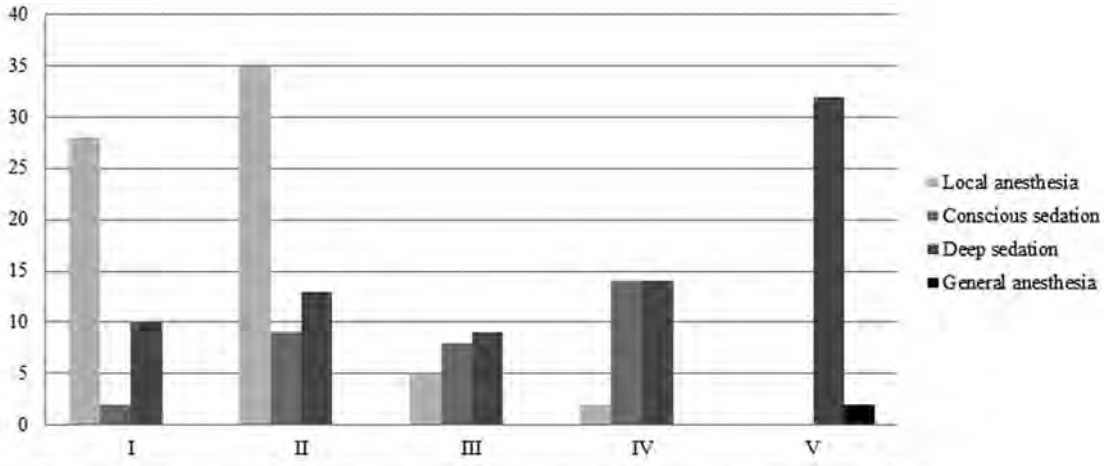


| | | | | | |
|---|---|---|---|---|---|
| Local anesthesia | 28 (70%) | 35 (61.4%) | 5 (22.7%) | 2 (6.6%) | 0 (0%) |
| Conscious sedation | 2 (5%) | 9 (15.8%) | 8 (36.4%) | 14 (46.7%) | 0 (0%) |
| Deep sedation | 10 (25%) | 13 (22.8%) | 9 (40.9%) | 14 (46.7%) | 32 (94.1%) |
| General anesthesia | 0 (0%) | 0 (0%) | 0 (0%) | 0 (0%) | 2 (5.9%) |
| Total (183) | 40 (21.9%) | 57 (31.1%) | 22 (12.0%) | 30 (16.4%) | 34 (18.6%) |

**FIG 2.** Distribution of patients according to clinical grade and depth of anesthesia.

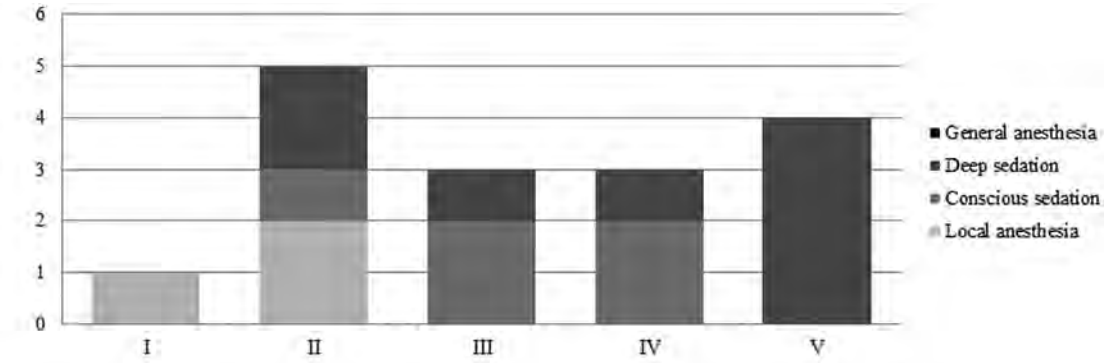


| | | | | | |
|---|---|---|---|---|---|
| Local anesthesia (70) | 1 | 2 | 0 | 0 | 0 |
| Conscious sedation (33) | 0 | 1 | 2 | 2 | 0 |
| Deep sedation (78) | 0 | 2 | 1 | 1 | 4 |
| General anesthesia (2) | 0 | 0 | 0 | 0 | 0 |
| Total (183) | 1/40 | 5/57 | 3/32 | 3/30 | 4/34 |

**FIG 3.** Procedure-related complications according to clinical grade and depth of anesthesia. Note:—( ) indicates number of patients.

## DISCUSSION

At most centers, EVT of ruptured aneurysms has been performed with the patient under general anesthesia.[5-8] In the present study, we were able to successfully perform procedures with the patient under local anesthesia or conscious sedation in 100%. Overall, the periprocedural complication rate was 8.7%, and the symptomatic events rate amounted to 7.7%. In patients with HH 1 or 2, the procedure-related complication rate was 4.1% under local anesthesia or conscious sedation. Local anesthesia or conscious sedation for the patients with HH 1 or 2 appears to be safe and feasible.

Overall, studies reporting EVT of ruptured aneurysms performed with the patient under local anesthesia or conscious sedation are scarce. Kan et al[9] reported the procedure-related compli-

**Table 3: Statistical analysis of complications with related factors**

| | | EVT (Complications, *n* = 16) | | |
|---|---|---|---|---|
| | All | Hemorrhagic | Thromboembolic | *P* Value |
| Age (yr) | | | | .399 |
| Younger than 40 | 5 | 2 | 3 | |
| 40–50 | 3 | 0 | 3 | |
| 50–60 | 5 | 2 | 3 | |
| 60–70 | 3 | 1 | 2 | |
| Older than 70 | 3 | 1 | 2 | |
| Sex | | | | |
| Female | 11 | 4 | 7 | .9026 |
| Location | | | | .6297 |
| ICA | 6 | 2 | 4 | |
| ACA | 3 | 2 | 1 | |
| MCA | 5 | 1 | 4 | |
| VB | 2 | 0 | 2 | |
| Aneurysm size ($n = 1230$) (mm) | | | | .3012 |
| ≤5 | 4 | 3 | 1 | |
| 5–10 | 11 | 2 | 9 | |
| 10–15 | 1 | 0 | 1 | |
| >15 | 0 | 0 | 0 | |
| Modalities of EVT | | | | .3919 |
| Simple catheter | 7 | 2 | 5 | |
| Double catheter | 6 | 2 | 4 | |
| Stent-assisted | 3 | 1 | 2 | |
| Anesthesia grade | | | | .3307 |
| Local anesthesia | 4 | 1 | 3 | |
| Conscious sedation | 5 | 3 | 2 | |
| Deep sedation | 7 | 1 | 6 | |
| General anesthesia | 0 | 0 | 0 | |
| Hunt and Hess grade | | | | .0731 |
| 1 | 1 | 0 | 1 | |
| 2 | 5 | 0 | 5 | |
| 3 | 3 | 1 | 2 | |
| 4 | 3 | 3 | 0 | |
| 5 | 4 | 1 | 3 | |
| Good (1 or 2) | 6 | 0 | 6 | .05438 |
| Poor (3, 4, or 5) | 10 | 5 | 5 | |

**Note:**—ACA indicates anterior cerebral artery; VB, vertebrobasilar artery.

cation rate of 9.4% (2.4% for symptomatic complications) in 79 aneurysms treated with EVT with the patient under conscious sedation. In their series, only the patients with good clinical grade underwent EVT under conscious sedation with local anesthesia. Qureshi et al[10] reported a complication rate of 8.6%. In their series, 58 procedures were performed with the patient under local anesthesia, and 53 cases (83%) were successfully completed. In a recent report of EVT of cerebral aneurysms with the patient under general anesthesia, Alanen et al[11] showed an 11.4% periprocedural complication rate with 491 ruptured cases, and Bradac et al[5] reported a 13% complication rate with 533 cases (including 448 with SAH). Our results are highly comparable with those studies reported above. In our study, there was an overall procedural complication rate of 8.7% (11 thromboembolic complications and 5 intraprocedural ruptures, 7.7% if only symptomatic complications were considered). Of the aforementioned 16 interventions with complications, 8 occurred with the patient under local anesthesia or conscious sedation, and of these, only 4 were observed in patients with a good clinical grade.

EVT with the patient under local anesthesia or conscious sedation has several potential drawbacks. First, if the patient does not tolerate the procedure due to restlessness or when an intraprocedural complication is observed, the procedure will need to be converted to general anesthesia, often on an emergent basis. Therefore, in such emergency cases, as stipulated in the conscious sedation protocol of our institution, the anesthesia team should be immediately available, and the conversion to general anesthesia is typically made within 10 minutes. Second, as argued by the proponents of general anesthesia, the best imaging quality is obtained when patient motion is completely eliminated. In addition, Fukuda et al[12] reported that the use of local anesthesia was independently associated with a higher risk of procedure-related rupture.

On the other hand, EVT of ruptured intracranial aneurysms with the patient under conscious sedation and local anesthesia has potential advantages. It helps avoid the inherent risk of general anesthesia, such as the need for invasive monitoring, endotracheal intubation, systemic effects of inhalational and intravenous agents, and cardiovascular complications.[13] In this respect, in 2 studies by Forrest et al,[14,15] general anesthesia–associated complications were reported in 17,201 patients. Seven of 19 recorded deaths were related to anesthetic agents. Adverse cardiovascular events were tachycardia (41%), hypotension (31%), hypertension (27%), bradycardia (19%), ventricular arrhythmias (6%), and myocardial ischemia (0.4%). In a previous report at our center, we suggested EVT of unruptured aneurysms under local anesthesia as an alternative for the patients with risk factors for general anesthesia.[16] The preparation of the procedure is simplified, and the overall cost is less without the need for general anesthesia.[16] The turnover time between procedures could also be reduced because conscious sedation avoids the prolonged induction and wake-up period accompanying general anesthesia.

Other advantages of conscious sedation include the ability for direct and frequent neurologic examinations of the patient without the necessity of interpreting the results of electrophysiologic monitoring. Furthermore, local anesthesia or conscious sedation might be helpful for the patients with comorbidities such as heart failure, cardiomyopathy, pulmonary edema, pulmonary emphysema, and severe liver or kidney dysfunction.[16] However, unlike patients with unruptured aneurysms, it is difficult to accomplish optimal sedation levels for patients with acute subarachnoid hemorrhage who present with various consciousness levels.[9] Specifically, the control of microcatheters can be hampered by unexpected body motion resulting from pain, discomfort, or anxiety, thus enhancing the risk of aneurysm rerupture. Even a

slight head movement with time and motion artifacts by respiration may detract from the quality of imaging under roadmap function, which is essential for safe navigation of the microcatheter. Furthermore, fluctuation of blood pressure accompanying local anesthesia is another a risk factor for procedure-related rupture.[17]

Our study suggests that local anesthesia or conscious sedation is a feasible and safe alternative to general anesthesia in most patients with good-grade SAH (Hunt and Hess 1 or 2) with ruptured aneurysms undergoing EVT. The main limitation of local anesthesia or conscious sedation is motion artifacts caused by the patient's movements or respiration. To determine and adjust the optimal working projection, we frequently generate high-quality roadmaps. These additional roadmaps increase the length of the procedural time and radiation dose delivered to the patient and the operator, which could be another disadvantage of local anesthesia or conscious sedation. However, we could not collect the data on the roadmaps.

Other limitations of our study are the retrospective data collection and the lack of a comparison group of patients with good-grade SAH (Hunt and Hess 1 or 2) treated under general anesthesia. A direct comparison between conscious sedation and general anesthesia in a randomized, controlled fashion would be necessary to identify the superior mode of anesthesia for EVT of patients with good-grade SAH (Hunt and Hess 1 or 2) with ruptured intracranial aneurysms. Moreover, future data pertaining to cost and turnover time associated with each technique will certainly strengthen the case for the use of local anesthesia or conscious sedation.

## CONCLUSIONS

The results of the present study demonstrate that local anesthesia or conscious sedation for patients with a good clinical grade SAH (HH 1 or 2) is safe and feasible. Local anesthesia or conscious sedation allows a direct evaluation of the patient's neurologic status, potentially leading to earlier detection and response to intraprocedural complications and thus helping to reduce complications related to general anesthesia.

## ACKNOWLEDGMENTS

This work was supported by Konyang University Myunggok Research Fund of 2017.

## REFERENCES

1. Abou-Chebl A, Lin R, Hussain MS, et al. **Conscious sedation versus general anesthesia during endovascular therapy for acute anterior circulation stroke: preliminary results from a retrospective, multicenter study.** *Stroke* 2010;41:1175–79 CrossRef Medline
2. Chamczuk AJ, Ogilvy CS, Snyder KV, et al. **Elective stenting for intracranial stenosis under conscious sedation.** *Neurosurgery* 2010;67:1189–93; discussion 1194 CrossRef Medline
3. Brinjikji W, Murad MH, Rabinstein AA, et al. **Conscious sedation versus general anesthesia during endovascular acute ischemic stroke treatment: a systematic review and meta-analysis.** *AJNR Am J Neuroradiol* 2015;36:525–29 CrossRef Medline
4. McDonald JS, Brinjikji W, Rabinstein AA, et al. **Conscious sedation versus general anaesthesia during mechanical thrombectomy for stroke: a propensity score analysis.** *J Neurointerv Surg* 2015;7:789–94 CrossRef Medline
5. Bradac GB, Bergui M, Stura G, et al. **Periprocedural morbidity and mortality by endovascular treatment of cerebral aneurysms with GDC: a retrospective 12-year experience of a single center.** *Neurosurg Rev* 2007;30:117–25; discussion 125–26 CrossRef Medline
6. Cardenas R, Connor D, Javalkar V, et al. **Coil embolization of intracranial aneurysms, the LSUHSC-S experience.** *J La State Med Soc* 2010;162:260–64 Medline
7. Friedman JA, Nichols DA, Meyer FB, et al. **Guglielmi detachable coil treatment of ruptured saccular cerebral aneurysms: retrospective review of a 10-year single-center experience.** *AJNR Am J Neuroradiol* 2003;24:526–33 Medline
8. Renowden SA, Benes V, Bradley M, et al. **Detachable coil embolisation of ruptured intracranial aneurysms: a single center study, a decade experience.** *Clin Neurol Neurosurg* 2009;111:179–88 CrossRef Medline
9. Kan P, Jahshan S, Yashar P, et al. **Feasibility, safety, and periprocedural complications associated with endovascular treatment of selected ruptured aneurysms under conscious sedation and local anesthesia.** *Neurosurgery* 2013;72:216–20; discussion 220 CrossRef Medline
10. Qureshi AI, Suri MF, Khan J, et al. **Endovascular treatment of intracranial aneurysms by using Guglielmi detachable coils in awake patients: safety and feasibility.** *J Neurosurg* 2001;94:880–85 CrossRef Medline
11. Alanen M, Pyysalo L, Jalava I, et al. **Procedural complications of endovascular treatment in patients with aneurysmal subarachnoid haemorrhage treated at a single centre.** *Acta Neurochir (Wien)* 2018;160:551–57 CrossRef Medline
12. Fukuda H, Handa A, Koyanagi M, et al. **Endovascular therapy for ruptured cerebral aneurysms in the elderly: poor accessibility of the guiding catheter and use of local anesthesia as the predictors of procedure-related rupture.** *Neurosurgery* 2015;77:544–52; discussion 552 CrossRef Medline
13. Ogilvy CS, Yang X, Jamil OA, et al. **Neurointerventional procedures for unruptured intracranial aneurysms under procedural sedation and local anesthesia: a large-volume, single-center experience.** *J Neurosurg* 2011;114:120–28 CrossRef Medline
14. Forrest JB, Cahalan MK, Rehder K, et al. **Multicenter study of general anesthesia, II: results.** *Anesthesiology* 1990;72:262–68 CrossRef Medline
15. Forrest JB, Rehder K, Cahalan MK, et al. **Multicenter study of general anesthesia, III: predictors of severe perioperative adverse outcomes.** *Anesthesiology* 1992;76:3–15 CrossRef Medline
16. Song J, Yang NR, Lee CY. **Local anesthesia for endovascular treatment of unruptured intracranial aneurysms: feasibility, safety, and periprocedural complications.** *World Neurosurg* 2017;104:694–701 CrossRef Medline
17. McDougall CG, Halbach VV, Dowd CF, et al. **Causes and management of aneurysmal hemorrhage occurring during embolization with Guglielmi detachable coils.** *J Neurosurg* 1998;89:87–92 CrossRef Medline

# Toward a Better Understanding of Dural Arteriovenous Fistula Angioarchitecture: Superselective Transvenous Embolization of a Sigmoid Common Arterial Collector

M. Shapiro, E. Raz, M. Litao, T. Becske, H. Riina, and P.K. Nelson

## ABSTRACT

**BACKGROUND AND PURPOSE:** Our aim was to propose a conceptually new angioarchitectural model of some dural arteriovenous fistulas based on subset analysis of transverse and sigmoid type lesions. The "common collector" notion argues for convergence of multiple smaller caliber arterial vessels on a common arterial collector vessel within the sinus wall. Communication of this single collector (or constellation of terminal collectors) with the sinus proper defines the site of arteriovenous fistula, which can be closed by highly targeted embolization, preserving the sinus and avoiding unnecessary permeation of indirect arterial feeders.

**MATERIALS AND METHODS:** One hundred consecutive dural arteriovenous shunts were examined. Thirty-six transverse/sigmoid fistulas were identified within this group and analyzed for the presence of a common arterial collector as well as other parameters, including demographics, grade, treatment approach, and outcome.

**RESULTS:** A common collector was identified in nearly all Cognard type I lesions (15 fistulas with 14 single collector vessels seen) and progressively less frequently in higher grade fistulas. Identification of the common collector requires careful angiographic analysis, including supraselective and intraprocedural angiographies during treatment, and final embolic material morphology.

**CONCLUSIONS:** Detailed evaluation of imaging studies allows frequent identification of a vascular channel in the sinus wall, which we argue reflects a compound, common arterial channel (rather than a venous collector) with 1 or several discrete fistulous points between this vessel and the sinus proper. Targeted closure of this channel is often feasible, with sinus preservation and avoidance of embolic material penetration into arteries remote from fistula site.

**ABBREVIATION:** dAVF = dural arteriovenous fistula

Dural arteriovenous fistulas (dAVFs) are pathologic arteriovenous shunts of the dural venous sinuses. Broad consensus exists regarding the relationship between the severity of dAVF-related cerebral venous congestion and disease morbidity, as reflected in the grading scales of Borden et al[1] and Cognard et al.[2] In contrast, there is less agreement on the nature of the pathologic angioarchitecture composing these lesions; the identity of the various vascular components, arterial or venous, in proximity to the fistula; the number and location of shunts in relation to the dural sinus; and the underlying mechanisms driving the evolution and occasional spontaneous involution of untreated lesions. Various treatment methods, transarterial[3,4] and transvenous,[5,6] have been used with generally successful results.[7,8] However, these treatments frequently lack target specificity, resulting in unnecessary permeation of arterial vessels remote from the site of shunting or sacrifice of venous structures likewise not directly involved in the shunt pathology. This article reviews the existing literature, which suggests that most transverse/sigmoid dAVFs consist of 1 or at most a limited number of direct arteriovenous connections. The seemingly complex angioarchitecture of these lesions is proposed to represent myriad artery-to-artery anastomoses, converging on a common collector vessel within the wall of the dural sinus. This collector, sometimes (we believe erroneously) referred to as a venous septation or pouch, in fact represents a final common arterial channel, with 1 opening (or a limited set of openings) into the dural sinus. The site of the fistulous communication thus involves a discrete point in the sinus wall where this common artery empties into the sinus, an arrangement best appreciated in lower grade fistulas. Highly targeted occlusion of this common channel and its

Received January 31, 2018; accepted after revision June 6.

From the Departments of Radiology (M.S., E.R., H.R., P.K.N.), Neurology (M.S., M.L.), and Neurosurgery (H.R., P.K.N.), NYU School of Medicine, New York, New York; and Department of Neurology (T.B.), Rochester Regional Health, Rochester, New York.

Please address correspondence to Maksim Shapiro, MD, Bernard and Irene Schwartz Interventional Neuroradiology Section, Center for Cerebrovascular Disease and Stroke, NYU Langone Medical Center, 660 First Ave, 7th floor, New York, NY 10016; e-mail: neuroangio@neuroangio.org; @neuroangio1; @neuroangio

http://dx.doi.org/10.3174/ajnr.A5740

**Breakdown by Cognard type, hemorrhage status on presentation, and presence of a common collector channel**

| Cognard Type | No. | Hemorrhagic Presentation (No.) | Common Channel (No.) (%) |
|---|---|---|---|
| I | 15 | 0 | 14 (93%) |
| IIa | 12 | 0 | 5 (42%) |
| IIb | 0 | 0 | NA |
| IIab | 3 | 0 | 1 (33%) |
| III | 6 | 4 | 2 (33%) |

**Note:**—NA indicates not applicable.

connection with the true sinus, when possible, minimizes collateral embolization with its associated hazards, procedural costs, and radiation dose.

## MATERIALS AND METHODS

NYU Institutional Board Review approved retrospective review of 100 consecutive dural arteriovenous shunts presenting for endovascular treatment from 2009 until 2017 was conducted by M.L. and M.S. to identify a subset of transverse and sigmoid sinus fistulas. A detailed examination of preprocedural MR and CT cross-sectional imaging and diagnostic and embolization angiographic studies was performed for evidence of the existence of a common arterial collector vessel and for assignment of fistula location by authors P.K.N., E.R., and M.S. Diagnostic angiography and embolization were performed on Axiom Artis or Q systems (Siemens, Erlangen, Germany) via femoral approach for both arterial and venous access at fluoroscopic and roadmap rates of 7.5 frames per second and digital subtraction angiography at 2 frames per second using the as low as reasonably achievable principles. Most diagnostic procedures were performed with the patient under local anesthesia, and all treatment was performed with the patient under general anesthesia. 3D-DSA was not acquired during diagnostic or therapeutic dAVF procedures. Data were also collected on the treatment strategy (arterial, venous, or both), number of treatment sessions, ultimate fistula status (closed or open), and any periprocedural complications, defined broadly as any new neurologic deficit or any delayed treatment-related neurologic issue. All authors were involved in performance of endovascular procedures. Fistulas in other locations were excluded from analysis at this stage.

## RESULTS

Thirty-six patients (mean age, 56 ± 14 years; 17 women) with transverse/sigmoid sinus fistulas were identified. The Table shows the breakdown by Cognard[2] type, hemorrhage status on presentation, and the presence of a common collector channel, which was identified in all but 1 of Cognard type I fistulas and progressively less frequently in higher grade lesions. A median of 1 embolization session (average, 1.47 sessions) was required to close 93% of fistulas by transarterial ($n = 19$), transvenous ($n = 9$), and combined ($n = 8$) approaches, incurring 1 permanent (lateral medullary infarct) and 1 transient (delayed venous sinus thrombosis resolved with anticoagulation) complication. Figures 1 and 2 illustrate normal and pathologic dAVF angioarchitecture according to a common collector theory and nonselective treatment approaches. The 2 cases shown in Figs 3–4 illustrate subselective transvenous embolization of the common collector vessels with coils (Fig 3) or *n*-BCA (Fig 4).

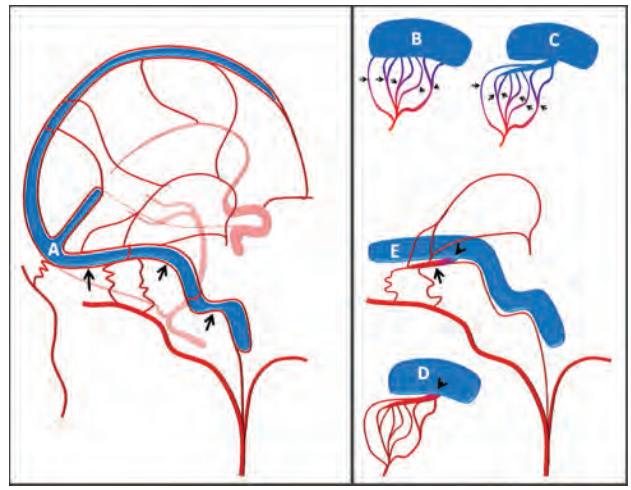


**FIG 1.** Schematic of normal dural arteriovenous architecture (*A*), with *arrows* pointing to the arterial arcade in the wall of the transverse/sigmoid sinuses. Schematic of dural fistula angioarchitecture according to a view of multiple arteriovenous shunts (*black arrows*) draining either separately via multiple discrete veins into the sinus (*B*) or into a common venous collector/pouch/septation (*C*) alongside the wall of the sinus proper. *D*, A low-grade dural fistula according to the common arterial collector view. Multiple arterial feeders converge on a common arterial channel in the sinus wall that empties into the sinus at a single fistulous point (*arrowhead*). *E*, Common arterial collector schematic relative to normal anatomy shown in *A*. The arterial supply converges on the common collector arterial channel within the sinus wall (*arrow*), with the fistulous point (*arrowhead*) at the confluence of this channel and the sinus proper.

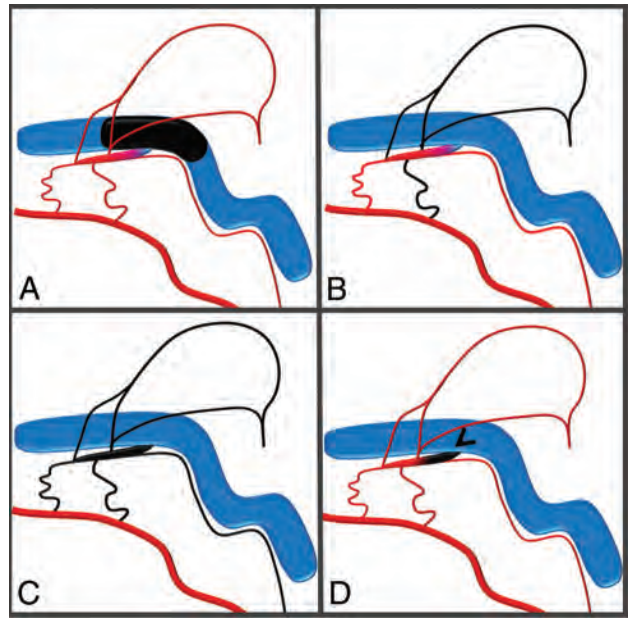


**FIG 2.** Schematic of typical transvenous sinus sacrifice (*A*) and incomplete (*B*) and complete (*C*) transarterial embolizations, each of which results in an unnecessary closure of arteries or sinus. Targeted occlusion of the shunt (*D*) at the entrance of the collector channel into the sinus preserves both the sinus and normal arterial structures.

## DISCUSSION

The existence of normal arterial channels within the walls of the dural sinuses is well-described and illustrated in works of Geibprasert el al,[9] Bernstein and Choi,[10] Lasjaunias et al[11] and others. These vessels comprise distal dural branches of the anterior, mid-

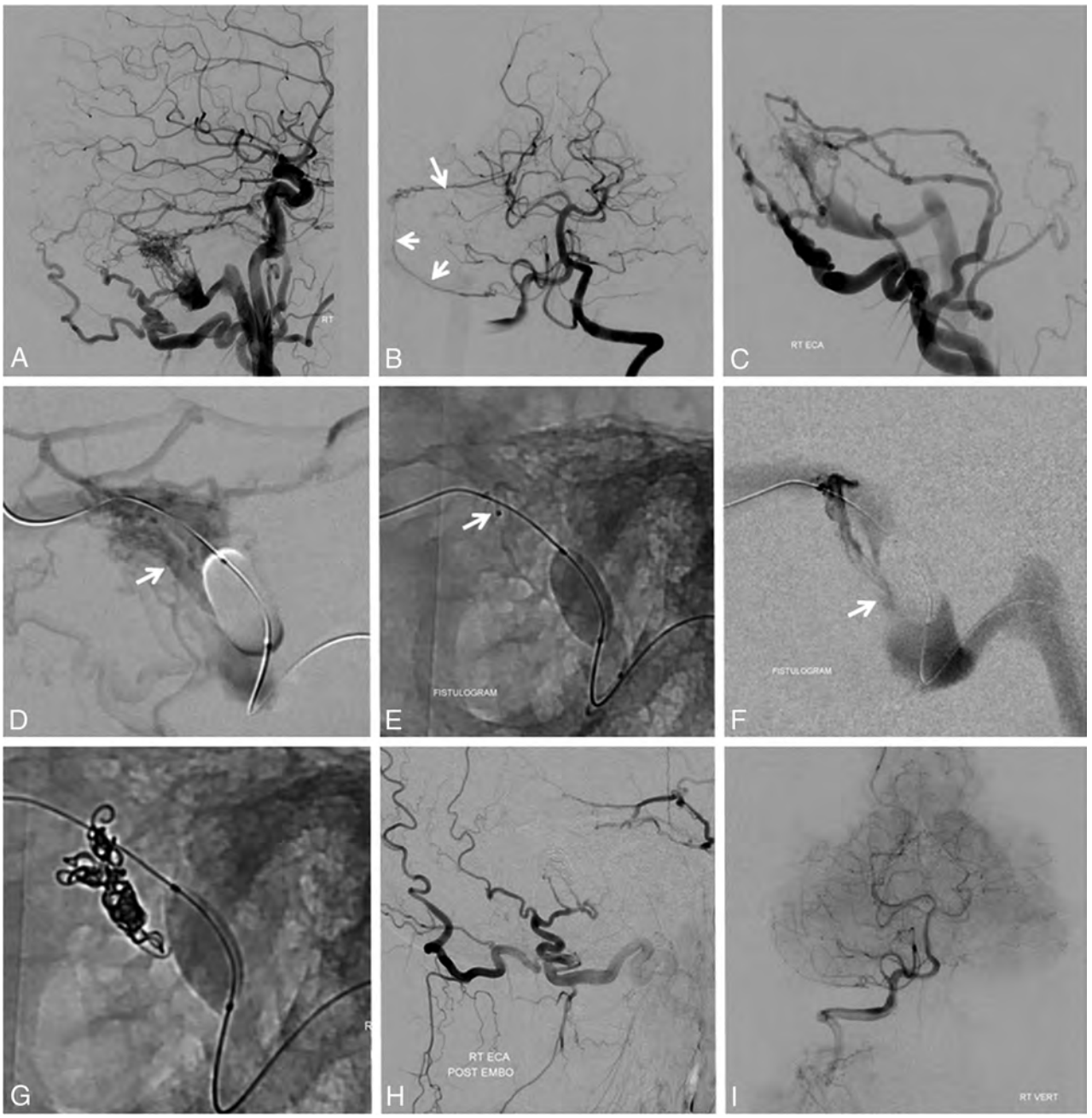


**FIG 3.** *A*, Left sigmoid sinus type I dural fistula. Posterior meningeal supply (*B*) proceeds via arteries in the wall of the transverse/sigmoid sinuses (*arrows*). Subselective external carotid artery injection (*C*) shows robust occipital and middle meningeal artery supply. *D*, Inflation of a compliant balloon within the sigmoid sinus reduces transfistulous flow to allow identification of a common collector channel (*white arrow*) inferior to the sinus proper. *E* and *F*, Transvenous microcatheterization of a common collector channel (*E*, distal catheter tip) and subsequent fistulogram (*F*) reduce the fistula to a single point where the collector joins the sinus (*white arrow*). Subselective coiling of this collector (*G*) results in fistula closure (*H* and *I*).

dle, posterior meningeal, ascending pharyngeal, and occipital arteries, as well as the meningohypophyseal and inferolateral trunks of the internal carotid artery, collectively forming a densely interconnected dural vascular network (Fig 1*A*). While occasionally visible angiographically in nonpathologic circumstances, the arterial vessels of the dural sinus wall are usually below the threshold of in vivo imaging resolution. They may, however, become angiographically visible in certain pathophysiologic conditions prevailing in the supply of the dAVF, dural-based vascular tumors such as meningiomas, hypertrophied collaterals in cerebral ischemic disease, or following meningeal arterial disruption (postcraniotomy). Close proximity of these arteries to the dural venous sinus and the vast collateral arcades through which they communicate with other dural arterial channels make these vessels a logical common conduit in the angioarchitectural evolution of a sinus dAVF. If we postulate that such a dural wall artery represents a common arterial collector that establishes an abnormal connection with the dural venous sinus to form the dAVF (Fig 1*D*, -*E*), the resulting vasculopathic picture may account for many empirically encountered phenomena related to the angio-

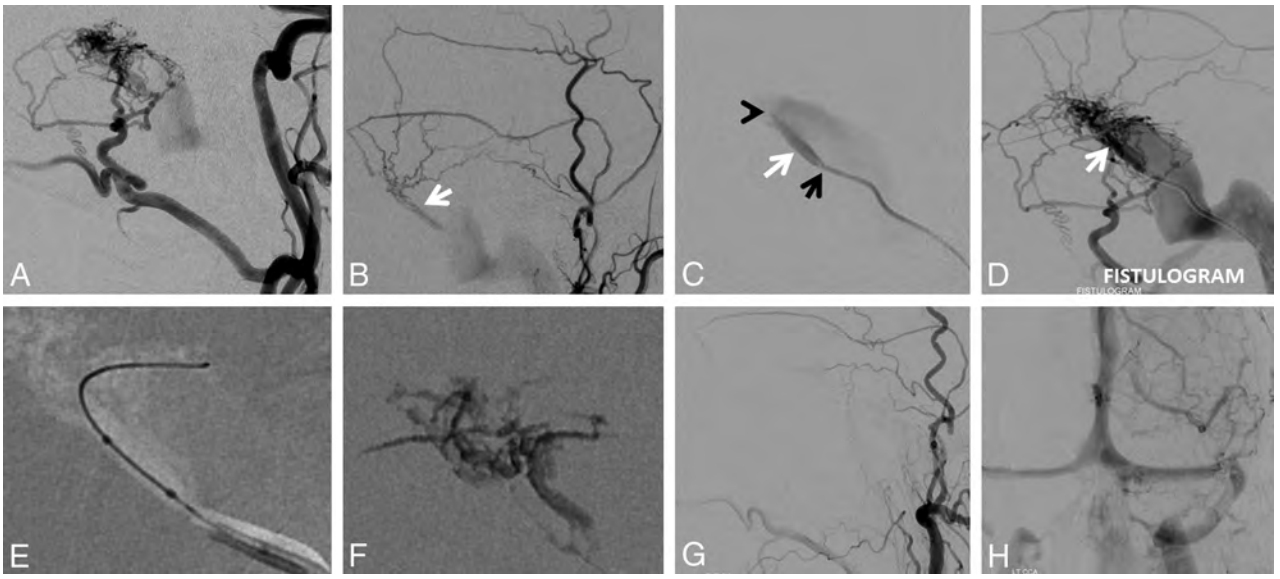


**FIG 4.** *A* and *B*, Left type I sigmoid sinus fistula with predominant occipital and middle meningeal supply. *C*, A 5F VERT (Cook, Bloomington, Indiana) catheter (tip marked by a *black arrow*) in the sigmoid sinus is wedged into the opening of the common collector (*white arrow*). Gentle injection of the VERT catheter identifies a second opening of the collector into the sinus shown by the *black arrowhead*. *D*, A stronger injection of the VERT (fistulogram) opacifies the entire arterial arcade in a retrograde fashion. *E*, Scepter C (MicroVention Tustin, California) subselective catheterization of the common collector, with a subsequent *n*-BCA cast in *F*. *G* and *H*, Postembolization angiography demonstrates occlusion of the fistula with preservation of the left sigmoid sinus.

graphic architecture of dAVFs and the success or failure of various treatment strategies, particularly in lower grade fistulas.

In the classic sigmoid sinus location, this collector is nearly always located inferior to the true sinus, as shown in Figs 1–5. Once its existence is recognized, prospective identification becomes substantially easier, despite the presence of overlapping regional collateral networks that communicate with and supply this common channel, frequently obscuring its detection. The implication of this model is that the true domain of shunting for a dAVF may be, in most cases, simplified to a single site (or small number of sites) where the common arterial channel is connected to the venous sinus rather than an innumerable tangle of arteriovenous shunts along a sinus segment, despite the apparently complex angiographic appearance of the mature lesion.

Literature support for the common collector concept may be found in articles describing the existence of channels alongside the sinus proper, first reported by Mironov[12] in 1998. Channels parallel to the venous sinus have been accessed successfully via a transvenous route and strategically embolized with coils, producing a durable cure. Piske et al[13] in 2005 described cases in which arteriovenous shunting was observed to involve what was described as a sinus compartment, which also could be selectively embolized with main sinus preservation. Similar results were reported earlier by Caragine et al in 2003.[14] Most recently, Kiyosue et al,[15] in agreement with our proposal, published results of rotational angiographic evaluation of 25 dAVFs, identifying the presence of "shunted pouches" immediately adjacent to the sinus in all 25 cases. Thirteen of these pouches were subselectively embolized via transvenous access, resulting in a durable cure. Baik et al[16] reported 8 cases in which a particularly direct arteriovenous connection allowed placement of coils into the venous compartment via the arterial route. These clinical examples each serve to demonstrate that closure of seemingly complex fistulas can be accomplished by strategic placement of embolic material at the location of the fistula rather than requiring extensive embolization of the innumerable, more proximal, indirect tributaries and strongly support the idea that most dAVFs can be reduced to 1 or a few aberrant arteriovenous communications, the opening of which defines the location of the shunt. In all the above articles, however, these compartments were considered venous. Alternatively, the "common arterial collector" hypothesis proposes that such compartments may represent the final arterial collectors supplying the shunt, rather than venous sinus septations.

For example, the arterial channel within the transverse and sigmoid sinuses most commonly communicates with the sinus at the sigmoid segment. However, the same vessel can develop fistulous connections at the torcular. The resulting complex arrangement that seemingly involves the entire sinus in fact may be reducible to several fistulous connections. At the more proximal end, fistulas involving the jugular bulb can be viewed as a collector artery deriving tributaries from ascending pharyngeal branches.

Several observations made during both transarterial and transvenous treatment approaches support this hypothesis. From transvenous embolizations, we have observed that placement of coils into the sinus may not result in substantial changes in the degree of shunting on control angiography until some critical location in the sinus is reached and the fistula is suddenly closed after placement of a few additional coils—corresponding to what might be expected from ultimate occlusion of a single fistulous site. In many of these transvenous cases, coiling the sinus is accompanied by continued flow immediately adjacent to the sinus coil mass (Fig 5*E*, -*F*), likely reflecting persistent patency of the common collector until flow within it is finally arrested when coil embolization reaches the shunting site where this collector opens into the sinus. If this common intradural channel were a vein rather than an artery, it would also be unclear why sacrifice of the

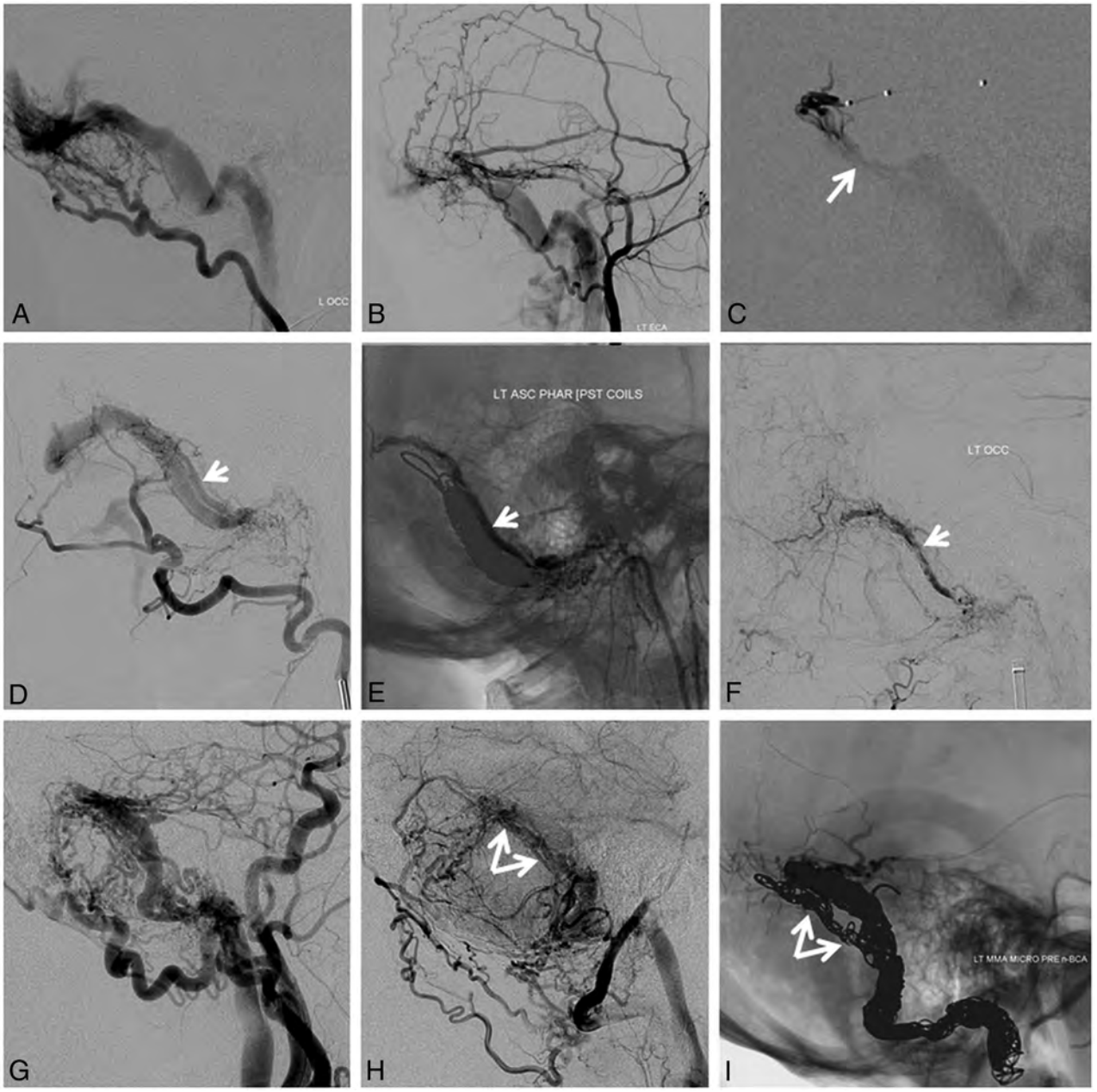


**FIG 5.** Additional examples of a common collector channel. Case 1 (*A–C*) of a type IIa fistula shows the collector channel inferior to the sinus (*C*, *white arrow*) during Onyx (Covidien, Irvine, California) injection via a Scepter C microcatheter (MicroVention). Case 2 (*D–F*) illustrates a relatively uncommon presence of a common collector superior to the sinus (*white arrows*), becoming more obvious after the sinus has been packed with coils. Case 3 (*G–I*) is another complex-appearing fistula, where the common collector channel (*white arrows*) is better seen via the left vertebral contributors (*H*) due to stenosis of the sinus proper. The collector channel is subsequently filled with coils (*I*, *white arrows*). In retrospect, cases 2 and 3 might have been cured by superselective embolization rather than sinus sacrifice.

venous sinus proper should result in a durable cure. Rather, one would expect this kind of embolization to be followed by development of alternative venous outflows, redirecting the drainage of the lesion possibly even into cortical veins. Moreover, the myriad arterial connections to the common channel would represent independent arteriovenous shunts if the channel were a vein, as opposed to collateral arterial-arterial connections if the conduit were the final common dural artery leading to a fistulous connection. If one assumed that the probability of forming an abnormal arteriovenous shunt is P, the likelihood of forming y independent shunts would be yP, which seems statistically less probable.

Arterial approaches typically require permeation of a liquid embolic into the sinus wall or the sinus itself to be effective. The most common pitfall of arterial embolization in treating dAVFs is a too-proximal deposition of embolic material. While this approach may be used deliberately in a partial or staged embolization, unless the common arterial collector is permeated, this exercise has no direct effect on the fistula, apart from temporary gross total flow reduction. The persistence or recurrence of shunting following proximal arterial embolizations is simply related to continued patency of the common arterial collector and its aberrant arteriovenous communication and inevitably will be fol-

lowed by enlargement of the remaining arterial routes comprising unembolized collaterals, which may be inaccessible or increasingly hazardous. Treatment succeeds when embolic material permeates the collector and extends to the terminal communication between the collector and the venous sinus, either with occlusion of the sinus or by using more sophisticated, sinus-sparing strategies that use temporary balloon protection of the sinus[17] or indwelling sinus stents.

As suggested above, the common collector hypothesis is consistent with successful transvenous and transarterial approaches and, in both instances, argues for more selective angiographic identification of the target-shunting site: that location where the common arterial collector (as we consider it, a "septation" or "shunted pouch" opening into the sinus proper, as described by Mironov,[12] Piske et al,[13] Caragine et al,[14] Kiyosue et al,[15] and others) abnormally communicates with the venous sinus. Identification of this terminal channel potentially allows preservation of the venous sinus proper during treatment and minimizes widespread collateral (nontarget) proximal arterial embolization, reducing the risk to regional cranial nerves.

Nevertheless, the common collector theory can be critiqued on several grounds. In 2 histopathologic studies, Nishigima et al[18] and Hamada et al[19] concluded that dAVFs consist of myriad microscopic arteriovenous connections within the sinus wall itself, ultimately communicating with the dural sinus (Fig 1*B*, -*C*). As suggested by our statistical argument, however, the development of numerous fistulas, in what appears fundamentally to be a reasonably rare event, seems unlikely. Moreover, Hamada et al[19] in their Fig 6 suggest that the final opening of these fistulas into the sinus proceeds via a common channel (which they, however, consider to be a vein) similar to Fig 1*C* in this article. However, if the fistulas are indeed numerous and located in the sinus wall, there appears to be no need to propose the existence of this common venous collector. From a probability standpoint, it also appears to be more likely that fistulas should be few rather than many if the entire angioarchitecture can be thus accounted for—an example of the Ockham razor. Additionally, from a histologic perspective, the existence of discrete mural veins that extend along the entire length of the dural venous sinuses under nonpathologic conditions has not been described, to our knowledge, while such arterial channels within the sinus walls are well-recognized. From the standpoint of the disease pathogenesis, if we hold that at least some dAVFs form because of sinus thrombosis and its subsequent lysis,[20] it seems more plausible that various lytic agents would act on the inner sinus wall to induce an aberrant arteriovenous connection between the sinus and an adjacent dural wall artery rather than establish myriad fistulous connections with the sinus itself or a parallel venous channel within the sinus wall.

Objection to the common arterial collector hypothesis may arise from apparent difficulty in defining this "common conduit" on routine angiography. However, the region of even relatively simple fistulas is often quite "busy" angiographically, and consistent identification of this channel is hampered by difficulty in its uniform opacification from 1 angiographic source in the face of competing unopacified inflow and overlap of the myriad collateral vessels, obscuring the underlying dAVF angioarchitecture. Some may find it counterintuitive to consider a terminal larger caliber vessel representing a collecting artery rather than vein. It is nevertheless a pathophysiologically coherent arrangement, accounting for collaterally fed high-flow networks. For example, proximal ligation of large vessels such as the external carotid or vertebral arteries frequently leads to reconstitution of their distal territory via multiple individually smaller-sized collaterals with maintenance of the original vessel caliber of the reconstituted segment.

Another critique concerns our inability to consistently identify collector channels in higher grade lesions. We postulate that this stems from the extensive asymmetric obliteration of normal anatomic structures in high-grade lesions, many of which are associated with narrowing or thrombosis of the native venous sinus. When the recipient sinus is occluded both retrograde and antegrade to the fistula, the common collector may come to drain through a trapped sinus segment (of variable dimensions) into regional cortical veins. This may limit the utility of subselective common collector embolization to anatomically lower grade lesions, many of which may be characterized by a more favorable natural history, and, instead, may be reasonably observed.[7,21] We agree, yet believe that subselective embolization of a common channel via a transvenous approach (Figs 3 and 4) is safe, effective, and elegant and that a good proportion of type IIa lesions also appear to have a common collector target. We do not believe that all common collectors can be embolized; for example, the collector may be too short or tortuous to allow subselective catheterization. Indeed, most of our cases were cured by transarterial embolization or sinus sacrifice.

The generalizability of the theory can be questioned on the basis of our exclusion of more complex fistulas of other sites (cavernous sinus, superior petrosal sinus, and torcular) from the analysis; however, observations reported by Satow et al[22] for cavernous sinus dural fistulas suggest the applicability of the principle in other settings. Volumetric imaging methods may be useful for better appreciation of the unique angioarchitecture in these areas.

Finally, the proposed model may be too simplistic, considering the variety of fistulas encountered in practice. The common arterial collector, like any theory, is open to the possibility of exceptions, variations, refutation, and improvement. It is our view that it represents an advance in our understanding of dAVF angioarchitecture and is useful as a guide to treatment.

## CONCLUSIONS

The seemingly complex lateral sinus dAVF angioarchitecture may be reduced in many instances to 1 or several discrete aberrant arteriovenous communications between arteries in the wall of the dural sinus and the sinus lumen itself. In the described model, an enlarged mural artery serves as the final common conduit supplying a simple fistulous site. This common arterial collector, in turn, receives the collective arterial inflow to the fistula through its numerous arterial anastomoses with an extensive collateral network, accounting for the convergence of myriad dural arteries near the region of shunting. Highly targeted occlusion of these artery-to-sinus communications allows occlusion of the shunt with sinus preservation and reduced inadvertent embolization of vessels not directly involved in the pathologic arteriovenous shunt.

Disclosures: Eytan Raz—*UNRELATED*: *Consultancy*: Medtronic; *Royalties*: Springer; *Stock/Stock Options*: Stryker and Penumbra; *Travel/Accommodations/Meeting Expenses Unrelated to Activities Listed*: Medtronic, MicroVention. Peter K. Nelson—*RELATED*: *Consulting Fee or Honorarium*: Medtronic, *Comments*: fees for clinical proctoring. Maksim Shapiro—*UNRELATED*: *Consulting Fee or Honorarium*: Medtronic, *Comments*: fees for clinical proctoring.

## REFERENCES


1. Borden JA, Wu JK, Shucart WA. **A proposed classification for spinal and cranial dural arteriovenous fistulous malformations and implications for treatment.** *J Neurosurg* 1995;82:166–79 CrossRef Medline
2. Cognard C, Gobin YP, Pierot L, et al. **Cerebral dural arteriovenous fistulas: clinical and angiographic correlation with a revised classification of venous drainage.** *Radiology* 1995;194:671–80 CrossRef Medline
3. Hu YC, Newman CB, Dashti SR, et al. **Cranial dural arteriovenous fistula: transarterial Onyx embolization experience and technical nuances.** *J Neurointerv Surg* 2011;3:5–13 CrossRef Medline
4. Kim DJ, Willinsky RA, Krings T, et al. **Intracranial dural arteriovenous shunts: transarterial glue embolization— experience in 115 consecutive patients.** *Radiology* 2011;258:554–61 CrossRef Medline
5. Roy D, Raymond J. **The role of transvenous embolization in the treatment of intracranial dural arteriovenous fistulas.** *Neurosurgery* 1997;40:1133–41; discussion 1141–1134 CrossRef Medline
6. Lekkhong E, Pongpech S, Ter Brugge K, et al. **Transvenous embolization of intracranial dural arteriovenous shunts through occluded venous segments: experience in 51 patients.** *AJNR Am J Neuroradiol* 2011;32:1738–44 CrossRef Medline
7. Cognard C, Januel AC, Silva NA Jr, et al. **Endovascular treatment of intracranial dural arteriovenous fistulas with cortical venous drainage: new management using Onyx.** *AJNR Am J Neuroradiol* 2008;29:235–41 CrossRef Medline
8. McConnell KA, Tjoumakaris SI, Allen J, et al. **Neuroendovascular management of dural arteriovenous malformations.** *Neurosurg Clin N Am* 2009;20:431–39 CrossRef Medline
9. Geibprasert S, Pereira V, Krings T, et al. **Dural arteriovenous shunts: a new classification of craniospinal epidural venous anatomical bases and clinical correlations.** *Stroke* 2008;39:2783–94 CrossRef Medline
10. Berenstein A, Choi IS. **Surgical neuroangiography of intracranial lesions.** *Radiol Clin North Am* 1988;26:1143–51 Medline
11. Lasjaunias PL, Berenstein A, Ter Brugge KG. *Surgical Neuroangiography*. Berlin: Springer-Verlag; 2001
12. Mironov A. **Selective transvenous embolization of dural fistulas without occlusion of the dural sinus.** *AJNR Am J Neuroradiol* 1998; 19:389–91 Medline
13. Piske RL, Campos CM, Chaves JB, et al. **Dural sinus compartment in dural arteriovenous shunts: a new angioarchitectural feature allowing superselective transvenous dural sinus occlusion treatment.** *AJNR Am J Neuroradiol* 2005;26:1715–22 Medline
14. Caragine LP, Halbach VV, Dowd CF, et al. **Parallel venous channel as the recipient pouch in transverse/sigmoid sinus dural fistulae.** *Neurosurgery* 2003;53:1261–66; discussion 1266–67 CrossRef Medline
15. Kiyosue H, Tanoue S, Okahara M, et al. **Angioarchitecture of transverse-sigmoid sinus dural arteriovenous fistulas: evaluation of shunted pouches by multiplanar reformatted images of rotational angiography.** *AJNR Am J Neuroradiol* 2013;34:1612–20 CrossRef Medline
16. Baik SK, Kim YW, Lee SW, et al. **A treatment option for nontraumatic adult-type dural arteriovenous fistulas: transarterial venous coil embolization.** *World Neurosurg* 2014;82:417–22 CrossRef Medline
17. Shi ZS, Loh Y, Duckwiler GR, et al. **Balloon-assisted transarterial embolization of intracranial dural arteriovenous fistulas.** *J Neurosurg* 2009;110:921–28 CrossRef Medline
18. Nishijima M, Takaku A, Endo S, et al. **Etiological evaluation of dural arteriovenous malformations of the lateral and sigmoid sinuses based on histopathological examinations.** *J Neurosurg* 1992;76: 600–06 CrossRef Medline
19. Hamada Y, Goto K, Inoue T, et al. **Histopathological aspects of dural arteriovenous fistulas in the transverse-sigmoid sinus region in nine patients.** *Neurosurgery* 1997;40:452–56; discussion 456–58 Medline
20. Houser OW, Campbell JK, Campbell RJ, et al. **Arteriovenous malformation affecting the transverse dural venous sinus: an acquired lesion.** *Mayo Clin Proc* 1979;54:651–61 Medline
21. Söderman M, Pavic L, Edner G, et al. **Natural history of dural arteriovenous shunts.** *Stroke* 2008;39:1735–39 CrossRef Medline
22. Satow T, Murao K, Matsushige T, et al. **Superselective shunt occlusion for the treatment of cavernous sinus dural arteriovenous fistulae.** *Neurosurgery* 2013;73(1 Suppl Operative):ons100–05 CrossRef Medline

# Adjunctive Efficacy of Intra-Arterial Conebeam CT Angiography Relative to DSA in the Diagnosis and Surgical Planning of Micro-Arteriovenous Malformations

A.S. Al-Smadi, A. Elmokadem, A. Shaibani, M.C. Hurley, M.B. Potts, B.S. Jahromi, and S.A. Ansari

## ABSTRACT

**BACKGROUND AND PURPOSE:** Micro-arteriovenous malformations are an underrecognized etiology of intracranial hemorrhage. Our study aimed to assess the adjunctive efficacy of intra-arterial conebeam CTA relative to DSA in the diagnosis and surgical planning of intracranial micro-AVMs.

**MATERIALS AND METHODS:** We performed a retrospective study of all micro-AVMs (≤1-cm nidus) at our institution. Blinded neuroradiologists qualitatively graded DSA and intra-arterial conebeam CTA images for the detection of specific micro-AVM anatomic parameters (arterial feeder, micronidus, and venous drainer) and defined an overall diagnostic value. Statistical and absolute differences in the overall diagnostic values defined the relative intra-arterial conebeam CTA diagnostic values, respectively. Blinded neurosurgeons reported their treatment approach after DSA and graded the adjunctive value of intra-arterial conebeam CTA to improve or modify treatment. Intra-arterial conebeam CTA efficacy was defined as interobserver agreement in the relative intra-arterial conebeam CTA diagnostic and/or treatment-planning value scores.

**RESULTS:** Ten patients with micro-AVMs presented with neurologic deficits and/or intracranial hemorrhages. Both neuroradiologists assigned a higher overall intra-arterial conebeam CTA diagnostic value ($P < .05$), secondary to improved evaluation of both arterial feeders and the micronidus, with good interobserver agreement ($\tau = 0.66$, $P = .018$) in the relative intra-arterial conebeam CTA diagnostic value. Both neurosurgeons reported that integrating the intra-arterial conebeam CTA data into their treatment plan would allow more confident localization for surgical/radiation treatment (8/10; altering the treatment plan in 1 patient), with good interobserver agreement in the relative intra-arterial conebeam CTA treatment planning value ($\tau = 0.73$, $P = .025$).

**CONCLUSIONS:** Adjunctive intra-arterial conebeam CTA techniques are more effective in the diagnostic identification and anatomic delineation of micro-AVMs, relative to DSA alone, with the potential to improve microsurgical or radiosurgery treatment planning.

**ABBREVIATIONS:** mAVM = micro-AVM; IA-CBCTA = intra-arterial conebeam CTA; 3DRA = 3D rotational angiography

Cerebral micro-arteriovenous malformations (mAVMs) are a rare subgroup, accounting for ~8% of intracranial AVMs in the surgical series by Stiver and Ogilvy[1] and may represent 21% of AVMs presenting with intracranial hemorrhage in young adults.[1,2] In 2013, Alén et al[3] reported approximately 87% of patients with mAVMs presenting with spontaneous hemorrhage, while previous studies reported a 100% incidence.[2,4,5] Yasargil defined mAVMs as a particular entity of pial AVMs characterized by an occult nidus of ≤1 cm and differentiated this subgroup, which could not be visualized on angiography or gross pathology specimens but could be identified on histopathology if the hematoma was carefully removed.[6]

Micro-AVMs may be suspected on cerebral DSA as an abnormal draining vein with variable detection of a feeding artery and/or micronidus, often only suggested by small coalescing arterioles. Subtle angiographic findings make the imaging diagnosis challenging and broaden the differential diagnosis to include the possibility of a dural or pial arteriovenous fistula. Additionally, the small mAVM size and associated hemorrhage add difficulty in lesion localization for treatment planning with either microsurgical resection or stereotactic radiation therapy.

Digital flat panel detector CT technology has improved the imaging capabilities of modern angiographic equipment with the

Received February 15, 2018; accepted after revision June 12.

From the Departments of Radiology (A.S.A.-S., A.E., A.S., M.C.H., M.B.P., B.S.J., S.A.A.), Neurology (S.A.A.), and Neurological Surgery (A.S., M.C.H., M.B.P., B.S.J., S.A.A.), Northwestern University, Feinberg School of Medicine, Chicago, Illinois.

Please address correspondence to Sameer A. Ansari, MD, PhD, Departments of Radiology, Neurology, and Neurological Surgery, Northwestern University, Feinberg School of Medicine, 676 N St. Clair St, Suite 800, Chicago, IL 60611-2927; e-mail: s-ansari@northwestern.edu

Indicates article with supplemental on-line tables.

http://dx.doi.org/10.3174/ajnr.A5745

feasibility of routinely performing 3D rotational angiography (3DRA) and intra-arterial conebeam CTA (IA-CBCTA). IA-CBCTA incorporates the high spatial vascular resolution of 3DRA with CT postprocessing techniques for increased contrast resolution to visualize the peripheral osseous and soft tissues. High spatial resolution is maintained and displayed in submillimeter multiplanar reconstructions for improved diagnostic sensitivity and cross-sectional mapping.[7] Prior studies have described the efficacy of IA-CBCTA for the anatomic localization of intracranial and spinal dural AVFs.[8,9] In this study, we hypothesized that the efficacy of IA-CBCTA relative to DSA would improve the diagnostic identification, localization, and treatment planning of mAVMs.

## MATERIALS AND METHODS

### Patient Study

Institutional review board approval was obtained for a retrospective study of patients presenting with intracranial mAVMs (≤1 cm) between January 2010 and February 2017. All patients were identified through the neuroangiographic database of our institution, and at least 1 pretreatment DSA study with adjunctive IA-CBCTA imaging was required for study inclusion. The clinical and radiologic findings of these patients and mAVM lesions were reviewed, including patient demographics, presentations, intracranial hemorrhage locations and volumes (gross manual calculations on presenting CT/MR imaging),[10] mAVM classification according to the Spetzler-Martin grading system, and subsequent management/treatment.

### Image Acquisition

Biplane DSA imaging studies were acquired at 2 tertiary academic institutions (Northwestern Memorial Hospital and Lurie Children's Hospital affiliated with Northwestern University, Chicago, Illinois) with identical biplane angiography suites (Artis Zee/Zeego flat detector biplane angiosuite; Siemens, Erlangen, Germany) and acquisition protocols. 3DRA or IA-CBCTA scanning was performed with a single flat panel detector rotational fluoroscopy and angiography unit (2k detector, amorphous silicon cesium iodide scintillator; 1920 × 2480 pixel resolution, 3.25 lp/mm; size, 30 × 40 cm). The motorized frontal C-arm was used to acquire 496 projection frames over a 200° arc with 5- to 8-second rotation times at 80 kV and 260 mA and a radiation dose of 1.2 μGy/frame. Although acquisition parameters remained constant, IA-CBCTA techniques varied slightly with respect to intra-arterial contrast injection rates dependent on vessel injection sites, including the internal carotid artery (4 mL/s) and vertebral artery (3–4 mL/s), with total volumes of 15–32 mL. Shorter acquisition times (5–8 seconds) and nondilute iodinated contrast assisted with opacification of subtle microvascular anatomy and abnormal early venous drainage without venous contamination.

IA-CBCTA acquisition data were transferred to an independent 3D postprocessing workstation (Leonardo; Siemens). Multiplanar, subtracted, and unsubtracted CT reconstructions (sagittal, coronal, and axial planes with overlapping 0.5-mm slice thickness) were generated and transferred to a PACS for direct visualization on the PACS workstation.

### Image Analysis

Images were retrospectively and independently reviewed by 2 interventional neuroradiologists and 2 vascular neurosurgeons on a de-identified PACS system (including the postprocessed multiplanar IA-CBCTA reconstructions). Both neuroradiologists graded the DSA (biplane, magnified, oblique views) and 3DRA images without access to the IA-CBCTA dataset. Subsequent IA-CBCTA images (subtracted/unsubtracted multiplanar reconstructions) acquired from the same intra-arterial injection site were scored by the observers. Qualitative image analyses were performed on high-definition liquid crystal display monitors routinely used for diagnostic reporting and, based on the level of image quality, anatomic and angiographic characterization on a scale of 0–2 (2, excellent/good; 1, relevant visibility with restrictions; 0, poor, nondiagnostic). The reviewers scored the following parameters: 1) arterial feeders (anatomic localization, origin/course, single versus multiple); 2) venous drainers (anatomic localization, course/destination, single versus multiple); and 3) nidus site (anatomic localization, size, and differentiation from arteriovenous shunting). The total score for each technique was defined as the overall diagnostic value for interpretation.

For evaluation of treatment-planning efficacy, the 2 vascular neurosurgeons reported their presumed treatment strategy and approach (if applicable) after evaluating DSA and 3DRA imaging and subsequently studied the IA-CBCTA multiplanar reconstructions. Both neurosurgeons then graded the adjunctive or relative treatment-planning values of IA-CBCTA according to a scale of 0–2 (2, altered treatment plan; 1, more confident treatment plan; or 0, no value). They were required to provide a reason if they determined that IA-CBCTA improved or altered the treatment plan (grade 1 or 2) in comparison with DSA imaging alone.

### Statistical Analysis

For each observer, the Wilcoxon test was used to assess statistical differences in DSA-versus-IA-CBCTA scoring for each of the 3 mAVM anatomic parameters and the overall diagnostic values (sum of all 3 parameter scores) between the 2 modalities. Statistical and absolute differences between the overall IA-CBCTA and DSA diagnostic value defined the relative IA-CBCTA diagnostic value/scores, respectively. A $P$ value $<.05$ was considered a statistically significant difference.

Interobserver agreement for DSA and IA-CBCTA scoring of each mAVM parameter and the overall diagnostic values were assessed using the Kendall $\tau$ coefficient. Interobserver agreement of the relative IA-CBCTA diagnostic value scores (absolute difference between overall IA-CBCTA and DSA diagnostic value scores), and relative IA-CBCTA treatment-planning value scores were also evaluated using the Kendall $\tau$ coefficient. Good or excellent agreement defined the efficacy of IA-CBCTA relative to DSA in the diagnosis and surgical planning of mAVMs, respectively. The $\tau$ coefficient varied between 0 and 1, with 0 representing no agreement and 1 representing complete agreement. $\tau$ values of $>0.8$, $>0.5–0.8$, $>0.2–0.5$, and $\leq 0.2$ were considered to indicate excellent, good, fair, and poor agreement, respectively. A $P$ value $< .05$ indicated statis-

**Table 1: Qualitative diagnostic scoring of DSA and IA-CBCTA imaging**

| | Observer 1 | | | | | | | | | Observer 2 | | | | | | | | |
|---|---|---|---|---|---|---|---|---|---|---|---|---|---|---|---|---|---|---|
| | Arterial Feeder | | Nidus | | Venous Drainage | | Overall | | Relative CBCTA Diagnostic Value[a] | Arterial Feeder | | Nidus | | Venous Drainage | | Overall | | Relative CBCTA Diagnostic Value[a] |
| | DSA | CBCTA | DSA | CBCTA | DSA | CBCTA | DSA | CBCTA | | DSA | CBCTA | DSA | CBCTA | DSA | CBCTA | DSA | CBCTA | |
| 1 | 1 | 2 | 0 | 2 | 2 | 2 | 3 | 6 | 3 | 0 | 2 | 0 | 2 | 2 | 2 | 2 | 6 | 4 |
| 2 | 0 | 2 | 1 | 2 | 2 | 2 | 2 | 6 | 4 | 0 | 2 | 1 | 2 | 2 | 2 | 3 | 6 | 3 |
| 3 | 1 | 2 | 1 | 2 | 2 | 2 | 4 | 6 | 2 | 0 | 2 | 1 | 2 | 2 | 2 | 3 | 6 | 3 |
| 4 | 1 | 2 | 0 | 2 | 1 | 2 | 2 | 6 | 4 | 1 | 2 | 0 | 2 | 1 | 2 | 2 | 6 | 4 |
| 5 | 1 | 2 | 1 | 2 | 2 | 2 | 4 | 6 | 2 | 1 | 2 | 0 | 2 | 2 | 2 | 3 | 6 | 3 |
| 6 | 2 | 2 | 0 | 2 | 2 | 2 | 4 | 6 | 2 | 2 | 2 | 1 | 2 | 2 | 2 | 5 | 6 | 1 |
| 7 | 1 | 2 | 1 | 2 | 2 | 2 | 4 | 6 | 2 | 2 | 2 | 1 | 2 | 2 | 2 | 5 | 6 | 1 |
| 8 | 2 | 2 | 2 | 2 | 0 | 1 | 4 | 5 | 1 | 1 | 2 | 2 | 2 | 0 | 1 | 3 | 5 | 2 |
| 9 | 2 | 2 | 2 | 2 | 2 | 2 | 6 | 6 | 0 | 2 | 1 | 2 | 2 | 2 | 1 | 6 | 4 | −2 |
| 10 | 2 | 2 | 0 | 2 | 2 | 2 | 4 | 6 | 2 | 1 | 2 | 1 | 2 | 2 | 2 | 4 | 6 | 2 |
| *P* | .02 | | .009 | | .157 | | .007 | | | .03 | | .009 | | .564 | | .016 | | |

$\tau$ coefficient = 0.66, $P$ = .018.

tically significant agreement. Statistical analysis was performed using SPSS statistical software (Version 23.0; IBM, Armonk, New York).

## RESULTS

### *Patient Demographics/Presentations and mAVM Characteristics*

Patients were nearly equivalent in sex (6 females, 4 males) with a mean age of 43.5 years (range, 10–69 years) at the time of presentation. Neurologic deficits were noted in 90% of patients, and half (50%) had headaches. Eight patients (80%) presented with intracranial hemorrhage, 1 patient (10%) had cerebellar/thalamic infarction, and a pediatric patient had altered mental status. All intracranial hemorrhage cases were intraparenchymal, except 1 with isolated intraventricular hemorrhage, with a mean volume of 20.3 mL (range, 0.5–55.5 mL). Intracranial hemorrhages were supratentorial in 5/8 (62.5%) patients and infratentorial in 3/8 (37.5%) patients. The On-line Table details patient demographics, clinical presentations, intracranial hemorrhage location/volume, mAVM classification/anatomy, and management/treatment.

CTA was performed at presentation in 3 patients, suggesting the possibility of a "small AVM" in patients 2 and 4 but was unremarkable in patient 10. MR imaging and MRA were performed for all patients at presentation; findings were questionable for an AVM in patient 4, while there was no report of an AVM in the remainder. DSA and IA-CBCTA were required for Spetzler-Martin grading of mAVMs that ranged from Spetzler-Martin grade I (40%), Spetzler-Martin grade II (40%), or Spetzler-Martin grade III (20%) due to deep venous drainage and/or eloquent location in 6/10 (60%). Most mAVMs, 7/10 (70%), consisted of a very small micronidus of <5 mm. Only a single flow-induced aneurysm arising from a splenial branch feeder of the pericallosal anterior cerebral artery was identified (patient 4).

Management of mAVMs included microsurgical resection in 6 patients, stereotactic radiosurgery in 2 patients, and conservative surveillance in the remaining 2 patients. No endovascular embolization procedures were performed. When intervention was planned, the IA-CBCTA imaging data for mAVM localization was imported into the neuronavigation software for intraoperative guidance (iPlan 3.0 Cranial; Brainlab, Munich, Germany) or treatment-planning software (Leksell GammaPlan 10; Elekta, Stockholm, Sweden) for stereotactic radiosurgery.

### *IA-CBCTA Diagnostic and Treatment-Planning Observer Studies*

Blinded observer analysis was performed on DSA and multiplanar IA-CBCTA images from 10 patients with suspected intracranial mAVMs (Table 1). Initial DSA evaluation revealed a micronidus with excellent visibility in only 2 patients (20%) per both observers (patients 8 and 9). In contrast, IA-CBCTA clearly identified the micronidus in all 10/10 (100%) patients, with both observers scoring the nidus as grade 2 (excellent visualization) with perfect interobserver agreement. Interobserver agreement in grading the rest of the individual anatomic parameters with IA-CBCTA or DSA ranged from good to excellent ($\tau$ coefficient between 0.55 and 1.0). Interobserver agreement for overall diagnostic value scores of IA-CBCTA and DSA was good ($\tau$ coefficient = 0.57 and 0.7, respectively).

Both neuroradiologists assigned significantly higher scores to IA-CBCTA for overall diagnostic value (both observers: $P < .05$; observer 1: $P = .007$; observer 2: $P = .016$), confirming the relative diagnostic value of IA-CBCTA. Although no significant differences were seen between DSA and IA-CBCTA scores when evaluating venous drainage (observer 1: $P = .157$; observer 2: $P = .564$), both observers assigned significantly higher scores to IA-CBCTA when evaluating arterial feeders (observer 1: $P = .02$; observer 2: $P = .03$) and the micronidus (observer 1: $P = .009$; observer 2: $P = .009$), resulting in relative IA-CBCTA diagnostic value scores with good interobserver agreement ($\tau$ coefficient = 0.66, $P = .018$).

Both neurosurgeons recorded more confidence in the treatment plan (grades 1–2) for nearly all patients after review of the IA-CBCTA and agreed that it provided better delineation and precise anatomic localization of the micronidus (Table 2). For example, IA-CBCTA led to both neurosurgeons altering their treatment plan (grade 2) in patient 1 (Fig 1, where the nidus could only be identified on IA-CBCTA) and recommending superselective catheterization and possible embolization before proceeding to an operation (grade 1) in patient 4. Overall, they reported that IA-CBCTA would increase confidence in their microsurgical or radiosurgery treatment by importing these data directly into a

**Table 2: Treatment-planning scoring of IA-CBCTA relative to DSA[a]**

| Patient | Neurosurgeon 1 | | Relative CBCTA Treatment Value | Neurosurgeon 2 | | Relative CBCTA Treatment Value |
|---|---|---|---|---|---|---|
| | DSA | CBCTA | | DSA | CBCTA | |
| 1 | Not sufficient | Operation | 2 | Not sufficient | Operation | 2 |
| 2 | Radiosurgery | Radiosurgery | 1 | Radiosurgery | Radiosurgery | 1 |
| 3 | Radiosurgery | Radiosurgery | 1 | Radiosurgery | Radiosurgery | 0 |
| 4 | Operation | Operation | 1 | Operation | Operation | 1 |
| 5 | Operation | Operation | 1 | Operation | Operation | 1 |
| 6 | Radiosurgery | Radiosurgery | 1 | Radiosurgery | Radiosurgery | 1 |
| 7 | Operation | Operation | 1 | Operation | Operation | 1 |
| 8 | Radiosurgery | Radiosurgery | 1 | Radiosurgery | Radiosurgery | 1 |
| 9 | Operation | Operation | 1 | Operation | Operation | 1 |
| 10 | Operation | Operation | 1 | Operation | Operation | 1 |

[a] $\tau$ coefficient = 0.73, $P = .025$.

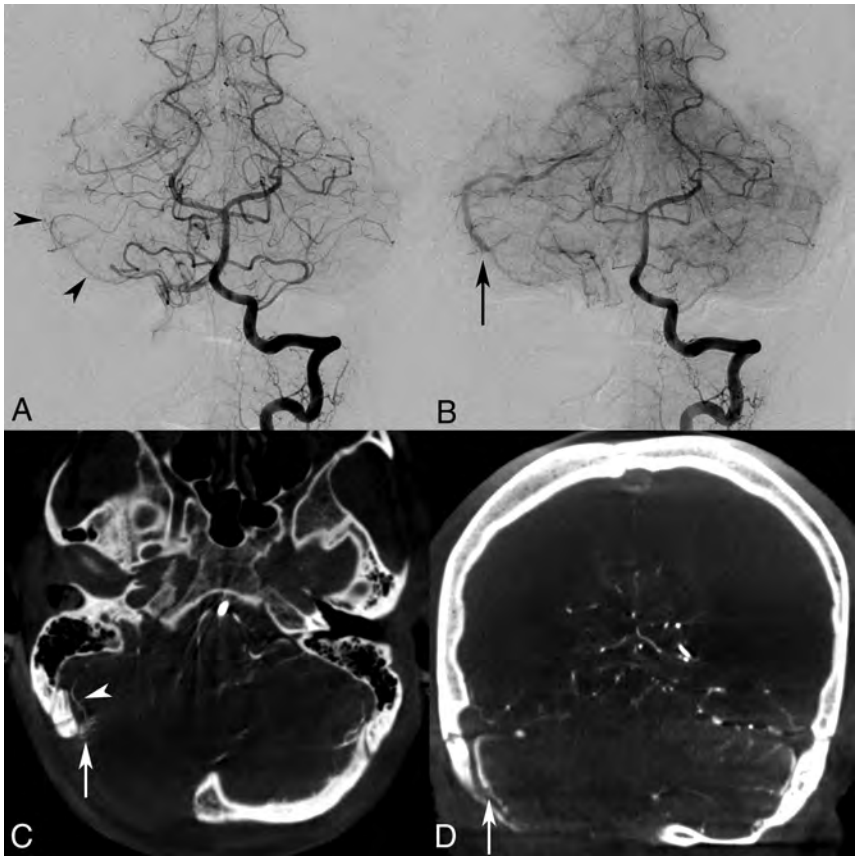


**FIG 1.** Anteroposterior DSA images demonstrate left vertebral artery injections in the early (*A*) and late (*B*) arterial phases, identifying arteriovenous shunting and early venous drainage into a hypertrophied superior cerebellar hemispheric vein (*arrow*) with tentorial venous outflow, but both observers were unable to appreciate an occult micronidus. Although arterial feeders are suggested to project into this region on DSA from the right anterior cerebellar artery and SCA (*A*, *arrowheads*), the SCA feeder is better appreciated on IA-CBCTA multiplanar axial reconstructions (*C*, *arrowhead*). Moreover, both observers identified a <5-mm micronidus under the lateral cerebellar surface and adjacent to the craniectomy site (*C*, *arrow*) with adjunctive IA-CBCTA reconstructions, consistent with an mAVM. IA-CBCTA coronal reconstruction (*D*) shows the nidal outflow to the early draining superior cerebellar hemispheric vein (*arrow*).

neuronavigation system. Interobserver agreement between the 2 vascular neurosurgeons for the relative IA-CBCTA treatment-planning value was good ($\tau$ coefficient = 0.73, $P = .025$).

### *Illustrative Cases*

**Patient 1.** A 30-year-old woman presented with a 3-year history of epilepsy, periventricular heterotopia was diagnosed with a presumed right cerebellar developmental venous anomaly after emergent outside imaging evaluation including DSA. Due to acute presentation with severe headache, visual impairment, quadriparesis, and rapid deterioration to unconsciousness, she required emergent craniectomy and decompression of a cerebellar parenchymal hemorrhage. Although initial MR imaging/MRA failed to detect a vascular malformation, a 3-month delayed DSA demonstrated findings suspicious for a pial AVF (Fig 1*A*, *B*). At 6 months, repeat DSA with 3DRA redemonstrated arteriovenous shunting and early venous drainage but also identified an occult <5-mm micronidus under the lateral right cerebellar surface, adjacent to the craniectomy site, and only visualized with IA-CBCTA reconstructions (Fig 1*C*, *D*).

**Patient 4.** A 21-year-old woman presented to our institution with sudden headache and dizziness for 1 hour. Initial CT/CTA and MR imaging/MRA brain studies revealed an acute paramedian right frontoparietal intracerebral hemorrhage and a distal pericallosal aneurysm with suspicion of an underlying occult vascular malformation, but no abnormal vascular flow voids or nidus was seen (Fig 2*A*). Subsequent DSA with the 3DRA/IA-CBCTA technique was performed 2 days later confirming a 2-mm pericallosal-splenial artery aneurysm/pseudoaneurysm with suggestion of an early draining vein (Fig 2*B*, *C*), but a definitive arterial feeder and <5-mm nidus were only visualized on IA-CBCTA multiplanar reconstructions to confirm the diagnosis of a micro-AVM (Fig 2*D*–*G*).

**Patient 9.** A 50-year-old man presented to an outside institution with confusion followed by right hemiparesis. Initial CT/MR imaging discovered a left parietal cortical hemorrhage, which was

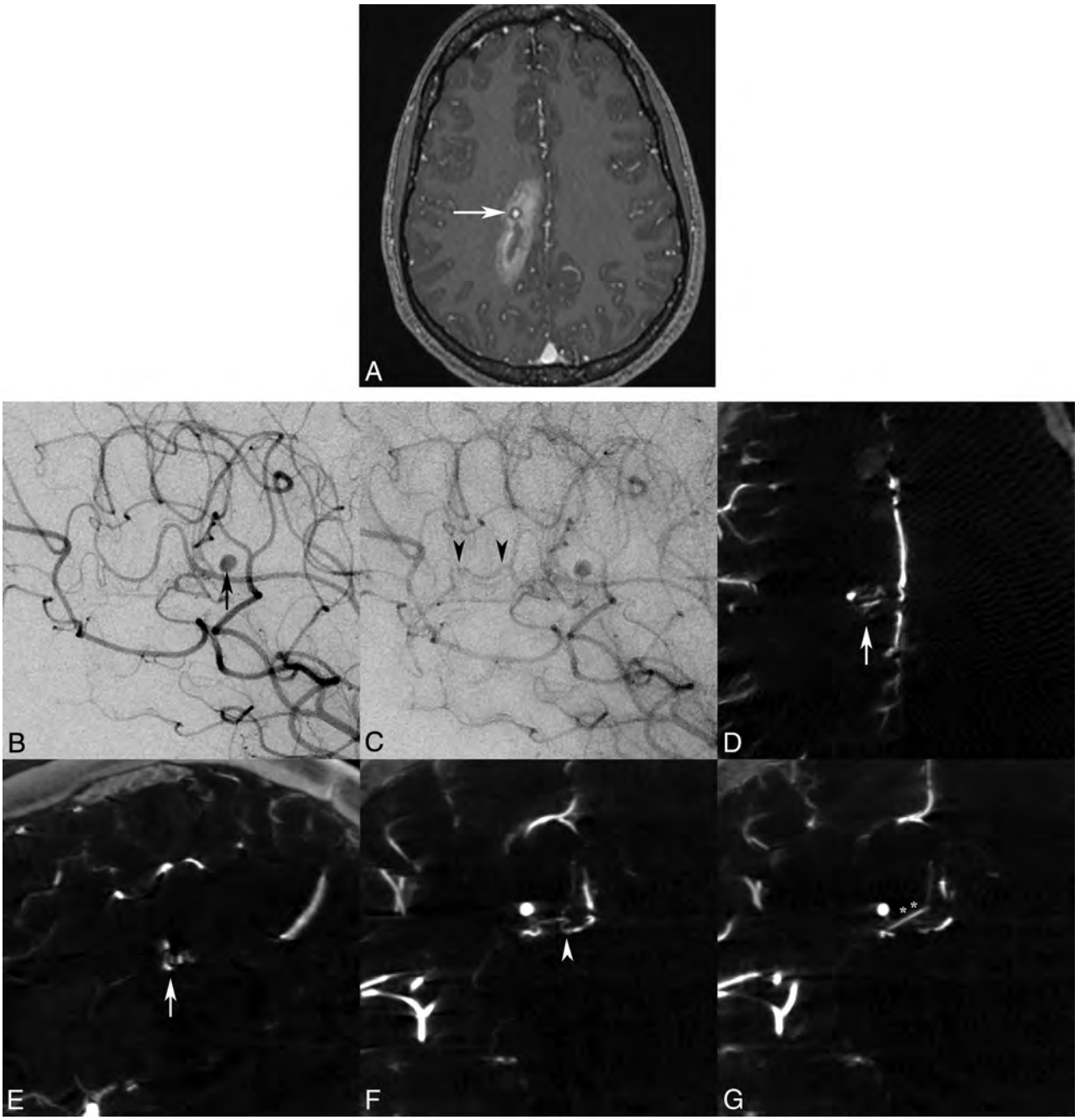


**FIG 2.** Axial MR imaging MPRAGE postgadolinium (*A*) image demonstrates a right parasagittal frontoparietal intraparenchymal hemorrhage with a contrast-enhancing pseudoaneurysm (*white arrow*), consistent with the rupture site. Lateral oblique DSA images in the early arterial phase confirm a pericallosal anterior cerebral artery aneurysm/pseudoaneurysm (*B*, *black arrow*), with a subtle early draining vein in the capillary phase (*C*, *black arrowheads*), but no distinct vascular nidus was identified by either observer. Only IA-CBCTA multiplanar reconstructions clearly delineate a <5-mm micronidus on axial and sagittal reconstructions (*D* and *E*, *white arrows*). Coronal multiplanar reconstructions also assist in identification of the small arterial feeder from the pericallosal-splenial artery branch (*F*, *white arrowhead*) and single draining vein (*G*, *double asterisks*) directly associated with the micronidus and flow-induced pseudoaneurysm.

conservatively managed. Delayed 2-month MR imaging findings were negative, but subsequent DSA reported a left parietal pial AVF, and embolization was planned. At our institution, a repeat DSA with the 3DRA/IA-CBCTA technique revealed a superficial left parietal mAVM with a nidus measuring <1 cm (Fig 3*A*, *B*). Left frontoparietal paramedian craniotomy and microsurgical resection were performed with IA-CBCTA imaging integrated into the neuronavigation system (Fig 3*C*, *D*).

## DISCUSSION

Prior literature emphasized the importance of identifying an mAVM and characterizing its anatomy for effective treatment. However, the diagnosis of mAVMs can be challenging. Alén et al[3] reported the role of high-resolution MR imaging fast spin-echo T2-weighted sequences in detecting subtle flow voids corresponding to small nidus volumes. In addition, they noted the supplementary value of contrast-enhanced MR imaging/MRA over

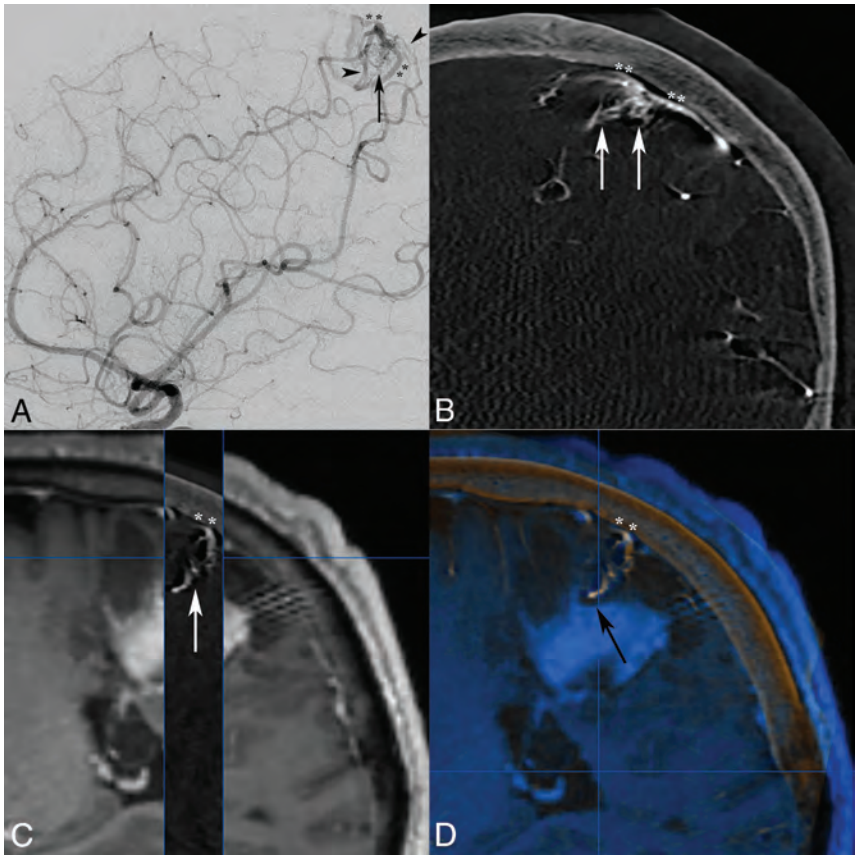


**FIG 3.** Lateral DSA (*A*) and coronal IA-CBCTA reconstruction (*B*) images both demonstrate a small <1-cm micronidus (*arrows*), supplied by tortuous parietal branches of the pericallosal anterior cerebral artery and inferior division of the MCA (*arrowheads*), with early venous drainage into bifurcating cortical veins (*double asterisks*). Although both observers did not report the improved diagnostic value of IA-CBCTA in this case, both neurosurgeons reported increased confidence in treatment planning, and IA-CBCTA was incorporated into the neuronavigation system for microsurgical resection. 3D IA-CBCTA and MR imaging datasets were merged with sagittal overlay (*C*) delineating the micronidus (*arrow*) and draining cortical vein (*double asterisks*) complex in relation to the adjacent hemorrhage. Both datasets were imported into the intraoperative neuronavigation system (*D*, BrainLAB), allowing anatomic localization of the micronidus within a specific sulcus guiding the surgical approach as well as the presumed deep nidal rupture site abutting the hematoma (*black arrow*).

time-of-flight MRA techniques for nidus delineation (especially when adjacent to a hematoma, due to background suppression of hyperintense methemoglobin). However, even combined MR imaging/MRA techniques failed to identify mAVMs in 6/21 patients, and they required DSA to confirm the diagnosis. Early DSA in the setting of hemorrhagic mass effect may also miss mAVMs secondary to diminished flow from various causes such as hemorrhage-related vasospasm, compression of the nidus or feeder/draining vessel, or intralesional thrombosis.[11] Some have reported initially negative DSA findings in patients with hemorrhage who were proven later to have an mAVM on histopathology or repeat angiography,[3,5,11] leading other authors to propose that negative or questionable conventional DSA findings in young adults with atypical hemorrhage patterns should prompt superselective angiography and/or a repeat study after hemorrhage resorption.[2,3,11,12]

In our series, even 2D and 3DRA techniques without IA-CBCTA reconstructions were relatively inferior in delineating the AVM arterial feeders and nidus, consistent with mAVMs possibly being very small occult lesions (<5 mm). We have shown that 3DRA with IA-CBCTA multiplanar reconstructions increases diagnostic power, enabling angiographic identification and precise localization of occult mAVMs over traditional 2D DSA techniques. IA-CBCTA techniques may thereby limit the need for superselective catheterization and repeat angiography. Additionally, while conventional DSA still maintains superior spatial and temporal resolution to diagnose arteriovenous shunting or an abnormal early draining vein, it has some limitations due to its 2D acquisition and inherent vessel overlap, which may interfere with arterial feeder and micronidus delineation.[9] In contrast, the precise cross-sectional localization of mAVMs, especially for surgical treatment planning, can be readily facilitated by IA-CBCTA.

Our results are in keeping with previous studies that have shown the feasibility and superiority of using IA-CBCTA in both preoperative planning and as an intraoperative reference for the microsurgical resection or stereotactic radiosurgery of larger brain AVMs.[13-15] In a case series of 16 patients with cerebral AVMs, Srinivasan et al[14] used CBCTA in a neuronavigation system, allowing complete and safe surgical resection of all lesions. In another case series by Safain et al[15] of 22 patients, CBCTA was used to target cerebral AVMs with radiosurgery, with only 4/22 lesions that had a micronidus of 1 cm and resulted in improved visualization of AVM components and treatment planning. Radvany et al[16] described a modified CBCTA imaging technique in 3 patients performed using an intra-arterial diluted iodinated contrast agent (35%) in the ascending aorta that lasted 22 seconds at a rate of 8 mL/s, which allows imaging of an entire AVM nidus receiving blood supply from >1 cervical artery in a single CBCTA acquisition. In this study, our intra-arterial technique was modified with shorter acquisition times (5–8 seconds) to avoid venous contamination and single cervical artery infusion of nondiluted contrast to optimize visualization of the micronidus and early draining vein. Rahal and Malek [17] reported a higher sensitivity of IA-CBCTA over DSA in identifying the occult nidal anatomy and angioarchitecture of brain AVMs in 3 patients presenting with intracranial hemorrhage as well providing anatomic guidance for either surgical or radiosurgery treatment. However, none of these studies included or discussed the value of CBCTA in cerebral AVMs with a micronidus of <1 cm.

Additionally, IA-CBCTA has been shown to improve the anatomic delineation and localization of both intracranial and spinal dural arteriovenous fistulas for preoperative or endovascular

treatment planning.[8,9,18] Flat panel detectors improve the signal intensity–to-noise ratio and suppress geometric distortion, enabling 3DRA and IA-CBCTA to produce high spatial and contrast-resolution imaging with radiation and contrast-dose reduction.[19] Isotropic CBCT volumetric datasets allow multiplanar and 3D reconstructions analogous to multidetector CT scanners.[9] Advantages over traditional intravenous CT angiography include submillimeter-spatial-resolution isotropic data with versatile postprocessing software analysis, selective intra-arterial contrast injections for territorial vascular analysis, rapid and variable acquisitions (5–8 seconds) to optimize early venous opacification versus venous contamination, subtraction and hemodynamic flow analysis (3DRA), and unsubtracted cross-sectional localization relative to the osseous structures and soft tissues (IA-CBCTA).[9,14]

Our study is subject to the inherent limitations of a retrospective series and qualitative grading of DSA images in comparison with IA-CBCTA as an adjunctive imaging technique. We attempted to partly mitigate this bias with blinded observer analysis and a protocol for grading DSA and IA-CBCTA imaging in series on a de-identified workstation that retained the ability to analyze IA-CBCTA multiplanar reconstructions with or without tissue subtraction. Furthermore, memory bias was limited, with an elapsed period of 6 years to accumulate our cases and only 2 observers in each arm of the study from a total of 6 neurointerventionalists involved in the initial diagnostic evaluation and 5 vascular neurosurgeons involved in the surgical/radiation treatment. Due to the rare incidence of mAVMs, sample sizes in all studies of this pathology remained small, and future studies with a larger population would require a multi-institutional cohort or registry.

## CONCLUSIONS

We compared DSA and adjunctive IA-CBCTA imaging to assess the relative efficacy of IA-CBCTA in the diagnosis and treatment planning of mAVMs. IA-CBCTA improves the diagnostic accuracy of mAVMs, particularly through enhanced anatomic identification and localization of subtle arterial feeders and/or a micronidus, and enables more confident surgical/radiosurgery treatment planning.


## ACKNOWLEDGMENTS

We thank Ms Saadia Sattar, MSc, who contributed to the statistical analysis of this study.

Disclosures: Sameer A. Ansari—*UNRELATED: Grants/Grants Pending*: MicroVention postdoctoral research training grant.* *Money paid to the institution.


## REFERENCES


1. Stiver SI, Ogilvy CS. **Micro-arteriovenous malformations: significant hemorrhage from small arteriovenous shunts**. *Neurosurgery* 2000;46:811–18; discussion 818–19 Medline
2. Andreou A, Ioannidis I, Lalloo S, et al. **Endovascular treatment of intracranial microarteriovenous malformations.** *J Neurosurg* 2008; 109:1091–97 CrossRef Medline
3. Alén JF, Lagares A, Paredes I, et al. **Cerebral microarteriovenous malformations: a series of 28 cases.** *J Neurosurg* 2013;119:594–602 CrossRef Medline
4. Stiver SI. **Microarteriovenous malformations.** *Neurosurg Clin N Am* 1999;10:485–501 Medline
5. Willinsky R, Lasjaunias P, Comoy J, et al. **Cerebral micro arteriovenous malformations (mAVMs): review of 13 cases.** *Acta Neurochir (Wien)* 1988;91:37–41 CrossRef Medline
6. Alexander E. **Microneurosurgery. IIIA: AVM of the brain, history, embryology, pathological considerations, hemodynamics, diagnostic studies, microsurgical anatomy: edited by M. G. Yasargil. 408 pages. New York: Georg Thieme Verlag, 1987 (book review)**. *Surg Neurol* 1988;29:494
7. Wallace MJ, Kuo MD, Glaiberman C, et al; Technology Assessment Committee of the Society of Interventional Radiology. **Three-dimensional C-arm cone-beam CT: applications in the interventional suite.** *J Vasc Interv Radiol* 2009;20:S523–37 CrossRef Medline
8. Honarmand AR, Gemmete JJ, Hurley MC, et al. **Adjunctive value of intra-arterial cone beam CT angiography relative to DSA in the evaluation of cranial and spinal arteriovenous fistulas.** *J Neurointerv Surg* 2015;7:517–23 CrossRef Medline
9. Aadland TD, Thielen KR, Kaufmann TJ, et al. **3D C-arm conebeam CT angiography as an adjunct in the precise anatomic characterization of spinal dural arteriovenous fistulas.** *AJNR Am J Neuroradiol* 2010;31:476–80 CrossRef Medline
10. Luby M, Hong J, Merino JG, et al. **Stroke mismatch volume with the use of ABC/2 is equivalent to planimetric stroke mismatch volume.** *AJNR Am J Neuroradiol* 2013;34:1901–07 CrossRef Medline
11. Elhammady MS, Baskaya MK, Heros RC. **Early elective surgical exploration of spontaneous intracerebral hematomas of unknown origin.** *J Neurosurg* 2008;109:1005–11 Medline
12. Willinsky R, TerBrugge K, Montanera W, et al. **Micro-arteriovenous malformations of the brain: superselective angiography in diagnosis and treatment.** *AJNR Am J Neuroradiol* 1992;13:325–30 Medline
13. van der Bom IM, Gounis MJ, Ding L, et al. **Target delineation for radiosurgery of a small brain arteriovenous malformation using high-resolution contrast-enhanced cone beam CT.** *J Neurointerv Surg* 2014;6:e34 CrossRef Medline
14. Srinivasan VM, Schafer S, Ghali MG, et al. **Cone-beam CT angiography (DynaCT) for intraoperative localization of cerebral arteriovenous malformations.** *J Neurointerv Surg* 2016;8:69–74 CrossRef Medline
15. Safain MG, Rahal JP, Raval A, et al. **Use of cone-beam computed tomography angiography in planning for gamma knife radiosurgery for arteriovenous malformations: a case series and early report.** *Neurosurgery* 2014;74:682–95; discussion 695–96 CrossRef Medline
16. Radvany MG, Ehtiati T, Huang J, et al. **Aortic arch injection with C-arm cone beam CT for radiosurgery treatment planning of cerebral arteriovenous malformations: technical note.** *J Neurointerv Surg* 2012;4:e28 CrossRef Medline
17. Rahal JP, Malek AM. **Benefit of cone-beam computed tomography angiography in acute management of angiographically undetectable ruptured arteriovenous malformations.** *J Neurosurg* 2013;119: 1015–20 CrossRef Medline
18. Ansari SA, Aoun SG, Bendok BR. **Cone beam computed tomography in the neurointerventional room: beyond vessels.** *World Neurosurg* 2012;77:659–61 CrossRef Medline
19. Lai CJ, Shaw CC, Chen L, et al. **Visibility of microcalcification in cone beam breast CT: effects of X-ray tube voltage and radiation dose.** *Med Phys* 2007;34:2995–3004 CrossRef Medline

# Investigation of a New Version of the Liquid Embolic Agent PHIL with Extra-Low-Viscosity in an Endovascular Embolization Model

D.F. Vollherbst, R. Otto, M. Hantz, C. Ulfert, H.U. Kauczor, M. Bendszus, C.M. Sommer, and M.A. Möhlenbruch

## ABSTRACT

**BACKGROUND AND PURPOSE:** The type and composition of an embolic agent have a relevant influence on the performance of endovascular embolization. The aim of this study was to investigate a new version of the liquid embolic agent precipitating hydrophobic injectable liquid (PHIL) with extra-low-viscosity in an in vivo embolization model.

**MATERIALS AND METHODS:** Twenty-four embolization procedures were performed in the porcine rete mirabile. Eight embolizations were performed with PHIL 25% low viscosity, Squid 12, and standard PHIL 25%, respectively. Procedure time, required volume of embolic agent, visibility of the embolic agent, embolization control, embolization extent (ie, penetration of the rete mirabile), amount of reflux, and degree of embolization distal to the rete mirabile were assessed.

**RESULTS:** All embolic agents were adequately visible. The embolization extent was not significantly different among the 3 investigated agents; however, there was a tendency toward a higher embolization extent for PHIL 25% low viscosity (median embolization extent: 88% [PHIL 25% low viscosity]; 65% [Squid 12]; 60% [PHIL 25%]; $P = .146$). The amount of reflux was significantly lower for the extra-low-viscosity agents PHIL 25% low viscosity and Squid 12 compared with the standard PHIL 25% (median reflux distance: 8 mm [PHIL 25% low viscosity]; 6 mm [Squid 12]; 17 mm [PHIL 25%]; $P = .011$). All other embolization features did not differ among agents.

**CONCLUSIONS:** PHIL 25% low viscosity is a promising liquid embolic agent for endovascular embolization, featuring effective distal penetration, adequate visibility, a low amount of reflux, and good flow control.

**ABBREVIATIONS:** APA = ascending pharyngeal artery; HR-DVT = high-resolution digital volume tomography; LEA = liquid embolic agent; LV = low viscosity; RM = rete mirabile

Endovascular embolization can be an effective treatment option for selected cerebral arteriovenous malformations and dural arteriovenous fistulas.[1,2] Although the success rate of endovascular embolization of these vascular entities has improved in recent years, there is still an obvious need for further improvement, especially regarding the effectiveness and safety of the endovascular treatment of AVMs.[3,4]

The choice of the embolic agent has a relevant impact on the success of the endovascular therapy.[4,5] For the endovascular treatment of AVMs and dural arteriovenous fistulas, liquid embolic agents (LEAs) are used most frequently. Different LEAs are currently available that basically differ in the following aspects: mechanism of hardening (ie, polymerization or precipitation), adhesiveness, active component, medium inducing radiopacity, and viscosity. A recently introduced LEA with potential advantages over the established LEAs is the precipitation hydrophobic injectable liquid (PHIL; MicroVention, Tustin, California). PHIL is a precipitating, nonadhesive embolic agent that uses 2 specific copolymers (polylactide-co-glycolide and polyhydroxyethylmethacrylate) as active components and a covalently bound iodine component (triiodophenol) for radiopacity. The safety and efficacy of PHIL has been demonstrated in several clinical and experimental studies.[6-10]

The treatment of complex AVMs with large nidi or dural arteriovenous fistulas with large vascular networks can be impeded by incomplete penetration of the target lesion by the LEA, resulting in an occlusion of the feeding arteries but not of the arteriovenous shunt itself.[11] LEAs with extra-low-viscosity could improve the success rate of these entities.[12,13] Of the commercially available LEAs, the standard low-viscosity versions are Onyx 18 (Covidien, Irvine, California), Squid 18 (Emboflu, Gland,

Received March 28, 2018; accepted after revision June 12.

From the Department of Neuroradiology (D.F.V., R.O., M.H., C.U., M.B., M.A.M.) and Clinic for Diagnostic and Interventional Radiology (D.F.V., H.U.K., C.M.S.), Heidelberg University Hospital, Heidelberg, Germany; and Clinic for Diagnostic and Interventional Radiology (C.M.S.), Klinikum Stuttgart, Stuttgart, Germany.

Please address correspondence to Markus A. Möhlenbruch, MD, Department of Neuroradiology, University Hospital Heidelberg, INF 400, 69120 Heidelberg, Germany; e-mail: markus.moehlenbruch@med.uni-heidelberg.de

http://dx.doi.org/10.3174/ajnr.A5750

Switzerland), and PHIL 25%. Currently, only Emboflu offers a commercially available extra-low-viscosity version (Squid 12).

The aim of this study was to investigate a new extra-low-viscosity version of the LEA PHIL in an in vivo endovascular embolization model. Squid 12 as a commercially available ethylene-vinyl alcohol copolymer–based extra-low-viscosity LEA and PHIL 25% as a standard low-viscosity LEA were used as control agents.

## MATERIALS AND METHODS

### Endovascular Embolization Model

The porcine rete mirabile (RM) is an established embolization model for the investigation of embolic agents and embolization techniques.[10,14-16] The RM is a reticular network of blood vessels, located bilaterally at the base of the skull in pigs with a connection through the midline. It is mainly supplied by the ascending pharyngeal artery (APA), a branch of the common carotid artery.

### Animal Procedure

State Animal Care and Ethics Committee approval was obtained. All experiments were performed in accordance with the Guide for the Care and Use of Laboratory Animals.

Healthy female pigs (German Landrace) with a body weight of 35–45 kg were used. Anesthesia was introduced with an intramuscular injection of azaperone (6 mg/kg; Stresnil; Janssen Animal Health, Beerse, Belgium), midazolam (0.4 mg/kg; Dormicum; Roche, Basel, Switzerland), and ketamine (10 mg/kg; Ketamin; Medistar, Hannover, Germany). For maintenance, intravenous injections of midazolam and ketamine were performed with a syringe driver, dosed according to the effect. Intubation was performed for airway management. After surgical cut-down, a 6F introducer sheath was inserted into the right femoral artery. The animals were sacrificed 2 hours after embolization with an intravenous injection of 20 mL of potassium chloride 7.5%. The RMs were explanted according to the technique described by Eliyas et al.[17] Subsequently, the RM were transferred to 4% buffered paraformaldehyde and embedded in paraffin.

### Embolization Technique

A 5F guiding catheter (Radifocus Glidecath Vertebral; Terumo Europe, Leuven, Belgium) was positioned in the common carotid artery, proximal to the origin of the APA under fluoroscopic guidance (Artis zee; Siemens, Erlangen, Germany). Subsequently, a diagnostic angiography of the respective side of the RM was performed via the guiding catheter. Afterward, a 1.3F microcatheter (Headway Duo; MicroVention), which was used with a 0.014-inch guidewire (Traxcess 14; MicroVention), was inserted through the guiding catheter and positioned in the base of the RM. After superselective angiography via the microcatheter for confirmation of the correct catheter position, the microcatheter was flushed with 1 mL of dimethyl-sulfoxide. A syringe-catheter interface adapter was connected to the microcatheter. Subsequently, embolization of the RM was performed by manual and pulsatile injection of the respective LEA. Per injection, a certain amount of reflux was tolerated, defined as a distance of 5 mm of the APA. In the case of reflux exceeding this limit or in the case of embolization of the efferent vessels of the RM, the injection was stopped and the procedure was paused for 60 seconds. At every pause and at the end of every procedure, an x-ray of the RM was performed for assessment of the intra- and postprocedural embolization extent. The procedure was terminated if the respective RM was completely embolized. The procedure was terminated prematurely in the following scenarios: 1) complete embolization of the APA with imminent embolization of the common carotid artery, 2) distal embolization with imminent embolization of the brain, or 3) embolization of the contralateral RM. One minute after termination of the embolization procedure, the microcatheter was removed under fluoroscopy while monitoring the LEA cast for stability. All interventions were performed by 2 interventionalists (D.F.V. and M.A.M. with 5 and 12 years of experience in endovascular interventions, respectively).

### PHIL 25% Low Viscosity

The chemical composition and the polymer backbone of PHIL 25% low viscosity (LV) are equivalent to those in the currently available versions of PHIL. The concentration of PHIL 25% LV is identical to that of the standard PHIL 25% (the numbers indicate the concentration in weight per weight). The difference between the extra-low-viscosity and the standard version of PHIL 25% is the length of the polymer chains. The polymer chains are shorter for PHIL 25% LV, resulting in a lower molecular weight of the single copolymer molecules. The lower molecular weight leads to the lower viscosity of PHIL 25% LV.

### Study Groups

In total, 24 embolization procedures were performed. We defined 3 study groups: PHIL 25% LV, Squid 12, and standard PHIL 25%, with 8 embolization procedures per study group, respectively.

### Study Goals

The aim of each embolization procedure was complete embolization of the respective side of the RM.

The total procedure time and the used volume of LEA per procedure (including the dead space of the microcatheter of 0.35 mL) were recorded. The ease of visualization in fluoroscopy and in x-ray was graded on a 3-point scale (1, definitely not visible; 2, probably visible; 3, definitely visible). The ability to stop forward flow when the injection stops was graded on a 5-point scale (1, uncontrolled high forward flow; 2, partially controlled high forward flow; 3, partially controlled moderate forward flow; 4, controlled low forward flow; 5, no forward flow). The degree of distal embolization was assessed by counting the number of events of embolization distal to the RM per procedure.

For the analysis of the embolization extent, the area of the respective side of the RM was determined in the preinterventional posteroanterior angiogram using the syngo Acquisition Workplace (Siemens) by delineating the perimeter of the RM (Fig 1*A*). The area of the embolized portion of the RM was delineated in the same fashion in the postinterventional x-ray (Fig 1*F*). The ratio of these 2 areas (preinterventional angiogram and postinterventional x-ray) was calculated and defined as the embolization extent, as described previously.[10,15]

For evaluation of the 3D distribution of the LEA in the RM, a high-resolution digital volume tomography (HR-DVT, 3D Accuitomo 170; J. Morita, Tokyo, Japan; FOV = 40 × 40 mm, volt-

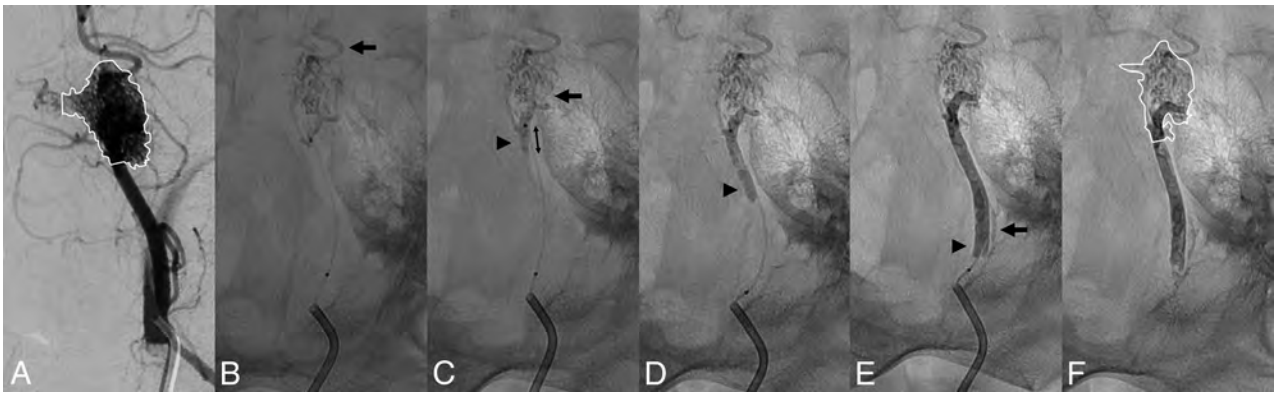


**FIG 1.** Representative embolization procedure with PHIL 25% LV. *A*, Before the embolization procedure, a diagnostic angiography is performed through a guiding catheter. The RM is delineated in the diagnostic angiography image with complete filling of the RM. *B*, X-ray after the first injection. After the first injection, most of the RM is already embolized. The injection is stopped because of embolization distal to the RM (*arrow*). *C*, X-ray after the second injection. The second injection leads to slight additional filling of the lateral parts of the RM (*black arrow*). The injection is stopped because of reflux (*arrowhead*). Retrospectively, this is the injection with which the maximal embolization extent was reached. Accordingly, the reflux distance is measured in this image (*double arrow*). X-rays after the fifth (*D*) and eighth (*E*) injections. No more filling of the RM is achieved with the following injections, which were all stopped because of reflux (*arrowheads*). After the eighth injection, the procedure is terminated because of reflux of the LEA into the APA (*arrow*). *F*, After termination of the procedure, the catheters are removed and the embolized portion of the RM is delineated. The area of the completely filled RM (*A*) and the area of the embolized RM (*F*) are related, resulting in the embolization extent.

**Summary of the results**[a]

| | PHIL 25% LV | Squid 12 | Standard PHIL 25% | *P* Value |
|---|---|---|---|---|
| Total procedure time (s) | 395 (310–528) | 436 (430–501) | 328 (239–479) | .386[b] |
| Required volume of embolic agent (mL) | 0.7 (0.7–0.9) | 0.8 (0.7–0.9) | 0.7 (0.6–0.7) | .121[b] |
| Visibility | 3 (3–3) | 3 (3–3) | 3 (3–3) | NA |
| Forward flow control | 5 (5–5) | 5 (5–5) | 5 (5–5) | .335[b] |
| Embolization extent (%) | 87.7 (68.0–100) | 64.6 (52.2–73.0) | 60.4 (27.0–75.9) | .146[b] |
| Reflux distance (mm) | 8 (6–8) | 6 (5–10) | 17 (14–21) | .011[b]<br>>.999[c]<br>.049[d]<br>.017[e] |
| Events of embolization distal to the RM per procedure (No.) | 0 (0–1) | 0 (0–0) | 0 (0–0) | .527[b] |

**Note:**—NA indicates that the *P* value was not available because all values are identical.
[a] Data are presented as median (lower quartile–upper quartile).
[b] Kruskal-Wallis test.
[c] Post hoc Dunn test, PHIL 25% LV vs Squid 12.
[d] Post hoc Dunn test, PHIL 25% LV vs standard PHIL 25%.
[e] Post hoc Dunn test, Squid 12 vs. standard PHIL 25%.

age = 90 kV, amperage = 8.0 mA, rotation = 360°, reconstruction with isotropic voxels with a slice thickness of 80 $\mu$m) of the explanted, paraffin-embedded RM was performed. The 3D distribution of the LEA was described qualitatively. An analysis of the embolization extent using the HR-DVT datasets was consciously not performed for 2 reasons: 1) preparation artifacts that occurred in a few specimens during the dissection of the RM, and 2) the nonembolized portions of the RM that could not be examined in HR-DVT due to the limited soft-tissue contrast in this technique.

To assess the amount of reflux, we measured the reflux distance, defined as the distance of LEA in the APA, on reaching the maximal embolization extent (Fig 1*C*). The reflux distance at the end of the procedure was consciously not used because for most the procedures, the APA was finally embolized completely or near-completely because of repeat reflux.

### *Statistics*

GraphPad Prism software (Version 7.02; GraphPad Software, San Diego, California) was used for data analysis. Quantitative data are presented as medians (lower quartile–upper quartile). To evaluate statistical differences among the study groups, we performed the Kruskal-Wallis test with a post hoc Dunn test with a *P* value of .05 as the threshold for statistical significance.

## RESULTS

All procedures were performed as planned. No event of technical failure, such as catheter occlusion or catheter entrapment, or indirect angiographic signs of vasotoxicity, such as embolization-induced vasospasm, were observed.

The results are summarized in the Table. A representative embolization procedure is shown in Fig 1.

All embolic agents were definitely visible on fluoroscopy and in x-ray (Fig 2). We observed a slightly better visibility for standard PHIL 25% compared with PHIL 25% LV and Squid 12.

The embolization extent (illustrated in Fig 3*A*) was not significantly different for the 3 study groups; however, there was a trend toward a higher embolization extent for PHIL 25% LV (medians:

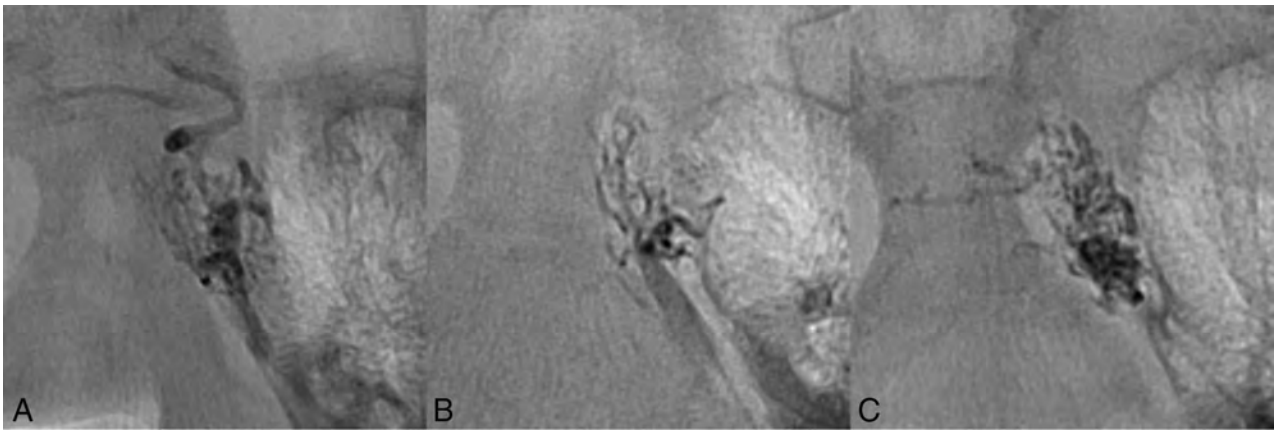


**FIG 2.** Visibility of the embolic agents. X-rays after the first injection shown for PHIL 25% LV (*A*), Squid 12 (*B*), and standard PHIL 25% (*C*). Note the adequate visibility of all 3 embolic agents.

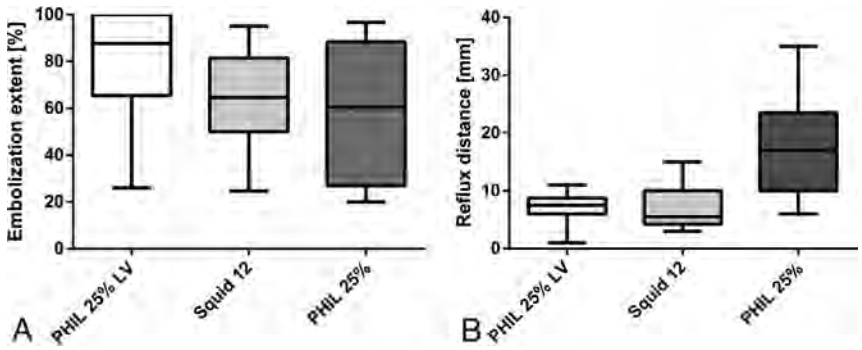


**FIG 3.** Illustration of embolization extent and reflux distance. *A*, The embolization extent tended to be higher for PHIL 25% LV, however, without reaching statistical significance. *B*, The reflux distance was significantly lower for the 2 extra-low-viscosity LEAs PHIL 25% LV and Squid 12 compared with standard PHIL 25%.

87.7%, 64.6%, and 60.4%, respectively). For PHIL 25% LV and for Squid 12, but not for standard PHIL 25%, the first 3 injections were assessed as the most effective. These effective injections were not accompanied by reflux or were accompanied by only low amounts of reflux. After these effective injections, in most of the embolization procedures, there was repeat reflux until complete or near-complete filling of the APA with subsequent termination of the procedure.

The 3D distribution of the LEAs in HR-DVT showed a good correlation qualitatively to the 2D distribution of the LEAs in x-ray (Fig 4). There were no substantial differences for the 3 LEAs regarding their 3D distribution. For procedures with complete or near-complete filling, there was homogeneous enhancement of the RM, whereas for procedures with low-embolization extents, various filling defects were identified.

The reflux distance (illustrated in Fig 3*B*) was lower for PHIL 25% LV and Squid 12 compared with standard PHIL 25% (medians: 8, 6, and 17 mm, respectively; $P = .011$), however, with no difference between the extra-low-viscosity LEAs PHIL 25% LV and Squid 12.

For PHIL 25% LV and Squid for 12, there was 1 case of controlled low forward flow for each of them. For the remaining 7 procedures of these study groups and for all procedures of standard PHIL 25%, there was excellent flow control with no event of unwanted forward flow. The total number of events of embolization distal to the RM was $n = 3$ for PHIL 25% LV; $n = 2$ for Squid 12; and $n = 2$ for standard PHIL 25% without significant differences.

The total procedural time and the volume of embolic agent used were also not significantly different among the 3 study groups.

## DISCUSSION

In this experimental study, the new extra-low-viscosity LEA PHIL 25% LV was investigated in an acute in vivo embolization model. The embolization extent tended to be higher for PHIL 25% LV compared with Squid 12 and standard PHIL 25%, while both extra-low-viscosity LEAs (PHIL 25% LV and Squid 12) featured a significantly lower amount of reflux compared with standard PHIL 25%. All investigated embolic agents showed good flow control.

Several different concentrations are available for each of the currently commercially available precipitating, nonadhesive LEAs: a low-viscosity version (Onyx 18, Squid 18, and PHIL 25%), a medium-viscosity version (Onyx 20 and PHIL 30%), and a high-viscosity version (Onyx 34 and PHIL 35%). For the low-viscosity versions Onyx 18 and PHIL 25%, it was shown in the experimental setting that embolization characteristics and embolization extent are similar.[9,10] Also Squid 18 seems to show embolization features that are like those in the equally viscous Onyx 18.[13] As initially indicated, of the commercially available precipitating, nonadhesive LEAs, Squid 12 is the only extra-low-viscosity version so far.

Intra- and postprocedural visibility in the angiography suite is a crucial requirement for the LEA being used.[18,19] Adequate visibility enables real-time embolization control and assessment of the current status of embolization (embolized and nonembolized portions of a lesion).[18,19] A decrease in viscosity could theoretically lead to a decrease in visibility. In this study, all investigated LEAs were definitely visible on fluoroscopy and x-ray. However, a slightly better visibility was noted for standard PHIL 25% compared with the extra-low-viscosity

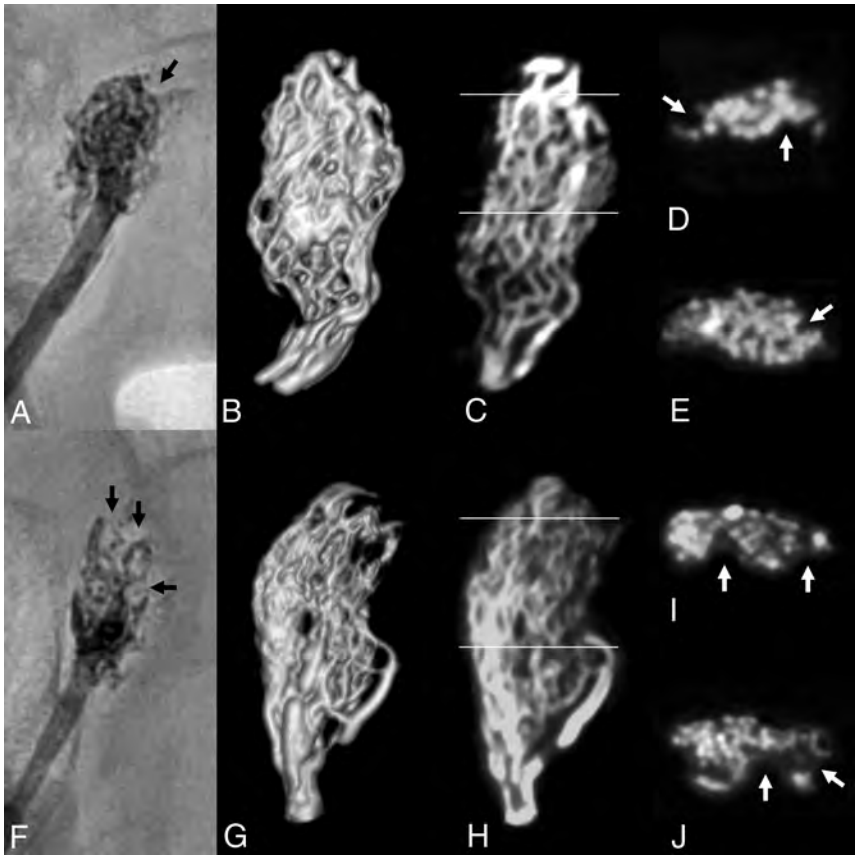


**FIG 4.** Distribution of the LEA in HR-DVT. The distribution of the LEA in HR-DVT is shown for 2 representative cases. *A–E*, PHIL 25% LV. *F–J*, Standard PHIL 25%. *A* and *F*, Postinterventional x-rays. *B* and *G*, Volume-rendering of the HR-DVT dataset. *C* and *H*, Coronal HR-DVT images. *D*, *E*, *I*, and *J*, Axial HR-DVT images of the middle (*E* and *J*) and the distal (*D* and *I*) parts of the RM (*lines* in *C* and *H* indicate the position of the axial planes). Note the perceptibility of single blood vessels of the RM in the high-resolution HR-DVT images. Well-circumscribed filling defects were identified in the axial HR-DVT images, which were particularly detected in the distal, only partially embolized parts of the RM (*white arrows*). The same filling defects were also seen in the 2D x-rays (*black arrows*).

LEAs PHIL 25% LV and Squid 12. Considering that the porcine RM is a rather simple vascular structure with a homogeneous organization, in complex vascular pathologies with embolized and nonembolized blood vessels of different sizes overlapping each other, the visibility of these LEAs could be different.

In this study, the embolization extent was highest for PHIL 25% LV, followed by Squid 12 and standard PHIL 25%, however, without reaching statistical significance. Nevertheless, these results indicate that for selected vascular entities, extra-low-viscosity LEAs may be advantageous over the currently available standard low-viscosity LEAs (Onyx 18, Squid 18, and PHIL 25%). Naturally, the requirements for the respective LEA in terms of the adequate viscosity differ for different lesions with regard to type (eg, AVMs or dural arteriovenous fistulas), flow (eg, high-flow or low-flow), extent (eg, small or large lesions), and configuration of the vessels of the lesion (eg, large vessels, small vessels, or aneurysms).[20,21] For Squid 12, previous studies in the literature have already noted that penetration of the nidus may be more effective than with standard low-viscosity embolic agents, such as Squid 18 or Onyx 18.[13,22,23]

Several advantages of PHIL over cyanoacrylates and ethylene-vinyl alcohol–based LEAs are discussed in the literature, including its ease of use, fast plug formation, consistent visibility, low artifacts on postinterventional CT, lower required volumes of LEA, and the lack of intraoperative hazards.[6,9,24,25] Given these potential advantages of the currently available versions of PHIL and the results of the present study, PHIL 25% LV appears to be an effective agent for endovascular embolization of selected pathologies.

We could show that the degree of reflux is significantly lower for the extra-low-viscosity LEAs PHIL 25% LV and Squid 12 compared with the standard PHIL 25%. This aspect can be highly relevant in clinical practice. Reflux carries the risk of closing the feeding artery prematurely and increases the probability of catheter entrapment; and especially in AVMs or dural arteriovenous fistulas with short feeding arteries, reflux increases the risk of unwanted embolization of arteries supplying healthy tissue, eventually leading to infarction.[18,26]

In this study, for PHIL 25% LV and Squid 12, embolization was most effective with approximately the first 3 injections. Afterward, in most of the cases, reflux occurred and no more penetration of the RM, especially of the distal parts, was possible. Accordingly, there was actually no plug formation with consecutive effective embolization for the 2 extra-low-viscosity LEAs. This concern can potentially be solved using a dual-lumen micro-balloon catheter for prevention of reflux.[27,28] Another option is to use small amounts of the more viscous versions of these LEAs for plug formation with subsequent filling of the lesion with extra-low-viscosity LEAs in a manner similar to the pressure cooker technique.[29] This approach was already described in the literature with respect to Squid, using Squid 18 for the initial plug formation followed by embolization with Squid 12.[13]

A conceivable drawback of extra-low-viscosity LEAs is poor flow control and early distal embolization, which risks premature closing of the draining veins, potentially leading to intra- or postprocedural hemorrhage, or embolization of healthy tissue distal to the lesion to be treated, potentially leading to stroke.[27,30] In this experimental study, flow control was good and the frequency of embolization distal to the RM was low for all 3 LEAs. However, in clinical practice, due to the more complex angioarchitecture and different flow patterns of AVMs and dural arteriovenous fistulas, flow characteristics could be different and the risk of distal embolization could be higher for extra-low-viscosity LEAs, especially for lesions with high-flow shunts. Therefore, especially the first injections should be of low volume and with a high extent of

caution concerning unwanted forward flow exceeding the distal parts of the treated lesion.

This study has limitations. First, PHIL 25% LV was only compared with 2 other LEAs. Comparison with other LEAs, such as Onyx 18, could have identified more characteristics and differences between PHIL 25% LV and the currently available embolic agents. However, as mentioned above, recent experimental studies showed that the embolization features of Onyx 18 and standard PHIL 25% are similar.[9,10] Accordingly, to reduce the number of required laboratory animals, the above-mentioned study groups were defined. Second, the number of experiments was relatively small; however, the findings were consistent in the different study groups. Third, the survival time after embolization was short, precluding a meaningful analysis on the biocompatibility of the LEAs. Fourth, the transferability of experimental models to clinical practice is generally limited. Fifth, the creation of an arteriovenous fistula would have made the embolization model more like an AVM. Sixth, the analysis of the embolization extent that was used in this study does not take into account central filling defects or the density of the LEA inside the RM.

## CONCLUSIONS

PHIL 25% LV is a promising LEA for endovascular embolization, featuring effective distal penetration, adequate visibility, a low amount of reflux, and good flow control.

Disclosures: Dominik F. Vollherbst—*UNRELATED*: *Travel/Accommodations/Meeting Expenses Unrelated to Activities Listed*: MicroVention and Stryker, *Comments*: Travel support*; *OTHER RELATIONSHIPS*: This study was technically supported by MicroVention. Christian Ulfert—*UNRELATED*: *Travel/Accommodations/Meeting Expenses Unrelated to Activities Listed*: MicroVention, Stryker*. Hans U. Kauczor—*UNRELATED*: *Payment for Lectures Including Service on Speakers Bureaus*: Siemens, Boehringer Ingelheim, Philips Healthcare, Bracco. Martin Bendszus—*UNRELATED*: *Board Membership*: Data and Safety Monitoring Board for Vascular Dynamics, Guerbet, Boehringer Ingelheim; *Consultancy*: Codman Neurovascular, Roche, Guerbet, Boehringer Ingelheim, Braun; *Grants/Grants Pending*: German Research Foundation Hopp Foundation, Novartis, Siemens, Guerbet, Stryker, Covidien, European Union*; *Payment for Lectures Including Service on Speakers Bureaus*: Novartis, Roche, Guerbet, Teva Pharmaceutical Industries, Bayer AG, Codman Neurovascular. Markus A. Möhlenbruch—*UNRELATED*: *Board Membership*: Codman Neurovascular; *Consultancy:* MicroVention, Medtronic, Stryker; *Grants/Grants Pending*: Balt, MicroVention*; *Payment for Lectures Including Service on Speakers Bureaus*: MicroVention, Medtronic, Stryker. *Money paid to the institution.

## REFERENCES

1. Pierot L, Cognard C, Herbreteau D, et al. **Endovascular treatment of brain arteriovenous malformations using a liquid embolic agent: results of a prospective, multicentre study (BRAVO).** *Eur Radiol* 2013;23:2838–45 CrossRef Medline
2. Gross BA, Albuquerque FC, Moon K, et al. **Evolution of treatment and a detailed analysis of occlusion, recurrence, and clinical outcomes in an endovascular library of 260 dural arteriovenous fistulas.** *J Neurosurg* 2017;126:1884–93 CrossRef Medline
3. Singfer U, Hemelsoet D, Vanlangenhove P, et al. **Unruptured brain arteriovenous malformations: primary ONYX embolization in ARUBA (A Randomized Trial of Unruptured Brain Arteriovenous Malformations)-eligible patients.** *Stroke* 2017;48:3393–96 CrossRef Medline
4. van Rooij WJ, Jacobs S, Sluzewski M, et al. **Curative embolization of brain arteriovenous malformations with Onyx: patient selection, embolization technique, and results.** *AJNR Am J Neuroradiol* 2012; 33:1299–304 CrossRef Medline
5. Gross BA, Du R. **Diagnosis and treatment of vascular malformations of the brain.** *Curr Treat Options Neurol* 2014;16:279 CrossRef Medline
6. Varadharajan S, Ramalingaiah AH, Saini J, et al. **Precipitating hydrophobic injectable liquid embolization of intracranial vascular shunts: initial experience and technical note.** *J Neurosurg* 2017 Dec 1:1–6. [Epub ahead of print] CrossRef Medline
7. Lamin S, Chew HS, Chavda S, et al. **Embolization of intracranial dural arteriovenous fistulas using PHIL liquid embolic agent in 26 patients: a multicenter study.** *AJNR Am J Neuroradiol* 2017;38: 127–31 CrossRef Medline
8. Samaniego EA, Kalousek V, Abdo G, et al. **Preliminary experience with Precipitating Hydrophobic Injectable Liquid (PHIL) in treating cerebral AVMs.** *J Neurointerv Surg* 2016 Jan 27. [Epub ahead of print] CrossRef Medline
9. Vollherbst DF, Sommer CM, Ulfert C, et al. **Liquid embolic agents for endovascular embolization: evaluation of an established (Onyx) and a novel (PHIL) embolic agent in an in vitro AVM model.** *AJNR Am J Neuroradiol* 2017;38:1377–82 CrossRef Medline
10. Vollherbst DF, Otto R, von Deimling A, et al. **Evaluation of a novel liquid embolic agent (precipitating hydrophobic injectable liquid (PHIL)) in an animal endovascular embolization model.** *J Neurointerv Surg* 2018;10:268–74 CrossRef Medline
11. Saatci I, Geyik S, Yavuz K, et al. **Endovascular treatment of brain arteriovenous malformations with prolonged intranidal Onyx injection technique: long-term results in 350 consecutive patients with completed endovascular treatment course.** *J Neurosurg* 2011; 115:78–88 CrossRef Medline
12. van Rooij WJ, Sluzewski M, Beute GN. **Brain AVM embolization with Onyx.** *AJNR Am J Neuroradiol* 2007;28:172–77; discussion 178 Medline
13. Akmangit I, Daglioglu E, Kaya T, et al. **Preliminary experience with Squid: a new liquid embolizing agent for AVM, AV fistulas and tumors.** *Turk Neurosurg* 2014;24:565–70 CrossRef Medline
14. Massoud TF, Ji C, Viñuela F, et al. **An experimental arteriovenous malformation model in swine: anatomic basis and construction technique.** *AJNR Am J Neuroradiol* 1994;15:1537–45 Medline
15. Haussen DC, Ashour R, Johnson JN, et al. **Direct continuous measurement of draining vein pressure during Onyx embolization in a swine arteriovenous malformation model.** *J Neurointerv Surg* 2015; 7:62–66 CrossRef Medline
16. Gentric JC, Raymond J, Batista A, et al. **Dual-lumen balloon catheters may improve liquid embolization of vascular malformations: an experimental study in swine.** *AJNR Am J Neuroradiol* 2015;36: 977–81 CrossRef Medline
17. Eliyas JK, Niekrasz M, Wardrip C, et al. **Focused post mortem dissection technique for harvest of rete mirabile in domestic swine (Sus scrofa).** *J Neurointerv Surg* 2016;8:973–76 CrossRef Medline
18. Weber W, Kis B, Siekmann R, et al. **Endovascular treatment of intracranial arteriovenous malformations with Onyx: technical aspects.** *AJNR Am J Neuroradiol* 2007;28:371–77 Medline
19. Duran R, Sharma K, Dreher MR, et al. **A novel inherently radiopaque bead for transarterial embolization to treat liver cancer: a pre-clinical study.** *Theranostics* 2016;6:28–39 CrossRef Medline
20. Ayad M, Eskioglu E, Mericle RA. **Onyx: a unique neuroembolic agent.** *Expert Rev Med Devices* 2006;3:705–15 CrossRef Medline
21. Diaz O, Scranton R. **Endovascular treatment of arteriovenous malformations.** *Handb Clin Neurol* 2016;136:1311–17 CrossRef Medline
22. Szatmáry Z, Hillman J, Finitsis S. **Meningioma embolization with the pressure cooker technique using Squid 12.** *Interv Neuroradiol* 2017;23:441–43 CrossRef Medline
23. Erbahceci Salik A, Islim F, Akgul A, et al. **Concomitant transarterial and transvenous embolization of a pelvic arteriovenous malformation using a new liquid embolic agent, Squid-12 and detachable coils.** *Case Rep Vasc Med* 2014;2014:972870 CrossRef Medline
24. Koçer N, Hanımoğlu H, Batur Ş, et al. **Preliminary experience with precipitating hydrophobic injectable liquid in brain arteriovenous malformations.** *Diagn Interv Radiol* 2016;22:184–89 CrossRef Medline

25. Leyon JJ, Chavda S, Thomas A, et al. **Preliminary experience with the liquid embolic material agent PHIL (Precipitating Hydrophobic Injectable Liquid) in treating cranial and spinal dural arteriovenous fistulas: technical note.** *J Neurointerv Surg* 2016;8:596–602 CrossRef Medline
26. Jagadeesan BD, Grigoryan M, Hassan AE, et al. **Endovascular balloon-assisted embolization of intracranial and cervical arteriovenous malformations using dual-lumen coaxial balloon microcatheters and Onyx: initial experience.** *Neurosurgery* 2013;73(2 Suppl Operative): ons238–43; discussion ons243 CrossRef Medline
27. Shi ZS, Loh Y, Gonzalez N, et al. **Flow control techniques for Onyx embolization of intracranial dural arteriovenous fistulae.** *J Neurointerv Surg* 2013;5:311–16 CrossRef Medline
28. Vollherbst DF, Otto R, Do TD, et al. **Extra-small dual-lumen microballoon catheters can improve endovascular embolization: an experimental in vivo and in vitro study.** *J Neurointerv Surg* 2018 Mar 19. [Epub ahead of print] CrossRef Medline
29. Chapot R, Stracke P, Velasco A, et al. **The pressure cooker technique for the treatment of brain AVMs.** *J Neuroradiol* 2014;41: 87–91 CrossRef Medline
30. Abud DG, Riva R, Nakiri GS, et al. **Treatment of brain arteriovenous malformations by double arterial catheterization with simultaneous injection of Onyx: retrospective series of 17 patients.** *AJNR Am J Neuroradiol* 2011;32:152–58 CrossRef Medline

# Five-Year Longitudinal Study of Neck Vessel Cross-Sectional Area in Multiple Sclerosis

L. Pelizzari, D. Jakimovski, M.M. Laganà, N. Bergsland, J. Hagemeier, G. Baselli, B. Weinstock-Guttman, and R. Zivadinov

## ABSTRACT

**BACKGROUND AND PURPOSE:** Alterations of neck vessel cross-sectional area in multiple sclerosis have been reported. Our aim was to investigate the evolution of the neck vessel cross-sectional area in patients with MS and healthy controls during 5 years.

**MATERIALS AND METHODS:** Sixty-nine patients with MS (44 relapsing-remitting MS, 25 progressive MS) and 22 age- and sex-matched healthy controls were examined twice, 5 years apart, on a 3T MR imaging scanner using 2D neck MR angiography. Cross-sectional areas were computed for the common carotid/internal carotid arteries, vertebral arteries, and internal jugular veins for all slices between the C3 and C7 cervical levels. Longitudinal cross-sectional area differences at each cervical level and the whole-vessel course were tested within study groups and between patients with MS with and without cardiovascular disease using mixed-model analysis and the related-samples Wilcoxon singed rank test. The Benjamini-Hochberg procedure was performed to correct for multiple comparisons.

**RESULTS:** No significant cross-sectional area differences were seen between patients with MS and healthy controls at baseline or at follow-up. During the follow-up, significant cross-sectional area decrease was found in patients with MS for the common carotid artery–ICAs (C4: $P = .048$; C7: $P = .005$; whole vessel: $P = .012$), for vertebral arteries (C3: $P = .028$; C4: $P = .028$; C7: $P = .028$; whole vessel: $P = .012$), and for the internal jugular veins (C3: $P = .014$; C4: $P = .008$; C5: $P = .010$; C6: $P = .010$; C7: $P = .008$; whole vessel: $P = .002$). Patients with MS without cardiovascular disease had significantly greater change than patients with MS with cardiovascular disease for internal jugular veins at all levels.

**CONCLUSIONS:** For 5 years, patients with MS showed significant cross-sectional area decrease of all major neck vessels, regardless of the disease course and cardiovascular status.

**ABBREVIATIONS:** CCA = common carotid artery; CSA = cross-sectional area; CVD = cardiovascular disease; EDSS = Expanded Disability Status Scale; HC = healthy controls; $HC_{CVD}$ = healthy controls with cardiovascular disease; $HC_{noCVD}$ = healthy controls without no cardiovascular disease; IJV = internal jugular vein; IQR = interquartile range; $MS_{CVD}$ = patients with MS with cardiovascular disease; $MS_{noCVD}$ = patients with MS without cardiovascular disease; RRMS = relapsing-remitting MS; PMS = progressive MS; VA = vertebral artery WV = whole vessel; MS = multiple sclerosis; ICA = internal carotid artery

Multiple sclerosis is a chronic immune-mediated inflammatory disease of the central nervous system characterized by demyelination and neurodegeneration. MS does not seem to be triggered by a single specific factor, and there is mounting evidence that genetic, environmental, and cardiovascular risk factors play an important role in the development of the disease.[1]

Although still elusive, the involvement of the vascular component in MS has been investigated across time from different points of view.[2-5] The disruption of the blood-brain barrier and the perivenular topography of MS lesions are recognized as well-established features of MS pathology.[2] Furthermore, MS lesions

Received April 19, 2018; accepted after revision June 6.

From the Department of Electronics Information and Bioengineering (L.P., G.B.), Politecnico di Milano, Milan, Italy; Istituto di Ricovero e Cura a Carattere Scientifico (L.P., M.M.L.), Fondazione Don Carlo Gnocchi ONLUS, Milan, Italy; and Buffalo Neuroimaging Analysis Center (D.J., N.B., J.H., R.Z.), Department of Neurology, Jacobs School of Medicine and Biomedical Sciences; Jacobs Multiple Sclerosis Center (B.W.-G.), Department of Neurology, School of Medicine and Biomedical Sciences; and Center for Biomedical Imaging at Clinical Translational Science Institute (R.Z.), University at Buffalo, State University of New York, Buffalo, New York.

Research reported in this publication was funded in part by the National Center for Advancing Translational Sciences of the National Institutes of Health under award Number UL1TR001412 and, in part, by the Annette Funicello Research Fund for Neurological Diseases and internal resources of the Buffalo Neuroimaging Analysis Center. In addition, we received support from the Jacquemin Family Foundation.

The content is solely the responsibility of the authors and does not necessarily represent the official views of the National Institutes of Health.

Please address correspondence to Robert Zivadinov, MD, PhD, University of Buffalo, Department of Neurology, Jacobs School of Medicine and Biomedical Sciences, University at Buffalo, 100 High St, Buffalo, NY 14203; e-mail: rzivadinov@bnac.net

Indicates open access to non-subscribers at www.ajnr.org
Indicates article with supplemental on-line tables and appendix.
Indicates article with supplemental on-line photo.

http://dx.doi.org/10.3174/ajnr.A5738

have been observed to be most commonly located in watershed areas of low arterial blood supply,[3] while in vitro experiments revealed that neural ischemia triggers tight junction disruption, increasing endothelial permeability.[4] Recently, alterations of neurovascular coupling have also been reported in terms of impaired cerebrovascular reactivity.[5]

In addition, the presence of vascular comorbidities, such as hypertension, dyslipidemia, diabetes, and heart disease, has been shown to be associated with more severe disability,[6,7] increased lesion burden,[8] higher risk of relapse,[9] greater brain atrophy,[10,11] and increased risk of stroke and heart failure[12] in patients with MS.

The association of MS with systemic diseases affecting the cardiovascular system suggests that vascular involvement in the pathology may not be limited to only the neurovascular interface. Because extracranial structural changes impact intracranial pressure and hemodynamics,[13] the investigation of the main routes of brain blood supply and drainage might help to better understand the involvement of the vascular component in MS.

In the past 10 years, some studies have investigated internal jugular vein (IJV) structure and hemodynamics in MS. However, contrasting results were reported,[14-16] and it was not possible to unequivocally conclude that patients with MS have a higher prevalence of IJV abnormalities with respect to healthy individuals. A recent large study shifted the focus of investigation from neck veins to the main arterial pathways of brain supply, showing reduced cross-sectional area (CSA) of the internal carotid artery and vertebral artery (VA) in patients with MS compared with healthy controls (HC).[17]

No longitudinal studies of neck vessel CSA have been reported in the literature so far. Thus, it is not clear whether altered neck vessel CSA is a primary or secondary phenomenon in MS. Therefore, the aim of this study was to investigate the evolution of ICA, VA, and IJV CSAs during 5 years in a group of patients with MS and HC. We also aimed to examine differences in neck vessel CSA evolution between patients with relapsing-remitting MS (RRMS) and progressive MS (PMS). Finally, we examined changes in the CSA across time in relation to cardiovascular comorbidities.

## MATERIALS AND METHODS

### Study Design and Population

The subjects are part of an ongoing prospective, longitudinal study of cardiovascular, environmental, and genetic risk factors in MS.[18] At baseline assessment, patients with MS and HC (an approximately 3:1 ratio) were originally enrolled at our center between 2009 and 2014.[19] The inclusion criteria for this substudy of cardiovascular, environmental, and genetic factors in MS were the following: 1) being a patient with RRMS or PMS, according to the criteria of Lublin and Reingold[20] or a healthy control at baseline examination; 2) 5-year follow-up from initial enrollment in the cardiovascular, environmental, and genetic study; 3) having neck MR imaging at baseline and follow-up using the same 3T scanner and protocol; 4) 18–75 years of age; and 5) a physical/neurologic examination within 30 days from the standardized MR imaging study protocol. Exclusion criteria were the following: 1) the presence of a relapse and steroid treatment within the 30 days preceding study entry; 2) pre-existing medical conditions known to be associated with brain or neck pathology; or 3) pregnancy.

Demographic and clinical information was collected for all participants. The body mass index was computed for each subject, and smoking status was recorded. For patients with MS, disability was quantified with the Expanded Disability Status Scale (EDSS) by an experienced neurologist. Furthermore, both MS and HC groups were split into 2 subgroups (ie, patients with MS with and without cardiovascular disease [$MS_{CVD}$ and $MS_{noCVD}$], healthy controls with and without cardiovascular disease [$HC_{CVD}$ and $HC_{noCVD}$]). Subjects who presented with hypertension and/or heart disease and/or hyperlipidemia and/or diabetes were classified as subjects with cardiovascular disease (CVD).

The study was approved by local institutional review board of the University at Buffalo, and all participants provided written informed consent.

### MR Imaging Acquisition

All participants were scanned twice, 5 years apart, with a 3T Signa Excite HD 12.0 TwinSpeed 8-channel scanner (GE Healthcare, Milwaukee, Wisconsin), using an 8-channel head and neck coil (HDNV; Medrad, Pittsburgh, Pennsylvania). No hardware and software changes occurred during the follow-up. The MR imaging examination consisted of a 2D neck time-of-flight MR angiography, which is described in the On-line Appendix.

### MR Imaging Analysis

Image quality control was performed by an experienced operator. Segmentation of the left and right common carotid arteries–internal carotid arteries (CCA–ICAs), VAs, and IJVs was performed semiautomatically for all slices between the C2–C3 and C7–T1 intervertebral spaces with the Jim 6.0 software package (http://www.xinapse.com/home.php). Specifically, the vessel contour was drawn by an operator on a single axial slice using the edge-detection and contour-following algorithm and propagated on the other slices with edge-seeking and 3D propagation modes.[21] The operator was blinded to the group status and verified the segmentation results, manually editing them, if necessary. Then, neck vessel CSA was computed for each segmented slice, and CSA-to-slice curves were resampled to obtain the same number of measures (ie, samples) for all the subjects, as described previously.[22] More details about segmentation and resampling methodology are reported in the On-line Appendix.

For each MRA image, CSA measures of the left and right corresponding vessels were summed at each sample to derive total CCA–ICA, VA, and IJV CSA values. Change in CSA ($\Delta$CSA) during the 5 years was computed for all total CSA values by subtracting the total CSA at baseline from the corresponding total CSA at follow-up.

### Statistical Analysis

All statistical analyses were performed with SPSS (Version 24; IBM, Armonk, New York). Demographic and clinical differences between groups and subgroups were assessed at baseline with the Fisher exact test, Student *t* test, and Mann-Whitney *U* test, as appropriate. The normality of data was assessed with the Shapiro-

**Table 1: Demographic and clinical characteristics of HC and MS groups**

| | HC (*n* = 22) | MS (*n* = 69) | RRMS (*n* = 44) | PMS (*n* = 25) | HC vs MS (*P* Value) | RRMS vs PMS (*P* Value) |
|---|---|---|---|---|---|---|
| Female (No.) (%) | 18 (81.8) | 48 (69.6) | 28 (63.6) | 20 (80.0) | .411[a] | .184[a] |
| Age (yr), (median) (range) | 48.0 (17.7–73.3) | 50.3 (18.8–68.29) | 45.6 (18.8–68.3) | 58.3 (33.1–66.9) | .240[b] | <.001[c,d] |
| BMI (median) (range) | 25.1 (18.1–44.9) | 27.3 (19.0–44.9) | 26.4 (19.0–44.9) | 28.97 (22.5–43.1) | .104[c] | .128[c] |
| Disease duration (yr) (median) (range) | NA | 13 (0–37) | 9.5 (0–35) | 20.0 (1–37) | NA | .001[c,d] |
| EDSS (median) (range) | NA | 2.5 (0–8) | 1.5 (0.0–6.5) | 6.0 (1.5–8.0) | NA | <.001[c,d] |
| Hypertension (No.) (%) | 4 (18.2) | 8 (11.6) | 2 (4.5) | 6 (24.0) | .474[a] | .023[a,d] |
| Heart diseases (No.) (%) | 1 (4.5) | 4 (5.8) | 3 (6.8) | 1 (4.0) | 1.000[a] | 1.000[a] |
| Hyperlipidemia (No.) (%) | 4 (18.2) | 13 (18.8) | 8 (18.2) | 5 (20.0) | 1.000[a] | 1.000[a] |
| Diabetes (No.) (%) | 1 (4.5) | 2 (2.9) | 1 (2.3) | 1 (4.0) | .569[a] | 1.000[a] |
| Smoking status (No.) (%) | 5 (22.7) | 32 (46.4) | 22 (50.0) | 10 (40.0) | .080[a] | .461[a] |

**Note:**—BMI indicates body mass index; NA, not applicable.

[a–c] The Fisher exact test (a), independent-samples Student *t* test (b), and independent-samples Mann-Whitney *U* test (c) were used to evaluate differences between MS and HC groups and between RRMS and PMS, as appropriate.

[d] *P* values < .05 were considered significant.

Wilk test, and CSA and ΔCSA data distributions were transformed if needed.

Group median and interquartile range (IQR) were computed for total CSA at baseline, total CSA at follow-up, and ΔCSA at each cervical level and for the whole-vessel (WV) course.

We tested these group comparisons: HC versus MS, RRMS versus PMS, $MS_{CVD}$ versus $MS_{noCVD}$, and $HC_{CVD}$ versus $HC_{noCVD}$. Baseline-to-follow-up CSA differences between groups were assessed with linear mixed-model analysis. Group differences at the same time point and baseline-to-follow-up differences within each group were tested on the WV with mixed-model analysis. At each cervical level, group differences were assessed for CSA at baseline, for CSA at follow-up, and for ΔCSA, either with the Mann-Whitney *U* test for matched groups or with linear mixed-model analysis, correcting for the demographic or clinical nonmatching factors. To evaluate differences between baseline and follow-up CSA within each group at each cervical level, we used the related-samples Wilcoxon singed rank test. The Benjamini-Hochberg procedure was performed to correct for multiple comparisons.

More details about mixed-model analysis are reported in the On-line Appendix. *P* values < .05 were considered significant.

## RESULTS

### Demographic and Clinical Characteristics

In total, 69 consecutive patients with MS (44 with RRMS and 25 with PMS, consisting of 23 with secondary-progressive and 2 with primary-progressive MS) and 22 age- and sex-matched HC were included in the study (Table 1). No significant differences in body mass index, prevalence of any CVD, and smoking status were observed between the MS and HC groups. There were significant differences between the RRMS and PMS subgroups regarding age ($P < .001$), EDSS ($P < .001$), disease duration ($P = .001$), and the prevalence of hypertension ($P = .023$). Fifty-five (79.7%) of 69 patients were on disease-modifying therapy (29 on interferon β, 18 on glatiramer acetate, and 8 on natalizumab). Demographic and clinical information related to $MS_{CVD}$, $MS_{noCVD}$, $HC_{CVD}$, and $HC_{noCVD}$ subgroups are summarized in On-line Table 1.

### Assessment of CSA in MS and HC Groups

All the acquired scans were classified as good-quality images. On-line Fig 1 shows an example of the segmented regions of interest (ROIs). Total CCA–ICA, VA, and IJV median CSA values at baseline and follow-up for the MS and HC groups and respective group-comparison results are reported in Table 2. The CSA-to-samples curves at baseline and at follow-up are shown for HC and patients with MS in Fig 1.

No significant differences were observed between MS and HC subjects in total CSA at baseline or at follow-up for any of the considered neck vessels. Furthermore, baseline-to-follow-up comparison between patients with MS and HC did not yield any significant differences.

In the MS group, significantly smaller total CSA at follow-up with respect to baseline was found for CCA–ICAs (C4: $P = .048$; C7: $P = .005$; WV: $P = .012$), for VAs (C3: $P = .028$; C4: $P = .028$; C7: $P = .028$; WV: $P = .012$), and for IJVs (C3: $P = .014$; C4: $P = .008$; C5: $P = .010$; C6: $P = .010$; C7: $P = .008$; WV: $P = .002$). No significant group differences were observed for CSA at baseline and follow-up or baseline to follow-up for any of the neck vessels or the cervical level in patients with MS with and without disease-modifying therapy.

HC showed significantly smaller total CSA at follow-up compared with baseline for only CCA–ICAs at the C7 level ($P = .03$).

### Assessment of CSA in RRMS and PMS

Neck vessel total CSA measures of RRMS and PMS and respective group comparison results are summarized in On-line Table 2. The CSA to sample curves at baseline and at follow-up are shown for RRMS and PMS in On-line Fig 2.

No significant CSA differences were found between RRMS and PMS groups at baseline or at follow-up. Furthermore, no significant baseline-to-follow-up differences between RRMS and PMS were observed.

Within the RRMS group, a significantly smaller CSA at follow-up with respect to baseline was observed for CCA–ICAs (C7: $P = .035$), for VAs (WV: $P = .030$), and for IJVs (WV: $P = .032$).

The PMS group showed significantly reduced CSA at follow-up with respect to baseline for CCA–ICAs (WV: $P = .036$) and for IJVs (C4: $P = .040$; C5: $P = .040$; C6: $P = .040$; C7: $P = .040$; WV: $P = .021$).

### Assessment of the CSA Association with CVD in MS and HC Groups

No significant CSA differences between $MS_{CVD}$ and $MS_{noCVD}$ were found at baseline (On-line Table 3). However, the CSA de-

**Table 2: Group medians and IQRs of neck vessel total cross-sectional area at baseline, and follow-up in HC ($n = 22$) and MS ($n = 69$) groups**

| Vessel/Cervical Level | HC BL CSA ($mm^2$) (Median) (IQR) | MS BL CSA ($mm^2$) (Median) (IQR) | BL CSA MS vs HC (*P* Value) | HC FU CSA ($mm^2$) (Median) (IQR) | MS FU CSA ($mm^2$) (Median) (IQR) | FU CSA MS vs HC (*P* Value) | HC CSA BL vs FU (*P* Value) | MS CSA BL vs FU (*P* Value) | BL-to-FU MS vs HC CSA (*P* Value) |
|---|---|---|---|---|---|---|---|---|---|
| CCA–ICAs | | | | | | | | | |
| C3 | 67.5 (28.1) | 54.5 (28.3) | .298[a] | 75.6 (30.7) | 57.6 (32.9) | .248[a] | .223[c] | .993[c] | .699[e] |
| C4 | 73.4 (19.9) | 79.3 (28.2) | .298[a] | 73.2 (12.9) | 77.5 (27.3) | .535[a] | .57[c] | .048[c,g] | .365[e] |
| C5 | 69.7 (14.7) | 75.7 (20.9) | .298[a] | 67.0 (7.9) | 70.9 (23.5) | .248[a] | .168[c] | .361[c] | .365[e] |
| C6 | 66.7 (10.8) | 71.5 (16.7) | .318[a] | 66.5 (9.7) | 67.8 (19.4) | .474[a] | .223[c] | .222[c] | .603[e] |
| C7 | 69.1 (8.9) | 69.7 (19.8) | .795[a] | 66.3 (7.9) | 66.5 (20.3) | .474[a] | .030[c,g] | .005[c,g] | .36[e] |
| WV | 68.8 (16.4) | 71.8 (26.2) | .605[b] | 68.1 (15.8) | 69.0 (26.7) | .632[b] | .206[d] | .012[d,g] | .967[f] |
| VAs | | | | | | | | | |
| C3 | 31.9 (6.5) | 31.7 (6.9) | .597[a] | 28.7 (11.5) | 30.3 (7.2) | .718[a] | .070[c] | .028[c,g] | .921[e] |
| C4 | 30.1 (8.5) | 30.0 (5.9) | .597[a] | 28.8 (10.8) | 29.7 (6.5) | .779[a] | .288[c] | .028[c,g] | .921[e] |
| C5 | 29.1 (8.0) | 29.4 (6.0) | .597[a] | 29.4 (10.6) | 29.4 (6.3) | .948[a] | .570[c] | .051[c] | .921[e] |
| C6 | 28.4 (7.6) | 29.7 (6.9) | .588[a] | 27.6 (8.4) | 28.9 (7.0) | .718[a] | .570[c] | .051[c] | .921[e] |
| C7 | 28.4 (9.2) | 29.2 (8.1) | .588[a] | 27.0 (8.0) | 28.6 (8.0) | .718[a] | .570[c] | .028[c,g] | .92[e] |
| WV | 29.7 (7.9) | 30.5 (7.5) | .406[b] | 28.5 (9.8) | 29.6 (7.9) | .377[b] | .119[d] | .012[d,g] | .866[f] |
| IJVs | | | | | | | | | |
| C3 | 100.8 (59.9) | 105.3 (59.7) | .956[a] | 94.8 (52.9) | 90.6 (60.8) | .970[a] | .444[c] | .014[c,g] | .987[e] |
| C4 | 111.4 (44.8) | 121.8 (67.9) | .956[a] | 107.6 (63.9) | 102.8 (74.0) | .970[a] | .444[c] | .008[c,g] | .987[e] |
| C5 | 117.1 (86.7) | 122.4 (59.8) | .956[a] | 103.9 (89.3) | 107.9 (71.6) | .970[a] | .444[c] | .010[c,g] | .987[e] |
| C6 | 116.7 (124.2) | 118.7 (91.6) | .956[a] | 86.7 (120.0) | 101.4 (86.9) | .970[a] | .444[c] | .010[c,g] | .987[e] |
| C7 | 116.9 (174.2) | 126.3 (95.4) | .956[a] | 109.4 (111.6) | 113.2 (90.7) | .970[a] | .935[c] | .008[c,g] | .987[e] |
| WV | 111.9 (87.0) | 119.5 (73.5) | .790[b] | 99.3 (76.1) | 103.8 (76.4) | .913[b] | .424[d] | .002[d,g] | .680[f] |

**Note:**—BL indicates baseline; FU, follow-up.

[a–f] Group medians and IQR of neck vessel total CSA at baseline and follow-up are reported for HC and MS at each cervical level and for the WV course. To evaluate CSA differences between HC and MS groups at baseline and at follow-up, an independent-samples Mann-Whitney *U* test (a) was used at each cervical level, while linear mixed models were used for the WV (b). To evaluate differences between baseline and follow-up within each group, the Wilcoxon signed-rank test (c) was used at each cervical level, while linear mixed models were used for the WV (d). To perform baseline-to-follow-up CSA comparison between groups, linear mixed models were used at each cervical level (e) and for the WV (f). The Benjamini-Hochberg procedure was performed to correct for multiple comparisons.

[g] An $\alpha$ level of .05 was considered significant.

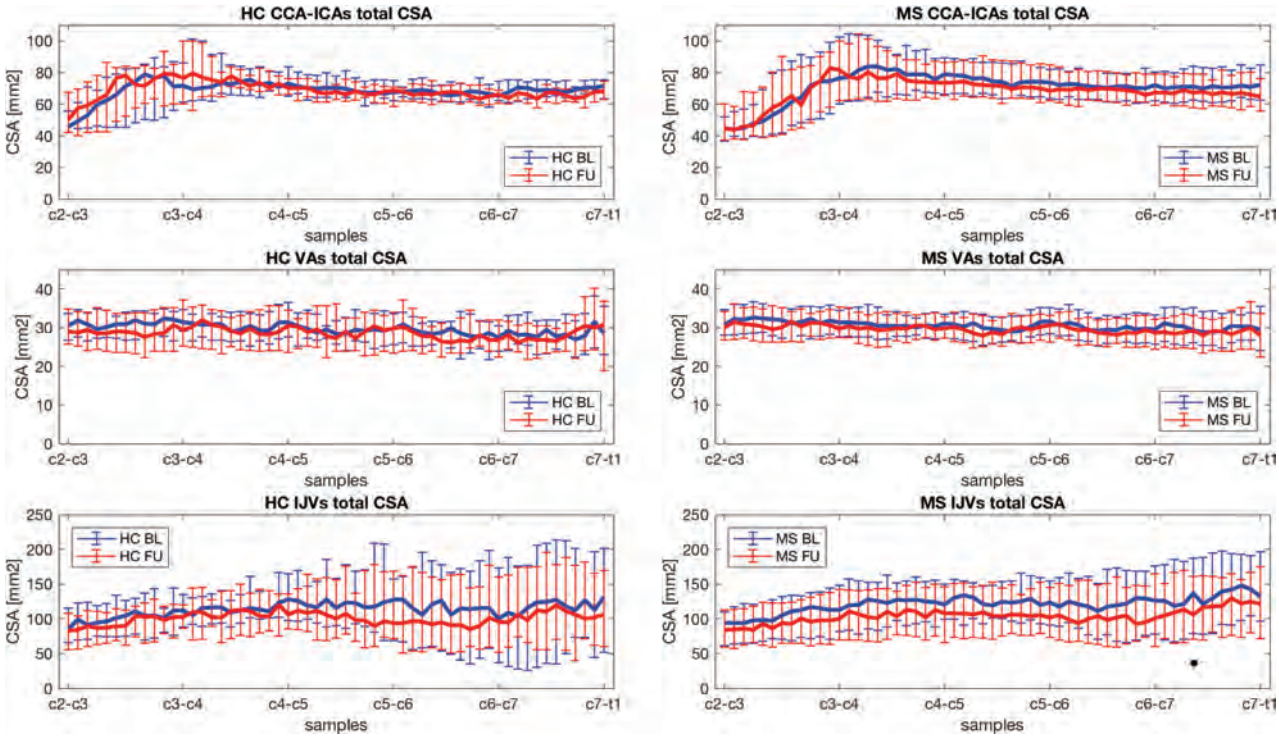


**FIG 1.** Total CSA of CCA–ICAs, VAs, and IJVs at baseline (blue) and at follow-up (red) for HC (*left*) and patients with MS (*right*). The median CSA values (*lines*) and the respective IQR (*bars*) are represented for all the samples along the C3-to-C7 cervical levels. BL indicates baseline; FU, follow-up.

creased with time, and ΔCSA was significantly larger in $MS_{noCVD}$ with respect to $MS_{CVD}$ for IJVs (C3: $P = .018$; C4: $P = .018$; C5: $P = .010$; C6: $P = .015$; C7: $P = .018$; WV: $P = .003$). The CSA-to-samples curves at baseline and follow-up are shown for both subgroups in Fig 2. No significant group differences were observed for CSA at baseline and follow-up or baseline to follow-up

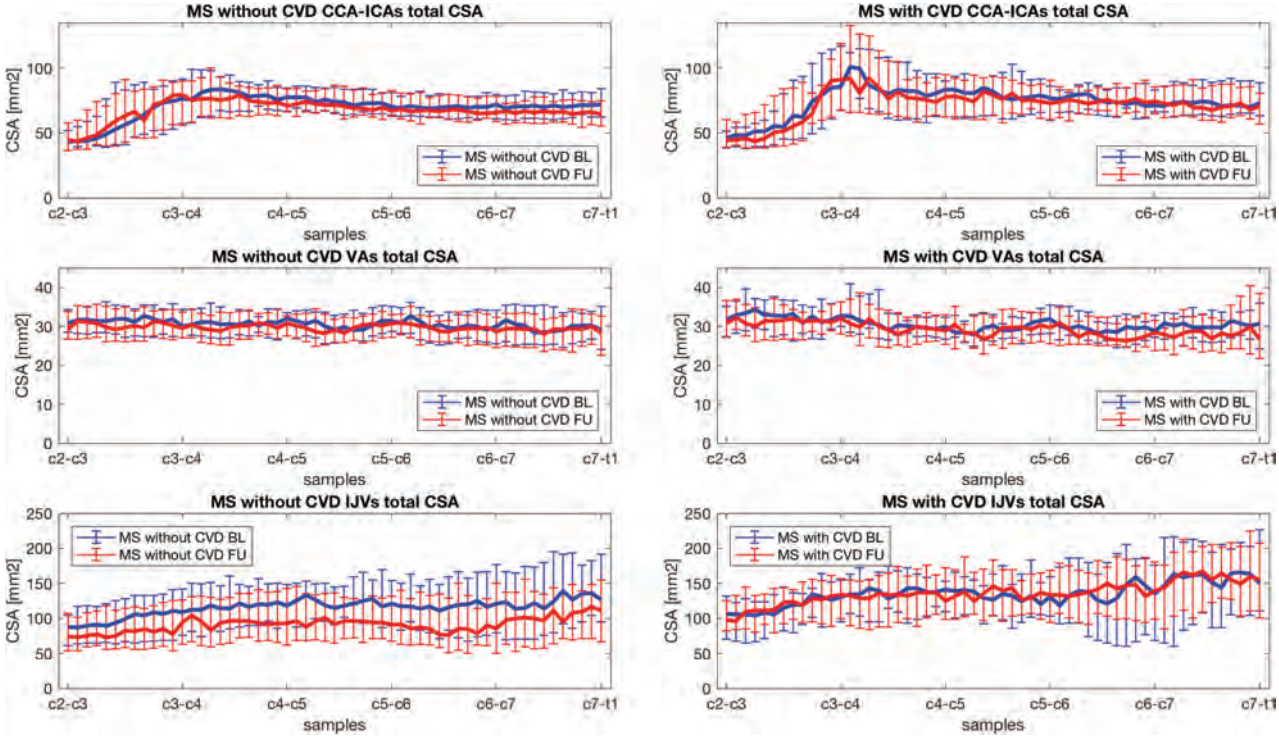


**FIG 2.** Total CSA of CCA–ICAs, VAs, and IJVs at baseline (blue) and at follow-up (red) for patients with MS without CVD (*left*) and for patients with MS with CVD (*right*). The median CSA values (*lines*) and the respective IQR (*bars*) are represented for all the samples along the C3-to-C7 cervical levels. BL indicates baseline; FU, follow-up.

for any of the neck vessels or cervical levels in patients with MS with ($n = 32$) and without ($n = 37$) smoking status.

Both CSA at baseline and ΔCSA were not significantly different between $HC_{CVD}$ and $HC_{noCVD}$ (On-line Table 4).

## DISCUSSION

To the best of our knowledge, this is the first longitudinal study assessing CCA–ICA, VA, and IJV CSA evolution across time in patients with MS. The main finding of this study is that a reduction of all major neck vessel CSA was observed during 5 years in patients with MS. A smaller CSA at follow-up was seen independent of disease phenotype and vascular comorbidity, while only sporadic changes were found for HC during the same time observation.

Most interesting, the CSA of both neck arteries for brain supply and veins for extracranial drainage was found to be affected at several cervical levels in patients with MS during the follow-up. A significant CSA decrease with time was also found in HC but only at the C7 cervical level for CCA–ICAs. Given the small sample size of HC, this isolated difference should be interpreted with caution.

Despite the emerging effects of the role of cardiovascular comorbidities in contributing to MS disease severity,[7,8,10-12] there is scarce evidence of the involvement of neck arterial structural changes. A recent study showed lower CCA–ICA and VA CSA in a group of 193 patients with MS compared with 193 HC.[17] Furthermore, significantly higher carotid intima-media thickness was observed in MS without CVD with respect to HC, suggesting that patients with MS have a predisposition to atherosclerosis.[24] Both MS and atherosclerosis are associated with an increase of plasma level of interleukin-6, tumor necrosis factor α, monocyte chemoattractant protein-1, soluble intercellular adhesion molecule-1, vascular cell adhesion molecule 1, and endothelial microparticles.[25-29] In addition, the progression and severity of both diseases are known to be associated with lipoproteins and cholesterol metabolism.[7,30,31] All this evidence and our results showing a consistent decrease of CCA–ICA and VA CSA with time in the MS group suggest that the 2 pathologies may share some mechanisms that cause or increase the inflammatory reaction.

The reduction of ICA and VA CSA may also be associated with hypoperfusion of normal-appearing brain tissue, which has been previously observed in MS.[32,33] Although the clinical correlations between MS and perfusion alterations have not been strongly established,[34] some studies showed an association between reduced gray matter cerebral blood flow, cognitive impairment,[32] and fatigue,[35] while 1 study showed an inverse correlation between periventricular normal-appearing white matter CBF and EDSS.[33] Because hypoperfusion was also observed in the absence of GM atrophy in early RRMS,[32] it may not only be an epiphenomenon in MS. Longitudinal combined studies of neck vessel CSA, brain perfusion, and GM volume could help to clarify the link existing among these different types of alterations.

In this work, a significant and consistent reduction of CSA with time in MS was also observed for IJVs. This result must be interpreted against a background of conflicting findings. Some previous cross-sectional studies have shown a greater prevalence of morphologic and hemodynamic alterations of extracranial venous drainage pathways in patients with MS with respect to HC.[14,16] On the other hand, some other studies reported an absence of significant differences between patients with MS and HC

regarding IJV CSA and flow rates.[15,36] Our results at baseline are in line with the latter group of findings. However, the IJV CSA changes that we observed longitudinally in this study in patients with MS may suggest a potential link between IJV CSA and the disease course. The clinical relevance of these observations remains elusive. Recently, extracranial venous angioplasty has been reported to be largely ineffective at impacting the course of MS[37]; therefore, caution should be used when drawing final conclusions. The investigation of fluid dynamics of the brain, including the recently discovered sinus-associated lymphatic vessels and the glymphatic pathways, may shed more light on the relation between vascular and immune/inflammatory factors in MS.[38] By interpreting the obtained IJV CSA reduction together with the CSA decrease of neck arteries with time in MS, one could also explain a decrease in IJV CSA because of a potential flow reduction in CCA–ICA and VA pathways.

Cardiovascular risk factors and CVD are well-known to adversely affect the course of MS.[1] Specifically, smoking was reported to be associated with increased BBB disruption, higher lesion volumes, greater brain atrophy,[23] and more rapid conversion from RRMS to a PMS disease course.[39] Obesity was shown to be linked with increased MS risk and higher disability.[40] Also diabetes, hypertension, dyslipidemia, and ischemic heart disease are associated with worse disability and a more severe disease course,[6,7] increased lesion burden, and more advanced brain atrophy.[10,11] Nevertheless, in the present study, greater change of IJV CSA at all cervical levels was observed for $MS_{noCVD}$ compared with $MS_{CVD}$. The limited sample size and the group inhomogeneity may have prevented us from highlighting CVD as an exacerbating factor for neck vessel CSA decrease. However, because CSA changes were also found in $MS_{noCVD}$, neck vessel CSA reduction with time in MS might not be necessarily driven by CVD only. Investigating the effect of CVD and other potential MS-related factors on CCA–ICA, VA, and IJV CSA in a larger cohort of subjects is warranted to make clearer speculations.

The relatively small sample size, especially of the HC group, is the main limit of this study, and it must be considered when interpreting our findings. Indeed, the comparison of neck vessel CSA between patients with MS and HC at baseline did not lead to any significant results, while a much larger recent study has reported a significantly lower CCA–ICA and VA CSA in patients with MS with respect to HC.[17] Furthermore, no significant CSA differences were found between MS and HC subjects at follow-up as well as in baseline-to-follow-up comparisons, probably due to the discrepancies in sample size between patients with MS and HC groups. Nevertheless, the extensive longitudinal CSA change that we observed in the MS group for all the neck vessels indirectly corroborates the previous findings of neck vessel CSA alterations in MS.[14,16]

Other limitations are that TOF MR imaging signal depends on flow velocity and that by measuring CSA on TOF MRA axial slices, vessels are assumed to be perpendicular to the axial plane. Slow flow and the presence of blood refluxes might produce inaccurate CSA estimation; however, as opposed to contrast-enhanced MRA, TOF MR imaging has the advantage of imaging neck vessels in a noninvasive way.[41] Furthermore, the assumption of the perpendicularity of the vessels to the axial plane was made for all vessels within the considered cervical levels; nevertheless, in future studies, CSA measures could be improved by considering the angle between the vessel longitudinal axis and the z-axis. Despite these limitations, the reliability and repeatability of the acquisition and segmentation methods used in this study were assessed and confirmed previously.[22]

To the best of our knowledge, this is the first longitudinal study assessing CCA–ICA, VA, and IJV CSA evolution with time in MS. The dependence of neck vessel CSA measures on many factors such as positioning, hydration, body mass index, and respiration have probably discouraged longitudinal evaluations so far. However, recent reports demonstrated the repeatability of neck vessel semiautomatic segmentation on TOF MRA images,[21,22] making longitudinal studies feasible.

Future studies, involving larger groups of subjects and the acquisition of more data such as intima-media thickness measures, perfusion MR imaging, and GM volume should be performed to better understand these preliminary findings.

## CONCLUSIONS

Patients with MS showed a decrease of CCA–ICA, VA, and IJV CSA during 5 years, regardless of the disease phenotype. Because neck vessel CSA evolution with time was found to be altered in MS even in the absence of CVD, CSA reduction might also be influenced by MS-related factors.

Disclosures: Giuseppe Baselli—*UNRELATED*: *Employment*: Politecnico di Milano, *Comments*: This work is part of my research duties as Full Professor of the Politecnico di Milano. Bianca Weinstock-Guttman—*UNRELATED*: *Consultancy*: Biogen Idec, Teva Pharmaceutical Industries, Novartis, Genentech, Celgene, EMD Serono; *Grants/Grants Pending*: Biogen, Teva Pharmaceutical Industries, Novartis, Genentech*; *Payment for Lectures Including Service on Speakers Bureaus*: Biogen, Teva Pharmaceutical Industries, Genentech. Robert Zivadinov—*UNRELATED*: *Consultancy*: Sanofi Genzyme, Novartis, Celgene, EMD Serono; *Grants/Grants Pending*: Biogen, Sanofi Genzyme, Novartis, Celgene, EMD Serono, Protembis*; *Payment for Lectures Including Service on Speakers Bureaus*: Sanofi Genzyme, Novartis, Celgene, EMD Serono. *Money paid to the institution.

## REFERENCES

1. Spencer JI, Bell JS, DeLuca GC. **Vascular pathology in multiple sclerosis: reframing pathogenesis around the blood-brain barrier.** *J Neurol Neurosurg Psychiatry* 2018;89:42–52 CrossRef Medline
2. Rae-Grant AD, Wong C, Bernatowicz R, et al. **Observations on the brain vasculature in multiple sclerosis: a historical perspective.** *Mult Scler Relat Disord* 2014;3:156–62 CrossRef Medline
3. Haider L, Zrzavy T, Hametner S, et al. **The topography of demyelination and neurodegeneration in the multiple sclerosis brain.** *Brain* 2016;139:807–15 CrossRef Medline
4. Desai RA, Davies AL, Tachrount M, et al. **Cause and prevention of demyelination in a model multiple sclerosis lesion.** *Ann Neurol* 2016;79:591–604 CrossRef Medline
5. Marshall O, Lu H, Brisset JC, et al. **Impaired cerebrovascular reactivity in multiple sclerosis.** *JAMA Neurol* 2014;71:1275–81 CrossRef Medline
6. Marrie RA, Rudick R, Horwitz R, et al. **Vascular comorbidity is associated with more rapid disability progression in multiple sclerosis.** *Neurology* 2010;74:1041–47 CrossRef Medline
7. Weinstock-Guttman B, Zivadinov R, Mahfooz N, et al. **Serum lipid profiles are associated with disability and MRI outcomes in multiple sclerosis.** *J Neuroinflammation* 2011;8:127 CrossRef Medline
8. Weinstock-Guttman B, Zivadinov R, Horakova D, et al. **Lipid profiles are associated with lesion formation over 24 months in interferon-β treated patients following the first demyelinating event.** *J Neurol Neurosurg Psychiatry* 2013;84:1186–91 CrossRef Medline

9. Kowalec K, McKay KA, Patten SB, et al; CIHR Team in Epidemiology and Impact of Comorbidity on Multiple Sclerosis (ECoMS). **Comorbidity increases the risk of relapse in multiple sclerosis: a prospective study.** *Neurology* 2017;89:2455–61 CrossRef Medline
10. Kappus N, Weinstock-Guttman B, Hagemeier J, et al. **Cardiovascular risk factors are associated with increased lesion burden and brain atrophy in multiple sclerosis.** *J Neurol Neurosurg Psychiatry* 2016;87:181–87 CrossRef Medline
11. Pichler A, Khalil M, Langkammer C, et al. **The impact of vascular risk factors on brain volume and lesion load in patients with early multiple sclerosis.** *Mult Scler* 2017 Oct 1. [Epub ahead of print] CrossRef Medline
12. Christiansen CF. **Risk of vascular disease in patients with multiple sclerosis: a review.** *Neurol Res* 2012;34:746–53 CrossRef Medline
13. Marcotti S, Marchetti L, Cecconi P, et al. **An anatomy-based lumped parameter model of cerebrospinal venous circulation: can an extracranial anatomical change impact intracranial hemodynamics?** *BMC Neurol* 2015;15:95 CrossRef Medline
14. Zamboni P, Galeotti R, Menegatti E, et al. **Chronic cerebrospinal venous insufficiency in patients with multiple sclerosis.** *J Neurol Neurosurg Psychiatry* 2009;80:392–99 CrossRef Medline
15. Zivadinov R, Lopez-Soriano A, Weinstock-Guttman B, et al. **Use of MR venography for characterization of the extracranial venous system in patients with multiple sclerosis and healthy control subjects.** *Radiology* 2011;258:562–70 CrossRef Medline
16. Sethi SK, Utriainen DT, Daugherty AM, et al. **Jugular venous flow abnormalities in multiple sclerosis patients compared to normal controls.** *J Neuroimaging* 2015;25:600–07 CrossRef Medline
17. Belov P, Jakimovski D, Krawiecki J, et al. **Lower arterial cross-sectional area of carotid and vertebral arteries and higher frequency of secondary neck vessels are associated with multiple sclerosis.** *AJNR Am J Neuroradiol* 2018;39:123–30 CrossRef Medline
18. Zivadinov R, Ramasamy DP, Vaneckova M, et al. **Leptomeningeal contrast enhancement is associated with progression of cortical atrophy in MS: a retrospective, pilot, observational longitudinal study.** *Mult Scler* 2017;23:1336–45 CrossRef Medline
19. Zivadinov R, Ramasamy DP, Benedict RR, et al. **Cerebral microbleeds in multiple sclerosis evaluated on susceptibility-weighted images and quantitative susceptibility maps: a case-control study.** *Radiology* 2016;281:884–95 CrossRef Medline
20. Lublin FD, Reingold SC. **Defining the clinical course of multiple sclerosis: results of an international survey—National Multiple Sclerosis Society (USA) Advisory Committee on Clinical Trials of New Agents in Multiple Sclerosis**. *Neurology* 1996;46:907–11 CrossRef Medline
21. Laganà MM, Pelizzari L, Scaccianoce E, et al. **Assessment of internal jugular vein size in healthy subjects with magnetic resonance and semiautomatic processing.** *Behav Neurol* 2016;2016:9717210 CrossRef Medline
22. Pelizzari L, Laganà MM, Jakimovski D, et al. **Neck vessel cross-sectional area measured with MRI: scan-rescan reproducibility for longitudinal evaluations.** *J Neuroimaging* 2018;28:48–56 CrossRef Medline
23. Zivadinov R, Weinstock-Guttman B, Hashmi K, et al. **Smoking is associated with increased lesion volumes and brain atrophy in multiple sclerosis.** *Neurology* 2009;73:504–10 CrossRef Medline
24. Yuksel B, Koc P, Kurtulus F, et al. **Is multiple sclerosis a risk factor for atherosclerosis?** *Multiple Sclerosis Journal*: Sage Publication LTD, London, England; 2016:455–455
25. Li J, Wang W, Han L, et al. **Human apolipoprotein A-I exerts a prophylactic effect on high-fat diet-induced atherosclerosis via inflammation inhibition in a rabbit model.** *Acta Biochim Biophys Sin (Shanghai)* 2017;49:149–58 CrossRef Medline
26. Hautecoeur P, Forzy G, Gallois P, et al. **Variations of IL2, IL6, TNF alpha plasmatic levels in relapsing remitting multiple sclerosis.** *Acta Neurol Belg* 1997;97:240–43 Medline
27. Dawson J, Miltz W, Mir AK, et al. **Targeting monocyte chemoattractant protein-1 signaling in disease.** *Expert Opin Ther Targets* 2003;7:35–48 CrossRef Medline
28. Damotte V, Guillot-Noel L, Patsopoulos NA, et al; International Multiple Sclerosis Genetics Consortium, Wellcome Trust Case Control Consortium 2. **A gene pathway analysis highlights the role of cellular adhesion molecules in multiple sclerosis susceptibility.** *Genes Immun* 2014;15:126–32 CrossRef Medline
29. Chironi GN, Boulanger CM, Simon A, et al. **Endothelial microparticles in diseases.** *Cell Tissue Res* 2009;335:143–51 CrossRef Medline
30. Orekhov AN, Sobenin IA. **Modified lipoproteins as biomarkers of atherosclerosis.** *Front Biosci (Landmark Ed)* 2018;23:1422–44 CrossRef Medline
31. Uher T, Fellows K, Horakova D, et al. **Serum lipid profile changes predict neurodegeneration in interferon-$\beta$1a-treated multiple sclerosis patients.** *J Lipid Res* 2017;58:403–11 CrossRef Medline
32. Debernard L, Melzer TR, Van Stockum S, et al. **Reduced grey matter perfusion without volume loss in early relapsing-remitting multiple sclerosis.** *J Neurol Neurosurg Psychiatry* 2014;85:544–51 CrossRef Medline
33. Adhya S, Johnson G, Herbert J, et al. **Pattern of hemodynamic impairment in multiple sclerosis: dynamic susceptibility contrast perfusion MR imaging at 3.0 T.** *Neuroimage* 2006;33:1029–35 CrossRef Medline
34. Lapointe E, Li DK, Traboulsee AL, et al. **What have we learned from perfusion MRI in multiple sclerosis?** *AJNR Am J Neuroradiol* 2018;39:994–1000 CrossRef Medline
35. Inglese M, Park SJ, Johnson G, et al. **Deep gray matter perfusion in multiple sclerosis: dynamic susceptibility contrast perfusion magnetic resonance imaging at 3 T.** *Arch Neurol* 2007;64:196–202 CrossRef Medline
36. Cocozza S, Canna A, Lanzillo R, et al. **Lack of correlation between extracranial venous abnormalities and multiple sclerosis: a quantitative MRI study.** *Brit J Radiol* 2016 Jun 27. [Epub ahead of print] CrossRef Medline
37. Zamboni P, Tesio L, Galimberti S, et al; Brave Dreams Research Group. **Efficacy and safety of extracranial vein angioplasty in multiple sclerosis: a randomized clinical trial.** *JAMA Neurol* 2018;75:35–43 CrossRef Medline
38. Louveau A, Da Mesquita S, Kipnis J. **Lymphatics in neurological disorders: a neuro-lympho-vascular component of multiple sclerosis and Alzheimer's disease?** *Neuron* 2016;91:957–73 CrossRef Medline
39. Healy BC, Ali EN, Guttmann CR, et al. **Smoking and disease progression in multiple sclerosis.** *Arch Neurol* 2009;66:858–64 Medline
40. Kavak KS, Teter BE, Hagemeier J, et al. **Higher weight in adolescence and young adulthood is associated with an earlier age at multiple sclerosis onset.** *Mult Scler* 2015;21:858–65 CrossRef Medline
41. Lindsay AC, Biasiolli L, Knight S, et al. **Non-invasive imaging of carotid arterial restenosis using 3T cardiovascular magnetic resonance.** *J Cardiovasc Magn Reason* 2014;16:5 CrossRef Medline

# Value of Contrast-Enhanced MRA versus Time-of-Flight MRA in Acute Ischemic Stroke MRI

T. Boujan, U. Neuberger, J. Pfaff, S. Nagel, C. Herweh, M. Bendszus, and M.A. Möhlenbruch

## ABSTRACT

**BACKGROUND AND PURPOSE:** Vessel imaging in acute ischemic stroke is essential to select patients with large-vessel occlusion for mechanical thrombectomy. Our aim was to compare the diagnostic accuracy of time-of-flight MR angiography and contrast-enhanced MR angiography for identification of vessel occlusion and collateral status in acute ischemic stroke.

**MATERIALS AND METHODS:** One hundred twenty-three patients with stroke with large-vessel occlusion before thrombectomy were included in this retrospective study. Before thrombectomy, 3T MR imaging, including conventional 3D TOF-MRA of the intracranial arteries and contrast-enhanced MRA of intra- and extracranial arteries, was performed. Both techniques were assessed independently by 2 neuroradiologists for location of the occlusion, imaging quality, and collateral status. Findings were compared, with subsequent DSA as the reference standard.

**RESULTS:** Both techniques had good interrater agreement of $\kappa = 0.74$ (95% CI, 0.66–0.83) for TOF-MRA and $\kappa = 0.72$ (95% CI, 0.63–0.80) for contrast-enhanced MRA. Occlusion localization differed significantly on TOF-MRA compared with DSA ($P < .001$), while no significant difference was observed between DSA and contrast-enhanced MRA ($P = .75$). Assessment of collaterals showed very good agreement between contrast-enhanced MRA and DSA (94.9% with $P = .25$), but only fair agreement between TOF-MRA and DSA (23.2% with $P < .001$).

**CONCLUSIONS:** Contrast-enhanced MRA offers better diagnostic accuracy than TOF-MRA in acute ischemic stroke. Contrast-enhanced MRA was superior in localizing vessel occlusion within a shorter acquisition time while providing a larger coverage, including extracranial vessels, and a more accurate assessment of collateral status. These results support inclusion of contrast-enhanced MRA in acute stroke MR imaging, perhaps making TOF-MRA superfluous.

**ABBREVIATION:** CE-MRA = contrast-enhanced MRA

In acute ischemic stroke, imaging plays a pivotal role in the initial diagnosis and treatment decisions. Especially in acute ischemic stroke due to large-vessel occlusion, vessel imaging, including CT angiography and MR angiography, is essential to select patients for thrombectomy as a highly effective treatment.[1]

Stroke MR imaging usually includes time-of-flight MRA for the detection of proximal vessel occlusion.[2-4] However, TOF-MRA has several major disadvantages: It provides only a small FOV, excluding extracranial vessels, and has a long acquisition time with the risk of motion artifacts[5] because the MR signal is generated by blood flow.[6]

Contrast-enhanced MR angiography (CE-MRA) with T1-shortening paramagnetic contrast medium induces the MR signal predominantly unaffected by blood flow disturbances, while providing a larger coverage from the aortic arch up to intracranial arteries,[7] and has a shorter acquisition time.

One of the most important questions in diagnostic imaging of acute stroke is, besides occlusion location as the principal indicator for further treatment, the assessment of pial collateral circulation as an independent predictor of outcome.[8-10]

Recently, TOF-MRA and CE-MRA have both been implemented in the evaluation of patients with acute stroke with promising results.[11,12] However, evaluation of CE-MRA as a method to identify intracranial occlusions and to assess collateral circulation has not yet provided conclusive results.[13,14] As more centers use MR imaging for triage (especially in the 6- to 24-hour time window), it is important to determine the best MR imaging protocol to assess proximal occlusion and collaterals.

The aim of this retrospective study was to assess the interrater agreement and diagnostic accuracy of TOF-MRA and CE-MRA in

Received April 15, 2018; accepted after revision June 17.

From the Departments of Neuroradiology (T.B., U.N., J.P., C.H., M.B., M.M.) and Neurology (S.N.), University of Heidelberg Medical Center, Heidelberg, Germany.

Timan Boujan and Ulf Neuberger contributed equally to this work.

Please address correspondence to Markus A. Möhlenbruch, MD, Department of Neuroradiology, University of Heidelberg Medical Center, Im Neuenheimer Feld 400, 69120 Heidelberg, Germany; e-mail: markus.moehlenbruch@med.uni-heidelberg.de

http://dx.doi.org/10.3174/ajnr.A5771

**Table 1: Acquisition parameters for MRA sequences**

| Parameter | CE-MRA | 3D TOF-MRA |
|---|---|---|
| Receive coil | 12-Channel head and neck coil combination | 12-Channel head and neck coil combination |
| TR/TE (ms) | 3.28/1.23 | 22/3.83 |
| Flip angle | 33° | 18° |
| Acquisition plane | Coronal | Axial |
| FOV (mm) | 300 × 300 | 200 × 200 |
| Reconstructed voxel size (mm) | 0.9 × 0.7 × 0.8 | 0.7 × 0.5 × 0.6 |
| Slice oversampling (%) | 9.1 | 20 |
| No. of slices per slab | 88 | 40 |
| No. of slabs | 1 | 3 |
| Slice thickness (mm) | 0.8 | 0.64 |
| Partial Fourier (phase and slice directions) | 7/8 and 6/8 | 6/8 and 6/8 |
| Total acquisition time | 64 sec | 3 min 7 sec |

identifying the location of occlusions and assessing the status of collaterals in the acute phase of ischemic stroke, compared with the reference standard DSA, in patients with large-vessel occlusion eligible for thrombectomy.

The hypothesis of this study was that CE-MRA is superior to TOF-MRA in determining the site of occlusion as the key element of acute stroke MR imaging before thrombectomy. Moreover, we hypothesized that CE-MRA offers better diagnostic assessment of collateral status. Additionally, by covering a larger FOV, including the supra-aortic vessels, CE-MRA offers the possibility of additional findings.

## MATERIALS AND METHODS

### *Patient Selection*

Due to the retrospective character of the study, individual written informed consent was waived by the institutional review board. One hundred twenty-three patients were prospectively included in a data base between January 2011 and July 2015.

Inclusion criteria for this study were the following: 1) clinical symptoms suggestive of acute stroke due to large-vessel occlusion, 2) DSA within 60 minutes after stroke MR imaging for thrombectomy, and 3) stroke MR imaging, including TOF- and CE-MRA, with the absence of motion artifacts impeding assessment of intracranial vessel occlusion.

### *MR Imaging*

All examinations were performed on a 3T MR imaging scanner (Magnetom Trio or Verio; Siemens, Erlangen, Germany) using a 12-channel head and neck coil array.

The complete acute stroke MR imaging protocol included parenchymal brain imaging sequences (axial DWI, T2 FLAIR, and SWI), angiographic sequences without contrast media (3D TOF), angiographic sequences with injection of a first bolus of contrast (CE-MRA), and perfusion-weighted imaging with the injection of a second bolus of contrast. The total average acquisition time for all MR imaging sequences was 17 minutes. The MRA acquisition parameters are provided in Table 1.

A volume of a 0.1-mmol/kg of body weight bolus of gadoterate meglumine, 0.5 mmol/mL, (Dotarem; Guerbet, Aulnay-sous-Bois, France) was administered via a peripheral venous catheter at 2 mL/s with an automatic power injector, followed by a 20-mL saline flush, with a bolus-tracking acquisition for the CE-MRA. A bolus-tracking sequence was started simultaneously with the injection. The image-acquisition sequence was launched manually after arrival of contrast media in the proximal common carotid artery. The second bolus of contrast (PWI) was identical, with injection of a volume of 0.1-mmol/kg of body weight bolus of gadoterate meglumine, 0.5 mmol/mL intravenously at 3.5 mL/s with an automatic power injector, followed by a 20-mL saline flush.

Source images and 3D maximum-intensity-projection images of CE-MRA and TOF-MRA were generated.

### *DSA Imaging*

Diagnostic DSA before thrombectomy was performed as the standard reference for extra- and intracranial artery analysis. All DSA examinations were performed by experienced neurointerventionalists on a biplanar system (Artis zee biplane; Siemens). Angiographic images were acquired at 4 frames per second with a manual injection of iodinated contrast media.

### *Data Analysis*

The TOF-MRA and CE-MRA sequences (MPR and MIP images) were evaluated independently and in random order on a commercially available 3D workstation by 2 neuroradiologists (T.B. and U.N.) with 8 and 2 years of experience, respectively. Results were compared with those of diagnostic DSA images in terms of occlusion location, quality of imaging, relevant vascular findings of supra-aortic vessels in CE-MRA, and assessment of collaterals. Readings occurred for several days, and cases were randomly assigned to prevent recall. Potential disagreements were discussed to reach a consensus.

The overall MR image quality was analyzed with a subjective interpretation score using a 3-point scoring scale: 0 = poor quality with a substantial number of artifacts, interpretation not possible; 1 = moderate quality with a mild-to-moderate number of artifacts, noise not interfering with diagnosis/interpretation; 2 = good/excellent image quality with no-to-minimal artifacts.

Occlusion location was defined as the proximal M1 segment (first half of the M1 segment), distal M1 segment (second half of the M1 segment), M2 segment, M3 segment, proximal internal carotid artery, distal ICA (subdivided into carotid-I, -L, and -T occlusions according to Liebeskind et al[15]), common carotid artery, and basilar artery.

Collaterals were evaluated according to a simplified 3-point scale based on the 4-point CT scale by Tan et al,[16] comparing the vascularity distal to the occlusion between the ischemic and the healthy hemisphere: 0 = no collaterals (no filling of the occluded area), 1 = poor collaterals (>0% but ≤50% filling of the occluded area), 2 = moderate/good collaterals (>50% filling of the occluded area).

Finally, we evaluated the relevant vascular findings of supra-aortic vessels, which may have influenced the choice of guiding or distal-access catheter (eg, vulnerable aortic arch and vascular variants).

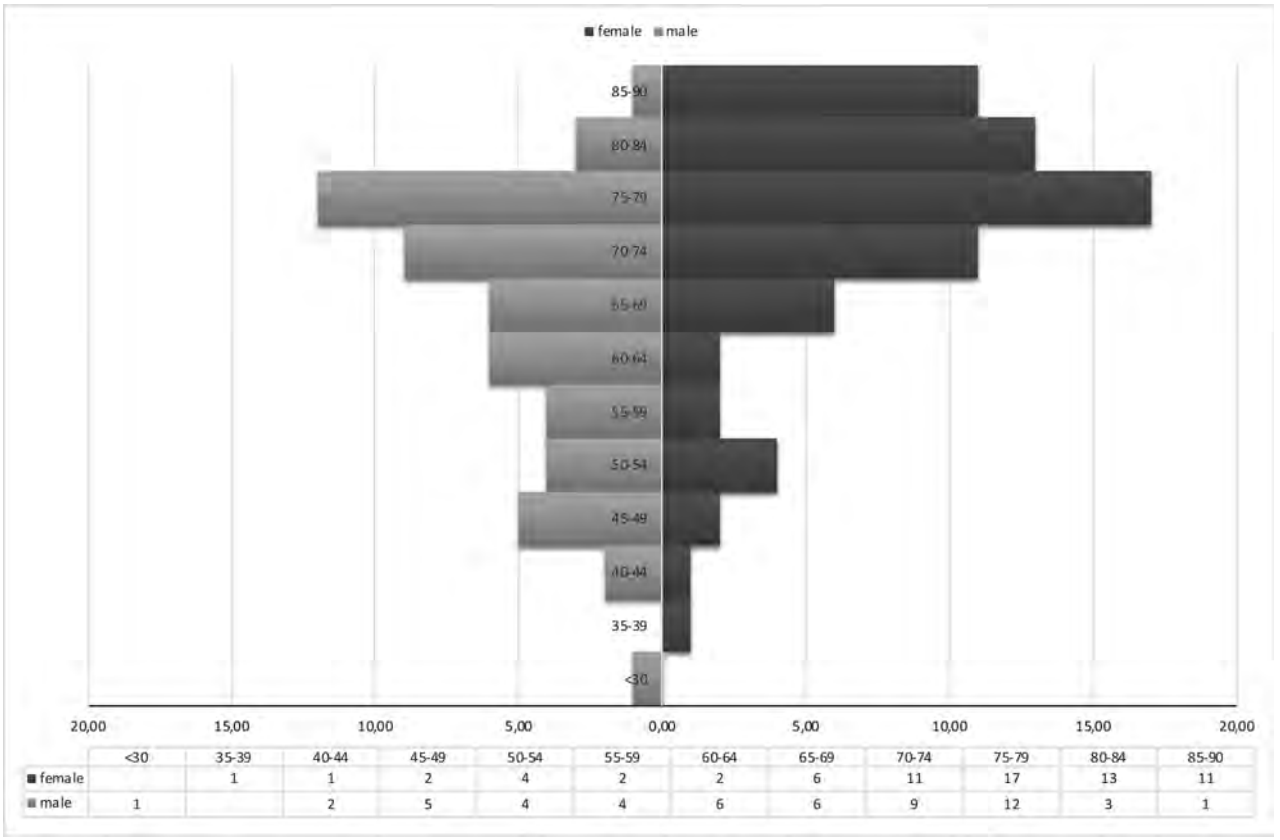


| | <30 | 35-39 | 40-44 | 45-49 | 50-54 | 55-59 | 60-64 | 65-69 | 70-74 | 75-79 | 80-84 | 85-90 |
|---|---|---|---|---|---|---|---|---|---|---|---|---|
| female | | 1 | 1 | 2 | 4 | 2 | 2 | 6 | 11 | 17 | 13 | 11 |
| male | 1 | | 2 | 5 | 4 | 4 | 6 | 6 | 9 | 12 | 3 | 1 |

**FIG 1.** Sex and age distribution (in absolute numbers).

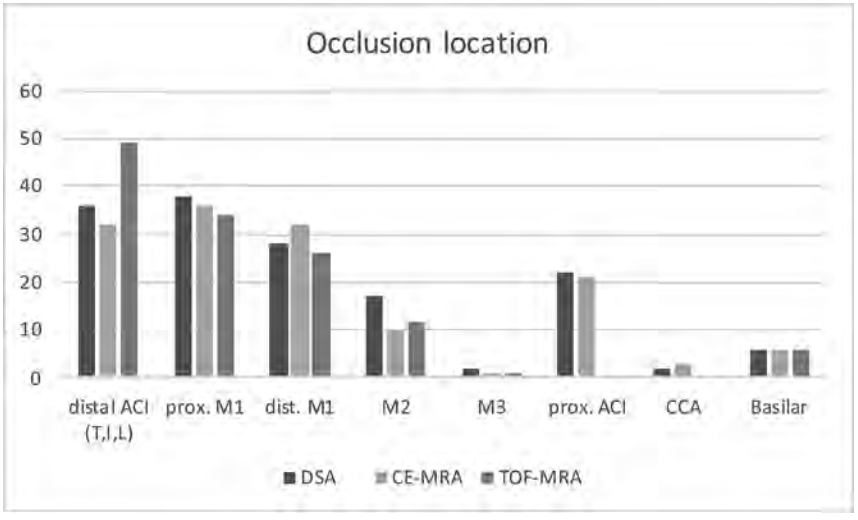


**FIG 2.** Site of occlusion (absolute numbers) based on the respective imaging technique.

### *Statistical Analysis*

Statistical analysis was performed using GraphPad Prism, Version 7 (GraphPad Software, San Diego, California) and Excel (Microsoft, Redmond, Washington). Interrater agreement was determined using the Cohen $\kappa$ coefficient. Agreement was graded according to Altman's definition[17] with $\kappa = 0.0–0.20$, poor; $\kappa = 0.21–0.40$, fair; $\kappa = 0.41–0.60$, moderate; $\kappa = 0.61–0.80$, good; and $\kappa = 0.81–1.00$, very good.

Measurements (occlusion location, collaterals) based on the 2 MRA sequences were compared with the reference imaging standard DSA using a Wilcoxon signed rank test. A variable was considered statistically significant only if $P < .05$.[18]

## RESULTS

### *Patient Selection*

Overall, 123 patients met the inclusion criteria (mean age, 70.3 ± 12.9 years; 70 women, 53 men) between January 2011 and July 2015. Sex and age distributions are given in Fig 1.

### *Evaluation of Image Quality*

Only 3.25% (4/123) of all TOF-MRAs and 1.62% (2/123) of all CE-MRAs could not be interpreted because of motion artifacts. The imaging quality was not statistically different between TOF-MRA (mean, 1.72 ± 0.49) and CE-MRA (mean, 1.83 ± 0.45) using the 3-step scoring scale. Interrater agreement for assessment of imaging quality was moderate for both CE-MRA (0.44; 95% CI, 0.25–0.64) and TOF-MRA (0.51; 95% CI, 0.35–0.68).

### *Occlusion Location*

In all 123 patients, an arterial occlusion was identifiable in 3D TOF and CE-MRA sequences. Interrater agreement for occlusion location was good for CE-MRA ($\kappa = 0.73$; 95% CI, 0.66–0.82) and TOF-MRA ($\kappa = 0.74$; 95% CI, 0.66–0.83).

**Table 2: Identification of intracranial occlusion location with 3D TOF-MRA and CE-MRA compared with DSA as the reference standard[a]**

| Occlusion Location | TOF-MRA | CE-MRA | DSA |
|---|---|---|---|
| CCA | 0 (0%) | 3 (66.7%) | 2 |
| Proximal ICA | 0 (0%) | 21 (90.5%) | 21 |
| Distal ICA | 53 (18.9%) | 34 (100%) | 36 |
| M1 | 54 (96.3%) | 68 (94.1%) | 66 |
| M2 | 14 (92.9%) | 13 (92.3%) | 17 |
| M3 | 1 (100%) | 1 (100%) | 2 |
| Basilar artery | 6 (100%) | 6 (100%) | 6 |

**Note:**—CCA indicates common carotid artery.
[a] Site of occlusion (absolute numbers), based on the respective imaging modality with percentage of agreement with DSA.

**Table 3: Cases with discrepancies in occlusion location between 3D TOF-MRA and CE-MRA compared with DSA as the reference standard[a]**

| Patient No. | TOF-MRA | CE-MRA | DSA |
|---|---|---|---|
| 2 | 1, 3 | 6, 3 | 6, 3 |
| 10 | 2 | 3 | 3 |
| 11 | 1, 2 | 7, 2 | 6, 2 |
| 12 | 1 | 6, 2 | 6, 2 |
| 16 | 1, 2 | 6, 2 | 6, 2 |
| 19 | 1 | 6, 2 | 6, 2 |
| 23 | 1 | 6, 3 | 6, 3 |
| 30 | 1 | 6, 1 | 1 |
| 34 | 1 | 7, 1 | 7, 1 |
| 42 | 1 | 6 | 6 |
| 59 | 1 | 6 | 6, 4 |
| 62 | 1, 3 | 6, 3 | 6, 3 |
| 65 | 4 | 3 | 4 |
| 66 | 1 | 6, 2 | 6, 2 |
| 70 | 1 | 6, 1 | 6, 1 |
| 71 | 1 | 6, 2 | 6, 2 |
| 79 | 1 | 6, 1 | 6, 1 |
| 80 | 1, 3 | 6, 2 | 6, 2 |
| 84 | 1 | 7 | 7, 1 |
| 87 | 1, 2 | 6, 2 | 6, 2 |
| 94 | 1 | 6, 2 | 6, 2 |
| 97 | 1 | 6, 2 | 1 |
| 98 | 1, 2 | 6, 2 | 6, 2 |
| 107 | 1 | 6, 1 | 6, 1 |
| 117 | 1 | 6, 1 | 6, 1 |
| 118 | 4 | 4 | 5 |
| 119 | 1 | 6, 1 | 6, 1 |
| 120 | 1 | 6, 2 | 6, 2 |

[a] Occlusion location: 1 = distal ICA; 2 = proximal M1; 3 = distal M1; 4 = M2; 5 = M3; 6 = proximal ICA; 7 = CCA.

Specificity and sensitivity for detecting the correct occlusion site compared with DSA were 92.0% and 91.7% for TOF-MRA and 99.0% and 92.0% for CE-MRA, respectively. Sensitivity for detecting a distal ICA occlusion was similar for both techniques (100% for TOF-MRA versus 94% for CE-MRA), whereas specificity was better for CE-MRA (100% versus 75% for TOF-MRA).

A Wilcoxon signed rank test revealed significant differences in the occlusion location between TOF-MRA and DSA ($P < .001$), whereas there was no statistically significant difference between CE-MRA and DSA ($P = .75$).

The occlusion locations are presented in Fig 2 and Table 2. The cases in which there were discrepancies among TOF MRA, CE MRA, and DSA are listed in Table 3. Imaging examples are shown in Fig 3.

### *Evaluation of Collaterals*

The assessment of collaterals is more sensitive to motion artifacts compared with occlusion location of proximal vessels because peripheral vessels/collaterals are much smaller; therefore, 3.25% (4/123) of all TOF-MRAs and 5.69% (7/123) of all CE-MRAs could not be interpreted. We only compared collaterals for M1 and M2 occlusions because pial collaterals could be retrogradely filled vessels from the ipsilateral anterior cerebral artery, posterior communicating artery, or lenticulostriate arteries. Because the assessment of collateral status was not possible for occlusions of the ICA and basilar artery, we excluded these.

Furthermore, the assessment of the collaterals on DSA was impossible in 9.7% (7/72) of the remaining cases because of the short series duration or lack of ipsilateral A1 or posterior communicating arteries. Therefore, the collateral score could be compared in 65 patients.

We analyzed the collateral status in the reference standard DSA with a very good interrater agreement with $\kappa = 0.92$ (95% CI, 0.80–0.99). Interrater agreement for assessing the collaterals was considered good for CE-MRA with $\kappa = 0.70$ (95% CI, 0.56–0.85) and moderate for TOF-MRA with $\kappa = 0.40$ (95% CI, 0.19–0.62). Imaging examples are given in Fig 3.

The collateral score was identical between DSA and CE-MRA in 87.7% of cases (57/65) with no statistically significant difference ($P = .125$), while there was a significant difference in collateral assessment between TOF-MRA and DSA ($P < .001$) and only 21.5% (14/65) of cases were assigned correctly. Imaging examples are shown in Fig 4.

### *Relevant Vascular Findings of Supra-Aortic Vessels*

CE-MRA demonstrated relevant vascular findings of the supra-aortic vessels, which were decisive for the endovascular treatment planning in 18.7% (23/123) of all patients. The relevant vascular findings are presented in Table 4.

## DISCUSSION

Both TOF-MRA[19] and CE-MRA[20-22] are frequently used and sensitive techniques for the triage of patients with acute stroke. Traditionally, TOF-MRA was primarily used to detect intracranial occlusions and occlusions in proximity to the skull base, while CE-MRA was usually performed to provide anatomic information from the aortic arch up to the skull base.

The advancement of stronger magnetic fields (ie, 3T), optimized sequences, and better receive coil arrays made it feasible to visualize intracranial cerebral arteries by CE-MRA at sufficient resolution. However, for more than a decade, multimodal CT has established itself as a less expensive and accessible alternative in the emergency assessment of patients with stroke, especially for patients with a short time window.[23] With the steady progress of neurointerventional therapy during recent years, mechanical thrombectomy has proved to be a highly effective therapy option,[24] well beyond the traditional time window of 6 hours, and up to 24 hours in eligible patients.[11,12] These recent developments stress the importance of MR imaging in acute stroke triage, especially in the 6- to 24-hour time window and necessitate determining the best MR images for assessment of the occlusion site and collateral status.

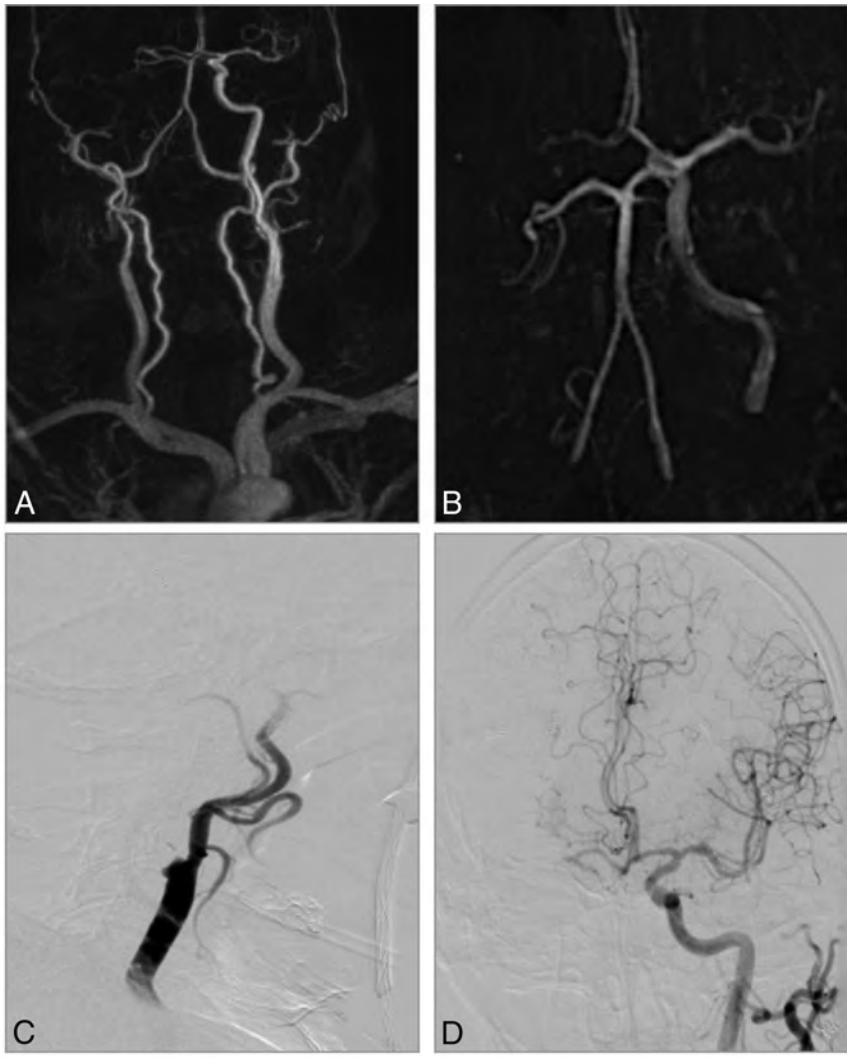


**FIG 3.** CE-MRA and TOF-MRA in an 81-year-old man with acute stroke symptoms before treatment. *A*, CE-MRA shows a tandem occlusion of the proximal ICA and right M1 segment with poor collaterals. *B*, TOF-MRA shows an occlusion of distal ICA (carotid-L). *C* and *D*, DSA confirms the tandem occlusion and CE-MRA diagnosis.

The present study indicates the superiority of CE-MRA in detecting the intracranial vessel occlusion and assessing intracranial collateral status, while simultaneously providing larger coverage at a shorter acquisition time compared with TOF-MRA.

The primary differences between TOF-MRA and DSA were found in patients with occlusions of the distal supraclinoid ICA (occlusions of the carotid-I, -L, and -T[15]) and proximal ICA. This difference is mostly due to distal occlusions mimicking proximal extracranial ICA occlusions ("pseudo-occlusion") and proximal occlusions mimicking distal intracranial ICA occlusions. This misapprehension could be a result of the nonenhanced nature of TOF-MRA, a technique that depends on the flow velocity and direction of blood. Previous studies have already reported this limitation of TOF-MRA when assessing these occlusion sites.[25-27] The better accuracy of CE-MRA was not dependent on image quality, which was not significantly different for the 2 techniques despite TOF-MRA having better spatial resolution. The better accuracy of CE-MRA, on the other hand, might be due to the T1-shortening effect of gadolinium. The effect compensates for the signal loss caused by spin dephasing occurring in TOF-MRA,[19] especially when the arterial flow is slow or oriented parallel to the section plane, which applies to imaging of the M2 segment. In these cases, TOF-MRA may indicate an incorrect occlusion site, with the level of occlusion more proximal than expected.

Similarly, for the assessment of collaterals as independent predictors of outcome,[8-10] CE-MRA was not affected by the signal loss observed in TOF-MRA. This particular signal loss might be due to low flow in vessels distal to the occlusion. Furthermore, slow collateral flow over leptomeningeal connections cannot be visualized on TOF-MRA.[28] This issue resulted in CE-MRA being significantly more accurate than TOF-MRA in assessing collaterals compared with the criterion standard of DSA. A previously performed study with 44 patients found similar results with CE-MRA, but not TOF-MRA, being a reliable predictor of infarct outcome in patients with stroke with proximal arterial occlusion of the anterior circulation using visual scoring.[29] The predictive performance could be increased by applying an automated atlas-based collateral assessment.

Besides assessment of the occlusion site and collaterals, CE-MRA offered additional advantages that could not be compared in the present study due to the limited FOV on TOF-MRA. CE-MRA showed relevant vascular findings of the supra-aortic vessels in 18.7% of patients, which are crucial for the planning of endovascular treatment. The choice of a guiding or distal-access catheter as well as selection of the vessel providing better access (in case of access from the vertebral artery) may be influenced by these findings as well as a priori knowledge of the internal carotid artery condition (eg, occlusion, site of occlusion, pseudo-occlusion).

### *Limitations of CE-MRA*

In comparison with TOF-MRA, CE-MRA requires more preparation with the following: 1) filling a power injector with contrast media, and 2) a sequence for bolus-tracking that takes additional time during stroke MR imaging (64 seconds). Currently, the use of contrast media is controversial due to potential risk of nephrogenic systemic fibrosis, in particular with unknown renal retention parameters,[30,31] and possible brain gadolinium deposition.[32] This risk is especially the case when not performing bolus PWI but instead using an arterial spin-labeling perfusion. Both risks

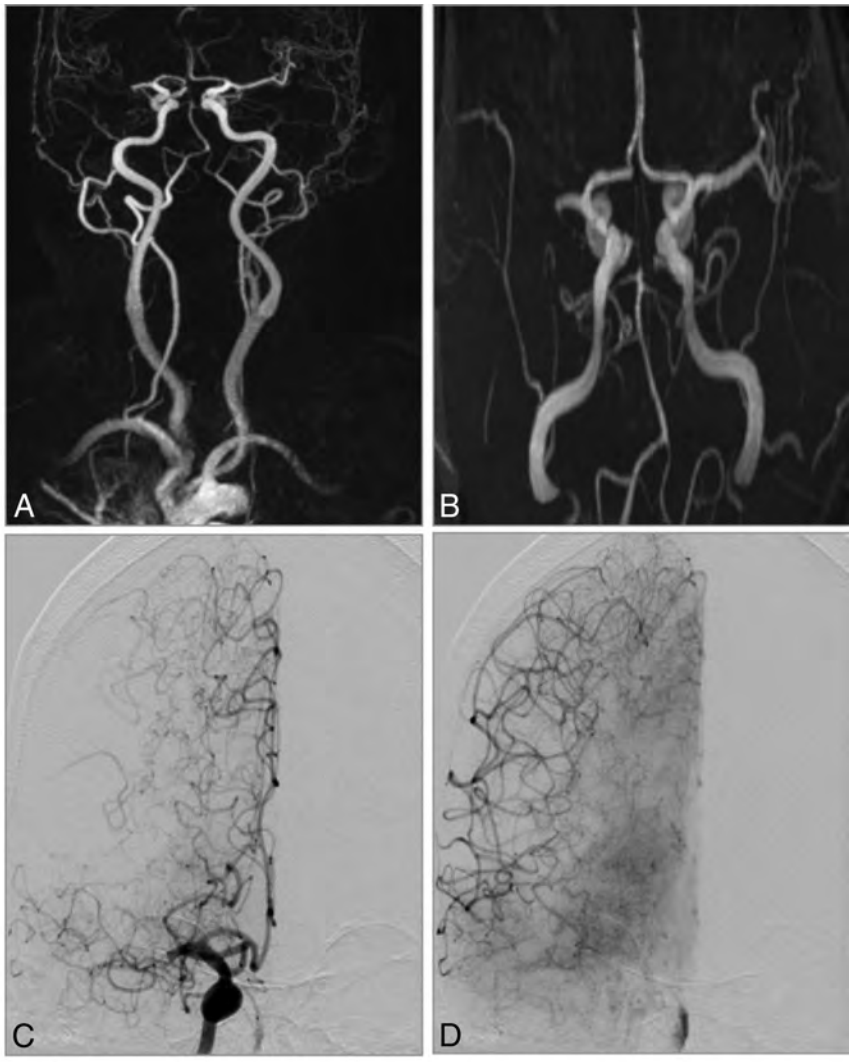


**FIG 4.** CE-MRA and TOF-MRA in a 72-year-old woman with acute stroke symptoms before treatment. *A*, CE-MRA shows an occlusion of right M1 segment with good collaterals. *B*, TOF-MRA shows an occlusion of the M1 segment and poor collaterals. *C* and *D*, DSA shows a right-sided M1 occlusion with good collaterals as in the CE-MRA.

**Table 4: Relevant vascular findings of supra-aortic vessels**

| Relevant Findings in CE-MRA | No. (%) |
|---|---|
| Vulnerable aortic arch (type III with at least 1 cervical vessel originating below the inferior margin of the aortic arch as described by Demertzis[35]) and a vascular variant (eg, severe vessel elongation) | 11 (8.9) |
| Dissection of the ipsilateral ICA | 2 (1.6) |
| PICA termination of hypoplastic vertebral artery, right or left, in case of basilar artery thrombosis | 5 (4.1) |
| Relevant ipsilateral ICA stenosis in case of M1–M2 thrombosis | 5 (4.1) |

can be minimized using macrocyclic gadolinium-based contrast agents.[33]

Furthermore, in our subjective experience, the first bolus of contrast media for CE-MRA did not affect the subsequent PWI analysis and was not a major limiting factor for the diagnostic interpretation, as was shown before.[34]

CE-MRA has lower spatial resolution compared with TOF-MRA, which could lead to poorer performance in addressing more precise characteristics of the clot, even if the localization is known.

### *Study Limitations*

The main limitation of this study is its retrospective design and the inclusion of nonconsecutive patients. However, the data were collected in a prospective data base. Moreover, a precise assessment of collateral status in DSA is only possible with 3-vessel angiography. Nevertheless, we performed only 1 injection at the site of occlusion to reach the clot as soon as possible and to avoid treatment delay. Another potential source of bias in this study might be the 30- to 60-minute delay between MRA examinations and DSA, with potential alterations of the findings (eg, thrombus migration, especially after intravenous thrombolysis). Moreover, the subjective assessment of image quality and collaterals, which is more sensitive to motion artifacts, may be a further limitation of the study.

## CONCLUSIONS

Our study indicates that CE-MRA is superior to TOF-MRA in identifying occlusion location and assessing the status of collaterals in patients with ischemic stroke, with shorter examination times. Moreover, CE-MRA can provide crucial information for the planning of endovascular treatment by covering a larger FOV. The inclusion of supra-aortic vessels, for example, can inform the selection of the appropriate guiding or distal-access catheters. These findings indicate that CE-MRA could replace TOF-MRA in the triage of patients with acute stroke and its use should be evaluated in future prospective trials.

Disclosures: Johannes Pfaff—*UNRELATED*: *Travel/Accommodations/Meeting Expenses Unrelated to Activities Listed*: Stryker, MicroVention. Simon Nagel—*UNRELATED*: *Consultancy*, Brainomix, Boehringer Ingelheim; *Payment for Lectures Including Service on Speakers Bureaus*: Medtronic, Bayer AG, Pfizer; *Travel/Accommodations/Meeting Expenses Unrelated to Activities Listed*: Brainomix. Christian Herweh—*UNRELATED*: *Consultancy*: Brainomix; *Payment for Lectures Including Service on Speakers Bureaus*: Medtronic, Bristol-Myers Squibb; *Travel/Accommodations/Meeting Expenses Unrelated to Activities Listed*: Stryker. Martin Bendszus—*UNRELATED*: *Board Membership*: Data and Safety Monitoring Board for Vascular Dynamics, Guerbet, Boehringer Ingelheim; *Consultancy*: Codman, Roche, Guerbet, Boehringer Ingelheim, B Braun; *Grants/Grants Pending*: Deutsche Forschungsgemeinschaft, Hopp Foundation, Novartis, Siemens, Guerbet, Stryker, Covidien, European Union*; *Payment for Lectures Including Service on Speakers Bureaus*: Novartis, Roche, Guerbet, Teva Pharmaceutical Industries, Bayer AG, Codman. Markus A. Möhlenbruch—*UNRELATED*: *Board Membership*: Codman; *Consultancy*: Medtronic, MicroVention, Stryker; *Grants/Grants Pending*: Balt, MicroVention*; *Payment for Lectures Including Service on Speakers Bureaus*: Medtronic, MicroVention, Stryker. *Money paid to institution.

## REFERENCES


1. Saver JL, Goyal M, van der Lugt A, et al; HERMES Collaborators. **Time to treatment with endovascular thrombectomy and outcomes from ischemic stroke: a meta-analysis.** *JAMA* 2016;316:1279–88 CrossRef Medline
2. Nagel S, Schellinger PD, Hartmann M, et al. **Therapy of acute basilar artery occlusion: intraarterial thrombolysis alone vs bridging therapy.** *Stroke* 2009;40:140–46 CrossRef Medline
3. Barlinn K, Alexandrov AV. **Vascular imaging in stroke: comparative analysis.** *Neurotherapeutics* 2011;8:340–48 CrossRef Medline
4. Stock KW, Radue EW, Jacob AL, et al. **Intracranial arteries: prospective blinded comparative study of MR angiography and DSA in 50 patients.** *Radiology* 1995;195:451–56 CrossRef Medline
5. Miyazaki M, Lee VS. **Nonenhanced MR Angiography.** *Radiology* 2008;248:20–43
6. Bash S, Villablanca JP, Jahan R, et al. **Intracranial vascular stenosis and occlusive disease: evaluation with CT angiography, MR angiography, and digital subtraction angiography.** *AJNR Am J Neuroradiol* 2005;26:1012–21 Medline
7. Yang CW, Carr JC, Futterer SF, et al. **Contrast-enhanced MR angiography of the carotid and vertebrobasilar circulations.** *AJNR Am J Neuroradiol* 2005;26:2095–101 Medline
8. Cheng-Ching E, Frontera JA, Man S, et al. **Degree of collaterals and not time is the determining factor of core infarct volume within 6 hours of stroke onset.** *AJNR Am J Neuroradiol* 2015;36:1272–76 CrossRef Medline
9. Kluytmans M, van der Grond J, van Everdingen KJ, et al. **Cerebral hemodynamics in relation to patterns of collateral flow.** *Stroke* 1999;30:1432–39 CrossRef Medline
10. Bang OY, Saver JL, Kim SJ, et al. **Collateral flow predicts response to endovascular therapy for acute ischemic stroke.** *Stroke* 2011;42:693–99 CrossRef Medline
11. Albers GW, Marks MP, Kemp S, et al; DEFUSE 3 Investigators. **Thrombectomy for stroke at 6 to 16 hours with selection by perfusion imaging.** *N Engl J Med* 2018;378:708–18 CrossRef Medline
12. Nogueira RG, Jadhav AP, Haussen DC, et al; DAWN Trial Investigators. **Thrombectomy 6 to 24 hours after stroke with a mismatch between deficit and infarct.** *N Engl J Med* 2018;378:11–21 CrossRef Medline
13. Hernández-Pérez M, Puig J, Blasco G, et al. **Dynamic magnetic resonance angiography provides collateral circulation and hemodynamic information in acute ischemic stroke.** *Stroke* 2016;47:531–34 CrossRef Medline
14. Martinon E, Lefevre PH, Thouant P, et al. **Collateral circulation in acute stroke: assessing methods and impact—a literature review.** *J Neuroradiol* 2014:41:97–107 CrossRef Medline
15. Liebeskind DS, Flint AC, Budzik RF; MERCI and Multi-MERCI Investigators. **Carotid I's, L's and T's: collaterals shape the outcome of intracranial carotid occlusion in acute ischemic stroke.** *J Neurointerv Surg* 2015;7:402–07 CrossRef Medline
16. Tan IYL, Demchuk AM, Hopyan J, et al. **CT angiography clot burden score and collateral score: correlation with clinical and radiologic outcomes in acute middle cerebral artery infarct.** *AJNR Am J Neuroradiol* 2009;30:525–31 CrossRef Medline
17. Altman DG. *Practical Statistics for Medical Research*. Chapman & Hall/CRC; 1990
18. Rosner B, Glynn RJ, Lee ML. **The Wilcoxon signed rank test for paired comparisons of clustered data.** *Biometrics* 2006;62:185–92 CrossRef Medline
19. Yang JJ, Hill MD, Morrish WF, et al. **Comparison of pre- and post-contrast 3D time-of-flight MR angiography for the evaluation of distal intracranial branch occlusions in acute ischemic stroke.** *AJNR Am J Neuroradiol* 2002;23:557–67 Medline
20. Nael K, Khan R, Choudhary G, et al. **Six-minute magnetic resonance imaging protocol for evaluation of acute ischemic stroke: pushing the boundaries.** *Stroke* 2014;45:1985–91 CrossRef Medline
21. Phan T, Huston J 3rd, Bernstein MA, et al. **Contrast-enhanced magnetic resonance angiography of the cervical vessels: experience with 422 patients.** *Stroke* 2001;32:2282–86 CrossRef Medline
22. Le Bras A, Raoult H, Ferré JC, et al. **Optimal MRI sequence for identifying occlusion location in acute stroke: which value of time-resolved contrast-enhanced MRA?** *AJNR Am J Neuroradiol* 2015;36:1081–88 CrossRef Medline
23. Meissner W, Sibon I, Rouanet F, et al. **MRI versus CT in acute stroke.** *Lancet* 2007;369:1342 Medline
24. Goyal M, Menon BK, van Zwam WH, et al; HERMES collaborators. **Endovascular thrombectomy after large-vessel ischaemic stroke: a meta-analysis of individual patient data from five randomised trials.** *Lancet* 2016;387:1723–31 CrossRef Medline
25. Saager C, Fitting T, Goebell E, et al. **Contrast-enhanced MR angiography improves detection of carotid-T occlusion by acute stroke MRI.** *Clin Neuroradiol* 2008;18:163–77
26. Igase K, Igase M, Matsubara I, et al. **Mismatch between TOF MR angiography and CT angiography of the middle cerebral artery may be a critical sign in cerebrovascular dynamics.** *Yonsei Med J* 2018;59:80–84 CrossRef Medline
27. Pedraza S, Silva Y, Mendez J, et al. **Comparison of preperfusion and postperfusion magnetic resonance angiography in acute stroke.** *Stroke* 2004;35:2105–10 CrossRef Medline
28. Heiserman JE, Drayer BP, Keller PJ, et al. **Intracranial vascular stenosis and occlusion: evaluation with three-dimensional time-of-flight MR angiography.** *Radiology* 1992;185:667–73 CrossRef Medline
29. Ernst M, Forkert ND, Brehmer L, et al. **Prediction of infarction and reperfusion in stroke by flow- and volume-weighted collateral signal in MR angiography.** *AJNR Am J Neuroradiol* 2015;36:275–82 CrossRef Medline
30. Cowper SE, Robin HS, Steinberg SM, et al. **Scleromyxoedema-like cutaneous diseases in renal-dialysis patients.** *Lancet* 2000;356:1000–01 CrossRef Medline
31. Thomsen HS, Webb JA, eds. *Contrast Media: Safety Issues and ESUR Guidelines*. Berlin Heidelberg: Springer Science & Business Media; 2014
32. Kanda T, Ishii K, Kawaguchi H, et al. **High signal intensity in the dentate nucleus and globus pallidus on images: relationship with increasing cumulative dose of a gadolinium-based contrast material.** *Radiology* 2014;270:834–41 CrossRef Medline
33. Radbruch A, Weberling LD, Kieslich PJ, et al. **Gadolinium retention in the dentate nucleus and globus pallidus is dependent on the class of contrast agent.** *Radiology* 2015;275:783–91 CrossRef Medline
34. Nael K, Meshksar A, Ellingson B, et al. **Combined low-dose contrast-enhanced MR angiography and perfusion for acute ischemic stroke at 3T: a more efficient stroke protocol.** *AJNR Am J Neuroradiol* 2014;35:1078–84 CrossRef Medline
35. Demertzis S, Hurni S, Stalder M, et al. **Aortic arch morphometry in living humans**. *J Anat* 2010;217:588–96 CrossRef Medline

# Breath-Hold Blood Oxygen Level–Dependent MRI: A Tool for the Assessment of Cerebrovascular Reserve in Children with Moyamoya Disease

N. Dlamini, P. Shah-Basak, J. Leung, F. Kirkham, M. Shroff, A. Kassner, A. Robertson, P. Dirks, R. Westmacott, G. deVeber, and W. Logan

## ABSTRACT

**BACKGROUND AND PURPOSE:** There is a critical need for a reliable and clinically feasible imaging technique that can enable prognostication and selection for revascularization surgery in children with Moyamoya disease. Blood oxygen level–dependent MR imaging assessment of cerebrovascular reactivity, using voluntary breath-hold hypercapnic challenge, is one such simple technique. However, its repeatability and reliability in children with Moyamoya disease are unknown. The current study sought to address this limitation.

**MATERIALS AND METHODS:** Children with Moyamoya disease underwent dual breath-hold hypercapnic challenge blood oxygen level–dependent MR imaging of cerebrovascular reactivity in the same MR imaging session. Within-day, within-subject repeatability of cerebrovascular reactivity estimates, derived from the blood oxygen level–dependent signal, was computed. Estimates were associated with demographics and intellectual function. Interrater reliability of a qualitative and clinically applicable scoring scheme was assessed.

**RESULTS:** Twenty children (11 males; 12.1 ± 3.3 years) with 30 MR imaging sessions (60 MR imaging scans) were included. Repeatability was "good" on the basis of the intraclass correlation coefficient (0.70 ± 0.19). Agreement of qualitative scores was "substantial" ($\kappa = 0.711$), and intrarater reliability of scores was "almost perfect" ($\kappa = 0.83$ and 1). Younger participants exhibited lower repeatability ($P = .027$). Repeatability was not associated with cognitive function ($P > .05$). However, abnormal cerebrovascular reactivity was associated with slower processing speed ($P = .015$).

**CONCLUSIONS:** Breath-hold hypercapnic challenge blood oxygen level–dependent MR imaging is a repeatable technique for the assessment of cerebrovascular reactivity in children with Moyamoya disease and is reliably interpretable for use in clinical practice. Standardization of such protocols will allow further research into its application for the assessment of ischemic risk in childhood cerebrovascular disease.

**ABBREVIATIONS:** BH = breath-hold; BOLD = blood oxygen level–dependent; CV = coefficient of variation; CVR = cerebrovascular reactivity; ICC = intraclass correlation coefficient; SCD = sickle cell disease

Arterial ischemic stroke remains a major cause of morbidity and mortality in children worldwide. The incidence ranges from 2 to 13 per 100,000 person-years in developed countries.[1,2] Childhood risk factors are multiple and include cardiac disease, sickle cell disease (SCD), arteriopathy, and infection.[3-5] More than two-thirds of previously healthy children presenting with their first arterial ischemic stroke have a steno-occlusive arteriopathy, the presence of which predicts recurrence and outcome.[6-8] Moyamoya disease is a major arteriopathy of childhood. It is a progressive steno-occlusive arteriopathy that typically affects the anterior circulation arteries of the circle of Willis. It confers a life-long risk of recurrent stroke and neurologic injury, and it is associated with early death due to chronic cerebral hypoperfusion and thrombotic vaso-occlusion.[9-11] However, the pathology of the primary arteriopathy is poorly understood.

A network of lenticulostriate collaterals develops to bypass the primary steno-occlusive arteriopathy, and vasodilation at the level of the capillary bed occurs to maintain cerebral blood flow, resulting in a reduction of cerebrovascular reserve.[12] Studies in adults with arteriopathy suggest that impairment of cerebrovas-

Received February 15, 2018; accepted after revision June 10.

From the Division of Neurology (N.D., G.d.V., W.L.), Neurosciences and Mental Health Program (N.D.), Child Health Evaluative Sciences Program (N.D., A.R., G.d.V.), Translational Medicine (J.L., A.K.), Diagnostic Imaging (P.S.-B., M.S.), Department of Neurosurgery (P.D.), and Department of Neuropsychology (R.W.), The Hospital for Sick Children, Toronto, Ontario, Canada; Institute of Medical Science (N.D., G.d.V.) and Department of Medical Imaging (A.K.), University of Toronto, Toronto, Ontario, Canada; Rotman Research Institute (P.S.-B.), Baycrest, Toronto, Ontario, Canada; and Developmental Neurosciences (N.D., F.K.), University College London, Great Ormond Street Institute of Child Health, London, UK.

Please address correspondence to Nomazulu Dlamini, Division of Neurology, The Hospital for Sick Children, 555 University Ave, Toronto, M5G 1X8, Canada, e-mail: nomazulu.dlamini@sickkids.ca

Indicates article with supplemental on-line tables.

Indicates article with supplemental on-line photos.

http://dx.doi.org/10.3174/ajnr.A5739

cular reserve is associated with an approximate 4-fold increased risk of developing stroke or transient ischemic attacks.[13] In vivo assessment of cerebrovascular reserve can be performed by measurement of cerebrovascular reactivity (CVR), defined as a change in CBF in response to vasoactive stimuli such as carbon dioxide. In the context of steno-occlusive arteriopathy and maximal microvascular vasodilation in response to falling CBF, exhaustion of cerebrovascular reserve and vasodilatory capacity may result in paradoxical reductions in CBF and CVR following a vasodilating stimulus.[12,14-16] This negative response, termed "steal," is an independent predictor of ischemic injury and stroke.[12,14,15]

Historically used techniques for assessing CBF and cerebrovascular reserve such as PET and SPECT require exposure to ionizing radiation and are hence undesirable.[16] Blood oxygen level–dependent (BOLD) MR imaging is a widely used technique for the noninvasive imaging of dynamic changes in CBF at the local and global levels. BOLD MR imaging harnesses the paramagnetic properties of deoxyhemoglobin using clinically available T2* gradient-echo MR imaging sequences and does not require intravenous contrast medium. Using carbon dioxide as a vasoactive stimulus, hypercapnic challenge BOLD MR imaging CVR (BOLD-CVR) can be used to generate high-spatial-resolution CVR maps. Thus, when cerebrovascular reserve is exhausted, negative or paradoxical reactivity on hypercapnic challenge BOLD-CVR maps represents steal and provides a visual representation of ischemic risk and impending tissue demise.[15]

Hypercapnia induced by computer-controlled carbon dioxide stimulus delivery for BOLD-CVR experiments has been validated in both adults and children in research settings.[17-21] In the only published study of the reliability of CVR measurements acquired in children (10 healthy children; mean age, 16.1 ± 1.6 years), intraclass correlations coefficients (ICCs) of within-day values were 0.857 and 0.895 in the GM and the WM, respectively.[22] However, this method relies on specialized MR imaging–compatible equipment, limiting its applicability in clinical settings. Additionally, the use of nasal prongs or a facemask to deliver and monitor the carbon dioxide stimulus serves as a barrier for CVR acquisition in young children.

An alternative approach for performing CVR assessment is breath-hold (BH), in which endogenous alveolar carbon dioxide naturally accumulates during short periods of voluntary apnea. Without the need for additional equipment and gas-delivery apparatus, BH is easier to implement and well-tolerated.[22] The repeatability and reliability of BH-BOLD-CVR (BH-CVR) in high-stroke-risk pediatric populations, however, remain unknown. The purpose of this study was to evaluate within-day, within-subject repeatability, qualitative scoring, and interrater reliability of the scoring of BH-CVR estimates. The relationship between clinical factors and intellectual function and BH performance and repeatability was also explored.

## MATERIALS AND METHODS

### Study Population

Children 6 years of age or older diagnosed with cerebral vasculopathy consistent with a diagnosis of Moyamoya disease (idiopathic or syndromic) between 2010 and 2017 were recruited from the Hospital for Sick Children Toronto Stroke Registry. All procedures were approved by our institutional Research Ethics Board, and informed written consent was obtained. Moyamoya disease was diagnosed if conventional or MR angiography demonstrated stenosis or occlusion of the distal internal carotid artery, the proximal middle cerebral artery, and/or the anterior cerebral artery with the appearance of lenticulostriate collaterals. Children with unilateral Moyamoya disease with collaterals (probable Moyamoya disease) were included.[23] Children without a previously diagnosed condition were diagnosed as having Moyamoya disease or idiopathic Moyamoya disease, while those with a previously diagnosed condition such as neurofibromatosis type 1 or SCD were diagnosed as having Moyamoya syndrome. Children with non-Moyamoya arteriopathy and children unable to complete a repeat study were excluded.

### Breath-Hold Paradigm

No minimum duration of BH was set for inclusion in the study. Children practiced the BH paradigm seated on a chair before entering the MR imaging scanner under the supervision of a research technologist. Each BH paradigm began with 10 seconds of normal breathing, followed by five 60-second periods of breath-holding and normal breathing (Fig 1*A*). Optimal BH duration was determined during practice in individual patients as the maximum number of seconds that they could hold their breath without discomfort. BH duration was subtracted from 60 seconds to calculate the within-cycle normal breathing duration. A 30-second rest period with normal breathing was included after the second cycle. To assess subject compliance and motion, we monitored real-time respiration signals using respiratory bellows throughout the scan. Any patients observed to deviate from the instructions (ie, unable to breath-hold and/or breathe normally when instructed by the research technologist or observed to move excessively) were flagged as "noncompliant."

### Breath-Hold CVR and MR Imaging Acquisition

Children underwent repeat BH-CVR studies (1A and 1B) on the same day during the same MR imaging session. Follow-up repeat studies were performed in a subset of patients at later time-points (2A–2B; 3A–3B; 4A–4B).

MR imaging data were acquired with a 3T scanner (Achieva; Philips Healthcare, Best, the Netherlands) using an 8-channel head coil. The BH-CVR protocol consisted of 2 separate BOLD acquisitions using EPI–gradient recalled echo lasting 6 minutes, 6 seconds (25 slices; TR/TE = 2000/30 ms; voxel size = 3.4 × 3.4 × 5 $mm^3$; FOV = 22 cm; 180 dynamics). The BH paradigm was used throughout the scan duration. A high-resolution 3D T1-weighted structural image (160 slices; voxel size = 0.86 × 0.86 × 1 $mm^3$; FOV = 22 cm) was acquired for tissue classification and coregistering the CVR maps.

### Image Postprocessing and CVR Estimation

MR imaging data processing was performed using functions from Analysis of Functional Neuro Images (AFNI, Version 16.1.04; http://afni.nimh.nih.gov/afni)[23] and FSL (Version 4.1.9; (http://www.fmrib.ox.ac.uk/fsl) toolboxes. The first 2 dynamics of the BOLD data were truncated and subjected to slice-timing correction. Dynamics were corrected for motion by including the 6

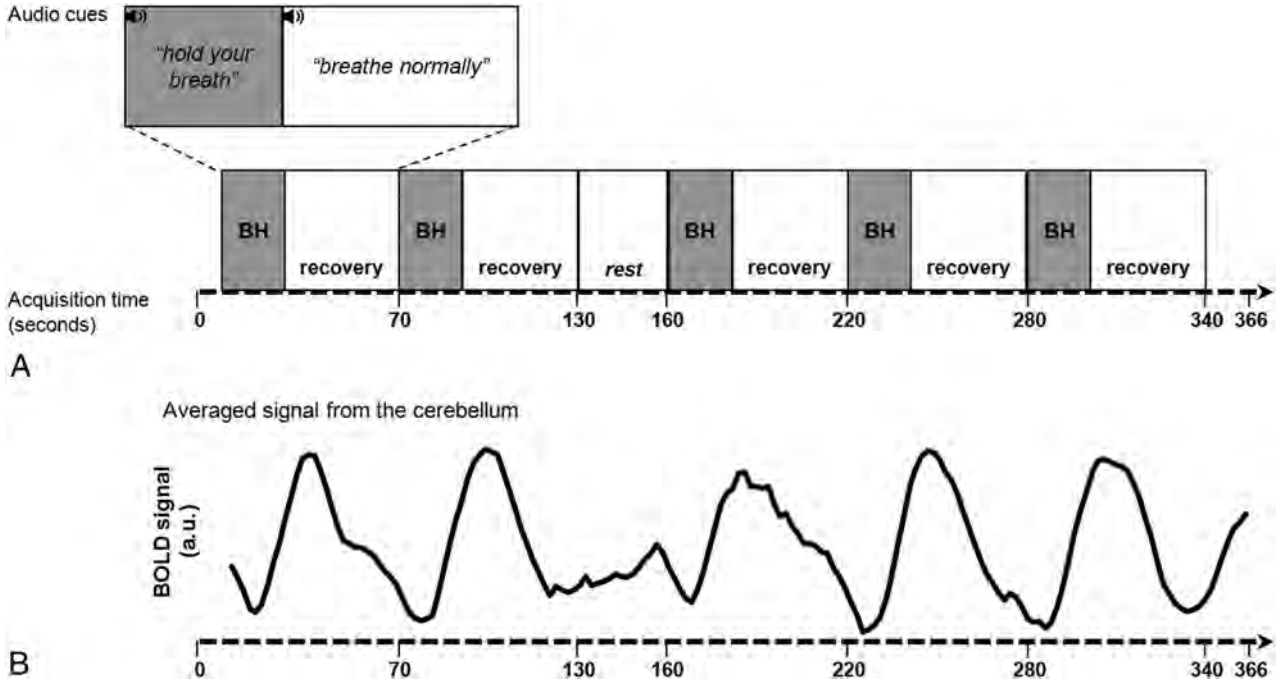


**FIG 1.** Schematic of breath-hold paradigm (*A*) and cerebellar BOLD signal time course (*B*) obtained from a representative participant (P11). a.u. indicates arbitrary units.

rigid-body-movement parameters as covariates in a generalized linear model. Spatial deviations with respect to a reference dynamic were also computed. BOLD dynamics exhibiting excessive motion (>0.3 mm/dynamic) were automatically labeled and disregarded in subsequent analyses. Data were spatially smoothed using a Gaussian kernel of 7 mm. The Automated Segmentation Tool of FSL (FAST; http://fsl.fmrib.ox.ac.uk/fsl/fslwiki/fast) was used for defining GM and WM masks.[24] The mask of the cerebellum from the Montreal Neurological Institute 152 atlas was coregistered to each patient to determine the cerebellar region.

For CVR maps, the patient's BOLD time-series in each voxel of the brain was subjected to generalized linear model analysis, using the corresponding averaged cerebellar time courses as a regressor (Fig 1*B*). The regression coefficients (or the $\beta$ weights) were then calculated for each voxel. Negative $\beta$ weights describing an inverse relationship with the regressor are the markers of steal. CVR maps consisting of voxelwise negative and positive $\beta$ weights (describing a negative and positive relationship with the regressor, respectively) were coregistered to the high-resolution T1 images in the native space for visualization.[25] A combined CVR measure was also computed as a weighted average of relative counts of positive and negative voxels.[19] In addition, all CVR measures were summarized by major vascular territory, namely the middle cerebral artery, anterior cerebral artery, and posterior cerebral artery, defined using the regions in the Harvard-Oxford Atlas.[26-29]

### Assessment of BH-CVR Performance

The quality of BH studies was assessed using the following: 1) BH compliance during data acquisition using a respiratory waveform from the bellows, and 2) evidence of excessive motion during postprocessing. The determination was based on a cutoff set at >15 dynamics, or 30 seconds, affected by motion in either BH repeat study.

**Criteria for scoring CVR maps**

| Visual Impression | Score |
|---|---|
| Normal CVR | 1 |
| Reduced positive reactivity ± minimal steal (<10%) | 2 |
| Significant steal (>10%) | 3 |

### Qualitative Scoring of BH-CVR Maps

Summative scoring of the ROIs (whole-brain and hemispheric vascular territories) of the BH-CVR maps was conducted by visual inspection for steal of the first repeat study (1A–1B) by neurologists, blinded to the patients' clinical information. Negative CVR reactivity observed in CSF-rich ventricular regions, including the peritrigonal regions, has been reported in healthy individuals.[30] It is physiologic and hence considered an artifact in CVR interpretation.[31] The visual impression of normal positive reactivity, reduced positive reactivity ± minimal steal, and significant (>10% of the ROI) steal was scored as 1, 2, and 3, respectively (Table). Hemispheric scoring by visual inspection was conducted independently by the same neurologists for patients with multiple time point studies (1A–1B; 2A–2B; 3A–3B; 4A–4B) (Fig 2).

### Moyamoya Subtype, Stroke, and Intellectual Function

Clinical records and high-resolution clinical T2-weighted images acquired at the time of each BH-CVR study were reviewed for Moyamoya subtype, history of stroke, and the presence of vascular territory ischemic infarction.

Standardized age-appropriate measures of intelligence using the Wechsler Intelligence Scale for Children (IV/V),[26,27] administered as part of routine clinical care within 3 years of BH-CVR collection, were reviewed and included in the analysis.

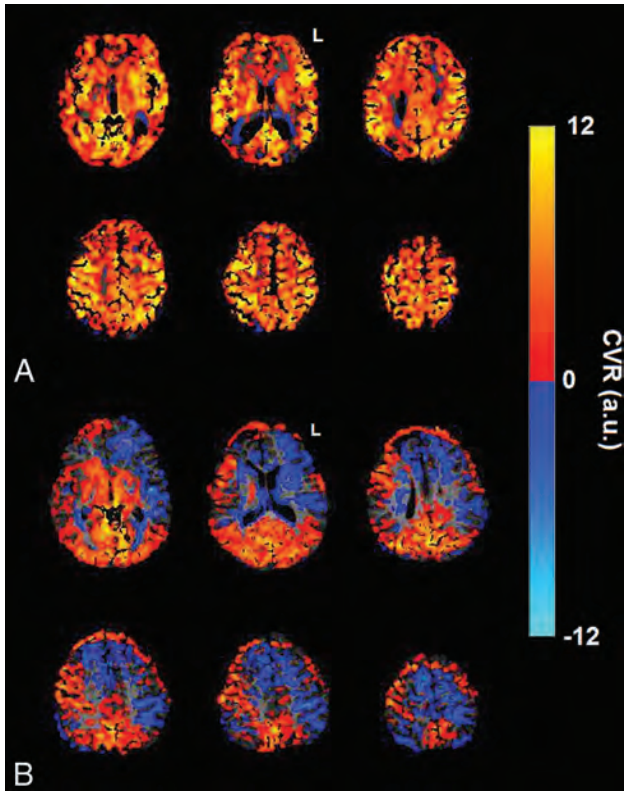


**FIG 2.** *A*, Normal-appearing BH-CVR maps demonstrating positive BH-CVR reactivity (P07: whole-brain score, 1; hemispheric score, 1:1). *B*, BH-CVR maps with abnormal findings demonstrating bilateral abnormal (left > right) negative reactivity (P15: whole-brain score, 3; hemispheric score, 3:3). L indicates left; a.u., arbitrary units.

### *Statistical Analysis*

To determine the repeatability, we computed the ICC and coefficient of variation (CV) of within-day repeat scans in the whole brain and in tissue (GM, WM) masks.[21] CV was computed as a ratio of the SD and mean of CVR estimates among repeat studies. Interpretation of ICC values was as follows: <0.41, "poor"; ≥0.41 and <0.59, "fair"; ≥0.59 and <0.74, "good"; and ≥0.74, "excellent."[32] Bland-Altman analysis was performed to determine the 95% limits of agreement among the repeat BH-CVR estimates. The Cohen $\kappa$ analysis was used to assess the following: 1) agreement among whole-brain scores, 2) agreement among scores by vascular territory, and 3) interrater reliability of hemispheric scoring of repeat scans. Interpretation of the $\kappa$ scores was as follows: 0.01, "poor"; 0.01–0.20, "slight"; 0.21–0.40, "fair"; 0.41–0.60, "moderate"; 0.61–0.80, "substantial"; and 0.81–1.00,"almost perfect" agreement.[33]

Means of positive, negative, and combined CVR estimates, representing the magnitude of CVR values, and their respective voxel counts were computed and compared among repeat scans using paired *t* tests. These estimates were also compared among repeat scans in the left and right hemispheric vascular territories, using 3-way repeat-measures ANOVA.

Exploratory analyses to examine relationships among ICC, CVR estimates, clinical factors (Moyamoya subtype, history of stroke), demographics (age at CVR), and intellectual function (full-scale intelligence quotient and intelligence quotient subscales) were conducted. One-way ANOVA was used for categoric variables; and linear regression, for continuous independent variables. Post hoc *t* tests were performed to assess significant ANOVA findings. Fisher exact tests were used for comparing 2 categoric variables.

## RESULTS

### *Study Population*

Twenty children (11 males; mean age, 12.1 ± 3.3 years; median, 11.7 years; range, 6.2–18.0 years) at the first BH-CVR were included. Follow-up repeat scans (2A–2B) were collected in 6 children, 3 children returned for a third scan (3A–3B), and 1 child returned for a fourth scan (4A–4B). Thirty pairs of within-day repeat BH-CVR studies (60 BH-CVR scans) were completed.

Eleven patients (55%) had idiopathic Moyamoya disease, 4 (20%) had neurofibromatosis type 1, two (10%) had SCD, while 3 others (15%) had familial, radiation-induced, or *ACTA2* mutation Moyamoya disease (On-line Table 1); the mean age at Moyamoya disease diagnosis was 7.9 ± 3.2 years (median, 8.0 years; range, 1.4–16.8 years). Three patients (15%) presented with stroke, and 7 patients (35%), with TIA. Seventeen patients (85%) had no prior history of stroke. Half of the children were either asymptomatic (7/20, 35%) or had headache only (3/20, 15%) at the time of Moyamoya disease diagnosis.

### *BH Performance, CVR Estimates, and Repeatability Measures*

In 6 of 30 studies (20%), the children were flagged as noncompliant, all of whom were undergoing first repeat studies (1A or 1B). Four of those were noted to be noncompliant during data acquisition. Two studies had excessive motion noted during postprocessing. All studies irrespective of compliance or motion were included in the assessment of repeatability (On-line Table 1).

Mean BH durations in the first (A) and the second (B) scans were 19.6 ± 3.3 seconds (range, 12–25 seconds) and 20.3 ± 3.4 seconds (range, 14–25 seconds), respectively ($P = .1$; median for A and B = 20 seconds). No significant differences between repeat scans were found for the positive, negative, or combined mean CVR estimates or the counts of positive and negative voxels in the GM and the WM (all $P > .05$; patient-wise estimates in On-line Table 2). The CVR estimates differed across the vascular territories but, most important, not among repeat scans (all $P > .05$; On-line Fig 1). All estimates differed between the anterior cerebral artery and posterior cerebral artery and MCA and posterior cerebral artery territories, with no difference between the anterior cerebral artery and MCA ($P < .05$, Bonferroni-corrected). Of 30 paired studies, repeatability for the whole-brain CVR estimates (ICC = 0.703 ± 0.190) was excellent in 18 (60%) and good in 5 (17%) studies. The remaining 7 studies (23%) fell into the fair-to-poor range (On-line Table 1). All except 1 (5/6) patient flagged as either noncompliant or for excessive motion had poor ICCs. The 2 patients with SCD also exhibited relatively low ICCs (0.51–0.48). The ICC tended to vary across vascular territories ($P = .07$) but fell in the good range (MCA = 0.67 ± 0.16; anterior cerebral artery = 0.65 ± 0.19; posterior cerebral artery = 0.71 ± 0.12; On-line Fig 2).

The mean CV was 9.1% ± 8.2% for positive CVR and 22.5% ± 18.3% for negative CVR in the GM. CV was reduced, on average,

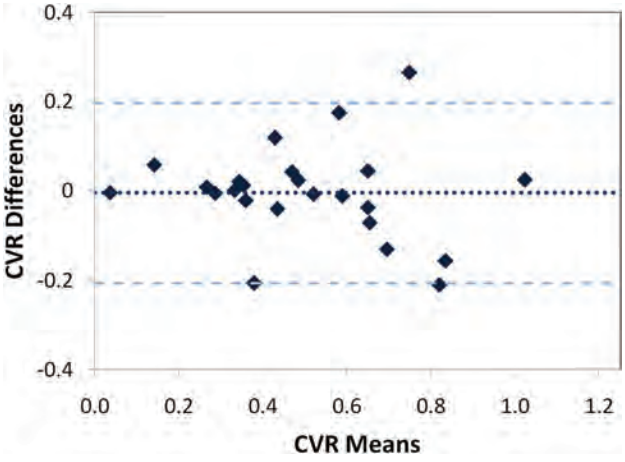


**FIG 3.** Bland-Altman plot showing a low mean between-scan difference of 0.004 (*dotted line*) with a critical difference of 0.202 (*broken lines*).

by 2.5% after excluding the studies flagged for noncompliance. CV and ICC were negatively correlated ($P < .05$). A Bland-Altman plot (Fig 3) illustrated the overall variation of whole-brain CVR with a test-retest difference of $-0.004 \pm 0.202$.

### *Qualitative Scoring by Visual Inspection*

Three (1A or 1B) repeat studies were excluded as not being suitable for scoring by visual inspection. In the remaining paired studies (17/20), there was 82.35% (14/17) agreement in whole-brain (1A–1B) scores. The Cohen weighted $\kappa$ was 0.75, in keeping with good strength of agreement. The Cohen weighted $\kappa$ by vascular territory was 0.95 (MCA), 0.8 (anterior cerebral artery), and 1.0 (posterior cerebral artery), suggestive of almost perfect strength of agreement. The interrater reliability for hemispheric scoring was 1.0 (left) and 0.83 (right), suggestive of perfect and very good strength of agreement among scorers, respectively.

### *Age, Moyamoya Subtype, Stroke, Intellectual Function, and Measures of BH-CVR Repeatability*

Neither Moyamoya subtype nor a history of stroke was associated with ICC ranks (excellent, fair/good, poor; $P > .05$). A significant effect of age at the time of BH-CVR on the ICC ranks was found (mean age in poor, excellent, and good ICC groups, $8.6 \pm 1.7$, $13.1 \pm 2.6$, and $14.2 \pm 2.9$ years, respectively; $F(2,20) = 4.3$; $P = .027$). The ICC was not associated with the full-scale intelligence quotient ($n = 9$) or subscales ($P > .05$). However, the count of negative CVR voxels was a significant predictor of the processing-speed index (GM, $P = .015$; WM, $P = .047$) after controlling for BH duration and age. In addition, the processing-speed index was significantly reduced in patients with whole-brain qualitative scores of 3 (ie, in patients exhibiting significant steal) ($P = .009$).

## DISCUSSION

Our study demonstrates that BH-CVR implemented using standard functional MR images provides a feasible, repeatable, and reliably interpretable tool for the assessment of CVR and cerebrovascular reserve in children with Moyamoya disease. On average, children older than 8.6 years, composing 80% of our cohort, had no difficulty with our BH paradigm. In this group, within-day repeatability was good-to-excellent, CV was <25%, and agreement of repeat measures was acceptable. Repeatability was not affected by clinical factors such as Moyamoya disease etiology, history of stroke, or intellectual abilities. Negative CVR or steal, however, was associated with a reduced processing-speed index in a subset of our cohort. Another important goal of our study was to explore whether BH-CVR maps are reliably interpretable among different clinical users. We found good-to-excellent agreement of within-day visual inspection scores and almost perfect interrater agreement.

A significant number of children with Moyamoya disease are asymptomatic at the time of diagnosis and therefore require lifelong surveillance. This was reflected in our study in which 35% of our patients were asymptomatic at diagnosis. Our study also included the youngest child with Moyamoya disease reported to date to successfully complete BH-CVR studies (6.2 years of age).[20,21,30] Lowering the age limit of feasibility to younger than 7 years for obtaining the CVR measures will facilitate earlier instigation of longitudinal surveillance in Moyamoya disease than is the current practice and will inform clinical management in the age group at highest risk of stroke.

A number of factors affect the BOLD response and thereby measures of repeatability. This was highlighted by our 2 patients with SCD who had notably lower repeatability, despite completing the BH-CVR without any issues with compliance or motion. This result may be attributed to the anemia in SCD driving a global impairment in CVR[34,35] and reducing the overall signal-to-noise ratio of the BOLD response. The increased influence of noise can adversely affect the correlation of repeat scans. In addition, negative CVR, which is frequently seen in SCD,[35] is especially prone to high variability and therefore can affect repeatability in these patients, as suggested by our data.

The BH execution and the duration of BH can also affect the BOLD response. A short BH of 3 seconds is adequate to produce a detectable BOLD response. However, a longer BH increases the magnitude and number of voxels exhibiting the response, resulting in more robust and repeatable measures of BOLD-CVR.[36] The mean BH duration in our study ranged from 19.6 to 20.3 seconds, suggestive of good BH duration overall. One of the limitations of the BH challenge is that it is limited to patients who can understand and comply with instructions. It therefore does not adequately address the challenge of conducting CVRs in the very young (eg, younger than 5 years of age). However, supervised practice of the paradigm and use of good BH practice guidelines such as paced breathing between challenges and breath-holding after expiration both at home and outside the MR imaging scanner before the BH-CVR study may help improve BH performance, reduce variability, and, in turn, improve repeatability.[22] Other strategies to minimize motion during scanning include measures to reduce distractibility among BH-CVR cycles such as visual fixation with videos and/or games.

Real-time monitoring of the carbon dioxide stimulus is the desirable method for CVR quantification.[22] Alternatively, as in our study, the dynamic cerebellar BOLD time course can be used.[37] In this method, the BOLD signal from the cerebellum represents changes in the blood flow corresponding to the accumulation of arterial carbon dioxide in each BH and provides a

dynamic trace reference for quantifying BOLD in the rest of the brain tissue. While this method is reliable for within-subject assessment of CVR, a limitation is that it cannot be used for group comparative analysis. The use of MR imaging–compatible technologies for real-time acquisition of carbon dioxide in conjunction with BOLD and BH will facilitate group-based and more sophisticated quantitative analysis in future studies.

## CONCLUSIONS

Measures of BH-CVR repeatability in children are good-to-excellent and CVR maps are reliably interpretable by clinical users. While clinical acquisition of MR imaging–CVR using computer-controlled devices has become increasingly feasible with recent iterations of this technology, the relative simplicity of BH-CVR is desirable for younger patients who can follow simple instructions. In addition, BH-CVR remains a practical substitute for many institutions when controlled-delivery carbon dioxide methods are not available or tolerable. Standardization of BH paradigms, image acquisition, and processing protocols will further allow the implementation of this promising technique for clinical assessment of cerebrovascular reserve and ischemic risk in childhood cerebrovascular disease.


## ACKNOWLEDGMENTS

We acknowledge the support of The Auxillium Foundation, the Stroke Imaging Laboratory for Children, and the Ontasian Imaging Laboratory.

Disclosures: Fenella Kirkham—*UNRELATED*: *Employment*: University College London Great Ormond Street Institute of Child Health; *Grants/Grants Pending*: National Institute of Health Research (UK), Actione Medical Research; *Payment for Lectures Including Service on Speakers Bureaus*: Fenella Kirkham; *Payment for Manuscript Preparation*: Shire plc Pharmaceutical Company, Paid to Fenella Kirkham; *Comments*: for epilepsy; *Royalties*: Mac Keith Press, *Comments*: small amount for previously published book on childhood stroke; *Travel/Accommodations/Meeting Expenses Unrelated to Activities Listed*: European Haemoglobinopathy Association, *Comments*: travel to Madrid and Cairo to give lectures.


## REFERENCES


1. Lynch JK, Hirtz DG, DeVeber G, et al. **Report of the National Institute of Neurological Disorders and Stroke workshop on perinatal and childhood stroke.** *Pediatrics* 2002;109:116–23 CrossRef Medline
2. Fullerton HJ, Wu YW, Zhao S, et al. **Risk of stroke in children: ethnic and gender disparities.** *Neurology* 2003;61:189–94 CrossRef Medline
3. Fullerton HJ, Wu YW, Sidney S, et al. **Risk of recurrent childhood arterial ischemic stroke in a population-based cohort: the importance of cerebrovascular imaging.** *Pediatrics* 2007;119:495–501 CrossRef Medline
4. Mackay MT, Wiznitzer M, Benedict SL, et al; International Pediatric Stroke Study Group. **Arterial ischemic stroke risk factors: the International Pediatric Stroke Study.** *Ann Neurol* 2011;69:130–40 CrossRef Medline
5. Wintermark M, Hills NK, deVeber GA, et al; VIPS Investigators. **Arteriopathy diagnosis in childhood arterial ischemic stroke: results of the vascular effects of infection in pediatric stroke study.** *Stroke* 2014;45:3597–605 CrossRef Medline
6. Ganesan V, Prengler M, Wade A, et al. **Clinical and radiological recurrence after childhood arterial ischemic stroke.** *Circulation* 2006;114:2170–77 CrossRef Medline
7. Braun KP, Bulder MM, Chabrier S, et al. **The course and outcome of unilateral intracranial arteriopathy in 79 children with ischaemic stroke.** *Brain* 2009;132:544–57 Medline
8. Amlie-Lefond C, Bernard TJ, Sebire G, et al; International Pediatric Stroke Study Group. **Predictors of cerebral arteriopathy in children with arterial ischemic stroke: results of the International Pediatric Stroke Study.** *Circulation* 2009;119:1417–23 CrossRef Medline
9. Dobson SR, Holden KR, Nietert PJ, et al. **Moyamoya syndrome in childhood sickle cell disease: a predictive factor for recurrent cerebrovascular events.** *Blood* 2002;99:3144–50 CrossRef Medline
10. Rafay MF, Armstrong D, Dirks P, et al. **Patterns of cerebral ischemia in children with moyamoya.** *Pediatr Neurol* 2015;52:65–72 CrossRef Medline
11. Guey S, Tournier-Lasserve E, Hervé D, et al. **Moyamoya disease and syndromes: from genetics to clinical management.** *Appl Clin Genet* 2015;8:49–68 CrossRef Medline
12. Sobczyk O, Battisti-Charbonney A, Fierstra J, et al. **A conceptual model for $CO_2$-induced redistribution of cerebral blood flow with experimental confirmation using BOLD MRI.** *Neuroimage* 2014;92:56–68 CrossRef Medline
13. Gupta A, Chazen JL, Hartman M, et al. **Cerebrovascular reserve and stroke risk in patients with carotid stenosis or occlusion: a systematic review and meta-analysis.** *Stroke* 2012;43:2884–91 CrossRef Medline
14. Conklin J, Fierstra J, Crawley AP, et al. **Impaired cerebrovascular reactivity with steal phenomenon is associated with increased diffusion in white matter of patients with Moyamoya disease.** *Stroke* 2010;41:1610–16 CrossRef Medline
15. Reinhard M, Schwarzer G, Briel M, et al. **Cerebrovascular reactivity predicts stroke in high-grade carotid artery disease.** *Neurology* 2014;83:1424–31 CrossRef Medline
16. Lee M, Zaharchuk G, Guzman R, et al. **Quantitative hemodynamic studies in moyamoya disease: a review.** *Neurosurg Focus* 2009;26:E5 CrossRef Medline
17. Slessarev M, Han J, Mardimae A, et al. **Prospective targeting and control of end-tidal CO2 and O2 concentrations.** *J Physiol* 2007;581:1207–19 CrossRef Medline
18. Kassner A, Winter JD, Poublanc J, et al. **Blood-oxygen level dependent MRI measures of cerebrovascular reactivity using a controlled respiratory challenge: reproducibility and gender differences.** *J Magn Reson Imaging* 2010;31:298–304 CrossRef Medline
19. Heyn C, Poublanc J, Crawley A, et al. **Quantification of cerebrovascular reactivity by blood oxygen level-dependent MR imaging and correlation with conventional angiography in patients with Moyamoya disease.** *AJNR Am J Neuroradiol* 2010;31:862–67 CrossRef Medline
20. Han JS, Mikulis DJ, Mardimae A, et al. **Measurement of cerebrovascular reactivity in pediatric patients with cerebral vasculopathy using blood oxygen level-dependent MRI.** *Stroke* 2011;42:1261–69 CrossRef Medline
21. Leung J, Kim JA, Kassner A. **Reproducibility of cerebrovascular reactivity measures in children using BOLD MRI.** *J Magn Reson Imaging* 2016;43:1191–95 CrossRef Medline
22. Bright MG, Murphy K. **Reliable quantification of BOLD fMRI cerebrovascular reactivity despite poor breath-hold performance.** *Neuroimage* 2013;83:559–68 CrossRef Medline
23. Fukui M. **Guidelines for the diagnosis and treatment of spontaneous occlusion of the circle of Willis ('moyamoya' disease): Research Committee on Spontaneous Occlusion of the Circle of Willis (Moyamoya Disease) of the Ministry of Health and Welfare, Japan.** *Clin Neurol Neurosurg* 1997;99(Suppl 2):S238–40 Medline
24. Zhang Y, Brady M, Smith S. **Segmentation of brain MR images through a hidden Markov random field model and the expectation-maximization algorithm.** *IEEE Trans Med Imaging* 2001;20:45–57 CrossRef Medline
25. Jenkinson M, Smith S. **A global optimisation method for robust affine registration of brain images.** *Med Image Anal* 2001;5:143–56 CrossRef Medline
26. Wechsler D. *Wechsler Intelligence Scale for Children: Fourth Edition Technical and Interpretive Manual.* San Antonio: PsychCorp; 2004
27. Wechsler D. *Wechsler Intelligence Scale for Children: Fifth Edition.*

*Technical and Interpretive Manual.* Bloomington: PsychCorp: Pearson; 2014
28. van der Zwan A, Hillen B, Tulleken CA, et al. **Variability of the territories of the major cerebral arteries.** *J Neurosurg* 1992;77:927–40 CrossRef Medline
29. Desikan RS, Ségonne F, Fischl B, et al. **An automated labeling system for subdividing the human cerebral cortex on MRI scans into gyral based regions of interest.** *Neuroimage* 2006;31:968–80 CrossRef Medline
30. Mandell DM, Han JS, Poublanc J, et al. **Mapping cerebrovascular reactivity using blood oxygen level-dependent MRI in patients with arterial steno-occlusive disease: comparison with arterial spin labeling MRI.** *Stroke* 2008;39:2021–28 CrossRef Medline
31. Thomas BP, Liu P, Aslan S, et al. **Physiologic underpinnings of negative BOLD cerebrovascular reactivity in brain ventricles.** *Neuroimage* 2013;83:505–12 CrossRef Medline
32. Lipp I, Murphy K, Caseras X, et al. **Agreement and repeatability of vascular reactivity estimates based on a breath-hold task and a resting state scan.** *Neuroimage* 2015;113:387–96 CrossRef Medline
33. Landis JR, Koch GG. **The measurement of observer agreement for categorical data.** *Biometrics* 1977;33:159–74 CrossRef Medline
34. Kosinski PD, Croal PL, Leung J, et al. **The severity of anaemia depletes cerebrovascular dilatory reserve in children with sickle cell disease: a quantitative magnetic resonance imaging study.** *Br J Haematol* 2017;176:280–87 CrossRef Medline
35. Prohovnik I, Hurlet-Jensen A, Adams R, et al. **Hemodynamic etiology of elevated flow velocity and stroke in sickle-cell disease.** *J Cereb Blood Flow Metab* 2009;29:803–10 CrossRef Medline
36. Abbott DF, Opdam HI, Briellmann RS, et al. **Brief breath holding may confound functional magnetic resonance imaging studies.** *Hum Brain Mapp* 2005;24:284–90 CrossRef Medline
37. Raut RV, Nair VA, Sattin JA, et al. **Hypercapnic evaluation of vascular reactivity in healthy aging and acute stroke via functional MRI.** *Neuroimage Clin* 2016;12:173–79 CrossRef Medline

# Contrast-Enhanced CISS Imaging for Evaluation of Neurovascular Compression in Trigeminal Neuralgia: Improved Correlation with Symptoms and Prediction of Surgical Outcomes

A.M. Blitz, B. Northcutt, J. Shin, N. Aygun, D.A. Herzka, D. Theodros, C.R. Goodwin, M. Lim, and D.P. Seeburg

## ABSTRACT

**BACKGROUND AND PURPOSE:** Thin-section MR imaging through the posterior fossa is frequently used for trigeminal neuralgia. Typical heavily T2-weighted imaging methods yield high anatomic detail and contrast between CSF and neurovascular structures, but poor contrast between vessels and nerves. We hypothesized that the addition of gadolinium-based contrast material to 3D-constructive interference in steady-state imaging would improve the characterization of trigeminal compression.

**MATERIALS AND METHODS:** Retrospective review of high-resolution MRIs was performed in patients without prior microvascular decompression. 3D-CISS imaging without contrast and with contrast for 81 patients with trigeminal neuralgia and 15 controls was intermixed and independently reviewed in a blinded fashion. Cisternal segments of both trigeminal nerves were assessed for the grade of neurovascular conflict, cross-sectional area, and degree of flattening. Data were correlated with symptom side and pain relief after microvascular decompression using the Fisher exact test, receiver operating curve analysis, and a paired *t* test.

**RESULTS:** Contrast-enhanced CISS more than doubled the prevalence of the highest grade of neurovascular conflict (14.8% versus 33.3%, $P = .001$) and yielded significantly lower cross-sectional area ($P = 8.6 \times 10^{-6}$) and greater degree of flattening ($P = .02$) for advanced-grade neurovascular conflict on the symptoms side compared with non-contrast-enhanced CISS. Patients with complete pain relief after microvascular decompression had significantly lower cross-sectional area on contrast-enhanced CISS compared with non-contrast-enhanced CISS on preoperative imaging ($P = 2.0 \times 10^{-7}$). Performance based on receiver operating curve analysis was significantly improved for contrast-enhanced CISS compared with non-contrast-enhanced CISS.

**CONCLUSIONS:** The addition of contrast material to 3D-CISS imaging improves the performance of identifying unilateral neurovascular compression for symptomatic trigeminal neuralgia and predicting outcomes after microvascular decompression.

**ABBREVIATIONS:** AUC = area under the curve; CSA = cross-sectional area; CE = contrast-enhanced; DOF = degree of flattening; MVD = microvascular decompression; NE = non-contrast-enhanced; TN = trigeminal neuralgia

It is generally accepted that vascular compression of the trigeminal nerve (CN V) is an etiologic factor in trigeminal neuralgia (TN).[1] Lingering controversy stems mainly from 2 frequently made observations: First, neurovascular contact of the cisternal segment of CN V is not uncommon in asymptomatic individuals, ranging in prevalence from 14% to 88%.[2-5] Second, it is not uncommon to find patients with TN who have no neurovascular contact at all.[5] However, more severe neurovascular conflict (eg, resulting in deformity or displacement of the nerve) is commonly seen in patients with TN, but not in patients without TN.[4,6,7] Moreover, both the presence and severity of trigeminal nerve root compression have been shown intraoperatively[4,8-10] and by imaging[11-13] to be predictive of favorable outcomes after microvascular decompression (MVD). Thus, from these studies, the concept emerges that it is the degree of compression of the CN V root, rather than simply whether there is any neurovascular contact, that is most predictive of symptoms of TN and favorable outcomes after MVD.

MVD is one of the most commonly performed surgical interventions for TN[14] and has shown high effectiveness in relieving pain.[9] MVD is an invasive procedure, however, and careful pre-

Received November 18, 2016; accepted after revision June 17, 2018.

From the Departments of Radiology and Radiological Science (A.M.B., B.N., J.S., N.A., D.P.S.), Biomedical Engineering (D.A.H.), and Neurosurgery (D.T., C.R.G., M.L.), Johns Hopkins University School of Medicine, Baltimore, Maryland.

Paper preciously presented at: Annual Meeting of the American Society of Head and Neck Radiology, September 9–13, 2015; Naples, Florida, by Seeburg et al; and Annual Meeting of the Congress of Neurological Surgeons, September 26–30, 2015; New Orleans, Louisiana, by Goodwin et al.

Please address correspondence to Ari M. Blitz, MD, Division of Neuroradiology, The Russell H. Morgan Department of Radiology and Radiologic Science, The Johns Hopkins Hospital, Phipps B-100, 600 North Wolfe St, Baltimore, MD, 21287; e-mail: ablitz1@jhmi.edu

Indicates article with supplemental on-line tables.

Indicates article with supplemental on-line photos.

http://dx.doi.org/10.3174/ajnr.A5743

operative patient selection is important. Although rare, complications like meningitis, CSF leak, wound infections, and short- or long-term deficits such as hearing loss may occur.[14]

High-resolution 3D T2-weighted steady-state free precession sequences, including 3D-CISS or FIESTA, yield high spatial resolution and high contrast between CSF and neurovascular structures and have become the standard sequence for preoperative imaging in TN.[15,16] However, these sequences have poor contrast between vessels and nerves because both are low in intensity, potentially limiting detection and characterization of higher grade neurovascular conflict when there is little or no intervening CSF. We hypothesized that the addition of intravenous contrast material to 3D-CISS sequences, which appear to be T2-weighted but, in fact, have both T2- and T1-weighting[17] and therefore demonstrate enhancement,[18-20] would improve the contrast between enhancing vessels and adjacent unenhanced trigeminal nerve roots. The aim of this study was to evaluate whether contrast-enhanced 3D-CISS (CE-CISS) improves our ability to predict the symptom side in patients with TN and further to predict which patients are most likely to have favorable outcomes after MVD, compared with 3D-CISS without contrast (NE-CISS).

## MATERIALS AND METHODS

### Study Design and Patient Sample

A retrospective review of 310 consecutive high-resolution 3D TN protocol MR imaging studies acquired between 2011 and 2014 at our institution was performed. The study was institutional review board–approved and Health Insurance Portability and Accountability Act–compliant. Of the 261 patients imaged for TN (49 studies belonged to subjects imaged more than once) with this protocol during this period, we selected all 116 patients with a history of TN who had imaging performed before undergoing MVD. Of those, 26 patients were excluded because they had had a previous intervention for TN (rhizotomy or gamma knife treatment). Nine studies were excluded because a full set of clinical characteristics was not available or the imaging data were incomplete. A total of 81 studies qualified for the pre-MVD TN group. Separately, 51 patients without the diagnosis of TN were imaged with the same parameters performed as a component of an evaluation of the skull base. Of these, 15 studies were chosen at random as non-TN controls. An equal number of cases and asymptomatic controls would bias the reader to overestimate the asymptomatic controls as TN cases because most asymptomatic individuals do not undergo the high-resolution trigeminal neuralgia imaging protocol. Assuming a statistical power of 80% and exposure defined by those undergoing the high-resolution trigeminal neuralgia imaging protocol, 1-$\beta$ is 20% exposure in controls (chance of type II error). Considering that the number of symptomatic cases was 81, fifteen (18.5%) were selected as the number of asymptomatic controls to remain below 20%.[21,22]

The mean age for the pre-MVD TN group was 49.2 years (range, 27–71 years), with 52 female and 29 male patients. The mean age for the control group was 44.6 years (range, 15–71 years), with 10 female and 5 male patients. There was no statistical difference in the age of the 2 groups ($P = .2$, two-tailed Student $t$ test).

The diagnosis of TN was based on clinical history and physical examination performed by the neurosurgery team (C.R.G. and M.L.). Demographic and baseline disease characteristics were collected during the presurgical work-up for MVD. Patients were classified as having either type 1 TN (classic TN, purely paroxysmal) or type 2 TN (TN with persistent facial pain). The clinical outcome of pain relief following MVD was assessed during follow-up clinic visits and classified as type 1: complete pain relief without need for medication; type 2: complete pain relief with continued need for medication; type 3: partial pain relief with continued need for medication; and type 4: no pain relief despite medication. The range of clinical follow-up was 3 days to 1228 days, with an average of 275 days. On-line Tables 1 and 2 list the patients and clinical outcomes. For one of the patients, clinical outcome data were not available because the patient was lost to follow up.

### Imaging Technique

All studies were conducted on Verio or Magnetom Trio 3T scanners (Siemens, Erlangen, Germany) ($n = 78$) or Magnetom Espree or Avanto 1.5T scanners (Siemens) ($n = 3$) using a standardized high-resolution TN protocol. The protocol included triplanar pre- and postcontrast 3D-CISS (slice thickness, 0.6 mm; matrix, 256 × 256; FOV, 16.9 × 24.6) and 3D time-of-flight MR angiography.

### Image and Data Analysis

The studies of patients with TN and controls were intermixed and reviewed independently by 2 neuroradiologists (D.S. and B.N., each with >5 years of experience) blinded to patient history, including the presence or absence and side of symptoms. The cisternal segment of CN V was assessed on both sides for the presence or absence of neurovascular conflict. The following types of data were acquired for each side: type of vessel involved (vein, artery, or both), nerve surface involved (superior, inferior, medial, or lateral), the grade of neurovascular conflict (0 = none, 1 = simple contact without displacement or distortion of the nerve, 2 = displacement and/or mild distortion, 3 = severe distortion or decrease in cross-sectional area of the nerve), the cross-sectional area (CSA) of CN V at the site of neurovascular conflict, orthogonal dimensions of the nerve root at the site of neurovascular conflict (degree of flattening [DOF]), and the distance of neurovascular conflict from the apparent origin of the nerve at the surface of the pons.

Orthogonal dimensions were obtained by first measuring the greatest possible dimension of the nerve in the coronal plane and then taking the measurement of the nerve orthogonal to and at the midportion of the first measurement (see illustrative drawing in Online Fig 1) from multiplanar reformats. For statistical analysis, we took the mean of the CSA, the distance of neurovascular conflict from the pons, and DOF between the 2 observers. For the type of vessel in conflict, grading of neurovascular conflict, and the surface of the nerve involved, if there was discrepancy between the 2 readers, those cases were re-reviewed jointly, blinded to study type, and a consensus was reached. 3D TOF MRA was used to help in the assessment of the type of vessel in conflict with the nerve (the artery is bright).

### Statistical Analysis

We calculated the sensitivity and specificity of characteristics of neurovascular conflict (grade and type of vessel) comparing the symptomatic (diseased) with the asymptomatic side or controls

(healthy). Statistical comparisons for CSA and DOF were performed by a paired *t* test with the Holm-Bonferroni method of *P* value adjustment for multiple comparisons after performing Shapiro-Wilk normality tests. Statistical comparisons between the area under the curves were performed as described in DeLong et al.[23] The Fisher exact test was applied when assessing associations of categoric variables such as grades of neurovascular conflicts or types of vascular involvement. The $\kappa$ statistic for interobserver agreement was calculated. All analyses were performed using R statistical and computing software, Version 3.2.2 (http://www.r-project.org) with packages caroline, plotrix, beeswarm, and pROC. A *P* value of $<.05$ was considered significant.

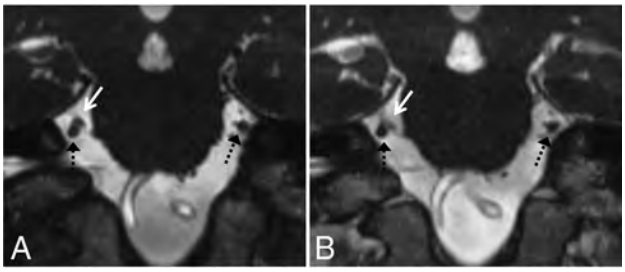


**FIG 1.** Grades 0 and 1 neurovascular conflict. Coronal NE-CISS (*A*) and CE-CISS (*B*) images show grade 1 (simple contact) on the patient's right side with a branch from the superior cerebellar artery (*white solid arrow*) contacting the cisternal segment of the trigeminal nerve root (*dashed black arrow*) from above. Note enhancement of the artery on the CE-CISS image. On the patient's left, the cisternal trigeminal nerve root (*dashed black arrow*) has no neurovascular conflict (grade 0).

## RESULTS

### *Comparison of Neurovascular Conflict on the Symptomatic and Asymptomatic Sides and in Controls on NE-CISS and CE-CISS Imaging*

Examples of the different grades of neurovascular conflict (0–3) and examples illustrating improvement in contrast between trigeminal nerve roots and adjacent vessels in advanced grades of neurovascular conflict are shown in Figs 1–4. On NE-CISS, neurovascular conflict in general (grade 1, 2, or 3) was common on the asymptomatic side and in controls (54/81 [66.7%] and 18/30 [60%], respectively), and it was even more common on the symp-

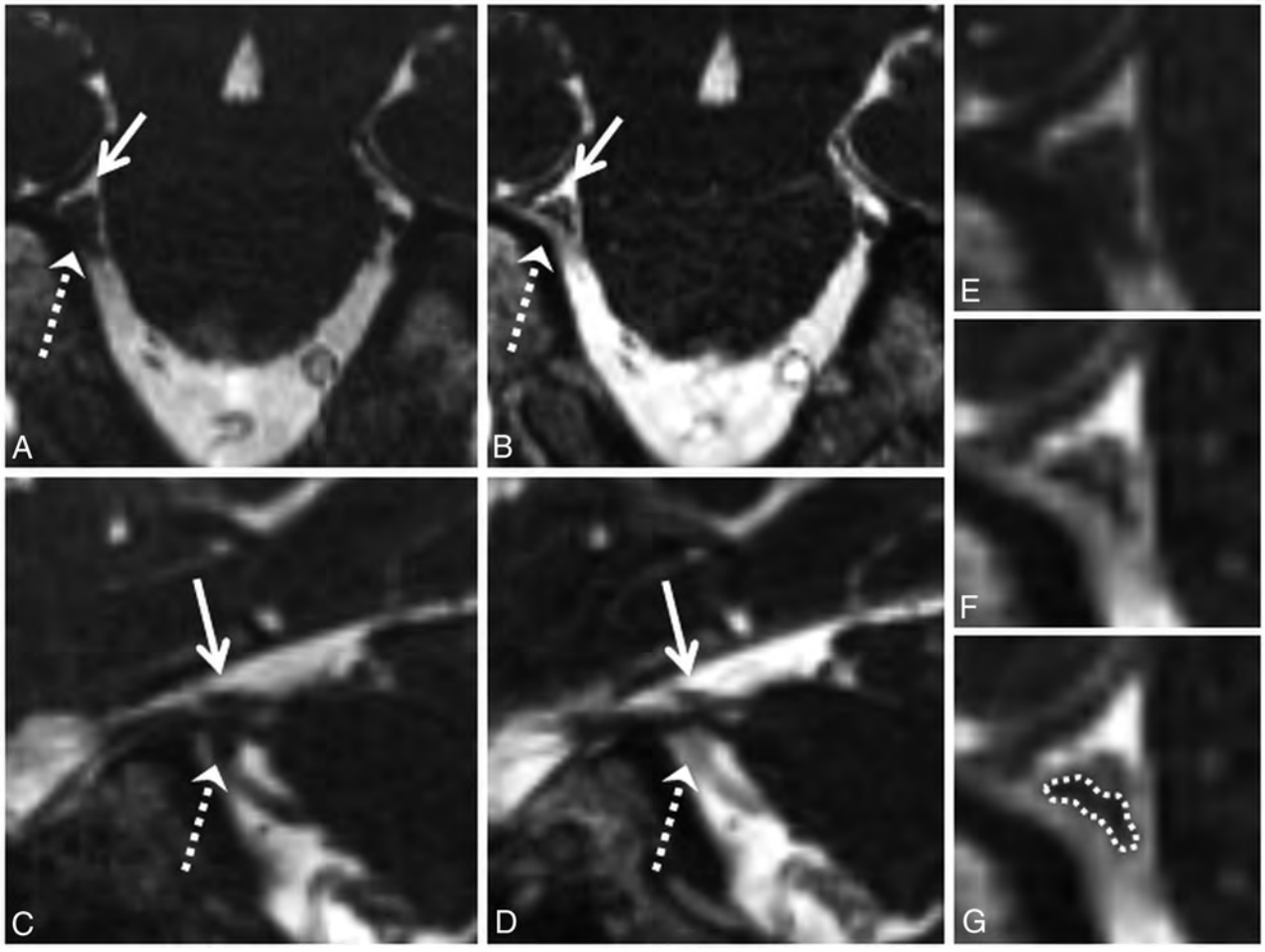


**FIG 2.** Grade 2 neurovascular conflict. Coronal NE-CISS (*A*) and CE-CISS (*B*) and sagittal NE-CISS (*C*) and CE-CISS (*D*) images show neurovascular conflict of the cisternal segment of the patient's right trigeminal nerve with a branch of the superior cerebellar artery from above (*solid white arrow*) and the superior petrosal vein from below (*dashed white arrow*), resulting in flattening of the nerve near the porus trigeminus. On the NE-CISS images (*A* and *C*), the nerve is not well-delineated from the adjacent vascular structures. On the CE-CISS images (*B* and *D*), the vessels enhance, outlining the compressed nerve between them. Zoomed-in images of the site of neurovascular conflict in the coronal plane (*E* and *F*) illustrate the poor contrast between vessels and nerve on the NE-CISS image (*E*) and the improved contrast after administration of gadolinium contrast material (*F*), allowing more confident delineation of the compressed nerve from the adjacent vessels (*G*). Both NE-CISS and CE-CISS images were interpreted as grade 2 compression. On the patient's left, grade 0 was given for both the NE-CISS and CE-CISS images.

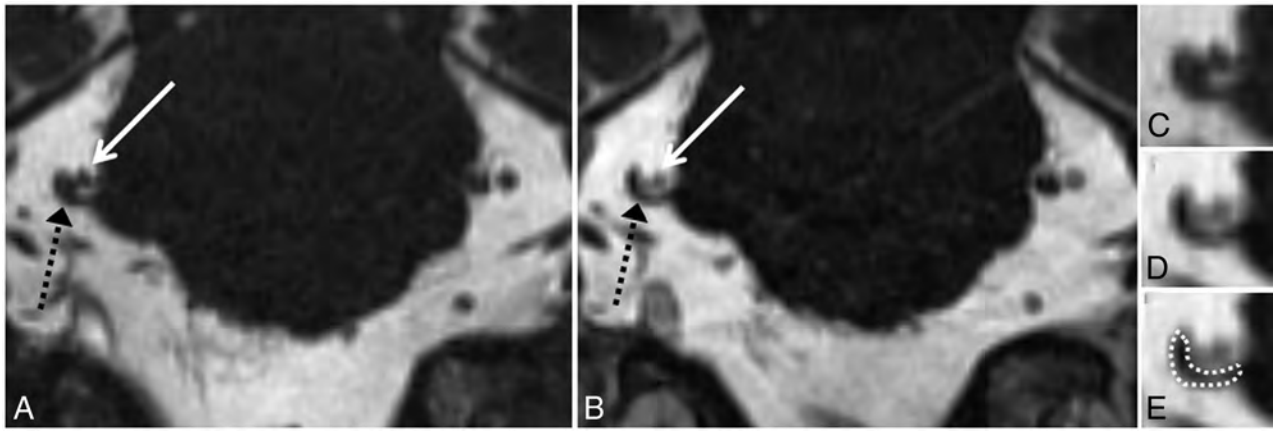


**FIG 3.** Grade 3 neurovascular conflict. Coronal NE-CISS (*A*) and CE-CISS (*B*) images show compression of the cisternal segment of the patient's right trigeminal nerve (*black dashed arrow*) by branches of the superior cerebellar artery from above (*solid white arrow*). On the unenhanced image (*A*), the nerve root is not well-distinguished from the compressing arterial branches. After contrast administration (*B*), at least 2 arterial branches enhance, allowing more confident delineation of the markedly compressed nerve. Zoomed-in images of the site of neurovascular conflict in the coronal plane (*C–E*) illustrate the poor contrast between vessels and nerve on the NE-CISS image (*C*) and the improved contrast after administration of gadolinium contrast material (*D*), allowing more confident delineation of the compressed nerve from the adjacent vessels (*E*). In this patient, grade 3 was given for both the NE-CISS and CE-CISS images, but the measured CSA was lower and the degree of flattening was more pronounced on the CE-CISS images. On the patient's left, grade 0 was given for both the NE-CISS and CE-CISS images.

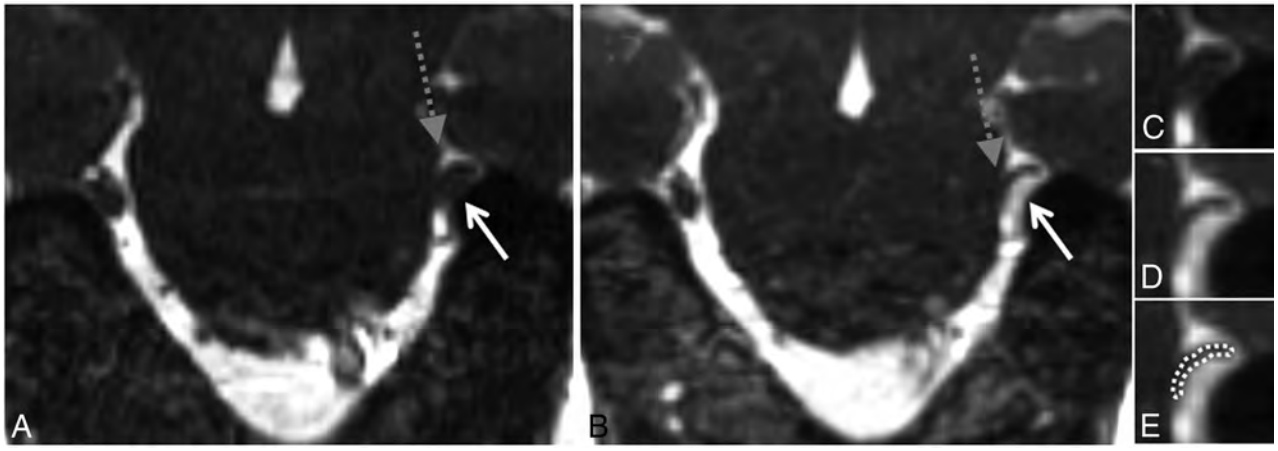


**FIG 4.** High-grade neurovascular conflict. Coronal NE-CISS (*A*) and CE-CISS (*B*) images show compression of the distal cisternal segment of the patient's left trigeminal nerve (*gray dashed arrow*) by a branch of the superior petrosal venous complex from below (*solid white arrow*). On the unenhanced image (*A*), the nerve root is not well-distinguished from the compressing venous branch. After contrast administration (*B*), the venous branch fills with contrast, showing a severely compressed unenhanced adjacent trigeminal nerve root at the level of the porus trigeminus. Zoomed-in images of the site of neurovascular conflict in the coronal plane (*C–E*) illustrate the poor contrast between vessels and nerve on the NE-CISS image (*C*) and the improved contrast after administration of gadolinium contrast material (*D*), allowing more confident delineation of the compressed nerve from the adjacent vessel (*E*). In this patient, grade 2 was given on the NE-CISS and grade 3 was given on CE-CISS images. On the patient's right, grade 1 was given on both the NE-CISS and CE-CISS images.

tomatic side (71/81 [87.7%]; Table 1). On the asymptomatic side and in controls, this consisted mostly of grade 1 neurovascular conflict (48/54 [88.9%] and 18/18 [100%] cases, respectively). Advanced-grade neurovascular conflict (grade 2 or 3) was encountered in 38/81 (46.9%; $n = 26$ for grade 2 and $n = 12$ for grade 3) cases on the symptomatic side versus in only 6/81 (7.4%, all grade 2) on the asymptomatic side and not at all in controls. Most of the advanced-grade cases of neurovascular conflict (grade 2 or 3) had involvement of an artery (33/38 [86.8%]), but venous involvement was found in more than half of these cases as well (22/38 [57.9%]).

Grade 3 neurovascular conflict was encountered only on the symptomatic side, so it was 100% specific for that group. Its sensitivity for the symptomatic side was 14.8% on NE-CISS imaging, which more than doubled to 33.3% on CE-CISS ($P = 9.6 \times 10^{-3}$, Tables 2 and 3). Advanced-grade neurovascular conflict (grade 2 or 3) had a specificity for the symptomatic side of 94.6% on both NE-CISS and CE-CISS and a sensitivity of 46.9% and 51.9% on NE-CISS and CE-CISS, respectively ($P = .64$). The $\kappa$ statistic for interobserver agreement in grading of neurovascular conflict was 0.68 for NE-CISS, which increased to 0.72 for CE-CISS.

Grade 1 neurovascular conflict occurred with similar frequency along the course of the cisternal segment of the trigeminal nerve root, with 8/29 (27.6%) occurrences between 0 and 3 mm from the surface of the pons, 11/29 (37.9%) between 3 and 6 mm, and 9/29 (31.0%) distal to 6 mm (On-line Fig 2). Advanced-grade neurovascular conflict (grade 2 or 3), on the other hand, was most prevalent between 3 and 6 mm from the surface of the pons (32/42

**Table 1: Prevalence of various grades of neurovascular conflict and types of vascular involvement in patients with TN and in controls**

| | Contrast Enhancement | Symptomatic Side (No.) (%) of 81 Cases | Asymptomatic Side (No.) (%) of 81 Cases | Control (No.) (%) of 30 Cases |
|---|---|---|---|---|
| Grades of neurovascular conflict | | | | |
| 0 | Contrast− | 10 (12.3) | 27 (33.3) | 12 (40.0) |
| | Contrast+ | 10 (12.3) | 27 (33.3) | 12 (40.0) |
| 1 | Contrast− | 33 (40.7) | 48 (59.3) | 18 (60.0) |
| | Contrast+ | 29 (35.8) | 48 (59.3) | 18 (60.0) |
| 2 | Contrast− | 26 (32.1) | 6 (7.4) | 0 (0.0) |
| | Contrast+ | 15 (18.5) | 6 (7.4) | 0 (0.0) |
| 3 | Contrast− | 12 (14.8) | 0 (0) | 0 (0.0) |
| | Contrast+ | 27 (33.3) | 0 (0) | 0 (0.0) |
| 1, 2, or 3 | Contrast− | 71 (87.7) | 54 (66.7) | 18 (60.0) |
| | Contrast+ | 71 (87.7) | 54 (66.7) | 18 (60.0) |
| 2 and 3 | Contrast− | 38 (46.9) | 6 (7.4) | 0 (0.0) |
| | Contrast+ | 42 (51.9) | 6 (7.4) | 0 (0.0) |
| Artery alone | | 27 (33.3) | 17 (21.0) | 4 (13.3) |
| Artery involved | | 49 (60.5) | 30 (37.0) | 5 (16.7) |
| Vein alone | | 22 (27.2) | 24 (29.6) | 12 (40.0) |
| Vein involved | | 44 (54.3) | 37 (45.7) | 13 (43.3) |
| Mixed | | 22 (27.2) | 13 (16.0) | 1 (3.3) |

**Note:**—Contrast+ indicates contrast enhancement; Contrast−, no contrast enhancement.

**Table 2: Statistical analysis**

| Grades of Neurovascular Conflict | Contrast Enhancement | *P* Values | | | Contrast vs Noncontrast | | Sensitivity | Specificity |
|---|---|---|---|---|---|---|---|---|
| | | Sym vs Asym | Sym vs Cntrl | Asym vs Cntrl | Sym | Asym | | |
| 0 | Contrast− | .002 | .002 | .51 | 1 | 1 | 12.3% | 66.7% |
| | Contrast+ | .002 | .003 | .51 | | | 12.3% | 66.7% |
| 1 | Contrast− | .03 | .09 | 1 | 0.63 | 1 | 40.7% | 40.5% |
| | Contrast+ | .004 | .03 | 1 | | | 35.8% | 40.5% |
| 2 | Contrast− | <.001 | <.001 | .19 | 0.07 | 1 | 32.1% | 94.6% |
| | Contrast+ | .06 | .01 | .19 | | | 18.5% | 94.6% |
| 3 | Contrast− | <.001 | .03 | 1 | 0.001 | 1 | 14.8% | 100.0% |
| | Contrast+ | <.001 | <.001 | 1 | | | 33.3% | 100.0% |
| 1, 2, or 3 | Contrast− | .002 | .003 | .51 | 1 | 1 | 87.7% | 35.1% |
| | Contrast+ | .002 | .002 | .51 | | | 87.7% | 35.1% |
| 2 and 3 | Contrast− | <.001 | <.001 | .19 | 0.64 | 1 | 46.9% | 94.6% |
| | Contrast+ | <.001 | <.001 | .19 | | | 51.9% | 94.6% |

**Note:**—Sym indicates symptomatic; Asym, asymptomatic; Cntrl, control; Contrast +, contrast enhancement; Contrast −, no contrast enhancement.

**Table 3: Characteristics of neurovascular involvement**

| Involvement of Neurovascular Conflict | *P* Values | | | Contrast vs | Noncontrast |
|---|---|---|---|---|---|
| | Sym vs Asym | Sym vs Cntrl | Asym vs Cntrl | | |
| Artery alone | 0.11 | 0.06 | 0.43 | 33.3% | 81.1% |
| Artery involved | .005 | <.001 | .06 | 60.5% | 68.5% |
| Vein alone | 0.86 | 0.25 | 0.36 | 27.2% | 67.6% |
| Vein involved | 0.35 | 0.39 | 1 | 54.3% | 55.0% |
| Mixed | 0.13 | 0.007 | 0.11 | 27.2% | 87.4% |

[76.2%]), with 6/42 (14.3%) cases occurring between 0 and 3 mm, and 4/42 (9.5%) cases occurring distal to 6 mm.

### *Comparison between NE-CISS and CE-CISS in the Evaluation of CSA and DOF*

When we compared CSA and DOF between the symptomatic and asymptomatic sides on either NE-CISS or CE-CISS, there was no significant difference in the setting of grade 1 neurovascular conflict (On-line Fig 1). However, with higher grades of neurovascular conflict (grade 2 or 3), there was a significant difference in CSA and DOF between the symptomatic and asymptomatic sides on both NE-CISS and on CE-CISS. Moreover, when we compared the CSA and DOF on the symptomatic side between NE-CISS and CE-CISS, there was a significant decrease in CSA and an increase in DOF on CE-CISS for higher grades of neurovascular conflict, but no significant difference in the setting of low-grade neurovascular conflict. There was also no significant difference when comparing the CSA or DOF on the asymptomatic side between NE-CISS and CE-CISS.

### *Correlation between Postsurgical Symptomatic Relief and the Metrics of Preoperative Neurovascular Conflict and Comparison of NE-CISS versus CE-CISS in Predicting the Symptomatic Side and Symptomatic Relief after MVD in Patients with TN*

On-line Table 3 shows the correlation between the grade of neurovascular conflict as determined on CE-CISS and NE-CISS with the type of postoperative outcome after MVD. There was a significant difference between the grades of compression found in patients with type 1 postsurgical outcome when comparing NE-CISS with CE-CISS images ($P = .031$), but not in patients with

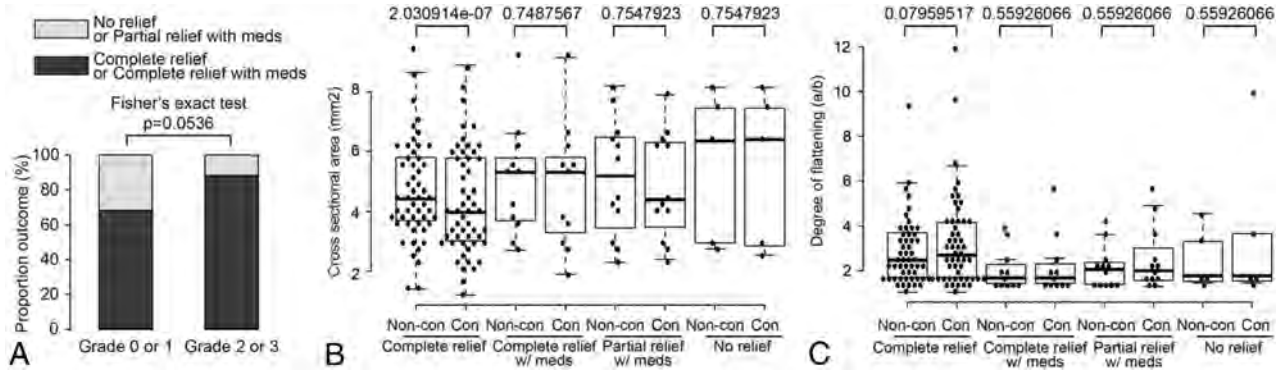


**FIG 5.** Correlation of the metrics of neurovascular conflict with postsurgical outcomes after MVD. Grades of neurovascular conflict (*A*), CSA (*B*), and DOF (*C*) were correlated with different postsurgical outcomes after MVD, as described in the individual graphs. Non-con indicates non-contrast; Con, contrast-enhanced.

type 2, 3, or 4 outcome. The proportion of patients with complete relief from pain postoperatively with or without a continued need for analgesics (type 1 and 2 outcomes, respectively) was 26/38 (68%) in patients with grade 0 or 1 neurovascular conflict and 37/42 (88%) in patients with grade 2 or 3 neurovascular conflict, a difference that did not quite reach statistical significance ($P = .054$, Fig 5*A*).

The CSA in patients with type 1 outcome was significantly lower on CE-CISS compared with NE-CISS ($P = 2.03 \times 10^{-7}$, Fig 5*B*). With the other types of outcome,[2-4] there was no significant difference between the CSA on NE-CISS and CE-CISS. Using receiver operating curve analysis, we compared the performance of NE-CISS versus CE-CISS in predicting the symptomatic side or relief of symptoms after MVD based on the grade of neurovascular conflict, CSA, and DOF (Fig 6). All tests were found to be useful in predicting the outcome in question (area under the curve [AUC] $> 0.65$). Optimum cutoffs to maximize sensitivity and specificity are given in Table 4. Using the grade of neurovascular conflict to predict complete relief after MVD yielded an AUC of 0.804 on NE-CISS and a significantly higher AUC of 0.835 on CE-CISS ($P = .017$, Fig 6*A*). The grade of neurovascular conflict was also the best predictor of the side of symptoms, with an AUC of 0.746 on NE-CISS and a significantly higher AUC of 0.767 on CE-CISS ($P = 1.7 \times 10^{-14}$, Fig 6*G*).

## DISCUSSION

We found that while neurovascular conflict in general was prevalent in both patients with TN and controls, higher grade (grade 2 or 3) neurovascular conflict was specific to the symptomatic side in patients with TN, but only about 50% sensitive, like findings in previous studies.[6,7] These findings imply that neurovascular compression is sufficient but not necessary to induce symptoms of TN.[1] Patients with little or no neurovascular conflict were less likely to experience pain relief after MVD compared with patients with advanced-grade neurovascular conflict; these results corroborate previous reports from preoperative imaging and intraoperative findings.[4,9-14] In these patients, other etiologic considerations, including pathology in or near the trigeminal root ganglion, may be in play[1,24] and an initial trial with rhizotomy of the trigeminal ganglion could be a rational alternative to MVD, especially if the patient is not an ideal surgical candidate.[1,12]

Most higher grade neurovascular conflict was found between 3 and 6 mm from the surface of the pons, corresponding to the location of the root entry zone, in line with findings in previous reports.[6,7,25,26] This relates to the proposed pathophysiologic mechanism (ignition hypothesis) of vascular compression resulting in microstructural damage to the nerve root at this vulnerable transition zone between central and peripheral myelin, making the axons hyperexcitable and giving rise to pain paroxysms as a result of synchronization after discharge activity.[1]

Like findings published by Zhou et al,[27] we found evidence of the known somatotopic organization of the trigeminal nerve,[28] which relates the surface of the compressed nerve to distribution of symptoms. Advanced-grade neurovascular conflict had a venous component in approximately 58% of the cases, most commonly along the inferior or lateral surface of the trigeminal nerve root, corresponding to the most common drainage pattern of the superior petrosal venous complex into the superior petrosal sinus between the porus trigeminus and porus acusticus.[29] Venous contribution to neurovascular compression has been reported previously, though typically as constituting less than half of the cases of neurovascular conflict.[6,7,11,26,28,30] The differences may be due to differences in technique, for instance related to increased sensitivity for venous detection after contrast administration. The reporting of a venous component in neurovascular conflict is important for presurgical planning because these cases may have a higher recurrence rate[31] and different surgical techniques have been proposed for decompression of culprit veins.[32] In a notable study of healthy subjects by Yousry et al,[33] the enhanced 3D-CISS sequence was determined to be superior for visualization of the trigeminal ganglion, sinus ganglion, and sinus lips. The current study, however, is unique in assessing symptomatic trigeminal compression.

Metrics (CSA, DOF, grading) of neurovascular conflict between NE-CISS and CE-CISS sequences in cases of little or no neurovascular conflict demonstrate little difference, which is expected because the nerve is mostly outlined by CSF in those cases and is thus well-characterized on NE-CISS. However, in cases of advanced-grade nerve root compression, significant differences in the metrics of neurovascular conflict between NE-CISS and CE-CISS emerged. These differences, in turn, resulted in significantly improved performance based on receiver operating curve analysis for CE-CISS compared with NE-CISS in predicting the

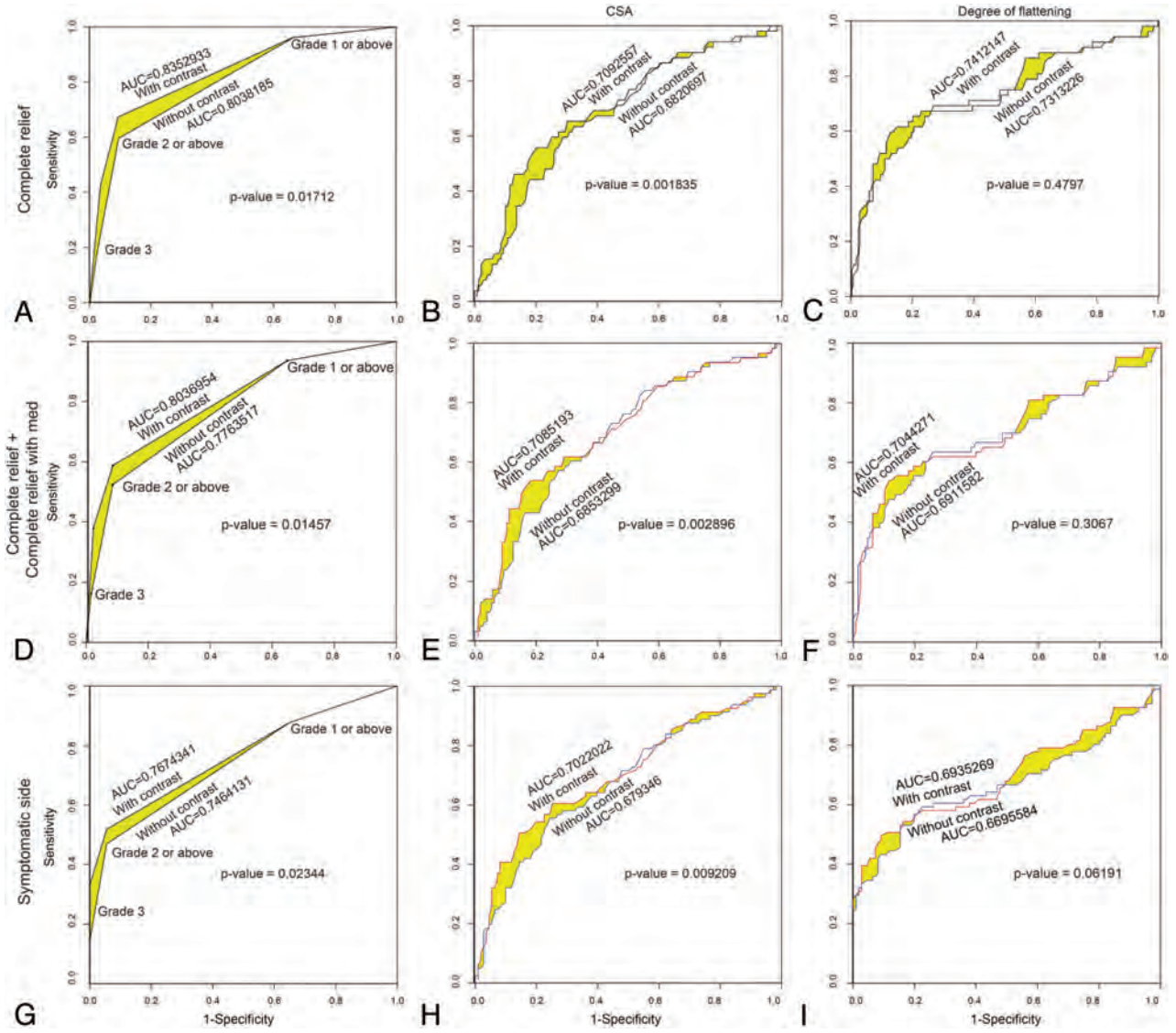


**FIG 6.** Receiver operating curves assessing the performance of the grade of neurovascular conflict (*A*, *D*, and *G*), CSA (*B*, *E*, and *H*), and DOF (*C*, *F*, and *I*) in predicting complete relief without further need for analgesic medication (type 1 outcome) after MVD (*A–C*), complete relief with or without further need for analgesic medication (type 1 or 2 outcome) after MVD (*D–F*), and symptom side in patients with TN (*G–I*) for both NE-CISS and CE-CISS images, as delineated in the graphs. The area under the curve and *P* values comparing the NE-CISS and CE-CISS curves are provided in the individual graphs.

symptom side and the degree of relief of symptoms after MVD. Notably, a cutoff of grade 2 neurovascular conflict or higher on CE-CISS predicted complete relief of symptoms after MVD, with a specificity of 90.7% and a sensitivity of 67.3% (AUC on the receiver operating curve analysis = 0.835), and the side of symptoms, with a specificity of 94.6% and a sensitivity 51.9% (AUC on the receiver operating curve analysis = 0.767). Given the invasiveness of MVD and potential risks to the patient, such advances in the optimization of preoperative imaging, allowing improved preoperative planning and patient selection, are of potential importance for clinical care.[14]

Limitations of our study include inherent biases associated with the retrospective study design and those of a single-institution cohort. In addition, although the reviewers were blinded to the type of subject (control versus patient with TN), it is not possible to blind the reviewers to the presence or absence of contrast in the grading of neurovascular conflict, CSA, and degree of flattening. Another limitation in this retrospective study was the range in duration of clinical follow-up for postoperative patients, raising the possibility that some patients might have had a different pain-relief outcome if they were followed for a shorter or longer time. Finally, our measurements of CSA and DOF were performed at the submillimeter level, which is at the limits of the spatial resolution of even high-resolution 3D-CISS volumetric imaging. However, spatial resolution for acquisition and measurement techniques during evaluation was consistent across all conditions.

## CONCLUSIONS

Low-grade neurovascular conflict is common in control patients and on the asymptomatic side in patients with TN, while the presence of higher grade neurovascular conflict is highly specific for

**Table 4: Cutoff values for grade of neurovascular conflict, CSA, and DOF to obtain the highest sum of sensitivity and specificity in predicting complete relief of pain after MVD (type 1 outcome), complete relief of pain with or without need for analgesic medication (type 1 or 2 outcome), or in predicting the side of symptoms in patients with TN**

| Outcome | Cutoff | Contrast | Sensitivity | Specificity |
|---|---|---|---|---|
| Type 1 | | | | |
| Grade | ≥2 | − | 59.6 | 90.7 |
| | ≥2 | + | 67.3 | 90.7 |
| CSA | ≤5.1 | − | 63.5 | 67.6 |
| | ≤4.15 | + | 55.8 | 79.9 |
| DOF | ≥2.0 | − | 69.2 | 73.4 |
| | ≥2.5 | + | 59.6 | 87.1 |
| Type 2 | | | | |
| Grade | ≥2 | − | 52.4 | 91.4 |
| | ≥2 | + | 58.7 | 91.4 |
| CSA | ≤4.7 | − | 57.1 | 72.7 |
| | ≤4.15 | + | 54 | 82 |
| DOF | ≥2.0 | − | 63.5 | 74.3 |
| | ≥2.5 | + | 54 | 88.3 |
| Predicting side of sym in patients with TN | | | | |
| Grade | ≥2 | − | 46.9 | 94.6 |
| | ≥2 | + | 51.9 | 94.6 |
| CSA | ≤4.7 | − | 55.6 | 75.7 |
| | ≤4.15 | + | 50.6 | 85.6 |
| DOF | ≥2.2 | − | 53.1 | 84.7 |
| | ≥2.5 | + | 49.4 | 91 |

**Note:**—sym indicates symptoms; −, absent; +, present.

the symptomatic side in TN and in predicting symptomatic relief after MVD. The addition of contrast material to 3D-CISS imaging improves characterization of higher grade neurovascular conflict and improves performance in predicting both the side of symptoms in patients with TN and favorable outcomes after MVD. These improvements in TN imaging may be helpful in optimizing patient selection and preoperative planning.

Disclosures: Ari M. Blitz—*UNRELATED*: *Board Membership*: Guerbet, *Comments*: Medical Advisory Board; *Grants/Grants Pending*: Aesculab, Siemens, National Institutes of Health, *Comments*: Aesculab, research funding on hydrocephalus; Siemens, in-kind support for a pulse programming course for graduate students; National Institutes of Health, support unrelated to this submission: R21 NS096497 (coinvestigator), FAIN U01DC013778 (lead radiologist)*; *Payment for Lectures Including Service on Speakers Bureaus*: Siemens, *Comments*: payment for an educational talk at a symposium. C. Rory Goodwin—*UNRELATED*: *Grants/Grants Pending*: Johns Hopkins Neurosurgery Pain Research Institute, Burroughs Wellcome Fund, United Negro College Fund-Merck Science Initiative.* Michael Lim—*UNRELATED*: *Consultancy*: Stryker; *Grants/Grants Pending*: Stryker*; *Payment for Lectures Including Service on Speakers Bureaus*: Stryker, *Comments*: consulting and speaking; *Payment for Development of Educational Presentations*: Stryker, *Comments*: speaker for education; *Travel/Accommodations/Meeting Expenses Unrelated to Activities Listed*: Stryker, *Comments*: pay for travel to consulting and speaking engagements. *Money paid to the Institution.

## REFERENCES

1. Devor M, Amir R, Rappaport ZH. **Pathophysiology of trigeminal neuralgia: the ignition hypothesis.** *Clin J Pain* 2002;18:4–13 CrossRef Medline
2. Peker S, Dinçer A, Necmettin Pamir M. **Vascular compression of the trigeminal nerve is a frequent finding in asymptomatic individuals: 3-T MR imaging of 200 trigeminal nerves using 3D CISS sequences.** *Acta Neurochir (Wien)* 2009;151:1081–88 CrossRef Medline
3. Miller JP, Acar F, Hamilton BE, et al. **Radiographic evaluation of trigeminal neurovascular compression in patients with and without trigeminal neuralgia.** *J Neurosurg* 2009;110:627–32 CrossRef Medline
4. Hamlyn PJ. **Neurovascular relationships in the posterior cranial fossa, with special reference to trigeminal neuralgia, 2: neurovascular compression of the trigeminal nerve in cadaveric controls and patients with trigeminal neuralgia— quantification and influence of method.** *Clin Anat* 1997;10:380–88 CrossRef Medline
5. Adams CB. **Microvascular compression: an alternative view and hypothesis.** *J Neurosurg* 1989;70:1–12 CrossRef Medline
6. Maarbjerg S, Wolfram F, Gozalov A, et al. **Significance of neurovascular contact in classical trigeminal neuralgia.** *Brain* 2015;138:311–19 CrossRef Medline
7. Antonini G, Di Pasquale A, Cruccu G, et al. **Magnetic resonance imaging contribution for diagnosing symptomatic neurovascular contact in classical trigeminal neuralgia: a blinded case-control study and meta-analysis.** *Pain* 2014;155:1464–71 CrossRef Medline
8. Sindou M, Leston J, Decullier E, et al. **Microvascular decompression for primary trigeminal neuralgia: long-term effectiveness and prognostic factors in a series of 362 consecutive patients with clear-cut neurovascular conflicts who underwent pure decompression.** *J Neurosurg* 2007;107:1144–53 CrossRef Medline
9. Sarsam Z, Garcia-Fiñana M, Nurmikko TJ, et al. **The long-term outcome of microvascular decompression for trigeminal neuralgia.** *Br J Neurosurg* 2010;24:18–25, 2010 CrossRef Medline
10. Szapiro J Jr, Sindou M, Szapiro J. **Prognostic factors in microvascular decompression for trigeminal neuralgia.** *Neurosurgery* 1985;17:920–29 CrossRef Medline
11. Leal PR, Barbier C, Hermier M, et al. **Atrophic changes in the trigeminal nerves of patients with trigeminal neuralgia due to neurovascular compression and their association with the severity of compression and clinical outcomes.** *J Neurosurg* 2014;120:1484–95 CrossRef Medline
12. Han-Bing S, Wei-Guo Z, Jun Z, et al. **Predicting the outcome of microvascular decompression for trigeminal neuralgia using magnetic resonance tomographic angiography.** *J Neuroimaging* 2010;20:345–49 CrossRef Medline
13. Duan Y, Sweet J, Munyon C, et al. **Degree of distal trigeminal nerve atrophy predicts outcome after microvascular decompression for type 1a trigeminal neuralgia.** *J Neurosurg* 2015;123:1512–18 CrossRef Medline
14. Zakrzewska JM, Coakham HB. **Microvascular decompression for trigeminal neuralgia: update.** *Curr Opin Neurol* 2012;25:296–301 CrossRef Medline
15. Casselman JW, Kuhweide R, Deimling M, et al. **Constructive inter-**

**ference in steady state-3DFT MR imaging of the inner ear and cerebellopontine angle.** *AJNR Am J Neuroradiol* 1993;14:47–57 Medline
16. Blitz AM, Macedo LL, Chonka ZD, et al. **High-resolution CISS MR imaging with and without contrast for evaluation of the upper cranial nerves: segmental anatomy and selected pathologic conditions of the cisternal through extraforaminal segments.** *Neuroimaging Clin N Am* 2014;24:17–34 CrossRef Medline
17. Chavhan GB, Babyn PS, Jankharia BG, et al. **Steady-state MR imaging sequences: physics, classification, and clinical applications.** *Radiographics* 2008;28:1147–60 CrossRef Medline
18. Shigematsu Y, Korogi Y, Hirai T, et al. **Contrast-enhanced CISS MRI of vestibular schwannomas: phantom and clinical studies.** *J Comput Assist Tomogr* 1999;23:224–31 CrossRef Medline
19. Blitz AM, Choudhri AF, Chonka ZD, et al. **Anatomic considerations, nomenclature, and advanced cross-sectional imaging techniques for visualization of the cranial nerve segments by MR imaging.** *Neuroimaging Clin N Am* 2014;24:1–15 CrossRef Medline
20. Amemiya S, Aoki S, Ohtomo K. **Cranial nerve assessment in cavernous sinus tumors with contrast-enhanced 3D fast-imaging employing steady-state acquisition MR imaging.** *Neuroradiology* 2009;51:467–70 CrossRef Medline
21. Greenland S, Thomas DC. **On the need for the rare disease assumption in case-control studies.** *Am J Epidemiol* 1982;116:547–53 CrossRef Medline
22. Noordzij M, Tripepi G, Dekker FW, et al. **Sample size calculations: basic principles and common pitfalls.** *Nephrol Dial Transpl* 2010;25:1388–93 CrossRef Medline
23. DeLong ER, DeLong DM, Clarke-Pearson DL. **Comparing the areas under two or more correlated receiver operating characteristic curves: a nonparametric approach.** *Biometrics* 1988;44:837–45 CrossRef Medline
24. Beaver DL. **Electron microscopy of the gasserian ganglion in trigeminal neuralgia.** *J Neurosurg* 1967;26(Suppl):138–50 CrossRef Medline
25. Yousry I, Moriggl B, Holtmannspoetter M, et al. **Detailed anatomy of the motor and sensory roots of the trigeminal nerve and their neurovascular relationships: a magnetic resonance imaging study.** *J Neurosurg* 2004;101:427–34 CrossRef Medline
26. Leal PR, Hermier M, Souza MA, et al. **Visualization of vascular compression of the trigeminal nerve with high-resolution 3T MRI: a prospective study comparing preoperative imaging analysis to surgical findings in 40 consecutive patients who underwent microvascular decompression for trigeminal neuralgia.** *Neurosurgery* 2011;69:15–25; discussion 26 CrossRef Medline
27. Zhou Q, Liu ZL, Qu CC, et al. **Preoperative demonstration of neurovascular relationship in trigeminal neuralgia by using 3D FIESTA sequence.** *Magn Reson Imaging* 2012;30:666–71 CrossRef Medline
28. Gudmundsson K, Rhoton AL Jr, Rushton JG. **Detailed anatomy of the intracranial portion of the trigeminal nerve.** *J Neurosurg* 1971;35:592–600 CrossRef Medline
29. Tanriover N, Abe H, Rhoton AL Jr, et al. **Microsurgical anatomy of the superior petrosal venous complex: new classifications and implications for subtemporal transtentorial and retrosigmoid suprameatal approaches.** *J Neurosurg* 2007;106:1041–50 CrossRef Medline
30. Matsushima T, Huynh-Le P, Miyazono M. **Trigeminal neuralgia caused by venous compression.** *Neurosurgery* 2004;55:334–37; discussion 338–39 CrossRef Medline
31. Lee SH, Levy EI, Scarrow AM, et al. **Recurrent trigeminal neuralgia attributable to veins after microvascular decompression.** *Neurosurgery* 2000;46:356–61; discussion 361–62 CrossRef Medline
32. Hong W, Zheng X, Wu Z, et al. **Clinical features and surgical treatment of trigeminal neuralgia caused solely by venous compression.** *Acta Neurochir (Wien)* 2011;153:1037–42 CrossRef Medline
33. Yousry I, Moriggl B, Schmid UD, et al. **Trigeminal ganglion and its divisions: detailed anatomic MR imaging with contrast-enhanced 3D constructive interference in the steady state sequences.** *AJNR Am J Neuroradiol* 2005;26:1128–35 Medline

# Comparison of a Photon-Counting-Detector CT with an Energy-Integrating-Detector CT for Temporal Bone Imaging: A Cadaveric Study

W. Zhou, J.I. Lane, M.L. Carlson, M.R. Bruesewitz, R.J. Witte, K.K. Koeller, L.J. Eckel, R.E. Carter, C.H. McCollough, and S. Leng

## ABSTRACT

**BACKGROUND AND PURPOSE:** Evaluating abnormalities of the temporal bone requires high-spatial-resolution CT imaging. Our aim was to assess the performance of photon-counting-detector ultra-high-resolution acquisitions for temporal bone imaging and compare the results with those of energy-integrating-detector ultra-high-resolution acquisitions.

**MATERIALS AND METHODS:** Phantom studies were conducted to quantify spatial resolution of the ultra-high-resolution mode on a prototype photon-counting-detector CT scanner and an energy-integrating-detector CT scanner that uses a comb filter. Ten cadaveric temporal bones were scanned on both systems with the radiation dose matched to that of the clinical examinations. Images were reconstructed using a sharp kernel, 0.6-mm (minimum) thickness for energy-integrating-detector CT, and 0.6- and 0.25-mm (minimum) thicknesses for photon-counting-detector CT. Image noise was measured and compared using adjusted 1-way ANOVA. Images were reviewed blindly by 3 neuroradiologists to assess the incudomallear joint, stapes footplate, modiolus, and overall image quality. The ranking results for each specimen and protocol were compared using the Friedman test. The Krippendorff $\alpha$ was used for interreader agreement.

**RESULTS:** Photon-counting-detector CT showed an increase of in-plane resolution compared with energy-integrating-detector CT. At the same thickness (0.6 mm), images from photon-counting-detector CT had significantly lower ($P < .001$) image noise compared with energy-integrating-detector CT. Readers preferred the photon-counting-detector CT images to the energy-integrating-detector images for all 3 temporal bone structures. A moderate interreader agreement was observed with the Krippendorff $\alpha = 0.50$. For overall image quality, photon-counting-detector CT image sets were ranked significantly higher than images from energy-integrating-detector CT ($P < .001$).

**CONCLUSIONS:** This study demonstrated substantially better delineation of fine anatomy for the temporal bones scanned with the ultra-high-resolution mode of photon-counting-detector CT compared with the ultra-high-resolution mode of a commercial energy-integrating-detector CT scanner.

**ABBREVIATIONS:** EID = energy-integrating detector; K-$\alpha$ = Krippendorff $\alpha$; MTF = modulation transfer function; PCD = photon-counting detector; UHR = ultra-high-resolution

Multidetector CT is an essential clinical diagnostic tool for evaluating abnormalities of the temporal bone and lateral skull base.[1-4] Temporal bone structures of clinical interest, such as the ossicles, facial nerve, and labyrinth, are submillimeter and require high-spatial-resolution imaging.[2,5] The detector size of a CT system is one of the major factors limiting the spatial resolution needed to resolve these fine structures. Commercially available multidetector CT scanners are built using energy-integrating detectors (EIDs), in which the detected signal is proportional to the total energy deposited by all photons without specific information about an individual photon or its energy. The effective detector pixel sizes range from 0.5 to 0.625 mm at the isocenter for the commercial EIDs. Several approaches have been investigated to further improve the spatial resolution of an EID system for temporal bone imaging. One approach is to place an attenuating comb (grid) filter on top of the detector to reduce the detector aperture size.[6-8] However, the attenuation of the filter inevitably reduces geometric dose efficiency because the filter blocks the

Received March 13, 2018; accepted after revision June 19.

From the Departments of Radiology (W.Z., J.I.L., M.R.B., R.J.W., K.K.K., L.J.E., C.H.M., S.L.) and Otolaryngology–Head and Neck Surgery (M.L.C.) and Division of Biomedical Statistics and Informatics (R.E.C.), Mayo Clinic, Rochester, Minnesota.

Research reported in this article was supported by the National Institutes of Health under award numbers R01 EB016966 and C06 RR018898 and in collaboration with Siemens.

The content is solely the responsibility of the authors and does not necessarily represent the official views of the National Institutes of Health.

Please address correspondence to Shuai Leng, PhD, Department of Radiology, Mayo Clinic, 200 First St SW, Rochester, MN 55905; e-mail: leng.shuai@mayo.edu

Indicates open access to non-subscribers at www.ajnr.org

http://dx.doi.org/10.3174/ajnr.A5768

photons after they have passed through the patient.[6,9] Other methods, such as using a flat panel detector, do not satisfy the clinical requirements for contrast-to-noise ratio, scan field of view, or temporal resolution.[10,11]

A whole-body photon-counting detector (PCD) CT scanner has been installed in our laboratory for research use (Somatom CounT; Siemens, Erlangen, Germany)[12-14] and is not yet commercially available. Different from the conventional EIDs that integrate deposited energies from all photons, PCDs use direct-conversion techniques and count individual photons while measuring energy information. Studies have demonstrated many benefits of PCDs over the conventional EIDS, such as less impact of electronic noise, a higher contrast-to-noise ratio, improved dose efficiency, and simultaneous multi-energy imaging.[15-22] PCDs can eliminate the septa between adjacent detector pixels required by EIDs to avoid cross-talk and maintain spatial resolution. This feature leads to a PCD detector size of 0.25 mm at the isocenter (compared with 0.5–0.6 mm for EIDs) without compromising dose efficiency. To date, preliminary phantoms and cadaveric studies have reported 150-$\mu$m limiting spatial resolution for this scan mode and have demonstrated the potential benefits of superior image quality from ultra-high-resolution (UHR) PCD-CT acquisitions.[23,24] However, none of the studies has evaluated specific clinical tasks and investigated how radiologists' reading performance could benefit from the higher resolution capability of PCD-CT. Therefore, the purpose of this study was to assess the performance of PCD-CT UHR acquisitions for temporal bone imaging and compare the results with those of EID-CT UHR acquisitions.

## MATERIALS AND METHODS

### Phantom Experiments to Evaluate Spatial Resolution

A 50-$\mu$m diameter tungsten wire inserted into a solid water phantom was scanned along the z-axis on the whole-body PCD-CT scanner using the UHR scan mode. The PCD-CT system was built on the platform of a second-generation dual-source CT scanner (Somatom Definition Flash; Siemens). Detailed descriptions of this system have been reported elsewhere.[12-14] The UHR acquisition on the PCD-CT system has an effective pixel size of 0.25 × 0.25 mm at the isocenter.[23] PCD-CT scans were obtained with the following parameters: spiral mode, 120-kV tube potential, 25- and 75-keV energy thresholds, 32 × 0.25 mm collimation, 0.8 pitch, and 1.0-second rotation time. For comparison, the wire phantom was also scanned on a second-generation dual-source CT scanner, the same platform on which the PCD-CT was built. Both the PCD-CT and EID-CT systems involved in this study use an identical UHR focal spot size of 0.7 mm.[25] EID-CT scans were obtained using the standard clinical protocol: UHR mode with a comb filter along the fan direction, spiral mode, 120-kV tube potential, 16 × 0.6 mm collimation, 0.8 pitch, and 1.0-second rotation time. All images were reconstructed with a standard weighted filtered back-projection algorithm, 0.6-mm slice thickness, and a sharp kernel (U70). Modulation transfer function (MTF) is commonly used to provide a comprehensive evaluation of spatial resolution for imaging systems by assessing the system response with respect to the input signal at each frequency. In this study, the MTF was calculated from the point spread function of the wire in the axial images to assess the in-plane spatial resolution. Spatial frequencies of 50%, 10%, and 2% MTF values were recorded.

### Temporal Bone Specimens

Ten formalin-fixed cadaveric temporal bone specimens were harvested by the department of anatomy using the block technique described by Schuknecht.[26] All specimens had no known history of a prior operation or trauma and were otherwise anatomically intact. Each specimen was placed within a 20-cm-diameter solid-water ring and placed in the supine position to replicate clinical temporal bone CT examinations.

### Imaging Protocol for Specimens

Each specimen was scanned using the UHR mode with the same imaging protocols for phantom experiments on PCD-CT and EID-CT systems, respectively. Automatic exposure control was off and effective milliampere-second was set to match the radiation dose of clinical examinations (volume CT dose index = 61 mGy). All images were reconstructed using the weighted filtered back-projection method with a sharp kernel (U70). For PCD-CT acquisitions, image thickness and increment were set to 0.6/0.3 and 0.25/0.25 mm (thinnest available), respectively. Image thickness and increment for the EID system were set to 0.6/0.3 mm (thinnest available). For simplification, the 3 CT-acquisition protocols are denoted as "detector type–image thickness" (in millimeters) (ie, PCD-0.6, PCD-0.25, and EID-0.6).

### Noise Measurements

Image noise was measured in the cadaveric images as the standard deviation (SD) of CT numbers in a circular ROI drawn in a uniform soft-tissue area for each dataset. The size and the location of the ROIs were matched among the 3 image sets (PCD-0.6, PCD-0.25, and EID-0.6). The mean and SD of image noise for each image set were calculated.

### Reader Assessment of Image Quality

The reading protocol was established on a clinical viewing station that was appropriately calibrated for routine diagnosis following the "ACR-AAPM-SIIM Technical Standard for Electronic Practice of Medical Imaging."[27] The 3 image sets (PCD-0.6, PCD-0.25, and EID-0.6) for each temporal bone specimen were displayed side by side in a random order with scanning and reconstruction information blinded to the readers. Three fellowship-trained neuroradiologists (R.J.W., K.K.K., L.J.E.), each with >10 years of experience, independently assessed the overall image quality and the delineation of 3 anatomic structures (modiolus, stapes footplate, incudomallear joint). For each specimen, images from 3 protocols were ranked from 1 to 3, with 1 being the most preferred and 3 being the least preferred. Equal rank was allowed. Thirty sets of images (10 specimens × 3 image sets/specimen) were reviewed by each of the 3 readers.

### Statistical Analysis

All statistical analyses were performed using free statistical software (R Project, Version 3.4.0; http://www.r-project.org/). The differences of image noise among the 3 protocols were evaluated

using 1-way ANOVA with subsequent Tukey honest significant difference analysis. The average ranking from the 3 readers for each specimen and protocol was compared using the Friedman test to evaluate the differences in overall image quality and diagnostic confidence for the 3 structures. Pair-wise comparisons were performed with Conover post hoc testing with a Bonferroni correction. $P < .05$ was considered statistically significant. The Krippendorff $\alpha$ (K-$\alpha$) was used to test the interreader agreement with the following scales: 0–.20 = poor agreement, 0.21–0.40 = fair agreement, 0.41–0.60 = moderate agreement, 0.61–0.80 = substantial agreement, and 0.81–1.00 = almost perfect agreement.[28]

## RESULTS

PCD-CT showed a slightly better MTF performance than EID-CT (Fig 1). The spatial frequencies at 50%, 10%, and 2% MTF (Table 1) were 11.2, 18.4, and 21.1/cm for the PCD-CT and 10.6, 17.5, and 20.1/cm for EID-CT.

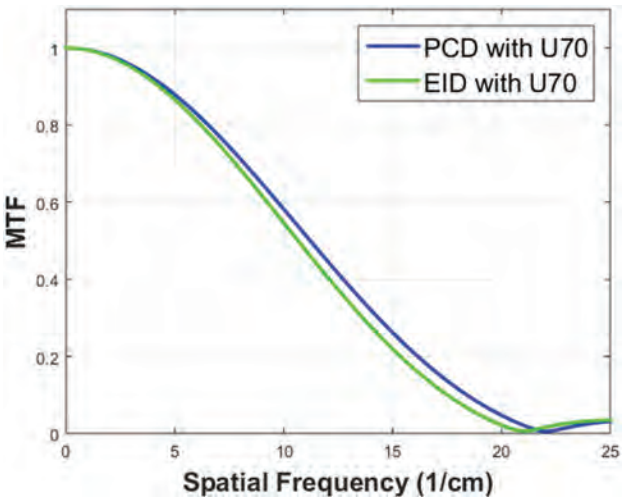


**FIG 1.** Comparison of MTF curves for UHR modes reconstructed with a sharp kernel (U70) on the PCD-CT and EID-CT systems.

**Table 1: Spatial frequencies of 50%, 10%, and 2% MTF values for UHR acquisitions on both PCD-CT and EID-CT systems with images reconstructed with a sharp kernel (U70)**

| MTF | 50% | 10% | 2% |
|---|---|---|---|
| PCD-CT with U70 kernel | 11.2/cm | 18.4/cm | 21.1/cm |
| EID-CT with U70 kernel | 10.6/cm | 17.5/cm | 20.1/cm |

Representative images of the modiolus (Fig 2), stapes footplate (Fig 3), and incudomallear joint (Fig 4), shown side-by-side for the 3 datasets (PCD-0.6, PCD-0.25, and EID-0.6), demonstrated the improved ability to resolve each of the evaluated structures. Decreased image thickness resulted in enhanced visualization of the 3 submillimeter structures evaluated.

Measurements for the same image thickness (0.6 mm, Fig 5) showed that images from the PCD scanner had significantly lower ($P < .001$) image noise (mean, 55.9 ± 5.2 HU) compared with images from the EID scanner (mean, 91.8 ± 6.5 HU). The thinner 0.25-mm PCD images (mean, 89.8 ± 8.3 HU) yielded noise like that of the 0.6-mm EID images ($P = .80$).

The rank distributions from all 3 readers demonstrated that PCD-0.25 images were the most preferred, followed by the PCD-0.6 images; the EID-0.6 images were the least preferred (Fig 6). The Friedman test showed statistically significant differences in rankings for the 3 protocols ($P = .02$). Pair-wise comparison demonstrated that the readers preferred the PCD-CT images to the EID images for all 3 temporal bone structures (Table 2). Among the 3 sets of PCD images, readers preferred the PCD-0.25 images over the PCD-0.6 images for visualizing the modiolus ($P = .002$) and the incudomallear joint ($P < .001$), but no significant preference was found when assessing the stapes footplates ($P = .12$). For overall image quality, both PCD-CT image sets were ranked significantly higher than the EID images ($P < .001$), and readers preferred thinner images (0.25 mm) over thicker images (0.6 mm) from PCD-CT ($P < .001$).

Fair-to-moderate interobserver agreement was observed among the 3 readers for ranking image quality (Table 3). Readers reached moderate agreement for the modiolus (K-$\alpha = 0.54$) and stapes footplate (K-$\alpha = 0.44$) and fair agreement for the incudomallear joint (K-$\alpha = 0.36$). For overall image quality, moderate agreement was observed with K-$\alpha = 0.50$.

## DISCUSSION

In this in vitro study, we investigated temporal bone imaging using a new PCD-CT system with a 0.25 × 0.25 mm detector size at its isocenter. Quantitative and qualitative image quality analyses

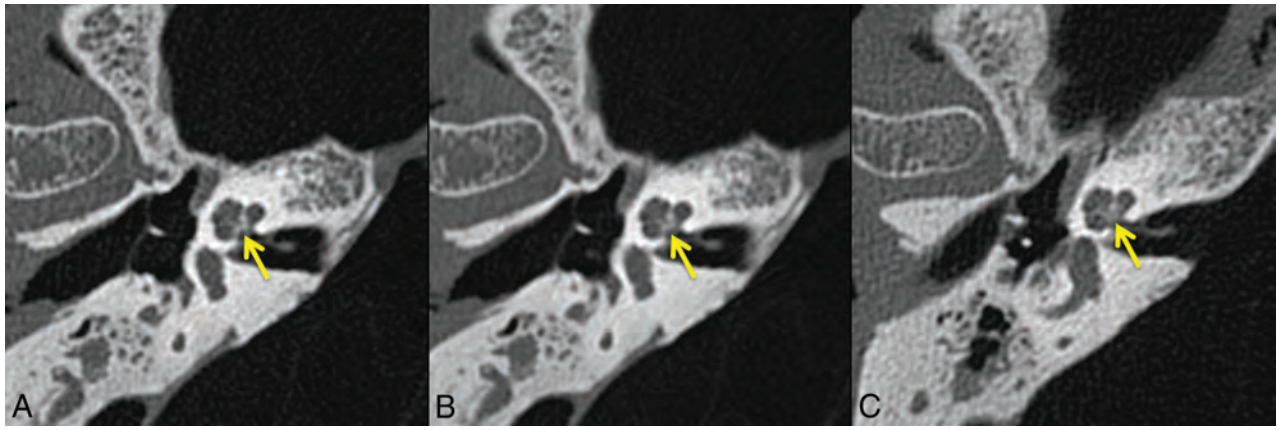


**FIG 2.** Representative axial images of the modiolus (*arrow*) from the same specimen scanned with UHR PCD-CT and reconstructed with 0.25- (*A*) and 0.6-mm (*B*) image thicknesses, and UHR EID-CT, with a 0.6-mm image thickness (*C*). The pyramid-shaped modiolus is better depicted with the PCD-CT.

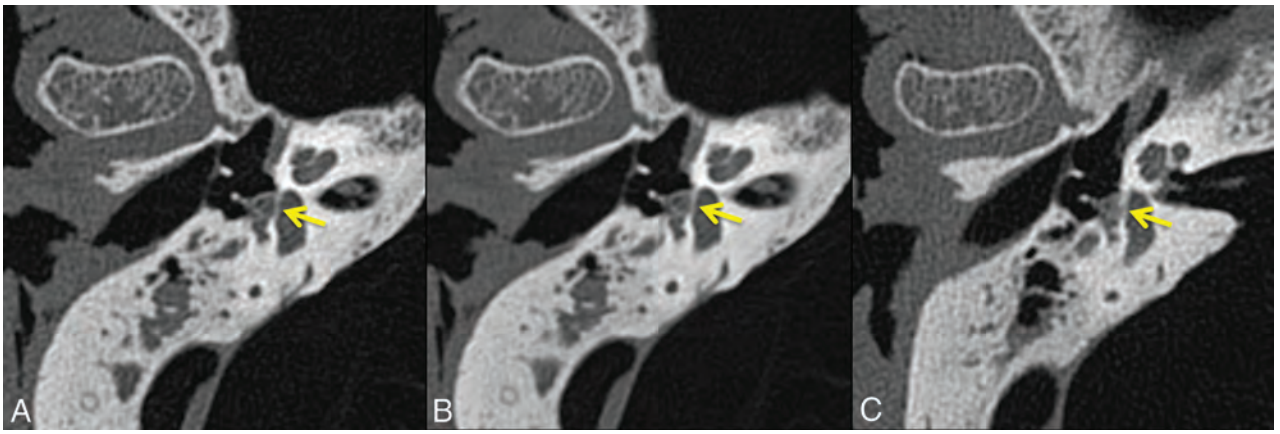


**FIG 3.** Representative axial images of the stapes footplate (*arrow*) from the same specimen scanned with UHR PCD-CT and reconstructed with 0.25- (*A*) and 0.6-mm (*B*) image thicknesses, and UHR EID-CT, with 0.6-mm image thickness (*C*). An improved illustration of the stapes footplate and the limbs of the stapes is observed for PCD-CT.

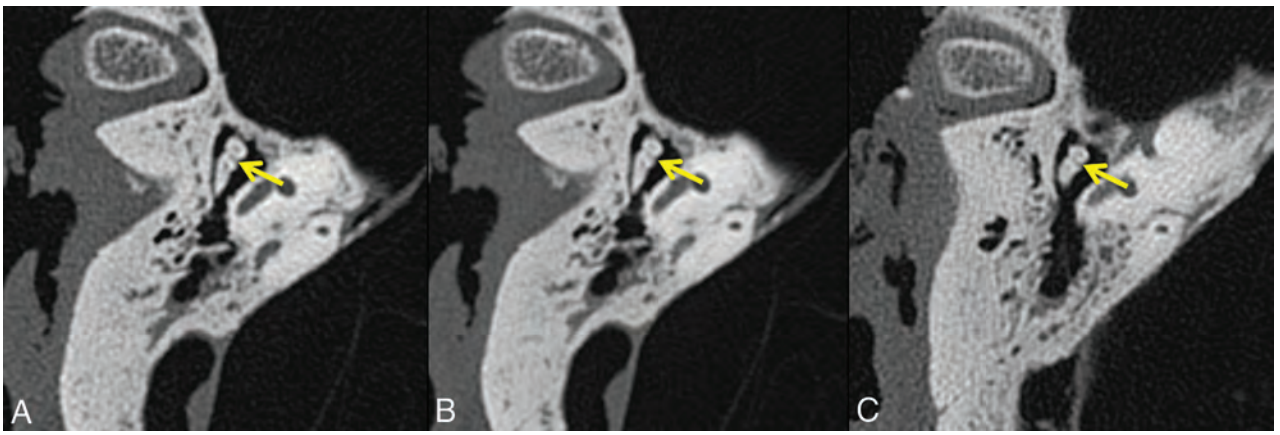


**FIG 4.** Representative axial images of the incudomallear joint (*arrow*) from the same specimen scanned with UHR PCD-CT and reconstructed with 0.25- (*A*) and 0.6-mm (*B*) image thicknesses, and UHR EID-CT, with 0.6-mm image thickness (*C*). The incudomallear joint between the incus and malleus is better defined in PCD-CT images compared with EID-CT images.

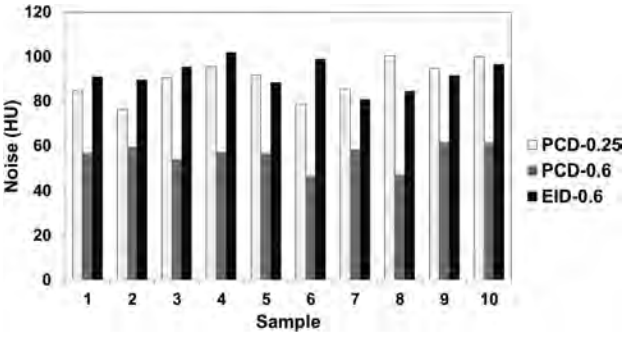


**FIG 5.** Image noise measured from 10 cadaveric specimens scanned with 3 UHR protocols. White indicates PCD with a 0.25-mm image; gray, PCD with a 0.6-mm image; black, EID with a 0.6-mm image.

showed superior image quality and better delineation of anatomic microstructures compared with the EID-CT system on which the PCD-CT was built.

Leng et al[23] reported the preliminary results of PCD-CT UHR imaging using various phantom and cadaveric test objects. Among these studies, 1 cadaveric temporal bone was scanned, and it was found that the PCD-CT UHR acquisition with a service-mode sharp kernel (S80) achieved 29% noise reduction compared with the EID-CT system. In this present work, with results from multiple cadaveric temporal bone specimens, we have demonstrated that with a clinical temporal bone reconstruction kernel (U70), the PCD-CT UHR mode could achieve ~40% noise reduction compared with an EID-CT system when scanning at the same dose level and reconstructing at the same image thickness (0.6 mm). The more aggressive noise reduction with PCD in this study compared with the previous report[23] is mainly due to the kernel difference (U70 is sharper than S80). Our results indicate the potential of a 64% reduction in dose using PCD-CT for clinical temporal bone imaging to achieve the same image noise as in EID-CT. This finding confirmed the previous conclusion that PCD-CT with its direct energy conversion could substantially increase the dose efficiency of UHR acquisitions compared with the EID-CT technique using a comb filter.[29]

Both PCD image sets (PCD-0.6 and PCD-0.25) were preferred compared with EID acquisitions because submillimeter structures were more evident on PCD images. One contribution was from the slightly improved in-plane resolution on the PCD-CT. At matched image thicknesses (0.6 mm), PCD-0.6 images had the additional benefit of significantly lower image noise than the EID-0.6 images. On the other hand, PCD-0.25 images had the benefit

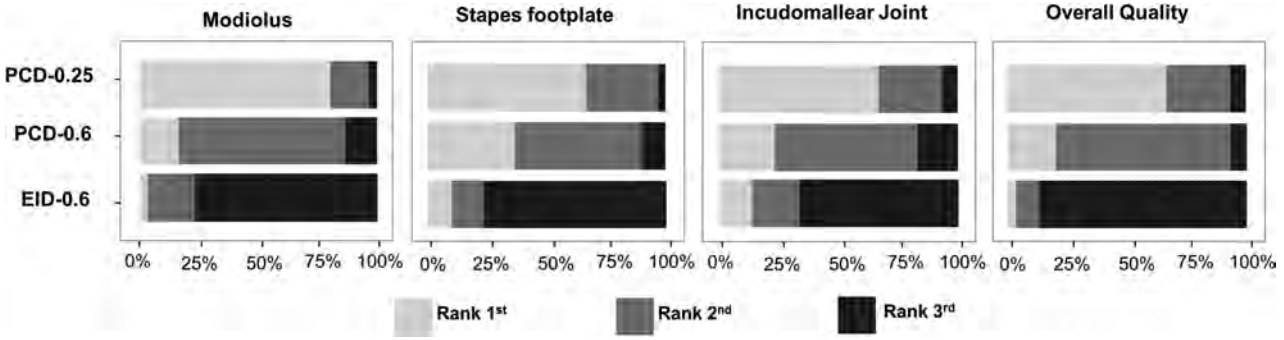


**FIG 6.** Rankings from 3 readers regarding overall image quality and delineation of 3 key anatomic structures. For all 3 structures and overall image quality, UHR PCD-CT images with 0.25-mm thickness have the highest rank (average, 1.2–1.4), while UHR EID-CT images with 0.6-mm thickness have the lowest rank (average, 2.5–2.8). White indicates the first rank; gray, the second rank; black, the third rank.

**Table 2: Visual assessment and comparison of image quality on 3 image sets acquired from PCD- and EID-CT scanners**

| | Average Rank | | | Pair-Wise Comparison *P* Value | | |
|---|---|---|---|---|---|---|
| | PCD-0.25 | PCD-0.6 | EID-0.6 | PCD-0.25 vs PCD-0.6 | PCD-0.25 vs EID-0.6 | PCD-0.6 vs EID-0.6 |
| Modiolus | 1.2 | 2.0 | 2.7 | .002 | <.001 | <.001 |
| Stapes footplate | 1.4 | 1.7 | 2.7 | .12 | <.001 | <.001 |
| Incudomallear joint | 1.4 | 1.9 | 2.5 | <.001 | <.001 | .02 |
| Overall quality | 1.4 | 1.9 | 2.8 | <.001 | <.001 | <.001 |

**Table 3: Interobserver agreement among 3 neuroradiologists for image-quality assessment of the 10 temporal bone cases[a]**

| | K-$\alpha$ | Successful Cases | Interobserver Agreement |
|---|---|---|---|
| Modiolus | 0.54 (0.37–0.69) | 7/10 | Moderate |
| Stapes footplate | 0.44 (0.27–0.59) | 7/10 | Moderate |
| Incudomallear joint | 0.36 (0.16–0.54) | 6/10 | Fair |
| Overall quality | 0.50 (0.33–0.67) | 7/10 | Moderate |

[a] Results were represented by K-$\alpha$ (95% confidence level). The number of cases with ranking agreement from majority of raters (≥2) was recognized as successful agreement cases.

of thinner images and less axial partial volume averaging compared with the EID-0.6 mm images, with no increase in image noise. Readers showed a strong preference for thinner PCD images despite their increased noise level.

Although this study focused on only temporal bone imaging, the demonstrated benefits may be applicable to other areas. For example, the use of thin CT images has been proved to increase the detectability of structural abnormalities in the temporal bone,[30] coronary artery,[31] and pulmonary nodules.[32,33] Recently, a prototype whole-body system using an EID detector at a smaller (0.25-mm) detector cell was introduced for lung imaging.[34] However, the loss of geometric efficiency from an increased density of septa substantially increased image noise. This is not an issue for PCD because no septa are required with its direct-conversion technique. Smaller image thicknesses reduce partial volume averaging and result in enhanced visualization of submillimeter structures.

In this study, the pyramid-shaped modiolus, the central bony pillar of the cochlea, was better depicted with the PCD system (Fig 2). The modiolus accommodates the fine terminal branches of the cochlear nerve, and hyperattenuation of the modiolus on CT can be observed in cases of cochlear nerve aplasia.[2] Determination of cochlear nerve aplasia can prove critical in the evaluation of patients with profound sensorineural hearing loss because it would preclude the possibility of successful cochlear implantation.[35] Similarly, a patulous modiolus is associated with intraoperative CSF leaks during cochlear implantation, and preoperative knowledge of this malformation would allow the surgeon to modify the approach accordingly. Likewise, in the evaluation of conductive hearing loss, confirming the integrity of the ossicular chain is critical to patient management. Our results suggest that PCD will be superior to EID in the detection of subtle ossicular abnormalities, including discontinuity, fibrous union, congenital fusion, and fixation (eg, otosclerosis, tympanosclerosis).

The PCD-CT scanner investigated in this study is a research system, and there is currently no commercial PCD-CT system available. More work is required to make the system more cost-effective and reliable, like the EID-CT systems, so that it can be used in routine clinical practice. This study represents the first step toward the adoption of the PCD-CT UHR mode for diagnostic neuroradiology practice. There were, however, several limitations to this study. First, this was an in vitro, cadaveric study. Cadaveric specimens were used because repeat scans could be easily performed in a well-controlled fashion. Because key anatomic structures were well-preserved in the cadaveric specimens, the results of our study represent what would be expected with patient imaging, though a future in vivo study is warranted. Second, the current study focused on image-quality assessment without evaluating diagnostic accuracy due to the lack of substantial pathology in the available cadaveric specimens. With these preliminary results showing the benefit of PCD-CT, our future studies will focus on diagnostic accuracy for in vivo patient examinations with specific pathology.

## CONCLUSIONS

This study demonstrated, for the first time, the improvement in image quality and reader preference in temporal bone imaging using the UHR PCD-CT technology. With the superior in-plane resolution and ultrathin (0.25-mm) image thickness, the

PCD-CT system demonstrated better delineation of anatomic microstructures of the temporal bones compared with UHR acquisitions performed on a commercial EID-CT system.

Disclosures: Cynthia H. McCollough—*RELATED*: *Grant*: Siemens*; *Provision of Writing Assistance, Medicines, Equipment, or Administrative Support*: Siemens *; *UNRELATED*: *Grants/Grants Pending*: Siemens, Bayer Healthcare*; *Royalties*: Bayer Healthcare.* Shuai Leng—*RELATED*: *Grant*: National Institutes of Health, *Comments*: Research reported in this article was supported by the National Institutes of Health under award numbers R01 EB016966 and C06 RR018898 and in collaboration with Siemens*. *Money paid to the institution.

## REFERENCES

1. Zayas JO, Feliciano YZ, Hadley CR, et al. **Temporal bone trauma and the role of multidetector CT in the emergency department.** *Radiographics* 2011;31:1741–55 CrossRef Medline
2. Lane JI, Lindell EP, Witte RJ, et al. **Middle and inner ear: improved depiction with multiplanar reconstruction of volumetric CT data.** *Radiographics* 2006;26:115–24 CrossRef Medline
3. Majdani O, Thews K, Bartling S, et al. **Temporal bone imaging: comparison of flat panel volume CT and multisection CT.** *AJNR Am J Neuroradiol* 2009;30:1419–24 CrossRef Medline
4. Jäger L, Bonell H, Liebl M, et al. **CT of the normal temporal bone: comparison of multi- and single-detector row CT.** *Radiology* 2005; 235:133–41 CrossRef Medline
5. Goldfeld M, Glaser B, Nassir E, et al. **CT of the ear in Pendred syndrome.** *Radiology* 2005;235:537–40 CrossRef Medline
6. Flohr TG, Stierstorfer K, Süss C, et al. **Novel ultrahigh resolution data acquisition and image reconstruction for multi-detector row CT.** *Med Phys* 2007;34:1712–23 Medline
7. McCollough CH, Leng S, Sunnegardh J, et al. **Spatial resolution improvement and dose reduction potential for inner ear CT imaging using a z-axis deconvolution technique.** *Med Phys* 2013;40:061904 CrossRef Medline
8. Meyer M, Haubenreisser H, Raupach R, et al. **Initial results of a new generation dual source CT system using only an in-plane comb filter for ultra-high-resolution temporal bone imaging.** *Eur Radiol* 2015;25:178–85 CrossRef Medline
9. Leng S, Diehn FE, Lane JI, et al. **Temporal bone CT: improved image quality and potential for decreased radiation dose using an ultra-high-resolution scan mode with an iterative reconstruction algorithm.** *AJNR Am J Neuroradiol* 2015;36:1599–603 CrossRef Medline
10. Gupta R, Grasruck M, Suess C, et al. **Ultra-high resolution flat-panel volume CT: fundamental principles, design architecture, and system characterization.** *Eur Radiol* 2006;16:1191–205 CrossRef Medline
11. Kalender WA, Kyriakou Y. **Flat-detector computed tomography (FD-CT).** *Eur Radiol* 2007;17:2767–79 CrossRef Medline
12. Kappler S, Hannemann T, Kraft E, et al. **First results from a hybrid prototype CT scanner for exploring benefits of quantum-counting in clinical CT.** *Proc SPIE* 2012;8313:30 CrossRef
13. Kappler S, Henning A, Kreisler B, et al. **Photon counting CT at elevated X-ray tube currents: contrast stability, image noise and multi-energy performance.** *Proc SPIE* 2014;9033:90331C CrossRef
14. Yu Z, Leng S, Jorgensen SM, et al. **Evaluation of conventional imaging performance in a research whole-body CT system with a photon-counting detector array.** *Phys Med Biol* 2016;61:1572–95 CrossRef Medline
15. Schlomka JP, Roessl E, Dorscheid R, et al. **Experimental feasibility of multi-energy photon-counting K-edge imaging in pre-clinical computed tomography.** *Phys Med Biol* 2008;53:4031–47 CrossRef Medline
16. Pourmorteza A, Symons R, Sandfort V, et al. **Abdominal imaging with contrast-enhanced photon-counting CT: first human experience.** *Radiology* 2016;279:239–45 CrossRef Medline
17. Shikhaliev PM. **Energy-resolved computed tomography: first experimental results.** *Phys Med Biol* 2008;53:5595–613 CrossRef Medline
18. Iwanczyk JS, Nygard E, Meirav O, et al. **Photon counting energy dispersive detector arrays for X-ray imaging.** *IEEE Trans Nucl Sci* 2009;56:535–42 CrossRef Medline
19. Taguchi K, Iwanczyk JS. **Vision 20/20: single photon counting x-ray detectors in medical imaging.** *Med Phys* 2013;40:100901 CrossRef Medline
20. Symons R, Pourmorteza A, Sandfort V, et al. **Feasibility of dose-reduced chest CT with photon-counting detectors: initial results in humans.** *Radiology* 2017;285:980–89 CrossRef Medline
21. Pourmorteza A, Symons R, Reich D, et al. **Photon-counting CT of the brain: in vivo human results and image-quality assessment.** *AJNR Am J Neuroradiol* 2017;38:2257–63 CrossRef Medline
22. Symons R, Reich DS, Bagheri M, et al. **Photon-counting computed tomography for vascular imaging of the head and neck: first in vivo human results.** *Invest Radiol* 2018;53:135–42 CrossRef Medline
23. Leng S, Yu Z, Halaweish A, et al. **Dose-efficient ultrahigh-resolution scan mode using a photon counting detector computed tomography system.** *J Med Imaging (Bellingham)* 2016;3:043504 CrossRef Medline
24. Zhou W, Montoya J, Gutjahr R, et al. **Lung nodule volume quantification and shape differentiation with an ultra-high-resolution technique on a photon counting detector CT system.** In: *Proceedings of SPIE Medical Imaging 2017: Physics of Medical Imaging.* Orlando, Florida; June 5, 2017
25. Schardt P, Deuringer J, Freudenberger J, et al. **New x-ray tube performance in computed tomography by introducing the rotating envelope tube technology.** *Med Phys* 2004;31:2699–706 CrossRef Medline
26. Schuknecht H. *Pathology of the Ear.* Boston: Harvard University Press; 1975
27. Norweck JT, Seibert JA, Andriole KP, et al. **ACR-AAPM-SIIM technical standard for electronic practice of medical imaging.** *J Digit Imaging* 2013;26:38–52 CrossRef Medline
28. Landis JR, Koch GG. **Measurement of observer agreement for categorical data.** *Biometrics* 1977;33:159–74 CrossRef Medline
29. Leng S, Gutjahr R, Ferrero AF, et al. **Ultra-high spatial resolution, multi-energy CT using photon counting detector technology.** *Proc SPIE Int Soc Opt* 2017;10132:101320Y CrossRef
30. Caldemeyer KS, Sandrasegaran K, Shinaver CN, et al. **Temporal bone: comparison of isotropic helical CT and conventional direct axial and coronal CT.** *AJR Am J Roentgenol* 1999;172:1675–82 CrossRef Medline
31. Nieman K, Cademartiri F, Lemos PA, et al. **Reliable noninvasive coronary angiography with fast submillimeter multislice spiral computed tomography.** *Circulation* 2002;106:2051–54 CrossRef Medline
32. Petrou M, Quint LE, Nan B, et al. **Pulmonary nodule volumetric measurement variability as a function of CT slice thickness and nodule morphology.** *AJR Am J Roentgenol* 2007;188:306–12 CrossRef Medline
33. Kawel N, Seifert B, Luetolf M, et al. **Effect of slab thickness on the CT detection of pulmonary nodules: use of sliding thin-slab maximum intensity projection and volume rendering.** *AJR Am J Roentgenol* 2009;192:1324–29 CrossRef Medline
34. Kakinuma R, Moriyama N, Muramatsu Y, et al. **Ultra-high-resolution computed tomography of the lung: image quality of a prototype scanner.** *PLoS One* 2015;10:e0137165 CrossRef Medline
35. Glastonbury CM, Davidson HC, Harnsberger HR, et al. **Imaging findings of cochlear nerve deficiency.** *AJNR Am J Neuroradiol* 2002; 23:635–43 Medline

# Pseudo-Leptomeningeal Contrast Enhancement at 3T in Pediatric Patients Sedated by Propofol

A.M. McKinney, A. Chacko Achanaril, B. Knoll, D.R. Nascene, and R.S. Gawande

## ABSTRACT

**BACKGROUND AND PURPOSE:** Propofol is a cerebral vasoconstrictor that modulates cerebral perfusion by decreasing the metabolic rate of oxygen. Because younger children often undergo intravenous sedation for MR imaging, this study set out to evaluate the degree of leptomeningeal contrast enhancement on 3T postcontrast brain MR imaging and to determine whether this phenomenon relates to sequence, sedation dosage, or patient age or weight.

**MATERIALS AND METHODS:** During a 2-year period, of 152 children 1–5 years of age who underwent MR imaging, 43 were included for MRI review. Of these, 37 underwent postcontrast imaging with either solely gradient-echo T1WI ($n = 20$) or spin-echo T1WI ($n = 17$); notably, 6 patients underwent both sequences. Three neuroradiologists separately graded the degree of leptomeningeal contrast enhancement (grades 0–3) that was correlated with various factors and calculated the interobserver reliability.

**RESULTS:** For the 43 patients, the mean patient age was 3.1 ± 1.4 years. The leptomeningeal contrast-enhancement grade was significantly greater ($P < .0001$) on spin-echo T1WI (1.9–2.1) versus gradient-echo T1WI (1.2–1.4). Patient weight ($r = -0.366$ to $-.418$, $P = .003$–$.01$) and age ($r = -0.315$ to $-0.418$, $P = .004$–$.032$) moderately and inversely correlated with the leptomeningeal contrast-enhancement grade, while the propofol dosage, sedation duration, and time to T1WI post-contrast administration did not (each, $P > .05$). The interobserver $\kappa$ was strong regarding the leptomeningeal contrast-enhancement grade on both spin-echo T1WI ($\kappa = 0.609–0.693$, $P < .0001$) and gradient-echo T1WI ($\kappa = 0.567–0.698$, $P < .0001$).

**CONCLUSIONS:** Leptomeningeal contrast enhancement (or "pseudo"-leptomeningeal contrast enhancement) occurs with a greater frequency and degree on 3T postcontrast spin-echo T1WI relative to gradient-echo T1WI in younger children sedated with propofol and should not be mistaken for disease. This phenomenon may be more prominent with lower age or size and may arise from propofol-induced vascular smooth-muscle dilation.

**ABBREVIATIONS:** GE = gradient-echo; LMCE = leptomeningeal contrast enhancement; SE = spin-echo; TTI = time to postcontrast T1-weighted imaging

Extra-axial enhancement in the CNS can be either leptomeningeal, occurring along the surface of the brain and subarachnoid space, or pachymeningeal, comprising the dura and its reflections.[1] The vessels within the pachymeninges do not have a blood-brain barrier, which causes the typical appearance of thin, linear, and smooth enhancement on postcontrast T1WI following the intravenous administration of gadolinium-based contrast agents; in contrast, the main mechanism of leptomeningeal contrast enhancement (LMCE) (ie, pial enhancement) is disruption of the blood-brain barrier.[1,2]

Often, children younger than 8 years of age require sedation to undergo a high-quality MR imaging examination. Anesthetic agents have been shown to cause changes in cerebral homeostasis and vascular reactivity.[3-5] Such agents can cause a global decrease in cerebral metabolism, with resultant decreases in both CBF and CBV.[3-5] Prior studies have also demonstrated that 2,6 diisopropyl phenol (propofol) can modulate CBF by decreasing the metabolic rate of oxygen; in addition, speculation based on animal studies suggests that propofol can dilate vascular smooth muscle in other regions of the body.[6]

The basis of this study is that the authors had noted prominent LMCE on brain MR imaging in some sedated children, but based on clinical notes, they neither were acutely ill nor exhibited meningeal signs. Thus, this study was initiated to determine whether

Received February 13, 2018; accepted after revision June 5.

From the Department of Radiology (A.M.M., A.C.A., D.R.N.), Neuroradiology Division, University of Minnesota, Minneapolis, Minnesota; Department of Radiology (B.K.), Hennepin County Medical Center, Minneapolis, Minnesota; and Department of Radiology (R.S.G.), Johns Hopkins University, Baltimore, Maryland.

Please address correspondence to Alexander M. McKinney, MD, University of Minnesota, Department of Radiology, 420 Delaware St SE, MMC 292, Minneapolis, MN 55455; e-mail: mckinrad@umn.edu

http://dx.doi.org/10.3174/ajnr.A5736

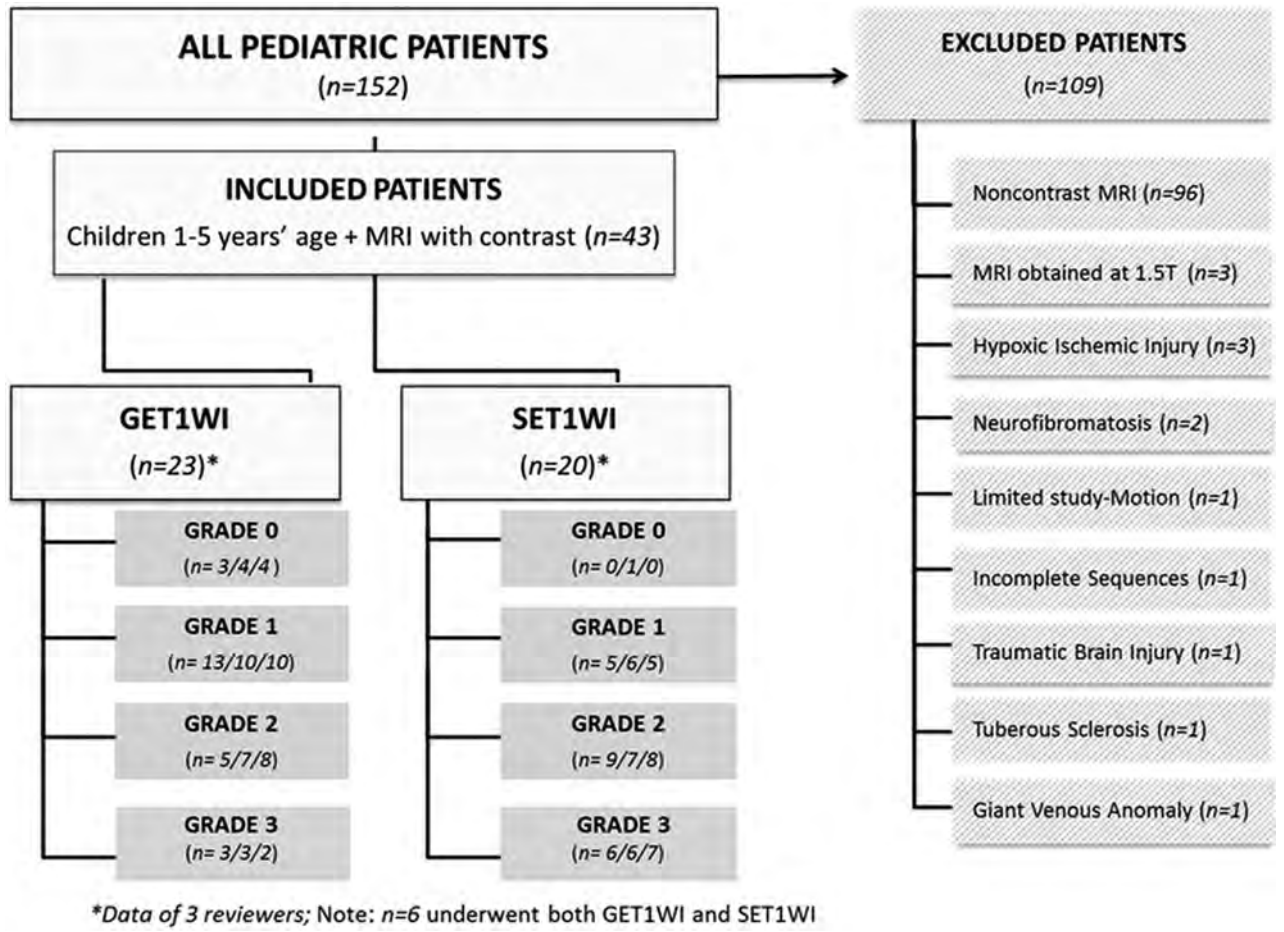


**FIG 1.** Organization chart showing the makeup of 43 children included in this study and grades per reviewer.

the degree of this phenomenon of apparent LMCE (termed here "pseudo"-LMCE) relates to the type of T1WI sequence, time to acquiring postcontrast T1WI, propofol dosage, or various patient demographics.

## MATERIALS AND METHODS

This retrospective study was performed after Hennepin County Medical Center, Minneapolis, Minnesota, review board approval. Review of the imaging data base and electronic clinical records yielded 152 healthy pediatric patients between the ages of 1 and 5 years who underwent 3T brain MR imaging and were sedated with intravenous propofol between November 2011 and November 2013. Inclusion criteria were the following: 1) ages were between 1 and 5 years; 2) either axial gradient-echo (GE) T1WI or spin-echo (SE) T1WI was performed; 3) the child received gadolinium-based intravenous contrast; 4) intravenous propofol was used for sedation; 5) the patient had either normal examination findings or only mild, nonacute, and noncongenital abnormalities (eg, <5 white matter foci); and 6) the patient had not had meningitis or other clinical diseases that could cause LMCE. Exclusion criteria consisted of the following: studies performed on a 1.5T magnet, an incomplete MR imaging examination, moderate-to-severe structural abnormalities, or clinical signs of meningitis (Fig 1). Anesthesia was induced via intravenous administration of propofol by a pediatric intensivist, without the use of inhalational anesthetics, akin to sedation methods described previously.[7]

### *MR Imaging Technique*

All studies were performed on a single 3T MR unit (Intera; Philips Healthcare, Best, the Netherlands), with sedation performed by a pediatric intensivist. The imaging parameters for GE TIWI were a volumetric acquisition of 9.8 ms/4.6 ms/8°/15–20 cm/1 (TR/TE/flip angle/FOV/NEX), a 169 × 169 to 240 × 240 matrix, 1-mm section thickness (0-mm gap), and an acquisition time of approximately 5 minutes; these scans were reconstructed in the axial plane at a section thickness of 3 mm. For SE T1WI, the parameters were 353–734 ms/10 ms/14–20 cm/1 (TR/TE/FOV/NEX), with a 168 × 132 to 265 × 205 matrix, axial 3-mm thickness (0.3–1.0 mm gap), and an acquisition time of about 5 minutes. We attempted to approximate and coregister the GE TIWI and SE TIWI to each other at the same thickness and level. Axial spin-echo T2WI, FLAIR, and DWI were also performed in each patient; the axial spin-echo T2WI and DWI acquisitions were performed after the intravenous administration of gadolinium-based contrast but prior to the postcontrast GE TIWI or SE TIWI acquisitions, to ensure a minimum delay of several minutes before the T1WI acquisitions were performed. The standard weight-based intravenous dose of gadolinium-based contrast was 0.1 mL/kg of body weight (0.1 mmol/kg) of gadobutrol (Gadavist; Bayer Schering Pharma, Berlin, Germany).

### *Imaging Interpretation*

Two staff neuroradiologists (A.M.M., B.K., each with >10 years of imaging experience) and 1 neuroradiology fellow (R.S.G., with

**Table 1: Demographics, TTI, dosages, and LMCE grades of the study patients**

| Parameter | Range | Mean | SD |
|---|---|---|---|
| Age (yr) | 1.3–5.0 | 3.1 | 1.4 |
| Weight (kg) | 5.7–24.6 | 15.3 | 4.5 |
| Propofol dose (mcg/kg/min) | 73–303 | 192 | 52 |
| Sedation duration (min) | 43–110 | 66.6 | 13.8 |
| TTI GE T1WI (min) | 8.0–17.0 | 12.6 | 2.2 |
| TTI SE T1WI (min) | 8.0–17.0 | 11.0 | 2.1 |
| LMCE score on SE T1WI | 1.9–2.1 | 2.0 | 0.8 |
| LMCE score on GE T1WI | 1.2–1.4 | 1.2 | 0.8 |

2 years of dedicated neuroradiology experience) independently graded the degree of LMCE as follows: grade 0, minimal thin vascular structures barely visible within the sulci; grade 1, thin vascular structures extending into the depths of the sulci; grade 2, smooth and slightly thickened LMCE; and grade 3, almost nodular, diffusely thickened LMCE or apparent involvement of adjacent parenchyma. The time between the commencement of the administration of intravenous contrast and the start of the postcontrast T1WI sequence was also recorded and was termed "time to imaging" (TTI).

### *Statistical Analysis*

The interobserver variability was calculated regarding LMCE grades using the Cohen κ. The LMCE grade was correlated with the propofol dosage, duration of sedation, patient age, weight, and TTI using the Spearman correlation. A Mann-Whitney *U* test was used to compare the grades of LMCE within the group ($n = 6$) who underwent both GE TIWI and SE TIWI. The significance threshold was set to $P < .05$.

## RESULTS

Of 152 pediatric patients (1–5 years of age) sedated by propofol for 3T MR imaging, 109 were excluded due to the lack of postcontrast T1WI ($n = 96$), the MR imaging being at 1.5T ($n = 3$), moderate-severe brain injury or congenital abnormalities, or several other factors, as listed under "Excluded Patients" within the organization chart of Fig 1. A total of 43 patients were ultimately included for MRI review; of these, 37 underwent postcontrast imaging with either solely gradient-echo T1WI ($n = 20/43$) or spin-echo T1WI ($n = 17/43$); notably, 6 patients underwent both sequences ($n = 6/43$). Table 1 lists the mean patient age, weight, propofol dosage, sedation duration, and TTI for both sequences. While the postcontrast TTI range was similar between sequences, it was slightly greater on SE TIWI than on GE TIWI (mean, 12.6 versus 11.0 minutes), being significantly different ($P = .01$).

As shown in Table 1, the range of LMCE grades of the reviewers was greater on SE TIWI (1.9–2.1) versus GE TIWI (1.2–1.4) and was significantly different ($P < .0001$). Interobserver κ between reviewers was strong for both GE TIWI ($\kappa = 0.567–0.698$, $P < .0001$) and SE TIWI ($\kappa = 0.609–0.693$, $P < .0001$). No patients had grade 0 LMCE on SE TIWI. Examples of the LMCE grades are provided in Figs 2–5.

Regarding the 6 patients who underwent both T1WI sequences, the mean LMCE grade on SE TIWI (1.83) was greater than that on GE TIWI (1.33) but was not significantly different ($P = .546$). Examples of LMCE on both sequences in the same patient are shown in Figs 3 and 5.

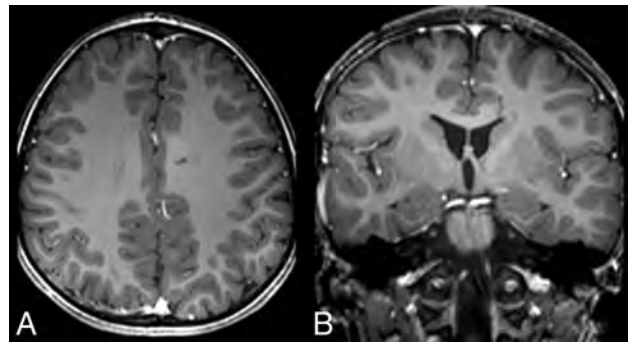


**FIG 2.** Grade 0 pseudo-LMCE in a 2-year-old girl post-trauma. Axial (*A*) and coronal (*B*) GE TIWI shows only minimal vasculature within the sulci. This grade of enhancement was present only on GE TIWI in 13%–17%, while no patients were graded as 0 on SE TIWI.

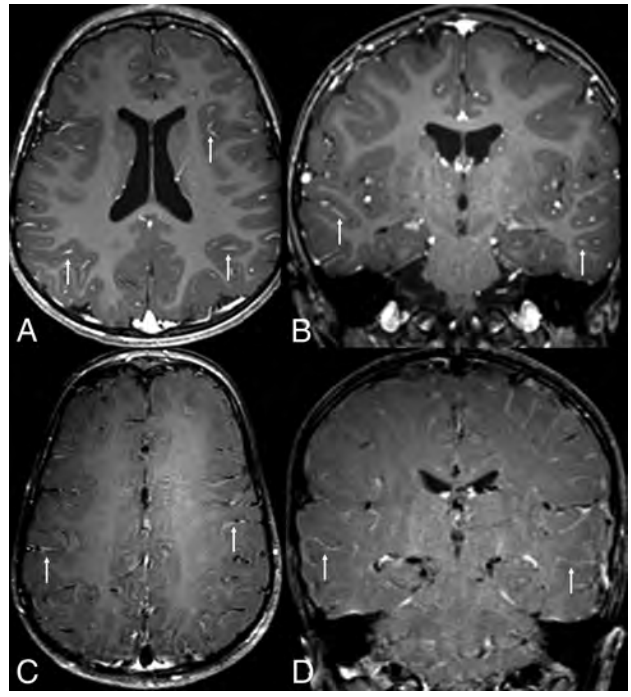


**FIG 3.** Grade 1 pseudo-LMCE on both sequences in a 3-year-old girl with seizures. Pseudo-LMCE appears as small vascular structures (*arrows*) within the depths of the sulci on GE TIWI axial (*A*) and coronal (*B*) images and on SE TIWI axial (*C*) and coronal (*D*) images. This grade was more frequent on GE TIWI (43%–57%) than on SE TIWI (25%–30%).

When we attempted to correlate various factors with the LMCE grade, there were significant, inverse, moderate correlations between patient weight and LMCE grade, as well as age and LMCE grade (each, $P < .05$; Table 2). Neither the propofol dose nor the sedation duration significantly correlated with the LMCE grade. The TTI did not correlate significantly with the grade of LMCE on GE TIWI, while on SE TIWI, there was a significant, moderate correlation between the LMCE grade and TTI with only 1 of the 3 observers (a staff neuroradiologist), but not the other 2 (Table 2).

## DISCUSSION

Because MR imaging is noninvasive and does not use ionizing radiation, it is often a technique of choice for pediatric patients requiring neuroimaging. However, its potentially long imaging

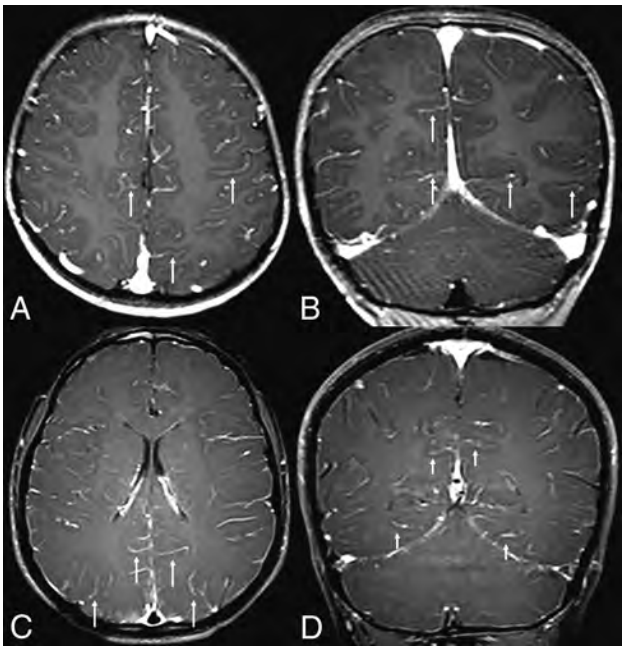


**FIG 4.** Examples of grade 2 pseudo-LMCE, demonstrated on both GE TIWI and SE TIWI in 2 different patients. In a 3-year-old girl with weakness, grade 2 pseudo-LMCE appears as smooth and slightly thickened enhancement (*arrows*) throughout the depths of the sulci on axial (*A*) and coronal (*B*) GE TIWI. In a 5-year-old boy with headaches, there is mildly thickened vasculature diffusely throughout the sulci (*arrows*) on axial (*C*) and coronal (*D*) SE TIWI. Note that grade 2 enhancement was slightly more frequent on SE TIWI (35%–45%) than on GE TIWI (22%–35%).

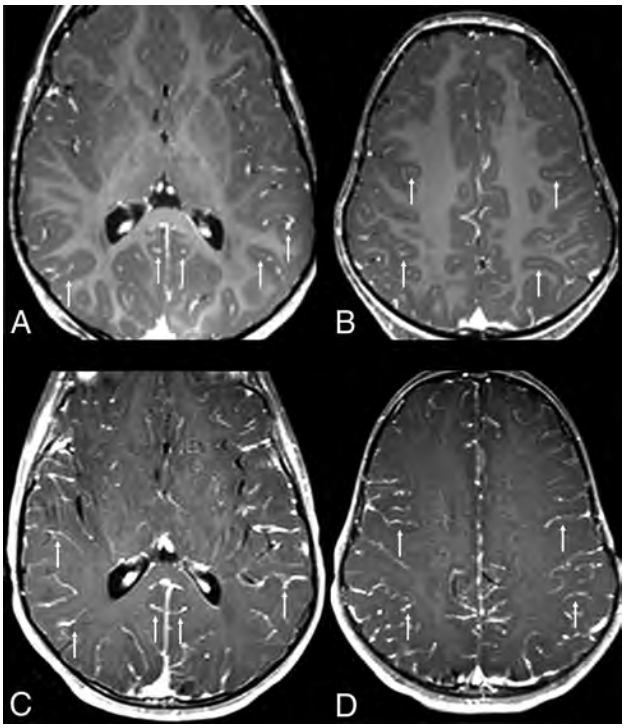


**FIG 5.** Discrepancy of the LMCE grade between sequences: grade 3 pseudo-LMCE on SE TIWI versus grade 2 on GE TIWI in a 3-year-old boy with fever. *A* and *B*, Axial GE TIWI depicts irregular enhancement (*arrows*) throughout many of the sulci, being slightly thickened, consistent with grade 2 pseudo-LMCE. *C* and *D*, Axial SE TIWI in the same patient demonstrates thicker pseudo-LMCE (*arrows*), appearing nearly nodular or parenchymal in some locations. This case demonstrates how such pseudo-LMCE is typically more prominent on SE TWI because grade 3 LMCE was much more frequent on SE TIWI (30%–35%) than on GE TIWI (8%–13%).

time often requires sedation in pediatric patients younger than 8 years of age. Thus, propofol is a lipid emulsion agent that is commonly the preferred anesthetic for children younger than 1 year of age who require intravenous sedation, due to its rapid onset, short duration, and infrequent side effects.[7-9] Because the presence of truly abnormal LMCE would be of concern in children, this study set out to determine whether pseudo-LMCE is a sequence-dependent (SE TIWI versus GE TIWI), TTI-dependent (time to postcontrast T1WI), propofol dosage–dependent phenomenon, or whether it is related to demographics such as age and weight. Ultimately, it was found that overall, the degree of apparent LMCE is significantly greater on SE TIWI compared with GE TIWI and that the only factors that correlated (inversely) with the degree of LMCE were patient weight and age. Hence, the type of T1WI sequence and patient size may be factors to consider when a pattern of apparent LMCE (so-called pseudo-LMCE) is identified, to distinguish this phenomenon from true meningeal abnormalities. Because this study focused solely on children between 1 and 5 years of age, future studies would be necessary to evaluate whether this phenomenon also occurs to some degree in older children and juveniles.

The mechanism of how this pattern of pseudo-LMCE occurs is not yet known, but there are several plausible explanations. The various determinants of cerebral blood flow are the patient's age, cerebral metabolic rate for oxygen, cerebral perfusion pressure, arterial oxygen, and carbon dioxide tensions. First, children under propofol sedation breathe spontaneously, but propofol causes a decrease in the tidal volume with a maintained respiratory rate and mild reduction in the partial pressure of oxygen in the blood, as well as a mild reduction in the fraction of inspired oxygen. By this phenomenon, one likely mechanism of pseudo-LMCE may be cerebral vasodilation secondary to an increase in the partial pressure of carbon dioxide (due to smooth-muscle relaxation); this increase in the partial pressure of carbon dioxide is likely due to the lack of "breathing off" $CO_2$.[9,10] Another factor could be that the leptomeninges may be more reactive or sensitive (in a sense "immature") in children compared with adults, an effect perhaps amplified by intravenous sedation. Additionally, because propofol sedation may affect respiration, studies have shown that the end-tidal volume of $CO_2$ has an inverse relationship with the degree of venous contrast, which could also contribute to LMCE.[11]

Hence, on the basis of reviewing the images within this study as well as the authors' experience, the authors opine that pseudo-LMCE on cerebral postcontrast T1WI often represents prominent venous vasculature of the subarachnoid space in younger children, being anecdotally described previously as less common in older children and adults; because older ages were not included in this study, this should be proved by a prospective study comparing age groups.[12] However, the finding in the current study of a significant, inverse correlation between patient weight and the grade of pseudo-LMCE suggests that smaller and younger patients have more vasoreactivity, perhaps because their vasculature is not as mature. This theory may be supported by a study by

**Table 2: Correlation coefficients and *P* values for LMCE versus other factors[a]**

| Correlation | TTI Overall (SE and GE T1WI) | TTI SE T1WI Only | TTI GE T1WI Only | Weight (kg) | Age (yr) | Dose/Weight (mg/kg) | Duration of Sedation (min) |
|---|---|---|---|---|---|---|---|
| LMCE ($\rho$) | −0.232 to −0.302 | −0.358 to −.475 | 0.016–0.190 | −0.366 to −0.418 | −0.315 to −0.418 | 0.103–0.210 | 0.023–0.147 |
| *P* value | .051–.130 | .036[b]–.122[c] | .371–.940 | .003–.011[b] | .004–.032[b] | .151–.484 | .318–.875 |

[a] Ranges provided are per the 3 reviewers.
[b] *P* values <.05.
[c] Only 1 reviewer (a staff neuroradiologist) had a significant correlation between TTI on SE T1WI and degree of LMCE ($\rho = -0.475$, $P = .036$).

Harreld et al,[4] which noted that in propofol-sedated children, the usual age-related decreases in CBF were reversed and increases in CBF and CBV were weight-dependent.

Unfortunately, exuberant pseudo-LMCE in children may simulate serious disorders that have implications for diagnosis therapy, such as leading to an unnecessary lumbar puncture to exclude meningitis. A radiologist should use other available imaging sequences to exclude true leptomeningeal abnormalities before the patient leaves the MR imaging scanner. The authors commonly experience the scenario in which a child with an unrelated diagnosis (eg, developmental delay, autism, and so forth) is imaged during sedation with propofol, in which the presence of pseudo-LMCE is spurious and varies with the postcontrast T1WI sequence used and the findings of other tests such as a resultant lumbar puncture, serum culture, and so forth are negative. This phenomenon being more common and greater in degree on SE TIWI versus GE TIWI is thought to be related to GE TIWI having a longer TR and lower contrast-to-noise ratio than SE TIWI; these features have been confirmed by studies noting that GE TIWI has a lower lesion detectability and visibility of contrast enhancement for a similar slice thickness.[13-15] While there was a small difference in slice gap between the 2 sequences in this study, the slice thickness and acquisition plane were coregistered between the 2 sequences, so this small gap is unlikely to account for the difference in the degree of LMCE.

Intravenous contrast is not required in most pediatric brain MR imaging examinations, and gadolinium-based contrast should be avoided when unnecessary due to the possibility of deposition within particular brain structures, especially with repeat administrations in children.[16-20] While this study did use a macrocyclic agent (the class of agents least likely to result in brain deposition), the use of most gadolinium-based agents is off-label for most gadolinium based intravenous contrast agents in the infantile population but is considered a standard of care in various clinical scenarios.[16-18] For example, particular known or suspected pathologies that may require either gadolinium-based contrast for diagnosis or follow-up or to exclude related pathology including infectious disorders (eg, abscess, empyema, or meningoencephalitis), neoplasms, syndromic disorders (eg, phakomatoses), vascular malformations, or vasculitis, to name a few. Hence, while stewardship is critical to lessen the use of gadolinium-based contrast, there will continue to be subsets of patients that necessitate such contrast in the foreseeable future, and an awareness of this appearance of pseudo-LMCE may help prevent a misdiagnosis of leptomeningeal disease in children.

This study has several limitations, including its retrospective nature and the relatively small sample size of groups that underwent both T1WI sequences. The role of supplemental oxygen during sedation was not accounted for, which may also affect cerebral hemodynamics and alter subarachnoid signal intensity on other sequences, such as previously noted on FLAIR.[21] In this regard, the authors found it difficult to obtain an accurate tabulation of the exact fractionation of oxygen and the length of time administered while the patient was under sedation, although the electronic record did note that there was titration of the supplemental oxygen in some patients. Thus, it is recommended that future studies prospectively tabulate the oxygen fraction accurately. Another potential limitation is that there was a small but significant difference between the TTI of both SE TIWI (12.6 minutes) and GE TIWI (11.0 minutes), which might create a bias toward having a greater LMCE score on SE TIWI; however, because no significant association was noted between the degree of LMCE and TTI, such bias (if present) was unlikely to affect the LMCE grade between sequences. Another limitation was that several factors such as CSF protein, fraction of inspired oxygen, end-tidal $CO_2$, and leakage of propofol across the BBB were not evaluated in this study. These factors, previously implicated on T2WI and FLAIR imaging, could be assessed with respect to T1WI in a future study.[21,22]

## CONCLUSIONS

The phenomenon of apparent LMCE, termed pseudo-LMCE herein, is relatively common on postcontrast T1-weighted MR imaging of younger children sedated by intravenous propofol and should not be mistaken for disease. This effect occurs more commonly and to a greater degree on SE TIWI compared with GE TIWI and inversely correlates with age and weight. The presence of this finding may relate to the immaturity of younger children's vasculature but needs to be studied further.

Disclosures: Alexander M. McKinney—*UNRELATED*: *Board Membership*: VEEV Inc Informatics, *Comments*: owner, Informatics Solutions.

## REFERENCES

1. Smirniotopoulos JG, Murphy FM, Rushing EJ, et al. **Patterns of contrast enhancement in the brain and meninges.** *Radiographics* 2007; 27:525–51 CrossRef Medline
2. McKinstry CS, Worthington BS, Niendorf HP, et al. **Demonstration of meningeal contrast enhancement on magnetic resonance imaging.** *Acta Radiol Suppl* 1986;369:564–67 Medline
3. Kaisti KK, Långsjö JW, Aalto S, et al. **Effects of sevoflurane, propofol, and adjunct nitrous oxide on regional cerebral blood flow, oxygen consumption, and blood volume in humans.** *Anesthesiology* 2003; 99:603–13 CrossRef Medline
4. Harreld JH, Helton KJ, Kaddoum RN, et al. **The effects of propofol on cerebral perfusion MRI in children.** *Neuroradiology* 2013;55: 1049–56 CrossRef Medline
5. Klein KU, Fukui K, Schramm P, et al. **Human cerebral microcirculation and oxygen saturation during propofol-induced reduction of bispectral index.** *Br J Anaesth* 2011;107:735–41 CrossRef Medline
6. Gragasin FS, Davidge ST. **The effects of propofol on vascular func-**

**tion in mesenteric arteries of the aging rat.** *Am J Physiol Heart Circ Physiol* 2009;297:H466–74 CrossRef Medline
7. Machata AM, Willschke H, Kabon B, et al. **Propofol-based sedation regimen for infants and children undergoing ambulatory magnetic resonance imaging.** *Br J Anaesth* 2008;101:239–43 CrossRef Medline
8. Martin LD, Pasternak LR, Pudimat MA. **Total intravenous anesthesia with propofol in pediatric patients outside the operating room.** *Anesth Analg* 1992;74:609–12 Medline
9. Szabó EZ, Luginbuehl I, Bissonnette B. **Impact of anesthetic agents on cerebrovascular physiology in children.** *Pediatr Anesth* 2009;19:108–18 CrossRef Medline
10. Remsen LG, Pagel MA, McCormick CI, et al. **The influence of anesthetic choice, PaCO2, and other factors on osmotic blood-brain barrier disruption in rats with brain tumor xenografts.** *Anesth Analg* 1999;88:559–67 Medline
11. Kwong KK, Wanke I, Donahue KM, et al. **EPI imaging of global increase of brain MR signal with breath-hold preceded by breathing O2.** *Magn Reson Med* 1995;33:448–52 CrossRef Medline
12. McKinney AM. *Atlas of Normal Imaging Variations of the Brain, Skull, and Craniocervical Vasculature*. New York: Springer-Verlag; 2017:413–26; chap 18
13. Komada T, Naganawa S, Ogawa H, et al. **Contrast-enhanced MR imaging of metastatic brain tumor at 3 Tesla: utility of T(1)-weighted SPACE compared with 2D spin echo and 3D gradient echo sequence.** *Magn Reson Med Sci* 2008;7:13–21 CrossRef Medline
14. Chappell PM, Pelc NJ, Foo TK, et al. **Comparison of lesion enhancement on spin-echo and gradient-echo images.** *AJNR Am J Neuroradiol* 1994;15:37–44 Medline
15. Mugler JP 3rd, Brookeman JR. **Theoretical analysis of gadopentetate dimeglumine enhancement in T1-weighted imaging of the brain: comparison of two-dimensional spin-echo and three-dimensional gradient-echo sequences.** *J Magn Reson Imaging* 1993;3:761–69 CrossRef Medline
16. Saunders DE, Thompson C, Gunny R, et al. **Magnetic resonance imaging protocols for paediatric neuroradiology.** *Pediatr Radiol* 2007;37:789–97 CrossRef Medline
17. American College of Radiology. ACR Appropriateness Criteria. http://www.acr.org/Quality-Safety/Appropriateness-Criteria. Accessed May 1, 2018
18. Soares BP, Lequin MH, Huisman TA. **Safety of contrast material use in children.** *Magn Reson Imaging Clin N Am* 2017;25:779–85 CrossRef Medline
19. Roberts DR, Chatterjee AR, Yazdani M, et al. **Pediatric patients demonstrate progressive T1-weighted hyperintensity in the dentate nucleus following multiple doses of gadolinium-based contrast agent.** *AJNR Am J Neuroradiol* 2016;37:2340–47 CrossRef Medline
20. Ryu YJ, Choi YH, Cheon JE, et al. **Pediatric brain: gadolinium deposition in dentate nucleus and globus pallidus on unenhanced T1-weighted images is dependent on the type of contrast agent.** *Invest Radiol* 2018;53:246–55 CrossRef Medline
21. Frigon C, Shaw DW, Heckbert SR, et al. **Supplemental oxygen causes increased signal intensity in subarachnoid cerebrospinal fluid on brain FLAIR MR images obtained in children during general anesthesia.** *Radiology* 2004;233:51–55 CrossRef Medline
22. Filippi CG, Ulug AM, Lin D, et al. **Hyperintense signal abnormality in subarachnoid spaces and basal cisterns on MR images of children anesthetized with propofol: new fluid-attenuated inversion recovery finding.** *AJNR Am J Neuroradiol* 2001;22:394–99 Medline

# Brachial Plexus Ultrasound and MRI in Children with Brachial Plexus Birth Injury

A. Gunes, E. Bulut, A. Uzumcugil, and K.K. Oguz

## ABSTRACT

**BACKGROUND AND PURPOSE:** Brachial plexus birth injury is caused by traction on the neck during delivery and results in flaccid palsy of an upper extremity commonly involving C5–C6 nerve roots. MR imaging and MR myelography help to assess the anatomic location, extent, and severity of brachial plexus injuries which influence the long-term prognosis along with the surgical decision making. Recently, sonography has been increasingly used as the imaging modality of choice for brachial plexus injuries. The aim of this study was to assess the degree of correlation among brachial plexus sonography, MR imaging, and surgical findings in children with brachial plexus birth injury.

**MATERIALS AND METHODS:** This prospective study included 55 consecutive patients (girls/boys = 32:23; mean age, 2.1 ± 0.8 months) with brachial plexus birth injury between May 2014 and April 2017. The patients were classified according to the Narakas classification and were followed up at 4- to 6-week intervals for recovery by the Modified Mallet system and sonography without specific preparation for evaluation. All patients had MR imaging under general anesthesia. Nerve root avulsion-retraction, pseudomeningocele, and periscalene soft tissue were accepted brachial plexus injury findings on imaging. Interobserver agreement for MR imaging and the agreement between imaging and surgical findings were estimated using the $\kappa$ statistic. The diagnostic accuracy of sonography and MR imaging was calculated on the basis of the standard reference, which was the surgical findings.

**RESULTS:** Forty-three patients had pre- and postganglionic injury, 12 had only postganglionic injury findings, and 47% of patients underwent an operation. On sonography, no patients had preganglionic injury, but all patients had postganglionic injury findings. For postganglionic injury, the concordance rates between imaging and the surgical findings ranged from 84% to 100%, and the diagnostic accuracy of sonography and MR imaging was 89% and 100%, respectively. For preganglionic injury, the diagnostic accuracy of MR imaging was 92%. Interobserver agreement and the agreement between imaging and the surgical findings were almost perfect for postganglionic injury ($\kappa$ = 0.81–1, $P < .001$).

**CONCLUSIONS:** High-resolution sonography can identify and locate the postganglionic injury associated with the upper and middle trunks. The ability of sonography to evaluate pre- and the postganglionic injury associated with the lower trunk was quite limited. Sonography can be used as a complement to MR imaging; thus, the duration of the MR imaging examination and the need for sedation can be reduced by sonography.

**ABBREVIATIONS:** BP = brachial plexus; GI = ganglionic injury; US = ultrasound; PST = periscalene soft tissue

Brachial plexus (BP) birth injury is caused by traction on the neck during delivery and results in flaccid palsy of an upper extremity commonly involving the C5–C6 nerve roots.[1] Imaging studies help to assess the anatomic location, extent, and severity of BP injuries, which influence the long-term prognosis along with the surgical decision-making.[1] MR imaging has been the preferred imaging technique for the evaluation of BP injuries with a high diagnostic accuracy (87%) and the ability to differentiate pre- and postganglionic injuries (GIs).[2-4] MR myelography is even superior to conventional MR imaging in detecting root avulsions, with a diagnostic accuracy of 92%.[5,6] Because of the ease of availability and superior spatial resolution for a quick, real-time evaluation of nerves without sedation or contrast administration,

Received March 9, 2018; accepted after revision June 25.

From the Department of Radiology (A.G.), University of Health Sciences, Ankara Child Health and Diseases Hematology Oncology Training and Research Hospital, Ankara, Turkey; and Departments of Radiology (E.B., K.K.O.) and Orthopedics and Traumatology (A.U.), Hacettepe University Faculty of Medicine, Ankara, Turkey.

Please address correspondence to Altan Gunes, MD, Department of Radiology, University of Health Sciences, Ankara Child Health and Diseases Hematology Oncology Training and Research Hospital, Dıskapı, 06130, Ankara, Turkey; e-mail: draltangunes@gmail.com

Indicates article with supplemental on-line tables.

http://dx.doi.org/10.3174/ajnr.A5749

ultrasound (US) has been increasingly used as the imaging technique of choice in recent years.[7-9] US can detect nerve injury in the form of a neuroma and/or scar tissue formation.[9,10] Detection of nerve root injuries has been reported to be 100% for C5–C7, 84% for C8, and 64% for T1 in adult patients.[11] These nerve roots can also be evaluated in children with similar detection rates except the C8 and T1 nerve roots because of difficulty in evaluating C8 and T1.[9]

The aim of this study was to assess the degree of correlation among BP US, MR imaging, and surgical findings in children with BP birth injury.

## MATERIALS AND METHODS

### Patients

The study was approved by the local ethics committee (Hacettepe University Faculty of Medicine Ethics Committee, Reference Number = 16969557–627), and the families of patients gave written informed consent. This prospective study included 55 patients (girls/boys = 32:23; mean age, 2.1 ± 0.8 months; range, 0.5–3 months) who were referred with the clinical diagnosis of BP birth injury from the Department of Orthopedics and Traumatology, between May 1, 2014, and April 1, 2017. The diagnosis was based on the clinical examination and risk factors (maternal diabetes [$n = 5$], high birth weight [$n = 21$], prolonged labor [$n = 8$], and assisted or difficult deliveries [$n = 5$]). Inclusion criteria for the patients in the study were having a BP birth injury and having a BP US and MR imaging studies with diagnostic quality. Exclusion criteria for the patients in the study included having inadequate medical records, not having regular follow-up, and having suboptimal/inadequate US and MR imaging scans due to motion or breathing artifacts.

### Clinical Follow-Up of Patients

The patients were classified according to the Narakas classification[12] of obstetric BP palsy: grade I = 20, grade II = 21, grade III = 2, and grade IV = 12. The patients were followed up to 2 years of age at 4- to 6-week intervals for recovery by the Modified Mallet system and US.[1] The same orthopedist (A.U.), with 11 years of experience in managing BP birth injury, examined and followed the patients throughout the study. Our clinical approach was consistent with that introduced by Gilbert et al.[13] The patients who demonstrated recovery in biceps function within the first 12 weeks of life were followed conservatively with functional rehabilitation. If the biceps function of the patients did not demonstrate recovery at 12 weeks, these patients were considered as possible surgical candidates, and the definitive surgery decision for the patients was made at 6 months. If the patient had total paralysis, especially when associated with Horner syndrome and no recovery at 3 months or insufficient recovery at 6 months, the operation would almost certainly to be required. The surgical intervention for all patients was performed by the same orthopedist (A.U.). No surgical laminectomies were performed to determine the nerve root avulsion to avoid increased morbidity and mortality of this procedure.[14] The nerve root integrity was determined by intraoperative neurophysiologic studies in which stimulating electrodes were used to observe the neuroelectrical responses. In these studies, the inability to receive a motor response distal to the nerve roots was considered a nerve root injury.

### Sonographic Technique

The US examinations were performed by 1 pediatric radiologist (A.G.), who had 7 years of experience in musculoskeletal imaging and US. The radiologist was not blinded to the indication for US but was blinded to the findings of the physical examination. All patients were examined with a high-frequency linear probe (Sonoline G40, Siemens, Erlangen, Germany [5–7.5 MHz]; Xario, Toshiba, Tokyo, Japan [5–12 MHz]) in a supine and contralateral (unaffected side) decubitus position without specific preparation for US. The examinations took an average of 5 minutes for each patient. The protocol of BP US was standardized and based on the detection of the anatomic landmarks in the neck such as the vertebral artery (for nerve root) and scalene muscles (for nerve root and trunk).[8,15] The probe was placed above the clavicle, and it was advanced from the supraclavicular area to the sternocleidomastoid muscle for evaluation of the interscalene-supraclavicular regions and the neural foraminal region in transverse and longitudinal views. The predefined findings of the nerve root avulsion, which include nonvisualization of the nerves on the affected side, pseudomeningocele (CSF collections due to dural tears in proximity to intervertebral foramina), and periscalene soft tissue (PST) that represent a posttraumatic neuroma or scar tissue, were evaluated on the affected side by US.[2,6,16] PST is defined as the asymmetric linear and/or nodular thickening of the nerve root trunks detected in the interscalene space.[16] The nerve root avulsion and pseudomeningocele were the accepted findings of pre-GI, and the PST was accepted as a sign of a post-GI finding.[2,6,16] The location, extension, size, echogenicity, and vascularity of the PSTs were evaluated. The size of the PSTs was measured in the transverse section. The changes in size and echogenicity of PSTs were followed up by the same radiologist (A.G.) throughout the study.

### MR Imaging Technique

All MR imaging examinations were performed on a 1.5T scanner (Symphony; Siemens) with a head and neck coil. Our MR imaging protocol for BP applied the conventional (spin-echo T1WI, TSE T2WI, STIR) and CISS sequences. No paramagnetic contrast agent was used. Both the left and right BPs were imaged to allow comparison and better detection of the abnormalities. The imaging technique included axial (C3 to inferior axilla) and coronal oblique (including both shoulders) T1WI (TR/TE = 450–600/12–15 ms, FOV = 16 cm, section thickness/gap = 3/1 mm); axial and sagittal T2WI for the cervical spine; coronal oblique fat-suppressed T2WI for the BP (TR/TE/TI = 3600–4000/70–80/160 ms, FOV = 16–20 cm, section thickness/gap = 3/1 mm); and axial and coronal CISS (TR/TE = 7.6/3.2 ms, FOV = 16–18 cm, section thickness/gap = 0.7–1/0.5 mm). The examinations took an average of 25–30 minutes, including the preparation of the patient. Each patient was scanned under general anesthesia. MR imaging of pre-GI can show the partial (ventral or dorsal rootlets) or complete nerve root avulsion seen as the discontinuity of the roots, nerve root retraction, displacement and/or signal abnormalities of cord, and pseudomeningocele.[2,6] MR imaging of post-GI shows the asymmetric linear and/or nodular thickening of the nerve roots and trunks that is detected in the interscalene space with imaging defined as a PST.[16] The location, extension, size, and the intensity of the PSTs were evaluated. The size of the PST was measured in the axial image.

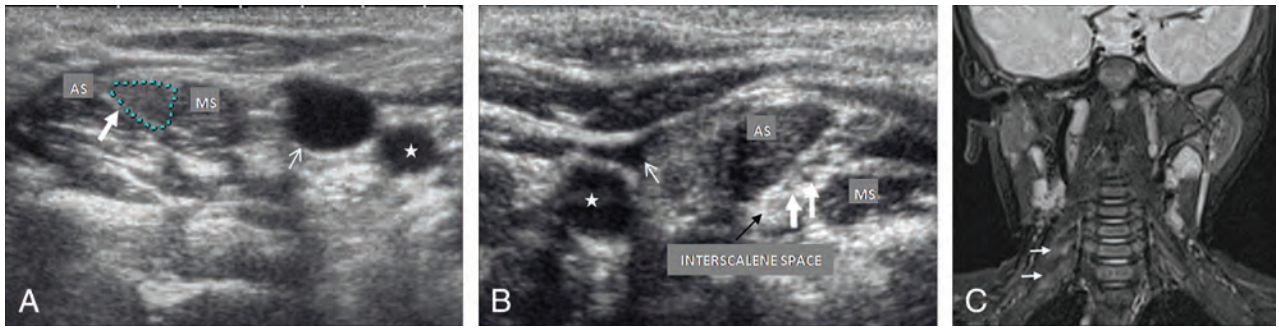


**FIG 1.** Case 25, in a 1-month-old infant with right-sided total brachial plexus paralysis with homogeneous periscalene soft tissue at the C5–7 level (*arrow*) between the anterior (AS) and middle scalene (MS) muscles on a transverse sonographic image (*A*). The *thin arrow* and *star* show the right internal jugular vein and carotid artery, respectively, on image *A*. *B*, The transverse scan sonographic image shows the normal interscalene space (*black arrow*) and nerve roots as hypoechoic oval cross-sections (*white arrows*) between the AS and MS muscles. The *thin arrow* and *star* show left internal jugular vein and carotid artery, respectively, on *B*. *C*, Coronal oblique fat-suppressed TSE T2WI shows periscalene soft tissues (*arrows*) coursing through the right interscalene space at the C5–7 level, findings similar to those in *A*.

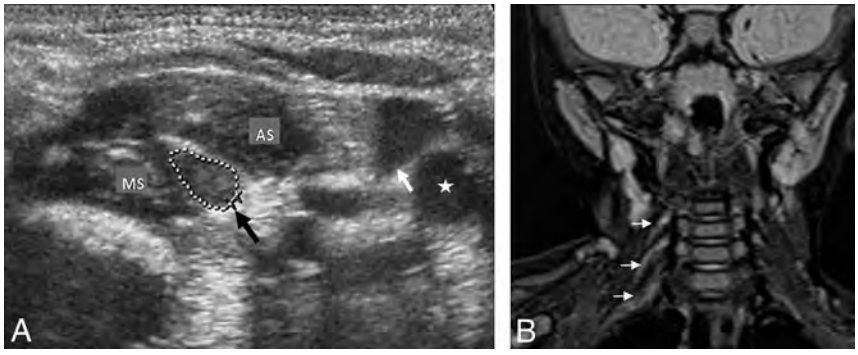


**FIG 2.** Case 20, a 2-month-old female patient with a right brachial plexus birth injury. *A*, Transverse scan sonography of the interscalene space shows homogeneous echogenicity periscalene soft tissue with fusiform morphology (*black arrow*) between the anterior (AS) and middle scalene (MS) muscles at the C4–7 level. The *white arrow* and *star* show the right internal jugular vein and carotid artery, respectively. *B*, Coronal oblique fat-suppressed TSE T2WI shows periscalene soft tissues (*arrows*) coursing through the right interscalene space at the C4–7 level, findings similar to those in *A*.

### *Analysis of Findings*

All patients had MR imaging (mean time = 5.4 months [range, 2–11 months]) after the US examinations (except 4 patients) because the BP birth injury is a medicolegal problem in our country and MR imaging can demonstrate this injury. All MR imaging was analyzed independently, without knowledge of the side of the injury, clinical and US findings, by 2 radiologists (E.B. with 8 years of experience in neuroimaging, and K.K.O. with 17 years of experience in neuroimaging). Finally, the degree of correlation among the clinical, imaging, and surgical findings was analyzed by all investigators in consensus. The surgical and histopathologic findings were the standard of reference for patients who underwent an operation. The standard reference was clinical follow-up for the patients who did not undergo surgery. No patient was excluded from the study for suboptimal US and MR imaging evaluation.

### *Statistical Analysis*

Comparative analysis was performed using a $\chi^2$ test for categoric variables and Mann-Whitney *U* and Kruskal-Wallis tests for nonnormally distributed continuous variables. Interobserver agreement for MR imaging and the agreement between imaging and surgical findings were estimated using the $\kappa$ statistic (range, $-1$ to $+1$), which is interpreted as follows: <0.40, poor to fair agreement; 0.41–0.60, moderate agreement; 0.61–0.80, substantial agreement; and 0.81–1.00, almost perfect agreement. The sensitivity, specificity, positive and negative predictive values, and accuracy were calculated for both US and MR imaging for the detection of pre- and post-GI using a $2 \times 2$ table based on the surgical findings. The statistical analysis was conducted with statistical software (SPSS, Version 21.0; IBM, Armonk, New York). A $P$ value $< .05$ was considered statistically significant.

## RESULTS

Forty-three patients had pre- and post-GI, and 12 had only post-GI. Twenty-six of 55 patients (47%) underwent an operation (24 with pre- and post-GI and 2 with only post-GI). There was no significant difference in the mean age between girls (2.1 ± 0.7 months; range, 0.5–3 months) and boys (2 ± 0.9 months; range, 0.5–3 months) ($P = .94$). No significant difference was found in the mean birth weight between girls (3865 g; interquartile range, 3600–4035 g) and boys (4000 g; interquartile range, 3830–4125 g) ($P = .05$). According to the Modified Mallet scoring system, the mean global abduction (72.1° [range, 0°–130°]) and external rotation (22.6° [range, 0°–90°]) scores were 2.57 and 2.22, respectively. The mean Modified Mallet scores for the ability to bring the hand to the neck, to the back, and to the mouth were 2.12, 2.46, and 2.50, respectively. Twelve patients had the Horner sign. Baseline characteristics, imaging findings, and the follow-up data of patients are presented in the Online Table.

All patients had PST on the affected side with no detectable pre-GI on US (Figs 1 and 2). The PST appeared as a smooth well-defined solid mass that usually extended laterally to the BP trunk region on US, with no internal vascularity. The echogenicity of PST (90%, 114/127) was usually similar to that of the scalene muscles, but some lesions had mixed echotexture (10%, 13/127). US revealed 127 PSTs that showed the affected number of nerve roots in 55 patients. The mean caliber of the PST was 6.6 ± 1.9

mm (range, 3.4–10.2 mm), and the thickness of the PST was not significantly different among the Narakas groups ($P = .26$) and between US and MR imaging examination (6.1 ± 2 mm [range, 3–11.6 mm]), ($P = .34$). Although the thickness of all PSTs was reduced in the follow-up period (at first evaluation, 6.3 ± 1.8 mm, [range, 3.3–9.6 mm], at the second evaluation, 6.1 ± 1.7 mm [range 3.1–9.3 mm]), PSTs remained persistent thereafter. All PSTs also did not show cystic/hemorrhagic degeneration or calcification on follow-up.

All patients had abnormal MR imaging findings on the affected side. The nerve root avulsion/retraction was seen in 43 patients in at least 1 level ($n = 25$) on MR imaging, and root avulsion without associated pseudomeningocele was seen in 4 patients (Fig 3*A*). The surgical electrophysiologic examination did not confirm the root avulsion diagnosis in 2 patients with a positive MR imaging finding, case 5 (C5) and case 49 (C5 and C6), and it revealed avulsion in 3 patients with negative MR imaging findings, cases 37 and 45 (C7, C8, and T1) and case 52 (C5). In clinical terms, there were also discrepancies between clinical findings and MR imaging in these patients (cases 5, 37, 45, 49, and 52). The pseudomeningocele without associated root avulsion was seen in 3 patients (cases 33, 39, and 42), and nerve root avulsion in the pseudomeningocele was not evaluated optimally in 3 patients (cases 5, 37, and 45) (Fig 3*B*). MR imaging showed 139 PSTs that usually showed signal similar to that of scalene muscles (93%, 129/139) on T1WI and higher signal (100%, 139/139) than muscles on T2WI. The locations and extensions of the PST were similar to those of US findings. The US and MR imaging showed concordance in 85% (47/55) of patients with PST (91%, 127/139) except in 8 cases (C8 [$n = 4$] and T1 [$n = 8$]) (Figs 1*C* and 2*B*). The clinical, US, and MR imaging findings were concordant in 85% of patients (47/55) with post-GI.

In the surgically proved cases, for the post-GI, the sensitivity, specificity, positive and negative predictive values, and diagnostic accuracy of US ranged from 81% to 100% (Table). The sensitivity, specificity, positive and negative predictive values, and the diagnostic accuracy of MR imaging ranged from 84% to 100% for pre- and post-GI (Table). The agreement among the US, MR imaging, and surgical findings was almost perfect for post-GI ($\kappa = 0.81$ and 1, respectively; $P < .001$). For pre- and post-GI, the $\kappa$ values between observers were 0.89 and 0.93 ($P < .001$), and there was almost perfect agreement.

Twenty-six surgical procedures were performed during the 3-year study period (mean time = 6.6 ± 1.1 months, [range, 5–9 months]; neurolysis [$n = 19$], nerve grafting [$n = 5$], and neurotization [$n = 2$]) without any surgical or early postoperative complications. Histopathologic studies were available in 9 patients: Five lesions were compatible with scar tissue, and 4 lesions were compatible with posttraumatic neuroma. The early results of shoulder and elbow function recovery demonstrated 66% success at 9 months postoperatively. In 29 patients who did not undergo an operation, the biceps function was recovered before 6 months in 22 (75%) patients and after 6 months in 7 patients (24%). Patients with C5–C6 palsy (90%, 18/20) had a statistically higher spontaneous functional recovery rate than patients with C5–C7 palsy (52%, 11/21) ($P = .008$). No patients with C5–T1 palsy had spontaneous functional recovery.

## DISCUSSION

The etiology and mechanism of BP birth injury is not completely known, though many maternal and fetal factors have been suggested as the cause such as shoulder dystocia and high birth weight.[17,18] Shoulder dystocia has been identified as the greatest risk factor in the etiology of BP birth injury in our study. Birth weight higher than 4500 g is the most important fetal factor for BP birth injury, increasing the risk by 10-fold.[18] Yet, in our study, the mean birth weight (3863 g) was <4500 g, and some BP birth injuries occurred in women without identifiable risk factors. In agreement with previous data, these findings suggest the unpredictability of BP birth injury occurrence.[17,18]

In our study, most of the infants (74%) had paralysis of the C5–C6 ± C7 roots, similar to findings in the previous report by Kozin.[19] Our study included patients with a diagnosis of BP birth injury on clinical grounds. Therefore, as expected, all patients had abnormal findings on the affected side on US. In these patients, US effectively showed the post-GI at the interscalene space, in concordance with MR imaging (82%–91%) and the surgical findings (90%). How-

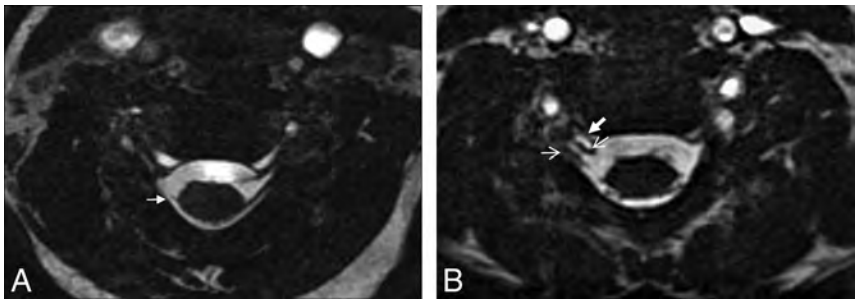


**FIG 3.** Case 31, in a 0.5-month-old male patient with right brachial plexus birth injury. C7 root avulsions (*arrow*) without associated pseudomeningocele were seen in the axial 3D-CISS image (*A*). Case 42, a 2-month-old female patient with right brachial plexus birth injury. The pseudomeningocele (*thick arrow*) without associated root avulsion (*thin arrows*) was seen at the C6–7 level in the axial 3D-CISS image (*B*).

**Sensitivity, specificity, positive and negative predictive values, and diagnostic accuracy of US and MRI in the surgically proven cases**

| | Sensitivity % | Specificity % | PPV % | NPV % | Accuracy % |
|---|---|---|---|---|---|
| For post-ganglionic injury | | | | | |
| US | 84 (66/78) | 100 (52/52) | 100 (66/66) | 81 (52/64) | 90 (118/130) |
| MRI | 100 (78/78) | 100 (52/52) | 100 (78/78) | 100 (52/52) | 100 (130/130) |
| For pre-ganglionic injury | | | | | |
| MRI | 84 (37/44) | 96 (83/86) | 92 (37/40) | 92 (83/90) | 92 (120/130) |

**Note:**—PPV indicates positive predictive value; NPV, negative predictive value.

ever, although all post-GIs at the C4–C7 levels were detected, US failed at the T1 and occasionally the C8 nerve root due to an improper window for the examination in 8 patients. In addition, the short necks of the patients and nerve root–bone relationship made evaluation difficult. Consequently, the lower nerve roots and trunks were not evaluated optimally in about 60% of patients. Previous studies with US mentioned similar technical challenges.[7-9]

The posttraumatic neuroma is a disorganized proliferation of regenerating axons at the proximal stump of a transected nerve, corresponding to lesion type III or IV in the Sunderland classification.[20] Thickening of the nerve root trunks might be related to neuroma and/or scar tissue, and the differentiation between them can be difficult by imaging methods. In the literature, the US and MR imaging criteria for the differential diagnosis between traction injury and neuroma have not been specified. We also could not find a distinguishing feature on US and MR imaging, in terms of the echogenicity, intensity, and size of the lesions, either at the initial diagnosis or during the follow-ups. Similarly, differentiation of the scar tissue from a neuroma was not possible in the studies by Abbott et al[3] and Wandler et al.[16] Therefore; imaging does not obviate the role of histopathologic examination for definitive diagnosis of these lesions.

Contrary to the post-GI, for the pre-GI, the US findings were not concordant with MR imaging and the surgical findings. This finding may be due to the technical insufficiency of US related to the artifacts caused by the transverse process of vertebrae. It has been reported that US can reveal root avulsion after traumatic BP injuries in adults.[21] However, the artifacts caused by vertebrae make it difficult to see intraspinal-intraforaminal injuries despite the high-frequency probes. Thus, US has a very limited value for showing the pre-GI and full extent of the injury. However, MR myelography is superior in the assessment of pre-GI compared with US because it allows obtaining high-quality, detailed anatomic images of the intraspinal-intraforaminal contents. Although MR myelography may have limitations related to CSF flow artifacts in showing the root avulsion, it is an effective method for demonstrating not only root avulsion but also the level of the injury.[6] Our study showed that MR myelography was successful in depicting the presence of the surgically proved root avulsion, and this finding was similar to those in previous studies.[6,22] The diagnostic accuracy of MR imaging was 92% in our study, which is also compatible with that in previous reports.[4] A pseudomeningocele can be seen with or without root avulsion, and the presence of a pseudomeningocele is highly indicative but not pathognomonic for a pre-GI.[3,23] There were 3 cases with pseudomeningocele but without root avulsion (cases 33, 39, and 42) in the present cohort.

In our study, those patients (75%) who recovered the upper trunk muscle strength spontaneously in the first 6 months of life had a complete neurologic recovery during the first 2 years of life, which is compatible with previous study findings.[12,24] The axon and its myelin covering (endoneurium) lose continuity with the cell body in grade III injury according to the Sunderland classification.[20] In addition to grade III injury, the perineurium is disrupted in grade IV injury; however, the nerve is still in continuity and surgical intervention is usually required to re-establish nerve transduction by removing the scar tissue.[20] In our study, 29 patients who improved spontaneously most likely had grade III injury. Compared with the range of 30%–90% recovery rate in the literature, our finding of 55% is still below the high expectations quoted in previous studies.[25,26] The varying degrees of the recovery rates show that patients need to be strictly monitored. For the diagnosis of BP injuries and treatment planning, a clinical assessment needs to be made in conjunction with an imaging examination. At this stage, US can play a complementary role to the clinical findings with its ability to visualize the interscalene space with high resolution. It yields information to clinicians about the presence, localization, and extension of the PST. When there is insufficient or no recovery in patients' follow-ups, MR myelography can be performed with superficial sedation instead of general anesthesia to show the pre-GI with fewer sequences such as STIR and 3D heavily T2WI, which, in turn, shortens the scan time. MR imaging can be performed earlier for patients with total BP palsy.

The strengths of our study are the prospective design, close follow-up of patients with the clinical examination and US, the presence of MR imaging of all patients, and the presence of the surgical findings for comparison. However, there are also some limitations: 1) The enhancement of the intradural nerve root and paraspinal muscles suggest functional impairment of the nerve despite morphologic continuity.[20] In our study, we did not use paramagnetic contrast agents in any of the examinations; thus, we could not demonstrate the possible damage to the nerve root, which could exist despite morphologic continuity, a form of pre-GI; 2) we did not evaluate the histopathology in all operated patients because of the limited biopsy specimen; 3) we did not evaluate the reproducibility and reliability of the US technique because of our patients' very young age (around 2 months); and 4) the follow-up period of 8 patients was <1 year, and these patients are still in follow-up at the time of this writing.

## CONCLUSIONS

High-resolution US can identify and locate the post-GI associated with the upper and middle trunks. The ability of US to evaluate pre- and the post-GI associated with the lower trunk was quite limited. US can be used as a complement to MR imaging; thus, the duration of MR imaging examination and the need for sedation can be reduced by US.

## REFERENCES


1. Abzug JM, Kozin SH. **Evaluation and management of brachial plexus birth palsy.** *Orthop Clin North Am* 2014;45:225–32 CrossRef Medline
2. Yoshikawa T, Hayashi N, Yamamoto S, et al. **Brachial plexus injury: clinical manifestations, conventional imaging findings, and the latest imaging techniques.** *Radiographics* 2006;26(Suppl 1):S133–43 CrossRef Medline
3. Abbott R, Abbott M, Alzate J, et al. **Magnetic resonance imaging of obstetrical brachial plexus injuries.** *Childs Nerv Syst* 2004;20:720–25 CrossRef Medline
4. Tagliafico A, Succio G, Serafini G, et al. **Diagnostic accuracy of MRI in adults with suspect brachial plexus lesions: a multicentre retrospective study with surgical findings and clinical follow-up as reference standard.** *Eur J Radiol* 2012;81:2666–72 CrossRef Medline
5. Carvalho GA, Nikkhah G, Matthies C, et al. **Diagnosis of root avulsions in traumatic brachial plexus injuries: value of computerized**

**tomography myelography and magnetic resonance imaging.** *J Neurosurg* 1997;86:69–76 CrossRef Medline
6. Gasparotti R, Ferraresi S, Pinelli L, et al. **Three-dimensional MR myelography of traumatic injuries of the brachial plexus.** *AJNR Am J Neuroradiol* 1997;18:1733–42 Medline
7. Demondion X, Herbinet P, Boutry N, et al. **Sonographic mapping of the normal brachial plexus.** *AJNR Am J Neuroradiol* 2003;24:1303–09 Medline
8. Graif M, Martinoli C, Rochkind S, et al. **Sonographic evaluation of brachial plexus pathology.** *Eur Radiol* 2004;14:193–200 CrossRef Medline
9. Smith EC, Xixis KI, Grant GA, et al. **Assessment of obstetric brachial plexus injury with preoperative ultrasound.** *Muscle Nerve* 2016;53:946–50 CrossRef Medline
10. Haber HP, Sinis N, Haerle M, et al. **Sonography of brachial plexus traction injuries.** *AJR Am J Roentgenol* 2006;186:1787–91 CrossRef Medline
11. Chen DZ, Cong R, Zheng MJ, et al. **Differential diagnosis between pre- and postganglionic adult traumatic brachial plexus lesions by ultrasonography.** *Ultrasound Med Biol* 2011;37:1196–203 CrossRef Medline
12. Narakas AO. **Obstetric brachial plexus injuries.** In: Lamb DW, ed. *The Paralysed Hand*. Edinburgh: Churchill Livingstone; 1987:116–35
13. Gilbert A, Razaboni R, Amar-Khodja S. **Indications and results of brachial plexus surgery in obstetrical palsy.** *Orthop Clin North Am* 1988;19:91–105 Medline
14. Amrami K, Port J. **Imaging the brachial plexus.** *Hand Clin* 2005;21:25–37 CrossRef Medline
15. Martinoli C, Bianchi S, Santacroce E, et al. **Brachial plexus sonography: a technique for assessing the root level.** *AJR Am J Roentgenol* 2002;179:699–702 CrossRef Medline
16. Wandler E, Lefton D, Babb J, et al. **Periscalene soft tissue: the new imaging hallmark in Erb palsy.** *AJNR Am J Neuroradiol* 2010;31:882–85 CrossRef Medline
17. Foad SL, Mehlman CT, Ying J. **The epidemiology of neonatal brachial plexus palsy in the United States.** *J Bone Joint Surg Am* 2008;90:1258–64 CrossRef Medline
18. Wolf H, Hoeksma AF, Oei SL, et al. **Obstetric brachial plexus injury: risk factors related to recovery.** *Eur J Obstet Gynecol Reprod Biol* 2000;88:133–38 CrossRef Medline
19. Kozin SH. **Brachial plexus microsurgical indications.** *J Pediatr Orthop* 2010;30:49–52 CrossRef
20. Laurent JP, Lee RT. **Birth-related upper brachial plexus injuries in infants: operative and nonoperative approaches.** *J Child Neurol* 1994;9:111–17 CrossRef Medline
21. Gruber H, Glodny B, Galiano K, et al. **High-resolution ultrasound of the supraclavicular brachial plexus: can it improve therapeutic decisions in patients with plexus trauma?** *Eur Radiol* 2007;17:1611–20 CrossRef Medline
22. Doi K, Otsuka K, Okamoto Y, et al. **Cervical nerve root avulsion in brachial plexus injuries: magnetic resonance imaging classification and comparison with myelography and computerized tomography myelography.** *J Neurosurg* 2002;96:277–84 Medline
23. Tharin BD, Kini JA, York GE, et al. **Brachial plexopathy: a review of traumatic and nontraumatic causes.** *AJR Am J Roentgenol* 2014;202:W67–75 CrossRef Medline
24. O'Brien DF, Park T, Noetzel MJ, et al. **Management of birth brachial plexus palsy.** *Childs Nerv Syst* 2006;22:103–12 CrossRef Medline
25. Greenwald AG, Schute PC, Shiveley JL. **Brachial plexus birth palsy: a 10-year report on the incidence and prognosis.** *J Pediatr Orthop* 1984;4:689–92 CrossRef Medline
26. Pondaag W, Malessy MJ, van Dijk JG, et al. **Natural history of obstetric brachial plexus palsy: a systematic review.** *Dev Med Child Neurol* 2004;46:138–44 CrossRef Medline

# Time Course of Cerebral Perfusion Changes in Children with Migraine with Aura Mimicking Stroke

K.M. Cobb-Pitstick, N. Munjal, R. Safier, D.D. Cummings, and G. Zuccoli

## ABSTRACT

**SUMMARY:** Hemiplegic migraine is a common cause of acute brain attack in pediatrics. MR imaging sequences useful in differentiating hemiplegic migraine from other entities include arterial spin-labeling, SWI, MRA, and DWI. There has been limited exploration on the simultaneous use of these sequences in pediatrics. We present 12 pediatric patients with acute hemiplegic migraine or migraine with aura who underwent MR imaging within 12 hours of symptom onset. Quantitative and qualitative analyses were performed on arterial spin-labeling; and qualitative analysis, on SWI and MRA sequences. All 12 patients had normal DWI and abnormal arterial spin-labeling findings. Furthermore, we observed a more rapid transition from hypoperfusion to rebound hyperperfusion in 3 patients compared with prior reports. These findings support the use of multimodal MR imaging to distinguish migraine with aura from stroke and the simultaneous use of these MR imaging sequences to improve understanding of perfusion changes during migraine with aura.

**ABBREVIATIONS:** ASL = arterial spin-labeling; rCBF = relative CBF

Hemiplegic migraine is one of the most common causes of acute brain attack (defined as acute onset of focal neurologic symptoms) seen in the pediatric emergency department, accounting for approximately one-third of pediatric brain attacks, and it can be difficult to differentiate from arterial ischemic stroke or TIA on initial presentation.[1,2] Hemiplegic migraine is defined according to the International Classification of Headache Disorders, 3rd edition[2] criteria by the presence of an aura characterized by fully reversible motor and visual, sensory, and/or speech/language symptoms and at least 2 of the following characteristics: 1) At least 1 aura symptom spreads gradually for ≥5 minutes and/or ≥2 symptoms occur in succession; 2) each individual aura symptom lasts 5–60 minutes, and motor symptoms generally last <72 hours (but may persist for weeks); 3) at least 1 aura symptom is unilateral; and 4) the aura is accompanied by or followed within 60 minutes by headache.[3] The pathophysiology of migraine and migraine with aura has not been determined, but leading hypotheses suggest a cortical spreading depression and subsequent local hypoperfusion as a trigger.[4,5]

Received January 19, 2018; accepted after revision April 11.

From the Department of Pediatrics (K.M.C.-P., N.M., R.S., D.D.C.), Division of Child Neurology, and Division of Pediatric Neuroradiology (G.Z.), Children's Hospital of Pittsburgh of University of Pittsburgh Medical Center, Pittsburgh, Pennsylvania.

Katherine M. Cobb-Pitstick and Neil Munjal contributed equally to this work.

Please address correspondence to Giulio Zuccoli, MD, Department of Radiology, Children's Hospital of Philadelphia, 3401 Civic Center Blvd, Wood Building 2115, Philadelphia, PA 19104; e-mail: giulio.zuccoli@gmail.com; zuccolig@email.chop.edu

http://dx.doi.org/10.3174/ajnr.A5693

MR imaging is becoming increasingly available for rapid assessment of pediatric brain attacks, even in patients who would previously have required sedation. Given the prevalence of migraine in the differential diagnosis of pediatric brain attack, reliable neuroimaging features differentiating migraine from acute ischemic stroke or TIA represent a valuable tool in guiding the appropriate level of initial work-up and management. MR imaging sequences that can be useful in differentiating hemiplegic migraine from other entities include arterial spin-labeling (ASL), SWI, and MRA. ASL implements a radiofrequency pulse that labels arterial blood water below the ROI and then captures the resulting signal as the labeled blood enters the ROI. These data are subtracted from the corresponding data obtained from a control sequence that does not label arterial blood water.[6] The degree of signal alteration correlates with the extent of arterial perfusion. SWI uses a gradient-echo pulse sequence to produce contrast and is blood oxygen level–dependent. The name derives from the use of the phase map of susceptibility difference in adjacent tissue and is the basis for blood oxygen level–dependent fMRI imaging. MRA provides a noninvasive, non-contrast-enhanced technique to image blood vessels. It can be viewed in the original 2D source or reconstructed into a 3D vessel image. Research has been published on the use of various MR imaging sequences to characterize the time course of perfusion changes in migraine, but there has previously been limited exploration of the simultaneous use of ASL, SWI, and MRA, particularly in pediatrics.[7-14] Our objective was to explore the use of multiple, noninvasive MR imaging sequences to better understand the relationship between clinical

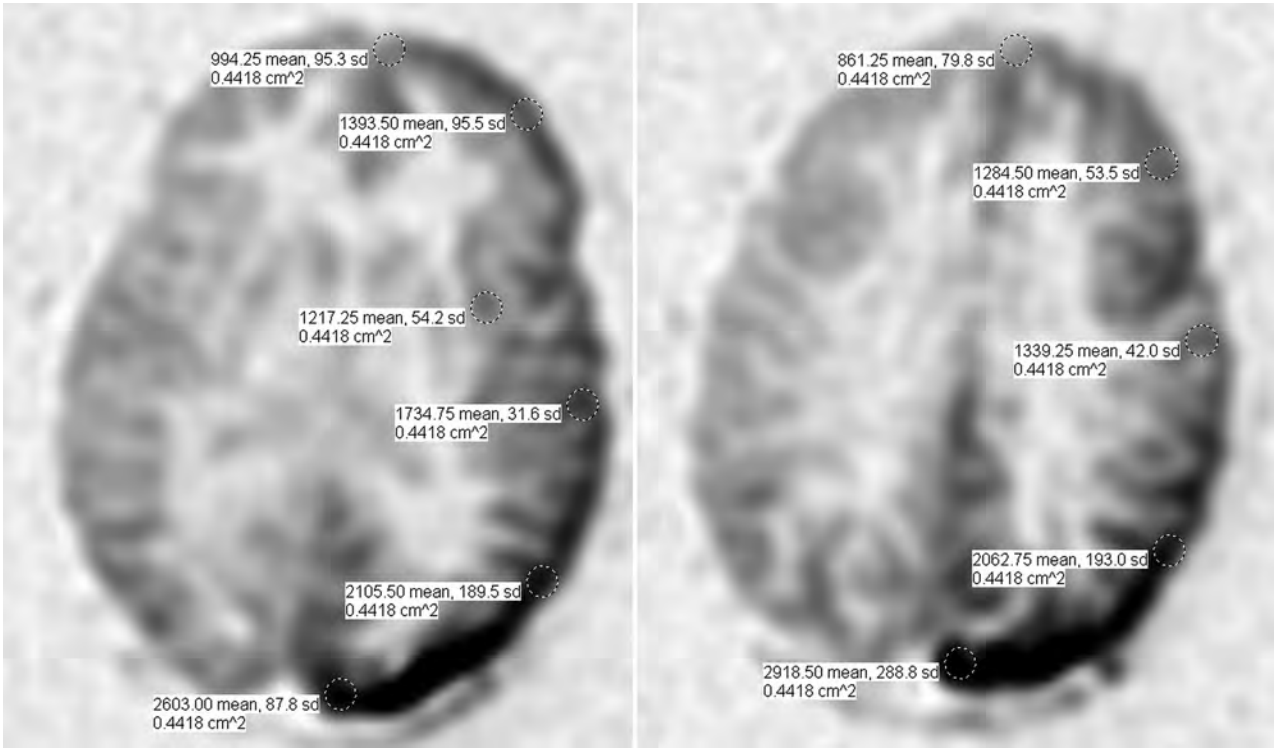


**FIG 1.** Modified ASPECTS system with 11 ROIs centered in the cortex at 2 contiguous levels on ASL imaging.

and MR imaging findings in pediatric hemiplegic migraine and migraine with aura.

### *Case Series*

This is a case series of children with migraine with focal neurologic symptoms and unilateral MR imaging findings who presented to the Children's Hospital of Pittsburgh emergency department. All cases were collected retrospectively under an institutional review board–approved study. Information was obtained from each patient's medical record and included clinical symptoms, family history, timing of MR imaging from the onset of symptoms, and headache severity. These data came from emergency department documentation and neurology consult notes. Patients were included in the study if they had undergone a stroke-protocol brain MR imaging within 12 hours of neurologic symptom onset, which included DWI, ASL, SWI, 3D-TOF MRA, and FLAIR imaging. Patients were excluded if symptoms were resolved at presentation, MR imaging was not performed before patient discharge from the emergency department or hospital, or MR imaging was performed >12 hours after symptom onset.

Qualitative MR imaging findings were identified for ASL, SWI, and MRA sequences. The images were obtained using a 1.5T scanner (Signa; GE Healthcare, Milwaukee, Wisconsin) with a 32-channel head coil. The technical factors used for ASL, SWI, and 3D-TOF MRA were the following: pseudocontinuous ASL—receiver bandwidth = 62.50, imaging mode = 3D, acceleration factor = 1.00, FOV = 24.0, slice thickness = 4.0, frequency = 512, phase = 8, frequency direction = anteroposterior, NEX = 3.00, autoshim = auto, phase correction = none; 3D SWI—flip angle, 15°, TE = 50.0 ms, TR = 78.3 ms, receiver bandwidth = 41.67, filter choice = none, FOV = 20.0, slice thickness = 3.0, slab = 32, overlap = 0, frequency = 288, phase = 224, frequency direction = anteroposterior, phase FOV = 1.00, autoshim = auto, phase correction = none; 3D-TOF—flip angle = 20°, TE = minimum, number of echoes = 1, TR = 23.0 ms, receiver bandwidth = 31.25, filter choice = none, imaging mode = 3D pulse sequence; TOF echo-spoiled gradient-echo—acceleration factor = 1.00, FOV = 16, slice thickness = 1.4, localizer per slab = 24, overlap locations = 6, frequency = 320, phase = 224, frequency direction = anteroposterior, FOV = 1.00.

Images were independently reviewed by 1 senior pediatric neuroradiologist and a pediatric neurologist blinded to the affected side for changes in brain perfusion on ASL, signal intensity of the cortical veins on SWI, and caliber of the intracranial arteries on 3D-TOF MRA, respectively. The final interpretation was reached by consensus in cases of disagreement between the readers. Eleven standard ROIs were selected in 2 axial planes on ASL sequences based on standard ASPECTS regions.[15]

Relative CBF (rCBV) values were calculated for standard 0.44-$cm^2$ circular regions at each ROI by using a PACS, and the affected side was subtracted from the nonaffected side. These rCBF differences were averaged to produce a net hemispheric blood flow difference. Of note, ROIs on the ASPECTS system are predominantly distributed in MCA territory. In this study, our extreme anterior and posterior ROIs were relocated as demonstrated in Fig 1 to provide anterior cerebral artery and posterior cerebral artery coverage. Quantitative statistical analysis was performed using the R statistical package (https://www.r-project.org).

Twelve patients met the inclusion criteria for this series. There were 6 female patients (50%) and 6 male patients (50%). Patients ranged from 9 to 16 years of age. Symptoms were localized to

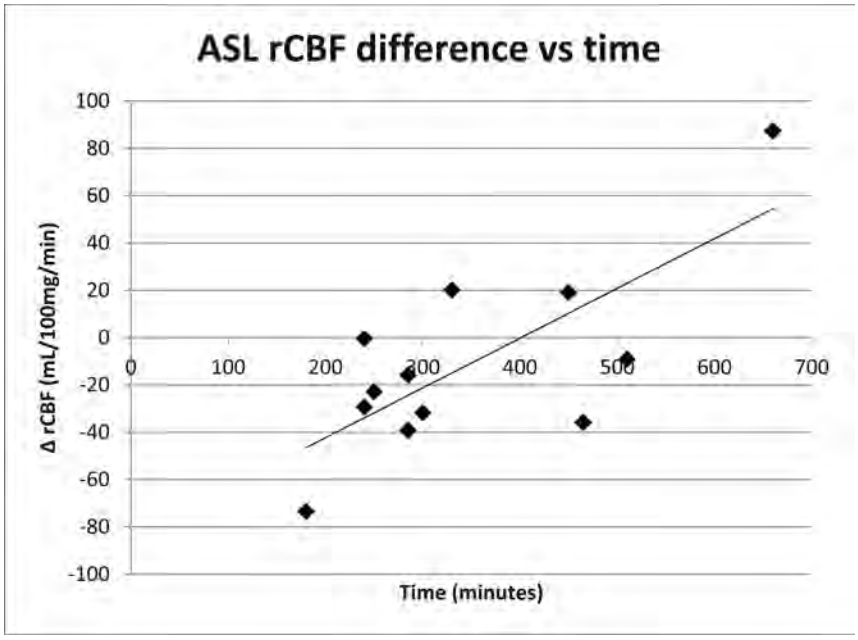


**FIG 2.** Time course of the brain perfusion changes in migraine with aura from symptom onset.

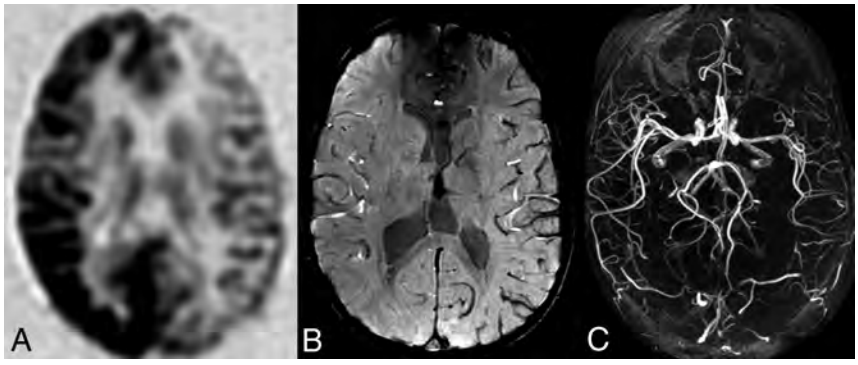


**FIG 3.** Patient 1. ASL demonstrates left hemispheric hypoperfusion (*A*). Note hypo-oxygenated cortical veins on SWI along the left cerebral hemisphere (*B*). MRA demonstrates thinning of the distal branches of the left MCA and posterior cerebral artery (*C*).

the right hemisphere in 4 patients and the left hemisphere in 8 patients. Brain MR imaging was performed between 3 and 11 hours from neurologic symptom onset. The median time of MR imaging following symptom onset was 4.9 hours. All patients demonstrated a difference in cerebral perfusion on ASL sequences compared with the unaffected hemisphere. Eight patients demonstrated a relative decrease in perfusion on ASL sequences. Of these patients, the 7 who had SWI and MRA available demonstrated a corresponding decreased signal and decreased caliber of vessels, respectively. Patient 12 did not have SWI or MRA sequences available for review. Patient 10 had normal SWI and MRA findings, and the ASL sequence demonstrated a signal difference of −0.4. Three patients had a relative increase in perfusion on ASL sequences. Patient 2 had normal SWI findings with an increased caliber of vessels on MRA. Patient 7 had normal SWI findings with a decreased vessel caliber on MRA. Patient 11 had normal SWI and MRA findings. DWI sequences for all patients were negative for restricted diffusion. The rCBF and time of MR imaging from symptom onset are shown in Fig 2. An example of the imaging findings during migraine with aura on multimodal MRI sequences for patient 1 is shown in Fig 3. The available demographic, clinical, time to MR imaging from symptom onset, and imaging features including relative cerebral blood flow are described in the Table. There was a significant positive relationship between the rCBF and time to MR imaging from symptom onset, $r(10) = 0.74$, $P < .05$.

## DISCUSSION

Information has been published on the use of various MR imaging sequences to characterize the time course of perfusion changes in migraine. Several case series on the use of noncontrast MR imaging in migraine have demonstrated prominent cerebral vasculature in the affected hemisphere on SWI sequences in the evaluation of the acute phase of migraine.[7-10] ASL is an increasingly more popular, available, and noninvasive MR imaging perfusion sequence that can provide insight into the pathophysiology of pediatric brain attacks, including pediatric migraine and stroke.[10] The presence of decreased relative cerebral perfusion on ASL in a DWI sequence with normal findings supports the simultaneous use of these sequences as the best MR imaging diagnostic tool for differentiating hemiplegic migraine from stroke. This combination was noted in 8 patients in this case series. ASL asymmetries in stroke or TIA would be localized to a specific vascular territory, while in our patients, migraine-with-aura asymmetries are seen throughout the affected hemisphere in multiple vascular territories. Moreover, lack of restricted diffusion while the patient is clinically symptomatic suggests migraine with aura over stroke.

Many studies have suggested the implementation of ASL in the evaluation of children presenting with focal neurologic symptoms, each with the finding of initial hypoperfusion followed by delayed hyperperfusion.[11-14] Boulouis et al[11] published a case series exploring the use of the ASL MR imaging sequence in children, which demonstrated decreased regional cerebral blood flow when obtained <14 hours after symptom onset and increased regional cerebral blood flow when obtained >17 hours after symptom onset. Lehman et al[12] demonstrated decreased pulsed ASL signal in 11 children who all had increased prominence of cortical or medullary veins on SWI, suggesting increased venous deoxyhemoglobin. In the Lehman et al study, ASL hypoperfusion persisted as long as 16.25 hours. Iizaku et al[13] also evaluated the changes in perfusion in 3 adult patients with focal neurologic symptoms and migraine whose MR imaging demonstrated initial hypoperfusion and delayed hyperperfusion on ASL >18–24

**Clinical and MRI findings in a cohort of patients presenting with atypical migraine**

| Patient No. | Age (yr) | Sex | Symptoms | Time of MRI from Symptom Onset (min) | SWI | MRA | ASL rCBF (mL/100 mg/min) |
|---|---|---|---|---|---|---|---|
| 1 | 10 | F | R paresis | 180 | ↓ | ↓ [a] | −73 |
| 2 | 13 | F | R paresis/anesthesia | 660 | Normal | ↑ | 87 |
| 3 | 13 | M | L paresis/anesthesia | 285 | ↓ | ↓ [a] | −15.8 |
| 4 | 12 | F | L anesthesia | 240 | ↓ | ↓ | −29.3 |
| 5 | 14 | M | R paresis | 510 | ↓ | ↓ | −9.0 |
| 6 | 15 | F | R paresis/anesthesia | 300 | ↓ | ↓ [b] | −31.7 |
| 7 | 13 | M | R paresis | 330 | Normal | ↓ | 20.2 |
| 8 | 9 | M | L anesthesia | 465 | ↓ | ↓ | −50.1 |
| 9 | 9 | M | L paresis | 285 | ↓ | ↓ [a] | −47.1 |
| 10 | 15 | F | R paresis/anesthesia | 240 | Normal | Normal | −0.4 |
| 11 | 16 | M | R paresis/anesthesia | 450 | Normal | Normal | 19.2 |
| 12 | 12 | F | R paresis/anesthesia | 250 | NA | NA | −22.8 |

**Note:**—L indicates left; R, right; SWI ↓, hypointensity; MRA ↓, decreased arterial caliber in the MCA territory; MRA ↑, increased arterial caliber in the MCA territory.
[a] Additional decrease in caliber of the posterior cerebral artery.
[b] Additional decrease in caliber of the posterior and anterior cerebral arteries.

hours after symptom onset. Pollock et al[14] similarly looked at a case series of 3 adults with migraine and noted cerebral hyperperfusion on ASL imaging >6 hours after the onset of neurologic symptoms.

Our results demonstrate a clear link between brain perfusion changes and the time course of migraine with aura. We observed a wide variation in the duration of perfusion changes, lasting up to at least 11 hours, the longest time to scan from symptom onset in this case series. Three patients in this series demonstrated increased perfusion on ASL within this time window, indicating the transition to hyperperfusion by 11, 5.5, and 7.5 hours. This is earlier than described in other studies.[11-13] Each technique reviewed in this study provided data supporting the following pattern: apparent constriction of distal vessels on MRA, the presence of deoxygenated blood in cerebral veins on SWI, and initial hypoperfusion followed by a rebound hyperperfusion on ASL in the affected hemisphere. Patient 10 in this series demonstrated normal SWI and MRA findings and an ASL sequence with rCBF of only −0.4 at 4 hours, which may represent near-resolution of MR imaging perfusion changes or the transition from hypoperfusion to pseudonormalization during this patient's migraine. Most interesting, patient 7 in this series demonstrated discordance between the MR imaging sequences with a normal SWI signal and decreased vessel caliber on MRA but increased rCBF on pseudocontinuous ASL 5.5 hours from symptom onset. The discordance between pseudocontinuous ASL and SWI could indicate that ASL is more sensitive than SWI sequences in detecting imaging changes related to hemiplegic migraine. It could also indicate that the transition from hypoperfusion to hyperperfusion may be occurring sooner in the progression of migraine than previously thought, as observed in other case reports.[14] The decreased vessel caliber on MRA with increased rCBF on ASL highlights the variability in neurovascular coupling and recovery characteristics with migraine. Migraine leads to reversible disturbances in neurovascular coupling that will affect the timing of ASL hyperperfusion and normalization of perfusion.[16]

Current models of migraine suggest that cortical spreading depression is a likely cause of the migraine aura. Spreading depression is a neurovascular phenomenon in which a self-propagating wave of depolarization results in spreading cortical hypoactivity and resultant vasoconstriction. Our data support this model through 2 observations: First, the distribution of changes across all sequences (ASL, SWI, MRA) cross vascular territories but respect the hemispheric boundary. Second, ASL findings demonstrate a trend of initial hemispheric hypoperfusion followed by remote rebound hyperperfusion hours later. In our imaging studies, the spatial resolution of ASL was not sufficient to allow more detailed analysis correlating symptoms and spreading depression localization.[5] The decreased caliber in the posterior and/or anterior circulation observed in 4 of 12 patients in the present study confirms that multiple vascular territories are affected during migraine with aura.[16]

One limitation of this series is the lack of standardized documentation detailing the time course of each patient's clinical symptoms, including aura/headache onset and duration. This may explain some of the variability in rCBF findings. This discordance also emphasizes the value of obtaining multiple imaging sequences to assist in interpreting the patient's symptoms. An additional limitation of this study is that brain MR imaging was performed at only 1 time point rather than ≥2 time points during the brain attack. Multiple samples of imaging data would allow more effective characterization of the evolution of perfusion changes during the migraine attack. Another limitation of this study is that for many of these patients, this was the first or only known attack of migraine with focal neurologic symptoms, which would not fulfill the International Classification of Headache Disorders, 3rd edition, criteria for migraine with aura or hemiplegic migraine.[2]

The management and disposition of migraine with aura differs remarkably from the entities in the differential diagnosis. Given the history and imaging findings, more than half of the patients in the series were not admitted to the hospital for a work-up and monitoring as would be typical for TIA; they were, instead, referred to the outpatient neurology clinic to establish headache care. Most patients were offered migraine prophylaxis treatment options (daily magnesium, riboflavin, tricyclic antidepressant, or antiepileptic). Given this difference, continuing to define criteria (both clinical and imaging) to identify and separate migraine from ischemic stroke in children by implementing noninvasive neuroimaging protocols in the emergency departments would be highly beneficial. This case series supports the addition of an ASL

sequence in the evaluation of pediatric patients presenting with an acute brain attack.

## CONCLUSIONS

The systematic use of multimodal MR imaging sequences including ASL, SWI, MRA, and DWI allows practitioners to distinguish hemiplegic migraine from stroke, with ASL being the most sensitive sequence to detect hemiplegic migraine. Our data suggest that the phenomenon of rebound hyperperfusion occurs earlier during a migraine attack than has been previously reported.

## REFERENCES


1. Mackay MT, Chua ZK, Lee M, et al. **Stroke and nonstroke brain attacks in children.** *Neurology* 2014;82:1434–40 CrossRef Medline
2. Headache Classification Committee of the International Headache Society (IHS). **The International Classification of Headache Disorders, 3rd edition.** *Cephalalgia* 2018;38:1–211 CrossRef Medline
3. Hadjikhani N, Sanchez Del Rio M, Wu O, et al. **Mechanisms of migraine aura revealed by functional MRI in human visual cortex.** *Proc Natl Acad Sci U S A* 2001;98:4687–92 CrossRef Medline
4. Pietrobon D. **Lessons from familial hemiplegic migraine and cortical spreading depression.** In: Dalkara T, Moskowitz MA, eds. *Neurobiological Basis of Migraine*. Hoboken: John Wiley & Sons; 2017:251–52
5. Grade M, Hernandez Tamames JA, Pizzini FB, et al. **A neuroradiologist's guide to arterial spin labeling MRI in clinical practice.** *Neuroradiology* 2015;57:1181–202 CrossRef Medline
6. Altinok D, Agarwal A, Ascadi G, et al. **Pediatric hemiplegic migraine: susceptibility weighted and MR perfusion imaging abnormality.** *Pediatr Radiol* 2010;40:1958–61 CrossRef Medline
7. Bosemani T, Burton VJ, Felling RJ, et al. **Pediatric hemiplegic migraine: role of multiple MRI techniques in evaluation of reversible hypoperfusion.** *Cephalalgia* 2014;34:311–15 CrossRef Medline
8. Fedak EM, Zumberge NA, Heyer GL. **The diagnostic role for susceptibility-weighted MRI during sporadic hemiplegic migraine.** *Cephalalgia* 2013;33:1258–63 CrossRef Medline
9. Gocmen R, Gunbey C, Arsava EM, et al. **Susceptibility-weighted magnetic resonance imaging findings of two pediatric migraine patients with aura.** *Neuropediatrics* 2016;47:46–50 CrossRef Medline
10. Chen J, Licht DJ, Smith SE, et al. **Arterial spin labeling perfusion MRI in pediatric arterial ischemic stroke: initial experiences.** *J Magn Reson Imaging* 2009;29:282–90 CrossRef Medline
11. Boulouis G, Shotar E, Dangouloff-Ros V, et al. **Magnetic resonance imaging arterial-spin-labeling perfusion alteration in childhood migraine with atypical aura: a case-control study**. *Dev Med Child Neurol* 2016;58:965–69 CrossRef Medline
12. Lehman LL, Danehy AR, Trenor CC 3rd, et al. **Transient focal neurologic symptoms correspond to regional cerebral hypoperfusion by MRI: a stroke mimic in children.** *AJNR Am J Neuroradiol* 2017;38:2199–202 CrossRef Medline
13. Iizaku T, Tominaga N, Kaneko J, et al. **Biphasic neurovascular changes in prolonged migraine aura in familial hemiplegic migraine type 2.** *J Neurol Neurosurg Psychiatry* 2015;86:344–53 CrossRef Medline
14. Pollock JM, Deibler AR, Burdette JH, et al. **Migraine associated cerebral hyperperfusion with arterial spin-labeled MR imaging.** *AJNR Am J Neuroradiol* 2008;29:1494–97 CrossRef Medline
15. Barber PA, Demchuk AM, Zhang J, et al; ASPECTS Study Group. **Validity and reliability of a quantitative computed tomography score in predicting outcome of hyperacute stroke before thrombolytic therapy.** *Lancet* 2000;355:1670–74 CrossRef Medline
16. Wolf ME, Held VE, Förster A, et al. **Pearls & oy-sters: dynamics of altered cerebral perfusion and neurovascular coupling in migraine aura.** *Neurology* 2011;77:e127–28 CrossRef Medline

# Feasibility of a Synthetic MR Imaging Sequence for Spine Imaging

M.I. Vargas, M. Drake-Pérez, B.M.A Delattre, J. Boto, K.-O. Lovblad, and S. Boudabous

## ABSTRACT

**BACKGROUND AND PURPOSE:** Synthetic MR imaging is a method that can produce multiple contrasts from a single sequence, as well as quantitative maps. Our aim was to determine the feasibility of a synthetic MR image for spine imaging.

**MATERIALS AND METHODS:** Thirty-eight patients with clinical indications of infectious, degenerative, and neoplastic disease underwent an MR imaging of the spine (11 cervical, 8 dorsal, and 19 lumbosacral MR imaging studies). The SyntAc sequence, with an acquisition time of 5 minutes 40 seconds, was added to the usual imaging protocol consisting of conventional sagittal T1 TSE, T2 TSE, and STIR TSE.

**RESULTS:** Synthetic T1-weighted, T2-weighted, and STIR images were of adequate quality, and the acquisition time was 53% less than with conventional MR imaging. The image quality was rated as "good" for both synthetic and conventional images. Interreader agreement concerning lesion conspicuity was good with a Cohen $\kappa$ of 0.737. Artifacts consisting of white pixels/spike noise across contrast views, as well as flow artifacts, were more common in the synthetic sequences, particularly in synthetic STIR. There were no statistically significant differences between readers concerning the scores assigned for image quality or lesion conspicuity.

**CONCLUSIONS:** Our study shows that synthetic MR imaging is feasible in spine imaging and produces, in general, good image quality and diagnostic confidence. Furthermore, the non-negligible time savings and the ability to obtain quantitative measurements as well as to generate several contrasts with a single acquisition should promise a bright future for synthetic MR imaging in clinical routine.

Radiologists base their diagnoses on morphologic and, increasingly more, quantitative imaging. The current trend in imaging is to reach a diagnosis based on not only morphologic and qualitative evaluation but also methods that can provide quantitative information. Quantitative imaging can be achieved by 2 different techniques: synthetic (used in clinical practice) and fingerprinting (used solely for research purposes).[1,2] Synthetic MR imaging is a method that can produce multiple contrasts from a single sequence, as well as quantitative T1, T2, STIR, and proton-density maps. This offers the possibility of shortening the study duration and the option of relying on more objective parameters to reach a diagnosis. Recently, this emerging technique has been applied to several brain diseases in adults[3,4] and children,[5-7] but to our knowledge, it has never been used in spine imaging. The purpose of this work was to apply synthetic MR imaging to the spine[6] and spinal cord and to compare the overall image quality, diagnostic confidence, and lesion conspicuity produced by synthetic MR imaging with conventional sequences.

## MATERIALS AND METHODS

### Patients

The local ethics committee on research involving humans approved this study (CCER 2016–1821).

A synthetic MR image was added to our usual spine imaging protocol in 38 patients referred to our institution with suspicion of multiple sclerosis or degenerative, infectious, and neoplastic diseases, or for postsurgical follow-up. Exclusion criteria were children, pregnant women, and motion artifacts on the images.

### Image Acquisition

Synthetic imaging was performed in addition to the conventional sequences (T1, FSE, T2, proton-density, and STIR) used in daily clinical practice at our hospital. The patients were

Received April 9, 2018; accepted after revision May 29.

From the Division of Diagnostic and Interventional Neuroradiology (M.I.V., J.B., K.-O.L.), Geneva University Hospitals and Faculty of Medicine of Geneva, Geneva, Switzerland; Department of Radiology (M.D.-P.), University Hospital Marqués de Valdecilla, IDIVAL, Santander, Spain; and Division of Radiology (B.M.A.D., S.B.), Geneva University Hospitals, Geneva, Switzerland.

Please address correspondence to Maria Isabel Vargas, MD, Geneva University Hospitals, Division of Diagnostic and Interventional Neuroradiology of Geneva University Hospitals, DISIM, Rue Gabrielle-Perret-Gentil 4, 1211 Genève 14, Switzerland; e-mail: maria.i.vargas@hcuge.ch

http://dx.doi.org/10.3174/ajnr.A5728

scanned on an Ingenia 1.5T scanner (Philips Healthcare, Best, the Netherlands).

The SyntAc sequence (Philips Healthcare) is based on a turbo spin-echo acquisition with a saturation pulse of 120°, four TIs, and 2 TEs, producing 8 images with different contrasts. These images are then used by the SyMRI software, Version 8 (SyntheticMR, Linköping, Sweden)[8] to generate T1, T2, and proton-density quantitative images and to create synthetic T1, T2, and STIR contrasts with specific TEs, TRs, and TIs, which are chosen in postprocessing.

The sequence parameters were the following: sagittal orientation, FOV = 200 × 321 mm, acquisition (reconstruction), voxel size = 0.89 × 1.48 mm (0.71 × 0.72 mm), 15 contiguous 4-mm-thickness slices, TE = 11/100 ms, TR = 2485 ms, TSE factor = 12, sensitivity encoding acceleration factor = 2. The acquisition time of the synthetic sequence is 5 minutes 40 seconds. Synthetic images were generated with matching TE/TR parameters and compared with the conventional sequences (T1, T2, and STIR when available) with an imaging acquisition time of 11 minutes 20 seconds. TI was chosen to maximize suppression of the fat signal.

Two sets of images were created for each patient: conventional and synthetic sequences.

### Image Evaluation

Two qualified readers, with 15 and 11 years of experience, respectively, reviewed the images. Image quality was evaluated on conventional T1, T2, and STIR images (when available) and on synthetic images for each patient in random order. Image quality was rated as "poor," "fair," or "good" (scores of 1, 2, and 3, respectively). The presence or absence of lesions was also assessed. Subsequently, both readers rated their degree of confidence regarding the presence or absence of a lesion, which was recorded as "certain" (score = 1) or "not certain" (score = 0). The presence or absence and the type of artifacts were also evaluated.

### Statistical Analysis

The medians of the scores for image quality and lesion conspicuity obtained with each method (synthetic versus conventional) were compared using the Wilcoxon test. The scores assigned by each reader were compared by the same method. Interreader agreement regarding the certainty of the presence or absence of a lesion was evaluated by the Cohen κ. All statistics were performed with RStudio (Version 3.3.2; http://rstudio.org/download/desktop).

## RESULTS

A total of 38 patients were included in this study (22 males, 16 females; mean age, 57 years; age range, 17–87 years). Clinical indications for MR imaging were as follows: degenerative pathology, multiple sclerosis, postsurgical follow-up, and diagnosis or follow-up of tumors. Eleven cervical, 8 dorsal, and 19 lumbosacral MR imaging studies were performed.

Image quality was rated as good in synthetic and conventional images by both readers. However, there was a statistically significant difference in the scores assigned for image quality by reader 2 ($P = .02$) but not reader 1 ($P = .053$). Figure 1 shows the distribution of scores for different methods and readers. Although the medians are similar, the synthetic method produced more "fair" and "poor" scores ($n = 3$ and $n = 2$, respectively, for reader 1 and $n = 6$ and $n = 0$ for reader 2).

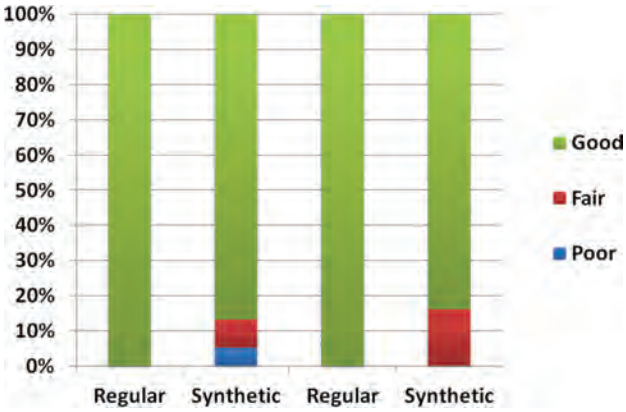


**FIG 1.** Distribution of scores for image-quality ratings for readers 1 (*left*) and 2 (*right*).

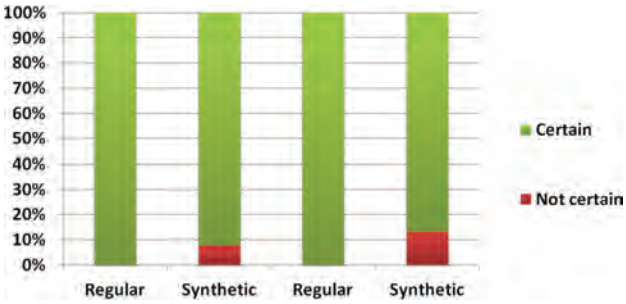


**FIG 2.** Distribution of scores for certainty of the presence or absence of a lesion for readers 1 (*left*) and 2 (*right*).

There was agreement between readers in identifying the presence or absence of lesions in all cases, except 1 case for reader 1 and 2 cases for reader 2. In these 3 cases, the lesions were not detected on the synthetic sequence but were easily identified on the conventional sequences. Lesions that were not present on the conventional images were also not incorrectly detected on the synthetic images (no false-positives).

The relative frequencies of certainty for the presence or absence of a lesion, with a median score of 1, are shown in Fig 2. Interreader agreement was good with a Cohen κ of 0.737, but there were cases in which there was discordance between the synthetic and conventional images ($n = 3$ for reader 1, $n = 5$ for reader 2). This difference was not statistically significant for reader 1 ($P = .149$), but it was significant for reader 2 ($P = .04$).

Artifacts consisting of white pixels/spike noise across contrast views and flow artifacts were more common in the synthetic sequences (except proton-density), especially in synthetic STIR (Fig 3).

There were no statistically significant differences between readers regarding the scores assigned for image quality or lesion conspicuity. The Table summarizes these results.

## DISCUSSION

The clinical use of synthetic MR imaging has focused mainly on brain pathology. The first mention of synthetic images possibly having a diagnostic value comparable with that of conventional sequences was in a study by Blystad et al[4] in 2012. Other studies

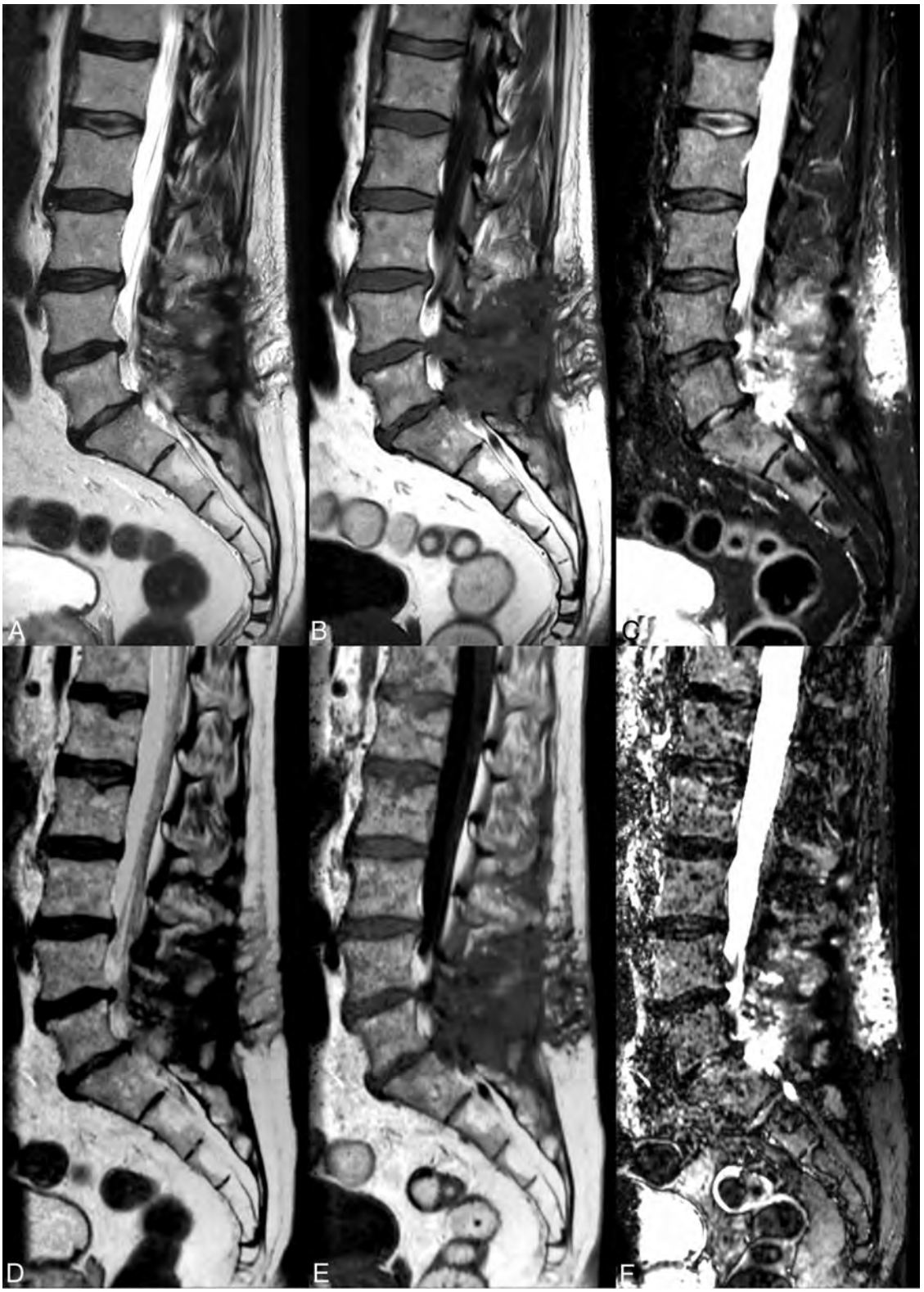


**FIG 3.** Conventional FSE T2 (*A*), spin-echo T1 (*B*), and STIR (*C*) images show a postsurgical lumbar spine with postoperative changes in the posterior soft tissues. The synthetic images (*D–F*) depict these changes with similar detail. Note the dirty appearance of the vertebral bodies observed in the synthetic reconstructions and flow artifacts from the aorta, especially in the synthetic STIR sequence.

have since assessed the clinical feasibility of synthetic MR imaging across different neurologic conditions[8,9] such as multiple sclerosis[10] and metastatic disease of the brain[11] and in the pediatric population.[5-7,12,13]

This technique has also been recently used for musculoskeletal imaging. A recent study, focusing on imaging of the normal knee,[14] assessed the feasibility and diagnostic accuracy of synthetic MR imaging compared with conventional MR imaging as

**Median scores for image quality and the certainty of the presence or absence of a lesion and statistical differences between methods and readers**[a]

| | Reader 1 | | | Reader 2 | | | Between Readers | |
|---|---|---|---|---|---|---|---|---|
| | Conventional | Synthetic | *P* | Conventional | Synthetic | *P* | Conventional | Synthetic |
| Image quality | 3 | 3 | .053 | 3 | 3 | .02 | 1.00 | .78 |
| Certainty of the presence or absence of a lesion | 1 | 1 | .149 | 1 | 1 | .04 | 1.00 | .35 |

[a] Scores for image quality: 1 = poor, 2 = fair, 3 = good; scores for the certainty of the presence or absence of a lesion: 0 = not certain, 1 = certain.

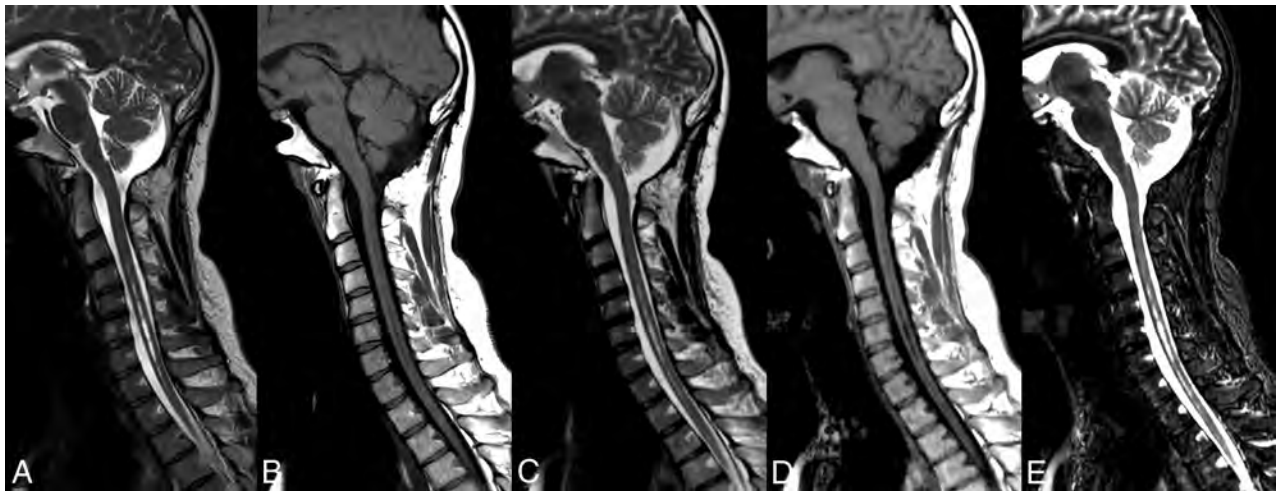


**FIG 4.** Sagittal conventional FSE T2 (*A*) and spin-echo T1 (*B*) images and synthetic T2 (*C*), T1 (*D*), and STIR (*E*) images illustrate a syrinx of the cervical cord. Note the same level of detail in both types of sequences.

well as the utility of synthetic quantitative T2 maps of the different knee structures compared with conventional T2 mapping sequences. The conclusion was that synthetic MR imaging provided comparable image quality and offered the potential to reduce the overall examination time. An exception was noted for bone marrow where the relative signal intensity and contrast of synthetic T1 images were lower than on conventional T1. Other studies focused on the feasibility of synthetic MR imaging for knee pathology.[15,16] To our knowledge, this is the first study exploring the potential utility of synthetic MR imaging for spine and spinal cord imaging in clinical routine (Figs 4 and 5). In this pilot study, synthetic MR has been shown to be a feasible alternative or complement to conventional T1WI, T2WI, and STIR sequences in spine imaging. Image quality was considered not significant different from that produced by conventional sequences, and both diagnostic confidence and lesion conspicuity were at acceptable levels. These results are in agreement with previous reports stating that synthetic and conventional imaging have similar diagnostic utility.[4,6,9,10]

Some differences were nevertheless observed between the 2 methods. The synthetic sequence, on occasion, had less contrast, a "dirty" appearance to the images, and less resolution (Fig 2), resulting in lower image-quality scores assigned by the readers in some cases. These differences were, however, not statistically significant and did not affect the overall perception of imaging quality or the diagnostic confidence. As previously reported, arbitrary signal changes found in the voxels containing 2 tissues that are particularly different are thought to be partial volume artifacts because they cannot be described using a monoexponential function. Consequently, fitted T1 and T2 relaxation appears as a combination of the 2 tissue values[3,17] and can represent a limitation in synthetic imaging. In contrast, some authors described synthetic T1-weighted images having higher but not significantly different mean overall image-quality scores than conventional images and less subjective noise.[6] This finding was due to the relatively low signal-to-noise ratio on conventional T1-weighted images.

The different backgrounds of the 2 readers (neuroradiology and musculoskeletal radiology, respectively) are probably the main factors affecting the lack of agreement observed in some cases. For example, some benign spine lesions, such as hemangiomas, were identified as abnormalities by reader 2, but minimized by reader 1.

With respect to the artifacts produced by synthetic MR imaging, it is known that synthetic FLAIR images of the brain have more pronounced artifacts,[18] requiring adding conventional FLAIR sequences to the imaging protocol. At the level of the spine, image artifacts were particularly noticeable in the synthetic STIR sequence, pulsatile (vascular) flow artifacts (Fig 2) being the most frequent ones. Additionally, a dirty appearance to the images was observed in all synthetic sequences. Artifacts secondary to the presence of metal in the spine were identified on the synthetic sequences but were not more pronounced than in the conventional sequences (Fig 6).

These artifacts occurred more often in the dorsal and lumbar spine, where the synthetic images showed more noise compared with scans of the cervical spine, almost certainly due to a higher number of channels and coils used to image this area (spine and cervical coils versus spine coil only in the dorsolumbar region).

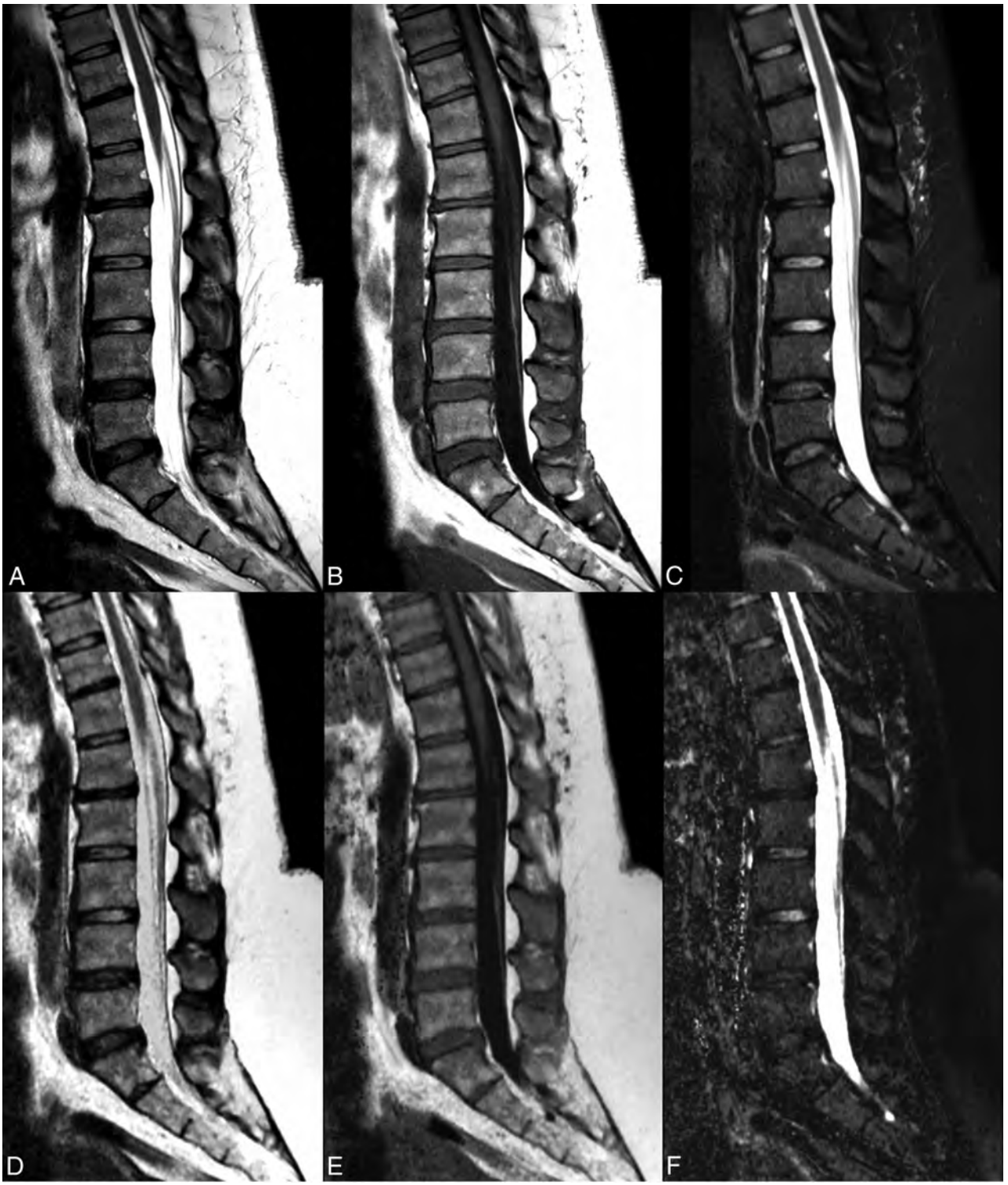


**FIG 5.** The normal dorsolumbar spine with conventional (*A–C*) and synthetic (*D–F*) sequences.

MR imaging time should be considered, especially in spine imaging due to the high prevalence of spinal pathology and, consequently, the high number of requests for MR imaging of this region. Furthermore, patients requiring spinal imaging frequently have back pain and find it more difficult to remain supine for long periods. Currently used imaging protocols for the spine have an average duration of approximately 30 minutes when the clinical indication does not warrant the use of contrast agent or only part of the spine needs to be imaged, as in disc herniation. When contrast administration is indicated or the whole spine needs to be imaged, the acquisition time is approximately 1 hour.

The SyntAc sequence was adapted for spine imaging and can produce at least 3 conventional sequences (T1, T2, STIR), which usually require an acquisition time of 11 minutes 20 seconds, offering the possibility of generating other contrasts if required. In

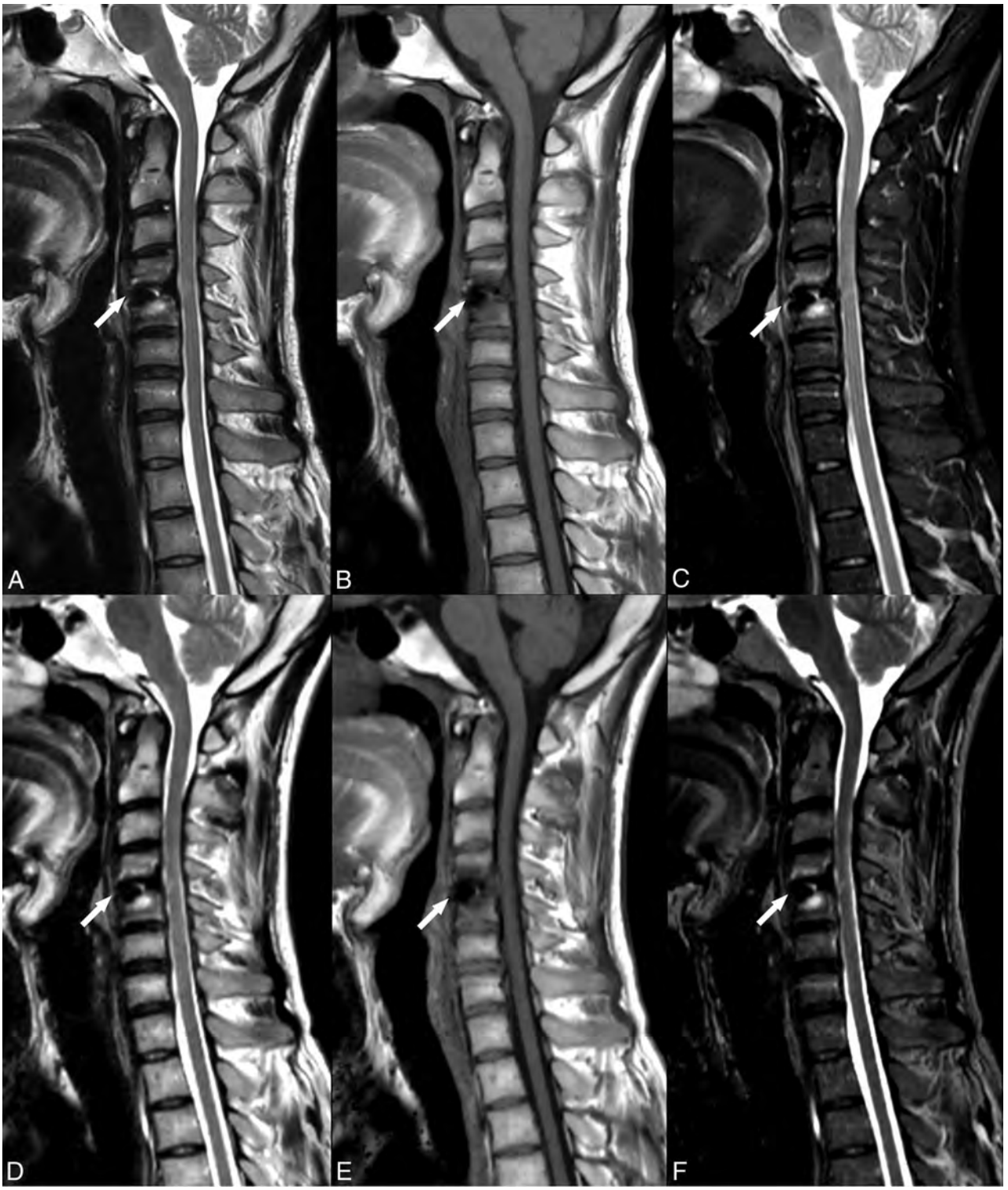


**FIG 6.** Sagittal conventional FSE T2 (*A*), spin-echo T1 (*B*), and STIR (*C*) sequences and corresponding synthetic sequences (*D–F*) in a patient with an intervertebral cage (*arrows*). Note that the degree of magnetic susceptibility artifacts is the same in both sequences.

the present study, the acquisition time of synthetic MR imaging (5 minutes 40 seconds) was approximately half of that required for conventional sequences. Sagittal synthetic spine MR imaging could therefore potentially replace conventional sagittal T1, T2, and STIR sequences for imaging 1 spinal region (cervical, dorsal, or lumbar) and halve the acquisition time. However, if fat-saturated postcontrast sequences were needed, they would be obtained separately by conventional methods.

In addition to allowing shorter acquisition times, synthetic sequences provide quantitative T1, T2, and proton-density maps (Fig 7). These can be used to derive relaxometry parameters of spinal components,[19] thus providing quantitative information of

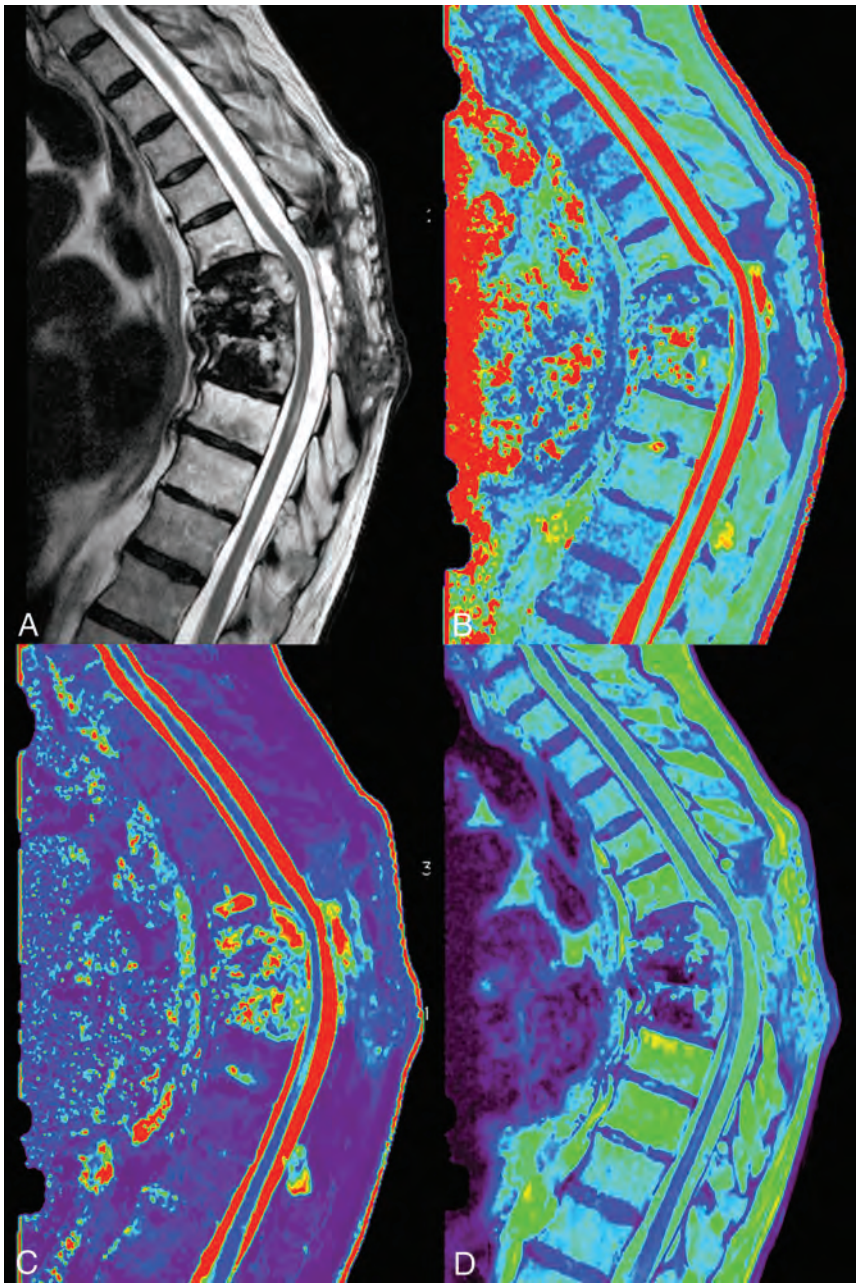


**FIG 7.** The dorsal spine in a patient with bone metastases illustrated by conventional FSE T2 (*A*) as well as T2 (*B*), T1 (*C*), and proton-density (*D*) maps.

interest for research and potentially clinical purposes with a view to using these quantified parameters daily in the assessment of common spine diseases (demyelinating diseases, degenerative conditions, spondylodiscitis).

In this study, identical TR and TE parameters were used in all patients to produce the synthetic sequences.

The main limitations of this study were the relatively small sample size and the limited number of pathologies in the patients included. From our observation, a compromise is still needed to increase the SNR while maintaining a reasonable acquisition time in the dorsolumbar region. This could potentially be improved with the implementation of this sequence on 3T MR imaging. Conversely, in our study, the image quality and diagnostic confidence were very good in the cervical area, where the SyntAc sequence currently produces the best results.

We believe that our findings could facilitate the integration of quantitative MR imaging in clinical routine.

## CONCLUSIONS

Synthetic MR imaging is feasible in spine imaging. However, some work and development are still required to improve synthetic STIR to reduce flow artifacts and increase the signal-to-noise ratio, particularly in the lumbar region. We believe that in the future, a significant reduction in acquisition time will be possible with this technique without sacrificing diagnostic accuracy. Furthermore, the quantitative information generated

with this method will allow a novel approach to the diagnosis of spine disease.

## REFERENCES


1. Liao C, Bilgic B, Manhard MK, et al. **3D MR fingerprinting with accelerated stack-of-spirals and hybrid sliding-window and GRAPPA reconstruction.** *Neuroimage* 2017;162:13–22 CrossRef Medline
2. European Society of Radiology (ESR). **Magnetic resonance fingerprinting: a promising new approach to obtain standardized imaging biomarkers from MRI.** *Insights Imaging* 2015;6:163–65 CrossRef Medline
3. Hagiwara A, Warntjes M, Hori M, et al. **SyMRI of the brain: rapid quantification of relaxation rates and proton density, with synthetic MRI, automatic brain segmentation, and myelin measurement.** *Invest Radiol* 2017;52:647–57 CrossRef Medline
4. Blystad I, Warntjes JB, Smedby O, et al. **Synthetic MRI of the brain in a clinical setting.** *Acta Radiol* 2012;53:1158–63 CrossRef Medline
5. Lee SM, Choi YH, You SK, et al. **Age-related changes in tissue value properties in children: simultaneous quantification of relaxation times and proton density using synthetic magnetic resonance imaging.** *Invest Radiol* 2018;53:236–45 CrossRef Medline
6. Lee SM, Choi YH, Cheon JE, et al. **Image quality at synthetic brain magnetic resonance imaging in children.** *Pediatr Radiol* 2017;47:1638–47 CrossRef Medline
7. McAllister A, Leach J, West H, et al. **Quantitative synthetic MRI in children: normative intracranial tissue segmentation values during development.** *AJNR Am J Neuroradiol* 2017;38:2364–72 CrossRef Medline
8. Warntjes JB, Leinhard OD, West J, et al. **Rapid magnetic resonance quantification on the brain: optimization for clinical usage.** *Magn Reson Med* 2008;60:320–29 CrossRef Medline
9. Tanenbaum LN, Tsiouris AJ, Johnson AN, et al. **Synthetic MRI for clinical neuroimaging: results of the Magnetic Resonance Image Compilation (MAGiC) prospective, multicenter, multireader trial.** *AJNR Am J Neuroradiol* 2017;38:1103–10 CrossRef Medline
10. Granberg T, Uppman M, Hashim F, et al. **Clinical feasibility of synthetic MRI in multiple sclerosis: a diagnostic and volumetric validation study.** *AJNR Am J Neuroradiol* 2016;37:1023–29 CrossRef Medline
11. Hagiwara A, Andica C, Hori M, et al. **Synthetic MRI showed increased myelin partial volume in the white matter of a patient with Sturge-Weber syndrome.** *Neuroradiology* 2017;59:1065–66 CrossRef Medline
12. Betts AM, Leach JL, Jones BV, et al. **Brain imaging with synthetic MR in children: clinical quality assessment.** *Neuroradiology* 2016;58:1017–26 CrossRef Medline
13. West H, Leach JL, Jones BV, et al. **Clinical validation of synthetic brain MRI in children: initial experience.** *Neuroradiology* 2017;59:43–50 CrossRef Medline
14. Park S, Kwack KS, Lee YJ, et al. **Initial experience with synthetic MRI of the knee at 3T: comparison with conventional T1 weighted imaging and T2 mapping.** *Br J Radiol* 2017;90:20170350 CrossRef Medline
15. Yi J, Lee YH, Song HT, et al. **Clinical feasibility of synthetic magnetic resonance imaging in the diagnosis of internal derangements of the knee.** *Korean J Radiol* 2018;19:311–19 CrossRef Medline
16. Boudabbous S, Neroladaki A, Bagetakos I, et al. **Feasibility of synthetic MRI in knee imaging in routine practice.** *Acta Radiol Open* 2018;7:2058460118769686 CrossRef Medline
17. Whittall KP, MacKay AL, Li DK. **Are mono-exponential fits to a few echoes sufficient to determine T2 relaxation for in vivo human brain?** *Magn Reson Med* 1999;41:1255–57 CrossRef Medline
18. Vargas MI, Boto J, Delatre BM. **Synthetic MR imaging sequence in daily clinical practice.** *AJNR Am J Neuroradiol* 2016 Jul 21. [Epub ahead of print] CrossRef Medline
19. Drake-Pérez M, Delattre BM, Boto J, et al. **Normal values of magnetic relaxation parameters of spine components with the synthetic MRI sequence.** *AJNR Am J Neuroradiol* 2018;39:788–95 CrossRef Medline

# Association between Type 1 Modic Changes and *Propionibacterium Acnes* Infection in the Cervical Spine: An Observational Study

M.M. Georgy, F. Vaida, M. Stern, and K. Murphy

## ABSTRACT

**BACKGROUND AND PURPOSE:** Research on the association between *Propionibacterium acnes* in the disc space and type 1 Modic changes in adjacent vertebrae is limited and has produced mixed results. The prevalence of bacteria in intervertebral discs contradicts the prior understanding that skeletal areas in the human anatomy are sterile; yet it opens new treatment possibilities. We investigated the relationship of *P acnes* and type 1 Modic changes in the cervical spine.

**MATERIALS AND METHODS:** Over a 36-month period, we collected intraoperative biopsies of patients undergoing a routine cervical spine operation for degenerative disc diseases. The disc material was cultured aerobically and anaerobically for 7 days. All preoperative MR images were evaluated for Modic changes by a board-certified neuroradiologist. Medical records were reviewed for other spine interventions before the operation.

**RESULTS:** The study population consisted of 48 patients. Of these, 14 patients tested positive for *P acnes* (29%) at ≥1 level. Additionally, 13 patients had type 1 Modic changes (27%) at ≥1 level; 54% (95% CI, 27%–84%) of patients who had type 1 Modic changes were also positive for *P acnes* compared with 20% (95% CI, 7%–33%) of patients without type 1 Modic changes. The difference between these proportions was 34% (95% CI, 4%–64%). The Fisher exact test produced a *P* value of .03 for the association between *P acnes* and MC1, and .53 for the association between *P acnes* and prior procedures.

**CONCLUSIONS:** We conclude that *P acnes* was prevalent in the degenerated cervical spine and that type 1 Modic changes were predictive of a culture positive for *P acnes*. We also found that the prevalence of *P acnes* was not associated with previous interventions. If these results are validated by future studies, they could have a major impact on the standard of care for back and neck pain.

**ABBREVIATION:** MC1 = type 1 Modic changes

During the past few years, several peer-reviewed publications concerning the correlation between type 1 Modic changes (MC1) on MR imaging and *Propionibacterium acnes* in the lumbar spine have produced polarized results. In 2013, Albert et al[1] performed a preoperative biopsy along with baseline and follow-up MR imaging for 61 patients planning to undergo a primary operation at a single level in the lumbar spine. Of the 61 patients, 43% had cultures positive for anaerobic bacteria, primarily *P acnes*. Of these positive discs, 80% developed new Modic changes.

Shortly after, the same group published a double-blind randomized controlled trial investigating the efficacy of antibiotic treatment for patients with chronic low back pain and MC1. A total of 162 patients were randomized into 4 groups: Forty-five were given 1-dose antibiotics, 45 were given double-dose antibiotics, 36 were given a 1-dose placebo, and 36 were given a double-dose placebo. The antibiotics used were a combination of 500 mg amoxicillin and 125 mg clavulanate acid under the brand name Bioclavid. The primary outcome measure was the disease-specific Roland-Morris Disability Questionnaire, used for its ability to capture short-term changes in back pain. At 1-year follow-up, the mean Roland-Morris Disability Questionnaire score of the treat-

Received March 3, 2018; accepted after revision June 8.

From the Division of Biostatistics and Bioinformatics (M.M.G., F.V.), Department of Family Medicine and Public Health, University of California, San Diego, La Jolla, California; Joint Department of Medical Imaging (K.M.), University Health Network, Toronto, Ontario; and Southern California Institute of Neurological Surgery (M.M.G., M.S.), Escondido, California.

Paper previously presented at: Annual Meeting of the American Society of Neuroradiology and the Foundation of the ASNR Symposium, April 22–27, 2017, Long Beach California; American Society of Spine Radiology Annual Symposium, February 14–18, 2018, Scottsdale, Arizona; and Griboi Meeting, an Interdisciplinary Research Conference on Image-Guided Spine Therapy, Biomaterials and Interventional Implants, March 17, 2018, Los Angeles, California.

Please address correspondence to Mark Georgy, MD, University of California, San Diego, Department of Family Medicine and Public Health, Southern California Institute of Neurological Surgery, 705 East Ohio Ave, Escondido, CA 92025; e-mail: mgeorgy@ucsd.edu, markmgeorgy@gmail.com

http://dx.doi.org/10.3174/ajnr.A5741

ment group dropped to 7 from 15, while the mean score of the control group dropped to 14 from 15. The differences in the scores produced a *P* value <.001. Although a trend toward a dose-response relationship was apparent, the relationship was not statistically significant. The authors concluded that Bioclavid could be considered a treatment option for a specific group of patients with chronic low back pain and MC1.[2]

In 2015 however, Rigal et al[3] published a prospective study in which they took disc biopsies from 313 patients undergoing L4–L5/L5–S1 fusion or disc prosthesis surgery. Arguing that a posterior approach has a high risk of contamination, they used an anterior retroperitoneal approach. They took intraoperative biopsies of 385 discs, 303 of which demonstrated MC1 on preoperative MR imaging. The biopsies were cultured for 4 weeks and subjected to histopathologic analysis. With 98.4% of all biopsies found sterile, only 6 cultures were positive, 2 of which were *P acnes* and proposed as contamination. In addition, postoperative monitoring at 1 year did not indicate any infection. The authors concluded that no correlation existed between infection and disc degeneration.[3]

Despite the relative abundance of studies focused on the relation of *P acnes* and MC1 in the lower back, there are very few regarding the same topic in the neck. Hence, we took the initiative to develop an observational study of this relationship in the cervical spine.

## MATERIALS AND METHODS

This was an observational study with approval from an institutional review board and run through a neurosurgery private practice operating in Tri-City and Palomar Medical Centers. During a 36-month period, 48 patients with 80 discs that were undergoing anterior/posterior cervical fusion, disc replacement, or discectomy were enrolled.

The study population comprised 24 women and 24 men, with an average age of 55 years and an age range of 18–87 years. MR imaging protocol included T1- and T2-weighted sagittal, T2-weighted axial, and gradient-echo axial imaging, and 40/48 patients also had STIR sagittal imaging. Patients underwent MR imaging, on average, 3 months before the procedure with a range of 1–10 months. All preoperative MR images were blindly evaluated for the presence, type, and levels of Modic changes by a board-certified neuroradiologist. In addition, discs were checked for narrowing, dissection, and bulges.

All biopsies were performed during open surgery with sterile pituitary rongeurs, and the cultures were carefully transported to the laboratory. The tissues were then ground and placed on a series of anaerobic and aerobic plates. The anaerobic plates used were the following: Brucella K1, Bacteroides Bile-Esculin, and Laked Blood with Kanamycin and Vancomycin. Aerobic incubation in $CO_2$ was accomplished with the following plates manufactured by Becton Dickinson: Columbia Agar with 5% Sheep Blood, Chocolate Agar, CNA Agar, and MacConkey Agar. *Propionibacterium* can take relatively longer to grow, so the cultures were incubated for up to 7 days.

Last, the medical records of all patients were checked for any interventions performed before enrollment, such as steroid injections or other operations. Sufficient information was found to confirm prior intervention status for 47 of the 48 enrolled patients.

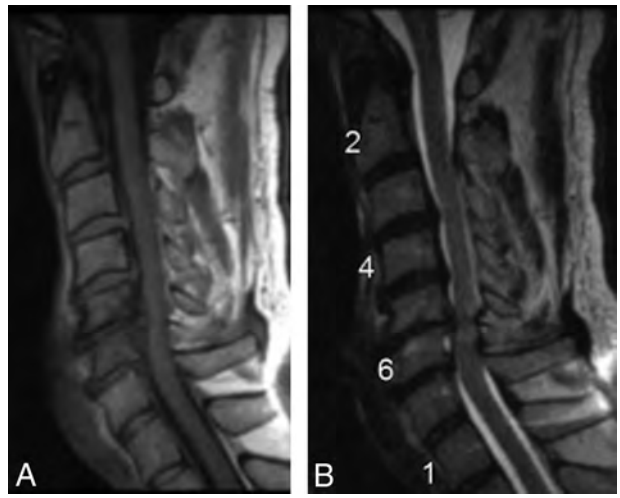


**FIG 1.** A 59-year-old male patient with neck pain who underwent discectomy at C5–C6 and was biopsy-positive for *P acnes*. Preoperative sagittal MR imaging (T1- and T2-weighted) shows MC1 and evidence of myelopathy at C5–C6.

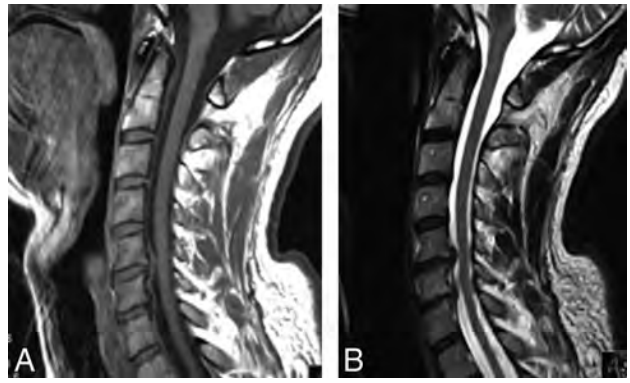


**FIG 2.** A 49-year-old male patient who underwent anterior fusion at C5–C6 and C6–C7 and was biopsy-positive for *P acnes* at both levels. Preoperative sagittal MR imaging (T1- and T2-weighted) shows disc bulges at C5–C6 and C6–C7 with no evidence of MC1.

SPSS Statistics, Version 24 (IBM, Armonk, New York) was used to record the data as well as perform the statistical analysis. All *P* values reported in this article were generated with the Fisher exact test.

## RESULTS

At the end of the study period, enrollment totaled 48 patients with 80 discs. The most common levels of the cervical spine that received treatment were the C3–4, C4–5, and C5–6 disc spaces. The types of operations each participant underwent were split as follows: Thirty-two had anterior fusion only, 9 had disc replacement only, 3 had anterior fusion and disc replacement, 3 had anterior and posterior fusion, and 1 had a discectomy.

Of the 48 patients, 14 were biopsy-positive for *P acnes* (29%) at ≥1 level. In addition, 13 of the 48 patients had MC1 (27%) at ≥1 level (Figs 1 and 2). The remaining 35 patients had either type 2 Modic changes, mixed types, or none. Of the patients with MC1,

**Fisher's exact test results**

| *P acnes* and MC1 |
|---|
| 48 patients, 24 women and 24 men, average age of 55 years |
| 14/48 patients had *P acnes* |
| 13/48 patients had MC1, 54% of which had *P acnes* (95% CI, 27%–84%) |
| *P* value = .03 |

54% were positive for *P acnes*, compared with 20% of those without MC1; 16% were positive for *Staphylococcus epidermis*, and these findings were considered a contamination. Patients with MC1 were significantly more likely to test positive for *P acnes* than patients without MC1 ($P = .03$) (Table). Thirty of the 47 patients with an accessible medical history had no intervention before study enrollment (64%), while the remaining 17 had a spinal injection, an operation, or both. Participants with a prior procedure were no more likely than patients without a prior procedure to test positive for *P acnes* ($P = .53$). Therefore, the prevalence of *P acnes* was unlikely to have been linked to contamination from prior procedures.

## DISCUSSION

de Roos et al[4] first identified bone marrow signaling changes in MR imaging of vertebrae adjacent to degenerative discs in 1987. These signal anomalies were attributed to degenerative disc disease rather than an infection or tumor. The following year, Modic et al[5,6] formally classified the signaling changes into 3 types, and MC1 is the most relevant to this study. Modic hypothesized that the signal intensity changes seen on MR imaging were not alone a causal pathologic process but rather a reflection of one, such as biomechanical stress or instability.[7] He found MC1 to be associated with disruption and fissuring of endplates and the formation of fibrovascular granulation tissue, which correspond to the inflammatory stage of degenerative disc disease and indicate an ongoing active process.[5,6] Later research by Kjaer et al[8] suggested that Modic changes constituted the crucial element in the degenerative process around the disc with regard to low back pain. They demonstrated that patients presenting with degenerative disc diseases and Modic changes together were more likely to have clinical symptoms than patients with degenerative disc diseases alone. Further, Toyone et al[9] investigated the 3 types of Modic changes to determine whether 1 specific type was more strongly associated with low back pain than the others. They observed that 73% of patients with MC1 had low back pain, compared with 11% of patients with type 2 Modic changes.

*P acnes* is an anaerobic, Gram-positive, rod-shaped bacterium that resides on the human skin, oral cavity, intestinal tract, and external ear canal as normal flora.[10] In bone and joint infections, *P acnes* is the most frequently isolated anaerobic microbe and has a strong correlation with vertebral osteomyelitis.[11] Multiple recent publications have proposed that *P acnes* is not only prevalent within spinal discs but may also play a pathogenic role in disc degeneration.

In this study, *P acnes* was isolated from 14/48 (29%) cultures taken intraoperatively from the cervical spine. Similarly, Javanshir et al[12] reported a prevalence of 9/25 (36%) for *P acnes* in disc material excised from the cervical spine. In the lumbar spine, at least 12 independent studies have reported a prevalence of *P acnes* between 2% and 44%.[13-15]

Still, many authors have raised concerns that positive cultures are likely due to contamination. Their arguments include the following: biopsy needles may be exposed to skin flora, an anterior approach is considered more sterile, and contamination may have occurred during prior operations or injections.[3,16] In this investigation, all biopsies were performed intraoperatively with an anterior approach, and no significant association was found between a prior procedure and the presence of *P acnes*. Further, Lambert et al[17] and Czaplewski[18] challenged the findings of Rigal et al[3] mentioned above, stating that *P acnes* could not have been efficiently recovered because incubation was only performed in aerobic conditions.[17,18]

The other part of this study concerned the relationship between *P acnes* in the disc space and MC1 in the adjacent vertebrae. We found that patients with MC1 were significantly more likely to produce a culture positive for *P acnes* ($P = .03$). This association could be indicative of pathogenic activity by *P acnes*, though additional experiments, such as with an animal model, are required. Other investigators have hypothesized the mechanisms by which *P acnes* may be instigating disc degeneration. In 2018, Yazhou et al[19] published an article in *Emerging Microbes & Infections* that demonstrated *P acnes* promoting apoptosis of nucleus pulposus cells within an animal model. Also, Zamora et al[20] found that injecting *P acnes* into rat tail discs increased degeneration but did not result in new Modic changes.

This study has limitations. First, this was an observational study with a relatively small number of patients. Second, it lacked accurate reporting of patient pain scores and functional status before and after the operation. This information would have been useful to determine whether the presence of *P acnes* in the disc had an association with increased pain reported by each patient. However, the primary goal was to investigate the prevalence of *P acnes* in the cervical spine and its relationship with MC1, considering the uncertainty stemming from 2-sided evidence in the recent literature. Third, there was potential bias in MR imaging grading because 1 neuroradiologist read the images. Last, in comparison with most other publications involving the detection of *P acnes* in the spine, this study did not include sophisticated methods such as polymerase chain reaction.

## CONCLUSIONS

The volume of academic commentary surrounding the prevalence of *P acnes* in the disc space of the spine and its possible pathogenicity has increased dramatically in recent years. If the findings of this article are replicated, there is the possibility of novel treatments for spinal pain. Therefore, the devotion of resources to further investigation in this area is justified.

Disclosures: Kieran Murphy—*UNRELATED*: *Board Membership*: IZI Medical Products, Active O, *Comments*: radiation therapy guidance systems and vertebroplasty devices, also ozone-generating devices; *Patents (Planned, Pending or Issued)*: IZI Medical Products, *Comments*: I have 66 patents; *Royalties*: IZI Medical Products; *Stock/Stock Options*: Syunaptive Medlantis, CoraMed, Active O, *Comments*: I have invented devices that are the basis of multiple companies; *Travel/Accommodations/Meeting Expenses Unrelated to Activities Listed*: IZI Medical Products, *Comments*: for a hands-on training courses in spine intervention.

## REFERENCES


1. Albert HB, Lambert P, Rollason J, et al. **Does nuclear tissue infected with bacteria following disc herniations lead to Modic changes in the adjacent vertebrae?** *Eur Spine J* 2013;22:690–96 CrossRef Medline
2. Albert HB, Sorensen JS, Christensen BS, et al. **Antibiotic treatment in patients with chronic low back pain and vertebral bone edema (Modic type 1 changes): a double-blind randomized clinical controlled trial of efficacy.** *Eur Spine J* 2013;22:697–707 CrossRef Medline
3. Rigal J, Thelen T, Byrne F, et al. **Prospective study using anterior approach did not show association between Modic 1 changes and low grade infection in lumbar spine.** *Eur Spine J* 2016;25:1000–05 CrossRef Medline
4. de Roos A, Kressel H, Spritzer C, et al. **MR imaging of marrow changes adjacent to end plates in degenerative lumbar disk disease.** *AJR Am J Roentgenol* 1987;149:531–34 CrossRef Medline
5. Modic MT, Steinberg PM, Ross JS, et al. **Degenerative disk disease: assessment of changes in vertebral body marrow with MR imaging.** *Radiology* 1988;166(1 Pt 1):193–99 CrossRef Medline
6. Modic MT, Masaryk TJ, Ross JS, et al. **Imaging of degenerative disk disease.** *Radiology* 1988;168:177–86
7. Modic MT. **Modic type 1 and type 2 changes.** *J Neurosurg Spine* 2007; 6:150–51; discussion 151 CrossRef Medline
8. Kjaer P, Korsholm L, Bendix T, et al. **Modic changes and their associations with clinical findings.** *Eur Spine J* 2006;15:1312–19 CrossRef Medline
9. Toyone T, Takahashi K, Kitahara H, et al. **Vertebral bone-marrow changes in degenerative lumbar disc disease: an MRI study of 74 patients with low back pain.** *J Bone Joint Surg Br* 1994;76:757–64 Medline
10. Perry A, Lambert P. **Propionibacterium acnes: infection beyond the skin.** *Expert Rev Anti Infect Ther* 2011;9:1149–56 CrossRef Medline
11. Walter G, Vernier M, Pinelli PO, et al. **Bone and joint infections due to anaerobic bacteria: an analysis of 61 cases and review of the literature.** *Eur J Clin Microbiol Infect Dis* 2014;33:1355–64 CrossRef Medline
12. Javanshir N, Salehpour F, Aghazadeh J, et al. **The distribution of infection with Propionibacterium acnes is equal in patients with cervical and lumbar disc herniation.** *Eur Spine J* 2017;26:3135–40 CrossRef Medline
13. Agarwal V, Golish SR, Alamin TF. **Bacteriologic culture of excised intervertebral disc from immunocompetent patients undergoing single level primary lumbar microdiscectomy.** *J Spinal Disord Tech* 2011;24:397–400 CrossRef Medline
14. Stirling A, Worthington T, Rafiq M, et al. **Association between sciatica and Propionibacterium acnes.** *Lancet* 2001;357:2024–25 CrossRef Medline
15. Wedderkopp N, Thomsen K, Manniche C, et al. **No evidence for presence of bacteria in Modic type I changes.** *Acta Radiol* 2009;50: 65–70 CrossRef Medline
16. Georgy M, Stern M, Murphy K. **What is the role of the bacterium Propionibacterium acnes in type 1 Modic changes? A review of the literature.** *Can Assoc Radiol J* 2017;68:419–24 CrossRef Medline
17. Lambert P, Elliott T, Worthington T, et al. **Letter to the Editor concerning "Prospective study using anterior approach did not show association between Modic 1 changes and low grade infection in lumbar spine" by Rigal J, et al. Eur Spine J 2016;25: Apr; 25(4): 1000–05.** *Eur Spine J* 2016;25:3377–78 CrossRef Medline
18. Czaplewski LG. **Letter to the Editor concerning "Prospective study using anterior approach did not show association between Modic 1 changes and low-grade infection in lumbar spine" by Rigal J, Thelen T, Byrne F, Cogniet A, Boissière L, Aunoble S, Le Huec JC (Eur Spine J [2016]; 25(4):1000–05. doi: 10.1007/s00586-016-4396-5).** *Eur Spine J* 2016;25:3379–80 CrossRef Medline
19. Lin Y, Jiao Y, Yuan Y, et al. **Propionibacterium acnes induces intervertebral disc degeneration by promoting nucleus pulposus cell apoptosis via the TLR2/JNK/mitochondrial-mediated pathway.** *Emerg Microbes Infect* 2018;7:1 CrossRef Medline
20. Zamora T, Palma J, Andia M, et al. **Effect of Propionibacterium acnes (PA) injection on intervertebral disc degeneration in a rat model: does it mimic Modic changes?** *Orthop Traumatol Surg Res* 2017;103:795–99 CrossRef Medline

# Simultaneous Bipedicular Radiofrequency Ablation Combined with Vertebral Augmentation for Local Tumor Control of Spinal Metastases

A. Tomasian, T.J. Hillen, R.O. Chang, and J.W. Jennings

## ABSTRACT

**BACKGROUND AND PURPOSE:** Percutaneous radiofrequency ablation combined with vertebral augmentation has emerged as a minimally invasive treatment for patients with vertebral metastases who do not respond to or have contraindications to radiation therapy. The prevalence of posterior vertebral body metastases presents access and treatment challenges in the unique anatomy of the spine. The purpose of this study was to evaluate the safety and efficacy of simultaneous bipedicular radiofrequency ablation using articulating bipolar electrodes combined with vertebral augmentation for local tumor control of spinal metastases.

**MATERIALS AND METHODS:** Imaging-guided simultaneous bipedicular radiofrequency ablation combined with vertebral augmentation was performed in 27 patients (33 tumors) with vertebral metastases selected following multidisciplinary consultations, to achieve local tumor control in this retrospective study. Tumor characteristics, procedural details, and complications were documented. Pre- and postprocedural cross-sectional imaging was evaluated to assess local tumor control rates.

**RESULTS:** Thirty-three tumors were successfully ablated in 27 patients. Posterior vertebral body or pedicle involvement or both were present in 94% (31/33) of cases. Sixty-seven percent (22/33) of the tumors involved ≥75% of the vertebral body volume. Posttreatment imaging was available for 79% (26/33) of the treated tumors. Local tumor control was achieved in 96% (25/26) of tumors median imaging follow up of 16 weeks. No complications were reported, and no patients had clinical evidence of metastatic spinal cord compression at the treated levels.

**CONCLUSIONS:** Simultaneous bipedicular radiofrequency ablation combined with vertebral augmentation is safe and effective for local tumor control of vertebral metastases. Articulating bipolar electrodes enable the placement and proximity necessary for optimal confluence of the ablation zones. Local tumor control may lead to more durable pain palliation, prevent disease progression, and reduce skeletal-related events of the spine.

**ABBREVIATIONS:** RF = radiofrequency; RFA = radiofrequency ablation

Approximately 1.7 million patients are diagnosed with cancer in the United States annually, most of whom will develop metastases that in 40% of cases will involve the spine.[1,2]

The vertebral column is the most common site of osseous metastasis as a result of vascular red marrow in adult vertebrae and communication of valveless vertebral venous plexuses with deep torso veins.[3] Approximately 90% of symptomatic patients with vertebral metastases present with pain due to pathologic fracture, biochemical stimulation of endosteal nociceptors, osteoclast-mediated osseous destruction, and spinal cord or nerve root compression, which occur in 10%–20% of patients and are most often due to tumor involvement of the posterior vertebral body.[4,5] Pain and neurologic deficits associated with vertebral metastases often lead to impaired mobility, deficient functional independence, and overall diminished quality of life.[6] Management of metastatic spine disease requires multidisciplinary input.[7]

Radiation therapy is the current standard of care for local control and pain palliation of vertebral metastases, but when used alone, it has important limitations. First, certain tumor histologies respond less favorably to radiation therapy, such as sarcoma, renal cell carcinoma, non-small cell lung cancer, and melanoma.[8] Second, radiation therapy of vertebral metastases is limited by the cumulative tolerance of the spinal cord, which often precludes retreatment of recurrent tumor or progressive tumor at adjacent

Received May 7, 2018; accepted after revision June 18.

From the Department of Radiology (A.T.), University of Southern California, Los Angeles, California; and the Mallinckrodt Institute of Radiology (T.J.H., R.O.C., J.W.J.), St. Louis, Missouri.

Please address correspondence to Anderanik Tomasian, MD, Department of Radiology, University of Southern California, 1500 San Pablo St, Los Angeles, CA 90033; e-mail: tomasian.andy@gmail.com

http://dx.doi.org/10.3174/ajnr.A5752

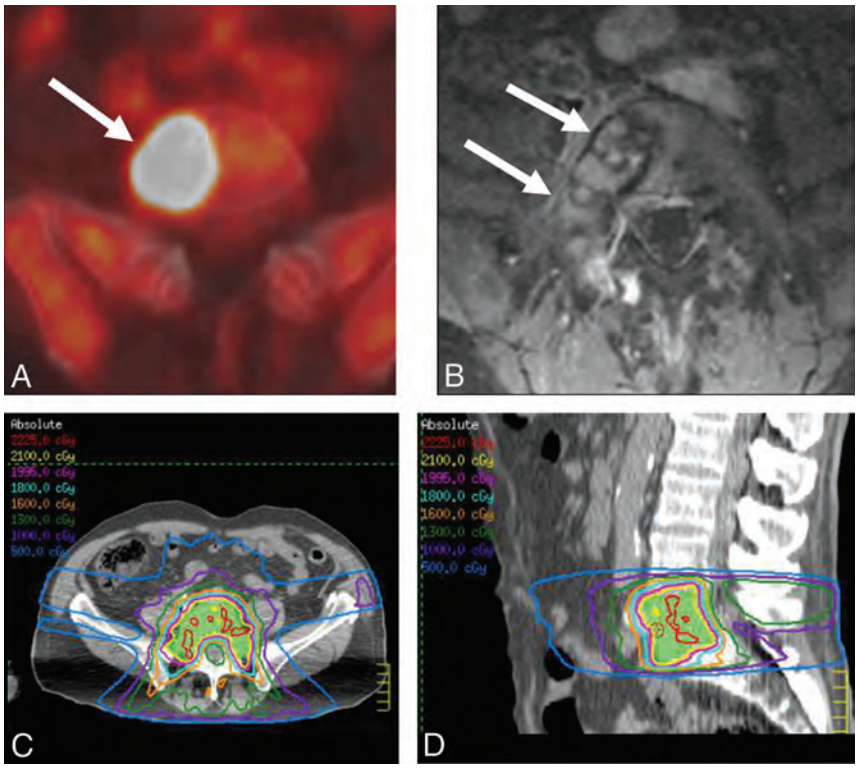


**FIG 1.** A 63-year-old man with chest wall melanoma and painful L5 metastasis. Axial FDG-PET/CT (*A*) and axial T1-weighted fat-saturated contrast-enhanced MR imaging (*B*) show hypermetabolic bone marrow replacing lesion in the L5 vertebral body extending to the right pedicle (*A* and *B*, *arrows*). Axial (*C*) and sagittal (*D*) stereotactic body radiation therapy planning CT images show stereotactic body radiation therapy contours with clinical target volume including the entire vertebral body and pedicles.

vertebrae.[9] Last, radiation therapy excludes patients from certain systemic chemotherapy clinical trials. Surgery (including stabilization, corpectomy, and gross tumor resection) is often of limited benefit in the management of spinal metastases due to its morbidity and patients' often poor functional statuses and short expected life span, and is typically considered for patients with neurologic compromise or spinal instability.

During the past few years, investigators have exploited minimally invasive percutaneous thermal ablation technologies, often combined with vertebral augmentation, for pain palliation and local tumor control of vertebral metastases. These may be performed in an outpatient setting with the patient under conscious sedation with short recovery and no compromise of adjuvant radiation or chemotherapy.[10-16] Percutaneous thermal ablation for vertebral metastases is performed to achieve pain palliation, local tumor control, or both (often with vertebral augmentation for fracture stabilization or prevention) in patients who have not responded to or have contraindications to radiation therapy.

There has been a recent paradigm shift in stereotactic spine radiosurgery for management of vertebral metastases with specific consensus recommendations by the International Spine Radiosurgery Consortium for the definition of clinical target volume versus gross tumor volume to account for microscopic tumor spread and marginal radiation therapy failures.[17] The consensus recommendations define clinical target volume (to be treated by stereotactic spine radiosurgery) to include gross tumor volume plus surrounding abnormal bone marrow signal intensity on MR imaging to account for microscopic tumor invasion and adjacent normal osseous expansion to account for subclinical tumor spread in the marrow space.[17] For example, tumor involving the posterior vertebral body would involve treating the entire vertebral body and both pedicles (Fig 1).

Simultaneous bipedicular radiofrequency ablation (RFA) is a novel technique that efficiently generates 2 confluent, coalescent, and overlapping ablation zones in close proximity that minimize the convective cooling effect (heat sink) and subsequently decrease the power required to conduct heat through tissue, decreasing the risk of thermal injury and minimizing charring and impedance-related issues. This technique may result in a more thorough ablation of the vertebral body and pedicles and supports the stereotactic spine radiosurgery paradigm to treat the entire vertebral body volume and pedicles (clinical target volume) for improved local tumor control rates and more durable pain palliation (Figs 1 and 2). However, the combination of transpedicular access being the safest approach to the vertebral body and the high prevalence of posterior vertebral body metastases (>95% of cases)[18] makes minimally invasive access and treatment challenging.

The purpose of this study was to evaluate the safety and efficacy of simultaneous bipedicular RFA using a navigational bipolar electrode system combined with vertebral augmentation for local tumor control of vertebral metastases.

## MATERIALS AND METHODS

Institutional review board approval was obtained to retrospectively review the institutional data base for all patients who underwent simultaneous bipedicular RFA and vertebral augmentation of vertebral metastases between May 2016 and July 2017 at a National Cancer Institute–designated Cancer Center.

Informed consent was waived for this retrospective study. Recorded data included patient demographics, primary tumor histology, vertebrae treated, and whether the lesion had been previously treated with radiation therapy. Available preprocedural cross-sectional imaging of each treated vertebra was reviewed to determine whether the tumor involved the posterior vertebral body and/or pedicles, had involved the posterior vertebral body cortex, and/or was associated with a pathologic vertebral fracture.

Procedural notes were reviewed to determine the total conscious sedation time and total ablation time for each radiofrequency (RF) electrode at each vertebral level. Procedural complications were documented according to the Society of

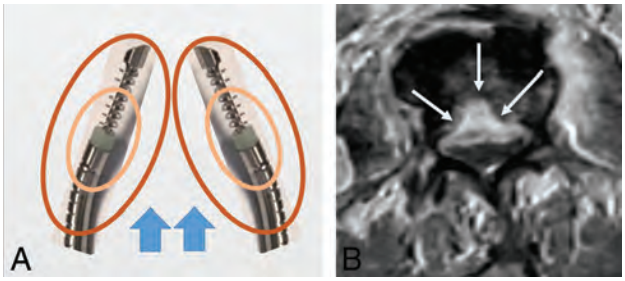


**FIG 2.** Illustration of simultaneous bipedicular RF ablation (*A*) depicts individual zones of resistive and conductive heating (central and peripheral ovoids, respectively) around 2 adjacent RF electrodes, resulting in a diminished convective cooling effect (ie, heat sink due to blood and CSF flow) (*A*, *arrows*). Adjacent areas of thermal spread result in reduction in the power required to conduct heat in tissue, decreased risk of thermal injury, and impedance-related issues. Axial T1-weighted fat-saturated contrast-enhanced MR imaging (*B*) following bilateral RF ablation using 2 straight electrodes shows ablation failure along the posterior third vertebral body centrally due to lack of confluent ablation zones (*B*, *arrows*).

Interventional Radiology classification.[19] Patients were clinically evaluated 2 hours after each procedure for evidence of acute complications, such as hematoma formation or neurologic injury, with routine follow-up by telephone 1 day, 1 week, and 1 month following the procedure. The duration of imaging follow-up was recorded for all patients, and electronic medical records were reviewed for possible delayed complications, such as infection.

### *Patient Selection for Radiofrequency Ablation and Vertebral Augmentation*

Patients were selected for RFA and vertebral augmentation by a multidisciplinary team of radiation and medical oncologists, interventional radiologists, and spine surgeons. Treatments were performed to achieve local tumor control and, in most cases, pain palliation. Patients selected for RFA treatment were either unable to undergo radiation therapy or had radiographic evidence of tumor progression at other sites of disease previously treated with radiation therapy. Exclusion criteria for RFA and vertebral augmentation included entirely osteoblastic metastases, the presence of pathologic compression fracture with spinal instability, or metastases causing spinal cord compression.

### *Radiofrequency Ablation and Vertebral Augmentation Procedure*

Written informed consent was obtained before all procedures. All procedures were performed using fluoroscopic guidance with patients under conscious sedation. Conscious sedation was decreased from moderate-to-mild sedation during the ablation portion of the procedure so that the patient could provide active biofeedback to prevent thermal nerve and or spinal cord injury. The vertebral body was accessed from a bipedicular approach with 10-ga introducer working cannulas, and a navigational osteotome was used to create channels in the marrow space along the planned placements of the ablation electrodes.

The ablation electrodes were then placed through both introducer cannulas and articulated until the tips were 5–10 mm apart as seen on the anteroposterior fluoroscopic images (approximately 1 width of the spinous process) (Fig 3). The first ablation was performed anteriorly, and the electrodes were then retracted and articulated within the posterior third of the vertebral body re-establishing the 5- to 10-mm tip distance, to treat the posterior vertebral body and pedicles. In each case, the goal was to generate confluent, coalescent, and overlapping ablation zones to encompass the entire vertebral body (and pedicles) to treat the clinical target volume in alignment with the International Spine Radiosurgery Consortium consensus recommendations.[17]

Simultaneous bipedicular RF ablations were performed with the STAR Tumor Ablation System (Merit Medical Systems, South Jordan, Utah) consisting of the 10/15 STAR ablation electrode and the MetaSTAR generator. The ablation device is a navigational bipolar electrode with an articulating distal segment that can be curved in various projections providing optimal lesion access and electrode proximity, both essential for accessing and ablating tumor in the posterior central vertebral body.[12,16] The electrode contains 2 active thermocouples embedded along its shaft 10 and 15 mm from the center of the ablation zone. These permit real-time monitoring of the temperatures at the periphery of the developing ablation zone, allowing accurate, intraprocedural assessment of the ablation zone size and providing passive thermal protection, which is especially important when treating the posterior vertebral body and pedicles. Based on the manufacturer's thermal distribution curves, the dimensions of the ellipsoid ablation volume are $20 \times 15 \times 15$ mm when the thermocouple located 10 mm from the center of the ablation zone (distal thermocouple) reaches 50°C and $30 \times 20 \times 20$ mm when the thermocouple located 15 mm from the center of the ablation zone (proximal thermocouple) reaches 50°C. The radiofrequency energy automatically stops when the proximal thermocouple registers 50°C, which is a valuable safety feature. Each individual ablation was performed until the proximal thermocouple registered 50°C, at which point the ablation was considered technically successful. The MetaSTAR generator provides 3-, 5-, 7.5-, and 10-W power settings, which allow slow ramping of temperatures and ablation size, improving efficacy and reducing undesired heat dispersion and impedance issues. Ablation is initiated at the 3-W setting until the temperatures registered at the thermocouples' plateau. The power is then sequentially increased using an identical strategy until the desired ablation volume is achieved. The generator displays ablation time, impedance, and the 2-thermocouple temperature readings, which allows precise real-time monitoring of the ablation zone geometry.

Vertebral augmentation was performed using the StabiliT Vertebral Augmentation System (Merit Medical Systems). In all cases, cement was injected through the same working cannulae used for ablation.

### *Local Control Assessment and Analysis*

All available postprocedural cross-sectional imaging was reviewed to determine the ablation extent, degree of local tumor control, possible complications, and evidence of systemic disease progression.[16,20] Local control failure was determined in accordance with previously established guidelines following thermal ablation of spinal metastases.[16,20]

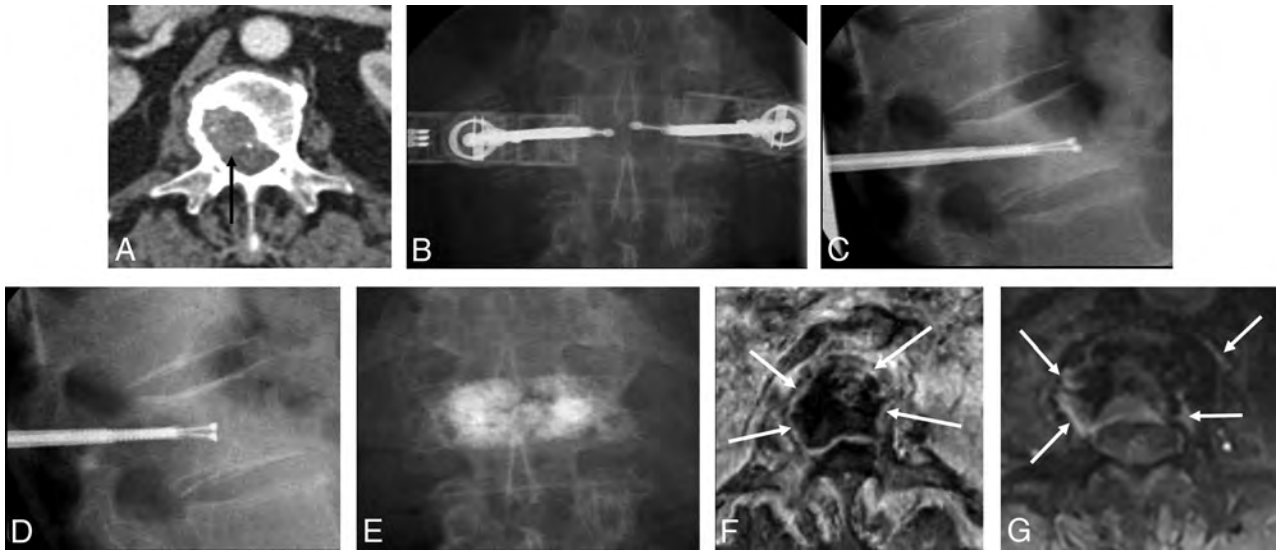


**FIG 3.** An 86-year-old man with metastatic melanoma and a painful L1 lesion. Axial contrast-enhanced CT (*A*) shows a destructive osteolytic mass within the vertebral body with partial disruption of the posterior wall and a small component extending to the anterior central canal (*A*, *arrow*). An anteroposterior fluoroscopic image during simultaneous bipedicular RF ablation (*B*) shows medial articulation of electrode tips, which are 5–10 mm apart (the width of the spinous process as a landmark). Lateral fluoroscopic images (*C*–*E*) show ablation of the anterior vertebral body first (*C*), followed by ablation of the posterior vertebral body and pedicles (*D*), and vertebral augmentation (*E*). Axial T1-weighted fat-saturated contrast-enhanced MR images obtained 2 weeks (*F*) and 52 weeks (*G*) following treatment show local tumor control with granulation tissues along the periphery of ablation zone (*F* and *G*, *arrows*).

## RESULTS

All RF ablation procedures were performed via a bipedicular approach as preoperatively planned and were technically successful. Thirty-three spinal metastases (in 27 patients, 17 men and 10 women; age range, 23–86 years) treated with simultaneous bipedicular RFA and vertebral augmentation were included in the study. Radiation-resistant histologies composed 70% (23/33) of treated tumors, including non-small cell lung cancer (30.3%, 10/33), sarcoma (18.2%, 6/33), renal cell carcinoma (12.1%, 4/33), and melanoma (9.1%, 3/33). Other histologies included multiple myeloma (6.1%, 2/33), epithelioid hemangioendothelioma (6.1%, 2/33), hepatocellular carcinoma (3%, 1/33), head and neck squamous cell carcinoma (3%, 1/33), breast adenocarcinoma (3%, 1/33), bladder carcinoma (3%, 1/33), prostate adenocarcinoma (3%, 1/33), and germ cell tumor (3%, 1/33). Thirty-six percent (12/33) of tumors involved thoracic vertebrae, 61% (20/33) involved lumbar vertebrae, and 3% (1/33) involved sacral vertebrae. Posterior vertebral body and/or pedicle involvement was present in 94% (31/33) of cases. Three percent (1/33) of tumors exclusively involved the pedicles. Sixty-seven percent (22/33) of tumors involved ≥75% of the vertebral body volume. Twenty-four percent (8/33) of lesions in 7 patients were treated with spinal radiation therapy before RFA.

The mean total ablation time per RF electrode was 18.3 minutes (range, 9.9–29.3 minutes). The mean total conscious sedation time was 102.6 ± 25.8 minutes (range, 55–168 minutes). According to the Society of Interventional Radiology classification, there were no acute or delayed procedure-related complications.

Follow-up imaging was available for 79% (26/33) of tumors in 23 of 27 patients and included MR imaging in 42% (14/33), CT in 52% (17/33), and PET/CT in 15% (5/33) of tumors. Follow-up imaging demonstrated local tumor control for 96% (25/26) of lesions (22 of 23 patients) with no evidence of residual or recurrent tumor during the median imaging follow-up of 16 weeks (range, 1–57 weeks; interquartile range, 29.5 weeks) (Fig 3). The patient thought to have progression had slightly more epidural tumor from the preoperative to the initial postoperative CT scan; however, it did not progress and remained unchanged at the 52-week follow-up in the setting of metastatic disease progression. Retraction of the epidural component of the tumor was identified in 3 lesions (Fig 4). On the basis of follow-up imaging, systemic metastatic disease progression was identified in 77% (17/22) of patients with local tumor control. Eight patients eventually died due to other causes, without symptoms of metastatic spinal cord compression, and 2 patients entered hospice care due to progression of visceral or intracranial metastatic disease.

## DISCUSSION

In the present study, simultaneous bipedicular RFA and vertebral augmentation achieved a radiographic local tumor control rate of 96% (25/26 tumors), with a median follow-up of 16 weeks with no immediate or delayed complications. Systemic metastatic disease progression was identified in 77% (17/22) of patients with local tumor control. These results support the clinical value of a novel percutaneous thermal ablation approach for management of vertebral metastatic disease that adapts consensus recommendations by the International Spine Radiosurgery Consortium to treat clinical target volumes (entire vertebral body and pedicles if there is posterior vertebral body involvement), to account for microscopic tumor spread and marginal treatment failures for improved local tumor control rates.[17]

Although radiation therapy is the standard of care for palliation and local control of osseous metastases, simultaneous bipedicular RFA and vertebral augmentation may be a robust and safe

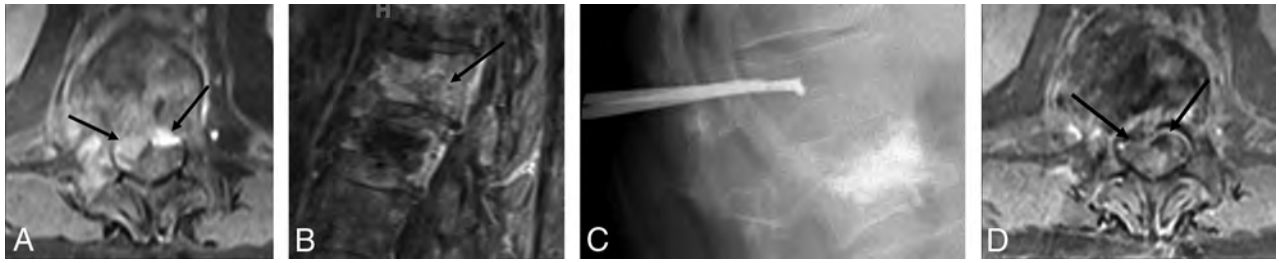


**FIG 4.** A 70-year-old man with thigh metastatic undifferentiated pleomorphic sarcoma and a painful T12 lesion. Axial and sagittal T1-weighted fat-saturated contrast-enhanced MR images (*A* and *B*, respectively) show bone marrow replacing lesion in the T12 vertebral body with posterior wall destruction, epidural extension of tumor, and thecal sac compression (*A* and *B*, *arrows*). Note the previously treated L1 lesion (*B*). Lateral fluoroscopic image during simultaneous bipedicular RF ablation (*C*) shows aggressive ablation of the posterior vertebral body and pedicles. Axial T1-weighted fat-saturated contrast-enhanced MR image (*D*) obtained 30 weeks following treatment shows local tumor control with no evidence of recurrence and retraction of epidural component (*D*, *arrows*).

alternative for patients who cannot be offered or cannot tolerate radiation therapy or have radiation-resistant tumors.

Simultaneous bipedicular RFA performed with an articulating device that permits optimal electrode placement has several important advantages: First, it effectively generates confluent and coalescent ablation zones at any given time to encompass as much vertebral volume as possible. This ablation zone is characterized by 2 regions of resistive and conductive heating in close proximity with the consequent reduction of the convective cooling effect (heat sink) (Fig 2).

Second, it minimizes the risk of undesired thermal injury by decreasing the power required to conduct heat through tissue via reduction of the temperature difference between regions of resistive heating and adjacent tissue, thus decreasing the distance that heat must be conducted. Consequently, there is less undesired heat propagation beyond the margins of ablation zones to generate the same ablation geometry compared with single-electrode RFA. This setup affords implementation of a low-power wattage protocol (with gradual increase in power), which also results in a decreased incidence of increased impedance, subsequently improving efficiency. Third, simultaneous ablation results in time savings and efficient treatment. In addition, the use of a bipolar navigational RF electrode system provides optimal tumor access, particularly within the posterior central vertebral body where access may be challenging using straight electrodes.[12,16] Finally, in cases of challenging pedicle anatomy, the articulation can help anchor the electrode in position. This constellation of advantages is particularly important for treatment of tumors in the posterior vertebral body, which is involved in >95% of vertebral metastases.[18] In these cases, aggressive ablation may be challenging due to proximity to the central canal and nerve roots and the associated risk of thermal injury, which increases the possibility of tumor recurrence and inadequate ablation. Similarly, based on dosimetry, the efficacy of radiation therapy declines with decreasing distance between the tumor and the spinal cord because of the risk of radiation-induced myelopathy.[9]

In a retrospective single-center study, Wallace et al[10] used combination RFA and vertebral augmentation for the management of spinal metastases and reported local tumor control rates of 74% and 70% at 6-month and 1-year follow-up time points. The authors reported that in 89% (8/9 cases) of cases in which radiographic local tumor control was not achieved, residual or recurrent tumor was present in the posterior vertebral body or epidural space.[10] A combination of radiation therapy and RFA has been used for improved local control rates of vertebral metastases.[21] In a retrospective single-center study, Greenwood et al[21] reported a local tumor control rate of 92% (12/13 tumors) at 3-month follow-up despite systemic metastatic disease progression. In the present study, 94% (31/33) of tumors involved the posterior vertebral body and/or the pedicles, and a local tumor control rate of 96% (25/26 tumors) was achieved. The safety of the procedure was supported by a lack of complications based on the Society of Interventional Radiology guidelines. Specifically, there were no thermal nerve or spinal cord injuries.

It is our practice to ablate as much vertebral body volume as possible plus the pedicles to account for microscopic tumor invasion and subclinical tumor spread in marrow space for improved local tumor control.[17] We perform spinal RFA with patients under conscious sedation, in part, to allow patients to express new radicular pain indicating impending spinal nerve or potential spinal cord injury. In such cases, ablation is immediately terminated to avoid thermal nerve injury. Active thermal protective techniques including perineural and epidural injections of carbon dioxide and/or 5% dextrose in water are then attempted. If these are unsuccessful, the result is often less thorough tumor ablation. Of note, these active thermoprotective techniques were not necessary in this group of patients, and it is theorized that this feature may be, in part, due to the ability to use lower wattages, 5W and 3W, when ablating posteriorly near the spinal canal and neuroforamina. The difficulty in achieving maximum benefit of simultaneous bipedicular ablation includes the requirement for optimal positioning of dual RF electrodes, which may be difficult due to operator inexperience, challenging anatomy, and /or suboptimal imaging guidance.

The limitations of the present study include the single-arm nature of the analysis with no control group, the retrospective methodology, the relatively small number of treated tumors, and the lack of standard follow-up imaging protocol.

## CONCLUSIONS

The results of this single-center retrospective study suggest that simultaneous bipedicular RF ablation using bipolar, articulating electrodes and the generation of confluent, coalescent, and overlapping vertebral body ablations, combined with vertebral augmentation, is safe and effective for local tumor control of vertebral metastases. The goal of treating the clinical target volume (the

entire vertebral body and pedicles) in those with posterior vertebral body and pedicle lesions and achieving local tumor control may lead to more durable pain palliation, prevent disease progression, and reduce spinal skeletal related events.

Disclosures: Travis J. Hillen—*UNRELATED: Other*: helped with cadaver lab training course sponsored by DFine. Jack W. Jennings—*RELATED: Consulting Fee or Honorarium*: Merit Medical, *Comments*: ablation training labs and a few talks at national/international meetings regarding spine ablation; *UNRELATED: Board Membership*: Medtronic, Merit Interventional Oncology Advisory Boards, *Comments*: They have only met 1 time for each; *Consultancy*: Bard, BTG, *Comments*: BTG was for Principal Investigator fees.

## REFERENCES


1. American Cancer Society. Cancer facts and figures 2018. https://www.cancer.org/content/dam/cancer-org/research/cancer-facts-and-statistics/annual-cancer-facts-and-figures/2018/cancer-facts-and-figures-2018.pdf. Accessed May 2, 2018
2. Witham TF, Khavkin YA, Gallia GL, et al. **Surgery insight: current management of epidural spinal cord compression from metastatic spine disease.** *Nat Clin Pract Neurol* 2006;2:87–94; quiz 116 CrossRef Medline
3. Coleman RE. **Clinical features of metastatic bone disease and risk of skeletal morbidity.** *Clin Cancer Res* 2006;12:6243s–49s CrossRef Medline
4. Bayley A, Milosevic M, Blend R, et al. **A prospective study of factors predicting clinically occult spinal cord compression in patients with metastatic prostate carcinoma.** *Cancer* 2001;92:303–10 CrossRef Medline
5. Klimo P Jr, Schmidt MH. **Surgical management of spinal metastases.** *Oncologist* 2004;9:188–96 CrossRef Medline
6. Kim JM, Losina E, Bono CM, et al. **Clinical outcome of metastatic spinal cord compression treated with surgical excision ± radiation versus radiation therapy alone: a systematic review of literature.** *Spine* 2012;37:78–84 CrossRef Medline
7. Wallace AN, Robinson CG, Meyer J, et al. **The Metastatic Spine Disease Multidisciplinary Working Group algorithms.** *Oncologist* 2015;20:1205–15 CrossRef Medline
8. Gerszten PC, Mendel E, Yamada Y. **Radiotherapy and radiosurgery for metastatic spine disease: what are the options, indications, and outcomes?** *Spine* 2009;34:S78–92 CrossRef Medline
9. Masucci GL, Yu E, Ma L, et al. **Stereotactic body radiotherapy is an effective treatment in reirradiating spinal metastases: current status and practical considerations for safe practice.** *Expert Rev Anticancer Ther* 2011;11:1923–33 CrossRef Medline
10. Wallace AN, Tomasian A, Vaswani D, et al. **Radiographic local control of spinal metastases with percutaneous radiofrequency ablation and vertebral augmentation.** *AJNR Am J Neuroradiol* 2016;37:759–65 CrossRef Medline
11. Tomasian A, Wallace A, Northrup B, et al. **Spine cryoablation: pain palliation and local tumor control for vertebral metastases.** *AJNR Am J Neuroradiol* 2016;37:189–95 CrossRef Medline
12. Wallace AN, Greenwood TJ, Jennings JW. **Radiofrequency ablation and vertebral augmentation for palliation of painful spinal metastases.** *J Neurooncol* 2015;124:111–18 CrossRef Medline
13. Pusceddu C, Sotgia B, Fele RM, et al. **Combined microwave ablation and cementoplasty in patients with painful bone metastases at high risk of fracture.** *Cardiovasc Intervent Radiol* 2016;39:74–80 CrossRef Medline
14. Callstrom MR, Dupuy DE, Solomon SB, et al. **Percutaneous image-guided cryoablation of painful metastases involving bone: multicenter trial.** *Cancer* 2013;119:1033–41
15. Bagla S, Sayed D, Smirniotopoulos J, et al. **Multicenter prospective clinical series evaluating radiofrequency ablation in the treatment of painful spine metastases.** *Cardiovasc Intervent Radiol* 2016;39:1289–97 CrossRef Medline
16. Hillen TJ, Anchala P, Friedman MV, et al. **Treatment of metastatic posterior vertebral body osseous tumors by using a targeted bipolar radiofrequency ablation device: technical note.** *Radiology* 2014;273:261–67 CrossRef Medline
17. Cox BW, Spratt DE, Lovelock M, et al. **International Spine Radiosurgery Consortium consensus guidelines for target volume definition in spinal stereotactic radiosurgery.** *Int J Radiat Oncol Biol Phys* 2012;83:e597–605 CrossRef Medline
18. Algra PR, Heimans JJ, Valk J, et al. **Do metastases in vertebrae begin in the body or the pedicles? Imaging study in 45 patients.** *AJR Am J Roentgenol* 1992;158:1275–79 CrossRef Medline
19. Ahmed M, Solbiati L, Brace CL, et al; International Working Group on Image-Guided Tumor Ablation, Interventional Oncology Sans Frontières Expert Panel, Technology Assessment Committee of the Society of Interventional Radiology, Standard of Practice Committee of the Cardiovascular and Interventional Radiological Society of Europe. **Image-guided tumor ablation: standardization of terminology and reporting criteria—a 10-year update.** *J Vasc Interv Radiol* 2014;25:1691–705.e4 CrossRef Medline
20. Wallace AN, Greenwood TJ, Jennings JW. **Use of imaging in the management of metastatic spine disease with percutaneous ablation and vertebral augmentation.** *AJR Am J Roentgenol* 2015;205:434–41 CrossRef Medline
21. Greenwood TJ, Wallace A, Friedman MV, et al. **Combined ablation and radiation therapy of spinal metastases: a novel multimodality treatment approach.** *Pain Physician* 2015;18:573–81 Medline

# Celebrating 35 Years of the AJNR

September 1983 edition

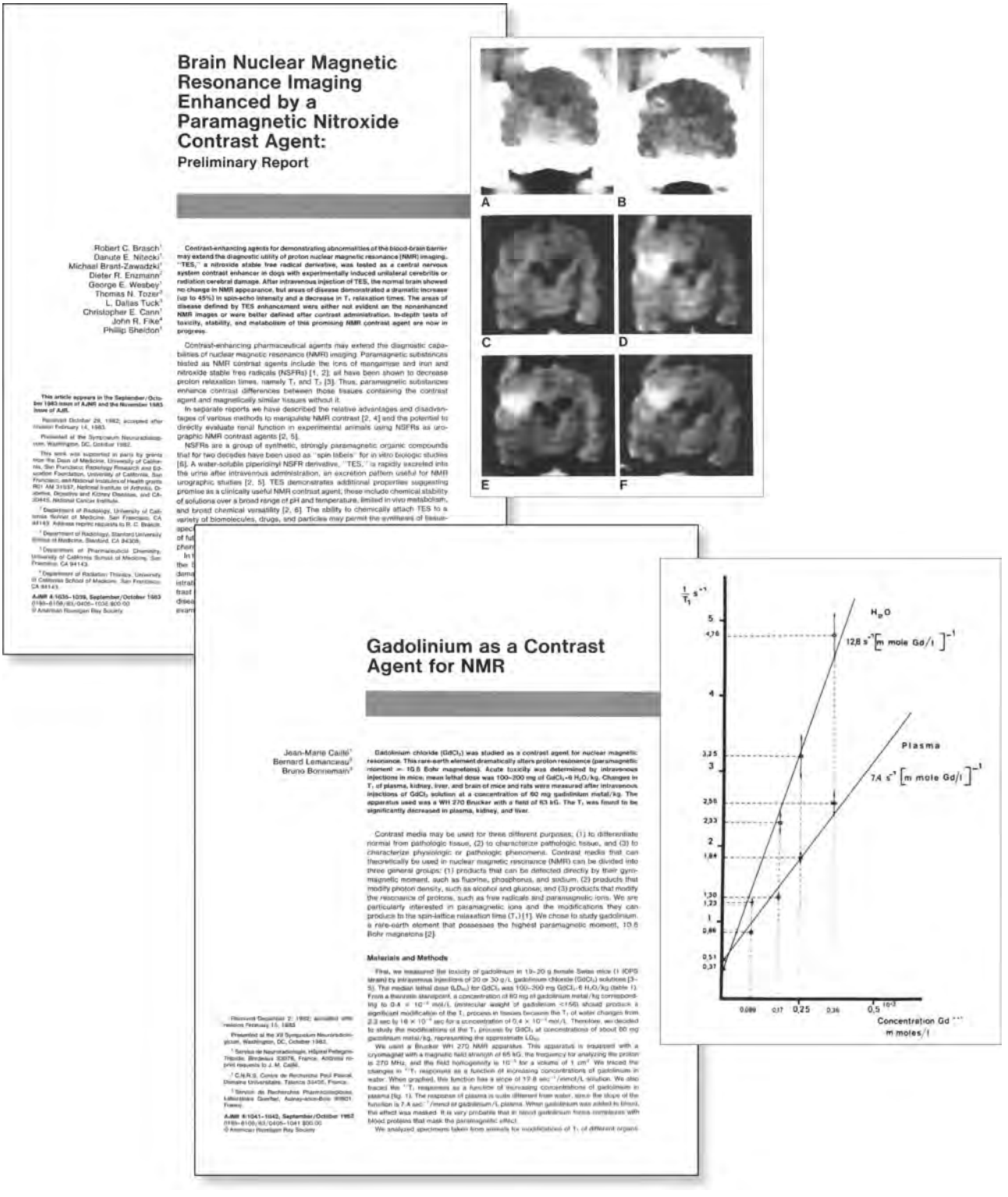

Brain Nuclear Magnetic Resonance Imaging Enhanced by a Paramagnetic Nitroxide Contrast Agent: Preliminary Report

Robert C. Brasch, Danute E. Nitecki, Michael Brant-Zawadzki, Dieter R. Enzmann, George E. Wesbey, Thomas N. Tozer, L. Dallas Tuck, Christopher E. Cann, John R. Fike, Phillip Sheldon

Gadolinium as a Contrast Agent for NMR

Jean-Marie Caillé, Bernard Lemanceau, Bruno Bonnemain

A B C D E F

$H_2O$

12,8 $s^{-1}$ [m mole Gd/l]$^{-1}$

Plasma

7,4 $s^{-1}$ [m mole Gd/l]$^{-1}$

Concentration Gd

m moles/l

# Memorial: Galdino Valvassori, MD, FACR

Galdino Valvassori, MD, FACR, distinguished Professor Emeritus of the Department of Radiology at the University of Illinois in Chicago, passed quietly in his sleep on February 13, 2018, in Florida. He was 91 years old.

Dr Valvassori, who was considered by most radiologists to be the father of head and neck radiology, was one of the founders and first President of the American Society of Head and Neck Radiology. Dr Valvassori authored the first definitive reference textbook in head and neck imaging. He went on to become his generation's leader in head and neck radiology in general and otoradiology, radiology of ear system and diseases of the ears evaluated by radiological modalities, in particular.

Dr Valvassori was born in Milan, Italy, on July 16, 1926. He was a man like no other. His tenacity and love of life were shared with everyone he touched in his life and career, and he had a good run of 91 incredible years. He came to the United States in 1955 to complete his training at Memorial Hospital Cornell Medical School in New York City. Dino married his first love Alessandrina and had 4 lovely children, who survive him and have families of their own.

Dr Valvassori had an amazing career as he pioneered the field of radiology in otolaryngology and ophthalmology. He pursued his teaching at the University of Illinois Eye and Ear Infirmary as well as his private practice with determination and boundless energy. We studied under Dr Valvassori when we were residents in the 1970s, and he impressed us not only by his knowledge but also by his continuous pursuit of excellence in his chosen field. He was known for his attention to detail that resulted in diagnoses that few could make. He became the mentor of one of us (M.M.), who succeeded him as the director of the department at University of Illinois Eye and Ear Infirmary. Dr Valvassori treated all staff with respect, and we admired and loved this larger-than-life man because of his charisma, energy, and brilliance.

Dr Valvassori loved the outdoors. He especially liked hiking in the mountains and engaged in downhill skiing well into his 80s.

Dr Valvassori was above all a family man who adored his grandchildren who were the love of his life. He is survived by his second wife, Eleanor, his 4 children: Danielle, Alex, Laura, and Pia, and his 8 grandchildren.

**M. Mafee**
Department of Radiology
University of California, San Diego
San Diego, California
**D. Spigos**
University of Illinois, Chicago
Chicago, Illinois

http://dx.doi.org/10.3174/ajnr.A5716

# MR Imaging Features of Adult-Onset Neuronal Intranuclear Inclusion Disease May Be Indistinguishable from Fragile X–Associated Tremor/Ataxia Syndrome

We have read with great interest the article by Sugiyama et al[1] published in the November 2017 edition of the *American Journal of Neuroradiology*, which described typical brain MR imaging findings in adult-onset neuronal intranuclear inclusion disease (NIID). The authors highlighted the paravermal signal changes on FLAIR sequences as well as the high-intensity signal on DWI along the corticomedullary junction as typical neuroimaging findings in NIID.

According to Sone et al,[2] who described clinical features, MR imaging findings, and pathologic features in a larger series of 57 patients with adult-onset NIID, the pathophysiology of fragile X–associated tremor/ataxia syndrome (FXTAS) and NIID overlaps, and it is not reliable for distinguishing both disorders based on either clinical presentation, imaging findings, or family history. Moreover, pathologic changes are also similar because FXTAS and NIID usually present with intranuclear eosinophilic inclusions. The study of Sugiyama et al[1] did not evaluate the CGG repeat length of the *FMR1* gene in their patients, which is a crucial step to support their conclusions. When we reviewed our institutional records, 3 recent patients were clinically evaluated and genetic studies confirmed FXTAS. Most interesting, our 3 patients with FXTAS presented with imaging findings (Figs 1 and 2) very similar to the those in patients described by Sugiyama et al, whose diagnoses were NIID.

Research in neuroradiology must concentrate on predicting specific neurologic disorders, identifying either radiophenotypes and/or useful algorithms for clinical practice. Considering that FXTAS seems to be more common than adult-onset NIID, it is reasonable that the algorithm using genetic studies (*FMR1* gene premutation) proposed by Sone et al[2] remains unpredictable because the pathologic changes and the imaging findings reported by Sugiyama et al[1] may occur in both disorders.

http://dx.doi.org/10.3174/ajnr.A5729

Disclosures: Orlando G.P. Barsottini—*UNRELATED*: *Employment*: Federal University of Sao Paulo, Brazil, *Comments*: Professor of Neurology.

## REFERENCES

1. Sugiyama A, Sato N, Kimura Y, et al. **MR imaging features of the cerebellum in adult-onset neuronal intranuclear inclusion disease: 8 cases.** *AJNR Am J Neuroradiol* 2017;38:2100–04 CrossRef Medline
2. Sone J, Mori K, Inagaki T, et al. **Clinicopathological features of adult-onset neuronal intranuclear inclusion disease.** *Brain* 2016; 139:3170–86 CrossRef Medline

**I.G. Padilha**
**R.H. Nunes**
**F.A. Scortegagna**
Division of Neuroradiology
Santa Casa de Sao Paulo School of Medical Sciences
Sao Paulo, Brazil
Division of Neuroradiology
Diagnosticos da America SA
Sao Paulo, Brazil
**J.L. Pedroso**
Ataxia Unit, Department of Neurology
Universidade Federal de São Paulo
Sao Paulo, Brazil
**V.H. Marussi**
Division of Neuroradiology
Med Imagem, Hospital da Beneficencia Portuguesa de Sao Paulo
Sao Paulo, Brazil
**M.R. Rodrigues Gonçalves**
Department of Neurology
Universidade de São Paulo
Sao Paulo, Brazil
**O.G.P. Barsottini**
Division of Neuroradiology
Med Imagem, Hospital da Beneficencia Portuguesa de Sao Paulo
Sao Paulo, Brazil
**A.J. da Rocha**
Division of Neuroradiology
Santa Casa de Sao Paulo School of Medical Sciences
Sao Paulo, Brazil
Division of Neuroradiology
Diagnosticos da America SA
Sao Paulo, Brazil

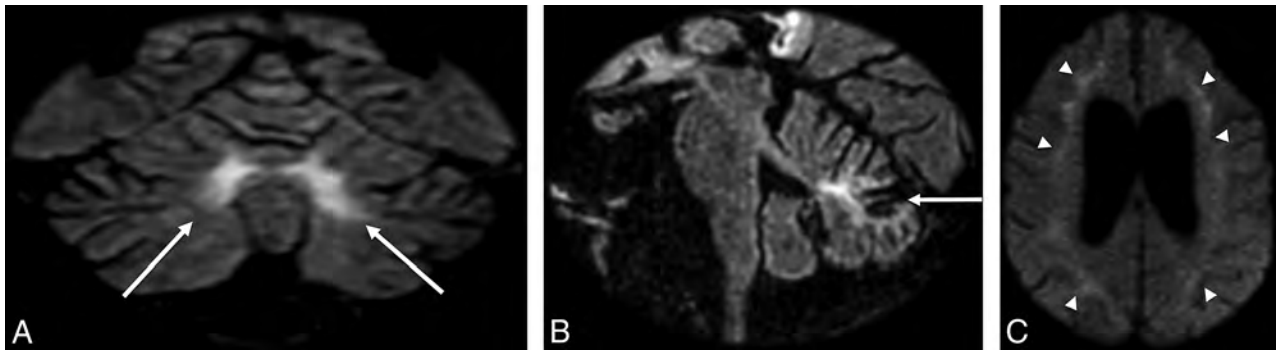


**FIG 1.** Representative case (patient 1). A 49-year-old male patient with a genetically confirmed diagnosis of FXTAS (CGG 115). Coronal (*A*) and sagittal (*B*) FLAIR images demonstrate cerebellar atrophy and a high signal intensity in the paravermal area (*arrows*). *C*, DWI shows abnormal high-intensity signal along the corticomedullary junction (*arrowheads*).

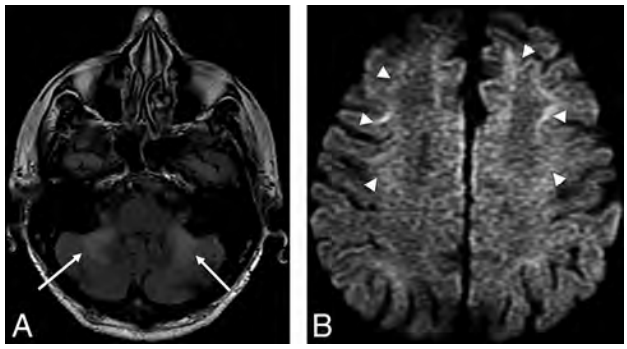


**FIG 2.** Representative case (patient 2). A 69-year-old male patient with slowly progressive ataxia, tremor, and paraparesis. Axial FLAIR image (*A*) shows bilateral abnormal high signal intensity in the middle cerebellar peduncles (*arrows*). Axial DWI ($b = 1000$ s/mm$^2$) (*B*) image depicts similar signal changes along the corticomedullary junction (*arrowheads*). Genetic investigation showed 100 CGG repetition (premutation) of the *FMR1* gene, which confirmed FXTAS.

***REPLY:***

We thank Dr Padilha and colleagues for the letter written in response to our recently published article, "MR Imaging Features of the Cerebellum in Adult-Onset Neuronal Intranuclear Inclusion Disease: 8 Cases." The authors stated that 3 patients with genetically confirmed fragile X-associated tremor/ataxia syndrome (FXTAS) presented with imaging findings similar to those in the patients described in our report. In addition, they actually show MR images of 2 cases, one presenting with both the paravermal signal changes on FLAIR images and abnormal high-intensity signal along the cortico-medullary junction on DWI and the other presenting with abnormal high-intensity signals both in the middle cerebellar peduncle on FLAIR and along the cortico-medullary junction on DWI.

Considering the cases described by the authors, we agree with their statement that the MR imaging features of adult-onset neuronal intranuclear inclusion disease (NIID) may be indistinguishable from FXTAS. Indeed, because the finding of an abnormal high intensity signal along the corticomedullary junction on DWI has been considered unique to NIID and useful for discriminating NIID from FXTAS,[1] we consider the cases described by the authors to be very important.

As the authors pointed out, *FMR1* permutation was not analyzed in our patients; thus, we cannot rule out the possibility that some patients with FXTAS were included in our subject group. Crucially, however, in 2 previous reports, the paravermal abnormal signal and abnormal signal in the middle cerebellar peduncle were observed in patients with NIID in whom a diagnosis of FXTAS was excluded by genetic testing of the *FMR1* gene.[2,3] Moreover, an abnormal high-intensity signal along the corticomedullary junction on DWI was also observed in a study in which a diagnosis of FXTAS was excluded in most subjects by genetic analysis.[4] Therefore, MR imaging features such as paravermal abnormal signals, abnormal signals in the middle cerebellar peduncle, and abnormal high-intensity signals along the corticomedullary junction on DWI are considered common findings that can be observed in both NIID and FXTAS. This point is very interesting. As the authors also noted, the histopathologic features of NIID resemble those of FXTAS and some cases of FXTAS present with dementia and peripheral neuropathy, which are common clinical manifestations of adult-onset NIID.[4] Because of their similar symptoms, pathology, and imaging findings, NIID and FXTAS are presumed to have a considerable degree of overlap in their pathophysiologies.

Finally, although the authors state that FXTAS seems to be more common than NIID, we note that this remains speculative. Since the usefulness of skin biopsy for the diagnosis of NIID was first described, the number of NIID diagnoses has increased, and reports describing cases with NIID have also increased, especially in Japan. It thus seems that adult-onset NIID is not as rare as previously thought.[5] On the other hand, the first case of FXTAS diagnosed in a living patient in Japan was reported in 2010,[6] and FXTAS continues to be considered a rare disease entity in Japan. There may be racial differences in the prevalence of these entities, with FXTAS being more common in whites and NIID more common in Japanese. In addition, patients with FXTAS may be mixed with those diagnosed with NIID by MR imaging findings and skin biopsy, and patients with NIID may be mixed with those clinically suspected of FXTAS without genetic confirmation. To clarify the accurate prevalences and racial differences of these entities, genetic analysis of the *FMR1* permutation in the diagnosis of NIID is a crucial first step, and such analysis was included in the diagnostic algorithm of NIID described by Sone et al.[4]

http://dx.doi.org/10.3174/ajnr.A5757

## REFERENCES


1. Sone J, Nakamura T, Koike H, et al. **Reply: neuronal intranuclear (hyaline) inclusion disease and fragile X-associated tremor/ataxia syndrome: a morphological and molecular dilemma.** *Brain* 2017;140:e52 CrossRef Medline
2. Sone J, Kitagawa N, Sugawara E, et al. **Neuronal intranuclear inclusion disease cases with leukoencephalopathy diagnosed via skin biopsy.** *J Neurol Neurosurg Psychiatry* 2014;85:354–56 CrossRef Medline
3. Hirose B, Hisahara S, Uesugi H, et al. **Sporadic adult-onset neuronal intranuclear inclusion disease with abnormal electroretinogram, nerve conduction studies and somatosensory evoked potential** [in Japanese]. *Rinsho Shinkeigaku* 2018;58:407–10 CrossRef Medline
4. Sone J, Mori K, Inagaki T, et al. **Clinicopathological features of adult-onset neuronal intranuclear inclusion disease.** *Brain* 2016;139:3170–86 CrossRef Medline
5. Takahashi-Fujigasaki J, Nakano Y, Uchino A, et al. **Adult-onset neuronal intranuclear hyaline inclusion disease is not rare in older adults.** *Geniatr Gernotol Int* 2016;16(Suppl 1):51–56 CrossRef Medline
6. Ishii K, Hosaka Ai, Adachi K, et al. **A Japanese case of fragile-X-associated tremor/ataxia syndrome (FXTAS).** *Intern Med* 2010;49:1205–08 CrossRef Medline


**A. Sugiyama**
Department of Radiology
National Center of Neurology and Psychiatry
Tokyo, Japan
Department of Neurology
Graduate School of Medicine, Chiba University
Chiba, Japan
**N. Sato**
Department of Radiology
National Center of Neurology and Psychiatry
Tokyo, Japan

# Blunt Cerebrovascular Injuries: Advances in Screening, Imaging, and Management Trends

We would like to commend Nagpal et al[1] for their study assessing the advances in screening, imaging, and management trends for blunt cerebrovascular injury (BCVI). However, we would like to point out a few persisting controversies regarding the management of patients with BCVI.

A major contributor to the confusion is the technique used for the diagnosis of BCVI. DSA has historically been the criterion standard. Increasingly, its use has been supplanted by CTA. However, the current role of DSA is not well-defined. Some groups recommend DSA for patients with negative CTA findings and persistent concern for BCVI, while other groups recommend DSA for patients with positive CTA findings. Paulus et al[2] justified CTA use despite showing only 68% sensitivity (and 92% specificity) for 64-channel multidetector CTA and recommended DSA for patients with CTA with negative findings with persistent neurologic symptoms. Subsequently, high false-positive rates of up to 47.9% have been reported with CTA, with the authors strongly recommending the use of DSA in all patients with positive findings on CTA with suspected BCVI to avoid unnecessary anticoagulation.[3] A possible explanation for the high false-positive rates is that the radiologists were overcalling vascular injury because of initial studies showing low sensitivity, bringing into question the need for a radiology review process. Unfortunately, most of these studies did not review the reasons for the reported low sensitivity or high false-positivity. Previous studies have also shown a learning curve with intervention, which resulted in the improved sensitivity of CTA without an increase in false-positives. Greater awareness of BCVI, the grading of injury, and imaging pitfalls would help improve noninvasive imaging diagnosis.

The justification for DSA after positive CTA findings is to avoid anticoagulation in false-positive reads. However, the same groups that showed a high false-positive rate with CTA also showed the relative safety of antithrombotic therapy, even in patients with traumatic brain injury and solid organ injury.[4]

Ultimately, it is the incidence and, hopefully, the prevention of subsequent stroke that would determine the utility of imaging. The true incidence of stroke in patients with BCVI is not well-understood. This is partly because detection of BCVI is imperfect, and most studies on BCVI report only the hospital course of these patients and not long-term outcomes. Studies that do report postdischarge outcomes have reported that up to 75% of strokes in BCVI may occur before the diagnosis is made on imaging.[5] This finding is important to recognize while discussing the role of imaging. For example, it would be interesting to know whether the patients with negative DSA findings and positive CTA findings have any strokes subsequently.

Optimized, selective CTA in high-risk populations may be the most cost-effective strategy for BCVI detection.[6,7]

## REFERENCES


1. Nagpal P, Policeni BA, Bathla G, et al. **Blunt cerebrovascular injuries: advances in screening, imaging, and management trends.** *AJNR Am J Neuroradiol* 2017 Oct 12. [Epub ahead of print] CrossRef Medline
2. Paulus EM, Fabian TC, Savage SA, et al. **Blunt cerebrovascular injury screening with 64-channel multidetector computed tomography: more slices finally cut it.** *J Trauma Acute Care Surg* 2014;76:279–83; discussion 284–85 CrossRef Medline
3. Shahan CP, Magnotti LJ, Stickley SM, et al. **A safe and effective management strategy for blunt cerebrovascular injury: avoiding unnecessary anticoagulation and eliminating stroke.** *J Trauma Acute Care Surg* 2016;80:915–22 CrossRef Medline
4. Shahan CP, Magnotti LJ, McBeth PB, et al. **Early antithrombotic therapy is safe and effective in patients with blunt cerebrovascular injury and solid organ injury or traumatic brain injury.** *J Trauma Acute Care Surg* 2016;81:173–77 CrossRef Medline
5. DiCocco JM, Fabian TC, Emmett KP, et al. **Functional outcomes following blunt cerebrovascular injury.** *J Trauma Acute Care Surg* 2013; 74:955–60 CrossRef Medline
6. Malhotra A, Wu X, Kalra VB, et al. **Screening for pediatric blunt cerebrovascular injury: review of literature and a cost-effectiveness analysis.** *J Pediatr Surg* 2015;50:1751–57 CrossRef Medline
7. Malhotra A, Wu X, Kalra VB, et al. **Evaluation for blunt cerebrovascular injury: review of the literature and a cost-effectiveness analysis.** *AJNR Am J Neuroradiol* 2016;37:330–35 CrossRef Medline



**A. Malhotra**
**X. Wu**
**K. Seifert**
Department of Radiology and Biomedical Imaging
Yale University School of Medicine
New Haven, Connecticut


http://dx.doi.org/10.3174/ajnr.A5733

***REPLY:***

We thank Drs Malhotra, Wu, and Seifert for their interest in our work and their comments regarding our recent article on blunt cerebrovascular injuries (BCVI).[1] As highlighted in our work, controversies exist regarding screening criteria, the modalities used for screening, and the treatment of these patients. The literature on the accuracy of CT angiography is diverse and is best studied by groups using both CTA and digital subtraction angiography for the diagnosis of BCVI in all patients.[2-6] The study by Eastman et al[2] showed that the overall sensitivity, specificity, positive predictive value, negative predictive value, and accuracy of 16-slice CTA for the diagnosis of BCVI were 97.7%, 100%, 100%, 99.3%, and 99.3%, respectively, with a single false-positive of a grade I vertebral injury. While most other studies have shown a modest sensitivity with good specificity, for example, Goodwin et al[3] showed a sensitivity and specificity of 41% and 97%, respectively, combined for 16- and 64-slice CT, and Paulus et al[4] showed a sensitivity and specificity of 68% and 92% for CTA on 64-slice CT.

In another study comparing CTA (16-slice) and DSA for diagnosis, Malhotra et al[6] showed that the sensitivity and specificity of CTA was 74% and 84%, but all the false-negative CTAs were obtained in the first half of the study period. In the latter part, the specificity and the negative predictive value was 100%, and the most likely explanation was the learning curve of the radiologists reading the studies. Malhotra et al and Shahan et al[7] have reported high false-positive rates of CTA with an incidence of approximately 43%[6] and 45%, respectively. The reason for this high false-positive rate is poorly understood, and we agree that it could be related to overcalling from radiologists due to reported poor sensitivity of CTA. Whether this is best addressed by the radiology review process, improved awareness of this entity among radiologists, or a multidisciplinary team consensus will be an interesting topic for further studies. A systematic review of studies comparing CTA and DSA for the diagnosis of BCVI showed that the pooled sensitivity and specificity of CTA are 66% (95% CI, 49%–79%) and 97% (95% CI, 91%–99%), respectively.[8] Hence, the authors concluded that CTA may have a low sensitivity for adequately ruling out a diagnosis but may be useful to rule in BCVI among patients with trauma with a high pretest probability of injury as highlighted by the Drs Malhotra, Wu, and Seifert in their letter.

Finally, in a study looking at the cost-effectiveness of various modalities for BCVI screening, CTA was shown to be the best test from the societal perspective with the most cost-effective screening strategy for patients at high risk for BCVI. From an institutional perspective, CTA was shown to prevent the most strokes at a reasonable cost.[9] Hence, the use of CTA for screening, though imperfect, is likely the most widely used and is suggested as preferred (or equivalent) over DSA for screening for BCVI in the existing guidelines.[10,11]

A recent multicenter study on stroke evaluation in patients with BCVI showed that most strokes occur in the first 72 hours after injury, and 22% of patients were on antithrombotic therapy when the stroke occurred.[12] Such findings highlight the need for early and accurate diagnosis of BCVI.

http://dx.doi.org/10.3174/ajnr.A5758

## REFERENCES


1. Nagpal P, Policeni BA, Bathla G, et al. **Blunt cerebrovascular injuries: advances in screening, imaging, and management trends.** *AJNR Am J Neuroradiol* 2017 Oct 12. [Epub ahead of print] CrossRef Medline
2. Eastman AL, Chason DP, Perez CL, et al. **Computed tomographic angiography for the diagnosis of blunt cervical vascular injury: is it ready for primetime?** *J Trauma* 2006;60:925–29; discussion 929 CrossRef Medline
3. Goodwin RB, Beery PR 2nd, Dorbish RJ, et al. **Computed tomographic angiography versus conventional angiography for the diagnosis of blunt cerebrovascular injury in trauma patients.** *J Trauma* 2009;67:1046–50 CrossRef Medline
4. Paulus EM, Fabian TC, Savage SA, et al. **Blunt cerebrovascular injury screening with 64-channel multidetector computed tomography: more slices finally cut it.** *J Trauma Acute Care Surg* 2014;76:279–83; discussion 284–85 CrossRef Medline
5. Utter GH, Hollingworth W, Hallam DK, et al. **Sixteen-slice CT angiography in patients with suspected blunt carotid and vertebral artery injuries.** *J Am Coll Surg* 2006;203:838–48 CrossRef Medline
6. Malhotra AK, Camacho M, Ivatury RR, et al. **Computed tomographic angiography for the diagnosis of blunt carotid/vertebral artery injury: a note of caution.** *Ann Surg* 2007;246:632–42; discussion 642–43 Medline
7. Shahan CP, Magnotti LJ, Stickley SM, et al. **A safe and effective management strategy for blunt cerebrovascular injury: avoiding unnecessary anticoagulation and eliminating stroke.** *J Trauma Acute Care Surg* 2016;80:915–22 CrossRef Medline
8. Roberts DJ, Chaubey VP, Zygun DA, et al. **Diagnostic accuracy of computed tomographic angiography for blunt cerebrovascular injury detection in trauma patients: a systematic review and meta-analysis.** *Ann Surg* 2013;257:621–32 CrossRef Medline
9. Kaye D, Brasel KJ, Neideen T, et al. **Screening for blunt cerebrovascular injuries is cost-effective.** *J Trauma* 2011;70:1051–56; discussion 1056–57 CrossRef Medline
10. Bromberg WJ, Collier BC, Diebel LN, et al. **Blunt cerebrovascular injury practice management guidelines: the Eastern Association for the Surgery of Trauma.** *J Trauma* 2010;68:471–77 CrossRef Medline
11. Biffl WL, Cothren CC, Moore EE, et al. **Western Trauma Association critical decisions in trauma: screening for and treatment of blunt cerebrovascular injuries.** *J Trauma* 2009;67:1150–53 CrossRef Medline
12. Burlew CC, Sumislawski JJ, Behnfield CD, et al. **Time to stroke: a Western Trauma Association multi-center study of blunt cerebrovascular injuries.** *J Trauma Acute Care Surg* 2018 May 25. [Epub ahead of print] CrossRef Medline



**P. Nagpal**
**B.A. Policeni**
**M. Kwofie**
**G. Bathla**
**C.P. Derdeyn**
Department of Radiology
University of Iowa Hospitals and Clinics
Iowa City, Iowa
**D. Skeete**
Trauma Services, Department of Surgery
University of Iowa Hospitals and Clinics
Iowa City, Iowa